# THE PHYSICS AND CHEMISTRY OF SOLIDS

## AN INTERNATIONAL JOURNAL

**VOLUME 7 1958**

VOL. 7 1958

*Editor-in-Chief* **HARVEY BROOKS** *Cambridge, Mass.*

*Associate Editors* **H. B. G. CASIMIR** *Eindhoven* · **G. J. DIENES** *Brookhaven* · **JACQUES FRIEDEL** *Paris*

**E. M. LIFSHITZ** *Moscow*

*Editorial Advisory Board*

*U.S.A.:* E. N. ADAMS, Pittsburgh · D. ALPERT, Illinois · L. APKER, Schenectady · J. BARDEEN, Illinois · D. S. BILLINGTON, Oak Ridge · R. G. BRECKENRIDGE, Cleveland · LEO BREWER, Berkeley, Calif. · E. BURSTEIN, Penn. J. A. BURTON, New Jersey · N. CABRERA, Virginia · C. C. DANIELSON, Iowa · I. ESTERMANN, Washington, D.C. J. C. FISHER, Schenectady · F. HERMAN, Princeton · CONYERS HERRING, New Jersey · A. R. VON HIPPEL, Cambridge, Mass. · J. H. HOLLOMON, Schenectady · W. V. HOUSTON, Houston · H. B. HUNTINGTON, Troy · H. M. JAMES, Purdue · JOHN G. KIRKWOOD, Yale · C. KITTEL, Berkeley, Calif. · W. KOHN, Pittsburgh · J. A. KRUMHANSL, Cleveland · A. W. LAWSON, Chicago · H. W. LEVERENZ, Princeton · O. T. MARZKE, Pittsburgh · B. T. MATTHIAS, New Jersey · L. R. MAXWELL, Silver Spring · JOSEPH E. MAYER, Chicago · E. W. MONTROLL, Maryland · DAVID PINES, Princeton · H. REISS, New Jersey · J. R. REITZ, Cleveland · A. ROSE, Princeton · O. C. SIMPSON, Argonne R. SMOLUCHOWSKI, Pittsburgh · F. H. SPEDDING, Iowa · D. TURNBULL, Schenectady · J. H. VAN VLECK, Harvard B. E. WARREN, Cambridge, Mass. · Eugene P. WIGNER, Princeton · B. H. ZIMM, Schenectady.

*Canada:* R. E. BURGESS, Vancouver · D. K. C. MACDONALD, Ottawa.

*United Kingdom:* A. CHARLESBY, Shrivenham, Berks · W. J. DUNNING and F. C. FRANK, Bristol · H. K. HENISCH, Reading · H. JONES, London · J. W. MITCHELL, Bristol · A. B. PIPPARD, Cambridge · M. H. L. PRYCE, Bristol R. A. SMITH, Malvern · K. W. H. STEVENS, Nottingham · F. C. TOMPKINS, London.

*France:* E. F. BERTAUT, Grenoble · A. GUINIER, PARIS · LOUIS NÉEL and LOUIS WEIL, Grenoble.

*Germany:* M. BORN, Bad Pyrmont · ULRICH DEHLINGER, Stuttgart · R. HILSCH and G. LEIBFRIED, Göttingen E. MOLLWO, Erlangen · H. PICK, Stuttgart · M. VON LAUE, Berlin · H. WELKER, Erlangen.

*Italy:* F. G. FUMI, Pavia.

*Czechoslovakia:* J. TAUC, Praha.

*Japan:* TOSHINOSUKE MUTO, Tokyo.

*The Netherlands:* A. MICHELS and G. W. RATHENAU, Amsterdam. *Sweden:* J. O. LINDE, Stockholm · PER-OLOV LÖWDIN, Uppsala.

*Switzerland:* G. BUSCH and P. SCHERRER, Zürich. *U.S.S.R.:* G. S. ZHDANOV, Moscow.

**PERGAMON PRESS** **NEW YORK · LONDON · PARIS · LOS ANGELES**

# NOTES FOR CONTRIBUTORS

## I. GENERAL

1. Submission of a paper to the *Journal of the Physics and Chemistry of Solids* will be taken to imply that it represents original research not previously published (except in the form of an abstract or preliminary report), that it is not being considered for publication elsewhere, and that if accepted, it will not be published elsewhere in the same form, in any language, without the consent of the editor-in-chief. It should deal with original research work in the field of the physics and chemistry of solids.

2. Papers should be submitted to the appropriate regional editor (all English-language papers to be sent to the U.S. editor).

3. Papers will be published as quickly as possible after acceptance, and, subject to space being available, should appear in the following issue, if this is due for publication not earlier than three months after the acceptance date. Short communications under the heading of "Letters to the Editors" will receive priority for publication, and will be published in the issue following receipt, if accepted not later than the beginning of the month preceding publication.

4. Fifty free reprints of each paper are supplied. Additional copies can be obtained at a reasonable cost if ordered when proofs are returned. A reprint order form will accompany first proofs.

## II. SCRIPT REQUIREMENTS

1. Papers submitted should be concise and written in a readily understandable style. Scripts should be typed and double spaced and submitted in duplicate to facilitate refereeing.

It will be appreciated if authors clearly indicate any special characters used. An abstract, not exceeding 200 words, should be provided in the language of the paper. French and German papers should be submitted with English abstract and titles, but if this is not possible the abstract will be translated by the publishers. To conserve space, authors are requested to mark less important parts of the paper, such as details of experimental technique, methods, mathematical derivations, etc. for printing in small type. The technical description of methods should be given in detail only when such methods are new. Authors will receive proofs for correction when their papers are first set; page proofs will be sent only when the amount of alteration makes it advisable.

2. Illustrations should not be included in the typescript of the paper, and legends should be typed on a separate sheet. Line drawings which require redrawing should include all relevant details and clear instructions for the draughtsman. If figures are already well drawn it may be possible to reproduce them direct from the originals, or from good photo-prints if these can be provided. It is not possible to reproduce from prints with weak lines. Illustrations for reproduction should normally be about twice the final size required. Photographs should only be included where they are essential.

Tables and figures should be so constructed as to be intelligible without reference to the text. Every table and column should be provided with an explanatory heading. Units of measure must always be clearly indicated. The same data should not be published in both tables and figures. The following standard symbols should be used on line drawings since they are easily available to the printers: ○, ●, +, ×, □, ■, △, ▲, ◇, ◆, ▽, ▼.

4. References are indicated in the text by superior numbers in parentheses, and the full reference should be given in a list at the end of the paper in the following form:

1. HILL R., *J. Iron St. Inst.* **158,** 177 (1948).
2. PEARSON C., *The Extrusion of Metals.* Chapman and Hall, London (1944).

Abbreviations of journal titles should follow those given for *Physics Abstracts.* It is particularly requested that authors' initials, and appropriate volume and page numbers, should be given in every case.

Footnotes, as distinct from literature references should be indicated by the following symbols—*, †, ‡, ‡‡, commencing anew on each page; they should *not* be included in the numbered reference system.

5. Due to the international character of the journal no rigid rules concerning notation and spelling will be observed, but each paper should be consistent within itself as to symbols and units.

VOL
7
195

VOL.
7
1958

VOL
7
195

# CONTENTS

## NUMBER 1


W. D. JOHNSTON, R. R. HEIKES and D. SESTRICH: The preparation, crystallography and magnetic properties of the $Li_xCo_{(1-x)}O$ system . . . . . 1

R. T. BATE and C. V. HEER: Some optical and magnetic properties of irradiated LiF . . . 14

PIERRE BRISSONNEAU: Contribution a l'etude quantitative du trainage magnetique de diffusion du carbone dans le fer $\alpha$ . . . . . 22

JAMES C. PHILLIPS: Exchange terms in the effective mass formalism. . . . . 52

ULRICH GONSER and BOUDEWYN OKKERSE: The question of radiation-induced phase changes . 55

G. A. ALERS and J. R. NEIGHBOURS: The elastic constants of zinc between 4·2° and 670°K . . 58

E. MOOSER and W. B. PEARSON: The crystal structure and properties of the Group VB to VIIB elements and of compounds formed between them . . . . . 65

R. F. WALLIS and H. J. BOWLDEN: Theory of impurity photo-ionization spectrum of semiconductors in magnetic fields . . . . . 78

C. R. VASSEL: L'effet des elements de la première longue période sur la résistivité du cuivre et de l'aluminium . . . . . 90

Letters to the Editors:

NILS BÄCKLUND: Electrical resistance of some noble-metal alloys at liquid-helium temperatures. 94

T. J. ROWLAND: $Pt^{195}$ nuclear magnetic resonance in metallic platinum . . . . . 95

B. T. MATTHIAS and W. H. ZACHARIASEN: Superconductivity of rhenium nitride . . . . 98

Contents list of Volume 5, Numbers 1–4 . . . . . 99


## NUMBERS 2/3


M. YA. AZBEL': The quantum theory of the high frequency surface impedance of a metal . . 105

KURT WEISER: Theoretical calculation of distribution coefficients of impurities in germanium and silicon, heats of solid solution . . . . . 118

MANUEL CARDONA and WILLIAM PAUL: A quadratic photoelectromagnetic effect in germanium . 127

KATHERINE WOLFSTIRN and C. S. FULLER: Comparison of radio-copper and hole concentrations in germanium . . . . . 141

N. T. MELAMED: Energy transfer in ZnS : Cu : Cl phosphors. . . . . 146

G. MEIJER: Infrared fluorescence of copper-activated zinc sulphide phosphors . . . . . 153

W. MARSHALL: The antiferromagneticism of $CuCl_2 \cdot 2H_2O$ . . . . . 159

MAURICE GOLDMAN: Résonance nucléaire des protons dans l'acide trichloracétique . . . . 165

CLIFFORD C. KLICK and W. DALE COMPTON: Polarized luminescent emission from KCl : Tl at low temperatures . . . . . 170

H. A. KLASENS: The intensity-dependence of photoconduction and luminescence of photoconductors in the stationary state . . . . . 175

A. M. CLOGSTON: Structure of the metastable state of $Mn^{++}$ and $Fe^{+++}$ . . . . . 201

T. E. SLYKHOUSE and H. G. DRICKAMER: The effect of pressure on the absorption edge in silver halides . . . . . 207

T. E. SLYKHOUSE and H. G. DRICKAMER: The effect of pressure on the optical absorption edge of germanium and silicon . . . . . 210

D. F. C. MORRIS: The instability of some dihalides of copper and silver . . . . . 214

J. F. LAURENT et J. BÉNARD: Autodiffusion des ions dans les halogenures alcaline polycristallins . 218

T. C. HARMAN, M. J. LOGAN and H. L. GOERING: Preparation and electrical properties of mercury telluride . . . . . 228

HENRY J. HROSTOWSKI and R. H. KAISER: Absorption spectrum of arsenic doped silicon . . 236

J. H. WERNICK, S. GELLER and K. E. BENSON: Constitution of the $AgSbSe_2$–$AgSbTe_2$–$AgBiSe_2$–$AgBiTe_2$ system . . . . . 240

R. J. WEISS and K. J. TAUER: Thermodynamics of the Au–Pt system . . . . . 249

J. KORRINGA: Dispersion theory for electrons in a random lattice with applications to the electronic structure of alloys . . . . . 252

B. S. Chandrasekhar and J. K. Hulm: The electrical resistivity and superconductivity of some uranium alloys and compounds . . . . . 259

John Rayne: Heat capacity of dilute magnesium–aluminum alloys below 4·2°K . . . . 268

Letters to the Editors:

T. E. Slykhouse and H. G. Drickamer: The effect of pressure on the absorption edge of sulfur. 275

L. E. Orgel: Lattice distortions due to *d–s* mixing . . . . . 276

F. A. Kröger: On the relation between non-stoichiometry and the formation of donor and acceptor centres in compounds . . . . . 277

Book Review:

"The Calculation of Atomic Structures", by D. R. Hartree (reviewed by Per-Olov Löwdin) . 279

Papers to be published in future issues . . . . . 280

## NUMBER 4

Eiji Hirahara and Miyuki Murakami: Magnetic and electrical anisotropies of iron sulfide single crystals . . . . . 281

G. J. Dienes: The temperature-dependence of the elastic moduli of vitreous silica . . . . 290

O. G. Folberth: Zur Frage des Dampfdrucks der Verbindungen InAs, GaAs, InP und GaP . 295

Alvin J. Cohen and Herbert L. Smith: Ultraviolet and infrared absorption of fused germania . 301

M. S. Wechsler and R. H. Kernohan: Neutron-irradiation effects on copper–aluminum alloys . 307

George Weiss and Alexei Maradudin: Thermodynamic properties of a disordered lattice . . 327

P-G De Gennes: Sur la relaxation nucleaire dans les cristaux ioniques . . . . . 345

D. G. Wickham and W. J. Croft: Crystallographic and magnetic properties of several spinels containing trivalent JA-1044 manganese . . . . . 351

Letter to the Editors:

Alvin J. Cohen and Edwin S. Hodge: Zonal specificity and nonspecificity of certain impurities during growth of synthetic α-quartz . . . . . 361

Contents list of Volume 6, Numbers 1–4 . . . . . 363

## AUTHOR INDEX TO VOLUME 7

(B) denotes book review

Alers, G. A. 58
Azbel', M. Ya. 105
Bate, R. T. 14
Bénard, J. 218
Benson, K. E. 240
Bowlden, H. J. 78
Brissonneau, Pierre 22
Cardona, Manuel 127
Chandrasekhar, B. S. 259
Clogston, A. M. 201
Cohen, Alvin J. 301, 361
Compton, W. Dale 170
Croft, W. J. 351
De Gennes, P-G. 345
Dienes, G. J. 290
Drickamer, H. G. 207, 210, 275
Folberth, O. G. 295
Fuller, C. S. 141
Geller, S. 240
Goering, H. L. 228
Goldman, Maurice 165
Gonser, Ulrich 55
Harman, T. C. 228
Hartree, D. R. 279 (B)
Heer, C. V. 14
Heikes, R. R. 1
Hirahara, Eiji 281
Hodge, Edwin S. 361
Hrostowski, Henry J. 236
Hulm, J. K. 259
Johnston, W. D. 1
Kaiser, R. H. 236
Kernohan, R. H. 307
Klasens, H. A. 175
Klick, Clifford C. 170
Korringa, J. 252
Kröger, F. A. 277
Laurent, J. F. 218
Logan, M. J. 228
Maradudin, Alexei 327
Marshall, W. 159
Matthias, B. T. 98, 327
Meijer, G. 153
Melamed, N. T. 146
Mooser, E. 65
Morris, D. F. C. 214
Murakami, Miyuki 281
Neighbours, J. R. 58
Okkerse, Boudewyn 55
Orgel, L. E. 276
Paul, William 127
Pearson, W. B. 65
Phillips, James C. 52
Rayne, John 268
Rowland, T. J. 95
Sestrich, D. 1
Slykhouse, T. E. 207, 210, 275
Smith, Herbert L. 301
Tauer, K. J. 249
Vassel, C. R. 90
Wallis, R. F. 78
Wechsler, M. S. 307
Weiser, Kurt 118
Weiss, George 327
Weiss, R. J. 249
Wernick, J. H. 240
Wickham, D. G. 351
Wolfstirn, Katherine 141
Zachariasen, W. H. 98, 276

VOL.
7
1958

VOL
7
195

*J. Phys. Chem. Solids* Pergamon Press 1958. Vol. 7. pp. 1–13.

# THE PREPARATION, CRYSTALLOGRAPHY, AND MAGNETIC PROPERTIES OF THE $Li_xCo_{(1-x)}O$ SYSTEM

**W. D. JOHNSTON, R. R. HEIKES and D. SESTRICH**

Westinghouse Research Laboratories, Pittsburgh 35, Pennsylvania

(*Received* 27 *January* 1958; *revised* 3 *March* 1958)

**Abstract**—The $Li_xCo_{(1-x)}O$ system has been prepared by the solid-state reaction between $Li_2O_2$ and CoO at 900°C. The material is a single-phase structure in the composition range $0 < x < 0{\cdot}2$, the lattice parameter of the cubic unit cell decreasing with increasing lithium content. At the composition $x = 0{\cdot}5$ (i.e. $LiCoO_2$) a rhombohedral structure is formed. A phase diagram for this system has been developed.

The crystal structure of material in the composition range $0 < x < 0{\cdot}2$ has been studied both above and below the antiferromagnetic Curie temperature. Both the antiferromagnetic Curie temperature and the related cubic–tetragonal transformation are found to occur at decreasing temperatures with increasing lithium content. In addition the magnitude of the crystallographic deformation decreases and finally vanishes with increasing lithium content.

The magnetic-susceptibility data indicate that the magnetic moment of $Co^{+2}$ is best understood if the multiplet splitting is small compared to $kT$. Further, the moment of $Co^{+3}$ is shown to be lowered by crystalline field effects. No effects attributable to the double exchange coupling were found. The absence of such a coupling is understood by consideration of the mechanism of electron transfer in the lithium-substituted compounds.

## 1. INTRODUCTION

In a recent paper[1] the preparation, structural evaluation, and magnetic properties of the $Li_xMn_{(1-x)}O$ system have been reported. The present paper describes some of the subsequent studies made on the analogous system $Li_xCo_{(1-x)}O$. This system has been prepared through the use of the method originally devised for $Li_xMn_{(1-x)}O$. The products have been studied both crystallographically and magnetically. The electrical properties of this system as well as those of the $Li_xMn_{(1-x)}O$, $Li_xNi_{(1-x)}O$ and $Li_xCu_{(1-x)}O$ systems have been previously reported.[2]

One of the reasons for initiating work on the lithium-substituted transition-metal oxides was the desire to gain a further understanding of the double-exchange interaction. This is an indirect interaction which is expected to occur between like ions in different valence states in crystallographically equivalent sites. Such an interaction was first proposed by ZENER[3] in order to understand the occurrence of ferromagnetism and metallic-type electrical conductivity in some substituted perovskites, e.g. $La_xSr_{(1-x)}MnO_3$. It was expected that the introduction of lithium into the divalent transition-metal oxides might induce ferromagnetism due to the formation of mixed valence states on equivalent sites. As has been reported previously,[1] no evidence for ferromagnetism was found in the $Li_xMn_{(1-x)}O$ system. To obtain further information as to the possibility of ferromagnetism in this type of system, the magnetic properties of $Li_xCo_{(1-x)}O$ were examined in detail.

The parent compound of this system, CoO, is antiferromagnetic. Many antiferromagnetic substances are known to have symmetry changes at the Curie point.[4,5] An interpretation of these symmetry changes was first given by GREENWALD and SMART[6] in terms of an "exchange-type magnetostriction". For example, neutron-diffraction experiments on NiO indicate that (111) planes are ferromagnetic, while the direction of magnetization alternates in going along the [111] direction. SMART postulated that the exchange interaction between neighboring (111) planes caused the observed rhombohedral distortion.

However, in the case of CoO, to which SHULL[7] assigned the same spin structure as NiO, a tetragonal distortion is found experimentally. LI[8] attempted to resolve this situation by a reinterpretation of SHULL's results. However, recent work[9–11] indicates that the axis of easy magnetization in these oxides is [111] instead of [100] as needed in LI's theory and as proposed originally by SHULL.[7] Apparently the issue is not yet settled, as ROTH[12] has shown that multispin-axis arrangements are to be preferred from single-crystal data.

The effect of foreign-ion substitution on the distortion in NiO was noted by SHIMOMURA.[13] He found that copper lessened the distortion while aluminum increased it. Further, he found that at high copper concentrations the material remained cubic even below the antiferromagnetic Curie temperature, $T_c$. BROWNLEE and MITCHELL[14] reported the qualitative observation that the rhombohedral deformation is less in $Li_xNi_{(1-x)}O$ than in pure NiO.

In the present work a detailed crystallographic study has been made of the structural changes which occur in the $Li_xCo_{(1-x)}O$ system below the antiferromagnetic Curie temperature. These results are discussed in connection with the magnetic data.

## 2. EXPERIMENTAL

### (a) *Preparation*

Cobalt oxide was prepared by dissolving Fisher nickel-free cobalt in concentrated nitric acid, filtering the solution, and then evaporating to dryness. The material, after heating in air to drive off all nitrous fumes, yielded a black oxide. This oxide was placed in a platinum crucible and was heated in air for 3 hr at 400° and 14 hr at 900°. It was finally heated for 14 hr at 1100°C in a pumped vacuum. The product was reddish-brown in color.

This material was analyzed spectroscopically for alkali-metal impurities. The results (in p.p.m.) are Na 1–10, Li $< 10$, K $< 50$, Rb $< 100$, and Cs $< 500$.

The preparation of $Li_2O_2$ has been previously described.[1] The preparation of samples in the $Li_xCo_{(1-x)}O$ system as well as for certain samples in the $Li_xNi_{(1-x)}O$ and $Li_xCu_{(1-x)}O$ system was performed as previously described for the $Li_xMn_{(1-x)}O$ system.[1] The divalent transition-metal oxide and $Li_2O_2$ were mixed and pressed into pellets under an argon atmosphere. The pellets were then fired for 24 hr in a sealed container of small volume, and finally quenched. By this method it was possible to prepare pure single-phase samples in the composition ranges CoO–$Li_{0.2}Co_{0.8}O$, NiO–$Li_{0.15}Ni_{0.85}O$, and CuO–$Li_{0.02}Cu_{0.98}O$. The products containing 1 atomic per cent lithium or more were black in color. The mechanical strength of the pellets has been observed to decrease in the order Mn $>$ Co $>$ Ni $>$ $>$ Cu. In the case of the $Li_xCo_{(1-x)}O$ system the upper limit of lithium concentration is due to the existence of a phase boundary in the system. On the other hand samples in the $Li_xNi_{(1-x)}O$ and $Li_xCu_{(1-x)}O$ systems containing more than the maximum amount of lithium indicated above attacked their platinum containers during the sintering reaction and resulted in samples of doubtful purity. It should be emphasized, however, that the maximum lithium concentrations in these two cases do not correspond to phase boundaries. Samples containing less than the limiting lithium contents for the various systems appear to be relatively free from platinum contamination. Spectroscopic analysis of these materials indicate less than 100 p.p.m. of platinum.

Analytical data for samples in the $Li_xCo_{(1-x)}O$ system are given in Table 1. In these materials it was impossible to correct the sample composition for loss by volatilization of $Li_2O$ in the same manner as was done in the case of $Li_xMn_{(1-x)}O$,[1] since there is considerable fragmentation of these pellets during preparation. This made any correction on the basis of weight loss of very doubtful accuracy. It will be noted from the analytical data that there is little need for such a correction.

Lithium was determined either gravimetrically as the sulfate or through the use of a flame photometer. Oxidizing power was measured by dissolving the sample in ferrous ammonium sulfate under argon and then titrating with ceric sulfate or potassium dichromate. The result is recorded as trivalent metal. Cobalt metal was determined by electro-deposition.

$LiCoO_2$, which occurs when $x = 0{\cdot}5$ in the general formula $Li_xCo_{(1-x)}O$, was prepared by both the present method as well as by a previously reported method[15] in which $Li_2CO_3$ is reacted with $CoCO_3$ in air at 900–1000°C. The two methods

VOL 7 195

*Table* 1. *Analytical data*

| Composition | Wt.-% Lithium | | Wt.-% $Co^{+3}$ | | Wt.-% Co Total | | At.-% $Li^{+1}$ / At.-% $Co^{+3}$ |
|---|---|---|---|---|---|---|---|
| | Calculated | Found | Calculated | Found | Calculated | Found | |
| CoO | | | 0·00 | 0·16 | 78·6 | 78·4 | |
| $Li_{0·01}Co_{0·99}O$ | 0·093 | 0·098 | 0·79 | 0·72 | 78·4 | 78·4 | 1·04 |
| $Li_{0·05}Co_{0·95}O$ | 0·48 | 0·42 | 4·1 | 3·6 | 77·4 | 78·4 | 1·00 |
| $Li_{0·08}Co_{0·92}O$ | 0·78 | 0·70 | 6·7 | 5·9 | 76·6 | 77·8 | 1·00 |
| $Li_{0·10}Co_{0·90}O$ | 1·00 | 0·90 | 8·4 | 7·6 | 76·1 | 77·1 | 1·01 |
| | | 0·93 | | 7·8 | | 77·3 | 1·02 |
| $Li_{0·15}Co_{0·85}O$ | 1·55 | 1·46 | 13·2 | 12·6 | 74·6 | 77·1 | 0·98 |
| $Li_{0·20}Co_{0·80}O$ | 2·15 | 2·26 | 18·3 | 18·9 | 73·1 | 75·2 | 1·02 |
| $Li_{0·25}Co_{0·75}O$ | 2·80 | 2·89 | 23·8 | 23·9 | 71·4 | 74·0 | 1·03 |
| $Li_{0·30}Co_{0·70}O$ | 3·50 | 3·45 | 29·8 | 28·9 | 69·5 | 70·8 | 1·01 |
| $Li_{0·35}Co_{0·65}O$ | 4·28 | 4·24 | 36·4 | 35·5 | 67·5 | 66·3 | 1·01 |
| $Li_{0·50}Co_{0·50}O$ | 7·09 | 7·37 | 60·2 | 59·3 | 60·2 | 61·3 | 1·05 |

yield the same product according to their X-ray patterns.

(b) *X-ray studies*

Much of the X-ray examination was carried out as previously described.[1] The samples were all ground and X-rayed as a mineral-oil mull in order to prevent reaction with the air. Cobalt radiation, $\lambda K\alpha_1$ and $\lambda K\alpha_2$ having wavelengths 1·78892 and 1·79278 Å, respectively, was used. In the single-phase regions, all X-ray patterns were sharp, indicating that the samples were homogeneous.

The structure of $LiCoO_2$ was indexed from the powder pattern obtained with an 11·54-cm-diameter Debye camera. The density was determined pycnometrically, using toluene. Integrated intensities were obtained with a North American Philips proportional counter unit. These data are given in Table 2. In several cases intensity data are recorded for lines which were too faint to be measured on the Debye film. The highest-angle line measured on the Debye film could not be scanned with the proportional counter and thus no intensity data are recorded.

Low-temperature X-ray measurements were made using the bottom of a 19-cm Unicam high-temperature camera. A rotating-anode X-ray tube, designed and built by Dr. A. TAYLOR of this laboratory, was employed and permitted exposures to be taken in $\frac{1}{2}$–1 hr, which considerably simplified the temperature-control problem. The sample was cooled by a stream of cold nitrogen gas impinging on it from above. The cold nitrogen gas was produced by energizing an electric heater submerged in a Dewar of liquid nitrogen. This gas was conducted to the sample through thermally insulated tubing. The rate of the gas stream, which determined the sample temperature, was controlled by manually varying the power input to the electric heater. Temperature was measured by a thermocouple placed within $\frac{1}{8}$ in. of the sample. Calibration showed that this thermocouple gave a true reading of sample temperature. A tube, concentric with the nitrogen gas jet, supplied a stream of dry air to the area to prevent frost formation. The concentric tubes both ended with 1-in. long Cellophane tubes which surrounded the sample and through which X-rays could readily pass. With this rather simple apparatus, temperatures could be held constant to within several degrees in the temperature range studied, −130 to +25°C.

The accuracy of these measurements is approximately ±2 parts in 10,000 and is somewhat less than would be expected for a 19-cm camera for the following reasons. First, the line splitting which was studied in this work was rather slight and often somewhat diffuse, making measurement difficult. In some cases only one split line (420) was measurable. Secondly, in the experimental set-up used, sample eccentricity was sometimes a problem. In a few cases where this effect was noted, it was minimized by using $\cos^2\theta$ as an extrapolation function

*Table 2. X-ray diffraction data for* $LiCoO_2$

Space group $R\bar{3}m - D_{3d}^5$
Hexagonal axes $a = 2{\cdot}8166$ Å
$c = 14{\cdot}052$ Å
Density calculated 5·16 g/cc.
Density found 5·05 g/cc.
Atomic co-ordinates
$(000; \frac{1}{3}\frac{2}{3}\frac{2}{3}; \frac{2}{3}\frac{1}{3}\frac{1}{3}) +$
Co 3*a*: 000
Li 3*b*: $00,\frac{1}{2}$
O 3*c*: $00z$, $00z$
$z = 0{\cdot}26$

| *hkl* | $\sin^2\Theta$ converted to CoλKα | | *F* | | $I_{obs}$ |
|---|---|---|---|---|---|
| | Obs. | Calc. | Obs. | Calc. | |
| 003 | 0·0366 | 0·0365 | 71·8 | 63·1 | 1068 |
| 101 | 0·1388 | 0·1387 | 46·4 | 42·0 | 163 |
| 006 | 0·1453 | 0·1461 | 26·6 | 24·1 | 32 |
| 012 | 0·1511 | 0·1509 | 24·0 | 21·8 | 48 |
| 104 | 0·1998 | 0·1996 | 82·5 | 76·0 | 377 |
| 015 | 0·2361 | 0·2361 | 33·7 | 31·4 | 56 |
| 009 | — | 0·3287 | 33·1 | 31·7 | 14 |
| 107 | 0·3333 | 0·3335 | 47·5 | 45·5 | 92 |
| 018 | 0·3946 | 0·3943 | 61·8 | 60·3 | 116 |
| 110 | 0·4041 | 0·4040 | 64·1 | 62·7 | 86 |
| 113 | 0·4407 | 0·4409 | 41·2 | 40·7 | 60 |
| 10,10 | 0·5417 | 0·5404 | 26·6 | 27·1 | 20 |
| 021 | 0·5436 | 0·5427 | 30·4 | 30·9 | 19 |
| 116 | 0·5499 | 0·5500 | 24·4 | 24·9 | 23 |
| 202 | — | 0·5549 | 19·7 | 23·8 | 9 |
| 00,12 | 0·5851 | 0·5843 | 48·0 | 49·5 | 28 |
| 024 | 0·6040 | 0·6036 | 50·6 | 52·4 | 49 |
| 01,11 | 0·6264 | 0·6256 | 38·1 | 39·7 | 40 |
| 205 | 0·6398 | 0·6401 | 24·5 | 25·7 | 13 |
| 119 | 0·7332 | 0·7327 | 19·9 | 21·4 | 21 |
| 027 | 0·7382 | 0·7375 | 31·5 | 34·0 | 32 |
| 208 | $\alpha_1$0·7985<br>$\alpha_2$0·7990 | 0·7983 | 40·7 | 44·6 | 56 |
| 10,13 | 0·8205 | 0·8204 | 16·5 | 18·2 | 13 |
| 00,15 | $\alpha_1$0·9128<br>$\alpha_2$0·9127 | 0·9130 | 31·8 | 36·0 | 32 |
| 01,14 | $\alpha_1$0·9300<br>$\alpha_2$0·9296 | 0·9299 | 21·4 | 24·4 | 26 |
| 02,10 | 0·9444 | 0·9441 | 17·1 | 19·6 | 22 |
| 211 | 0·9468 | 0·9470 | 22·1 | 25·3 | 45 |
| 122 | $\alpha_1$0·9589<br>$\alpha_2$0·9587 | 0·9591 | 16·9 | 19·4 | 38 |
| 11,12 | $\alpha_1$0·9880<br>$\alpha_2$0·9878 | 0·9892 | — | — | — |

instead of the more general function of Taylor and Sinclair (ref. in KLUG and ALEXANDER.[16]

(c) *Phase diagrams*

Data from which a phase diagram for $Li_xCo_{(1-x)}O$ was derived are given in Table 3. In order to demonstrate that equilibrium was attained, samples were prepared in such a manner that equilibrium was approached from two directions. One approach to equilibrium involves reacting

*Table 3. X-ray data for phase diagram (Original composition* $= Li_{0.3}Co_{0.7}O$)

| Sample heat-treatment (°C) | Lattice parameter of cubic phase (Å) | Composition of cubic phase |
|---|---|---|
| Prep. 900°, anneal 600° | 4·244 | $Li_{0.045}Co_{0.955}O$ |
| Prep. 650° | 4·239 | $Li_{0.060}Co_{0.940}O$ |
| Prep. 650° | 4·236 | $Li_{0.065}Co_{0.935}O$ |
| Prep. 700° | 4·212 | $Li_{0.125}Co_{0.875}O$ |
| Prep. 900°, anneal 700° | 4·216 | $Li_{0.115}Co_{0.885}O$ |
| Prep. 900°, anneal 750° | 4·206 | $Li_{0.14}Co_{0.86}O$ |
| Prep. 760° | 4·206 | $Li_{0.14}Co_{0.86}O$ |
| Prep. 810° | 4·185 | $Li_{0.185}Co_{0.815}O$ |
| Prep. 900°, anneal 850° | 4·174 | $Li_{0.210}Co_{0.790}O$ |

CoO and $Li_2O_2$ for at least 20 hr at the temperature being studied. The other involves preparing the $Li_xCo_{(1-x)}O$ material at a high temperature, 900°C, and then annealing for at least 20 hr at the proper lower temperature. The agreement of the data obtained by these two methods indicates that equilibrium has been achieved. All lines in the X-ray patterns of the products in the two-phase region are accounted for on the basis of the NaCl and $CsCl_2I$ structures. The composition of the NaCl phase of $Li_xCo_{(1-x)}O$ in the two-phase mixtures was obtained by comparing the lattice parameter of this phase with a plot of lattice parameter versus composition.

The $LiCoO_2$ phase shown on the diagram is believed to have a negligible range of solid solution. The *c*-axis of its hexagonal unit cell is independent of annealing temperature in the two-phase region, while the *a*-axis changes from that of the stoichiometric material by a maximum of only 5 parts in 10,000 at very low temperatures. The change of volume of the cell is negligible when compared with the change in volume versus composition of the phase with the rock-salt structure and would suggest a change in $x$ of only 0·0025. Admittedly such an analysis is far from rigorous, but it is believed to give a qualitatively correct result.

(d) *Magnetic measurements*

The gradient method used in making the magnetic measurements has been previously described.[1] Samples were contained in small sealed Vycor bulbs to prevent reaction with the atmosphere during magnetic testing.

## 3. DISCUSSION

(a) *Preparation*

The system $Li_xCo_{(1-x)}O$, as well as $Li_xNi_{(1-x)}O$ and $Li_xCu_{(1-x)}O$, has been successfully prepared by the method originally devised for the preparation of $Li_xMn_{(1-x)}O$,[1] indicating that the following reaction between $Li_2O_2$ and a divalent transition-metal oxide is a general one for the preparation of lithium-substituted transition-metal oxides.

$$\frac{x}{2}Li_2O_2+(1-x)MO \rightarrow Li_xM_{(1-x)}O$$
$$\equiv Li_x^{+}M_x^{+3}M_{(1-2x)}^{+2}O^{=}.$$

The compositions of the products in the $Li_xCo_{(1-x)}O$ system are probably best indicated by the ratio of atomic per cent $Li^+$ to oxidizing power (which is recorded as $Co^{+3}$). As can be seen from the above formula, such a ratio should equal unity. Table 1 shows that the experimental ratios are very close to this value.

(b) *X-ray study*

The values of the X-ray lattice parameter versus composition for $Li_xCo_{(1-x)}O$ are plotted on Fig. 1 with our corresponding data for $Li_xNi_{(1-x)}O$ included for comparison. In both cases there is a decrease in cell dimensions with increased lithium content. This decrease in the $Li_xCo_{(1-x)}O$ system is due to a twofold effect. First, $Li^+$ is smaller than $Co^{+2}$, and secondly, the $Co^{+3}$ formed is smaller than either $Li^+$ or $Co^{+2}$. In the $Li_xNi_{(1-x)}O$ system the decrease in lattice parameter with lithium content is not as pronounced, since $Li^+$ and $Ni^{+2}$ are

more nearly equal in size and thus the change in the cell dimension will be primarily due to the smaller size of the $Ni^{+3}$ formed. The introduction of small amounts of lithium into the tenorite lattice of CuO causes only a very small decrease in lattice spacing.

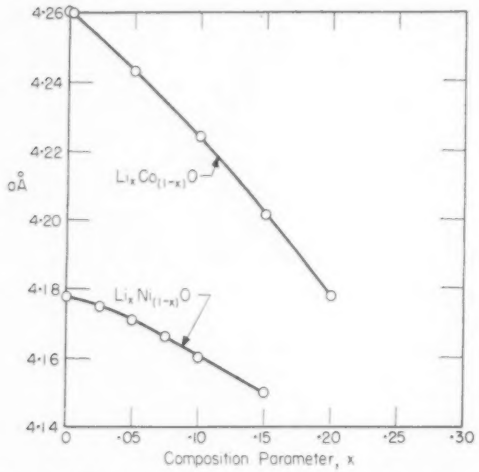


FIG. 1. X-ray lattice parameter of NaCl phase of $Li_xCo_{(1-x)}O$ and $Li_xNi_{(1-x)}O$ versus composition.

Samples of $Li_xCo_{(1-x)}O$ having values of $x$ near 0·5 gave a new X-ray pattern. These lines were indexed and the material was found to be $LiCoO_2$, having a rhombohedral $CsCl_2I$ structure. The hexagonal cell contains three formula weights. This structure has recently been reported by BONGERS.[17] Such a structure has also been reported for the similar compound $LiNiO_2$.[18] The cell dimensions given in Table 2 are referred to hexagonal axes. These values are in agreement with those of BONGERS, who gives $a = 2{\cdot}81$ and $c = 14{\cdot}0$ Å. The intensity data for $LiCoO_2$ give the best agreement with the calculated data with an oxygen parameter $z = 0{\cdot}26$. With this parameter the agreement index or residual as defined by

$$R = \frac{\Sigma \, | \, |F_0| - |F_c| \, |}{\Sigma \, |F_0|},$$

where $F_0$ and $F_c$ are the observed and calculated structure factors, is found to be 0·11. The corresponding values for $z = 0{\cdot}25$ and $z = 0{\cdot}27$ are 0·19 and 0·16, respectively. The calculated values of $F_c$ in the table have been corrected for the effect of temperature. It may be noted that in all cases the (00*l*) reflections are much stronger than the calculated values. This suggests either a preferred orientation of the sample crystallites or that the atomic scattering factors are markedly anisotropic.

Each $Co^{+3}$ or $Li^{+1}$ ion in the crystal is surrounded by a distorted octahedron of oxygen with the cobalt–oxygen distance about 8 per cent smaller than the lithium–oxygen distance. The cobalt–oxygen distance is also somewhat smaller than the nickel–oxygen distance in $LiNiO_2$, where $z$ was found to have a value of 0·25. There is little difference between the lithium–oxygen distances of the two compounds.

(c) *Phase diagram*

After the characterization of the $LiCoO_2$ phase was completed, it became possible to examine the phase diagram of the $Li_xCo_{(1-x)}O$ system in the range $0 \leqslant x \leqslant 0{\cdot}5$. It seemed possible that this system might have a phase diagram similar to that found for $Li_xMn_{(1-x)}O$. The diagram for this system (Fig. 2) shows that the phase having the

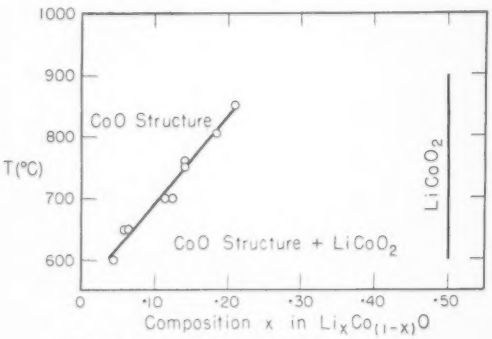


FIG. 2. Phase diagram for $Li_xCo_{(1-x)}O$.

rock-salt structure which has been studied here is actually a high-temperature phase. The transformation from the phase with NaCl structure to the lower-temperature two-phase mixture is slow enough that by quenching preparations from 900° the high-temperature phase can be retained. In none of the cases where samples were quenched from 900° and in which $x < 0{\cdot}2$ was any line of the $LiCoO_2$ phase observed in the X-ray pattern. The lines of the phase with rock-salt structure were

always sharp. Further, the samples prepared in this manner are quite stable and do not transform at moderate temperatures. This behavior is exactly what was observed in the $Li_xMn_{(1-x)}O$ system. Thus, in both cases pure samples of the high-temperature phase can be readily prepared and retained by the normal preparation procedure.

(d) *Low-temperature X-ray study*

As pointed out earlier, pure antiferromagnetic oxides such as MnO, CoO, and NiO undergo structural modifications at their antiferromagnetic Curie temperature as a result of magnetic ordering. In order to examine this effect more closely, a study was made of both the magnetic susceptibility and the structural transformation of the $Li_xCo_{(1-x)}O$ system. This system was chosen for study first because the antiferromagnetic Curie temperature is located at a convenient temperature, room temperature, and secondly because the deformation in pure CoO has been thoroughly studied.[4]

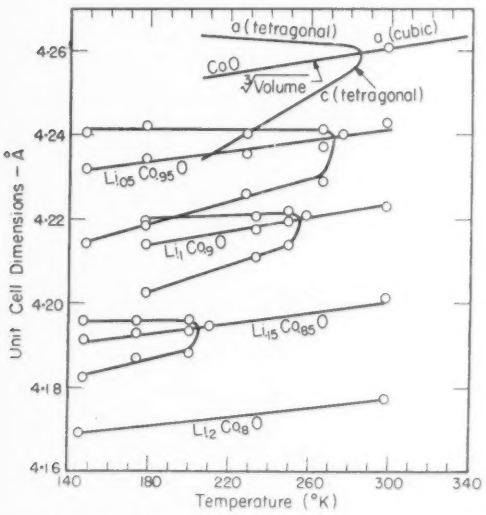


FIG. 3. Unit cell dimensions for $Li_xCo_{(1-x)}O$ versus temperature.

The low-temperature crystal-structure data for the $Li_xCo_{(1-x)}O$ system are graphically shown in Fig. 3. GREENWALD's data on pure CoO are included for comparison. In all but one case a crystallographic distortion to tetragonal symmetry occurs as the temperature is lowered, with the parameter $a$ increasing slightly and $c$ decreasing. The cube root of volume (which, of course, is equal to $a$ in the cubic case) is linear throughout. The distortion to tetragonal is always quite abrupt. One of the most significant features of these data is that the temperature at which the distortion occurs decreases with increased lithium content. With the exception of $Li_{0.2}Co_{0.8}O$, the temperature of this crystallographic distortion is in relatively good agreement with the antiferromagnetic Curie temperature obtained from susceptibility measurements, as can be seen in Fig. 4. Secondly, the

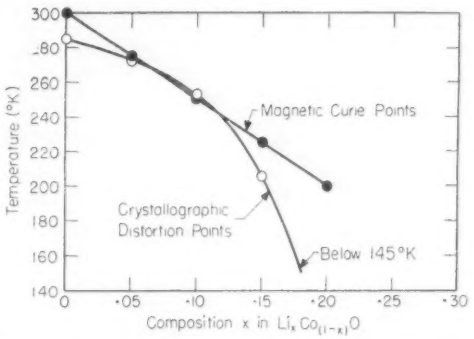


FIG. 4. Antiferromagnetic Curie points and crystallographic distortion points versus composition $x$ in $Li_xCo_{(1-x)}O$.

amount of crystallographic distortion generally decreases with increased lithium concentration. Both this decrease in the deformation temperature and the decrease in the amount of distortion are in agreement with what would be expected on the basis of a decreased magnetic coupling due to the dilution of the cobalt ions. In $Li_{0.2}Co_{0.8}O$ sufficient lithium has entered the lattice to suppress the transformation, as the data show that 55° below $T_c$ there is no structural distortion. It is impossible to say whether the structural distortion is completely eliminated in this material, whether it is too small to be observed, or whether it is moved to a much lower temperature.

The abrupt nature of the deformation at constant lithium content as the temperature is decreased has been previously noted. In addition it should be pointed out that the deformation is also abrupt as lithium content is varied at constant temperature. A three-dimensional plot summarizing these data is presented in Fig. 5. In this plot the

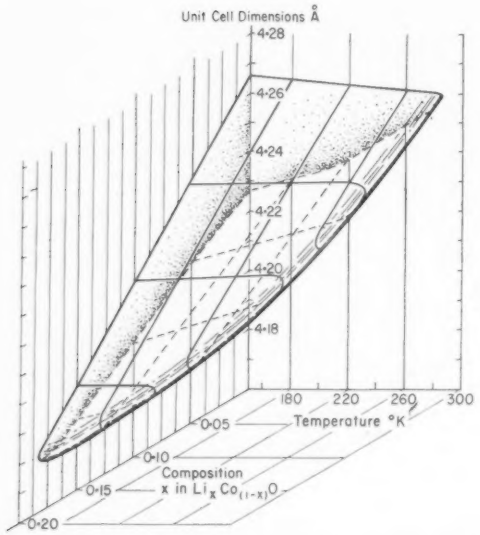


FIG. 5. Surface showing X-ray lattice parameters of $Li_xCo_{(1-x)}O$ as a function of composition and temperature.

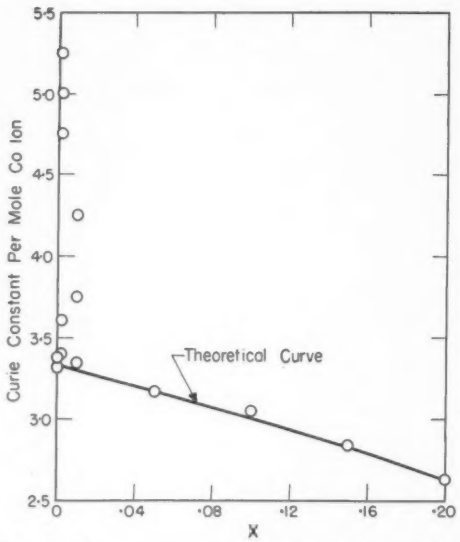


FIG. 7. Curie constant versus mole fraction of lithium.

amount of distortion in the antiferromagnetic range is given as a function of both temperature and composition. This plot emphasizes the equivalent roles of temperature and composition in defining the distortion region and also illustrates the abrupt nature of the onset of the crystallographic deformation.

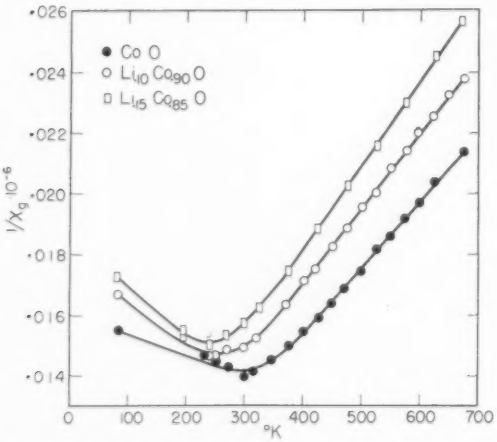


FIG. 6. Reciprocal susceptibility versus absolute temperature for $Li_xCo_{(1-x)}O$.

### (e) *Magnetism*

The experimental magnetic data will now be examined to determine the magnitude of the magnetic moments of the ions and the magnitude of the various interactions. The situation with regard to double exchange will also be discussed.

Fig. 6 shows the reciprocal susceptibility plotted against temperature for several of the compositions in the single-phase region of $Li_xCo_{(1-x)}O$. From an analysis of such susceptibility data above the antiferromagnetic Curie temperature, the values of $C$ (Curie constant/mole of Co) and $\Theta$ (paramagnetic Curie temperature) can be determined. These are

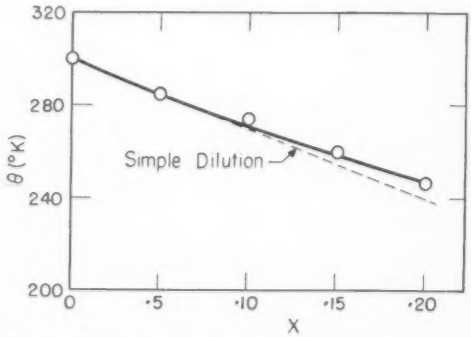


FIG. 8. Paramagnetic Curie temperature versus mole fraction of lithium.

plotted in Figs. 7 and 8. An examination of Fig. 7 shows that from $Li_{0.05}Co_{0.95}O$ to $Li_{0.20}Co_{0.80}O$ the Curie constant follows a smooth curve; however, for smaller lithium contents the data scatter considerably. Only the data from $0.05 < x < 0.20$ are to be considered as completely meaningful. The large scatter for $0 < x < 0.05$ is believed to be due to the presence of traces of cobalt metal. This point is discussed in Appendix I.

The data for $C$ will now be analyzed. In Appendix II it is shown that $C$ can be written

$$C = \frac{N\beta^2}{3k}\left[\frac{1-2x}{1-x}\cdot n_A{}^2 + \frac{x}{1-x}\cdot n_B{}^2\right],$$

where $\beta$ is the Bohr magneton, $N$ is Avogadro's number, and $n_A$ and $n_B$ are the magnitudes (in units of $\beta$) of the magnetic moments of the $Co^{+2}$ and $Co^{+3}$ ions respectively.

Using the experimental results at $x = 0.05$ and $x = 0.20$, the magnetic moments of $Co^{+2}$ and $Co^{+3}$ can be evaluated. These numbers are found to be

$$n_A{}^2 = 26.6,$$

$$n_B{}^2 = 4.4.$$

The solid curve in Fig. 7 was drawn using these values. Thus, for pure CoO we find the extrapolated value of $C$ to be 3·32. This value should be compared with $C = 3.21$ obtained by ELLIOT[19] and 3·42 obtained by SINGER.[20] It is now necessary to get an understanding of the magnitude of the magnetic moments of the two ions.

Before attempting to understand the magnitude of the magnetic moments of the specific ions in question, a brief survey of the situation might be helpful. In rare-earth salts it is generally found (samarium and europium are exceptions) that the magnetic moment is simply $g\beta\sqrt{J(J+1)}$, where $g$ is the Landé factor and $J$ is the total angular momentum quantum number (as determined for the free ion). In deriving the above-quoted value for the moment, it is assumed that all other $J$ values are so high energetically that their occurrence is negligible in the temperature range of measurement, i.e. the multiplet splitting is much greater than $kT$. On the other hand, if the multiplet splitting is much less than $kT$, the moment is found to be $\beta[4S(S+1)+L(L+1)]^{\frac{1}{2}}$.[21] This situation is not commonly discussed. Finally, in the iron-group dilute salts, it is generally found that the moment is best represented by $\beta\sqrt{4S(S+1)}$. In other words the orbital angular momentum $L$ is quenched.

As indicated above, $Co^{+2}$ has a moment of $\sqrt{26.6}\beta$. Pure CoO is cubic above room temperature. One therefore does not expect quenching of the orbital moment.[21] If the $Co^{+2}$ is assumed to be in a $^4F_{9/2}$ state (the ground state for the free ion), the above expressions for wide and narrow multiplet splitting give $\sqrt{43.5}\beta$ and $\sqrt{27}\beta$, respectively. From the excellent agreement between the latter value and the experimental one, it would appear that this is a case of narrow multiplet splitting. As evidence that this agreement is no coincidence, the data of SINGER[20] on NiO can also be cited. He finds the experimental moment of $Ni^{++}$ to be $\sqrt{21}\beta$, while the narrow multiplet moment is calculated to be $\sqrt{20}\beta$. In the calculation the free ion state ($^3F_4$) for $Ni^{+2}$ is used.

Unfortunately, the $Co^{+3}$ ion is not so simple. The narrow multiplet moment ($^5D_4$) is $\sqrt{30}\beta$, as compared to the experimental value of $\sqrt{4.4}\beta$. A possible explanation of this anomalously small moment may be found in the effect of the crystalline electric field on the $d$-electron levels. It is known[22] that the five $d$-levels of an ion in an octahedral site are split into a triplet and a doublet, the doublet being the higher energy level. The $d$-level configuration for the ion in the octahedral site of a cubic lattice is shown in Fig. 9a. If the

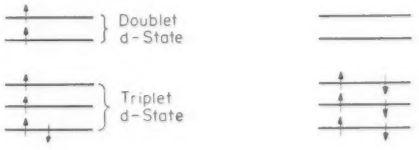


FIG. 9. $d$-Electron configuration for $Co^{+3}$.

crystalline fields cause sufficient splitting, it can become energetically advantageous for the electrons in the doublet level to drop into the triplet level and cancel the magnetic moment, as indicated in Fig. 9b. It only requires that the splitting is greater than the increase in exchange energy

accompanying the transfer. This interpretation would, of course, require zero moment for the $Co^{+3}$ instead of $\sqrt{4\cdot4}\beta$ as calculated. However, when the presence of monovalent lithium is considered, it is not surprising that this simple concept breaks down. $Co^{+3}$ ions in one set of surroundings may have a zero moment while in another set of surroundings they may have a non-zero moment due to insufficient splitting of the $d$ levels. Therefore the moment of $\sqrt{4\cdot4}\beta$ for $Co^{+3}$ should be considered as an average value over all $Co^{+3}$ ions. It is quite likely that this average moment will be a function of lithium content. However, considering the experimental error in susceptibility ($\pm1$ per cent), it does not seem fruitful to refine the model further.

It should be pointed out that such a behavior for $Co^{+3}$ is not uncommon. This ion is frequently found to be weakly paramagnetic or even diamagnetic.[23] If this model is accepted, it is necessary to indicate why it does not also occur in $Co^{+2}$. Because of the extra charge on $Co^{+3}$, the surrounding oxygen octahedron will be smaller, thereby increasing the perturbing effect on the $d$-levels due to the crystalline field.

Another significant quantity for the understanding of these materials is the paramagnetic Curie temperature $\Theta$. As $\Theta$ is essentially a measure of the Weiss internal field in the crystal, a qualitative interpretation can first be given. The replacement of a $Co^{+2}$ by $Li^{+1}$ has two effects. (1) It reduces by one the number of interactions for those Co ions neighboring to a $Li^{+1}$. (2) It replaces one $Co^{+2}$–$Co^{+2}$ interaction. Since $\Theta$ initially follows closely to a dilution law, the $Co^{+2}$–$Co^{+3}$ interaction must be approximately of the same magnitude and sign. As more lithium is introduced, $Co^{+3}$–$Co^{+3}$ interactions will arise. The number of such interactions will be proportional to the square of the $Li^{+1}$ concentration. Since $\Theta$ begins to deviate positively from the dilution law, we expect that the $Co^{+3}$–$Co^{+3}$ interaction is larger than the other interactions. Using the molecular field treatment given in Appendix II, a quantitative expression for $\Theta$ can be derived. $C_A$ and $C_B$, the Curie constants of the $A$ and $B$ ions for one formula weight of compound, are given by the following expressions:

$$C_A = \frac{N\beta^2(1-2x)}{3k}\cdot n_A^2 \quad \text{and} \quad C_B = \frac{N\beta^2 x}{3k}\cdot n_B^2.$$

Substituting these in equation (1) of the Appendix

$$\Theta = -\frac{N\beta^2 n_A^2\gamma_{AA}}{3k}\left[1-\left\{2+\frac{n_B^2}{n_A^2}\left(1-\frac{2\gamma_{AB}}{\gamma_{AA}}\right)\right\}x+\right.$$
$$\left.+\frac{n_B^4}{n_A^4}\left(1+\frac{\gamma_{BB}}{\gamma_{AA}}-\frac{2\gamma_{AB}}{\gamma_{AA}}\right)\frac{x^2}{1-2x}\right].$$

The interaction constants, $\gamma$, are defined in the Appendix. This equation is seen to have all the qualitative features mentioned above. By fitting this equation at two points, the ratios $\gamma_{BB}/\gamma_{AA}$ and $\gamma_{AB}/\gamma_{AA}$ can be determined.

$$\frac{\gamma_{BB}}{\gamma_{AA}}\simeq 10 \qquad \frac{\gamma_{AB}}{\gamma_{AA}}\simeq 4.$$

Thus, all interaction in this phenomenological model are antiferromagnetic. This is especially to be noted in the case of the $\gamma_{AB}$ where the ferromagnetic double exchange might be anticipated. This point is discussed below.

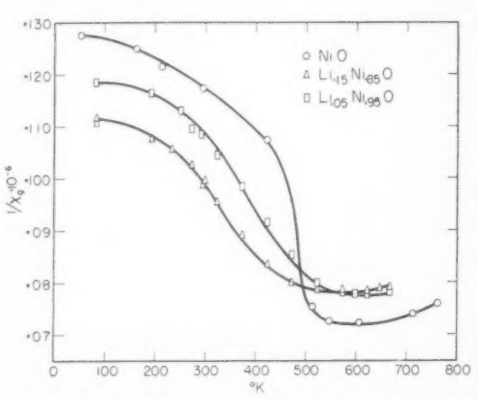


FIG. 10. Reciprocal susceptibility versus absolute temperature for $Li_xNi_{(1-x)}O$.

In Fig. 10 is plotted the $1/\chi$ versus $T$ curves for several compositions in the $Li_xNi_{1-x}O$ system. Again in the composition range studied this system does not exhibit ferromagnetism down to liquid-nitrogen temperature. Due to the work of PERAKIS *et al.*,[24] a separate study was made of $Li_{0.02}Ni_{0.98}O$.[25] The ferromagnetism reported by PARRAVANO for this composition was not confirmed. In the curves of the nickel system, the transition region from antiferromagnetism to paramagnetism becomes more gradual with increasing lithium concentration. This is similar to the results of

SHIMOMURA and TSUBOKAWA,[26] who replaced nickel by copper.

In the case of CuO, only a small amount of $Li^{+1}$ could be added. Except for the fact that $\chi$ is slightly higher, the lithium has not caused any significant change.

It remains to review the situation with regard to the double-exchange interaction. This interaction, as described by ZENER,[3] should result in a ferromagnetic coupling and metallic type conductivity. The present paper has shown that a ferromagnetic coupling does not arise. Furthermore, a previous paper[2] shows that the conductivity is semiconducting in type over the whole composition range.

The semiconductivity is interpreted as being due to a trapping of the positive holes caused by a local ionic polarization.[2] In a recent paper[27] it was shown that this trapping energy should decrease as the electronic polarizability of the ions increases. This can be understood qualitatively as follows. The introduction of a positive hole into the CoO lattice causes a certain amount of distortion. Part of the distortion occurs as a shift in the electron distribution of the ions and part as a shift in the ions themselves. It is only the ionic shift which is believed to contribute to the trapping.[28] Therefore, the introduction of an ion having a large electronic polarizability should decrease the trapping energy. It is possible that the trapping effect can disappear completely. If such a case happens, then a double-exchange type of interaction can occur; for this interaction requires that the electrons have no activation energy for motion. It is expected that the substitution of selenium or tellurium for oxygen in the present compound might be a case in point. This substitution is now being attempted.

## APPENDIX I

### *Effect of Metallic Cobalt on Magnetic Data*

The large scatter of the magnetic data for small lithium content will now be examined. First, it must be pointed out that duplicate samples of the same nominal composition show significant differences in $C$ and $\chi$. Secondly, this is not due to scatter in the magnetic measurements. Furthermore, X-rays show no observable difference between samples with widely different values of $C$. It is observed that all the scatter is on the high side of the theoretical curve. Also for a particular value of $x$ the $\chi$ is found to be higher the higher the $C$. This leads to a consideration of the presence of small quantities of free cobalt metal. The susceptibility for a sample containing a small amount of free cobalt can be written

$$\chi_g(\text{exp}) = (1-f)\chi_g + f\frac{I_{Co}}{H} \tag{1}$$

where $\chi_g$ = value of susceptibility for pure sample ($f = 0$), $\chi_g(\text{exp})$ = measured value per $g$, $f$ = weight fraction of free cobalt, and $I_{Co}$ = magnetization of Co/g.

As the $Li_{0.002}Co_{0.998}O$ samples show the widest deviation, they will be examined in detail. It will be assumed that sample No. 2 (see below), with a Curie constant almost on the theoretical curve, has $f = 0$. Then, examining sample No. 1, the difference in $\chi$ and $C$ will be attributed to free cobalt. Using (1) $f$ can be calculated from the following data:

| | $\chi_g$(exp)(at 400°K) | $C_g$(Curie constant/g) |
|---|---|---|
| No. 1 | $76\times10^{-6}$ | 0·071 |
| No. 2 | $64\times10^{-6}$ | 0·045 |

It is found that $f \sim 10^{-3}$ or 0·1 per cent free cobalt. Such amounts could not be detected by X-rays. As a check, the amount of free cobalt needed to affect $C$ can be calculated in the following way:

$$\chi = \frac{(1-f)C_g}{T+\Theta} + f\frac{I_{Co}}{H}.$$

The equation can then be put in the standard form for paramagnetic substances:

$$\chi = \frac{(1-f)C_g + f\dfrac{I_{Co}}{H}(T+\Theta)}{T+\Theta}.$$

Then

$$C_{\text{eff}} = (1-f)C_g + f\frac{I_{Co}}{H}(T+\Theta).$$

Using the data above, $f \sim 0{\cdot}2$ per cent. Therefore, free cobalt appears to be a satisfactory explanation.

## APPENDIX II

### *Molecular Field Treatment*

In order to interpret the results of the magnetic measurements, it is necessary to derive an expression for the susceptibility above $T_c$ in terms of the lithium concentration and the various interaction parameters. A molecular field treatment will be given here. As the basis for such a treatment is well known,[29] it will not be discussed here.

Consider a f.c.c. lattice containing $x Co^{+3}$ ions (designated $B$), $(1-2x)Co^{+2}$ ions (designated $A$), and $x$ Li ions randomly distributed. Previous work[2] on the electrical conductivity of these systems indicates that random distribution of $Co^{+2}$ and $Co^{+3}$ is a good assumption. Nearest-neighbor and next-nearest-neighbor interactions will be treated. The interaction between an

ion—an $A$ ion, for example—with its neighbors will be assumed to be of the form

$$-2\alpha_{Ai}\bar{J}_A\sum_i\bar{J}_i,$$

where $\bar{J}$ represents the total angular momentum quantum number and $i$ is summed over all nearest and next-nearest neighbors. (It is recognized that the double-exchange interaction can not be put in this form.[30] However, for this phenomenological treatment the $Co^{+2}$–$Co^{+3}$ will be expressed in this way.) The standard approximation is to replace $\bar{J}$ by an appropriate average. Thus

$$V_A=-2\bar{J}_A\alpha^1_{AA}Z_1(1-2x)\frac{I_A}{N(1-2x)g\beta}+$$
$$+\alpha^1_{AB}Z_1x\frac{I_B}{Nxg\beta}+\alpha^2_{AA}Z_2(1-2x)\frac{I_A}{N(1-2x)g\beta}+$$
$$+\alpha^2_{AB}Z_2x\frac{I_B}{Nxg\beta}.$$

Here $\alpha^1_{AA}$ = nearest-neighbor $A$–$A$ interaction, $\alpha^2_{AA}$ = next-nearest-neighbor $A$–$A$ interaction, $Z_1$ = no. of nearest neighbors, $Z_2$ = no. of next-nearest neighbors and $I_A$ = magnetization of the $A$ ions.

In the above equation, the average value of $J_A$ is replaced by

$$\frac{I_A}{N(1-2x)g\beta}$$

Now

$$V_A=\frac{-2}{Ng^2\beta^2}[Z_1(\alpha^1_{AA}I_A+\alpha^1_{AB}I_B)+Z_2(\alpha^2_{AA}I_A+$$
$$+\alpha^2_{AB}I_B)\bar{M}_A,$$

where $\bar{M}_A=g_i\beta\bar{J}_A$ is the magnetic moment of an $A$ ion. From this equation one finds the effective field for the $A$ ion to be

$$H^{\text{eff}}_A=\frac{2}{Ng^2\beta^2}[Z_1(\alpha^1_{AA}I_A+\alpha^1_{AB}I_B)+$$
$$+Z_2(\alpha^2_{AA}I_A+\alpha^2_{AB}I_B)].$$

The effective field for a $B$ ion is found by simply interchanging indices. We now use the Curie–Weiss law, which states that

$$I=\frac{C}{T}(H_0+H^{\text{eff}}),$$

where $C$ is the Curie constant and $H_0$ is the applied field.

Thus,

$$I_A=\frac{C_A}{T}[H_0+\gamma_{AA}I_A+\gamma_{AB}I_B]$$

$$I_B=\frac{C_B}{T}[H_0+\gamma_{BB}I_B+\gamma_{AB}I_B],$$

where

$$\gamma_{AA}=Z_1\alpha^1_{AA}+Z_2\alpha^2_{AA}.$$

Solving for $I_A$ and $I_B$

$$I_A=\frac{H_0\left[\frac{T}{C_B}-\gamma_{BB}+\gamma_{AB}\right]}{\left(\frac{T}{C_A}-\gamma_{AA}\right)\left(\frac{T}{C_B}-\gamma_{BB}\right)-\gamma_{AB}^2}$$

$$I_B=\frac{H_0\left[\frac{T}{C_A}-\gamma_{AA}+\gamma_{AB}\right]}{\left(\frac{T}{C_A}-\gamma_{AA}\right)\left(\frac{T}{C_B}-\gamma_{BB}\right)-\gamma_{AB}^2}.$$

As

$$1/\chi=\frac{H_0}{I_A+I_B},$$

it can now be determined. To a second approximation this result can be written

$$\frac{1}{\chi}=\frac{T-(\gamma_{BB}C_B+\gamma_{AA}C_A)+\dfrac{C_AC_B(\gamma_{AA}+\gamma_{BB}-2\gamma_{AB})}{C_A+C_B}}{C_A+C_B}$$

using the form

$$1/\chi=\frac{T+\Theta}{C},$$

where

$$C=C_A+C_B \text{ and } \Theta$$
$$=-(\gamma_{BB}C_B+\gamma_{AA}C_A)+\frac{C_AC_B(\gamma_{AA}+\gamma_{BB}-2\gamma_{AB})}{C_A+C_B}.$$

It is easily seen that the Curie constant per formula weight can be written

$$C_{\text{F.W.}}=\frac{N\beta^2}{3k}[(1-2x)N_A^2+xN_B^2].$$

To convert this expression to Curie constant per mole of cobalt ion, it is necessary only to divide by the factor $(1-x)$.

## REFERENCES


1. JOHNSTON W. D. and HEIKES R. R. *J. Amer. Chem. Soc.* **78,** 3255 (1956).
2. HEIKES R. R. and JOHNSTON W. D. *J. Chem. Phys.* **26,** 582 (1957).
3. ZENER C. *Phys. Rev.* **82,** 403 (1951).
4. GREENWALD S. *Acta Cryst.* **6,** 396 (1953).
5. TOMBS N. C. and ROOKSBY H. P. *Nature Lond.* **165,** 442 (1950).
6. GREENWALD S. and SMART J. S. *Nature Lond.* **166,** 523 (1950).
7. SHULL C. G. and SMART J. S. *Phys. Rev.* **76,** 1256 (1949).
8. LI Y. Y. *Phys. Rev.* **100,** 627 (1955).
9. KEFFER F. and O'SULLIVAN W. *Phys. Rev.* **108,** 637 (1957).
10. CORLISS L., ELLIOTT N. and HASTINGS J. *Phys. Rev.* **104,** 924 (1956).
11. LOEB A. L. and GOODENOUGH J. B. Conference on Magnetism and Magnetic Materials, Boston, Oct. 1956.
12. ROTH W. L. *Bull. Amer. Phys. Soc.* **2,** 119 (1957).
13. SHIMOMURA Y. *J. Japan Inst. Metals* **17,** 421 (1951).
14. BROWNLEE L. D. and MITCHELL E. W. J. *Proc. Phys. Soc.* B **65,** 710 (1952).
15. ELLESTAD R. B. and BABBITT B. R. U.S. Patent 2,545,424.
16. KLUG H. P. and ALEXANDER L. E. *X-ray Diffraction Procedures.* John Wiley and Sons, New York (1954).
17. BONGERS P. F. Thesis, Univ. of Leiden, July 4, 1957.
18. DYER L. D., BORIE B. S. Jr. and SMITH G. P. *J. Amer. Chem. Soc.* **76,** 1479 (1954).
19. ELLIOT N. *J. Chem. Phys.* **22,** 1924 (1954).
20. SINGER J. R. *Phys. Rev.* **104,** 928 (1956).
21. VAN VLECK J. H. *Electric and Magnetic Susceptibilities.* Oxford University Press (1932).
22. VAN VLECK J. H. *J. Chem. Phys.* **3,** 807 (1935).
23. COSSEE P. *Rec. Trav. Chim. Pays-Bas* **75,** 1089 (1956).
24. PERAKIS N., SERRES A., PARRAVANO G. and WUCHER J. *C.R. Acad. Sci., Paris* **242,** 1275 (1956).
25. JANUSZ T. P., HEIKES R. R. and JOHNSTON W. D. *J. Chem. Phys.* **26,** 973 (1957).
26. SHIMOMURA Y. and TSUBOKAWA I. *J. Phys. Soc. Japan* **9,** 19 (1954).
27. ZENER C. and HEIKES R. R. Conference on Magnetism and Magnetic Materials, 1956.
28. MOTT N. F. and GURNEY R. W. *Electronic Processes in Ionic Crystals* p. 87. Oxford University Press (1940).
29. SMART J. S. *Rev. Mod. Phys.* **25,** 327 (1953).
30. ANDERSON P. W. and HASEGAWA A. *Phys. Rev.* **100,** 675 (1955).

*J. Phys. Chem. Solids* Pergamon Press 1958. Vol. 7. pp. 14–21.

# SOME OPTICAL AND MAGNETIC PROPERTIES OF IRRADIATED LiF*

**R. T. BATE† and C. V. HEER**

Department of Physics and Astronomy, Ohio State University, Columbus, Ohio

(*Received* 9 *January* 1958; *revised* 18 *February* 1958)

**Abstract**—The optical oscillator strength of the *F*-band in LiF is determined as $f_L = 0{\cdot}82$ from combined optical and magnetic measurements on X-irradiated and neutron-irradiated samples. The number of *F*-centers formed in LiF as a function of neutron dosage was measured over a broad range of dosage by either optical or magnetic techniques. The formation of *F*-centers saturates in the vicinity of $8 \times 10^{19}$ centers/cm$^3$; and saturation occurs for neutron dosages considerably smaller than those required for saturation of vacancies and interstitials. Experimental evidence is presented to indicate that *F*-centers are separated by more than six lattice units in the most densely colored samples.

## 1. INTRODUCTION

THE correlation of the magnetic and optical properties of the *F*-centers formed in LiF by neutron and X-ray irradiation, and some of the magnetic properties of these centers, form the basis of this research. Their correlation for other additively colored alkali halides was treated in a previous publication,[1] henceforth referred to as I. The maximum concentration of *F*-centers in alkali halides additively colored with the alkali vapor was limited by the coloration techniques to less than $4 \times 10^{18}$/cm$^3$. In this investigation the large cross-section of $^6$Li for slow neutrons, $^6\text{Li}(n, \alpha)^3\text{H}$, with the resulting $\alpha$ and tritium particles with 4·7 MeV energy, yields a large amount of coloration for immediately accessible slow-neutron fluxes. The amount of coloration as a function of dosage is followed over a broad range of dosage by means of optical techniques for small dosages and magnetic techniques for large dosages. The optical investigation of the absorption lines formed by X-ray or neutron irradiation is less detailed than that of DELBECQ and PRINGSHEIM,[2] the primary concern being the *F*-band and *M*-band absorption.

* This research was supported by the USAF through the Office of Scientific Research of the Air Research and Development Command.

† Now at Battelle Memorial Institute, Columbus, Ohio.

## 2. THEORETICAL ASPECTS

The absorption spectrum in irradiated LiF consists of a strong main band, the *F*-band, and a somewhat weaker band to the long-wavelength side, the *M*-band; and, using the model of an electron trapped at a vacancy or a group of vacancies, the spectrum may be regarded as an electronic transition from the ground state to an excited state.[3] If one assumes, as in reference (1), that the wave function depends parametrically upon the co-ordinates of the surrounding nuclei, i.e. the Born–Oppenheimer approximation, the "Condon" approximation that the electric dipole matrix element is independent of the nuclear co-ordinates, and that the local field seen by the electron is the Lorentz local field, the product of the number of centers, $N$, and the oscillator strength, $f$, is given by

$$Nf = 8{\cdot}21 \times 10^{16}[n/(n^2+2)^2] \times \times \begin{bmatrix}\text{area under absorption}\\ \text{curve in cm}^{-1}\times\text{eV}\end{bmatrix}\text{cm}^{-3}. \qquad (1)$$

The "area under the absorption curve" $= (\pi/2)\alpha_{max}\Delta\gamma_{\frac{1}{2}}$ for a Lorentz line shape, and $(\pi/4 \ln 2)^{\frac{1}{2}}\alpha_{max}\Delta\gamma_{\frac{1}{2}}$ for a gaussian line shape, where $\alpha_{max}$ is the maximum absorption coefficient of the color center in cm$^{-1}$, and $\Delta\gamma_{\frac{1}{2}}$ the band width at half-maximum in electron volts. The index of

refraction, $n$, was taken as 1·42 for the $F$-band and 1·39 for the $M$-band.

The magnetic sublevels of the color centers give rise to a paramagnetism characteristic of an electron in an atomic $s$-state. For small interactions, one obtains a Curie-law temperature-dependence, and the number of centers is related to the magnetic susceptibility by

$$\chi = [Ng^2\beta^2/4kT][1-\tfrac{1}{3}(g\beta H/2kT)^2-\delta(T)] \quad (2)$$

where $g$ represents the $g$-value, $\beta$ the Bohr magneton, $k$ the Boltzmann constant, $H$ the external magnetic field, and $\delta(T)$ a correction due to the interaction between centers. KORRINGA and DAUNT[4] have discussed the correction due to the hyperfine interaction, but this correction is too small to be of importance in our measurements. A correction due to the overlap of the wave functions of neighboring color centers is discussed in the Appendix and is of the form $\delta(T)$. Saturation effects due to the term in $(H/T)^2$ are small for the magnetic fields and temperatures used, and may be corrected for in the calculations. The optical oscillator strength of the absorption line is determined from a comparison of the number of centers measured magnetically and the number measured optically, as was done in reference (1).

### 3. EXPERIMENTAL TECHNIQUES

The lithium fluoride crystals used for this investigation were cleaved from high-purity optical-grade crystals obtained from the Harshaw Chemical Company. X-irradiation of the crystals was carried out by means of a Picker X-ray machine at a potential of 35 kV and a current of 10 mA with a copper target. Large-dosage neutron irradiations were carried out at the Oak Ridge National Laboratories in hole 10 at a thermal neutron flux of $5\times10^{11}$ neutrons/cm$^2$/sec for the indicated periods of time. None of the crystals used were thicker than about 0·4 mm, so that there was no appreciable extinction of the neutron flux. The crystals were wrapped in aluminum foil and sealed in aluminum cans prior to irradiation, and then kept in aluminum foil until the time of use. Irradiations at small dosages were obtained by suspending the crystals in a water-filled tank at a distance of a few centimeters from several polonium–beryllium neutron sources, and by pile irradiation. Although the flux accuracy is poor, these points are included for completeness.

Optical absorption measurements of the small thin crystals were made with a Beckman Model DU spectrophotometer. Absorption curves were limited to optical densities of less than three by the instrument.

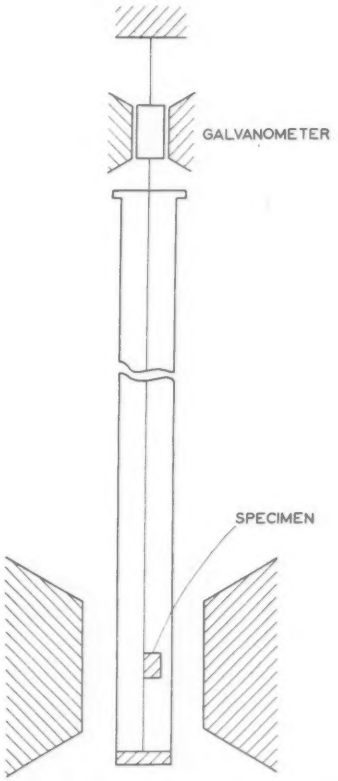


FIG. 1. Torsion balance for magnetic measurements.

The paramagnetic susceptibility of the color centers was determined by measuring the torque on the sample when placed in an inhomogeneous magnetic field. Both optical and magnetic measurements were made on the same sample. The force on a small sample[5] of volume $v$ is given by, force $=$ $\frac{1}{2}\chi v$ grad $H^2$; and the torque depends on the force and the average lever arm of the sample. A torsion balance shown in Fig. 1 is used to measure the torque on small crystals, i.e. of the order of $0{\cdot}4\times5\times$ $\times5$ mm, or smaller in most cases. The inhomogeneous field is supplied by an electromagnet with

tapered poles. A galvanometer, which is at room temperature, and has one suspension at room temperature and the other at liquid-nitrogen or liquid-helium temperatures, is used to measure the small torques. The current required to restore the galvanometer to the position before the application of the magnetic field provides a measure of the torque. A self-balancing feature is introduced by means of a split photocell and a d.c. amplifier, and the operator need only record the voltage across a standard resistor to have a measure of the torque. The balance is quite sensitive and may be used to measure the paramagnetic susceptibility of samples with more than $10^{14}$ magnetic spins.

The number of magnetic centers is determined by noting that in the high-temperature region, above 2°K for these samples, the magnetic susceptibility is given by

$$\chi = C/T + \chi_d \qquad (3)$$

where $C$ is the Curie constant; $\chi_d$ is the diamagnetic susceptibility and is equal to $\chi_d = -1{\cdot}15 \times 10^{-6}$ emu/cm$^{-3}$ for LiF.[6] An absolute determination of $C$ or the paramagnetic contribution can be made by noting the point at which the torque on the sample is zero, and then $C/T = -\chi_d$. Using equation (2), the number of magnetic centers is related to the Curie constant by,

$$N = 1{\cdot}62 \times 10^{24} C \text{ centers/cm}^3. \qquad (4)$$

## 4. EXPERIMENTAL RESULTS AND DISCUSSION

### (a) *Optical Oscillator Strengths*

Optical-absorption and magnetic-susceptibility measurements were made on two X-irradiated LiF crystals and on a number of neutron-irradiated crystals. The optical-absorption curves are shown in Fig. 2 for one of the X-irradiated samples and in Fig. 3 for the neutron-irradiated samples, and

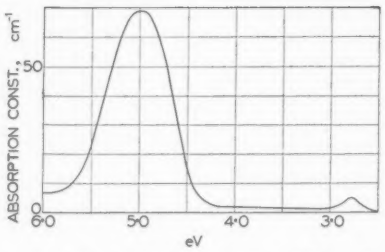


FIG. 2. Optical absorption curve for X-irradiated LiF.

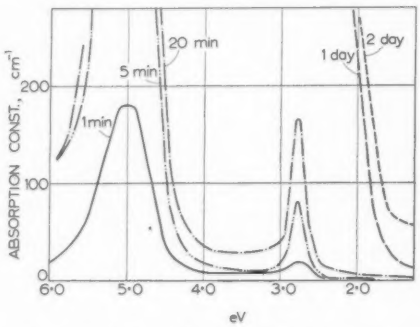


FIG. 3. Optical absorption curves for neutron-irradiated LiF.

Neutron dosage: ——— 1 min; — — — — 5 min; —— — —— 20 min; —— —— —— 1 day; – – – – – – 2 day.

*Table* 1. *Optical and magnetic data for* LiF*

| Crystal No. | coloration technique | $N_m$ (cm$^{-3}$) | *F*-center | | *M*-center | | $f_L$ | $f_g$ | $f_a$ |
|---|---|---|---|---|---|---|---|---|---|
| | | | $\alpha_{max}$ (cm$^{-1}$) | $\Delta\gamma_{\frac{1}{2}}$ (eV) | $\alpha_{max}$ (cm$^{-3}$) | $\Delta\gamma_{\frac{1}{2}}$ (cm$^{-1}$) | | | |
| 1 | X-ray | $7{\cdot}6 \times 10^{17}$ | 68·7 | 0·79 | 5 | 0·2 | 0·81 | 0·55 | 0·54 |
| 2 | X-ray | $13{\cdot}1 \times 10^{17}$ | 121 | 0·79 | 10 | 0·2 | 0·83 | 0·56 | |
| 3 | Neutrons (1 min) | $18{\cdot}4 \times 10^{17}$ | 170 | 0·79 | 17 | 0·2 | 0·82 | 0·56 | |
| 4 | Neutrons (5 min) | $48{\cdot}0 \times 10^{17}$ | 450 | 0·79 | 75 | 0·20 | 0·84 | 0·57 | |

* $N_m$ is the number of centers/cm$^3$ measured magnetically; $\alpha_{max}$ the maximum absorption coefficient of the *F*- or *M*-band; $\Delta\gamma_{\frac{1}{2}}$ the width at half-maximum absorption in electron volts; $f_L$, $f_g$, and $f_a$ are the oscillator strengths determined for a Lorentz, gaussian, and the observed line shape.

the experimental results used for the determination of the optical oscillator strengths are shown in Table 1. These absorption data for the $F$- and $M$-bands are in agreement with the more detailed study of DELBECQ and PRINGSHEIM.[2] Data for two of the neutron-irradiated samples are included, but the data for the more opaque sample, number 4, are less accurate, since the maximum absorption of the $F$-band was determined by an extrapolation of the measurements taken on the long-wavelength side of the band to the known line center at 4·95 eV. This technique avoids some of the error which is introduced by the presence of the 222 band or other bands which cause a large amount of background on the short-wavelength side. The oscillator strengths determined from the area under the curve and for a Lorentzian line shape are determined by neglecting the magnetic contribution of the $M$-band. This introduces an error of a few per cent if the oscillator strength of the $F$- and $M$-centers are comparable. If the oscillator strength for the $M$-band is as small as suggested by LORD[7] from his analysis of the second moment of the $F$- and $M$-center spin resonance, i.e. $f \simeq 0{\cdot}08$, then a considerable upward revision in the oscillator strength for the $F$-center is required.

Since the ratio of the peak absorption of the $F$- and $M$-bands in the neutron-irradiated crystal, $\alpha_M/\alpha_F = 75/450$, is a factor of two larger than in the X-irradiated crystal, $\alpha_M/\alpha_F = 10/121$, a closer examination is of interest. If one assumes that the two oscillator strengths are equal, and both types of center contribute to the temperature-dependent paramagnetism, then one obtains an oscillator strength of 0·87 for the neutron-irradiated and 0·84 for the X-irradiated crystals. A very low value of the oscillator strength for the $M$-band, such as that suggested by LORD, would require an oscillator strength of the order of 1·6 for the neutron-irradiated and 0·97 for the X-irradiated crystal. It may be noted that LORD's value would require that approximately one-half of the magnetic contribution in the neutron-irradiated samples is due to the $M$-center, or the $M$- and $F$-centers are equally prevalent.

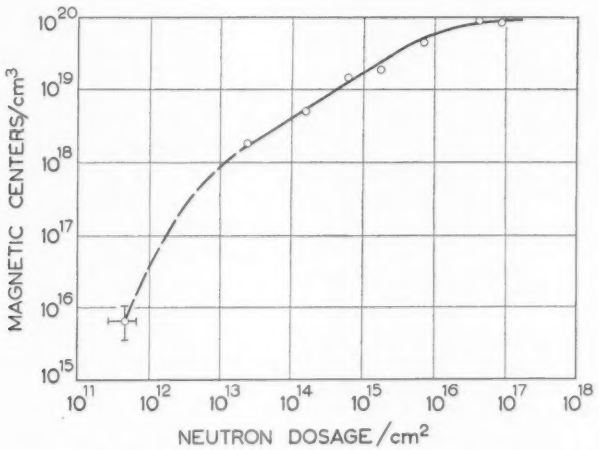


FIG. 4. Magnetic centers as a function of neutron dosage.

Since some of our samples contained a large number of $M$-centers, the microwave absorption spectra* for the samples irradiated with neutrons for periods of 20 min and of 1 day were obtained for comparison with prevision work on the hyperfine structure of the $F$-center. In both crystals a $g$-value of 2·002 and a line width at half maximum of approximately 140 G were observed. These values are in agreement with the previous work, but since the hyperfine structure was not resolved, no comparison could be made with the suggestion

* We are indebted to Mr. GEUSIC of the Dept. of Physics, Ohio State University, for making these microwave absorption measurements.

of LORD[7] that the second moment of the *F*-center alone is 1460 G.[2] In this respect it should be noted that the conclusions regarding the oscillator strength of the *M*-center from microwave measurements is very dependent on the value taken for the second moment of the *F*-center.

### (b) *Effects in Neutron-Irradiated* LiF

The number of magnetic centers formed in LiF as a function of integrated thermal neutron flux or dosage is shown in Fig. 4, and the results are tabulated in Table 2. The optical absorption curves for various dosages are shown in Fig. 3. After the rapid initial rise, the number of magnetic centers formed as a function of dosage is the order of 10,000 magnetic centers per thermal neutron absorbed over a broad range of dosage until saturation occurs in the vicinity of $8\times10^{19}$ centers/cm$^3$. The rapid initial growth of centers is attributed to coloration via Schottky defects. It is quite difficult to produce more than $4\times10^{18}$ *F*-centers/cm$^2$ in alkali-halide crystals by low-energy X-irradiation or additive coloring; although concentrations comparable to the neutron-irradiated crystals were obtained by BUCKEL and HILSCH[8] for thin films formed from evaporated layers of the alkali halide and the alkali vapor. A reasonable explanation of this behavior seems to be that a large number of vacancy interstitial pairs, or Frenkel defects, are created in the lattice by neutron bombardment. The principal source of energy for the production of Frenkel defects is the 4·7 MeV energy of the $\alpha$ particles and tritons produced in the $^6$Li $(n, \alpha)^3$H reaction. By combining X-ray diffraction and gravimetric density measurements, BINDER and STURM[9] have shown that at least 94 per cent of the lattice expansion in neutron-irradiated lithium flouride is due to the interstitial ions or atoms. The increased magnetism is interpreted as due to electrons or holes trapped at vacancies, or to interstitial atoms or ions having an odd number of electrons. Comparison with the data for X-irradiated crystals indicates that the predominant contribution to the paramagnetism is due to the *F*-center, and in our discussion the magnetic contribution of other type centers such as the *M*-centers have been regarded as small.

*Table 2. Neutron-irradiated* LiF

| Neutron irradiation time | Integrated neutron dosage (neutrons/cm$^2$) | Number of magnetic centers (centers/cm$^3$) |
|---|---|---|
| 1 min | $3\cdot0\times10^{13}$ | $1\cdot8\times10^{18}$ |
| 5 min | $1\cdot5\times10^{14}$ | $4\cdot8\times10^{18}$ |
| 20 min | $6\cdot0\times10^{14}$ | $1\cdot4\times10^{19}$ |
| 20 min | $6\cdot0\times10^{14}$ | $1\cdot2\times10^{19}$ |
| 60 min | $1\cdot8\times10^{15}$ | $2\cdot6\times10^{19}$ |
| 4 hr | $7\cdot2\times10^{15}$ | $4\cdot2\times10^{19}$ |
| 1 day | $4\cdot3\times10^{16}$ | $8\cdot7\times10^{19}$ |
| 2 days | $8\cdot6\times10^{16}$ | $8\cdot3\times10^{19}$ |

If, for intermediate dosages, one assumes that one Frenkel defect or vacancy interstitial pair is produced for each magnetic center observed, then approximately 15,000 defects are produced for each thermal neutron absorbed at a dosage of $3\times10^{13}$ neutrons, 5000 at a dosage of $6\times10^{14}$, and 500 at $4\cdot3\times10^{16}$. The number of magnetic centers formed saturates at approximately $8\times10^{19}$/cm$^3$, and at a dosage of $3\times10^{16}$ neutrons/cm$^2$. The results of MAYER *et al.*[10] and of SMALLMAN and WILLIS[11] indicate that the lattice parameter of lithium flouride as a function of neutron dosages increases linearly up to dosages ten times greater than the dosage at which the magnetism saturates. ESHELBY[12] has shown that interstitials will give rise to a uniform lattice expansion which is proportional to the concentration of interstitials. Thus one may interpret the results on lattice expansion as indicating that the production of vacancies and interstitials persists up to dosages of the order of $3\times10^{17}$ neutrons/cm$^2$, while the magnetic color-center concentration saturates at a dosage of the order of $3\times10^{16}$. The rate of lattice expansion[12] for dosages greater than $10^{16}$ is consistent with the value of 1900 Frenkel defects per neutron absorbed, as suggested by SEITZ and KOEHLER.[13] The production of magnetic centers and *F*-centers does not appear related to this value, and is much greater over most of the range of neutron dosage. The conversion of electron excitation into atomic displacements near dislocations or imperfections,[14] or the production of atomic displacements by multiple ionization[15] may be necessary to explain the larger rate of production. The early saturation of the production of magnetic defects is in accordance with the suggestion that *F*-centers are separated by more than six lattice units. In this

respect it is interesting to note that CRAWFORD and WITTELS[16] observed a similar value for the saturation of paramagnetic centers in their investigation of the optical and magnetic properties of neutron-irradiated quartz. It is not apparent to us at this time how the separation of *F*-centers may be correlated with the size of defects observed by small-angle X-ray scattering.[11,17]

### (c) *Magnetic Effects*

In view of the large spatial extent suggested by the various models for the wave functions of the *F*-center,[18] it appeared of interest to see if any effects due to the overlap of the wave functions of neighboring *F*-centers could be observed in the more densely colored crystals. If, as discussed in the Appendix, hydrogen-like wave functions are used and an interaction between neighboring *F*-centers similar to that in a hydrogen molecule is assumed, then a splitting between the triplet state of parallel spins and the singlet state of the anti-parallel spins is expected. This splitting will cause a deviation from Curie's law at temperatures comparable to the splitting. A more detailed discussion of the expected splitting and the correction to the temperature-dependent paramagnetism is given in the Appendix. In Fig. 5 the torque on one of the most densely colored crystals, neutron irradiation for 2 days, as a function of the reciprocal temperature is shown. Since the torque is a direct measure of the paramagnetic susceptibility, this may be regarded as a plot of the susceptibility as a function of reciprocal temperature. Within the experimental accuracy, the temperature-dependent paramagnetism follows that indicated by equation (2) with a value of $\delta$ less than 0·01 at 1°K. The absent or very small correction term $\delta$ may be explained by assuming that either the *F*-centers are spatially separated by more than six lattice units, or that the spatial extent of the wave functions is considerably less than suggested by the hydrogen-like wave functions.

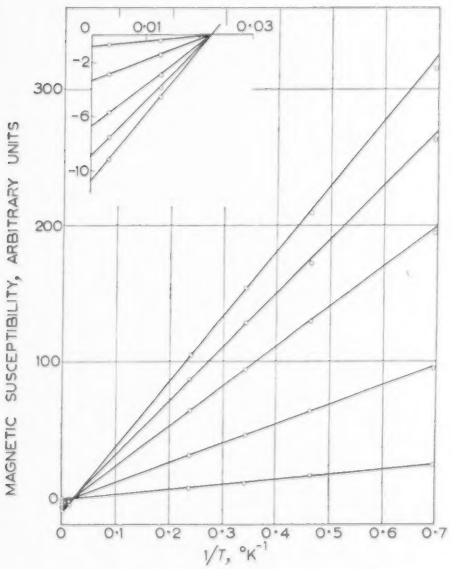


FIG. 5. Magnetic susceptibility as a function of $1/T$ for the 2-day neutron dosage.

## 5. CONCLUSIONS

It is not possible to deduce with certainty the optical oscillator strengths from this correlation of optical and magnetic data. Under the assumption that the magnetic contributions of the *M*-band and bands on the short-wavelength side of the *F*-band are negligible, the oscillator strength of the *F*-band determined for the X-irradiated LiF is the same as for the neutron-irradiated. The ratio of the peak absorption of the *F*- and *M*-bands varied between samples, and allow the conclusion that the observations are consistent with either a magnetic *M*-center with an oscillator strength comparable to the *F*-center, or with a non-magnetic *M*-center. An error of 5 per cent is introduced in the first and none in the second. The investigations of F. J. REID[19] on X-irradiated KCl yield a value of oscillator strength for the *F*-band the same as found by RAUCH and HEER[1] for additively colored KCl. He also investigated the change in paramagnetism as the *F*–*M* conversion took place under irradiation in the *F*-band at room temperature. The rapid growth of the *R*-bands and the distortion of the *F*-band caused considerable difficulty in separating the absorption of the *F*-band from the background. A change in paramagnetism by a factor of two was accompanied by a change in the peak *F*-band absorption by a similar amount. Recently SEITZ[20] has called our attention to the desireability of performing similar experiments in which the *F*–*M* conversion takes place at temperatures well below room temperature. The investigations of VAN DOORN[21] indicate that the *R*-bands may be avoided at these lower temperatures, and

it should be possible to obtain data considerably superior to that obtained by REID. Although our results are not conclusive, we interpret them to indicate that additive coloration, X-irradiation, and neutron irradiation yield similar values for the $F$-band oscillator strength in those samples in which the predominant coloration is due to the $F$-band. From this we conclude that within approximately 5 per cent the oscillator strength of the $F$-band in LiF is given by $f_L = 0{\cdot}82$.

The number of color centers in LiF saturates at a value of approximately $8 \times 10^{19}$ centers/cm$^3$. This saturation occurs at a dosage which is ten times smaller than the dosage producing saturation in vacancies and interstitials, and is consistent with the interpretation of the magnetic data. The absence of a correction to the Curie-type paramagnetism at the lowest temperatures indicates that $F$-centers are probably spaced more than six lattice units apart.

*Acknowledgements*—The authors wish to thank Mr. F. J. REID and Mr. J. GERSTNER for their assistance in this research work.

## APPENDIX

In order to estimate the effect of the overlap of the wave functions of neighboring $F$-centers on the paramagnetic susceptibility, the system of $F$-centers has been considered as similar to a dilute gas of hydrogen atoms in which the nuclear co-ordinates are "frozen" into a random configuration. The interaction as a function of nuclear separation can then be computed as a function of internuclear separation of two hydrogen atoms in analogy with the Heitler–London theory of the hydrogen molecule. Since pairs will give rise to the predominant interaction, the paramagnetic susceptibility of a pair for a particular internuclear separation and temperature can be computed, and then summed over the pairs for various separations. Following the Heitler–London theory of the hydrogen molecule,[22] the energy difference between the spatially symmetric and the anti-symmetric states is given by

$$\Delta = E_A - E_S = \int \psi_A(1)\psi_B(2)\psi_A(2)\psi_B(1) \times \times \{e^2/r_{12} - e^2/r_{B1} - e^2/r_{A2}\}\, d\tau \qquad (5)$$

where $A$ and $B$ refer to the halide vacancy sites, and 1 and 2 refer to the electrons. The above expression is evaluated using the hydrogen-like wave functions which were suggested by INUI and UEMURA[23] for their simplified model of an $F$-center, i.e.

$$\psi = 1/\sqrt{\pi}\beta^{3/2} \exp(-\beta r) \qquad (6)$$

where $\beta = 1{\cdot}36 \times 10^{-8}$ cm. If the separation between vacancies, $R$, is greater than three lattice units, the energy difference, $\Delta$, between the anti-symmetric and symmetric levels is approximately given by

$$\Delta \simeq 140 \exp(-2{\cdot}46R)\, \text{eV}, \qquad (7)$$

where $R$ is measured in lattice units, $2{\cdot}01 \times 10^{-8}$ cm for LiF.

The paramagnetic susceptibility of such an interacting pair of $F$-centers is estimated by assuming the anti-symmetric state has parallel magnetic spins, and the ground state anti-parallel spins. Then the susceptibility of a pair is

$$\chi_{\text{pair}} = (g\beta)^2/2kT[\tfrac{1}{4}\exp(\Delta/kT) + \tfrac{3}{4}]^{-1}. \qquad (8)$$

A summation over a random distribution of pairs yields for the paramagnetic susceptibility per unit volume

$$\chi = \chi_0 \int_0^{1/N} [\tfrac{1}{4}\exp(\Delta/kT) + \tfrac{3}{4}]^{-1} 4\pi R^2\, dR \qquad (9)$$

where $\chi_0 = N(g\beta)^2/4kT$ is the susceptibility in the absence of interaction, and $N$ is the number of $F$-centers per unit volume. Since $\Delta$ is such a strong function of $R$, the susceptibility is approximately given by

$$\chi = \chi_0[1 - NV^*] \qquad (10)$$

where $V^*$ is the volume in which the interaction energy between a pair exceeds the thermal energy, i.e. $\Delta > kT$. If the centers are randomly distributed, then $NV^* = \delta(T)$, the correction terms referred to in equation (2). If, by virtue of some non-random process, centers do not occur closer than a specified distance, then the definition of $\delta$ must be suitably modified. Thus if no centers occur inside $V^*$, the term $\delta$ is zero. An examination of the curve shown in Fig. 5 indicates that no temperature-dependent correction from that for normal paramagnetics is required. Since $V^*$ is highly dependent on the temperature, this suggests that no appreciable number of centers are closer than six lattice units in the sample with the highest concentration of $F$-centers.

## REFERENCES

1. RAUCH C. J. and HEER C. V. *Phys. Rev.* **105,** 914 (1957).
2. DELBECQ C. J. and PRINGSHEIM P. *J. Chem. Phys.* **21,** 794 (1953).
3. SEITZ F. *Rev. Mod. Phys.* **26,** 7 (1954).
4. KORRINGA J. and DAUNT J. G. *Phys. Rev.* **102,** 92 (1956).
5. See, for example, BATES L. F. *Modern Magnetism* 3rd Edn. Cambridge University Press (1953).
6. RAUCH C. J. Dissertation, Ohio State University (1953).
7. LORD N. M. *Phys. Rev.* **106,** 1100 (1957).
8. BUCKEL W. and HILSCH R. *Z. Phys.* **131,** 420 (1952).

VOL 7 195

9. BINDER D. and STURM W. J. *Phys. Rev.* **96,** 1519 (1954).
10. MAYER G., PERIO P., GIGON J. and TOURNARIE M. *Proc. Internat. Conf. Peaceful Uses Atomic Energy* (*Geneva* 1955) Vol. 7, Session 13B, pp. 647, 685. United Nations, New York (1956).
11. SMALLMAN R. E. and WILLIS B. T. *Phil. Mag.* **2,** 1018 (1957).
12. ESHELBY J. *J. Appl. Phys.* **25,** 255 (1954).
13. SEITZ F. and KOEHLER J. *Solid State Physics* (Ed. F. SEITZ and D. TURNBULL) Vol. 2, p. 444. Academic Press, New York (1956).
14. SEITZ F. and KOEHLER J. *Proc. Internat. Conf. Peaceful Uses Atomic Energy* (*Geneva* 1955) Vol. 7, Session 13B, p. 615. United Nations, New York (1956).
15. VARLEY J. H. O. *Nature, Lond.* **174,** 886 (1954); *J. Nuclear Energy* **1,** 130 (1954).
16. CRAWFORD J. H. and WITTELS M. C. *Proc. Internat. Conf. Peaceful Uses Atomic Energy* (*Geneva* 1955) Vol. 7, Session 13B, p. 654. United Nations, New York (1956).
17. LAMBERTM. and GUINIER A. *C.R. Acad. Sci., Paris* **244,** 2791 (1957).
18. See, for example:
SIMPSON J. H. *Proc. Roy. Soc.* A**197,** 269 (1949).
MUTO T. *Progr. Theor. Phys.* **4,** 243 (1949).
INUI T. and UEMURA Y. *Progr. Theor. Phys.* **5,** 252 (1950).
GOURARY B. S. and ADRIAN F. J. *Phys. Rev.* **105,** 1180 (1957).
19. REID F. J. M.S. Thesis, Ohio State University (1957)
20. SEITZ F. Private communication.
21. VAN DOORN C. Z. *Philips Res. Rep.* **12,** 309 (1957).
22. PAULING L. and WILSON E. B. *Introduction to Quantum Mechanics* pp. 340–345. McGraw-Hill, New York (1935).
SUGIURA Y. *Z. Phys.* **45,** 484 (1927).
23. INUI T. and UEMURA Y. *Progr. Theor. Phys.* **3,** 252 (1950).

VOL. 7 1958

*J. Phys. Chem. Solids* Pergamon Press 1958. Vol. 7. pp. 22–51.

# CONTRIBUTION A L'ETUDE QUANTITATIVE DU TRAINAGE MAGNETIQUE DE DIFFUSION DU CARBONE DANS LE FER α

**PIERRE BRISSONNEAU**

Laboratoire d'Electrostatique et de Physique du Métal, Grenoble, France

(*Received* 13 *February* 1958)

VOL
7
195

**Sommaire**—Sur des solutions solides très diluées de carbone dans du fer nous avons rencontré et mesuré un traînage magnétique de diffusion d'amplitude considérable. Nous interprêtons complètement nos résultats à partir de la théorie de L. NÉEL. Les mesures de désaccommodation de l'induction permettent d'évaluer le champ de traînage de diffusion dont la théorie fournit une expression simple. Dans ce champ de traînage proportionnel à la concentration des solutions solides, nous avons mis en valeur les contributions respectives des parois de BLOCH à 90° et 180°. Le mécanisme de la diffusion ne peut être correctement représenté qu'à l'aide d'un spectre de constantes de temps relativement étalé.

En champ alternatif nous avons trouvé un grand nombre d'anomalies que nous interprétons. Les études quantitatives sont alors considérablement entravées par l'existence de l'hystérésis et des courants induits.

Ces résultats permettent d'envisager la mesure du champ de traînage de diffusion comme une méthode de dosage des impuretés en solution. L'intérêt principal de cette méthode réside dans son extrême sensibilité.

**Abstract**—A magnetic diffusion after-effect of considerable magnitude has been found and measured in very dilute solid solutions of carbon in iron. The results are interpreted by NÉEL's theory. Measurements of the time decrease of the induction allow the determination of the diffusion after-effect field, which can be separated into the contributions due to the 90° and 180° BLOCH walls and for which theory gives a simple expression. The diffusion mechanism can be accurately represented only by introducing a fairly wide range of time constants.

A large number of anomalies has been found and interpreted in a.c. fields, but in this case, the quantitative measurements are greatly hindered by hysteresis and eddy currents.

It seems that the measurement of the diffusion after-effect field could be used as a very sensitive method for the quantitative determination of dissolved impurities.

## 1. INTRODUCTION

DANS un premier travail, nous avons passé en revue les principaux aspects du traînage magnétique de diffusion. De nombreux auteurs, parmi lesquels nous citons en tout premier lieu RICHTER[1] et SNOEK[2] l'ont observé dans les aciers à structure de cube centré. Ses effets dépendent de la susceptibilité reversible de la substance et beaucoup de la température. Ses causes sont aujourd'hui bien connues. La plupart des observateurs attribuent ce traînage à la diffusion dans le réseau cristallin ferromagnétique, d'atomes de carbone ou d'azote interstitiels. Par contre, les mécanismes qui nous rendent sensible cette diffusion sont beaucoup moins bien connus.

L'existence simultanée du traînage mécanique et du traînage magnétique dans les mêmes échantillons a conduit SNOEK à penser que la migration des atomes étrangers tend à relâcher les contraintes élastiques dans le réseau. Le relâchement des contraintes de magnétostriction conduirait dans ces mêmes échantillons au traînage magnétique observé. Mais NÉEL a démontré[3] que ce mécanisme, s'il existe, n'est certainement pas prépondérant, car incapable en particulier de rendre compte des énergies mises en jeu. Il

propose[4] de lui substituer un couplage du type magnétocristallin entre chaque atome étranger et le réseau. Par l'intermédiaire de cette théorie, qui nous a guidés tout au long de notre travail, nous rendrons compte des faits expérimentaux d'une manière plus satisfaisante que dans tous les essais antérieurs, confirmant ainsi les hypothèses de départ.

Nous rappellerons d'abord les bases de la théorie de NÉEL, ses conclusions et nous en discuterons les possibilités de vérifications expérimentales. Après avoir décrit très brièvement la préparation des solutions solides de carbone sur lesquelles ont porté nos mesures, nous étudierons en détail le phénomène connu sous le nom de désaccommodation de la perméabilité et nous le présenterons sous un jour nouveau. Nous interprèterons ensuite certains aspects du comportement de ces mêmes substances dans un champ alternatif sinusoïdal. Enfin, pour terminer, nous envisagerons une application du traînage de diffusion.

VOL. 7 1958

## 2. RAPPEL DE LA THEORIE DU TRAINAGE DE DIFFUSION

### (a) *Schéma cristallin*

Considérons un cristal de fer α, à structure de cube centré et désignons par $OX$, $OY$ et $OZ$ les directions des axes quaternaires. Un tel cristal peut contenir en solution solide métastable à température ordinaire une très faible quantité de carbone. Si les mesures de densité conduisent à penser que chaque atome de carbone est en position interstitielle, le doute est permis quant à la place réelle qu'il occupe dans le réseau. On peut l'imaginer à priori au centre d'un octaèdre, en position $(\frac{1}{2}, 0, 0)$ ou au centre d'un tétraèdre en position $(\frac{1}{2}, \frac{1}{4}, 0)$. Les rayons $X$ sont impuissants à préciser sa place exacte, le numéro atomique du carbone étant trop petit et les solutions solides toujours très diluées.

L'ambiguïté entre ces deux configurations ne revêt aucune importance pour le problème du traînage de diffusion, si l'on remarque que chaque arrangement présente, à l'échelle des quelques atomes proches voisins, un axe de symétrie parallèle à $OX$, $OY$ ou $OZ$. Si cet axe de symétrie est dirigé suivant $OX$, nous dirons que l'atome de carbone occupe un site $X$. A partir d'une certaine température, sa position ne peut plus être considérée comme immuable. A la faveur de l'agitation thermique, l'hétéroatome se déplace par bonds successifs. Il peut gagner indifféremment l'un des quatre sites voisins les plus proches (2 sites $Y$ et 2 sites $Z$) distants de 1,4 ou 1 Å selon la place qù'il occupe initialement.

Pour passer d'un site quelconque à l'un des sites immédiatement voisins, l'atome de carbone doit franchir une barrière de potentiel de hauteur $W_a$ et pour celà, posséder une énergie thermique suffisante. La barrière de potentiel $W_a$ étant très sensible aux positions relatives des atomes de fer voisins du site, il semble difficile de la définir avec précision. Elle peut varier d'un point à un autre en raison des défauts du réseau, et d'un instant à l'autre, en un point donné, à cause des vibrations thermiques du cristal. Nous pouvons toutefois espérer rendre compte de la diffusion, en imaginant que le cristal peut être divisé en domaines très petits, ne comportant que quelques atomes chacun, à l'intérieur desquels les barrières de potentiel entre les différents sites ont une hauteur $W_a$ bien définie et indépendante du temps. Nous appellerons alors $q(W_a)dW_a$ la probabilité de rencontrer un domaine dont les hauteurs des barrières de potentiel sont comprises entre $W_a$ et $W_a+dW_a$.

Supposons maintenant un déséquilibre quelconque dans les populations des différents sites. La diffusion tend à ramener une répartition d'équilibre avec une constante de temps $\theta$ pour chaque domaine de la forme:

$$\theta = C \exp(W_a/kT) \qquad (1)$$

où $k$ est la constante de BOLTZMANN. Le facteur $C$ varie lentement avec $W_a$ et la température absolue $T$. La migration des atomes dans tout le cristal dépend alors de la probabilité $p(\theta)d\theta$ de trouver une constante de temps comprise entre $\theta$ et $\theta+d\theta$. Dans l'état actuel de nos connaissances $q(W_a)$ étant inconnu, nous ne pouvons pas en déduire $p(\theta)$, et nous devons nous limiter à une première approximation utilisée avec succès par RICHTER, BECKER et NÉEL. Ces auteurs supposent $q(W_a)$ constant entre deux limites $W_{a1}$ et $W_{a2}$, et nul en dehors de cet intervalle. Les constantes de temps $\theta$ sont alors réparties dans un spectre dont nous appellerons $\theta_1$ et $\theta_2$ les limites. Il résulte de l'équation (1):

$$p(\theta) = \frac{1}{\theta(\log\theta_2 - \log\theta_1)}. \qquad (2)$$

Une telle distribution est désignée sous le nom de répartition logarithmique des constantes de temps. L'agitation thermique des atomes de fer ne peut pas expliquer, à elle seule, la présence d'un spectre étalé de constantes de temps de diffusion.

(b) *Hypothèse de Néel*

Ce mécanisme de diffusion étant admis, comment peut-il influencer les propriétés magnétiques du cristal? C'est ici que NÉEL[4] introduit une hypothèse particulièrement fructueuse. Il suppose que les sites $X$, $Y$ et $Z$ ne sont pas équivalents du point de vue énergétique, en présence de l'aimantation spontanée. Chaque site occupé par un atome étranger est couplé au réseau ferromagnétique par une énergie de la forme:

$$E = w \cos^2 \phi \qquad (3)$$

où $\phi$ désigne l'angle de la direction d'anisotropie du site avec la direction de l'aimantation spontanée.

NÉEL souligne que cette énergie est d'origine purement magnétocristalline. Elle ne fait pas intervenir la magnétostriction et n'exige à priori aucune déformation du réseau; mais une telle déformation très localisée de la maille existe vraisemblablement, car, à moins de supposer les atomes de carbone interstitiels très fortement ionisés, on ne saurait les loger librement dans les sites proposés. Si nous remplaçons le cristal de fer par un empilement de sphères rigides, les deux sites envisagés n'acceptent sans déformation, selon DIJKSTRA[5] que des atomes de rayon 0,19 et 0,36 Å respectivement. Or, le rayon atomique du carbone est voisin de 0,8 Å d'après GOLDSCHMIDT et PAULING. Toutefois, cette déformation possède la même direction d'anisotropie que le site, et, dans ces conditions, elle n'affecte nullement la forme de l'équation (3). En résumé, devant l'insuffisance de nos connaissances sur les couplages à l'échelle atomique, il semble raisonable de penser que l'arrangement uniaxial autour de l'hétéroatome est à l'origine d'une énergie d'anisotropie dont un développement, limité à son premier terme, doit avoir obligatoirement la forme prévue par NÉEL.

(c) *Conséquences*

L'état d'équilibre étant obtenu quand l'énergie du système est minimum, il en résulte, pour une direction d'aimantation spontanée, une répartition anisotrope des atomes de carbone sur les différents sites. Nous dirons que nous avons alors une «surstructure d'orientation», c'est-à-dire un arrangement atomique qui dépend de la direction de l'aimantation spontanée. Toutefois, il n'est pas possible de dire à priori, le signe de $w$ étant inconnu, si le fait de diriger l'aimantation suivant une direction $OX$ contribue à un enrichissement ou un appauvrissement des sites $X$. $w$ étant d'ailleurs beaucoup plus petit que $W_a$ l'enrichissement ou l'appauvrissement de la population des sites privilégiés reste toujours suffisamment faible pour que la répartition d'équilibre s'écarte peu de la répartition isotrope. Ces transferts de population s'effectuent par diffusion, à une vitesse déterminée par la répartition $p(\theta)$ des constantes de temps $\theta$. Nous appellerons état stabilisé celui qui correspond à la répartition d'équilibre des atomes de carbone sur les différents sites. Cet état stabilisé, quand il n'est pas déjà réalisé, est certainement en cours de réalisation par l'intermédiaire des mécanismes de diffusion à la faveur de l'agitation thermique.

Nous n'avons considéré jusqu'ici que des déplacements des atomes de carbone consécutifs à un changement de structure magnétique de l'échantillon, c'est-à-dire, à proprement parler, l'établissement d'une surstructure d'orientation. Nous allons envisager maintenant un autre aspect de la question. Considérons à un instant donné la substance dans un état différent de l'état stabilisé. Un certain nombre de sites préférentiels sont vides et un nombre équivalent de sites défavorables occupés. Au lieu d'attendre suffisamment longtemps pour que la diffusion modifie cette répartition, on peut changer convenablement la direction de l'aimantation spontanée pour abaisser instantanément l'énergie du système et par conséquent le stabiliser. Au cours de cette opération, tout se passe comme si les sites défavorables précédents devenaient des sites préférentiels et vice versa. En d'autres termes, pour un système non stabilisé, on peut trouver généralement une structure magnétique différente de la structure existante, et qui minimise l'énergie totale de la substance. Chaque paroi de BLOCH qui sépare deux domaines élémentaires de WEISS est alors soumise à une pression de la part du réseau ferromagnétique. Cette pression $P(t)$, appelée pression de traînage, tend à déplacer la paroi jusqu'à obtenir la structure magnétique d'énergie minimum. Ces deux aspects, surstructure d'orientation d'une part, traînage

magnétique d'autre part, sont complémentaires et indissociables. Ainsi, pour calculer la pression de traînage qui est toujours une fonction du temps à cause de la diffusion, il est nécessaire de se fixer arbitrairement au départ une certaine surstructure d'orientation. NÉEL la suppose nulle, c'est-à-dire qu'il imagine une répartition isotrope des atomes de carbone à l'origine des temps. Il obtient alors pour $P(t)$ l'expression suivante :

$$P(t) = -W_0 \int_0^t f(U) g(t-\tau)\, d\tau \qquad (4)$$

§—La pression $W_0$ est liée à l'énergie $w$ introduite précédemment par la relation:

$$W_0 = \frac{cw^2}{3kT} \qquad (5)$$

où $c$ est le nombre d'atomes de carbone par cm³ de fer, $k$ la constante de BOLTZMANN et $T$ la température absolue.

§—$\tau$ doit être considéré comme une variable d'intégration et désigne un temps quelconque compris entre 0 et $t$.

§—A chaque instant $t$, la pression de traînage dépend non seulement de la position $u(t)$ de la paroi de BLOCH mais aussi de toutes les positions $u(\tau)$ antérieures qui, chacune pour leur propre compte, ont influencé la distribution des atomes de carbone. Cette histoire magnétique de la paroi se manifeste par l'intermédiaire du déplacement :

$$U(t) = u(\tau) - u(t). \qquad (6)$$

§—La nature de la paroi de BLOCH définit la fonction $f(U)$.

C'est une fonction impaire de $U$. Pour une paroi à 90°, $-f(U)$, que NÉEL note $-f'(U)$, est uniformément croissante et tend vers l'unité dès que la paroi s'est déplacée d'une distance supérieure à sa propre épaisseur. Pour une paroi à 180°, $-f''(U)$ croît jusqu'à une valeur très voisine de 2, obtenue pour un déplacement $U$ de l'ordre de la moitié de son épaisseur, puis tend rapidement vers zéro pour un déplacement double. Nous reproduisons dans les Figs. 1 et 2 l'allure générale des fonctions $-f'(U)$ et $-f''(U)$.

§—Le processus de diffusion des atomes de carbone impose la forme suivante pour la fonction $g(t-\tau)$ :

$$g(t-\tau) = \int_0^\infty p(\theta) \cdot e^{-\frac{t-\tau}{\theta}}\, d\theta. \qquad (7)$$

La pression de traînage $P(u, t)$ est donc entièrement définie.

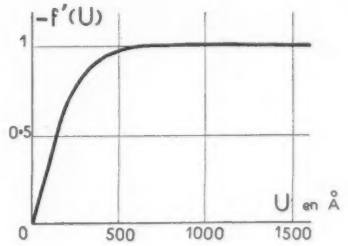


FIG. 1

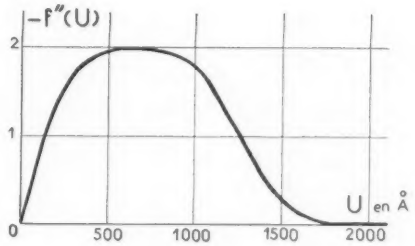


FIG. 2

Considérons une paroi de BLOCH à laquelle nous appliquons au temps $t$ un champ extérieur $\boldsymbol{H}(t)$. Cette paroi se déplace jusqu'à annuler la résultante des pressions qui s'exercent sur elle.

$$\boldsymbol{H}(t) \cdot (\boldsymbol{J}_1 - \boldsymbol{J}_2) + R(u) + P(u, t) = 0 \qquad (8)$$

$\boldsymbol{J}_1$ et $\boldsymbol{J}_2$ étant les vecteurs aimantation de part et d'autre de la paroi. Le premier terme de l'équation (8) représente la pression du champ extérieur appliqué. $R(u)$ s'oppose au déplacement. Cette pression rappelle la paroi vers quelques positions privilégiées, en rapport avec les différentes perturbations du réseau ferromagnétique. Elle ne dépend nullement du temps $t$, et LLIBOUTRY l'appelle[6] «(l'opposition)».

L'équation intégrale (8) résoud en principe le problème du déplacement de la paroi au cours du temps. C'est l'équation fondamentale du traînage.

Mais sous cette forme générale, elle n'est pas d'une utilisation commode pour l'expérimentateur. Les deux premiers termes varient d'une paroi à l'autre, ils ne sont accessibles que statistiquement. Nous allons donc simplifier le problème en imaginant, pour l'instant, que la substance ne comporte que deux domaines élémentaires de WEISS, séparés par une seule paroi, de surface constante, d'orientation et d'opposition convenables. Le déplacement $u$ d'une telle paroi, proportionnel à l'aimantation moyenne mesurée, est alors accessible. Il reste à déterminer sous quelles conditions la pression de traînage $P(u, t)$ peut prendre une forme plus maniable.

### 3. POSSIBILITIES DE VERIFIER EXPERIMENTALEMENT LA THEORIE DU TRAINAGE DE DIFFUSION

Nous désirons nous placer dans des conditions expérimentales où nous pourrons obtenir avec précision une expression commode de la pression de traînage $P(u, t)$.

(a) *Méthode des approximations successives*

NÉEL propose de résoudre l'équation intégrale (8) par approximations successives. Nous supposons d'abord la pression de traînage négligeable et nous déterminons le déplacement de paroi $u_0$ qui satisfait à l'équation :

$$H(J_1-J_2)+R(u_0)=0. \tag{9}$$

Nous utilisons ce déplacement $u_0$ pour le calcul d'une pression de traînage $P(u_0, t)$ qui, reportée dans l'équation (8), permet d'obtenir une première approximation $u_1$ du déplacement de la paroi. En répétant cette opération, $P(u_1, t)$ fournit une deuxième approximation $u_2$, etc.

Cette méthode n'est d'un emploi commode, que si nous pouvons la limiter à un nombre réduit d'opérations, une ou deux pour préciser. Pour que la suite $u_0, u_1, \ldots u_n$ soit rapidement convergente, il faut $P(u, t)$ petit vis-à-vis des deux autres termes de l'équation (8). L'expérience nous a montré que cette condition n'est jamais réalisée dans les échantillons que nous avons préparés, le terme $W_0/J_s$ n'étant jamais petit vis-à-vis des champs appliqués. Pour qu'il le devienne, il faudrait opérer sur des solutions solides tellement diluées (à des concentrations pondérales de l'ordre de $10^{-7}$ pour fixer les idées), que toute précision expérimentale serait bannie. On éprouverait en outre de très grosses difficultés à réaliser des solutions solides homogènes en supposant qu'on ait encore des moyens de contrôle. Nous ne pouvons donc confronter l'expérience et la théorie qu'à la faveur de cas particuliers. Nous proposons l'étude de deux d'entre eux.

(b) *Etude de la désaccommodation de l'induction*

A l'origine des temps, nous désaimantons l'échantillon dans un champ alternatif décroissant. Nous admettons pour l'instant, en nous réservant d'y revenir ultérieurement, que cette opération réalise une distribution isotrope des atomes de carbone sur les différents sites. La substance reste alors au repos pendant un certain temps au cours duquel s'établit un début de surstructure d'orientation suivant les directions d'aimantation spontanée des domaines élémentaires. Au temps $t$, nous appliquons un champ $H$, et nous effectuons une mesure aussi instantanée que possible de l'induction correspondante $B(H, t)$, par exemple à l'aide d'un montage comprenant un galvanomètre balistique.

Les conditions d'expérience correspondent à $u(\tau) = 0$ pour la paroi de BLOCH, puisqu'elle est toujours restée immobile jusqu'au temps $t$. D'après la formule (6), $U(t) = -u(t)$ et $f(-u)$ peut être extrait de l'intégrale (4). Il vient :

$$P=-W_0 \cdot f(-u) \int_0^t g(t-\tau)\, d\tau \tag{10}$$

$$P=W_0 \cdot f(u) \cdot G(t) \tag{11}$$

avec
$$G(t)=\int_0^t g(t-\tau)\, d\tau. \tag{12}$$

Nous obtenons ainsi une véritable séparation des variables $u$ et $t$. Le déplacement de la paroi est alors solution de l'équation beacoup plus simple :

$$H \cdot (J_1-J_2)+R(u)+W_0 \cdot f(u) \cdot G(t)=0. \tag{13}$$

Pour un champ $H$ donné, le déplacement $u$ observé décroît donc d'une valeur $u_0$ solution de l'équation (9) à une valeur $u_\infty$ quand $G(t) = 1$ au bout d'un temps $t$ suffisamment long. En d'autres termes, la valeur de $B(H, t)$ mesurée décroît entre

deux limites $B(H, 0)$ et $B(H, \infty)$. C'est le phénomène connu sous le nom de désaccommodation de la perméabilité ou de l'induction. Nous verrons dans un prochain paragraphe comment raccorder la mesure de $B(H, t)$ à l'équation (13) précédente.

(c) *Etude du comportement em champ alternatif de grande amplitude*

Nous désaimantons toujours l'échantillon à l'origine des temps et nous le laissons au repos jusqu'au temps $t_1$ où nous lui appliquons un champ alternatif sinusoïdal.

NÉEL a développé[4] le calcul de la pression de traînage exercée dans ces conditions sur une paroi à 90° animée d'un mouvement alternatif de grande amplitude. Son résultat correspond à la première approximation que nous avons appelée $P(u_0, t)$ précédemment. Mais $f'(u)$ ne dépend pratiquement que du signe de $u$ [$f'(u) = \pm 1$]. Une modification d'amplitude du déplacement ne modifie nullement alors la pression de traînage et dans ce cas particulier, $P(u_0, t)$ s'identifie avec tous les termes suivants qu'on peut obtenir par approximations successives : $P(u_1, t)$, $P(u_2, t)$, ... $P(u_n, t)$. Nous justifierons ultérieurement l'utilisation directe des résultats obtenus par NÉEL pour les seules parois à 90°.

En résumé, nous pouvons obtenir une expression relativement simple de $P(u, t)$ dans deux cas particuliers : d'une part, au cours de la désaccommodation de l'induction, d'autre part, dans les champs alternatifs suffisamment forts. Nous nous limiterons donc à ces deux types d'expériences.

## 4. PREPARATION DES ECHANTILLONS

Les nombreux alliages du commerce qui manifestent un traînage de diffusion plus ou moins important ne peuvent pas faire l'objet d'une étude quantitative, car ils ne sont jamais suffisamment bien définis. Ils contiennent en général tellement d'impuretés qu'on ne peut pas mettre en cause le comportement d'une seule d'entre elles avec certitude. Nous préparons donc les échantillons sur lesquels portent ensuite les mesures magnétiques. Ce sont des solutions solides de carbone dans du fer à des concentrations pondérales de l'ordre de 0,01 pour-cent.

Nous utilisons au départ des anneaux de fer commercialement pur, du type Armco, de diamètre extérieur 48 mm, diamètre intérieur 33 mm et épaisseur 0,3 mm. Nous les purifions très soigneusement par un séjour de 8 hr à 1350°C dans un courant permanent d'hydrogène humide. La substance obtenue possède alors une perméabilité initiale voisine de 1000 G/Oe, une perméabilité maximum égale à 15 000 G/Oe et un champ coercitif de 0,35 Oe. Après décarburation et trempe, nous n'avons jamais constaté la moindre trace de traînage de diffusion aux températures voisines de l'ambiante et inférieures. Il n'y a pas alors de carbone en solution solide. Nous admettons qu'il n'y en pas non plus à l'état précipité.

Nous effectuons la carburation des anneaux à une température voisine de 700°C, en atmosphère d'hydrogène contenant 1 pour-cent environ d'hydrocarbure. La Fig. 3 représente un schéma du dispositif utilisé. En fin

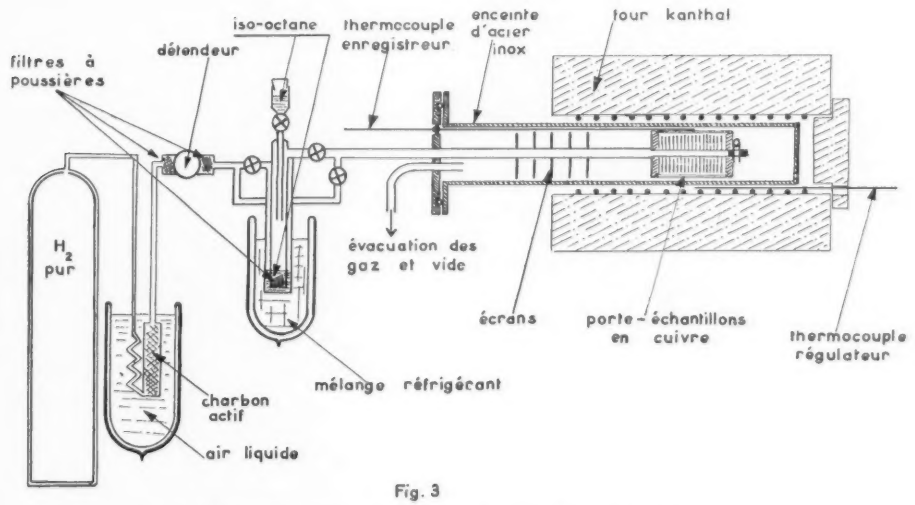


Fig. 3

FIG. 3. Schéma du montage utilisé pour la carburation des échantillons.

d'opération, nous trempons énergiquement dans un bain d'eau froide l'enceinte étanche et son contenu.

La pureté des gaz mis en oeuvre au cours des différents traitements a tout particulièrement retenu notre attention. Grâce à la collaboration du Laboratoire des Basses Températures, dont nous tenons à remercier le Directeur, M. WEIL, nous avons pu utiliser de l'hydrogène contenant moins de $4 \cdot 10^{-6}$ volume d'impuretés par volume de gaz. Tout caoutchouc a été systématiquement éliminé sur le circuit des gaz et les anneaux n'étaient en contact avec de l'alumine pure qu'en trois points seulement.

Le carbone total contenu dans les échantillons est évalué par pesées. Les poids n'étant malheureusement pas reproductibles à mieux de $5 \cdot 10^{-6}$ après chaque traitement, la précision de nos déterminations reste assez limitée aux faibles concentrations.

Toutes nos mesures sont effectuées sur des ensembles de seize anneaux aussi homogènes que possible. Nous avons rencontré de très grosses difficultés pour réaliser des solutions satisfaisantes sur ce point. Pour contrôler cette homogénéité nous mesurons les variations de résistance électrique, à la température d'ébullition de l'oxygène liquide, de quatre anneaux fendus, préparés spécialement pour cet usage, et régulièrement répartis parmi les autres échantillons. Nous avons rejeté systématiquement les préparations pour lesquelles on a constaté, sur l'un des anneaux, une variation de résistance $\Delta R/R$ différente de 15 pour-cent du $\Delta R/R$ moyen.

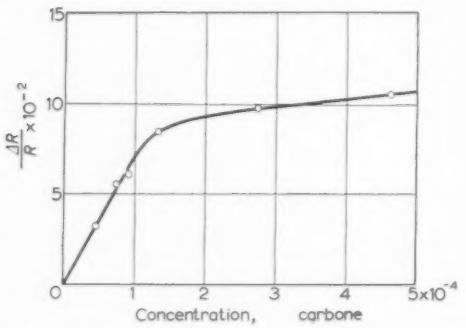


FIG. 4. Variation de résistance électrique du fer (mesurée à 90°K) pour différentes concentrations en carbone.

La plupart des mesures qui suivent se rapportent à un échantillon exceptionnellement homogène (concentration du carbone 0,0046 pour-cent, et $3{,}19 \cdot 10^{-2} \leqslant \Delta R/R \leqslant 3{,}37 \cdot 10^{-2}$). Nous avons reporté Fig. 4 les variations moyennes de résistance observées pour différentes concentrations en carbone. Aux faibles concentrations, le comportement linéaire de $\Delta R/R$ confirme l'efficacité des trempes. Au delà de 0,013 pour-cent un précipité de carbone apparaît dans les conditions de préparation.

## 5. MESURES DE DESACCOMMODATION DE L'INDUCTION A L'AIDE DU GALVANOMETRE BALISTIQUE

(a) *Mécanisme et contrôle des désaimantations*

Nous nous proposons de confronter la formule (13) rappelée précédemment avec l'expérience. Or, pour établir cette formule, NÉEL suppose une distribution isotrope des atomes de carbone à l'origine des temps sur les différents sites possibles. Nous préciserons d'abord cette hypothèse. Nous verrons ensuite par quel mécanisme nous pouvons espérer aboutir à cet état initial et enfin comment contrôler sa réalisation.

(i) *Etat initial de la substance.* Au temps $t = 0$, nous plaçons la substance dans un champ alternatif d'amplitude lentement et régulièrement décroissante depuis une valeur qui assure l'aimantation à saturation jusqu'à une valeur nulle. Cette opération comme chacun sait, produit une redistribution des domaines élémentaires de WEISS et l'aimantation moyenne résultante est alors nulle. Mais une telle désaimantation ne nous satisfait pas forcément. Nous lui demandons en outre de posséder un caractère nouveau indispensable à l'étude du traînage de diffusion. Nous lui demandons de réaliser l'état statistiquement isotrope que NÉEL suppose à l'origine des temps. A quelle échelle doit-on exiger que s'annule cette surstructure d'orientation? Certainement pas à l'échelle de quelques atomes, le nombre des sites occupés étant très réduit. Certainement pas non plus à une échelle macroscopique où, du fait de l'existence des domaines élémentaires, on peut très bien trouver une disposition anisotrope à l'intérieur de chaque domaine et une surstructure résultante nulle. En particulier, une désaimantation quelconque suivie d'une stabilisation réalise un milieu isotrope à trop grande échelle. L'état isotrope exigé par la théorie de NÉEL doit s'annuler à une échelle intermédiaire, disons de quelques centaines à quelques milliers de sites occupés pour fixer les idées. C'est en volume une échelle nettement inférieure à celle des domaines élémentaires.

Au cours de cette étude du traînage, nous dirons qu'une désaimantation est ((efficace)) si elle réalise une surstructure d'orientation nulle à une échalle suffisamment petite pour que la théorie de NÉEL soit valable.

(ii) *Mécanismes possibles des désaimantations ((efficaces)).* NÉEL[4] propose deux mécanismes permettant d'obtenir des désaimantations ((efficaces)).

D'une part, nous pouvons imaginer que nous appliquons à la substance un champ alternatif décroissant de grande amplitude vis-à-vis du champ coercitif, de période petite vis-à-vis de la plus petite constante de temps de traînage, et ceci, pendant un temps très grand vis-à-vis de la plus grande constante de temps de traînage. En chaque point du cristal, l'aimantation prend non seulement une valeur moyenne nulle, mais encore avec une égale probabilité, toutes les directions de facile aimantation si la forme de l'échantillon le permet et ceci, en un temps de l'ordre de grandeur des constantes de temps de diffusion. L'énergie de couplage (3) devient alors statistiquement isotrope et la diffusion elle-même rétablit des populations identiques sur les sites $X$, $Y$, et $Z$.

NÉEL propose d'autre part le deuxième mécanisme suivant. Supposons que la désaimantation bouleverse complètement la structure des domaines élémentaires en établissant à la fin de l'opération une nouvelle disposition des parois de BLOCH sans aucun rapport avec l'ancienne. On disposait précédemment d'une surstructure d'orientation à l'échelle de chaque domaine ancien que l'opération de désaimantation n'a pas détruite, mais chaque domaine nouveau est formé en réalité, de deux ou plusieurs morceaux accolés, chacun de ces morceaux ayant une surstructure indépendante de celle de ses voisins. Dans ces conditions, la répartition des atomes de carbone peut être considérée comme isotrope en moyenne, mais dans un volume plus grand que pour le mécanisme précédent, ce volume étant au moins de l'ordre d'un domaine élémentaire et peut être de plusieurs. Les pressions de traînage partielles qui s'exercent alors sur les parois de BLOCH à l'instant $t = 0$ ne sont pas nulles. La désaimantation sera-t-elle ((efficace)) dans ces conditions? Pratiquement oui si la nouvelle disposition de parois est absolument sans aucun rapport avec l'ancienne, auquel cas les pressions de traînage partielles possèdent des orientations diverses et leur comportement global ne diffère pas sensiblement de celui qu'on aurait avec une désaimantation suivant le premier mécanisme. Certainement pas d'autre part, si les parois reviennent même partiellement, là où elles étaient avant désaimantation, car elles bénéficient alors de la stabilisation acquise antérieurement.

(iii) *Contrôle de l'efficacité des désaimantations.* D'après les résultats de la théorie rappelés précédemment, les mesures de désaccommodation de la perméabilité magnétique dans un champ constant se caractérisent nécessairement après une désaimantation ((efficace)) par une décroissance de $\mu$ monotone. Aussitôt après une désaimantation la perméabilité mesurée est maximum, et le résultat obtenu ne diffère pas de celui qu'on aurait sur le même échantillon sans carbone (équation (9)).

En conséquence, nous dirons qu'une désaimantation est efficace :

(1°) Si la perméabilité magnétique de l'échantillon mesurée dans un champ faible quelconque est reproductible quel que soit le nombre des désaimantations successives effectuées.

(2°) Si cette même perméabilité mesurée est insensible à toute modification apportée au processus de la désaimantation elle-même, qu'il s'agisse de sa durée, de la fréquence du champ appliqué, de la température de l'échantillon, etc.

La reproductibilité de nos mesures au temps $t = 0$ représente le seul critère permettant de juger de l'efficacité d'une désaimantation.

(iv) *Résultats obtenus.* Un échantillon contenant 0,0046 pour cent de carbone donne des résultats parfaitement reproductibles (à 0,5 pour-cent au moins) après des désaimantations au cours desquelles le champ appliqué décroît de 2 Oe environ à une valeur nulle en 86 sec.

Comme les plus grandes constantes de temps atteignent plusieurs heures dans les conditions d'expérience, le premier mécanisme doit être alors rejeté. L'efficacité ne peut être due qu'au second mécanisme.

C'est d'autant plus vrai que ce type de désaimantation cesse d'être efficace si la concentration en carbone $c$ des solutions, devient voisine de 0,01 pour-cent. L'énergie de stabilisation $W_0$ proportionnelle à $c$ est alors considérable. Les positions dans lesquelles les parois ont séjourné un certain temps représentent des positions d'énergie minimum. Si, par rapport aux autres minima d'énergie qui résultent normalement du couplage de la paroi avec les défauts du réseau cristallin, ces minima dus à la stabilisation sont suffisamment prononcés, certaines dispositions primitives des parois se retrouvent après désaimantation. La stabilisation acquise ne s'efface alors que progressivement au fur et à mesure des désaimantations successives à moins qu'on ne fasse appel au premier mécanisme envisagé.

Un tel comportement caractérise tous les échantillons qui contiennent plus de 0,007 à 0,008 pour-cent de carbone en solution. Pour désaimanter ces substances, nous les avons portées à une température généralement comprise entre 0° et +10°C, pendant une demi-heure, dans un champ alternatif d'amplitude égale à 2 Oe. Elles ont été ensuite refroidies lentement sous champ alternatif et désaimantées normalement à la température des mesures.

La plus grande partie de notre étude est relative à des solutions plus diluées pour lesquelles ces difficultés n'existent pas.

(b) *Réalisation des désaimantations*

Nous avons obtenu une excellente reproductibilité dans nos mesures de désaccommodation en effectuant des désaimantations aussi régulières et aussi identiques que possible. Notre générateur de courant alternatif d'amplitude décroissante est constitué par un transformateur dont nous déplaçons l'enroulement secondaire, à vitesse constante, d'une position où le coefficient d'induction mutuelle avec le circuit primaire est maximum jusqu'à une position où il s'annule pratiquement. Au début de la désaimantation, nous appliquons un champ dont l'amplitude est voisine de six fois le champ coercitif de la substance. Au cours de l'opération qui dure 86 sec, l'amplitude du champ magnétique décroît d'un facteur 30 000 environ.

(c) *Le circuit de mesures*

Nous effectuons nos mesures sur des ensembles de seize anneaux disposés en forme de tore. Chaque anneau isolé de ses voisins est maintenu à l'intérieur d'une fine carcasse en araldite qui supporte deux enroulements de 80 et 2000 spires environ. Cette carcasse évite d'une part, les court-circuits entre les spires de l'enroulement, et d'autre part, annule l'effet des tensions mécaniques du bobinage sur les mesures. Bien entendu, le champ appliqué varie d'un point à un autre du tore. Nous n'envisageons dans la suite que des champs moyens, pris sur la spire médiane de diamètre $\phi = 40{,}5$ mm. De même, nous ne parlerons dans tout ce travail que d'inductions moyennes obtenues en divisant le flux d'induction au travers d'une spire de l'enroulement par la section.

Notre montage est représenté Fig. 5. Nous étalonnons le circuit galvanométrique à partir d'une bobine de mutuelle inductance connue $M$. Pour cette opération, nous substituons à l'enroulement secondaire du tore une

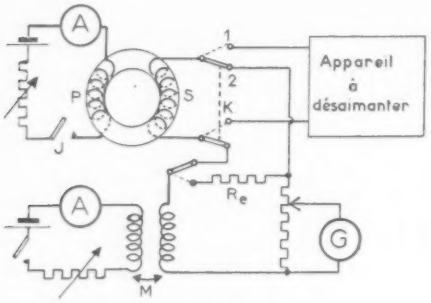


FIG. 5. Schéma du montage utilisé pour les mesures au galvanomètre balistique.

résistance pure égale. Nous assurons cette égalité par une mesure au pont de WHEATSTONE en courant continu. Cette opération s'est révélée indispensable pour obtenir un étalonnage du galvanomètre balistique indépendent de l'état magnétique de la solution solide constituant l'échantillon. L'enroulement de mesures se comporte en effet, comme une self à très grande constante de temps. Sous l'effet d'une impulsion de courant, les parois de BLOCH se déplacent et elles sont alors soumises à une pression de traînage qui varie suivant l'état de stabilisation de la substance. Sans précautions particulières, l'expérience conduit pour l'étalonnage du circuit de mesure à une incertitude qui peut atteindre 2 à 3 pour-cent dans certains cas défavorables.

L'utilisation de contacts appropriés permet d'éliminer la plupart des forces électromotrices parasites du circuit galvanométrique. Nous pouvons effectuer une première mesure quinze secondes seulement après la fin d'une désaimantation. On ne gagnerait pratiquement rien à réduire cet intervalle de quelques secondes, car nous verrons que l'origine des temps pour l'étude de la désaccommodation de l'induction se situe en réalité avant la fin de la désaimantation.

Le séjour moyen de chaque atome de carbone sur un site du réseau n'atteint un ordre de grandeur à l'échelle humaine, de quelques minutes pour fixer les idées, que dans le domaine des températures inférieures à l'ambiante. Nous maintenons donc nos échantillons dans une enceinte isotherme représentée Fig. 6. Les frigories sont apportées par une réserve d'air liquide qui s'évapore lentement. Une série d'écrans supportés par des tiges isolantes, ralentit les échanges de chaleur. Enfin, un mélange eutectique glace et sel à son point de congélation constitue le tampon thermique régulateur. L'échantillon séjourne au centre du mélange dans un bain d'éther de pétrole. Pour un réglage convenable (nombre de tiges du support, volume de la réserve d'air liquide) l'apport de frigories compense les pertes et la température du bain d'éther de pétrole se maintient constante pendant 24 heures environ à $\pm 0{\cdot}2$°C. L'immense avantage de ce système réside dans sa simplicité et dans l'absence de vibrations communiquées à l'échantillon. Nous avons utilisé au cours de cette étude une série de mélanges eutectiques pour obtenir les températures désirées : NaCl—21,3°C, NaBr—27,3°C, $MgCl_2$—33,8°C, et plus rarement $CaCl_2$—55°C.

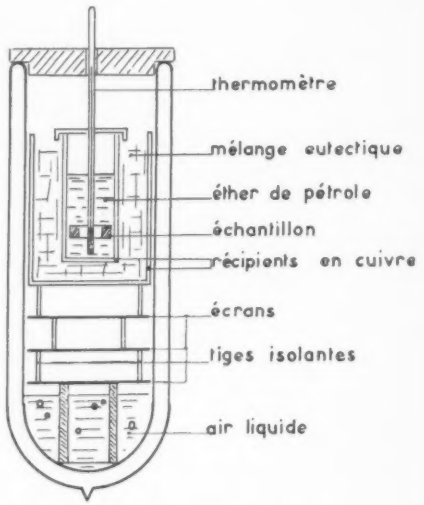


FIG. 6. Schéma de l'enceinte isotherme.

(d) *Mode opératoire et résultats des mesures*

Supposons un tore à la température de —27,3°C porteur de deux enroulements et intégré dans le montage décrit précédemment. La clé $K$ étant en position 1, (voir Fig. 5), nous le désaimantons. La fin de la désaimantation marque l'origine des temps. Nous ramenons alors la clé $K$ en position 2 et au temps $t'$, nous fermons le circuit primaire $P$ par l'interrupteur $J$. L'élongation maximum du galvanomètre balistique permet de calculer l'induction $B(H_0, t')$ prise par l'échantillon dans le champ $H_0$ au temps $t'$. Nous effectuons de la sorte une série de mesures, en prenant bien soin de désaimanter chaque fois la substance, en conservant la même valeur du champ $H_0$ appliqué et ceci, pour des temps $t'$ différents. La courbe $B(H_0, t')$ constitue ce que nous appelons une courbe de désaccommodation de l'induction magnétique dans le champ $H_0$.

Une telle courbe obtenue sur l'échantillon contenant $4{,}6 \cdot 10^{-5}$ de carbone est représentée Fig. 7. Le champ moyen appliqué vaut alors 32 mOe, et

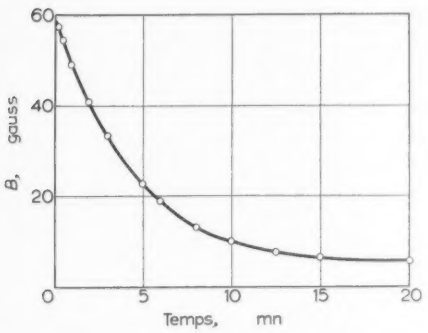


FIG. 7. Désaccommodation de l'induction. Température: −27,3°C, $c = 0{,}0046$ pour-cent, $H = 32$ mOe.

les mesures sont parfaitement reproductibles à 0,5 pour cent environ. L'amplitude de cette désaccommodation de l'induction est surprenante pour une concentration en carbone aussi faible. Il ne faut surtout pas voir le traînage de diffusion comme un phénomène qui provoque des variations du second ordre des propriétés magnétiques de la solution.

Si la plus grande partie du traînage s'observe dans les dix premières minutes, on ne peut pourtant pas en conclure que la variation de perméabilité est exponentielle. Une évolution se manifeste encore 2 heures et même une journée : après désaimantation à des vitesses toujours de plus en plus faibles. Ce fait apparait clairement dans la Fig. 8 relative au même échantillon que précédemment placé dans les mêmes conditions. Un simple examen condamne donc à priori toute interprétation quantitative à partir d'une loi de forme exponentielle ne comportant qu'une seule constante de temps.

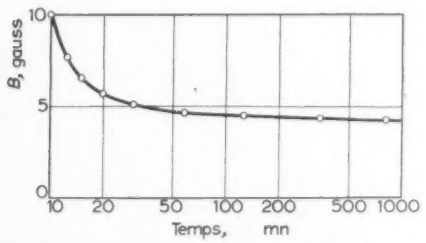


FIG. 8. Désaccommodation de l'induction dans les temps longs. Température: −27,3°C, $c = 0{,}0046$ pour-cent, $H = 32$ mOe.

(e) *Les diagrammes $B(H, t')$ et les courbes isochrones*

Au cours de très nombreuses mesures du type précédemment décrit, nous avons étudié le comportement d'un échantillon porté à −27,3°C. Nous avons fait varier le champ $H_0$ entre 4 et 80 mOe environ et le temps $t'$ entre 15 sec et 1000 min. En possession de ces valeurs de $B$, nous les avons reportées dans un diagramme $B(H, t')$ avec $H$ en abscisse et $t'$ en paramètre. Dans un tel diagramme, nous obtenons une courbe $B(H, t' = 15\text{ sec})$ une courbe $B(H, t' = 30\text{ sec})$, etc. Les valeurs adoptées pour le paramètre $t'$ sont arbitraires. Nous les avons choisies de façon à espacer assez régulièrement ces courbes que nous appellerons désormais des courbes isochrones.

Puis, nous avons recommencé ces opérations en modifiant la température de l'échantillon. Finalement, nous possédons pour la même substance trois diagrammes $B(H, t')$ relatifs aux températures : −21,3°C, −27,3°C et −33,8°C (Figs. 9–11). Aux températures plus élevées et plus basses, l'évolution du traînage devient trop rapide ou trop lente pour qu'on puisse en suivre facilement les étapes.

(f) *Extrapolation des courbes isochrones $t = 0$ et $t = \infty$*

Supposons une variation d'induction $B_0$ produite 15 sec après désaimantation, par un champ appliqué $H_{15\,\text{sec}}$. Pour produire le même effet en attendant plus longtemps après la désaimantation, il faut appliquer un champ notablement supérieur à $H_{15\,\text{sec}}$. Le champ supplémentaire nécessaire est représenté par un décalage vers la droite, pour des temps croissants, des différentes courbes isochrones du diagramme $B(H, t')$. Ainsi nous pouvons tirer immédiatement de cette représentation ce que NÉEL a appelé le champ fictif de traînage, soit au signe près, le champ qui, appliqué à la substance, permet de compenser exactement la pression de traînage. C'est un champ croissant au cours du temps, théoriquement nul pour $t' = 0$. S'il n'y avait qu'une seule constante de temps de diffusion $\theta$ pour le carbone, ce champ varierait avec $t'$ comme : $1 - \exp(-t'/\theta)$, c'est-à-dire qu'il serait linéaire en fonction du temps, pour $t'$ suffisamment petit. Nous constatons d'après les diagrammes $B(H, t')$ que cette condition est assez grossièrement respectée. Nous pouvons donc espérer obtenir facilement par extrapolation la

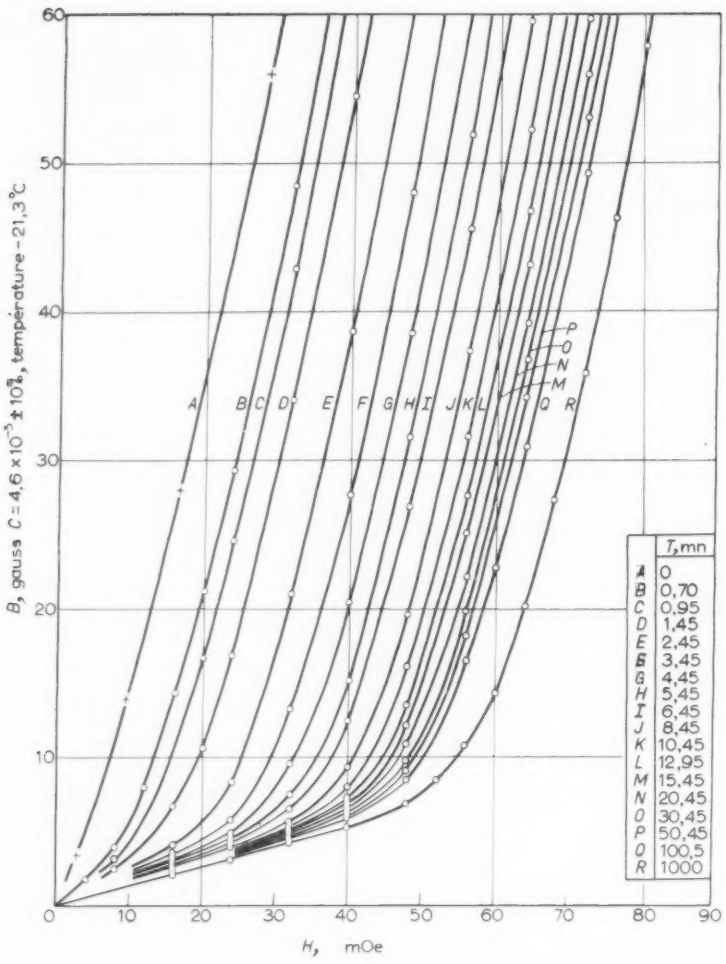


FIG. 9

courbe isochrone $B(H,\ t' = 0)$ théoriquement identique à la courbe d'induction $B(H)$ de la substance sans carbone. L'expérience montre alors que la courbe extrapolée ainsi obtenue dépend beaucoup de la température.

Dans les trois diagrammes $B(H,\ t')$, nous trouvons trois isochrones $B(H,\ t' = 0)$ parallèles nettement distinctes. Or, nos mesures sur des échantillons décarburés nous ont toujours donné au contraire une perméabilité indépendante de la température dans les champs faibles. Entre 20 et —50°C, la variation de perméabilité n'excède pas 1 pour-cent en l'absence de carbone et les trois courbes $B(H,\ t' = 0)$ devraient être confondues à la précision des mesures (0,5 pour-cent environ). Cette anomalie s'explique parfaitement si on admet que l'origine des temps pour le traînage doit être prise un peu avant la fin de la désaimantation. Pour chaque valeur de $B$, les trois courbes $H(t')$ convergent en effet, au temps $t' = -0{,}45$ min (Fig. 12). Nous avons par conséquent changé d'origine des temps et nous appellerons $t$ les temps rapportés à la nouvelle origine. Tous les paramètres $t$ des courbes isochrones sont alors décalés de 0,45 min par rapport aux paramètres $t'$ correspondants. La mesure effectuée 0,25 min après

désaimantation se retrouve sur la courbe isochrone $t = 0{,}70$ min, celle effectuée 0,5 min après désaimantation appartient à la courbe isochrone $t = 0{,}95$ min, etc. (Figs. 9–11).

une quinzaine de Gauss, les déplacements des différentes parois de BLOCH rappelées vers leur position d'équilibre par des forces extrêmement variables, sont alors notablement inférieurs à leur

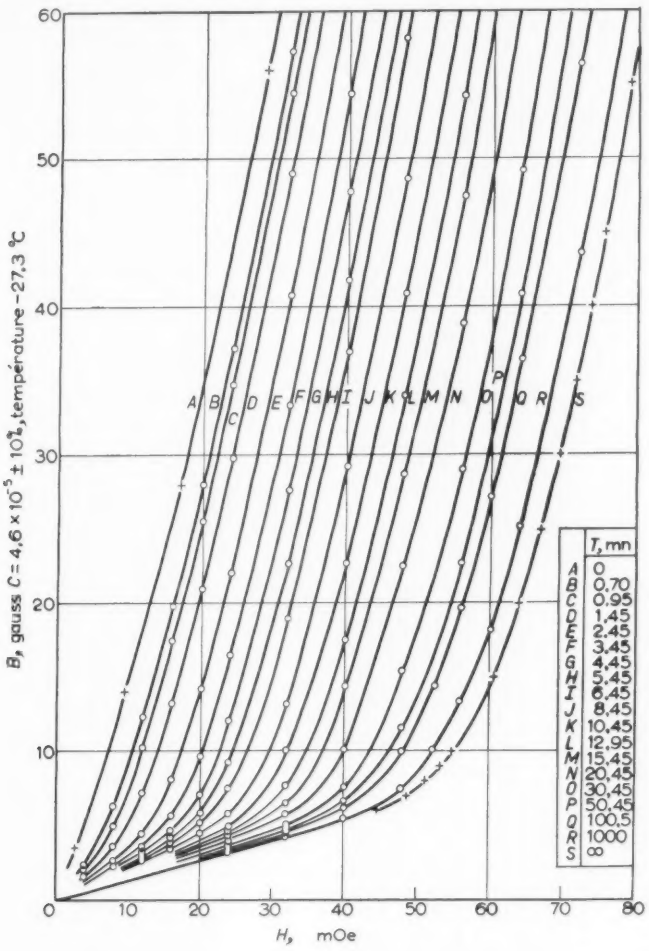


FIG. 10

Que représente cette nouvelle origine des temps dans le processus de désaimantation? L'amplitude du champ alternatif appliqué 0,45 min avant la fin de la désaimantation est de l'ordre de 15 mOe. Il lui correspond une induction voisine de 15 G. C'est précisément pour cette valeur de l'induction que les différentes courbes isochrones présentent un coude plus ou moins accentué. Nous montrerons que pour des champs d'induction inférieurs à

propre épaisseur. La stabilisation de chaque paroi commence dès que ses déplacements deviennent suffisamment petits. En toute rigueur, on devrait considérer une origine des temps variable d'une paroi à l'autre. Mais nos mesures ne permettent de déceler qu'un comportement moyen, d'où l'intérêt de ne pas trop étaler la phase finale des désaimantations.

Ainsi les courbes isochrones $B(H,\ t = 0)$

coïncident dans les trois diagrammes. Ultérieurement, nous montrerons que le décalage entre les courbes isochrones $B(H, t = 0)$ et $B(H, t = \infty)$ doit être proportionnel à l'énergie $W_0$. Quand la température absolue décroit l'isochrone $t = \infty$ s'éloigne donc indéfiniment dans la direction des champs croissants (formule 5). Mais cet effet se trouve complètement masqué par un ralentissement considérable des processus de diffusion, qui nous oblige pratiquement, à un choix arbitraire de l'isochrone $t = \infty$, en présence des grandes constantes de temps rencontrées.

Si nous observons à —27,3°C (Fig. 8), un traînage encore sensible 1000 min après désaimantation, une évolution est plus difficile à mettre en évidence dans le même champ appliqué à —21,3°C. Nous ne pensons pas toutefois que la répartition d'équilibre des atomes de carbone soit vraiment atteinte à la précision de nos expériences. Mais indépendamment du temps que prendrait une telle étude, notre appareillage ne nous permet pas d'assurer la reproductibilité des conditions extérieures nécessaire à des mesures dans des temps plus longs. Nous avons donc choisi comme courbe limite $B(H, t = \infty)$ pour les diagrammes relatifs à —27,3 et —33,8°C, la courbe isochrone $B(H,$

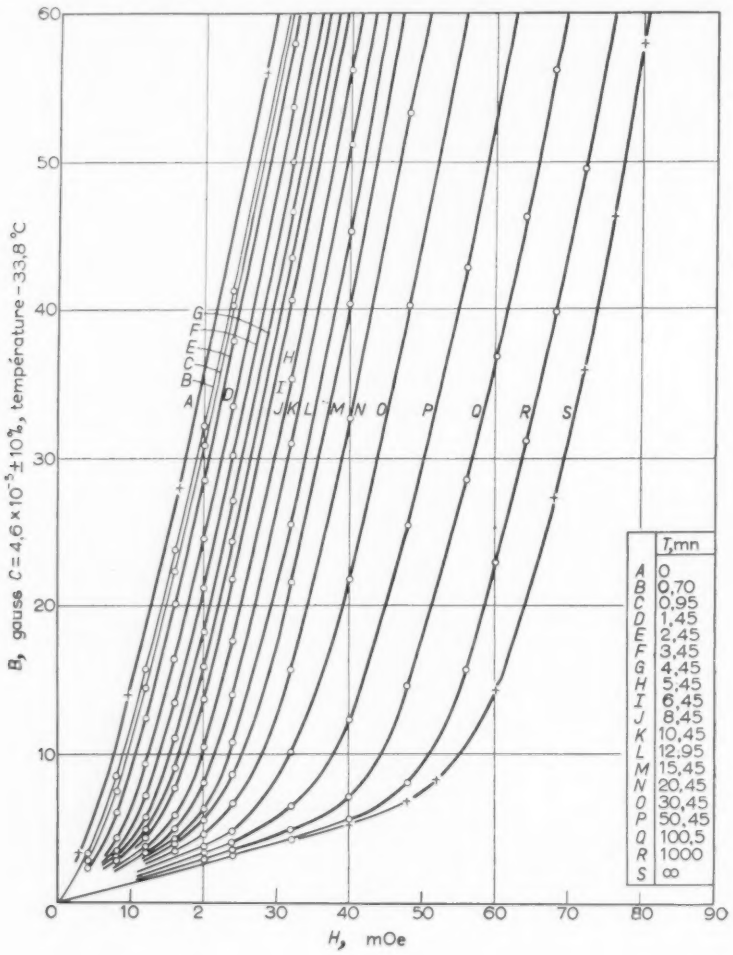


FIG. 11

$t = 1000$ min) du diagramme à —21,3°C (courbes $S$ des Figs. 10 et 11).

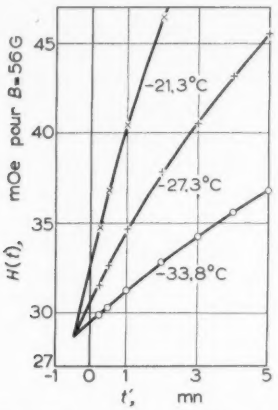


FIG. 12. Détermination de l'origine des temps pour l'étude de la désaccommodation.

(g) *Interprétation des diagrammes* $B(H, t)$

(i) *Cas d'une paroi de* BLOCH *unique*. Imaginons un échantillon divisé en deux domaines élémentaires seulement, dont les aimantations respectives sont $J_1$ et $J_2$, séparés par une seule paroi de BLOCH de surface $S$. Appliquons lui un champ $H$ et appelons $u$ le déplacement de la paroi parallèlement à elle-même sous l'effet de ce champ. Si la substance ferromagnétique est caractérisée par une grande perméabilité, on peut identifier pratiquement l'induction moyenne $\boldsymbol{B}$ mesurée et $4\pi J$, $J$ représentant l'aimantation de la substance. Le déplacement $u$ est alors proportionnel à la variation d'induction mesurée $B$. Posons $u = \gamma B$. Nous pouvons écrire l'équation (9) précédente sous une forme similaire :

$$H(J_1-J_2)+R(\gamma B)+W_0 \cdot f(\gamma B) \cdot G(t)=0. \qquad (14)$$

Cette équation traduit analytiquement un comportement absolument identique à celui que mettent en évidence les diagrammes $B(H, t)$. Nous avons rappelé précédemment comment elle rend compte des mesures de désaccommodation de l'induction. Mais nous pouvons aussi l'interpréter d'une manière plus fructueuse en essayant d'en déduire l'expression du champ fictif de traînage. A l'origine des temps, c'est-à-dire à la fin d'une désaimantation efficace, la courbe isochrone $t = 0$ satisfait à l'équation :

$$H_0(J_1-J_2)+R(\gamma B)=0. \qquad (15)$$

Nous appliquons au temps $t$ un champ $H(t) = H_0+h(t)$ qui produit la même variation d'induction $B_0$ que précédemment. Le champ fictif de traînage $h$ obéit alors à une relation de la forme :

$$h \cdot (J_1-J_2) = -W_0 \cdot f(\gamma B_0) \cdot G(t). \qquad (16)$$

Cette expression analytique de $h$, grâce à la séparation des variables $B$ et $t$, permet d'exploiter les diagrammes $B(H, t)$. On en déduit tous les paramètres introduits par NÉEL dans l'édification de la théorie. Par exemple, pour $t$ suffisamment grand, $G(t) = 1$; d'où le champ total de traînage $h_\infty$ :

$$h_\infty \cdot (J_1-J_2) = -W_0 \cdot f(\gamma B_0) \qquad (17)$$

$h_\infty$ atteint sa valeur maximum $(h_\infty)_{max}$ quand $f(\gamma B_0)$ vaut —1 ou —2, selon qu'il s'agit d'une paroi à 90° ou 180°. Il en résulte alors pour un champ $H$ parallèle à $J_1$ :

$$(h_\infty)_{max} \cdot J_s = W_0. \qquad (18)$$

Enfin, les fonctions $f(\gamma B_0)$ et $G(t)$ peuvent être obtenues respectivement en effectuant les rapports $h_\infty/(h_\infty)_{max}$ et $h_t/h_\infty$.

(ii) *Cas d'un grand nombre de parois de* BLOCH. Une substance polycristalline réelle comporte un grand nombre de parois de BLOCH, les unes à 90°, les autres à 180°, qui peuvent avoir toutes les orientations possibles. Ces parois séjournent à l'état désaimanté dans des positions d'énergie minimum. Quand on les déplace sous l'action d'un champ extérieur, elles sont rappelées vers leurs positions d'équilibre par des oppositions $R(u)$ extrêmement variables. Nous ne connaissons malheureusement rien de ces forces de rappel ni de leur dispersion. Seul, un comportement moyen des parois nous est accessible. Dans l'état actuel de nos connaissances il est alors impossible d'obtenir une expression rigoureuse du champ fictif de traînage. Pour simplifier le problème, nous supposerons que chaque structure des domaines élémentaires est une fonction univoque de l'aimantation moyenne prise par la substance. Le déplacement $u$ d'une paroi quelconque n'est plus alors fonction de la durée de stabilisation $t$, pour une même valeur de l'induction mesurée. Les couplages qui existent entre domaines élémentaires

proches voisins, lesquels nous empêchent de considérer isolément les déplacements de chaque paroi de BLOCH, pourraient justifier en partie cette hypothèse qui rend compte, en outre, d'une manière simple et très satisfaisante du traînage magnétique de diffusion observé.

Considérons donc un ensemble de parois de BLOCH et appelons $B(t)$ l'induction moyenne mesurée au temps $t$. Les équations (14) à (17) restent applicables à chaque instant avec un coefficient $\gamma$ qui varie d'une paroi à l'autre. Nous obtenons la fonction de traînage $G(t)$ comme précédemment. Par contre, la fonction $f(\gamma B_0)$ expérimentale ne représente qu'un comportement moyen de l'ensemble des parois et elle n'a plus la forme analytique prévue par NÉEL. Il devient difficile dans ces conditions d'atteindre l'énergie de stabilisation $W_0$. Au cours des prochains paragraphes, nous exploiterons dans cette voie, les résultats expérimentaux fournis par les diagrammes $B(H, t)$.

(h) *Variation avec l'induction du champ total de traînage*

(i) *Définition.* Nous appelons champ total de traînage $h_\infty$ la valeur limite du champ de traînage obtenue au bout d'un temps de stabilisation très grand. Dans les diagrammes $B(H, t)$, $h_\infty$ est représenté par le champ qui sépare les isochrones $t = 0$ et $t = \infty$ pour une même valeur de l'induction $B$ prise par la substance. Nous avons dit précédemment comment ces courbes isochrones sont obtenues. Toute détermination de $h_\infty$ nécessite donc deux extrapolations d'où une incertitude sur la valeur trouvée, incertitude encore aggravée par une détermination relativement arbitraire de l'isochrone $t = \infty$.

Pour étudier $h_\infty$ aux différentes inductions, nous mesurons un champ de traînage voisin $h_0 = H_{1000\ \mathrm{min}} - H_{0,70\ \mathrm{min}}$ directement accessible. $h_0$ est proportionnel au champ total de traînage en toutes circonstances d'après l'interprétation du paragraphe précédent. Nous obtenons pour un échantillon contenant 0,0046 pour-cent de carbone, à $-33{,}8°$C, et pour $B$ voisin de 50 G $h_0 = 44{,}5 \cdot 10^{-3}$ Oe et $h_\infty = 50{,}5 \cdot 10^{-3}$ Oe. L'écart entre ces deux valeurs bien qu'assez faible n'est pas négligeable surtout si nous sous-estimons $h_\infty$ lui-même.

(ii) *Détermination expérimentale de $h_0$.* Les diagrammes $B(H, t)$ des Figs. 9 à 11 sont limités à des champs d'induction de 60 G, mais nous avons étendu le domaine de mesures de $h_0$ bien au-delà vers les hautes inductions. Sur un échantillon contenant 0,0075 pour-cent de carbone en particulier, nous avons effectué des mesures jusqu'à $B = 6000$ G. Les dernières déterminations sont d'ailleurs difficiles car la variation relative d'induction, constamment décroissante à mesure que $B$ augmente, n'est plus alors que de l'ordre de 3 à 4 pour-cent. Pour éviter les erreurs d'étalonnage du circuit de mesures, nous opérons de la façon suivante. L'échantillon soigneusement désaimanté reste au repos à une température égale à $-33{,}5°$C pendant 1000 min. Nous appliquons ensuite le champ $H$ et nous lisons une déviation $\delta$ du galvanomètre. Nous effectuons immédiatement une série de désaimantations suivies à 15 sec de nouvelles mesures. Pour ces mesures, nous réglons le courant dans l'enroulement primaire du tore jusqu'à obtenir la même élongation $\delta$ que précédemment. Nous calculons $h_0$ à partir de la différence entre les deux courants d'excitation qui sont évalués, quant à eux, par une méthode potentiométrique et connus par conséquent avec toute la précision souhaitable. Les erreurs sur $h_0$ ne sont dues pratiquement qu'à l'irreproductibilité des états stabilisés.

(iii) *Résultats.* Nous avons porté ci-contre (Fig. 13a et 13b) les valeurs de $h_0$ obtenues. Le champ fictif commence par croître linéairement avec $B_0$, passe par un maximum très aplati puis décroît vers une valeur non nulle pratiquement atteinte pour $B_0 = 2000$ G. L'équation (17) permet effectivement d'expliquer un tel comportement.

§—Pour les faibles déplacements de parois $f(u)$ étant proportionnel à $u$, $f(\gamma B_0)$ et $h_0$ sont bien proportionnels à $B_0$ (Fig. 13a).

§—Pour les grands déplacements de parois, $f'(u)$ est égal à l'unité tandis que $f''(u)$ est nul. Le champ de traînage observé, uniquement dû aux parois à 90°, est effectivement constant pour des inductions supérieures à 2000 G (Fig. 13b).

§—Aux inductions moyennes, comprises entre 10 et 200 G, le champ de traînage passe par un maximum grâce à la contribution des parois à 180°.

Nous avons confirmé cette interprétation en cherchant l'ordre de grandeur du déplacement des parois à 180° quand on observe une induction

VOL 7 195

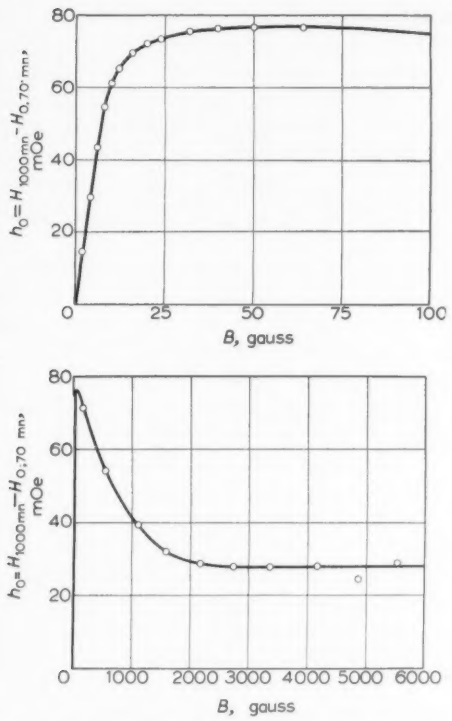


FIG. 13. Variation du champ de traînage $h_0$ en fonction de $B$ $c = 0{,}0075$ pour-cent, temperature: $-33{,}5°C$.
(a) faibles inductions
(b) inductions moyennes ou grandes.

moyenne $B_0 = 600$ G. Après polissage électrolytique d'un échantillon désaimanté, nous avons mis en évidence les domaines élémentaires par la méthode des figures de BITTER. Sur quelques cristaux convenablement orientés, nous avons observé la structure en feuillets bien connue, l'épaisseur $e$, de ces feuillets variant de 7 à 10 $\mu$ environ. Avec une telle structure, deux parois voisines à 180° se déplacent en sens contraire sous l'effet d'un champ appliqué. L'aimantation change de signe pour un déplacement de paroi égal à la largeur d'un domaine, de $-e/2$ à $+e/2$. Quand l'aimantation du cristal change de signe, compte tenu de son orientation quelconque par rapport au champ de mesure, l'induction moyenne passe de $-12000$ G à $+12000$ G soit une variation totale de 24 000 G. Une induction de 600 G doit donc correspondre à un déplacement $e/40$ environ d'une paroi à 180°, soit 2 000 Å, en accord avec la théorie (Fig. 2).

(iv) *Application: Perméabilités comparées des parois* à 180° *et* 90°. Le traînage magnétique de diffusion permet donc de différencier les parois selon leur nature. Quand l'induction moyenne de la substance dépasse 2000 G, la Fig. 13 montre que la contribution des parois à 180° dans $h_0$ est nulle et celle des parois à 90° constante. Moyennant quelques hypothèses simplificatrices, nous pouvons en tirer le rapport des perméabilités respectives $\mu''$ et $\mu'$ des parois à 180° et 90°.

Appelons $h'$ le champ de traînage moyen relatif aux seules parois à 90° ($h''$, pour les parois à 180°, étant nul). Aussitôt désaimantation, nous avons :

$$B_0 = (\mu' + \mu'')H_0. \tag{19}$$

Après stabilisation, nous retrouvons la même induction $B_0$ en appliquant un champ $H_0 + h_0$. Dans ces conditions, les parois à 90° sont soumises à un champ réel: $H_0 + h_0 - h'$. D'où :

$$B_0 = (\mu' + \mu'')H_0 = \mu'(H_0 + h_0 - h') + \mu''(H_0 + h_0) \tag{20}$$

il en résulte :

$$1 + \frac{\mu''}{\mu'} = \frac{h'}{h_0}. \tag{21}$$

Nous avons mesuré $h_0$ et nous pouvons calculer une valeur maximum de $h'$ en supposant, pour ces valeurs élevées de l'induction moyenne $f'(u) = \pm 1$ pour toutes les parois. Pour chacune d'elles, nous obtenons donc la relation :

$$h_\infty \cdot J_s |\cos\phi_1 - \cos\phi_2| = W_0, \tag{22}$$

où $\phi_1$ et $\phi_2$ désignent les angles que font les aimantations $\boldsymbol{J}_1$ et $\boldsymbol{J}_2$ avec $\boldsymbol{H}$. La valeur moyenne de $|\cos\phi_1 - \cos\phi_2|$ pour toutes les parois dans un polycristal vaut $\frac{1}{2}$ d'où :

$$h' = \frac{2W_0}{J_s}. \tag{23}$$

Malheureusement, nous ne connaissons pas $W_0$. Si nous posons $W_0/Js = (h_\infty)_{max}$ nous obtenons finalement d'après les mesures (Fig. 13b) $\mu''/\mu' = 4{,}5$. Sur un autre échantillon, contenant $10^{-5}$ de carbone seulement, nous avons obtenu en partant des mêmes hypothèses : $\mu''/\mu' = 4{,}2$. Il ne faut pas sous-estimer la fragilité de ce résultat qui dépend beaucoup trop de $W_0$ pour qu'on puisse le considérer autrement que comme une simple indication.

(v) *Forme de* $(\mu_0-\mu_\infty)/\mu_\infty$ *en fonction du champ de mesure.* Dans un travail remarquable déjà ancien, WEBB et FORD[8] ont introduit ce que nous appellerons la variation relative de perméabilité. Considérons un échantillon présentant du traînage de diffusion. Nous mesurons sa perméabilité magnétique dans un champ $H$, d'une part, aussitôt la désaimantation (soit $\mu_0$ la valeur obtenue), d'autre part après la stabilisation complète (soit $\mu_\infty$ cette seconde valeur). La variation relative de perméabilité est la quantité sans dimensions suivante : $(\mu_0-\mu_\infty)/\mu_\infty$, dont nous nous proposons l'étude en fonction du champ $H$ appliqué.

L'expérience montre que ce rapport croît à partir d'une valeur finie jusqu'à une valeur maximum, puis décroît ensuite rapidement en tendant vers zéro. Un tel comportement s'explique clairement si nous nous reportons à un diagramme $B(H, t)$ comme celui de la Fig. 9 par exemple.

On y voit que $\mu_\infty$ est constant quand le champ $H$ appliqué est inférieur à 40 mOe. La variation relative de perméabilité croît donc dans les champs faibles parce que $\mu_0$ lui-même est une fonction croissante. Pour les champs supérieurs à 60 mOe d'autre part, $B_0-B_\infty$ est pratiquement constant et $(\mu_0-\mu_\infty)/\mu_\infty$ décroît comme $1/\mu_\infty$ c'est-à-dire beaucoup plus rapidement que $1/H$.

Le maximum de $(\mu_0-\mu_\infty)/\mu_\infty$ est obtenu précisément au coude de la courbe isochrone $t = \infty$. La forme des diagrammes $B(H, t)$ explique donc non seulement l'allure de $(\mu_0-\mu_\infty)/\mu_\infty$ mais encore la position de son maximum, indépendante de la température. Soit $H_M$ le champ pour lequel nous observons ce maximum. On peut s'attendre à trouver le produit $\mu_\infty H_M$ indépendant de la nature des atomes qui diffusent, et grossièrement constant pour des supports ferromagnétiques voisins. En effet, d'après l'interprétation précédente, le produit $\mu_\infty H_M$ est égal à l'induction qu'on observe au coude de la courbe isochrone $B(H, t = \infty)$. Pour cette valeur de l'induction, on a un déplacement moyen donné des parois de BLOCH, en rapport avec leur propre épaisseur. Si $S$ représente la surface des parois et $u$ leur déplacement, $\mu_\infty \cdot H_M$ est proportionnel à $J_s S u$, où $J_s$ et $u$ sont imposés par la nature même du corps ferromagnétique. $\mu_\infty H_M$ varie donc comme $S$, c'est-à-dire assez peu, car la taille des domaines élémentaires reste du même ordre de grandeur dans la plupart des substances polycristallines courantes de même nature. Cette propriété du produit $\mu_\infty H_M$ remarquée par WEBB et FORD dans leur mémoire, n'avait reçu jusqu'à présent aucune explication. Pour d'autres valeurs de l'épaisseur des parois et de l'aimantation à

*Tableau* 1

| Auteurs | Nature de la substance (l'élément qui diffuse est inconnu) | $H_M$ (Oe) | $\mu$ (G/Oe) | $\mu_\infty H_M$ (G) |
|---|---|---|---|---|
| WEBB et FORD[8] | Tôles de transformateur | 0,02 | 350 | 7 |
| ,, ,, | Fer électrolytique | 0,04 | 302 | 12 |
| ,, ,, | Fer suédois | 0,03 | 183 | 5,5 |
| ,, ,, | Fer–Si faible teneur | 0,03 | 284 | 8,5 |
| ,, ,, | ,, ,, ,, | 0,02 | 292 | 6 |
| ,, ,, | ,, ,, ,, | 0,06 | 332 | 20 |
| ,, ,, | Fer–Si (forte teneur en Si) | 0,025 | 327 | 8 |
| ,, ,, | ,, ,, | 0,02 | 435 | 9 |
| ,, ,, | ,, ,, | 0,018 | 428 | 8 |
| ,, ,, | ,, ,, | 0,018 | 409 | 7 |
| ,, ,, | ,, ,, | 0,038 | 400 | 15 |
| ,, ,, | ,, ,, | 0,009 | 516 | 5 |
| ,, ,, | ,, ,, | 0,018 | 450 | 8 |
| ,, ,, | ,, ,, | 0,018 | 513 | 9 |
| ,, ,, | Fer–Al | 0,06 | 163 | 10 |
| FERRO et MONTALENTI[9] | Fer–Si | 0,014 | 600 | 8,4 |
| WEBB et FORD[8] | Fer–Ni (50 pour-cent) | 0,013 | 2120 | 28 |
| FERRO et MONTALENTI[9] | Fer–Ni | 0,0125 | 3000 | 37 |

saturation $J_s$, dans un alliage fer–nickel par exemple, on trouve des valeurs de $\mu_\infty H_M$ nettement différentes. Ce comportement est illustré par le tableau 1 où nous avons rassemblé les résultats de WEBB et FORD[8] d'une part, et de FERRO et MONTALENTI[9] d'autre part. La dispersion des constantes de temps de traînage ne nous semble donc pas à prendre en considération pour expliquer l'allure de la variation de perméabilité $(\mu_0 - \mu_\infty)/\mu_\infty$ dans les champs faibles. Enfin, si nous voulons mettre en évidence dans un champ donné un processus de désaccommodation difficilement observable, nous aurons intérêt à réaliser des conditions de mesure telles que le produit $\mu_\infty H$ soit de l'ordre de 10 G dans le cas d'un support ferromagnétique voisin du fer pur, et cela, indépendamment de l'impureté qui diffuse.

(j) *Variation de* $h_0$ *avec la concentration en carbone : determination de* $W_0$

$W_0$ étant par définition proportionnel à la concentration en carbone $c$ de la solution solide, si on suppose dans tous les échantillons une même répartition des forces de rappel des différentes parois de BLOCH, le champ total de traînage $h_\infty$ doit être proportionnel lui aussi à $c$ pour chaque valeur de $B$. Nous avons donc mesuré $(h_0)_{max}$ pour différentes substances. Nos résultats consignés dans la Fig. 14 montrent que cette proportionnalité est bien

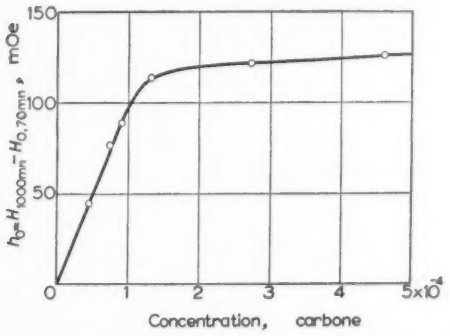


FIG. 14. Variation du champ de traînage $h_0$ en fonction de la concentration en carbone des échantillons ($B$ = 50 G environ, température: −33,8°C).

assurée à la précision des expériences pour des concentrations inférieures à 0,013 pour-cent. Au delà de cette valeur, la limite de solubilité du carbone est atteinte dans les conditions de préparation des échantillons et, la concentration de la solution n'augmentant plus, $(h_0)_{max}$ reste pratiquement stationnaire. Le carbone précipité n'intervient donc pas dans le traînage magnétique. Les variations de résistance observées confirment la valeur trouvée pour la solubilité du carbone au voisinage de 700°C.

Nous avons souligné précédemment l'impossibilité d'obtenir rigoureusement l'énergie de stabilisation $W_0$ à partir de la mesure de $h_\infty$ étant donné son caractére statistique. Pour une paroi telle que l'aimantation $J_1$ soit parallèle au champ de mesure, nous savons que :

$$(h_\infty)_{max} \cdot J_s = W_0. \qquad (18)$$

En présence d'un grand nombre de parois, nous devons compter avec des orientations de $J_1$ et $J_2$ quelconques et des déplacements qui peuvent être très différents sous l'effet d'un même champ extérieur. Or, il faut bien voir que ces deux facteurs jouent en sens opposés sur $h$. La diversité des orientations des parois de BLOCH tend à faire croître la valeur de $(h_\infty)_{max}$. La valeur limite $2W_0/J_s$ calculée précédemment ne se rapporte toutefois qu'au cas où tous les déplacements des parois permettent de réaliser simultanément la condition $f(u)$ = maximum. Cette condition n'est certainement pas remplie aux inductions moyennes de quelques dizaines de gauss. Les parois qui ont une orientation défavorable ou qui sont douées de forces de rappel assez élévées, se déplacent alors très peu et, $f(u)$ étant petit, leur contribution au champ total de traînage reste négligeable. Pour des inductions plus élevées, les parois à 180° les plus mobiles se déplacent suffisamment pour que $f''(u)$ s'annulant, elles ne soient plus soumises à aucune pression de traînage. Tout se passe donc comme si le champ total de traînage $h_\infty$ n'était dû pour chaque induction, qu'à la contribution d'un nombre limité de parois de BLOCH. Plus la dispersion de leurs déplacements dans un champ extérieur donné est grande, plus le maximum du champ de traînage est aplati.

En réalité, de ces deux facteurs qui provoquent l'étalement du maximum de $h_\infty$, le premier au moins est commun à toutes les substances polycristallines; seul, le deuxième peut varier d'une substance à l'autre. Il est difficile de dire à priori lequel d'entre eux est prépondérant.

Nous arrivons ainsi à la conclusion suivante : un certain champ total de traînage $(h_0)_{max}$ n'est pas

caractéristique d'une impureté dans un corps ferromagnétique à une concentration donnée. Il dépend aussi, mais dans une mesure à déterminer, de l'étalement du spectre des forces de rappel des parois de BLOCH vers leurs positions d'équilibre.

Dans l'hypothèse la plus simple, nous retiendrons la formule (18) pour estimer l'ordre de grandeur de $W_0$. Avec 0,0046 pour-cent de carbone en solution, nous obtenons alors $W_0 = 88$ ergs/cm$^3$; c'est là une énergie considérable pour le petit nombre des atomes de carbone mis en jeu : $1{,}8 \cdot 10^{19}$ par cm$^3$. D'où il résulte une énergie de couplage $w$ par atome de carbone :

$$w = \sqrt{W_0 \cdot 3kT/c} = 0{,}71 \cdot 10^{-15}\,\text{erg} = 0{,}44 \cdot 10^{-3}\,\text{eV}.$$

Cette valeur est remarquablement voisine de celle proposée par NÉEL pour justifier sa théorie ($0{,}6 \cdot 10^{-15}$erg.)

(k) *Etude de la fonction de traînage* $G(t)$

(i) *Détermination expérimentale.* Nous déterminons une fonction de traînage $G(t)$ expérimentale à partir d'un diagramme $B(H, t)$. D'après l'interprétation précédente :

$$G(t) = h(t)/h_\infty \qquad (24)$$

$h$ étant une fonction de $B_0$, nous pouvons procéder à une infinité de déterminations de $G(t)$. La théorie prévoit en principe des résultats identiques pour chaque valeur de $B_0$.

Nous avons remarqué précédemment la nécessité d'utiliser un spectre étalé de constantes de temps pour rendre compte des faits expérimentaux. Nous cherchons donc la répartition logarithmique qui s'accorde le mieux avec nos mesures, en première approximation. Appelons $\theta_1$ et $\theta_2$ les limites inférieure et supérieure du spectre. Nous définissons en outre une constante de temps moyenne

$$\theta_0 = \sqrt{\theta_1 \cdot \theta_2} = C \exp(W_{a0}/kT)$$

et une largeur de spectre : $k^2 = \theta_2/\theta_1$.

D'après la définition de $G(t)$ nous obtenons alors :

$$G(t) = 1 + \frac{1}{2 \log k}\left[Ei\left(-\frac{t}{k\theta_0}\right) - Ei\left(-\frac{kt}{\theta_0}\right)\right]. \qquad (25)$$

Nous avons représenté sur la Fig. 15, plusieurs fonctions $G(t)$ pour différentes valeurs du paramètre $k (k = 1, 3, 5, 10)$. Nous utilisons en abscisses

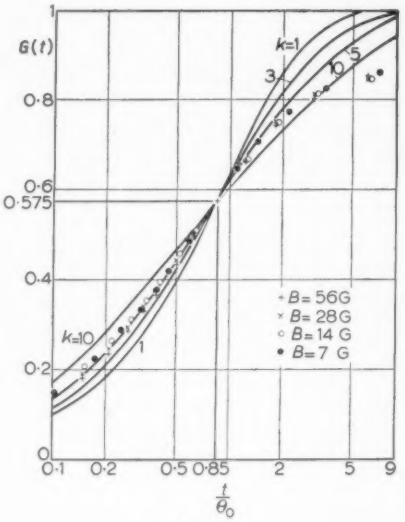


FIG. 15

un temps réduit $t/\theta_0$. Toutes ces courbes possèdent pratiquement en commun le point

$$\begin{cases} G(t) = 0{,}575 \\ t/\theta_0 = 0{,}85 \end{cases}$$

quelle que soit la valeur du paramètre $k$.

Pour déterminer $\theta_0$ et $k$ qui caractèrisent le mieux une fonction $G(t)$ expérimentale, nous procédons donc de la façon suivante. Soit $t_0$ le temps pour lequel $G(t_0) = 0{,}575$.

$$\theta_0 = t_0/0{,}85.$$

Nous obtenons ensuite une évaluation grossière du paramètre $k$ en reportant sur la Fig. 15 les valeurs expérimentales de $G(t)$.

(ii) *Résultats.* Pour la solution solide qui a fait l'objet des diagrammes $B(H, t)$ précédents (Figs. 9–11), nous obtenons les valeurs suivantes de la constante de temps moyenne $\theta_0$ :

*Tableau* 2

| $B$ (G) | $\theta_0$ (min) | | |
|---|---|---|---|
| | −21,3°C | −27,3°C | −33,8°C |
| 3,5 | 4,6 | 10,5 | 28 |
| 7 | 5,8 | 14,1 | 44 |
| 14 | 6,2 | 16,1 | 46 |
| 28 | 6,5 | 16,7 | 47 |
| 56 | 6,6 | 16,7 | 47 |

Nous avons porté sur la Fig. 15 les valeurs expérimentales de $G(t)$ déterminées à $-27{,}3$°C pour différentes valeurs de $B$. Une largeur du spectre $k^2 = 25$ est en bon accord avec ces points, mais pour les 3/4 de l'évolution totale seulement. Dans les temps longs, l'évolution de $G(t)$ est très lente. Cet effet souligne la présence de grandes constantes de temps, plus nombreuses qu'il n'est prévu par une répartition logarithmique.

(iii) *Etude des constantes de temps moyennes* $\theta_0$. Les valeurs de $\theta_0$ proposées précédemment peuvent difficilement être considérées comme caractéristiques du traînage de diffusion du carbone dans le fer, étant donné leur extrême sensibilité à la température. Nous avons observé en outre des variations inexpliquées entre deux échantillons qui peuvent atteindre 10 à 15 pour-cent. Une telle incertitude reste d'ailleurs négligeable devant la variation systématique de $\theta_0$ avec les déplacements moyens des parois d'une part, et d'autre part, devant l'étendue du spectre des constantes de temps.

L'expérience montre que $\theta_0$ croît avec $B_0$ et tend vers une limite pratiquement atteinte pour $B_0 = 20$ G. Aucune variation ultérieure n'a pu être décelée, même en poussant les mesures dans un cas jusqu'à une induction $B_0 = 355$ G. Quelle que soit la concentration de la solution solide, la variation de $\theta_0(B_0)$ garde la même allure.

Pour interpréter ces constations, il faut introduire une relation entre les constantes de temps de diffusion du carbone $\theta$ et la nature des éléments de volume balayés par les parois de BLOCH pendant leurs déplacements. On peut penser par exemple que la paroi se trouve à l'état désaimanté au moins partiellement dans une région perturbée du cristal. Quand on applique le champ de mesure, la paroi s'écarte de la zone perturbée et gagne une région de «bon cristal» où la diffusion est plus lente, les barrières de potentiel entre les sites voisins étant plus hautes. Toutes les parois quittent pratiquement la zone perturbée dès qu'on enregistre une variation d'induction de 20 G. Comme d'autre part, nous avons montré que *toutes* les parois se déplacent d'au moins leur propre épaisseur quand on enregistre une variation d'induction de 2 000 G, la zone de «mauvais cristal» s'étendrait au maximum à 1/100 d'épaisseur de paroi de part et d'autre du plan central de celle-ci, soit 6 à 7 distances interatomiques environ. Nous obtenons ainsi l'étendue maximum du défaut de réseau qui fixerait la paroi à l'état désaimanté.

(iv) *Etude de la dispersion des constantes de temps.* Une répartition logarithmique des constantes de temps ne rend compte que très imparfaitement de la diffusion observée puisque les points expérimentaux s'écartent notablement de la courbe théorique dès que $t/\theta_0$ devient plus grand que 2. En d'autres termes, si les 3/4 environ de la croissance du champ fictif sont assez bien représentés au moyen d'une répartition logarithmique de dispersion $\theta_2/\theta_1$ voisine de 25, il existe en outre des constantes de temps notablement plus grandes que prévu et nous avons cherché à déterminer directement les limites du spectre. Nous considérons pour cela la fonction $[1-G(t)]$ comme équivalente à la superposition de $n$ fonctions simples de la forme : $\exp(-t/\theta)$ où $\theta$ varie d'une façon discontinue. La pente, en un point d'abscisse $t_0'$ de la courbe représentative de la fonction $\log[1-G(t)]$ en fonction de $t$ est alors égale, au signe près, à l'inverse de la constante de temps dont l'effet prédomine au temps $t_0'$ considéré. Nous avons appliqué cette méthode à la recherche des valeurs $\theta_{max.}$ et $\theta_{min.}$ qui prédominent respectivement pour $B_0 = 28$ G quand $G(t_0') = 0{,}9$ et pour $B_0 = 3{,}5$ G quand $G(t_0') = 0{,}1$. Nous avons obtenu les résultats suivants :

| Températures | $-21{,}3$°C | $-27{,}3$°C | $-33{,}8$°C |
|---|---|---|---|
| $\theta_{min.}$ (min) | 3,5 | 6,0 | 11,3 |
| $\theta_{max.}$ (min) | 270 | 920 | 3390 |

Il est normal de trouver $\theta_{min.}$ notablement supérieur à $\theta_0/5$ car la répartition logarithmique paraît constituer une assez bonne approximation en début d'évolution et $G(t_0') = 0{,}1$ ne représente précisément pas ce début. Par contre la valeur de $\theta_{max.}$ est très supérieure à 5 $\theta_0$ comme il fallait s'y attendre.

Nous avons vérifié en outre que chacune des constantes de temps proposées précédemment varie avec la température selon une loi de la forme :

$$\theta = C \exp(W_a/kT) = C \exp(Q/RT). \qquad (1)$$

Les différentes énergies d'activation $W_a$ représentent autant de hauteurs des barrières de potentiel entre deux sites voisins.

Les énergies nécessaires pour passer d'un site à un autre site voisin sont donc considérables par

*Tableau* 3

| | $\theta_{min.}$ | $\theta_0(B_0 = 3{,}5$ G) | $\theta_0(B_0 = 56$ G) | $\theta_{max.}$ |
|---|---|---|---|---|
| Température d'activation $W_a/k$(0°K) | 5.675 | 8.650 | 9.460 | 12.200 |
| Energies d'activation Q (cal/mole) | 11.300 | 17.200 | 18.800 | 24.300 |
| Energies $W_a$ (eV) | 0,49 | 0,745 | 0,815 | 1,05 |

rapport à l'énergie de couplage $w$ introduite par NÉEL. Nous rappelons que nous avons obtenu $w$ de l'ordre de 0,001 eV.

Si nous confrontons ces résultats avec ceux publiées antérieurement sur cette question, nous trouvons un excellent accord. Là où SNOEK trouve une température d'activation de 8·700°K[2] nous avons obtenu 8.650°K. Le traînage mécanique étudié par le même auteur[15] conduit à une température d'activation de 9.200°K qu'il faut rapprocher de notre propre résultat pour les grands déplacements de parois : 9.460°K. Le traînage mécanique intéresse en effet, tout le cristal simultanément et non pas seulement des régions plus ou moins perturbées autour des positions de repos des parois de BLOCH. Enfin, RICHTER[1] a obtenu une énergie d'activation egale à 10 200°K en utilisant uniquement la fin du processus d'évolution du traînage à chaque température. Son résultat s'inscrit en bonne place à l'intérieur des limites auxquelles nous avons été conduits.

En résumé, nous avons mis en évidence un spectre de constantes de temps très étalé en opérant sur un fer particulier. Dans ces conditions, la dispersion des résultats fournis antérieurement par les différents auteurs nous semble avoir une origine physique et non pas accidentelle. D'après ces expériences, on ne peut pas parler de constantes de temps ou d'énergies d'activation moyennes pour la diffusion d'un hétéroatome sans préciser de quelle manière elle sont obtenues.

## 6. COMPORTEMENT DES SOLUTIONS SOLIDES DE CARBONE DANS UN CHAMP SINUSOIDAL

Au cours du paragraphe précédent, nous avons vu qu'on pouvait rendre compte du traînage en imaginant la présence d'une seule paroi de BLOCH de nature non précisée et soumise à un champ de traînage $h$ représenté sur les Figs. 13a et 13b. Nous rappelons que ce champ de traînage croît linéairement avec $B$ jusqu'à des inductions de l'ordre de 7 à 8 G. A partir de 15 à 20 G et jusqu'à 200 ou 300 G, $h$ garde une valeur pratiquement constante. Il s'agit là précisément de deux cas particuliers développés par NÉEL dans sa théorie et appelés par lui cas des déplacements de paroi de petite amplitude et cas des déplacements de grande amplitude. Nous pouvons donc confronter sur deux points la théorie et l'expérience, d'une part dans les champs faibles en limitant l'induction dans notre échantillon à une valeur de l'ordre de 7 G, d'autre part, dans les champs forts pour des inductions maxima de l'ordre de 200 à 300 G. Nous appliquerons dans ce dernier cas à l'ensemble des parois de BLOCH les formules établies par NÉEL pour les seules parois à 90°.

### (a) *Trainage dans les champs faibles*

Soit un échantillon de fer contenant en solution solide des traces de carbone, maintenu en permanence à une température inférieure à l'ambiante pour éviter toute précipitation de la solution métastable. A −20°C les constantes de temps de traînage $\theta$ sont au moins de l'ordre de la minute. Nous désaimantons cette substance au temps $t = 0$, et nous lui appliquons au temps $t_1$ un champ alternatif sinusoïdal de la forme :

$$H = H_m \cos(\omega t + \phi). \qquad (27)$$

Pour que l'effet des courants induits soit négligeable, nous utilisons une fréquence aussi basse que possible, la limite inférieure imposée par le générateur et les circuits de mesure étant de l'ordre de 20 Hz. Dans ces conditions, nous trouvons $\omega\theta$ de l'ordre de $10^{+4}$ et l'étude du traînage aux faibles amplitudes perd tout intérêt.

En effet, l'expérience montre que les déplacements des parois de BLOCH sont alors réversibles, d'où :

$$B = B_m \cos(\omega t + \phi) \text{ avec } B_m \leqslant 7\text{G}. \qquad (28)$$

Nous ne pouvons obtenir la pression de traînage que par une méthode d'approximations successives. Le terme d'ordre 0 a été calculé par NÉEL.

Appliquons directement son résultat avec $\omega\theta \gg 1$:

$$P(u_0, t) = -\frac{2W_0 u_0}{3d}\left[1-\exp\left(-\frac{t}{\theta}\right)\right]\cos(\omega t+\phi) \tag{29}$$

où $d$ est une distance égale à 160 Å dans le fer. La première approximation de la pression de traînage étant en phase avec $B$, la $n^{\text{ième}}$ l'est également. Le champ alternatif de traînage provoque dans ce cas particulier une variation monotone de perméabilité indépendante de $t_1$, sans introduire aucun déphasage sensible de l'induction sur le champ appliqué. Il ne permettrait pas, par conséquent, d'expliquer des pertes résiduelles du type de celles mises en évidence par JORDAN.

(b) *Traînage-dans-les champs forts*

Examinons dans les champs forts le comportement de la paroi de BLOCH fictive que nous avons introduite précédemment. Appelons $u_0$ sa position d'équilibre aussitôt désaimantation, position repérée par celle de son plan médian par exemple. Pour déplacer cette paroi, il faut vaincre une pression d'opposition $R(u)$ qui, pour de faibles déplacements, fluctue également, en première approximation, de part et d'autre d'une valeur moyenne nulle. A l'image d'un schéma utilisé par LLIBOUTRY[6] pour rendre compte de l'interprétation par NÉEL des lois de RAYLEIGH, nous la représentons par une ligne brisée, dessinée en pointillé sur la Fig. 16a, l'axe $u$ étant vertical et l'axe $R$ horizontal. Supposons maintenant la paroi immobile dans la position $u_0$ pendant un temps $t_1$ très grand devant les constantes de temps de diffusion. La paroi se stabilise dans la position $u_0$ et la pression de traînage $P(u, t_1)$ vient s'ajouter à l'opposition $R(u)$ (équation (8)). Nous nous proposons de rendre compte de cet état stabilisé en introduisant une nouvelle opposition $R'$ de forme convenable. $R'$, dessiné en traits discontinus, contient donc la pression de traînage $P(u, t_1)$.

D'après certains résultats antérieurs, nous savons que pour $u$ compris entre $u_0$ et une certaine valeur $u_1$ pour laquelle nous mesurons une induction moyenne $B$ de l'ordre de 10 G, l'écart entre $R$ et $R'$ est proportionnel à $u-u_0$. Quand $u$ est supérieur à $u_1$, l'écart entre $R$ et $R'$ est constant et égal à $W_0 = h_\infty \cdot J_s$. Cette partie de la nouvelle fonction d'opposition $R'$ résulte donc d'une translation pure et simple de la partie de $R$ correspondante.

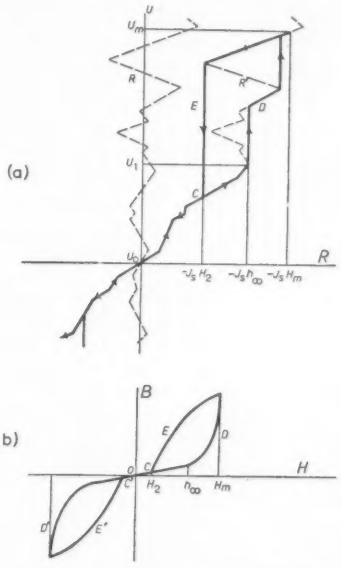


FIG. 16. Interprétation des cycles d'hystérésis ((étranglés)).

Appliquons à cet échantillon stabilisé un champ extérieur $H = H_m \cos(\omega t+\phi)$, la paroi se déplace jusqu'à obtenir un équilibre entre la pression $HJ_s$du champ extérieur et l'opposition $R'(u)$; l'équilibre étant stable si $dR'/du > 0$. Le point représentatif du mouvement de la paroi $u(H)$ n'a donc accès qu'à certaines parties de la courbe $R'(u)$.

Pour $H_m < h_\infty$ la pression du champ extérieur reste toujours inférieure à $W_0$, et le déplacement de la paroi plus petit que $u_1$. L'expérience conduit alors à une perméabilité magnétique constante (Figs. 9–11). L'aimantation prise par la substance est exclusivement reversible. Nous en avons tenu compte pour le tracé de la portion correspondante de la courbe $R'$. En aucun de ses points, elle ne comporte une pente $dR'/du$ négative.

Pour $H_m > h_\infty$, le déplacement de la paroi est supérieur à $u_1$ et compte un certain nombre de sauts de BARKHAUSEN. Sur une alternance positive du champ, le point représentatif du mouvement de la paroi décrit une portion de cycle, tel que $U_0CDECU_0$, indiquée en trait gras.

Un déplacement $u$ de la paroi entraînant une aimantation $B$ proportionnelle à $u$, le cycle en question représente en réalité une moitié de cycle d'hystérésis élémentaire, ramenée à des échelles convenables. Ainsi, le cycle d'hystérésis à l'état stabilisé, doit nous apparaître, comme formé de deux boucles décalées l'une par rapport à l'autre dans la direction du champ (Fig. 16b).

Nous avons effectivement rencontré systématiquement cet aspect (Fig. 17) signalé en premier lieu par FELDTKELLER[12] et nous dirons que nous avons obtenu des cycles d'hystérésis «étranglés»

(c) *Etude des cycles d'hystérésis «étranglés»*

(i) *Dispositif expérimental.* Nous avons pris toutes précautions pour définir avec précision nos conditions expérimentales. Tous nos essais sont effectués à une température de $-21{,}3°C$. Nous alimentons l'enroulement primaire du tore à travers un filtre sélectif LC sans fer, par un générateur basse fréquence stabilisé du type RC. Le générateur nous fournit un courant sinusoïdal avec une distorsion très inférieure à 1 pour cent dans les conditions d'utilisation. Il ne nécessite donc aucune correction. Nous intégrons la tension aux bornes de l'enroulement secondaire du tore à l'aide d'un circuit RC classique de constante de temps égale à 1,2 sec, la fréquence du fondamental étant généralement $f = 28$ Hz.

La tension intégrée est connectée à l'entrée d'un excellent oscillographe dont les amplificateurs n'introduisent aucun déphasage sensible dans les conditions d'expériences et possèdent une bande passante très supérieure à nos besoins.

(ii) *Résultats.* Le champ $H$ étant appliqué au temps $t_1$, nous suivons l'évolution du cycle d'hystérésis au cours du temps, toutes choses égales d'ailleurs. Nous obtenons à différentes époques $t_2$ les cycles étranglés de la Fig. 17 pour différentes valeurs de l'amplitude $H_m$ du champ appliqué. Une évolution très nette se manifeste au cours de laquelle l'étranglement initial disparaît progressivement, mais le cycle obtenu pour $t_2$ très grand ne s'identifie pas du tout avec le cycle normal à l'état désaimanté. Dans les limites où les courants induits restent négligeables, nous n'avons trouvé aucune influence notable de la fréquence de balayage sur la forme ou sur l'évolution du cycle.

Il est intéressant de constater les dispositions respectives des différents cycles d'hystérésis relatifs à l'état stabilisé, $H_m$ étant variable. Nous avons superposé Fig. 18 sur la même photographie dans la minute qui a suivi l'application du champ, plusieurs cycles relatifs à des amplitudes $H_m$ respectivement égales à : 79, 85, 93, 101, 106 et 112 mOe, après une stabilisation $t_1 = 30$ min. Malgré une dérive des amplificateurs de l'oscillographe qui a déplacé légèrement les cycles les uns par rapport aux autres, il apparaît sur cet ensemble que les parties $OD$ et $OD'$ (Fig. 16b) sont approximativement communes à tous les cycles quelle que soit la valeur de $H_m$. Nous expliquons ceci très simplement dans notre schéma d'interprétation (Fig. 16a). Le chemin $U_0CD$ est commun à tous les déplacements, puisque les petits déplacements autour de $U_0$ sont uniquement reversibles, tandis que les chemins $EC$ et $E'C'$ dépendent beaucoup de $H_m$.

La Fig. 19 résulte d'un montage réalisé à partir de la photographie précédente. Nous avons coupé la Fig. 18 suivant l'axe des abscisses et nous avons décalé les deux moitiés l'une par rapport à l'autre de 48 mOe environ. Ce décalage rétablit pour les différents cycles une disposition plus habituelle. Les phénomènes qu'on vient d'exposer peuvent donc être facilement interprétés en première approximation en supposant la présence d'un champ de traînage $\delta h(t_1)$ opposé au champ appliqué et représenté par une fonction en créneaux de même période que $H$. Pour $t_1 = 30$ min, ce champ $\delta h(t_1)$ conserve une valeur constante $\delta h_0 = \pm 24$ mOe à chaque alternance. Nous nous garderons bien d'assimiler $\delta h_0(t_1)$ et $h(t_1)$. Les mesures au galvanomètre balistique indiquent par exemple pour $t_1 = 30$ min un champ de traînage $h(t_1) = 43$ mOe.

La valeur $\delta h = \pm 24$ mOe mise en évidence précédemment ne représente d'ailleurs qu'un décalage moyen pour les différents cycles de la Fig. 18. La Fig. 16 a permet de prévoir que $\delta h$ décroît quand $H_m$ augmente, $t_1$ restant constant. En effet, comme la fonction d'opposition $R(u)$ fluctue également de part et d'autre de la valeur 0, $R'(u)$, pour $u > u_1$, fluctue également de part et d'autre de $W_0$, et, les déplacements de parois pour $u > u_1$ étant principalement des déplacements irréversibles, la boucle du cycle se referme au point $C$ pour un champ $H_2$ tel que statistiquement : $h_\infty - H_2 \# H_m - h_\infty$. Ainsi pour une solution contenant 0,0046 pour cent de carbone avec $h_\infty \neq 51$ mOe et $H_m = 102$ mOe, nous devons trouver $H_2 = 0$. L'expérience vérifie effectivement cette conclusion. Pour $H_m = 103$ mOe (Fig. 17) les points $C$ et $C'$ (Fig. 16b) sont confondus.

Il ne semble pas possible dans ces conditions

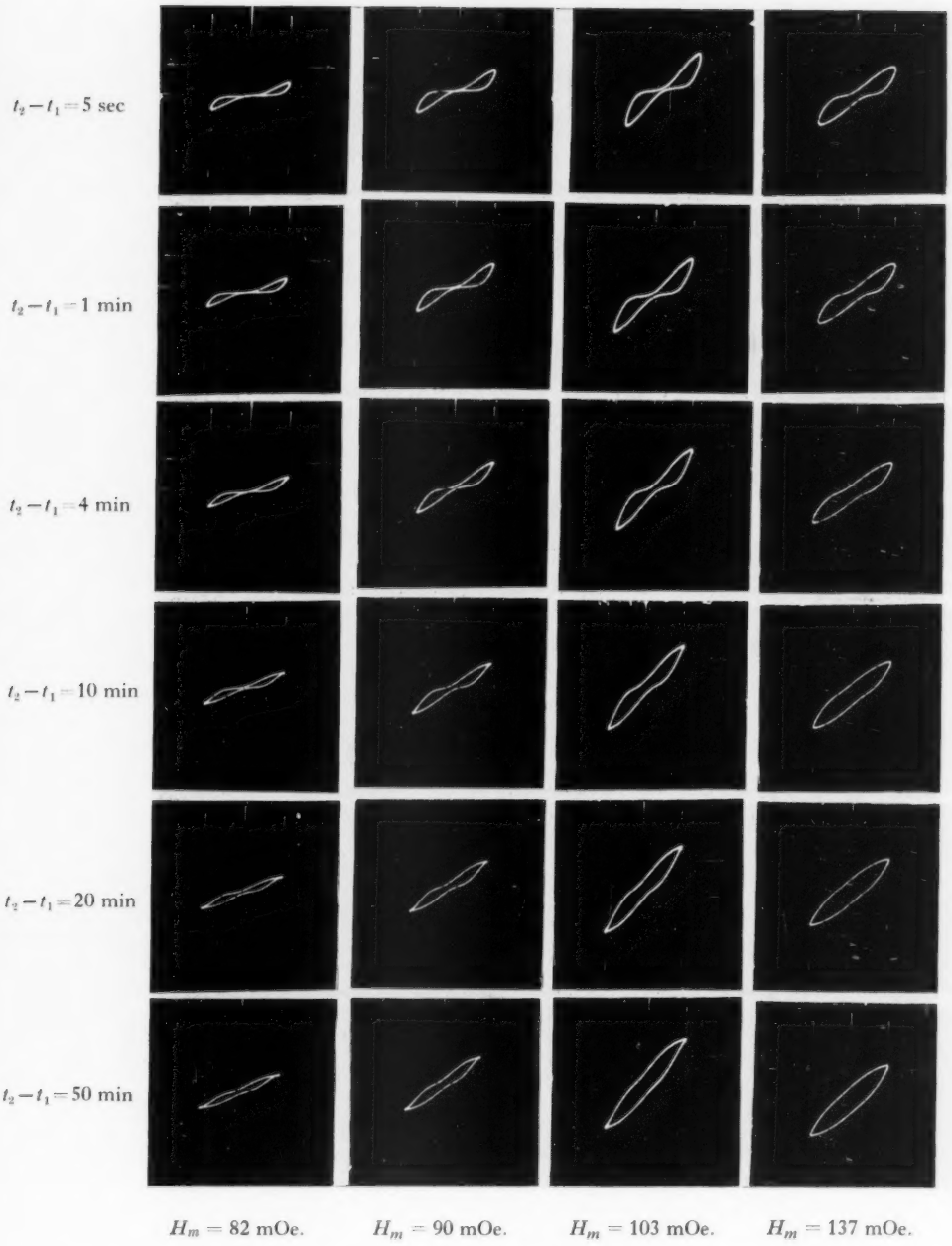


FIG. 17. Cycles d'hystérésis, après stabilisation, d'un échantillon de fer contenant des traces de carbone en solution. Température : $-21{,}3$°C, $c = 0{,}0046$ pour-cent, $t_1 = 10^3$ min.

*(facing page 44)*

FIG. 18

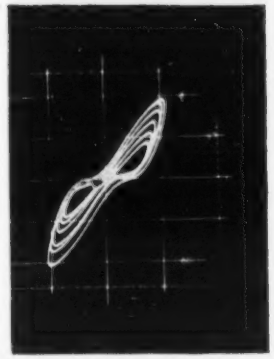

FIG. 19

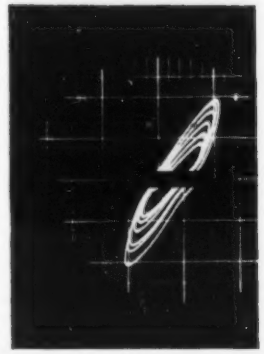

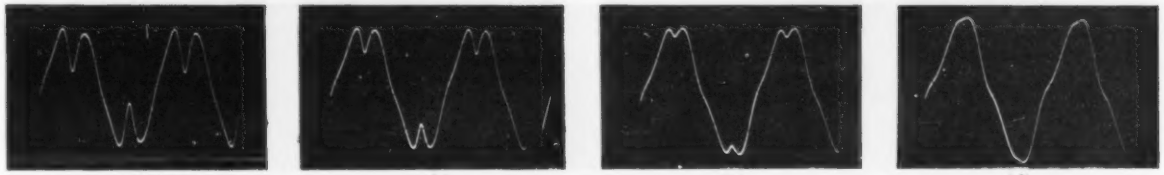

(a) (b) (c) (d)

FIG. 22. $V(t)$ pour différentes valeurs de $t-t_1$. Température : $-21{,}3°C$. $c = 0{,}0046$ pour-cent, $t_1 = 1080$ min.
(a) $t-t_1 = 0$ min; (b) $t-t_1 = 4$ min; (c) $t-t_1 = 12{,}5$ min; (d) $t-t_1 = 233$ min.

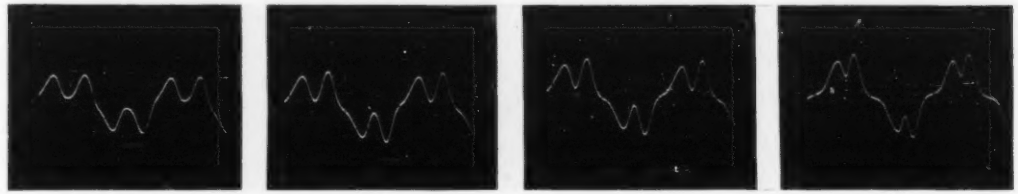

(a) (b) (c) (d)

FIG. 25. $V(t)$. Cas d'une solution saturée. $t_1 = 1000$ min; $H_m = 242$ mOe; $c = 0{,}027$ pour-cent.
(a) $t-t_1 = 0$ min; (b) $t-t_1 = 4$ min; (c) $t-t_1 = 10$ min; (d) $t-t_1 = 200$ min.

VOL.
7
1958

d'obtenir $\delta h = h_\infty$ sauf pour $H_m = h_\infty$, mais un tel cas particulier ne présente aucun intérêt car la théorie développée par NÉEL ne peut pas s'y appliquer, les déplacements de parois étant alors trop petits. Dans ces conditions, les phénomènes d'hystérésis excluent au départ toute interprétation quantitative des expériences, dans le but d'arriver jusqu'à l'énergie de stabilisation $W_0$.

Enfin, nous voulons souligner la parenté qui lie ces cycles étranglés aux cycles d'hystérésis des alliages du type Perminvar et de certains ferrites contenant de l'oxyde de cobalt[10] refroidis lentement au-dessous du point de Curie. NÉEL explique les propriétés des Perminvar en supposant un couplage entre la position des atomes de substitution du réseau et la direction de l'aimantation spontanée. Il s'agit donc du même mécanisme fondamental à l'échelle atomique que pour le traînage de diffusion. Seuls diffèrent l'ordre de grandeur des constantes de temps de diffusion d'une part, et les énergies mises en jeu d'autre part. Les difficultés qu'on rencontre pour obtenir l'énergie de stabilisation à partir du seul tracé du cycle d'hystérésis sont alors d'autant plus regrettables qu'une telle détermination présente certainement un grand intérêt technique.

(d) *Etude des harmoniques de l'induction*

(i) *Pression de traînage alternative.* Les cycles d'hystérésis étranglés que nous avons rencontrés précédemment montrent que l'induction magnétique dans ces échantillons est une fonction très complexe du temps. Nous avons rendu compte de l'état stabilisé en introduisant un champ de traînage $\delta h(t)$ représenté par une fonction en créneaux d'amplitude $\pm\delta h_0$. En toute rigueur $\delta h(t)$ reste constamment inférieur à $H$ en module, et sa dérivée première ne subit aucune discontinuité quand $B$ s'annule. Cette première approximation permet toutefois de prévoir l'évolution des phénomènes. On peut rapprocher en effet $\delta h(t)$ du champ de traînage qui s'exerce sur une paroi de BLOCH à 90°, animée d'un mouvement sinusoïdal de grande amplitude; et nous appliquerons directement le résultat obtenu par NÉEL dans ce dernier cas. Compte tenu de la condition $\omega\theta \gg 1$, il vient :

$$\delta h(t) = -\frac{4}{\pi}\delta h_0\Big\{[e^{-(t-t_1)/\theta} - e^{-t/\theta}]\times$$
$$\times(\cos\omega t - \tfrac{1}{3}\cos 3\omega t + \tfrac{1}{5}\cos 5\omega t - \ldots) +$$
$$+\frac{2}{\pi}(1-e^{-(t-t_1)/\theta})\times$$
$$\times(\cos\omega t + \tfrac{1}{9}\cos 3\omega t + \tfrac{1}{25}\cos 5\omega t + \ldots)\Big\} \quad (30)$$

En présence de nombreuses constantes de temps de traînage, nous avons posé par définition :

$$G(t) = \int_0^\infty (1-e^{-(t/\theta)})p(\theta)\,d\theta \quad (31)$$

d'ou : $$\delta h(t) = -\frac{4}{\pi}\delta h_0\Big\{[G(t)-G(t-t_1)]\times$$
$$\times(\cos\omega t - \tfrac{1}{3}\cos 3\omega t + \tfrac{1}{5}\cos 5\omega t - \ldots) +$$
$$+\frac{2}{\pi}G(t-t_1)(\cos\omega t + \tfrac{1}{9}\cos 3\omega t +$$
$$+\tfrac{1}{25}\cos 5\omega t + \ldots)\Big\}. \quad (32)$$

Ce résultat qui suppose un grand nombre d'approximations, ne paraît pas des plus faciles à exploiter. Comme l'a montré NÉEL,[4] le terme fondamental rend compte qualitativement des résultats de mesures de WEBB et FORD.[8] Nous confirmons cette interprétation. Pour $t_1$ suffisamment grand, la perméabilité apparente $\mu$ augmente d'une façon monotone conformément à l'équation (32). Mais l'effet de la composante fondamentale du champ de traînage $h(t)$ est alors difficile à séparer de l'effet du champ extérieur appliqué. Nous pouvons espérer par contre une mise en évidence plus directe des différents harmoniques 3, 5, 7, ... L'harmonique 3 retiendra tout spécialement notre attention.

(ii) *Dispositif expérimental.* Nous partons du montage utilisé pour le tracé du cycle d'hystérésis. Le circuit intégrateur étant supprimé, nous connectons directement les deux extrémités de l'enroulement secondaire à l'entrée de l'amplificateur $Y$ de l'oscillographe. Nous utilisons donc notre tore comme un transformateur en circuit ouvert alimenté au primaire par un courant sinusoïdal pur. Avec un balayage linéaire, nous relevons à l'oscillographe l'allure de la tension $V(t)$ aux bornes du secondaire. $V(t)$ est une fonction périodique décomposable en série de FOURIER.

$$V(t) = A_\omega \sin \omega t + A_{3\omega} \sin 3\omega t + B_{3\omega} \cos 3\omega t + \\ + A_{5\omega} \sin 5\omega t + B_{5\omega} \cos \omega t + \ldots \qquad (33)$$

Les différents coefficients $A_{n\omega}$ et $B_{n\omega}$ sont des fonctions lentement variables du temps et nous choisissons l'origine des temps de façon à annuler le coefficient $B_\omega$ du développement précédent. L'amplitude du fondamental se réduit donc à $A_\omega$. Nous appellerons $V_{3\omega}$, $V_{5\omega}$ etc. les amplitudes des harmoniques d'ordre 3, 5 etc.

Pour étudier les différents termes $A_{n\omega}$ et $B_{n\omega}$, nous photographions les courbes $V(t)$ sur l'écran de l'oscillographe et nous les analysons ensuite par les méthodes classiques de calcul numérique. Nous pouvons aussi obtenir directement à l'aide d'un voltmètre électronique très sélectif les différentes composantes $V_{n\omega}$ indépendamment les unes des autres (toute perturbation à $\pm 10$ Hz de la fréquence de mesure est atténuée de 30 dbs et à $\pm 30$ Hz de 60 dbs).

Les méthodes d'analyse graphique proposées ne sont valables qu'en présence de composantes $V_{n\omega}$ suffisamment importantes vis-à-vis du fondamental. Cette condition est précisément remplie. Pour $t = t_1$, l'expression approchée (32) conduit à $V_{n\omega} = V_{(n+2)\omega}$ pour tous les harmoniques. En pratique, les premiers termes de la suite $V_\omega$, $V_{3\omega}$, $V_{5\omega}$ ... décroissent comme $1/n$, et nous obtenons les différents termes $A_{3\omega}$ et $B_{3\omega}$ avec une précision suffisante de quelques centièmes.

(iii) *Résultats des mesures.* Soit une solution solide de carbone à la concentration 0,0046 pour-cent désaimantée à l'origine des temps et abandonnée au repos, à température constante (−21,3°C), pendant

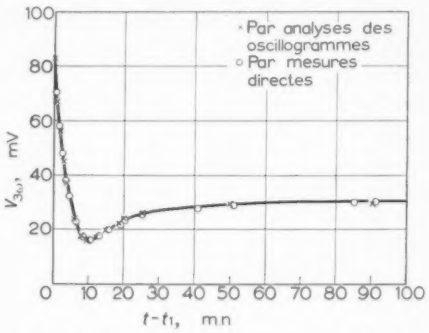


FIG. 20. Variation de $V_{3\omega}$ au cours du temps. Température: −21,3°C, $t_1 = 1080$ min, $c = 0{,}0046$ pour-cent $H_m = 141$ mOe.

un temps très long vis-à-vis des constantes de temps de traînage. Au temps $t_1 = 1080$ min, nous lui appliquons un champ sinusoïdal de fréquence 28 Hz, et d'amplitude constante $H_m = 141$ mOe. Nous avons représenté sur la Fig. 20 la composante $V_{3\omega}$ de la tension induite aux bornes de l'enroulement secondaire du tore en fonction du temps $t - t_1$ écoulé depuis l'application du champ.

$V_{3\omega}$ commence par décroître très rapidement,

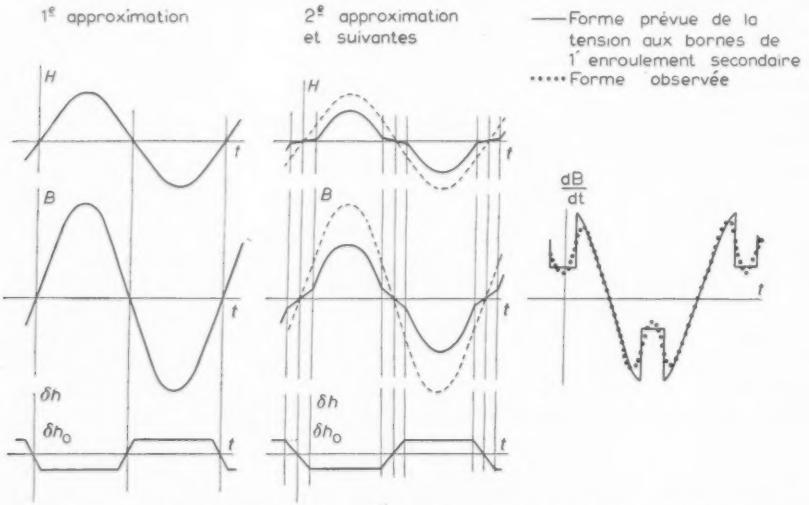


FIG. 21. Comportement de la substance dans un champ alternatif: méthode des approximations successives.

passe par un minimum et tend ensuite vers une limite par valeurs croissantes. Son amplitude est considérable par rapport au fondamental $V$. (Pour $t = t_1$, $V_{3\omega} = 83$ mV et $A_\omega = 240$ mV). FELDTKELLER[12] a déjà signalé un comportement analogue concernant un fer–silicium du commerce sans fournir à notre avis une interprétation satisfaisante.

La force électro-motrice d'induction relevée aux bornes de l'enroulement secondaire est donc très différente d'une sinusoïde comme en témoignent les oscillogrammes reproduits sur la Fig. 22. Leur allure varie au cours du temps d'application du champ $t-t_1$. Au temps $t = t_1$, la méthode d'approximations successives proposée par NÉEL permet de prévoir remarquablement la forme de $V(t)$ observée (Fig. 21).

Pour pousser plus avant la confrontation entre la théorie et l'expérience, nous avons calculé les composantes $A_{3\omega}$ et $B_{3\omega}$ de l'harmonique $V_{3\omega}$ et nous proposons d'expliquer leur évolution à partir de l'équation (32) précédente. Dans un plan défini à partir de deux axes rectangulaires, le point de coordonnées $A_{3\omega}$ et $B_{3\omega}$ représente l'extrémité d'un vecteur $\boldsymbol{V}_{3\omega}$. A mesure que la durée d'application du champ croît depuis $t-t_1 = 0$ jusqu'à $t-t_1 = \infty$, le vecteur $\boldsymbol{V}_{3\omega}$ pivote autour de l'origine d'un angle un peu inférieur à 180°, son extrémité libre décrivant une portion de courbe. Dans les conditions d'expérience décrites précédemment, nous obtenons un segment de droite (Fig. 23). Le minimum

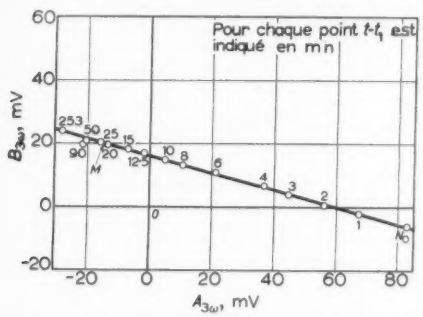


FIG. 23. Variation au cours du temps des composantes $A_{3\omega}$ et $B_{3\omega}$ (analyse de la figure 20).

de $V_{3\omega}$ est observé dans ces conditions à l'instant $t-t_1$ où le vecteur $V_{3\omega}$ est orthogonal à cette droite.

(iv) *Interprétation.* Soit $B(t)$ l'induction magnétique moyenne à chaque instant obtenue en évaluant le flux d'induction dans l'enroulement secondaire. $B(t)$ comporte un grand nombre d'harmoniques $B_3$, $B_5$ etc. Chacun de ces harmoniques, dont en particulier $B_3$, résulte de la composition en phase et en amplitude de deux termes d'origines différentes : l'un $B_3'$ est dû au traînage de diffusion proprement dit, l'autre $B_3''$, à l'hystérésis. Nous allons considérer $B_3'$ et $B_3''$ séparément.

La composante $B'_3$ résulte en première approximation de l'application à la substance du champ fictif de traînage, c'est-à-dire d'après l'équation (32) :

$$\delta h_{3\omega}(t) = \frac{4}{3\pi}\delta h_0\left[G(t)-\left(1+\frac{2}{3\pi}\right)G(t-t_1)\right]\cos 3\omega t \tag{34}$$

d'où l'expression de $B'_3$ :

$$B_3' = \frac{4\mu}{3\pi}\delta h_0\left[G(t)-\left(1+\frac{2}{3\pi}\right)G(t-t_1)\right]\times \\ \times\cos(3\omega t-\phi'). \tag{35}$$

Les cycles d'hystérésis de la Fig. 17 permettent d'évaluer $\delta h_0$. On trouve approximativement $\delta h_0 = 25$ mOe, et on en déduit $\mu$ voisin de 3 000 G/Oe. Le retard de phase $\phi'$, doit être attribué en tout premier lieu à l'effet des courants induits. Avec $f_{3\omega} = 84$ Hz, $\rho = 10^4$uem, pour une épaisseur de l'anneau $e = 3\cdot10^{-2}$ cm, les formules classiques[11] conduisent à tg $\phi' \neq 0{,}24$. Cette composante $B_3'$ s'annule pour $G(t) = 1{,}21\ G(t-t_1)$, soit pour $t-t_1 \neq 3{,}6\theta_0 = 23$ min. L'harmonique $B_3$ se réduit alors à sa seule composante $B_3''$ que nous allons évaluer. Avec $\delta h_0 = 25$ mOe, le champ réellement appliqué à la substance $H+\delta h$ conserve toujours une amplitude voisine de 120 mOe. Pour $H \leqslant 120$ mOe, nous obtiendrons une idée valable du comportement de la substance en écrivant qu'elle obéit aux lois de RAYLEIGH. Il en résulte :

$$\mu = \mu_0+\alpha H. \tag{36}$$

Nous avons trouvé expérimentalement : $\mu_0 = 1900$ G/Oe et $\alpha = 15\,000$ G/Oe$^2$. Nous appliquons alors le champ réel: $H = H_0\cos(\omega t+\phi)$ avec $H_0 = 120$ mOe. $B(t)$ ne comportant aucune composante en sin $\omega t$, il vient :[16]

$$tg\phi = 0{,}21$$

$$\text{et : } B_3'' = -\frac{4\alpha}{15\pi}H_0^2\sin 3(\omega t+\phi).$$

On voit que $B_3''$ est constant dans la mesure où $H_0$ l'est aussi et sa contribution dans le développement (33) conduit à des composantes $A_{3\omega}$ et $B_{3\omega}$ respectivement négative et positive.

En résumé, nous pensons que le vecteur $V_{3\omega}$ est la somme de deux vecteurs. L'un est dû à l'hystérésis. Il est constant en première approximation pour $H_m$ et $t_1$ donnés, et fait avec l'axe $B_{3\omega}$ un angle voisin de $+3\phi$. L'autre vecteur fait avec l'axe des abscisses un angle $-\phi'$ et son module est proportionnel à : $G(t)-(1+2/3\pi)G(t-t_1)$.

Un tel schéma rend compte d'une façon satisfaisante des résultats expérimentaux de la Fig. 23.

(v) *Position du minimum de* $V_{3\omega}$. Nous observons le minimum de $V_{3\omega}$ non pas à l'instant $t$ où la composante $\delta h_{3\omega}$ s'annule, mais à une époque $t-t_1$ différente, fonction de la durée $t_1$ de la stabilisation.

Quand $t_1$ diminue, le point $N_0$ se rapproche du point $M$ et le minimum a lieu pour une durée $t-t_1$ plus petite. Par exemple, pour $t_1 = 155$ min, toutes choses égales d'ailleurs nous avons trouvé le minimum de $V_{3\omega}$ pour $t-t_1 = 6{,}5$ min environ. A l'aide des résultats de mesures de désaccommodation on peut prévoir le position de ce minimum pour $t-t_1 = 7{,}1$ min. L'accord avec l'expérience est donc réalisé à 10 pour-cent. Pour des stabilisations plus incomplètes encore, le minimum a lieu pour $t-t_1$ très petit. $V_{3\omega}$ évolue alors rapidement dans les temps courts et la détermination du minimum devient plus difficile. Les valeurs de ces minima décroissent d'ailleurs quand la durée de la stabilisation $t_1$ augmente, ce qui s'explique aisément. En effet, le champ effectif n'est pas le même dans les différents cas, car $H_m-\delta h$ décroît à mesure que $t_1$ croît. La composante $\boldsymbol{OM}$ du à l'hystérésis est donc une fonction décroissante de $t_1$ pour un champ extérieur d'amplitude $H_m$ donnée.

Un résultat digne d'intérêt obtenu au cours de ces expériences réside dans la certitude que la stabilisation du matériau est encore incomplète au bout de 1 000 min à $-21{,}3$°C. Après une stabilisation $t_1 = 8.100$ min nous observons dans les mêmes conditions que précédemment (Fig. 20) un minimum de $V_{3\omega}$ de 13,9 mV seulement, situé pour $t-t_1 = 60$ min. Ce résultat, en confirmant les mesures au galvanomètre balistique, souligne le caractère arbitraire de notre détermination de la courbe isochrone $t = \infty$ dans un diagramme $B(H, t)$.

(vi) *Influence de l'amplitude du champ appliqué.* Nous avons reproduit l'étude de l'harmonique 3 décrite précédemment sur un échantillon contenant 0,027 pour-cent de carbone. La pression de traînage était alors maximum, voisine de 120 mOe et la perméabilité magnétique anormalement basse. L'étude décrite précédemment a donc été conduite dans des champs assez élevés (de l'ordre de 300 mOe) pour obtenir des inductions d'un bon ordre de grandeur. Sur la Fig. 24, nous avons porté les

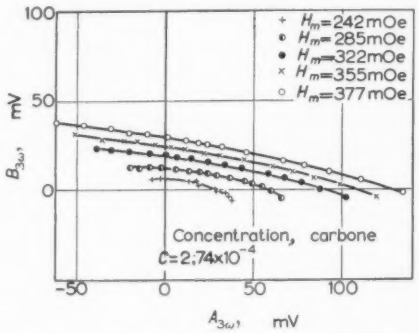


FIG. 24. Influence de l'amplitude du champ alternatif sur $A_{3\omega}$ et $B_{3\omega}$ $t_1 = 930$ min. Température: $-21{,}3$°C.

composantes $A_{3\omega}$ et $B_{3\omega}$ de la tension au secondaire du tore pour différentes valeurs du champ alternatif appliqué. Elles sont intéressantes à plus d'un titre.

L'extrémité libre du vecteur $V_{3\omega}$ décrit d'autant moins une droite que le champ appliqué est plus faible. L'interprétation donnée précédemment ne peut constituer ici qu'une première approximation assez grossière. La perméabilité magnétique de cette substance est beaucoup trop mauvaise pour qu'un schéma comme celui de la Fig. 16a puisse être appliqué avec succès dans les champs faibles. Pour $H_m = 242$ mOe, $B_m$ est en effet inférieur à 100 G pour $t = t_1$.

La Fig. 24 montre en outre l'influence des variations de perméabilité sur l'ordre de grandeur de $V_{3\omega}$. Alors que $\delta h_0$ doit être plutôt légèrement décroissant, $B_3'$ est une fonction de $H_m$ très nettement croissante. En mesurant le fondamental $V_\omega$ au voisinage du minimum de $V_{3\omega}$ nous avons trouvé que la perméabilité variait de 500 G/Oe pour $H_m = 242$ mOe à 2200 G/Oe pour $H_m = 377$ mOe. On retrouve bien approximativement ce même rapport entre les valeurs correspondantes de l'harmonique d'ordre 3.

Enfin, cet échantillon, à cause de la valeur

particulièrement élevée de son champ de traînage, est très difficile à désaimanter. Ainsi 200 min après l'application d'un champ d'amplitude $H_m = 242$ mOe la substance reste encore dans un état partiellement stabilisé qu'on reconnaît à l'existence du creux caractéristique au sommet de la sinusoïde. Les oscillogrammes de la Fig. 25 sont à rapprocher de ceux de la Fig. 22, obtenus dans les mêmes conditions de température et à l'aide du même appareillage, sur une solution beaucoup plus diluée. Parmi toutes les parois de BLOCH, celles qui sont rappelées vers leur position d'équilibre par les forces les plus grandes se déplacent alors suffisamment peu pour retomber à chaque alternance dans les mêmes creux de potentiel. Elles y restent stabilisées pratiquement indéfiniment, sans que les constantes de temps de diffusion soient en cause.

(vii) *Comportement des harmoniques supérieurs* $V_{5\omega}$ *et* $V_{7\omega}$. Revenons à l'étude de l'échantillon contenant 0,0046 pour-cent de carbone. Nous avons mesuré les composantes $V_{5\omega}$ et $V_{7\omega}$ dans les mêmes conditions que précédemment.

La théorie prévoit que les harmoniques $\delta h_{3\omega}$, $\delta h_{7\omega}$, $\delta h_{(4n-1)\omega}$, peuvent s'annuler pour une certaine valeur de $t-t_1$. On peut donc penser que dans la mesure où l'hystérésis n'intervient pas, seuls les harmoniques $V_{3\omega}$, $V_{7\omega}$, ... $V_{(4n-1)\omega}$ passeront par un minimum, inexistant pour les harmoniques $V_{5\omega}$, ... $V_{(4n+1)\omega}$. Nous avons effectivement pu mettre en évidence le minimum de $V_{7\omega}$ pour $t_1$ suffisamment court.

Par contre, nous avons toujours trouvé une décroissance monotone de l'harmonique 5 quelle que soit la durée $t_1$ de la stabilisation. Ce résultat conforme à la théorie est en contradiction avec certaines mesures de FELDTKELLER.[12] Nous pensons que des différences assez faibles dues à l'hystérésis et aux courants induits peuvent être rendues responsables des écarts importants enregistrés. En particulier, si la substance obéït aux lois de RAYLEIGH, et si les courants induits restent constamment négligeables, on peut montrer que l'existence d'un minimum est effectivement possible pour tous les harmoniques d'ordre impair.

(e) *Conclusion*

Nous avons mis en évidence sur des solutions solides connues de carbone dans du fer, placées dans un champ alternatif d'amplitude convenable, un très grand nombre de faits expérimentaux apparemment très complexes. Bien que ces phénomènes ne soient pas nouveaux à proprement parler,[12,13] nous les avons rencontrés avec une intensité jamais encore signalée; leur étude quantitative en a été grandement facilitée, et nous en interprétons les principaux aspects sur la base de la théorie du traînage de diffusion de NÉEL.

D'une manière générale, les résultats obtenus sont beaucoup plus difficiles à utiliser que ceux qui résultent des mesures de désaccommodation. L'intervention de l'hystérésis et des courants induits complique alors réellement les problèmes sans aucun profit.

## 7. APPLICATION DES MESURES DE TRAINAGE MAGNETIQUE A LA DETERMINATION DE LA SOLUBILITE DU CARBONE DANS LE FER

Au cours de nos mesures de désaccommodation, nous avons obtenu des variations considérables de perméabilité sur des solutions solides de carbone extrêmement diluées. Si les mesures magnétiques permettent inversement d'évaluer la teneur en carbone dissous d'un échantillon quelconque, nous disposons là d'une méthode de dosage d'une sensibilité exceptionnelle.

(a) *Comparaison de* $(h_0)_{max}$ *et c*

Aux faibles concentrations, la variation apparente de résistance électrique de nos échantillons à la température de l'oxygène liquide est proportionnelle à la quantité de carbone en solution (Fig. 4). Nous retrouvons la loi de MATTHIESSEN. Pour des concentrations supérieures à 0,01 pour-cent la solution précipite. Le précipité qui en résulte affecte lui aussi la résistivité de la substance, mais les perturbations qu'il provoque sont moins importantes.

Nous admettrons que ces perturbations sont également linéaires en fonction de la quantité de carbone mise en jeu. On en déduit la solubilité limite du carbone dans le fer à la température de préparation des échantillons, (légèrement inférieure à 700°C), $c_{limite} \simeq 0{,}013$ pour-cent, valeur voisine de celle obtenue par DIJKSTRA.[14]

Portons sur un même graphique (Fig. 26): d'une part en abscisses les variations de résistance $\Delta R/R$ mesurées pour différents échantillons en ne retenant, pour les solutions les plus concentrées, qu'une variation égale à 9,1 pour-cent représentant la contribution maximum du carbone dissous,

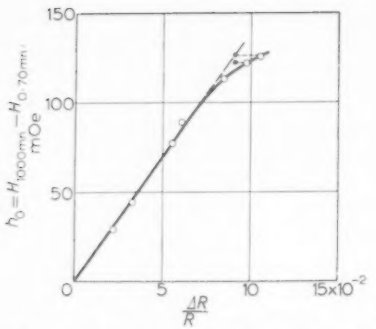


FIG. 26. Champ total de traînage $(h_0)_{max}$ et variation de résistance (90°K) pour différents échantillons.

d'autre part, en ordonnées, les valeurs correspondantes de $(h_0)_{max.}$ Aux erreurs d'expérience près, les points obtenus s'alignent sur une droite passant par l'origine. Le champ de traînage est donc bien proportionnel à $c$ dans toute l'échelle des concentrations réalisables et par conséquent, une mesure de $(h_0)_{max.}$ permet d'évaluer la quantité du carbone en solution.

Ce dosage se distingue toutefois d'un dosage absolu. Le coefficient de proportionnalité qui relie $(h_0)_{max.}$ et $c$ n'est certainement pas insensible aux propriétés magnétiques de la substance et plus spécialement à la dispersion des forces de rappel des parois de BLOCH et à la dispersion de leurs orientations. Dans quelles mesure ces deux facteurs affectent-ils la correspondance entre $(h_0)_{max.}$ et $c$? Seules, des études ultérieures permettront de répondre à cette question.

Nous avons obtenu sur les échantillons précédents un champ de traînage $(h_0)_{max.} = 100$ mOe pour une concentration en carbone dissous égale à 0,01 pour-cent. Mais sur une solution d'origine différente, l'application du même coefficient de proportionnalité ne fournirait qu'un ordre de grandeur. Pour un dosage précis, il serait indispensable de carburer à une concentration connue un échantillon témoin de même nature et de déterminer sur ce témoin la nouvelle correspondance entre $(h_0)_{max.}$ et $c$.

(b) *Avantages et inconvenients des dosages par mesure du traînage*

Envisagée comme permettant des dosages relatifs, la mesure du traînage présente des possibilités exceptionnelles. La qualité la plus précieuse de cette méthode réside certainement dans sa sensibilité. Non seulement, elle permet de déceler et mesurer facilement sur nos échantillons des concentrations en carbone dissous de l'ordre de 0,0001 pour-cent, mais encore sa sensibilité est à vrai dire d'autant meilleure que la concentration à mesurer est plus petite. Nous lui trouvons là une qualité particulièrement précieuse. Plus la substance est pure en effet, plus sa perméabilité est grande et, dans un diagramme $B(H, t)$ les mesures de désaccommodation sont d'autant plus sensibles à un petit déplacement latéral $h$ des isochrones que la pente de ces isochrones est plus grande. Pour une reproductibilité des mesures d'induction donnée, la concentration limite décelable est inversement proportionnelle à la perméabilité magnétique apparente de l'échantillon. D'où le soin apporté à purifier les anneaux avant carburation.

Des grosses difficultés subsistent néanmoins pour l'utilisation de ces dosages relatifs. D'une part, il faut s'assurer que le traînage observé est bien dû à l'impureté visée. La détermination des constantes de temps s'impose alors. Mais nous avons constaté au cours de cette étude une dispersion considérable de ces constantes et nous savons aussi combien sont voisins les comportements de certaines impuretés comme le carbone et l'azote. Il faut donc être prudent pour caractériser une substance par son traînage. D'autre part, aux très faibles concentrations qu'on peut aborder, on rencontre toujours de réelles difficultés à fabriquer un échantillon témoin absolument sûr. Nous nous y sommes heurtés au cours de ce travail et nous avons dit précédemment combien l'irréproductibilité de nos pesées limite la précision de nos résultats.

(c) *Solubilité du carbone dans le fer à température ordinaire*

Un échantillon contenant 0,0075 pour-cent de carbone d'après les pesées présentait initialement une pression de traînage de 77 mOe à —33,5°C nous l'avons conservé à la température ambiante dans un bain d'huile de vaseline. Deux ans après sa préparation, le champ de traînage n'était plus que de 3 mOe. Plus récemment, nous avons obtenu 2,30 mOe, 3 ans après sa préparation. La solubilité du carbone dans le fer $\alpha$ à 20°C est donc extrêmement faible, inférieure à 0,00023 pour-cent. En pratique, nous devons la considérer comme

nulle puisque la précipitation se poursuit pour des concentrations aussi faibles.

La variation relative de perméabilité dans les mesures de désaccommodation au voisinage de $B = 10$ G est alors voisine de 10 pour-cent pour $c = 2{,}3.10^{-6}$. Nous rappelons que la reproductibilité de nos mesures est de l'ordre de 0,5 pour-cent. Une concentration aussi faible reste donc encore mesurable. Ces résultats confirment la très grande sensibilité et par conséquent l'intérêt des mesures de traînage envisagées comme méthode de dosage des solutions solides très diluées.

**Remerciements**—Les travaux qui font l'objet de ce mémoire ont été effectués au Laboratoire d'Electrostatique et de Physique du Métal de Grenoble. J'exprime ma profonde et très respectueuse reconnaissance à M. le Professeur L. NÉEL qui m'a proposé cette étude et m'a constamment guidé, me faisant bénéficier de sa grande expérience au cours d'entretiens fréquents et particulièrement féconds.

Je remercie M. le Professeur L. WEIL, Directeur du Laboratoire des Basses Températures, qui a mis à ma disposition des moyens et des techniques modernes indispensables à mes recherches.

Je remercie également M. le Professeur FALLOT pour l'intérêt avec lequel il a suivi mes recherches et l'obligeance avec laquelle il m'a fait profiter des précieuses ressources de son Laboratoire.

Je remercie enfin, tous mes camarades et amis des différents services pour le dévouement qu'ils ont toujours manifesté à mon égard.

## BIBLIOGRAPHIE

1. RICHTER G. *Ann. Phys., Leipzig* **29,** 605 (1937).
2. SNOEK J. L. *Physica* **5,** 663 (1938).
3. NÉEL L. *J. Phys. Radium* **12,** 339 (1951).
4. NÉEL L. *J. Phys. Radium* **13,** 249 (1952).
5. DIJKSTRA L. J. *Philips Res. Rep.* **2,** 357 (1947).
6. LLIBOUTRY L. *Ann. Phys., Paris* **6,** 736 (1951).
7. SNOEK J. L. *New Developments in Ferromagnetic Materials* p. 123. Elsevier, Amsterdam (1947).
8. WEBB C. E. et FORD L. H. *J. Instn. Elect. Engrs.* **75,** 787 (1934).
9. FERRO A. et MONTALENTI G. *Metallurg. Ital.* **48,** 124 (1956).
10. BOZORTH R. M. *Ferromagnetism* p. 125. D. Van Nostrand, New York (1951).
    KORNETZSKI M., BRACKMANN J. et FREY J. *Siemens-Z.* **29,** 434 (1955).
11. BOZORTH R. M. *loc. cit.* p. 770.
12. FELDTKELLER R. *Z. angew. Phys.* **4,** 281 (1952).
13. SCHREIBER F. *Z. angew. Phys.* **8,** 539 (1956).
14. DIJKSTRA L. J. *Trans. Amer. Inst. Min. (Metall.) Engrs.* **188,** 252 (1949).
15. SNOEK J. L. *Physica* **8,** 711 (1941).
16. BECKER R. et DÖRING W. *Ferromagnetismus* p. 220. Springer, Berlin (1939).

*J. Phys. Chem. Solids* Pergamon Press 1958. Vol. 7. pp. 52–54.

# EXCHANGE TERMS IN THE EFFECTIVE MASS FORMALISM

**JAMES C. PHILLIPS**

Bell Telephone Laboratories, Inc., Murray Hill, New Jersey

(*Received* 24 *March*; *revised* 3 *April* 1958)

**Abstract**—The magnitude of the exchange terms recently discussed by KANE is evaluated for silicon and germanium. The non-local corrections lead to the expression $[r^\mu, H] = (1+\epsilon)(i\hbar p^\mu)/m$; the quantity $\epsilon$ measures the non-local correction. For silicon $\epsilon = 0{\cdot}29 \pm 0{\cdot}10$ and for germanium $\epsilon = 0{\cdot}26 \pm 0{\cdot}10$.

VOL. 7 1958

RECENTLY KANE[1] has discussed the effect of exchange terms in the effective mass formalism.* He concludes his paper with a qualitative estimate of their magnitude. In this note we shall show that by combining cyclotron mass and optical data with certain results of OPW (orthogonalized plane wave) band calculations, one can obtain a quantitative estimate of the magnitude of non-local corrections in silicon and germanium.

The corrections due to exchange arise because of its non-local character. Thus when one includes the exchange operator in the Hamiltonian, one obtains, as KANE[1] shows, corrections to the commutators important to the effective mass formalism. These are

$$[r^\mu, H] = \frac{i\hbar}{m} p^\mu + [r^\mu, W], \tag{1}$$

where $W$ is the exchange operator written in a space representation:

$$W = -e^2 \sum_i \frac{\Psi_i(r_1)\Psi_i^*(r_2)}{|r_1 - r_2|}. \tag{2}$$

The second term on the right in equation (1) represents the exchange correction. It can be evaluated approximately by writing $\Psi(r) = e^{ik\cdot r} u_k(r)$ and expanding $u_k(r)$ in a power series:

$$u_k(r_2) \simeq u_k(r_1) + (r_2 - r_1) \cdot \nabla u_k(r_1) + \ldots, \tag{3}$$

where we discard all terms higher than the first, which makes the first non-vanishing contribution. Inserting equations (2) and (3) into the commutator, one finds

$$\langle k', n' | [r^\mu, W] | k, n \rangle$$
$$= -e^2 \int (r_1^\mu - r_2^\mu) \Psi_{k'n'}^*(r_1)(r_2 - r_1) \cdot \nabla \Psi_{kn}(r_1) \sum_i \frac{\Psi_i(r_1)\Psi_i^*(r_2)}{|r_1 - r_2|} dr_1 d(r_2 - r_1). \tag{4}$$

If one now assumes that the exchange hole is isotropic,

$$\sum_i \Psi_i(r_1)\Psi_i^*(r_2) = f(|r_1 - r_2|), \tag{5}$$

then

$$[r^\mu, W] = +\frac{e^2 i}{3\hbar} p^\mu \int |r_2 - r_1| f(|r_2 - r_1|)\, d(r_2 - r_1)$$
$$= \frac{me^2 F}{\hbar^2} \left( \frac{i\hbar}{m} p^\mu \right), \tag{6}$$

where

$$F = \tfrac{1}{3} \int |r_2 - r_1| f(|r_2 - r_1|)\, d(r_2 - r_1). \tag{7}$$

We have repeated KANE's derivation primarily to correct an error in the sign of the result (6). However, from the derivation it is also clear that other non-local corrections, such as those due to correlation will also in first order yield a correction proportional to $\nabla$. Thus to lowest order, the

* I am indebted to Prof. G. F. DRESSELHAUS for calling this paper to my attention.

commutators appearing in the effective mass formalism should have the form

$$[r^\mu, H] = (1+\epsilon)\frac{i\hbar}{m}p^\mu, \tag{8}$$

where $\epsilon$ measures corrections due to non-local potentials. (If one includes exchange effects only, then $\epsilon = (me^2F)/\hbar^2$.) We shall now estimate $\epsilon$ in germanium and silicon crystals for states near the band gap.

Such estimates can be made by comparing experimental values for band-structure parameters with those obtained theoretically. At first sight this procedure would appear to have little quantitative significance because of the qualitative state of energy-band calculations at present, which in turn derives chiefly from uncertainties in the crystal potential. The situation is redeemed, however, by several features. To calculate effective masses one needs to know wave functions and energy values. In silicon and germanium the terms making the principal contributions at the center of the zone are those directly across the energy gap, and these energy differences have been measured optically by DASH and NEWMAN.[2] To obtain matrix elements in the OPW formalism one needs mainly the coefficient of the principal component of the wave function in a Fourier expansion e.g. the coefficient of the $\langle 111 \rangle$ plane waves in expansions of the wave functions near the top of the valence band. Since calculations for diamond,[3] silicon,[4] and germanium[5] have shown similar convergence properties, it is reasonable to conclude that these coefficients are relatively insensitive to the exact nature of the crystal potential (unlike the term values, which we obtain as much as possible from experiment).

We first indicate that the errors in the calculation are sufficiently small to show that non-local effects make a significant contribution to the experimental effective mass parameters for the valence bands in silicon and germanium. In the notation of DRESSELHAUS *et al.*,[6] one measures the band parameters $A, |B|$, and $|C|$. These are in turn related to the quantities $L$, $M$, and $N$ which describe the bands in the absence of spin-orbit coupling by the following equations:[6]

$$A = \hbar^2/2m + (L+2M)/3, \tag{9}$$

$$B^2 = [(L-M)/3]^2, \tag{10}$$

$$3C^2 = N^2 - (L-M)^2. \tag{11}$$

The quantities $L$, $M$, and $N$ are expressed according to second-order perturbation theory in terms of the matrix elements of $[r^\mu, H]$ between various wave functions. To indicate the uncertainties of the calculation, we evaluate $M$ for silicon. Assuming $[r^\mu, H] = i\hbar/mp^\mu$, we have

$$M_S \simeq \frac{\hbar^2}{m^2}\frac{|(\Gamma_{25'}^{(1)}|p_y|\Gamma_{15}^{(1)})|^2}{E_0 - E_1}, \tag{12}$$

where $|\Gamma_{15}^{(1)})$ denotes a suitable basis function as defined by DRESSELHAUS[7] and $E_1 - E_0 \simeq (2{\cdot}5 \pm \pm 0{\cdot}1)$ eV, according to DASH and NEWMAN.[2] One now expands $|\Gamma_{15}^{(1)})$ and $|\Gamma_{25'}^{(1)})$ in terms of symmetrized plane waves:

$$\begin{aligned} |\Gamma_{15}^{(1)}) &= a_0\langle 111\rangle + a_2\langle 220\rangle + \ldots, \\ |\Gamma_{25'}^{(1)}) &= b_0\langle 111\rangle + b_1\langle 200\rangle + b_2\langle 220\rangle + \ldots, \end{aligned} \tag{13}$$

where $\langle 111 \rangle$ denotes an appropriate symmetrized plane wave basis function. Now one finds

$$|(\Gamma_{25'}^{(1)}|p_y|\Gamma_{15}^{(1)})| \sim a_0b_0 + \sqrt{2}a_2b_2 + \ldots \tag{14}$$

The correction terms due to $a_2b_2 \ldots$ are smaller than the uncertainties in $a_0b_0$, so that they can be neglected. From HERMAN's study of diamond,[8] one guesses $a_0 \simeq 0{\cdot}91$ with a probable error of 0·02 and $b_0 \simeq 0{\cdot}76 \pm 0{\cdot}04$. Thus altogether one finds

$$M_S \simeq -3{\cdot}7 \pm 0{\cdot}6, \tag{15}$$

in units of $\hbar^2/2m$. The other parameters can be obtained in a similar way. The fractional errors will be larger because the term values are known less accurately, but the absolute errors will not be any larger, because the other terms are considerably smaller. The results of these calculations for silicon are shown in Table 1, where they are compared with the experimental values.

Somewhat more care must be exercised in carrying out similar calculations for germanium. The chief contribution in this case comes from $|\Gamma_{2'}^{(1)})$, and if $|\Gamma_{2'}^{(1)})$ is expanded as before,

$$|\Gamma_{2'}^{(1)}) = c_0\langle 111\rangle + c_1\langle 200\rangle + c_3\langle 311\rangle + \ldots, \tag{16}$$

one must determine $c_0$ and $c_1$. From HERMAN's calculations[5] for germanium, it is evident that $c_0$ and

*Table 1. Comparison of experimental and theoretical values for the cyclotron mass constants for the valence bands of silicon and germanium. The experimental values are taken from* DRESSELHAUS *et al.*,[7] *while the method of deriving the theoretical values is described in the text.*

| Silicon | $A$ | $\|B\|$ | $\|C\|$ |
|---|---|---|---|
| Exper. | $-4{\cdot}0\pm0{\cdot}2$ | $1{\cdot}6\pm0{\cdot}2$ | $3{\cdot}3\pm0{\cdot}5$ |
| Theory | $-2{\cdot}2\pm0{\cdot}7$ | $0{\cdot}5\pm0{\cdot}2$ | $2{\cdot}0\pm0{\cdot}6$ |
| Germanium | $A$ | $\|B\|$ | $\|C\|$ |
| Exper. | $-13{\cdot}0\pm0{\cdot}2$ | $8{\cdot}9\pm0{\cdot}1$ | $10{\cdot}3\pm0{\cdot}1$ |
| Theory | $-6{\cdot}3\pm1{\cdot}5$ | $6{\cdot}0\pm1{\cdot}0$ | $8{\cdot}5\pm8{\cdot}5$ |

$c_1$ are determined by $\delta\Gamma_{2'}$, the decrease in the $\Gamma_{2'}$ level when 15 instead of 9 plane waves are included in the calculation. We have assumed $\delta\Gamma_{2'} = (0{\cdot}7\pm0{\cdot}2)$ Ryd, and calculated the matrix element

$$|(\Gamma_{25'}{}^{(1)}|p_z|\Gamma_{2'}{}^{(1)})| \sim b_0c_0+3^{-\frac{1}{2}}\cdot 2b_1c_1+\ldots \quad (17)$$

The results of the calculations for germanium are also shown in Table 1. It is clear from this table that non-local effects must be included to obtain consistent results.

Thus we now reverse the calculation and estimate $\epsilon$ in silicon and germanium. We find in silicon $\epsilon = 0{\cdot}29\pm0{\cdot}10$ and in germanium $\epsilon = 0{\cdot}26\pm0{\cdot}10$. It is interesting to compare these values of $\epsilon$ with those obtained KANE,[1] using the Slater free-electron approximation for exchange with the valence electrons. KANE finds $\epsilon \simeq 0{\cdot}65$. This is about twice the value obtained for silicon and germanium, which is the result usually encountered when the Slater approximation is made.[9–11]

From these results it appears that the non-local part of the exchange interaction between the valence electrons and the $3d$ shell is not as large as the non-local interaction between the valence electrons themselves. A more accurate calculation of exchange effects, e.g. including screening, does not appear to be warranted by the data.

*Acknowledgement*—The author is pleased to acknowledge several conversations with M. LAX.

## REFERENCES

1. KANE E. O. *J. Phys. Chem. Solids* **6,** 236 (1958).
2. DASH W. C. and NEWMAN R. *Phys. Rev.* **99,** 1151 (1955).
3. HERMAN F. *Phys. Rev.* **93,** 1214 (1954).
4. WOODRUFF T. O. *Phys. Rev.* **103,** 1159 (1956).
5. HERMAN F. *Physica* **20,** 801 (1954).
6. DRESSELHAUS G. F., KIP A. F. and KITTEL C. *Phys. Rev.* **98,** 368 (1955).
7. DRESSELHAUS G. F. Ph.D. Thesis, Univ. of California (1955) (unpublished).
8. HERMAN F. Ph.D. Thesis, Columbia Univ. (1953) (unpublished).
9. SLATER J. C. *Phys. Rev.* **81,** 385 (1951).
10. PRATT G. W. *Phys. Rev.* **88,** 1217 (1952).
11. HARTREE D. R. *The Calculation of Atomic Structures* p. 61. John Wiley and Sons, New York (1957).

*J. Phys. Chem. Solids* Pergamon Press 1958. Vol. 7. pp. 55–57.

# THE QUESTION OF RADIATION-INDUCED PHASE CHANGES*

**ULRICH GONSER and BOUDEWYN OKKERSE†**

Department of Physics, University of Illinois, Urbana, Illinois

(*Received* 4 *September* 1957; *revised* 14 *January* 1958)

**Abstract**—Radiation-induced phase changes can give valuable information about the nature of thermal-spike regions. Recent experiments suggest the following classification: (1) If $dV/dT$ is always positive, even at the transformation point, the thermal spike is a region containing Frenkel pairs or many displaced atoms, as in the "displacement spike" of BRINKMAN. (2) If $dV/dT$ has an anomaly, corresponding to an increase of density due to the formation of a more closely packed phase, one may expect the more dense phase to be produced in a "structure spike". In the latter case the high pressure which a thermal spike exerts on the surrounding matrix is an important factor in creating the high-temperature phase.

IN recent years most of the results of radiation-damage experiments have been discussed on the basis of induced Frenkel defects and on the more generalized model of a thermal spike. The duration of such a thermal pulse was estimated by SEITZ[1] to be of the order of $10^{-11}$ sec. The atomic vibration frequency in solids is about $10^{13}$/sec, so that the lifetime of the pulse is of the order of 100 atomic oscillations. The heated region is quenched rapidly to ambient temperature. Consequently a model of the processes occurring during a thermal spike can be based only on the observation of the defects introduced by the thermal spike into the matrix material.

The short lifetime of a thermal spike causes one to ask whether time and space will allow the nucleation of a second phase being the stable phase at high temperature in the spike region, and whether it is possible for the group of atoms which are heated during the thermal spike to follow all the phase changes associated with the phase diagram of the material. Materials which have a characteristic and relatively unusual behavior at high temperatures, such as those which have a high-temperature phase, may be very helpful in the study of the effects of a thermal spike. It might then be possible to quench-in the high temperature behavior and to measure the effects at lower temperature.

The III–V compounds which have attracted so much attention in recent years because of their highly interesting electrical properties[2] are very suitable for this purpose. They contract considerably on melting, as is shown for gallium antimonide in Fig. 1.[3] The behavior of germanium is very similar. At the melting point a new configuration exists in the liquid state which is stable only in a form possessing short-range order under normal conditions. In the case of indium antimonide[4] and germanium,[5] X-ray measurements showed that the number of nearest neighbors increases at the melting point from 4 to 6 and 8, respectively. The present authors irradiated single crystals of gallium antimonide with 12-MeV deuterons at liquid-nitrogen temperature.[6] The shape of the X-ray reflections suggested very strongly that the material contracted on irradiation. This bulk contraction was interpreted as being due to spike regions which probably are in a liquid-like lattice configuration having a higher density than the normal solid.

$$\mathrm{GaSb}_{\substack{\text{solid}\\\text{configuration}}} \underset{\text{Annealing}}{\overset{\text{Irradiation}}{\rightleftarrows}} \mathrm{GaSb}_{\substack{\text{liquid}\\\text{configuration}}} \qquad (1)$$

* This research was supported by the United States Atomic Energy Commission and the National Academy of Sciences.

† Present address: Philips Research Laboratories, Eindhoven, The Netherlands.

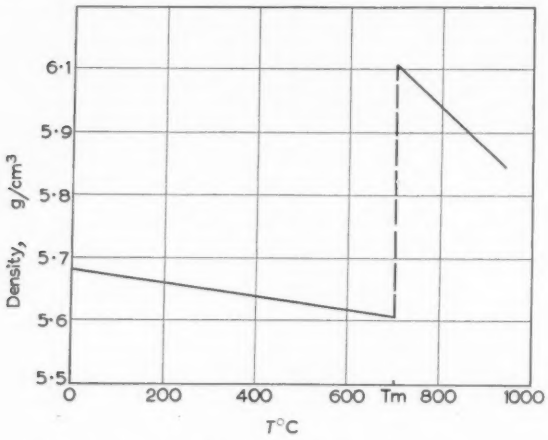


FIG. 1. Density change of GaSb with temperature (*after* MICROVSKII *and* REGEL[3]).

These spike regions do not fulfil the Bragg condition, whereas the surrounding single matrix does, resulting in a lower X-ray intensity from the irradiated crystal. Broad rings were observed with a modified Debye–Scherrer technique. This means that in the spike regions randomly distributed "micro-crystals" are present which have a well-defined structure. This structure must be different from the matrix material, for otherwise no contraction would have been observed. Reasoning along the lines of BRINKMAN,[7] one could call this model a structure spike. A structure spike region then is that part of the spike in which a phase different from the matrix is formed during or after the temperature pulse. Annealing experiments showed that the material of the spike regions transforms into the surrounding stable matrix at −110°C according to the reaction (1) mentioned above.

So far no general rules have been established for the occurrence of radiation-induced phase changes. The following transformations have been investigated: uranium ($\alpha \rightleftarrows \beta$) by TUCKER and SENIO,[8] tin (white → gray) by FLEEMAN and DIENES[9] $ZrO_2$ (monoclinic → cubic) by WITTELS and SHERILL,[10] and the precipitation of α-Fe in Cu ($Fe_\alpha \rightarrow Fe_\gamma$) by DENNEY.[11] It is remarkable that in the case where no transformation is observed (uranium) the high-temperature phase has the lower density, whereas in the cases where a transformation seems to occur ($ZrO_2$, GaSb, Fe) the high-temperature phase has the higher density. Apparently transformation is favored in these cases by a negative volume change. The transformation temperature varies with pressure according to the well-known Clausius–Clapeyron equation:

$$\frac{dT}{dp} = \frac{V_{\text{high } T} - V_{\text{low } T}}{S} \qquad (2)$$

in which $S$ is the transformation entropy. In Table 1 the value of $dT/dp$ is given for iron, tin, germanium, bismuth and copper.

*Table* 1. *Values of* $dT/dp$

| Transformation | $(dT/dp)(10^{-3}$ C° atm$^{-1})$ |
|---|---|
| $Fe_\alpha \rightarrow Fe_\gamma$ | − 8 |
| $Sn_{gray} \rightarrow Sn_{white}$ | −60 |
| $Ge_{solid} \rightarrow Ge_{liquid}$ | − 3 |
| $Bi_{solid} \rightarrow Bi_{liquid}$ | − 4 |
| $Cu_{solid} \rightarrow Cu_{liquid}$ | + 4·5 |

The volume change on melting is −5·5 per cent for germanium and is even higher for the III–V compounds (of the order of −10 per cent). The entropies of melting for the III–V compounds are not known, but the similarities to germanium suggest that a large change in transformation temperature is to be expected. In the case of germanium, HALL[12] verified this relation by applying

very high pressure. He found that the melting point decreases linearly with increasing pressure from 936°C at 1 atm to 347°C at 180,000 atm.

$$\frac{dT}{dp} = -3{\cdot}3 \times 10^{-3}\ \mathrm{C^\circ\ atm^{-1}}.$$

It should be noted that FLEEMAN and DIENES[9] investigated the reverse transformation, where such considerations are not applicable.

The pressure $p$ which a spherical spike region exerts on the surrounding matrix, treated as an infinite solid, can be estimated from the equation given by SEITZ and KOEHLER[13]

$$\frac{\Delta V}{V} = \frac{3p}{4\mu} \qquad (3)$$

in which $\Delta V$ is the expansion of the initial volume $V$ of the spike region and $\mu$ is the shear modulus. As a first approximation $V\mu$ may be set equal to the energy of the primary knocked-ons. In the case of fast neutron irradiation this energy is of the order of $10^4$ eV. The volume $V$ was estimated by BRINKMAN[7] and measured by ARONIN[14] on the basis of disordering, and is about $10^{-19}$ cm$^3$ or $10^4$ atom sites. Using these data, one finds a pressure of the order of $2 \times 10^5$ atm. On the basis of relation (2), it then seems reasonable to assume that the transformation temperature is lowered by several hundred degrees in spike regions of materials like iron, germanium, bismuth, and gallium antimonide. From a macroscopic point of view, it is therefore important to emphasize that both temperature and the associated pressure are responsible for the actual transformation of a thermal-spike region from the original phase into the high-temperature phase. With a better knowledge of the constants used in the calculation, one should be able to predict whether an irradiation-induced phase change is thermodynamically possible.

The foregoing discussion does not take into consideration factors such as thermal conductivity, incubation time, metastability of the high-temperature phase, and so forth. At present it seems impossible to make a complete theoretical evaluation of all factors involved.

Experiments are in progress[15] to determine the size and number of spike regions in germanium by means of the small-angle scattering of X-rays. Preliminary results show that the size is of the order of $10^4$ atoms, in agreement with the number used in the present paper.

*Acknowledgements*—The authors are indebted to Professor F. SEITZ and to Professor J. S. KOEHLER for valuable discussions.

## REFERENCES

1. SEITZ F. *Phys. To-day* **5,** 6 (1952).
2. WELKER H. and WEISS H. *Solid-State Physics* (Ed. F. SEITZ and D. TURNBULL) Vol. 3, p. 1. Academic Press, Inc., New York (1956).
3. MICROVSKII N. I. and REGEL A. R. *Zh. tekhn. fiz.* **22,** 1281 (1952).
4. BUSCHERT R. C. Thesis, Purdue University (1957).
5. HENDUS H. *Z. Naturf.* **2a,** 505 (1947).
6. GONSER U. and OKKERSE B. *Phys. Rev.* **105,** 757 (1957).
7. BRINKMAN J. A. *J. Appl. Phys.* **25,** 961 (1954).
8. TUCKER C. W. and SENIO P. *J. Appl. Phys.* **27,** 207 (1956).
9. FLEEMAN J. and DIENES G. J. *J. Appl. Phys.* **26,** 652 (1955).
10. WITTELS M. C. and SHERILL F. H. *J. Appl. Phys.* **27,** 643 (1956).
11. DENNEY J. M. *Phys. Rev.* **94,** 1417 (1954).
12. HALL H. T. *J. Phys. Chem.* **59,** 1144 (1955).
13. SEITZ F. and KOEHLER J. S. *Solid-State Physics* (Ed. F. SEITZ and D. TURNBULL) Vol. 2, p. 305. Academic Press, Inc., New York (1956).
14. ARONIN L. R. *J. Appl. Phys.* **25,** 344 (1954).
15. FUJITA F. E. and GONSER U. To be published.

*J. Phys. Chem. Solids* Pergamon Press 1958. Vol. 7. pp. 58–64.

# THE ELASTIC CONSTANTS OF ZINC BETWEEN 4·2° AND 670°K

**G. A. ALERS and J. R. NEIGHBOURS**

Scientific Laboratory, Ford Motor Company, Dearborn, Michigan

(*Received* 7 *February* 1958)

**Abstract**—The five adiabatic elastic constants of single crystals of zinc have been measured from 4·2°K to within 20°K of the melting point, using the ultrasonic-pulse technique. Although the temperature variation is not exactly linear, no very rapid changes occur even as the melting point is approached. The room-temperature values agree well with other data. The 4·2°K values are: $C_{11} = 17{\cdot}909$, $C_{33} = 6{\cdot}880$, $C_{44} = 4{\cdot}595$, $\frac{1}{2}(C_{11}-C_{12}) = 7{\cdot}080$, $C_{12} = 3{\cdot}75$ and $C_{13} = 5{\cdot}54$ in units of $10^{11}$ dynes/cm².

VOL. 7 195

## 1. INTRODUCTION

THE elastic constants of metals are of value in theories of lattice dynamics, metallic binding, and mechanical properties. However, only a very few have been measured over a wide temperature range extending down to 4·2°K. These low-temperature values are of fundamental interest, since they can be compared with theory and can also be used to determine the Debye $\theta_0$ useful in specific-heat measurements.

There have been no low-temperature measurements on the hexagonal metals until very recently,[1] and the present investigation was undertaken in order to provide such measurements. Zinc was chosen because of the ease in preparation of oriented single crystals and because its low melting point (419°C) made it possible to measure the elastic constants near the melting point where there are almost no data available for any metal.

## 2. EXPERIMENTAL PROCEDURE

For a medium of hexagonal symmetry, the three sound-wave velocities (two transverse and one longitudinal) are given by the three roots of the factored secular equation[2]

$$(\rho v^2-a)[(\rho v^2)^2-b\rho v^2+c]=0 \qquad (1)$$

Here $v$ is the velocity of a sound wave traveling at an angle $\phi$ to the hexagonal axis and $\rho$ is the medium density. The coefficients $a$, $b$, and $c$ are defined in terms of $\phi$ and the elastic constants by the equations

$$a=\beta^2\frac{C_{11}-C_{12}}{2}+\gamma^2C_{44} \qquad (2)$$

$$b=\beta^2C_{11}+C_{44}+\gamma^2C_{33} \qquad (3)$$

and

$$c=\gamma^2\beta^2(C_{11}C_{33}-2C_{44}C_{13}-C_{13}^2)+ +C_{44}(\gamma^4C_{33}+\beta^4C_{11}) \qquad (4)$$

where $\gamma = \cos\phi$ and $\beta = \sin\phi$.

The ultrasonic-pulse technique yields measurements of the three velocities at a particular value of $\phi$ and thus determines the coefficients $a$, $b$, and $c$ associated with that angle. Since there are five elastic constants, it is necessary to determine these coefficients for more than one angle $\phi$, in order to obtain five independent relations. The pure wave orientations $\phi = 0°$ and $\phi = 90°$ yield simple results, but allow only four of the five constants to be determined[3] because the fifth constant, $C_{13}$, appears only in the coefficient $c$ when $\phi$ is not equal to 0° or 90°. Furthermore the coefficient $c$ is a quadratic function of $C_{13}$ and thus there are two possible values of $C_{13}$ which are consistent with the measured coefficient $c$. In order to choose between these solutions, some other piece of information must be used. There are certain inequalities between the elastic constants which must exist in order to preserve the lattice stability.[4] For a hexagonal metal, those which involve $C_{13}$ are

$$C_{13}^2 > C_{11}C_{33}$$

and

$$C_{13}^2 > \tfrac{1}{2}C_{33}(C_{11}+C_{12}).$$

In the case of zinc at room temperature, the two possible values of $C_{13}$ which can be obtained from the measured wave velocities are $5{\cdot}30\times10^{11}$ dynes/cm$^2$ and $-13{\cdot}06\times10^{11}$ dynes/cm$^2$. The latter value does not satisfy either stability condition. Thus the former value must be the correct root.

There are materials for which both values of $C_{13}$ satisfy the stability conditions. In these cases it is necessary to use some other measurement (Young's modulus or the compressibility) in order to decide which value of $C_{13}$ is correct. Cobalt is such a case, and the wave velocities measured by McSkimin[5] at $\phi = 45°$ can be obtained for $C_{13} = 1{\cdot}027\times10^{12}$ dynes/cm$^2$ or from $C_{13} = -2{\cdot}537\times10^{12}$ dynes/cm$^2$. The former value must be accepted, since the latter leads to a compressibility which is quite different from the directly measured value.

The zinc single crystals used in the present investigation were grown at the State University of Iowa by one of us,[6] using the Bridgman technique. Their purity was determined to be 99·98 per cent zinc.* The crystals were grown in the form of $1\frac{1}{2}\times\frac{3}{4}\times7$ in. blocks and the two specimens used for this investigation were cut from these with a fine-toothed circular saw attached to a small milling machine. One specimen, referred to as Zn I, was cleaved at liquid-nitrogen temperature in order to obtain two parallel surfaces whose normals exactly coincided with the hexagonal axis of the zinc lattice. Using these surfaces for reference another pair of surfaces oriented at exactly right angles to the hexagonal base plane were prepared. In this way, the resulting zinc specimen had two surfaces parallel to the base plane and two surfaces perpendicular to it. The specimen was then lapped and polished on emery paper to remove the severely cold-worked layer left by the cutter while keeping the surfaces smooth and exactly parallel. After the mechanical polishing, the specimen was carefully etched in dilute HCl and in a solution suggested by Gilman and DeCarlo[7] to remove 0·1 mm of material from each surface. These etched surfaces showed slightly elongated Laue back-reflection X-ray spots. The crystal was then annealed at 390°C for 4 hr in an argon atmosphere. No recrystallization was observed to result from this anneal, and the Laue spots became sharp.

A second crystal, referred to as Zn II, having a different crystallographic orientation, was prepared by the same procedure. It had two parallel surfaces oriented at an angle to the hexagonal axis and another pair of parallel surfaces oriented at 90° to the base plane. The first pair of surfaces were required for the measurements of the constant $C_{13}$. The second pair was prepared in order to provide a cross-check on the results obtained from the first specimen.

Measurements made on these two crystals at various times during their preparation showed that the elastic constants were changed by no more than 0·1 per cent when the polished surface was removed and the crystals annealed. It therefore seems reasonable to conclude that the distortions introduced by the preparation technique had a negligible effect on the final results.

A modified ultrasonic-pulse technique[8] was used in measuring the elastic wave velocities. The electronic apparatus consisted of a type VR Sperry Reflectoscope with its output displayed on a Tektronix Type-535 oscilloscope and triggered by a Type-180 Tektronix time-mark generator. By using the double-sweep attachment, it was possible to determine the time of arrival of an echo by measuring the time difference between the first cycle of the echo signal and a particular time mark. This could be done to $\pm0{\cdot}01$ μsec. The unrectified echos were used in order to determine the leading edge of the echo more accurately. It was found that the attenuation of the sound in the solid caused the first cycle of the echo to disappear into the amplifier noise after a few trips through the specimen. The times of arrival of the subsequent echos were then measured to the second cycle of the echo signal and the result corrected by 0·10 μsec (since a 10-mc/sec echo signal was used). This technique greatly improved the internal consistency of the entire set of measurements. Furthermore we feel that this method made the transit time error[9] sufficiently small to be neglected. Hence no correction for this "error" has been applied to the data. Tests made on aluminum samples of several different lengths indicated that this point of view was justified since no clearly defined transit-time correction greater than the experimental error of 0·01 μsec was apparent.

The measurements at elevated temperatures were made in an argon atmosphere in a furnace equipped with a Wheelco temperature controller. A chromel–alumel thermocouple in contact with the specimen was used to measure its temperature. The glue used to fasten the quartz transducer onto the specimen was Sauereisen P-31 cement.

For the measurements between room temperature and 77°K, a small furnace was built, using polystyrene foam for insulation. This was immersed in a liquid-nitrogen bath and the same Wheelco temperature-control system used again to obtain any temperature between 77 and 300°K. In this range, a copper–constantan thermocouple was used to determine the specimen temperature. Measurements below 77°K were obtained only at 4·2°K by simply placing the specimen in liquid helium. For all of these low-temperature measurements, the glue used was machine oil, stopcock grease, or glycerine. All three were equally satisfactory.

In order to determine $C_{13}$ from the wave-velocity measurements, it was necessary to know the angle $\phi$ between the hexagonal axis and the propagation direction in crystal Zn II. This angle was measured by the back-reflection Laue technique, by observation of reflected light from the cleavage plane and by an acoustic method, i.e. by requiring internal consistency among the three wave velocities measured at the angle $\phi$ at room temperature. The average value obtained from all three methods was $\phi = 16{\cdot}60\pm0{\cdot}1°$.

At temperatures different from room temperature, it

* Spectroscopic analysis by Mr. E. Runge of this laboratory showed Cu 0·010, Ca 0·003, Mg 0·003, Cd 0·002, Fe 0·002, Pb 0·001, Sn $<$ 0·001, and Al $<$ 0·005 weight per cent.

is necessary to correct the density and the wave velocities for thermal expansion. Because the expansion is anisotropic, a correction to the angle $\phi$ must also be made. These corrections were determined from the thermal-expansion coefficients given by GRÜNEISEN and GOENS.[10]

### 3. RESULTS

Using zinc crystal Zn I, the velocities of propagation of the transverse and longitudinal waves traveling at $\phi = 0°$ and $\phi = 90°$ were measured. For $\phi = 0°$, equation (1) has the solutions $\rho v_1^2 = C_{44} = \rho v_2^2$, and $\rho v_3^2 = C_{33}$. For $\phi = 90°$, the solutions are $\rho v_4^2 = \frac{1}{2}(C_{11} - C_{12})$, $\rho v_5^2 = C_{44}$ and $\rho v_6^2 = C_{11}$. Fig. 1 shows the temperature-dependence of these quantities from 4·2°K to 97

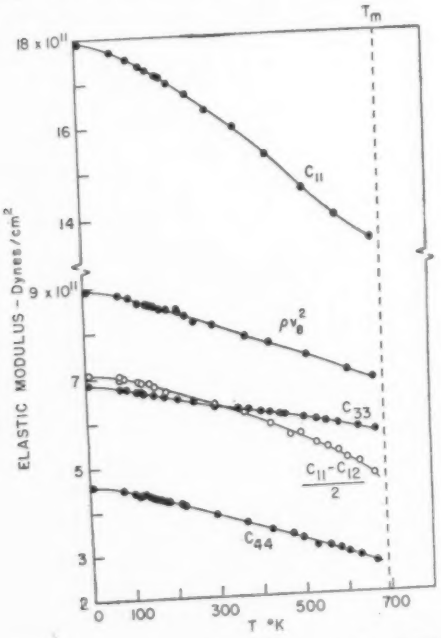


FIG. 1. Temperature-dependence of the directly measured adiabatic elastic constants of zinc. The quantity $\rho v_8^2$ comes from the velocity of a longitudinal wave traveling at 16·6° to the hexagonal axis. The line marked Tm defines the melting temperature.

per cent of the melting point (i.e. 670°K). The curve marked $\rho v_8^2$ was obtained from measurements of the velocity $v_8$ of a quasi-longitudinal wave traveling at 16·6° to the hexagonal axis in crystal Zn II. Equation (1), when solved for $\rho v_8^2$, yields

$$2\rho v_8^2 = (C_{11}+C_{44}) - \gamma^2(C_{11}-C_{33}) + \\ + \{[\beta^2(C_{11}-C_{44}) - \gamma^2(C_{33}-C_{44})]^2 + \\ + 4\gamma^2\beta^2(C_{13}+C_{44})^2\}^{\frac{1}{2}} \quad (5)$$

where $\gamma = \cos 16{\cdot}60°$ and $\beta = \sin 16{\cdot}60°$.

Using the measurements at $\phi = 0°$ and $\phi = 90°$ with $\rho v_8^2$, equation (5) was used to deduce the constant $C_{13}$. The constant $C_{12}$ was easily calculated from $\rho v_6^2$ and $\rho v_4^2$. The temperature-dependence of these two constants is shown in Fig. 2. Since

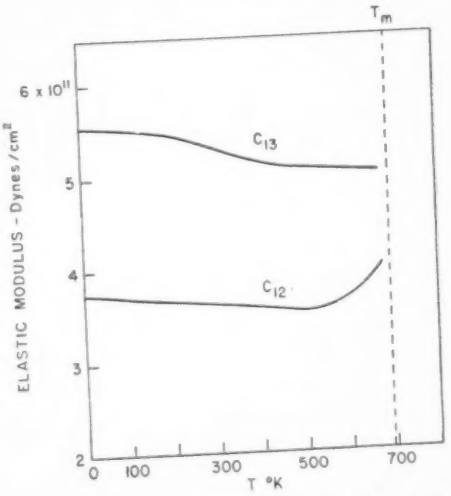


FIG. 2. Temperature-dependence of the adiabatic elastic constants $C_{12}$ and $C_{13}$. These were deduced from directly measured quantities.

they are deduced from smooth curves drawn through measured data, there are no experimental points on these curves.

Determination of the transit time of the sound pulse was accomplished to $\pm 0{\cdot}01$ $\mu$sec or about $\pm 0{\cdot}1$ per cent at all temperatures. The specimen length was measured at room temperature to an accuracy of $\pm 0{\cdot}05$ per cent. The sound-wave-propagation direction, i.e. the angle $\phi$, must be known, but for the important cases of $\phi = 0°$ and 90° errors from this source were negligibly small. For the case of $\phi = 16{\cdot}6°$, the angle was measured carefully as discussed previously. For computing the important quantity $\rho v^2$, the density of zinc was taken from the X-ray measurements of SWANSON and TATGE[11] to be 7·134 g/cm³ at room temperature. Assuming the density is correct to 0·1 per cent, the elastic constants $C_{11}$, $C_{33}$, $C_{44}$, and

*Table* 1. *Internal consistency of the measured quantities between the two zinc crystals*

Units of $10^{11}$ dynes/cm$^2$. $\gamma^2 = \cos^2\phi$ and $\beta^2 = \sin^2\phi$

| Crystal | Propagation direction | Quantity Measured | Associated elastic constant | Quantity calculated from data on Zn I |
|---|---|---|---|---|
| Zn I | $\phi = 0°$ | $\rho v_1^2 = 3{\cdot}880$ | $C_{44}$ | |
| | | $\rho v_2^2 = 3{\cdot}880$ | $C_{44}$ | |
| | | $\rho v_3^2 = 6{\cdot}347$ | $C_{33}$ | |
| | $\phi = 90°$ | $\rho v_4^2 = 6{\cdot}378$ | $\frac{1}{2}(C_{11}-C_{12})$ | |
| | | $\rho v_5^2 = 3{\cdot}887$ | $C_{44}$ | |
| | | $\rho v_6^2 = 16{\cdot}398$ | $C_{11}$ | |
| Zn II | $\phi = 90°$ | $\rho v_4^2 = 6{\cdot}344$ | $\frac{1}{2}(C_{11}-C_{12})$ | 6·378 |
| | | $\rho v_5^2 = 3{\cdot}867$ | $C_{44}$ | 3·887 |
| | | $\rho v_6^2 = 16{\cdot}362$ | $C_{11}$ | 16·398 |
| | $\phi = 16{\cdot}6°$ | $\rho v_7^2 = 4{\cdot}092$ | $\gamma^2 C_{44}+\frac{1}{2}\beta^2(C_{11}-C_{12})$ | 4·082 |
| | | $\rho v_8^2+\rho v_9^2 = 11{\cdot}055$ | $(C_{11}+C_{44})+\gamma^2(C_{33}-C_{11})$ | 11·044 |
| | | $\rho v_8^2-\rho v_9^2 = 5{\cdot}167$ | $\{[\beta^2(C_{11}-C_{44})+\gamma^2(C_{44}-C_{33})]^2+4\gamma^2\beta^2(C_{13}+C_{44})^2\}^{\frac{1}{2}}$ | 5·148 |

$\frac{1}{2}(C_{11}-C_{12})$ as well as $\rho v_8^2$ should then be accurate to $\pm 0{\cdot}5$ per cent. Actually repeated measurements of the same constant on the same crystal differed from one another by at worst 0·3 per cent. However, measurements of the same constant on two different crystals differed by approximately 0·5 per cent. These conclusions are exhibited in Table 1, which shows the internal consistency of all twelve measurements made on the two zinc single crystals prepared for this experiment.

The deduced constants $C_{12}$ and $C_{13}$ cannot be determined to $\pm 0{\cdot}5$ per cent accuracy because of propagation of errors. The calculation of $C_{12}$ is simple but leads to an uncertainty of $\pm 2$ per cent because it involves a difference of two quantities. $C_{13}$ presents a much more difficult problem, not only because equation (5) is elaborate, but also because the angle $\phi$ must be known quite accurately. An uncertainty of 0·1° in $\phi$ results in a 1 per cent uncertainty in $C_{13}$. The final accuracy of $C_{13}$ is estimated to be $\pm 5$ per cent.

Once all five of the elastic modulii have been determined, it is possible to compute the five elastic compliances $S_{11}$, $S_{12}$, $S_{33}$, $S_{44}$, and $S_{13}$ and the two linear compressibilities $K_\perp$ and $K_\parallel$. Some of these quantities have been measured previously,[12–14] and Table 2 shows a comparison of these results at room temperature. Considering the propagation of errors in converting the $C$ constants to the $S$ constants, the agreement is remarkably good. In fact the measured value of $C_{13}$ must be much closer to the true value than its estimated error of $\pm 5$ per cent would indicate. If $C_{13}$ were changed by 1 per cent, the overall agreement with other measurements would become much worse.

Figs. 3 and 4 show the temperature dependence of the compliances and of the linear compressibilities. The flags on these curves represent the uncertainties which arise from the propagation of errors. The dotted curves are the measurement of WERT and TYNDALL.[13] They measured $S_{11}$ nearly directly and here the agreement is quite good. Their measurement of $S_{33}$ was more indirect, and the agreement is not as good in this case. They also show that $2S_{13}+S_{44}$ goes through a maximum

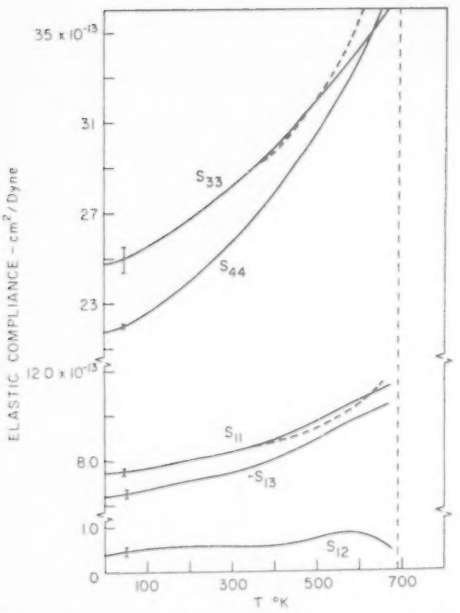


FIG. 3. Temperature-dependence of the adiabatic elastic compliances as deduced from the measurements. The flags represent the uncertainty expected from propagation of errors in the calculations. The dashed curves show the results of WERT and TYNDALL.[13]

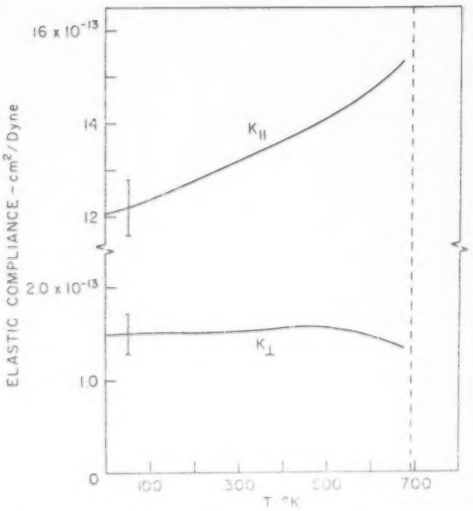


FIG. 4. Temperature-dependence of the two linear compressibilities of zinc. The flags represent the uncertainty expected from propagation of errors in the calculations.

near 500°K. The present results, however, show a continuous rise of this quantity over the entire temperature range. The reason for this difference is not clear.

Tables 3 and 4 give the values of all the elastic constants and compliances from 4·2 to 670°K. The tables were obtained by drawing smooth curves through the measured points and then reading off the values of $C_{11}$, $C_{33}$, $C_{44}$, $\frac{1}{2}(C_{11}-C_{12})$ and $\rho v_8^2$ at particular temperatures. These "smoothed" constants appearing in Table 3 were then used to compute the temperature variation of $C_{12}$, $C_{13}$, the $S$ constants, and the compressibilities.

## 4. DISCUSSION

One of the most striking features of zinc is its high anisotropy. This can be expressed by the ratio of the linear compressibilities $K_\parallel/K_\perp$ which for zinc extrapolated to 0°K, is 7·9. For magnesium, which is considered very isotropic, this ratio is 1·04 at 0°K.[1] Such a large anisotropy is not surprising in view of the large $c/a$ ratio of zinc (1·86). This ratio means that the atoms are more closely packed in the base plane and hence comparatively less compressible in that plane. As a function of temperature, the $c/a$ ratio increases and with it the

*Table 2. Comparison of the present room temperature results with those of other workers*

Units of $10^{-13}$ cm²/dyne

| | $S_{11}$ | $S_{33}$ | $S_{44}$ | $S_{12}$ | $S_{13}$ | $\frac{K_\parallel}{(2S_{13}+S_{33})}$ | $\frac{K_\perp}{(S_{11}+S_{12}+S_{13})}$ |
|---|---|---|---|---|---|---|---|
| Present work | 8·41 | 28·23 | 25·78 | 0·55 | −7·47 | 13·29 | 1·48 |
| GRÜNEISEN and GOENS[12] | 8·4 | 28·7 | 26·4 | 1·1 | −7·7 | | |
| WERT and TYNDALL[13] | 8·38 | 28·38 | 26·1 | $0·5_8$ | −7·31 | | |
| BRIDGMAN[14] | | | | | | 13·77 | 1·60 |

$K_\parallel/K_\perp$ ratio, as is to be expected from the argument above. However, unlike the $c/a$ ratio in which both $c$ and $a$ increase with temperature, the increase in $K_\parallel/K_\perp$ is almost entirely due to the numerator alone since the denominator, $K_\perp$, remains nearly constant. This means that even though all the atoms get farther apart at high temperatures, the base plane retains its resistance to being compressed while the $c$ direction becomes more compressible. Such an effect is quite strange, but it could imply that the binding in the base plane is different from that along the $c$-axis. That is, it implies that there is a separate contribution to the binding in the base plane, which has a small or negative temperature coefficient. The existence of covalent bonds operating only in the base plane has been proposed by WALLACE,[15] but the use of his bonding scheme to explain the present results would require a detailed calculation and discussion beyond the scope of this paper. We simply conclude that our results are compatible with his proposal.

*Table 3. Adiabatic elastic constants of zinc*

Units of $10^{11}$ dynes/cm²

| $T$(°K) | $C_{11}$ | $C_{33}$ | $C_{44}$ | $\frac{C_{11}-C_{12}}{2}$ | $\rho v_s^2$ | $C_{13}$ | $C_{12}$ |
|---|---|---|---|---|---|---|---|
| 4·2 | 17·909 | 6·880 | 4·595 | 7·080 | 8·956 | 5·54 | 3·75 |
| 77 | 17·677 | 6·766 | 4·479 | 7·000 | 8·814 | 5·52 | 3·68 |
| 150 | 17·336 | 6·620 | 4·296 | 6·837 | 8·609 | 5·48 | 3·66 |
| 200 | 17·047 | 6·523 | 4·158 | 6·689 | 8·443 | 5·45 | 3·67 |
| 250 | 16·730 | 6·428 | 4·018 | 6·533 | 8·278 | 5·37 | 3·66 |
| 295 | 16·368 | 6·347 | 3·879 | 6·361 | 8·111 | 5·30 | 3·64 |
| 350 | 16·002 | 6·257 | 3·724 | 6·194 | 7·934 | 5·21 | 3·61 |
| 400 | 15·590 | 6·168 | 3·573 | 6·006 | 7·756 | 5·15 | 3·58 |
| 450 | 15·138 | 6·077 | 3·417 | 5·792 | 7·583 | 5·11 | 3·55 |
| 500 | 14·648 | 5·982 | 3·261 | 5·567 | 7·408 | 5·08 | 3·51 |
| 550 | 14·219 | 5·887 | 3·098 | 5·340 | 7·234 | 5·06 | 3·54 |
| 600 | 13·843 | 5·793 | 2·933 | 5·095 | 7·060 | 5·04 | 3·65 |
| 670 | 13·395 | 5·661 | 2·667 | 4·655 | 6·818 | 5·02 | 4·08 |

A binding force operating only in the base plane is certainly not a central force. Thus, we cannot expect the Cauchy relations to be satisfied. For a hexagonal metal, these are $C_{13}-C_{44}=0$ and $C_{11}-3C_{12}=0$. Reference to Table 3 shows that indeed they are not satisfied at 0°K. At higher temperatures the difference $C_{13}-C_{44}$ increases, but $C_{11}-3C_{12}$ decreases and actually approaches zero as the melting point is approached. The significance of having only one relation satisfied near the melting point is not clear. It should be noted, however, that the deviation from the Cauchy relations is not proof that there is a non-central binding force active only in the base plane. The electron gas also contributes a non-central binding force. In fact, it can be shown that for a simple model[1,16] of a metal the difference $C_{13}-C_{44}=B_e$ may be interpreted as the bulk modulus of an electron gas. Using the present measurements at 0°K, $B_e$ is $0{\cdot}9\times10^{11}$ dynes/cm². From free-electron theory[16] and using a valence of 2, $B_e=13\times10^{11}$ dynes/cm². Such disagreement is not surprising, since the model is an oversimplification and the electrons in zinc cannot be considered free.

A very important use of the low-temperature elastic constants is the computation of the Debye temperature at 0°K. This requires the determination of the average value of the sum of the reciprocals of the cubed wave velocities. A value of $\theta_0=320$°K was determined by graphical integration, while a value of 327°K was obtained from the series-expansion method of BETTS *et al.*[17]. The value of 320°K is more nearly correct, since the series-expansion method is actually an approximation to the graphical method, and is expected to fail for highly anisotropic metals like zinc. In the

*Table 4. Adiabatic elastic compliances and linear compressibilities calculated from the elastic-constant measurements*

Units of $10^{-13}$ cm²/dyne

| $T$(°K) | $S_{11}$ | $S_{33}$ | $S_{44}$ | $S_{13}$ | $S_{12}$ | $K_\perp$ | $K_\parallel$ |
|---|---|---|---|---|---|---|---|
| 4·2 | 7·45 | 24·70 | 21·76 | −6·31 | 0·392 | 1·53 | 12·07 |
| 77 | 7·62 | 25·57 | 22·23 | −6·61 | 0·481 | 1·49 | 12·35 |
| 150 | 7·85 | 26·63 | 23·28 | −6·95 | 0·540 | 1·44 | 12·72 |
| 200 | 8·03 | 27·26 | 24·05 | −7·17 | 0·555 | 1·42 | 12·93 |
| 250 | 8·20 | 27·77 | 24·89 | −7·31 | 0·549 | 1·44 | 13·15 |
| 295 | 8·41 | 28·23 | 25·78 | −7·47 | 0·547 | 1·48 | 13·29 |
| 350 | 8·61 | 28·68 | 26·85 | −7·62 | 0·539 | 1·53 | 13·44 |
| 400 | 8·89 | 29·40 | 27·99 | −7·90 | 0·567 | 1·56 | 13·60 |
| 450 | 9·27 | 30·47 | 29·27 | −8·33 | 0·637 | 1·58 | 13·81 |
| 500 | 9·73 | 31·82 | 30·66 | −8·90 | 0·750 | 1·58 | 14·03 |
| 550 | 10·19 | 33·26 | 32·28 | −9·47 | 0·831 | 1·55 | 14·32 |
| 600 | 10·64 | 34·61 | 34·09 | −9·97 | 0·823 | 1·49 | 14·67 |
| 670 | 11·20 | 35·99 | 37·49 | −10·33 | 0·456 | 1·32 | 15·32 |

case of an isotropic metal like magnesium, the two methods agree to better than 1°K.

There are several determinations of $\theta_0$ from low-temperature specific-heat measurements. The earliest of these, by KEESOM and VAN DER ENDE,[18] gives the result $\theta_0 = 320$°K, while the more recent measurement of DAUNT and SILVIDI[19] in the liquid-helium range gives $\theta_0 = 291$°K. SMITH[20] gives the value $\theta_0 = 306$°K and shows that $\theta$ decreases rapidly with increasing temperature. The reason for this wide separation between the acoustic and the calorimetric results is being investigated in this laboratory by repeating the specific-heat measurements and by re-examining the methods of calculation $\theta_0$ from elastic-constant values.

*Acknowledgement*—The authors wish to thank Dr. E. P. T. TYNDALL of the State University of Iowa for his co-operation in providing the zinc single crystals used for these measurements.

## REFERENCES

1. SLUTSKY L. J. and GARLAND C. W. *Phys. Rev.* **107,** 972 (1957).
2. MUSGRAVE M. J. P. *Proc. Roy. Soc.* A**226,** 356 (1954).
3. NEIGHBOURS J. R. *J. Acoust. Soc. Amer.* **26,** 865 (1954).
4. ALERS G. A. and NEIGHBOURS J. R. *J. Appl. Phys.* **28,** 1514 (1957).
5. MCSKIMIN H. J. *J. Appl. Phys.* **26,** 406 (1955).
6. ALERS G. A. *Phys. Rev.* **97,** 863 (1955).
7. GILMAN J. J. and DECARLO V. J. *Trans. Amer. Inst. Min. (Metall.) Engrs.* **206,** 511 (1956).
8. HUNTINGTON H. B. *Phys. Rev.* **72,** 321 (1947).
9. OVERTON W. C. and GAFFNEY J. *Phys. Rev.* **98,** 969 (1953).
10. GRÜNEISEN E. and GOENS E. *Z. Phys.* **29,** 141 (1924).
11. SWANSON H. E. and TATGE E. *Circ. Nat. Bur. Stand.* No. **539,** Vol. 1, 16 (1953).
12. GRÜNEISEN E. and GOENS E. *Z. Phys.* **26,** 235 (1924).
13. WERT C. A. and TYNDALL E. P. T. *J. Appl. Phys.* **30,** 587 (1949).
14. BRIDGMAN P. W. *Phys. Rev.* **47,** 393 (1945).
15. WALLACE W. E. *J. Chem. Phys.* **23,** 2281 (1955).
16. DELAUNAY J. *Solid State Physics* (Ed. F. SEITZ and D. TURNBULL) Vol. 2. Academic Press, New York (1956).
17. BETTS D. D., BHATIA A. B. and HORTON G. K. *Phys. Rev.* **104,** 43 (1956).
18. KEESOM W. H. and VAN DER ENDE J. N. *Proc. K. Akad. Wetensch. Amsterdam* **35,** 143 (1932).
19. DAUNT J. G. and SILVIDI A. A. *Phys. Rev.* **77,** 125 (1950).
20. SMITH P. L. *Phil. Mag.* **46,** 744 (1955).

*J. Phys. Chem. Solids* Pergamon Press 1958. Vol. 7. pp. 65–77.

# THE CRYSTAL STRUCTURE AND PROPERTIES OF THE GROUP VB TO VIIB ELEMENTS AND OF COMPOUNDS FORMED BETWEEN THEM

**E. MOOSER and W. B. PEARSON**

Division of Pure Physics, National Research Council, Ottawa, Canada

(*Received* 10 *February* 1958)

VOL. 7 1958

**Abstract**—The crystal structures of the Group VB to VIIB elements and of compounds formed between them are discussed on the basis of the valence-bond theory. A consistent bond scheme is proposed and applied to derive qualitative band structures for these materials. The band structures, which in many cases deviate from the usual semiconductor band model, afford a satisfactory interpretation of the anomalous electrical and optical properties observed in some of the substances under consideration. Thus, for instance, they provide an explanation of the anomalous sign reversals of the Hall coefficients observed in both tellurium and $Bi_2Te_3$. Semiconducting properties are predicted for a series of ternary compounds.

## 1. INTRODUCTION

MOST of the semiconducting compounds known at present contain elements lying on both sides of the Zintl border. While their properties can readily be interpreted on the basis of the usual semiconductor band scheme, this is not, in general, the case for compounds containing Group VB to VIIB elements* only. Thus, the properties of $Bi_2Se_3$ and of $Bi_2Te_3$, for example, can be explained within the framework of the semiconductor theory only if additional assumptions are made; this is true also for selenium and tellurium. Using the "valence-bond approach",[1,2] MOOSER and PEARSON[3] therefore put forward an alternative description of these elements. Even though at that time few experimental data were available on the properties of compounds formed between Group VB to VIIB elements, it was suggested that the same description applied to at least some of them also. Since then new results, especially on the properties of compounds of the type $A_2^{V}B_3^{VI}$, have been published, and they can now be included in our discussion.

Although the valence-bond treatment as applied to solids is based on fundamental quantum-mechanical principles, it is not suited for any *quantitative* band calculations. It can, however, very well be used as a guide in *qualitative* discussions of band structures, and one of its most useful assets is that it affords an understanding of whole families of chemically and/or structurally related substances. Thus, in the present paper we apply the valence-bond theory to derive qualitative band structures for the family of substances containing only Group VB to VIIB elements. In many cases these band structures deviate from that normally found in semiconductors, and it will follow from our discussion that they provide a satisfactory explanation for the anomalies observed in many of the substances under consideration.

In Section 2 we will briefly discuss the bonds formed by the Group VB to VIIB atoms. The findings of Section 2 will then be applied to discuss the structures and electrical properties of a series of elements and compounds. Anomalies such as the double reversal of the sign of the Hall coefficients observed in both tellurium and $Bi_2Te_3$ will be interpreted. Finally, semiconducting properties will be predicted for a series of ternary compounds.

* For convenience we shall consider this designation also to include sulphur.

*Table* 1.

| Group number | Valence state | Valence | Bond type | Co-ordination number | Bond number |
|---|---|---|---|---|---|
| VB | *A* | 3 | $p^3$ | 3 | 1 |
| | $A^+$ | (2) | $p^3$ resonance | 6 | 1/3 |
| | *B* | 3 | $sp^3$ | 3 | 1 |
| | *C* | 3 | $p^3d^3$ resonance | 6 | 1/2 |
| | $D^-$ | (6) | $sp^3d^2$ | 6 | 1 |
| VIB | *A* | 2 | $p^2$ | 2 | 1 |
| | *B* | 2 | $sp^3$ | 2 | 1 |
| | *C* | 4 | $p^3d^3$ resonance | 6 | 2/3 |
| | *D* | 6 | $sp^3d^2$ | 6 | 1 |
| VIIB | *A* | 1 | *p* | 1 | 1 |
| | *B* | 1 | $sp^3$ | 1 | 1 |

## 2. THE BONDS FORMED BY THE GROUP VB TO VIIB ATOMS

The valence-bond theory offers no rigorous criteria for selecting the valence states best suited to describe the chemical bonding in a solid. However, the stoichiometric formula, the co-ordination of the atoms, and the interatomic distances of any particular substance often leave little doubt about the best choice. Thus we readily recognize that valence states *A* and *B* listed in Table 1 will be the most important ones in the Group VB to VIIB elements and in compounds formed between them. However, in some modifications of these substances the co-ordination numbers exceed the maximum numbers of possible *p* (or $sp^3$) bonds, which are three, two, and one in the Group VB, VIB, and VIIB atoms, respectively. We therefore have to assume either that the bonds undergo pivotal resonances among various positions leading to bond numbers smaller than unity, or that hybrid bonds are formed which involve the *s* electrons (e.g. types *D* and $D^-$ in Table 1.* The number of such hybrid bonds may then be high enough to satisfy the atomic co-ordination.

PAULING[1] has discussed the conditions under which pivotal resonance of bonds can develop, the most important being that empty ("metallic") orbitals must be available in at least one of any two atoms which are linked by a resonating bond. Unless electrons are removed from the *p* orbitals by ionization (type $A^+$), the only means by which empty orbitals become available for the valence electrons of the Group VB to VIIB atoms is a degeneracy in the solid of the vacant *d* orbitals of the valence shell with the occupied *p* orbitals. This degeneracy can take the form of a *p*–*d* hybridization such as is indicated in state *C* (Table 1). The conditions for the occurrence of resonating bonds are such that in a compound it is sufficient to postulate the availability of empty orbitals on the "cations" only, as long as the bonds only form between "cations" and "anions". The valence states of the anions are then of type *A* and/or *B*, and the bonding will lead to a filling of the *s* and *p* orbitals on the anions. Thus, in accordance with the concept of the "semiconducting bond",[2, 4]

* We shall ignore the possibility of ionic-bond formation.

semiconducting or insulating properties will result. If, however, resonating anion–anion bonds are formed, then states with empty orbitals have to be admixed to states $A$ and $B$ of the anions to an extent which depends on the strength of the anion–anion bonds.* Similarly, if in an elemental structure resonating bonds occur at all, states with empty orbitals have to be provided. In whatever way these empty orbitals are produced, they represent a violation of the requirements of the semiconducting bond and hence will affect the electrical properties.

In the present paper we attribute any increase of the co-ordination numbers beyond the normal valences to the occurrence of pivotal resonance rather than to the formation of single bonds of the hybrid $sp^3d^2$ type for the following reasons:

(1) This treatment is in better agreement with the stoichiometric formulae and interatomic distances.

(2) It can be applied to describe the bonding in all substances considered. This is not true for non-resonating bonds.

(3) The assumption of resonating bonds leads to a satisfactory interpretation of the anomalous electrical properties found in selenium, tellurium, $Bi_2Se_3$, and $Bi_2Te_3$.

With regard to the arbitrariness introduced by any particular choice of valence states, we observe that it is of no great importance to our treatment what the actual choice is, provided that it allows for the pivotal resonance to develop whenever the co-ordination numbers exceed the normal valences of the Group VB to VIIB atoms.

### 3. THE GROUP VB ELEMENTS As, Sb and Bi

The bond scheme of the Group VB elements, as well as the band structure to which this scheme leads, has been discussed previously by MOOSER and PEARSON.[3] While going more into details, the present discussion also forms the basis of our interpretation of selenium, tellurium, iodine, and of compounds of the types $A_2{}^{V}B_3{}^{VI}$, $A^{V}B^{VI}C^{VII}$, and $A^{V}C_3{}^{VII}$.

In the amorphous modifications of arsenic and antimony, which are both semiconductors, double layers of atoms are found, each atom being surrounded by three neighbours. The double layers form tiny flakes which are randomly arranged with respect to one another, thus causing the "amorphous" nature of these substances (see KREBS *et al.*[5] and KREBS and SCHULTZE-GEBHARDT[6]). The 3-co-ordination of the atoms is characteristic of covalent bonds based on valence states of types $A$ and $B$. Since through the sharing of electrons the octet on each atom is completed, this bonding leads to semiconducting properties. Amorphous arsenic and antimony are both semiconductors.

On the basis of the valence states $A$ and $B$, no resonating bonds can form. However, if states such as $C$, which involve a $p$–$d$ hybridization, are admixed to $A$ and $B$, empty orbitals become available for the valence electrons, and pivotal resonances can develop. Thus, the ordering of the double layers which takes place as the amorphous phases transform into the crystalline ones and which results in a drastic reduction of the second-nearest-neighbour distances (see Table 2) can be interpreted as the onset of resonances involving $p$–$d$ hybridization. The empty orbitals required for the formation of resonating bonds lead to metallic properties, in good agreement with experiment.

When the metal bismuth melts, the short-range order is completely changed,[7] each atom acquiring 7–8 neighbours at an average distance of 3·32 Å. This change can readily be interpreted in terms of better developed resonances, extensive use being made of the empty $d$ orbitals. As would be expected from better developed resonances, the resistivities of liquid bismuth and antimony are appreciably smaller than those of the solid phases.[8,9] Thus we see that the valence-bond theory accounts rather well for the changes in electrical properties which accompany the structural transformations, and it seems reasonable to use it as a guide in deriving a qualitative band scheme of the Group VB elements.

The properties of the amorphous phases of arsenic and antimony can be interpreted in terms of a normal semiconductor band structure. The valence band and the conduction band are formed

* The stoichiometric formulae indicate that in all the compounds to be considered in the present paper the anions strive to complete their $s$ and $p$ orbitals through electron sharing. States involving empty $d$ orbitals are therefore admixed to a very small extent only, as is substantiated also by the weakness of the anion–anion bonds. The corresponding anion–anion distances usually lie about half-way between the single bond diameters and the van der Waals' diameters.

*Table 2.*

| | Crystalline | | Amorphous | | Liquid | | van der Waals' diameter (Å) |
|---|---|---|---|---|---|---|---|
| | Interatomic distance (Å) | Number of neighbours | Interatomic distance (Å) | Number of neighbours | Interatomic distance (Å) | Number of neighbours | |
| As | 2·51 | 3 | 2·5 | 3·1 | | | 4·0 |
| | 3·15 | 3 | 3·75 | | | | |
| Sb | 2·87 | 3 | 2·87 | ~ 3 | | | 4·4 |
| | 3·37 | 3 | 3·75 | 2·6 | | | |
| Bi | 3·10 | 3 | — | — | 3·32 | 7–8 | |
| | 3·47 | 3 | — | — | (6·6) | | |
| Se | 2·32 | 2 | 2·35 | 2·1 | 2·36 | 2·3 | 4·0 |
| | 3·46 | 4 | 3·7 | | 3·7 | | |
| | | | | | At 465°C / At 610°C | | |
| Te | 2·86 | 2 | — | — | 2·93 / 2·9 | 2·3 | 4·4 |
| | 3·46* | 4 | — | — | 3·5 | | |
| | | | | | 4·4 / 4·3 | | |

* In *Strukturbericht* I, a next-nearest-neighbour distance of 3·74Å has erroneously been given for tellurium.

by the bonding and anti-bonding states arising from the atomic 4*p* and 5*p* states (see e.g. DEHLINGER[10]). The conduction band will also contain states stemming from the atomic 4*d* and 5*d* states. As the double layers of atoms arrange themselves in the crystalline form, the conduction band and the valence band will not be affected very much, since the immediate neighbourhood of each atom is retained in the ordering process. However, as a result of the short next-nearest-neighbour distances observed in the crystals, some of the *d* orbitals of the valence shell of each atom overlap with similar orbitals of its next-nearest neighbours. The energy of the *d* states is therefore depressed, and some of them become available for the valence electrons. In the valence-bond treatment, this corresponds to the proposed admixture of valence states of type *C* to states of types *A* and *B*. In the band picture, on the other hand, it means that the *d* states form a band which bridges the gap between the conduction and valence bands and actually overlaps with the latter, giving rise to the metallic properties exhibited by the crystalline phases. In the liquid phases, the various bands are completely smeared out.

The three-band model proposed here for the crystalline state is well supported by photoelectric measurements on arsenic and antimony made by TAFT and APKER.[11,12] From their experimental data, these authors conclude that the valence bands found in amorphous arsenic and antimony are not much affected by crystallization. "Between the edge of the occupied band of the semiconductor (amorphous phase) and the Fermi level, however, a relatively low but clearly discernable group of occupied energy levels appears on crystallization. It is this group, of course, which is responsible for the characteristic poorly metallic behaviour of these crystals."

#### 4. THE GROUP VIB ELEMENTS Se and Te

Selenium and tellurium both crystallize in the same hexagonal structure in which the atoms form infinite spiral chains. Each atom has two nearest neighbours in its own chain and four more neighbours lying at a somewhat greater distance in the adjacent chains. Since the next-nearest-neighbour distances are much too short to be due to van der Waals' bonds only (Table 2), the resulting distorted octahedral co-ordination must, according to our views, be based on a mixture of valence states *A*, *B*, and *C*. While states *A* and *B* account for the bonds between nearest neighbours, state *C*, containing empty orbitals, allows for the bond

resonances necessary to explain the short interchain distances.*

In Group VB elements the formation of resonating bonds gives rise to a band overlap and hence to metallic properties. From the above bond scheme, we expect a similar overlap to occur in hexagonal selenium and tellurium. However, these elements are usually considered to be semiconductors, and we therefore have to look into the details of their band structures. REITZ[14] has calculated the band model corresponding to a single infinite chain of selenium or tellurium atoms, assuming to the first order of approximation the bond angles to be 90°. His results show a splitting of the $p$ levels into three separate bands, the lowest of which contains the bonding states. The middle band arises from the non-bonding $p$ orbitals, and the highest band is formed by anti-bonding states. The middle and upper bands constitute the valence and the conduction bands of a semiconductor, the first being completely filled with electrons and the latter empty. In addition to these bands, REITZ finds a series of unoccupied $d$ bands which he assumes either to overlap with or to lie above the conduction band. This model does not, however, take into account interactions between neighbouring chains, which, according to the discussion given above, are appreciable. Rather than applying to the crystalline state, it describes the amorphous and liquid phases of selenium in which the same spiral chains occur as in the crystals. Here the chains are, however, arranged randomly with respect to one another, the average interchain distance being 3·7 Å,[15,16] i.e. considerably greater than the corresponding distance (3·46 Å) observed in crystalline selenium. The interactions between neighbouring chains are therefore negligible here, and it is indeed well known that amorphous and liquid selenium are semiconductors, both having an activation energy of 2·3 eV.

The valence-bond picture describes the properties of amorphous and of liquid selenium equally well. Since the bigger separation between the chains and their random arrangement destroy all resonances, one is left with bonds based on valence states $A$ and $B$ which lead to a complete filling of the $s$ and $p$ orbitals and hence to semiconducting properties. However, the valence-bond treatment goes one step further, since, as in the Group VB elements, the proposed $p$–$d$ hybridization implies that some $d$ states are depressed into the valence band when the chains rearrange themselves in the crystalline state.* Taking account of experimental data as well, we are thus led to propose the following three-band model for crystalline selenium and tellurium:

(1) The valence and conduction bands corresponding to a single chain of atoms are also found in the crystals, the gap between them being 2·3 eV in selenium and 0·35 eV in tellurium.

(2) Some $d$ states are depressed across the band gap and dip into the valence band, thus forming a third band of low state density which bridges the "forbidden" zone and empties some $10^{13}$–$10^{16}$ $cm^{-3}$ states of the valence band.

Because of the low density of states which has to be assumed for the overlapping third band in order to comply with experimental results, this band scheme is very similar to that of a semiconductor containing $10^{13}$–$10^{16}$ $cm^{-3}$ acceptors. The main difference is that here the empty states in the valence band are an intrinsic property of the crystals.

Some of the properties of selenium and tellurium have already been interpreted in terms of this band model.[3] In the present discussion we therefore mainly include recent experimental results. KOZYREV[18] has found in selenium a remarkable decrease in the concentration of holes with increasing temperature. This decrease, which is quite contrary to what one expects in a semiconductor, can, in our model, be explained by a weakening of the resonances due to enhanced thermal vibrations. At the melting point, the resonances are completely destroyed and, because of the resulting reduction of the charge-carrier concentration, a decrease of the conductivity is observed (see e.g. BORELIUS *et al.*[19]). The magnetic-susceptibility measurements on solid and liquid selenium made by BUSCH and

* The use of resonating bonds to explain the structures of selenium and tellurium was first proposed by VON HIPPEL.[13]

* Recently GASPAR[17] has proposed a band structure for selenium and tellurium which is very similar to the one given by REITZ.[14] GASPAR does, however, allow for interchain interactions and, in accordance with our views, he concludes that the close approach of the chains results in an overlap of some of the $d$ orbitals on next-nearest neighbours and hence in a modification of the $d$ bands.

VOGT[20] lead to a similar conclusion: the semiconducting character of selenium increases as one goes from the solid to the liquid phase.

Tellurium, on the other hand, behaves quite differently on account of its small energy gap. As shown by the exponential dependence on temperature of the electrical conductivity, electrons are excited across the "forbidden" zone, which here is only 0·35 eV wide. Because of this excitation, more and more vacant orbitals are formed in the valence band, so that the resonances can develop better as the temperature rises. This then explains why with increasing temperature the ratio $c/a$ of the crystallographic axes of tellurium decreases towards the value of 1·225,[21] which corresponds to an ideal octahedral co-ordination of the atoms. In selenium, on the other hand, where the resonances decrease, $c/a$ moves away from this value as the temperature is raised.[21] The fact that the melting point of tellurium (450°C) is higher than that of selenium (220°C) supports the assumption of

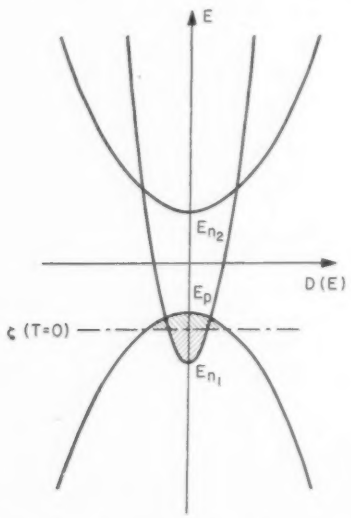


FIG. 1. The three-band model used to calculate the charge-carrier concentrations in tellurium and $Bi_2Te_3$.

better developed resonances, i.e. stronger interchain bonds in tellurium.

The most striking anomalies of tellurium are the two sign reversals of the Hall constant in the solid phase, followed by a third one in the liquid phase.[22] TANUMA[23] has interpreted the second reversal in the solid by assuming a temperature-dependent number of acceptors. However, the number of thermally generated acceptors actually

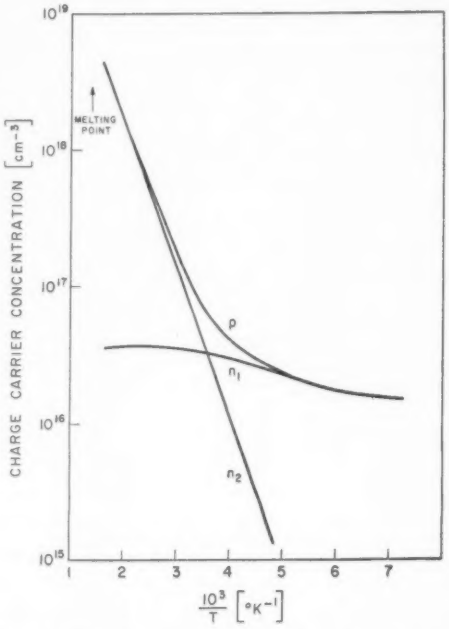


FIG. 2. The charge-carrier concentrations in intrinsic tellurium, as calculated from the band structure (Fig. 1).

found in tellurium[24] is much too small to account for such a reversal. Another interpretation, put forward by CALLEN,[25] is based on a wrong band structure (see e.g. the criticism by GASPAR[17]).

To demonstrate that the band structure proposed here accounts for the anomalous temperature-dependence, let us assume the density of states in both valence and conduction band to be that of free electrons (see Fig. 1). The density of states of the third overlapping band is chosen to be $10^{-4}$ times smaller. If then the energies of the band edges are $E_{n_1} = -0{\cdot}175$ eV, $E_p = -0{\cdot}15$ eV, and $E_{n_2} = +0{\cdot}15$ eV (see Fig. 1), we find by graphical methods[26] the charge-carrier concentrations $n_1$, $n_2$, and $p$ as given in Fig. 2. Next we make the usual assumption that the mobilities $\mu_{n_2}$ and $\mu_p$ of the electrons and holes in the conduction and valence band, respectively, are proportional to $T^{3/2}$. The mobility $\mu_{n_1}$ of the electrons

VOL. 7 1958

in the third band, however, is taken to be proportional to $T^{-1}$, since the electrons in this band are strongly degenerate. If then at $T = 300°K$

$$\mu_{n_1} : \mu_{n_2} : \mu_p = 1{\cdot}3 : 1 : 1{\cdot}05,$$

we find from

$$R = \frac{-n_1\mu_{n_1}{}^2 - n_2\mu_{n_2}{}^2 + p\mu_p{}^2}{e\cdot(n_1\mu_{n_1} + n_2\mu_{n_2} + p\mu_p)^2}$$

the values of the Hall coefficient $R$ as given in Fig. 3. The result shows that our model does readily

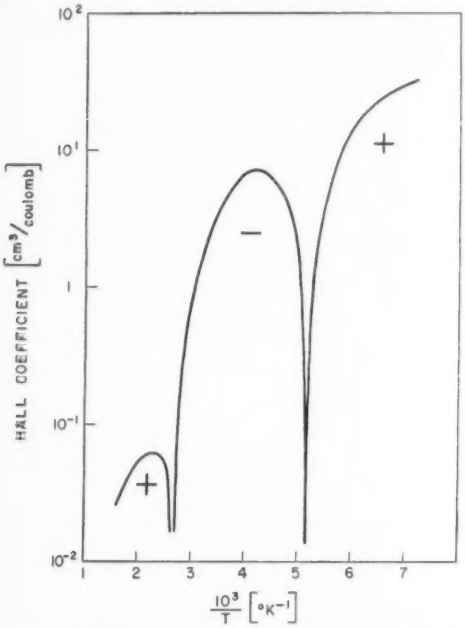


FIG. 3. Calculated dependence on temperature of the Hall coefficient of tellurium.

account for the observed double reversal. The absolute values of $R$ as calculated from the above assumptions do, however, differ appreciably from the experimental values, and while state densities and mobilities could readily be adjusted to give better agreement with experiment, such adjustments would be rather arbitrary with our present knowledge of tellurium.

On melting, the interchain bonds are broken, and the overlapping band is shifted towards higher energies. Since, according to our model, the conduction and the valence bands are essentially those arising from non-interacting chains and since, according to Fig. 2, $n_1 \ll n_2 \approx p$ at the melting point, fusion should not affect the number of free charge carriers. However, in tellurium the difference between the strengths of intrachain and interchain bonds is considerably smaller than in selenium. As soon as the interchain bonds start to break up, some of the intrachain bonds will break also. This leads to a change of the short-range order[16] and hence to a change of the charge-carrier concentrations as the temperature of the melt is increased. New resonances of the type observed in liquid bismuth develop, and the behaviour of the melt becomes more and more metallic.[27] While the positive Hall constant found near the melting point[22] is still characteristic for non-interacting chains (liquid selenium also shows $p$-type conduction), the sign reversal at higher temperatures clearly indicates metallic properties.

The interpretation of the sign reversals given here is very qualitative. Nevertheless, it shows that our model is compatible with the unusual behaviour of tellurium.

### 5. THE GROUP VIIB ELEMENT I

Strong support for our views comes from the nuclear quadruple coupling found in solid iodine. The structure of iodine consists of layers of diatomic molecules. The distance between the two atoms of a molecule is 2·70 Å, and the shortest distance between two molecules of the same layer is 3·54 Å, indicating that the intermolecular bonds in a layer are stronger than van der Waals' bonds. According to our model, we would suggest that states involving $p$–$d$ hybridization are admixed to states of types $A$ and $B$. ROBINSON *et al.*[28] have, indeed, proposed that $5s^25p^45d$ states must be admixed to the ground state $5s^25p^5$ to explain the quadrupole coupling observed in solid iodine, and their findings have since been confirmed by ITOH and KAMBE.[29] ROBINSON *et al.*[28] actually speak of a superposition of localized (intramolecular) and non-localized (intermolecular) bonds, thus indicating that in iodine, also, there exists a finite, if only very small, number of intrinsically free charge carriers.

### 6. COMPOUNDS OF THE TYPE $A_2{}^{V}B_3{}^{VI}$

(a) *Phases with the C33 structure*

Compounds of the type $A_2{}^{V}B_3{}^{VI}$, and especially

those crystallizing in the rhombohedral *C*33 type of structure, have in recent years become of great interest because of their thermoelectric applications. As a result, a number of papers on their properties have been published.[30–37] Unfortunately the interpretations of the experimental results are somewhat confusing, partly because of the difficulties in preparing good samples and partly because of the anomalous behaviour of these substances. However, the following facts are at present well established:

(1) Samples of $Sb_2Te_3$ and $Bi_2Te_3$ grown from a melt of stoichiometric composition are always *p*-type conductors. Under the same conditions, samples of $Bi_2Se_3$ show *n*-type conduction.

(2) In all such samples the number of free charge carriers is essentially constant to well above room temperature.

(3) The number is far greater than would be expected from the impurity content of the initial material from which the samples were made.

(4) Experimental results from various sources show a remarkable agreement of the number of free charge carriers (see Table 3).

(5) Zone melting does not produce any appreciable effect on the number of free charge carriers.

Not only are all these results compatible with a band scheme similar to that proposed for selenium and tellurium, but, on the basis of a normal semiconductor band structure, they can only be interpreted if additional and somewhat arbitrary assumptions are made. It is therefore worthwhile to investigate whether the structural features of these compounds support our band model.

The *C*33 structure in which $Sb_2Te_3$, $Bi_2Se_3$, $Bi_2Te_3$, and $Bi_2Te_2S$ crystallize is built up of multiple layers, each of which contains five atomic sheets in the sequence *B–A–B–A–B*. The stacking of these sheets is such that each atom inside one of the five-fold layers acquires a slightly distorted octahedral neighbourhood. The *B* atoms (Se, Te) at the boundaries of each multiple layer, however, have three nearest *A* neighbours (Sb, Bi) in the same multiple layer and three next-nearest *B* neighbours at a somewhat greater distance in the adjacent multiple layer. The co-ordination of the boundary atoms is, therefore, very similar to the co-ordination of the atoms in crystalline arsenic, antimony and bismuth, and a band scheme of the proposed type is, indeed, indicated.

Consideration of the bond lengths in $Bi_2Se_3$ and $Bi_2Te_3$* suggests that the actual bonding in these materials is mainly due to a mixture of the following valence structures:†

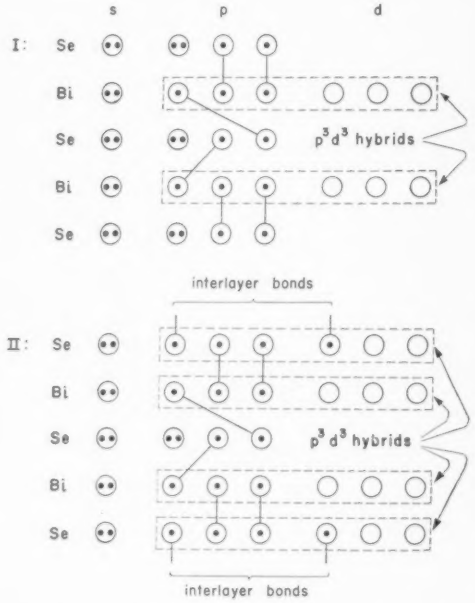


The bonds between the Se(Te) atoms of the central sheet and their six Bi neighbours make use of the empty orbitals on Bi to resonate among six positions, and their bond number should therefore be $\frac{1}{3}$. This value is in fair agreement with the bond number 0·23 (0·28) as calculated from the Pauling covalent radii. The remaining discrepancy, is probably due to the fact that the radii of bonds involving *d* orbitals of the valence shell are longer than the normal single bond radii (see e.g. PAULING[38]). A similar discrepancy is found for the distances between the boundary Se(Te) atoms and the Bi atoms. Here a bond number of $\frac{2}{3}$ would be expected, while the value 0·32 (0·41) is calculated.

In $Bi_2Te_2S$ the observed length of the Bi–S distance corresponds very nearly to $\frac{1}{6}$ bonds (bond

* The atomic positions in $Sb_2Te_3$ are not known accurately.

† The same pictorial representation is used here as in an earlier paper.[2]

*Table* 3.

| | Sign of charge carriers | Concentration of charge carriers ($cm^{-3}$) | | | | | | |
|---|---|---|---|---|---|---|---|---|
| | | A | B | C | D | E | F | G |
| $Sb_2Te_3$ | + | | | | $7\times10^{19}$ | $1\times10^{20}$ | | |
| $Bi_2Se_3$ | − | | | $2\text{–}4\times10^{19}$ | | $2\times10^{19}$ | | |
| $Bi_2Te_3$ | + | $1{\cdot}7\times10^{19}$ | $1{\cdot}4\times10^{19}$ | $2\text{–}3\times10^{19}$ | $0{\cdot}8\times10^{19}$ | $1\times10^{19}$ | $0{\cdot}9\text{–}3{\cdot}4\times10^{19}$ | $2\times10^{19}$ |

A. VLASOVA and STILBANS[30]
B. SHIGETOMI and MORI[31]
C. KONOROV[32,33]
D. HARMAN *et al.*[34]
E. BLACK *et al.*[35]
F. LAGRENAUDIE[36]
G. SATTERTHWAITE and URE[37]

number 0·15) and indicates a transfer of one electron from the Bi atoms to each S atom, which, because of the high electronegativity of sulphur, is to be expected. Such a charge transfer results in an electrostatic repulsion between neighbouring multiple layers, and indeed the Te–Te distance in $Bi_2Te_2S$ is 3·69 Å as compared to 3·57 Å in $Bi_2Te_3$.

Structure I above corresponds to no covalent bonding between neighbouring multiple layers and, according to the concept of the semiconducting bond, leads to semiconducting properties. From optical and electrical measurements, we indeed know that two separate bands exist in these compounds, the gap between them being 0·3 eV in $Sb_2Te_3$, 0·35 eV in $Bi_2Se_3$, and 0·16 eV in $Bi_2Te_3$. However, as indicated by the distance 3·30 (3·57) between the boundary Se(Te) atoms of neighbouring multiple layers, the bonding between these layers is stronger than would be expected from van der Waals' forces only. Thus our bond scheme provides for some covalent interlayer bonding by structure II. The promotion of one of the *p* electrons into a *d* orbital allows additional bonds to form between the layers and at the same time points to an overlap of some *d* states with the valence band.

SATTERTHWAITE and URE[37] have recently measured the electrical properties of $Bi_2Te_3$ samples grown from a melt containing excess tellurium. Their results show that the number of free holes decreases with an increasing excess of tellurium until finally *n*-type conduction is observed. In their interpretation of these results, SATTERTHWAITE and URE assume that the maximum of the liquidus curve is displaced somewhat towards the bismuth-rich side of the phase diagram, so that in fact all samples grown from a stoichiometric melt are bismuth-rich. However, this interpretation can account for the double reversal of the sign of the Hall coefficient observed in *n*-type samples only if a rather unlikely dependence on temperature of the charge-carrier mobilities is assumed. If, on the other hand, we consider a band model similar to the one used in interpreting tellurium, we first note that the reduction of the number of holes can very well be explained as a "compensation" of the

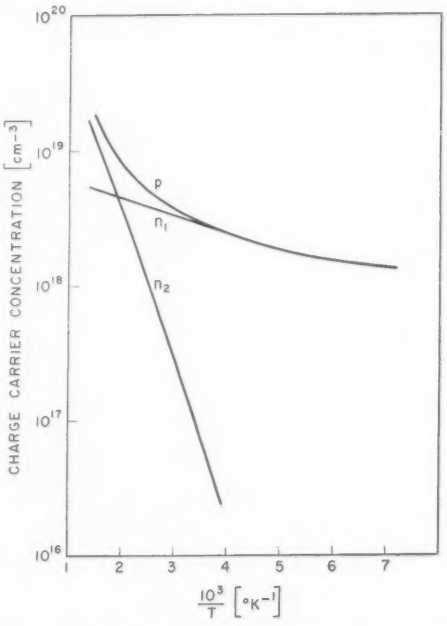


FIG. 4. The charge-carrier concentrations in intrinsic $Bi_2Te_3$ as calculated from the band structure in Fig. 1.

intrinsic holes in the valence band by the additional donor electrons. Moreover, assuming the density of states in both conduction and valence bands to be that of free electrons and, taking a value 40 times smaller for the state density of the overlapping band (see Fig. 1), we find, with $E_{n_1} = -0{\cdot}125$ eV, $E_p = -0{\cdot}1$ eV, and $E_{n_2} = +0{\cdot}1$ eV, the charge-carrier concentrations given in Figs. 4 and 5 for intrinsic $Bi_2Te_3$ and for $Bi_2Te_3$ containing $2\times10^{18}$ cm$^{-3}$ donors (excess tellurium atoms). If then the same dependences of the mobilities on

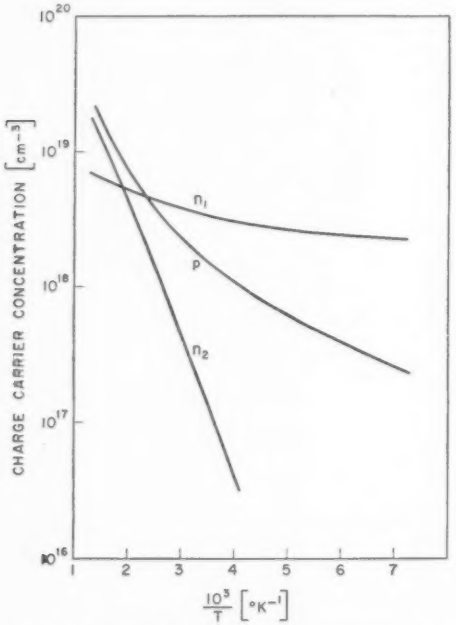


FIG. 5. The charge-carrier concentrations in $Bi_2Te_3$ containing $2\times10^{18}$ cm$^{-3}$ donors (excess tellurium).

temperature are used as in the case of tellurium, and if at 300°K.

$$\mu_{n_1} : \mu_{n_2} : \mu_p = 0{\cdot}6 : 1{\cdot}1 : 1,$$

we find the two $R = R(T)$ curves given in Fig. 6. Thus we see that our model not only accounts for the high number of holes in intrinsic samples, but that it also explains the anomalous behaviour of the Hall coefficient in *n*-type samples. Obviously, the two sign reversals of the thermoelectric power observed by KONOROV[33] in an *n*-type sample of $Bi_2Te_3$ can be explained along the same lines.

The *n*-type conduction found in $Bi_2Se_3$ requires a higher mobility of the electrons in the *d* band. This is not astonishing in view of the Se–Se

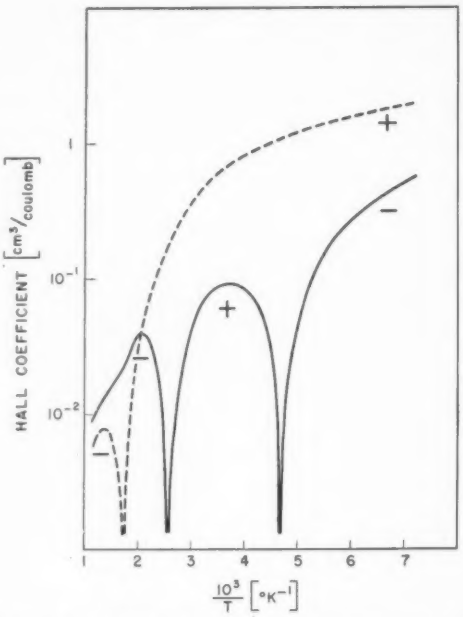


FIG. 6. Calculated dependence on temperature of the Hall coefficient in (*a*) intrinsic $Bi_2Te_3$ (dashed line), (*b*) $Bi_2Te_3$ containing $2\times10^{18}$ cm$^{-3}$ donors (full line).

distance of 3·30 Å in this substance, which is considerably smaller than the next-nearest-neighbour distance of 3·46 Å in elemental selenium. The corresponding distance in $Bi_2Te_3$ is 3·57, i.e. appreciably greater than the next-nearest-neighbour distance of 3·46 Å in tellurium. This may also be the reason why $Bi_2Se_3$ has a more metallic behaviour than $Bi_2Te_3$.

The infrared transmission measurements on $Bi_2Se_3$ and $Bi_2Te_3$ made by BLACK *et al.*,[35] which show a very low transmission even in the long-wavelength region and which therefore call for a high concentration of free charge carriers, give further support to our model.

The high resistivity and true semiconductor behaviour of amorphous $As_2Se_3$ reported by GORIUNOVA and KOLOMIETS[39] are exactly what we would expect from our model (if $As_2Se_3$ has indeed a *C*33 type of structure in the crystalline form[40]), since the interlayer resonances are

destroyed in the amorphous modification (cf. arsenic and antimony).

(b) *Phases with* $D5_8$ *structure*

The compounds $Sb_2S_3$, $Sb_2Se_3$, and $Bi_2S_3$, which all crystallize in the $D5_8$ structure, have not so far been investigated to any great extent. The few data available do, however, indicate a rather different behaviour as compared to that of the $C33$ phases. Along with a series of ternary and quaternary compounds, GORIUNOVA and KOLOMIETS[39,41] and GORIUNOVA *et al.*[42] have measured the resistivities and thermal and optical activation energies of $Sb_2S_3$, $Sb_2Se_3$, and $Bi_2S_3$. Their measurements were carried out on polycrystalline samples of rather low purity, and hence their results show an appreciable scatter. The room-temperature resistivities and the activation energies are listed in Table 4, together with similar data given by BLACK *et al.*[35] In spite of the appreciable discrepancies between the various results, it is clear that the $D5_8$ phases have considerably higher activation energies and resistivities than the $C33$ phases.*

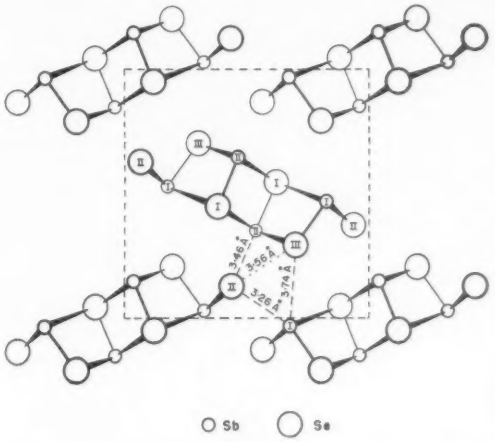


FIG. 7. Projection of the crystal structure of $Sb_2Se_3$ along the chains $(Sb_4Se_6)_n$.

chains of composition $(A_4B_6)_n$. The chains run parallel to the $c$-axis, and their projection on the (001) plane is represented in Fig. 7 for the case of $Sb_2Se_3$. The bond lengths within one chain vary from 2·58 to 3·22 Å, and the bond angles lie between 86° and 99°. Nevertheless, it is readily recognizable that the chains are distorted sections cut out of an NaCl type of structure. This resemblance to the NaCl structure, as well as a discussion of the bond numbers (see TIDESWELL *et al.*[43]), indicates the presence in this structure of resonating $p$ bonds. The empty orbitals required for the resonances are provided by a partial electron transfer from the cations (Sb, Bi) to the anions (S, Se) and/or by a hybridization of $p$ and $d$ orbitals on the cations.

*Table* 4.

| | A | | | B | | | C | | | D | | |
|---|---|---|---|---|---|---|---|---|---|---|---|---|
| | $\Delta E_{opt}$ (eV) | $\Delta E_{therm}$ (eV) | $\rho$ (Ωcm) | $\Delta E_{opt}$ (eV) | $\Delta E_{therm}$ (eV) | $\rho$ (Ωcm) | $\Delta E_{opt}$ (eV) | $\Delta E_{therm}$ (eV) | $\rho$ (Ωcm) | $\Delta E_{opt}$ (eV) | $\Delta E_{therm}$ (eV) | $\rho$ (Ωcm) |
| $Sb_2S_3$ | | | | | | | 1·55 | 0·9 | $10^6$–$10^7$ | 1·7 | | $10^8$ |
| $Sb_2Se_3$ | 1·20 | 1·22 | $4\times10^4$ | | 0·5 | $6\times10^1$ | | | | 1·2 | 1·4 | $10^6$ |
| $Bi_2S_3$ | | | | | | | 1·4 | 0·55 | $2\times10^1$ | 1·3 | (1) | $10^{-2}$ |

A. GORIUNOVA and KOLOMIETS[41]
B. GORIUNOVA and KOLOMIETS[39]
C. GORIUNOVA *et al.*[42]
D. BLACK *et al.*[35]

phases.* Moreover, the transmission in the infrared, as reported by BLACK *et al.*,[35] is fairly high, indicating a small number of free charge carriers, and we conclude that these compounds, unlike the $C33$ phases, are true semiconductors.

This conclusion is supported by the structural features of the $D5_8$ phases. In the orthorhombic $D5_8$ structure, the atoms are held together by essentially covalent bonds in such a way as to form

* The low resistivity of $Bi_2S_3$ reported by BLACK *et al.*[35] is considered by these authors as not representative for this material, but as being due rather to inhomogeneities in the composition.

The distances between some of the atoms of neighbouring chains (dashed lines in Fig. 7) are short enough to suggest the presence between these atoms of weak resonating bonds. Thus the distance between $Sb_I$ and $Se_{II}$ is $r = 3{\cdot}26$ Å, corresponding to a bond number of $b = 0{\cdot}08$. For the $Sb_{II}$–$Se_{II}$ and $Sb_I$–$Se_{III}$ bonds, these values are $r = 3{\cdot}46$ Å, $b = 0{\cdot}03$, and $r = 3{\cdot}74$ Å, $b = 0{\cdot}01$, respectively.

Unlike the interlayer bonds in the $C33$ structure, the interchain bonds here occur between anions and cations. Their presence does not, therefore, call for empty orbitals on the anions, and the conditions of the semiconducting bond are still fulfilled. Nevertheless, it should be noted that the distance between $Se_{II}$ and $Se_{III}$ (dotted line) is 3·56 Å, i.e. not much longer than the next-nearest-neighbour distance in selenium. It appears, however, that this distance is not due to any direct Se–Se bonding, but arises from the weak Sb–Se bonds between neighbouring chains.

### 7. COMPOUNDS OF THE TYPE $A^{V}B^{VI}C^{VII}$

DÖNGES[44,45] has found that the following nine compounds all crystallize in the same orthorhombic structure:

| | | BiSCl | |
|---|---|---|---|
| SbSBr | SbSeBr | BiSBr | BiSeBr |
| SbSI | SbSeI | BiSI | BiSeI |

Chains of composition $(A_2B_2C_2)_n$ run parallel to one of the crystallographic axes, and it is readily seen from a comparison of Figs. 7 and 8 that their structure is closely related to the $D5_8$ structure. Again the atoms in one chain are bound together by resonating bonds, and weak anion–cation bonds are formed between neighbouring chains (dashed line in Fig. 8). The anion–anion distances between neighbouring chains are too long to be due to any direct bonding, and we therefore predict that all these substances should show semiconducting properties similar to those found in the $D5_8$ phases.

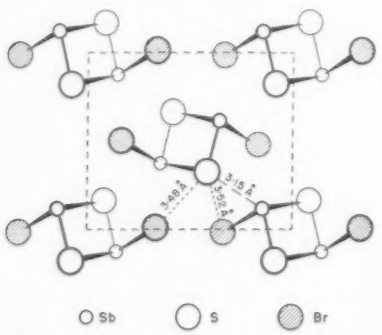


FIG. 8. Projection of the crystal structure of SbSBr along the chains $(Sb_2S_2Br_2)_n$.

### 8. COMPOUNDS OF THE TYPE $A^{V}C_3^{VII}$

Finally, mention should be made of the $D0_5$ type of phases $AsI_3$, $SbI_3$, and $BiI_3$. Multiple layers of atoms are formed in these materials, each layer being built up of three sheets in the sequence $C$–$A$–$C$. The stacking of the layers is such as to result in a slightly distorted hexagonal close-packing of the $C$(I) atoms. The $A$ atoms (As, Sb, Bi) fill up one-third of the octahedral holes in this close-packed array, thus acquiring a distorted octahedral neighbourhood, and resonances involving the empty $d$ orbitals on the $A$ atoms develop. The expected bond number for the $A$–$C$ bonds is $\frac{1}{2}$, and in $BiI_3$ a value of 0·4 is found. This discrepancy can be attributed to an abnormally long bond radius of bismuth caused by the participation of $6d$ orbitals in the bonding. Thus, an increase of the bismuth bond radius from its normal value of 1·52 to 1·58 Å produces bond numbers of 0·29, 0·35, and 0·51 in $Bi_2Se_3$, $Bi_2Te_3$, and $BiI_3$, respectively, which are in good agreement with the expected values of $\frac{1}{3}$, $\frac{1}{3}$, and $\frac{1}{2}$.

The distances between the boundary atoms of neighbouring multiple layers are much too long to lead to any anion–anion bonding such as is observed in the $C33$ phases. In $AsI_3$ and $BiI_3$* they are 4·09 and 4·10 Å, respectively, i.e. they correspond quite well to the van der Waals' diameter of iodine (4·06–4·46 Å). We therefore conclude that the $D0_5$ phases are true semiconductors, and this conclusion is supported by the high resistivities found by FISCHER[46] for $SbI_3$ and $BiI_3$ in a series of preliminary measurements.

### 9. CONCLUSION

Our discussion demonstrates how the valence-bond theory as applied to the Group VB to VIIB elements and to compounds formed between them leads to a consistent description of their structural

* The interatomic distances in $SbI_3$ are not known accurately.

features as well as of their electrical properties. While it is often difficult in a particular substance to decide what the actual bonding is, especially if *d* orbitals are involved, the consistency of our model nevertheless strongly supports our initial assumption of resonating bonds of the $p^3$ and $p^3d^3$ type.

We realize, of course, that the band models for selenium, tellurium, and the *C*33 phases which evolve from our bond considerations and which, admittedly, have been reached by a somewhat intuitive reasoning are in conflict with the semiconductor model normally used in describing these materials. We wish, however, to emphasize that no deductions drawn from our proposed model are contradicted by such experimental data as are available at present. In fact, many of the arbitrary assumptions which previously had been made to adjust the normal semiconductor model to the needs of these substances are relieved by our model.

*Acknowledgements*—We are glad to acknowledge the stimulating correspondence which we have had on this subject with Mr. C. H. L. GOODMAN and Dr. J. R. DRABBLE.

## REFERENCES


1. PAULING L. *Proc. Roy. Soc.* A**196,** 343 (1949).
2. MOOSER E. and PEARSON W. B. *J. Electronics* **1,** 629 (1956).
3. MOOSER E. and PEARSON W. B. *Canad. J. Phys.* **34,** 1369 (1956).
4. MOOSER E. and PEARSON W. B. *Proceedings of a Semiconductor Conference* (*Ashorne Hill*, 1956), p. 65. The Physical Society, London (1957).
5. KREBS H., SCHULTZE-GEBHARDT F. and THEES R. *Z. anorg. Chem.* **282,** 177 (1955).
6. KREBS H. and SCHULTZE-GEBHARDT F. *Z. anorg. Chem.* **283,** 263 (1956).
7. HENDUS H. *Z. Naturf.* **2a,** 505 (1947).
8. MOTT N. F. and JONES H. *The Theory of the Properties of Metals and Alloys*. Oxford University Press (1936).
9. BUSCH G. and VOGT O. *Helv. Phys. Acta* **27,** 241 (1954).
10. DEHLINGER U. *J. Phys. Chem. Solids* **1,** 279 (1957).
11. TAFT E. and APKER L. *Phys. Rev.* **75,** 1181 (1949).
12. TAFT E. and APKER L. *Phys. Rev.* **96,** 1496 (1954).
13. VON HIPPEL A. *J. Chem. Phys.* **16,** 372 (1948).
14. REITZ J. R. *Phys. Rev.* **105,** 1233 (1957).
15. RICHTER H., KULCKE W. and SPECHT H. *Z. Naturf.* **7a,** 511 (1952).
16. BUSCHERT R. C. Dissertation, Purdue Univ. (1957).
17. GASPAR R. *Acta Phys. Hung.* **7,** 289 (1957).
18. KOZYREV P. T. *Zh. Tekh. Fiz.* **27,** 35 (1957).
19. BORELIUS G., PIHLSTRAND F., ANDERSSON J. and GULLBERT K. *Ark. Mat. Astr. Fys.* **30,** No. 14 (1944).
20. BUSCH G. and VOGT O. *Helv. Phys. Acta* **30,** 224 (1957).
21. STRAUMANIS M. *Z. Krist.* A**102,** 432 (1940).
22. EPSTEIN A. S., FRITZSCHE H. and LARK-HOROVITZ K. *Phys. Rev.* **107,** 412 (1957).
23. TANUMA S. *Sci. Rep. Res. Insts. Tôhoku Univ.* **6,** 159 (1954).
24. KRONMÜLLER H., JAUMANN J. and SEILER K. *Z. Naturf.* **11a,** 243 (1956).
25. CALLEN H. B. *J. Chem. Phys.* **22,** 518 (1954).
26. MOOSER E. *Z. angew. Math. Phys.* **4,** 433 (1953).
27. JOHNSON V. A. *Purdue Univ. Rep.* (1954); *Phys. Rev.* **98,** 1567 (1955).
28. ROBINSON H., DEHMELT H. G. and GORDY W. *J. Chem. Phys.* **22,** 511 (1954).
29. ITOH T. and KAMBE K. *J. Phys. Soc. Japan* **12,** 763 (1957).
30. VLASOVA R. M. and STILBANS L. S. *Zh. tekh. fiz.* **25,** 569 (1955).
31. SHIGETOMI S. and MORI S. *J. Phys. Soc. Japan* **11,** 915 (1956).
32. KONOROV P. P. *Soviet Phys. Tech. Phys.* **1,** 1365 (1957).
33. KONOROV P. P. *Soviet Phys. Tech. Phys.* **1,** 1371 (1957).
34. HARMAN T. C., PARIS B., MILLER S. E. and GOERING H. L. *J. Phys. Chem. Solids* **2,** 181 (1957).
35. BLACK J., CONWELL E. M., SEIGLE L. and SPENCER C. W. *J. Phys. Chem. Solids* **2,** 240 (1957).
36. LAGRENAUDIE T. *J. Phys. Radium* **18,** 39A (1957).
37. SATTERTHWAITE C. B. and URE R. W. *Phys. Rev.* **108,** 1164 (1957).
38. PAULING L. *The Nature of the Chemical Bond.* Cornell University Press, Ithaca, N.Y. (1945).
39. GORIUNOVA N. A. and KOLOMIETS B. T. *Zh. tekh. fiz.* **25,** 2069 (1955).
40. RAMSDELL L. S. *Amer. Min.* **15,** 119 (1930).
41. GORIUNOVA N. A. and KOLOMIETS B. T. *Zh. tekh. fiz.* **25,** 984 (1955).
42. GORIUNOVA N. A., KOLOMIETS B. T. and MALKOVA A. A. *Soviet Phys. Tech. Phys.* **1,** 1583 (1957).
43. TIDESWELL N. W., KRUSE F. H. and MCCULLOUGH J. D. *Acta Cryst.* **10,** 99 (1957).
44. DÖNGES E. *Z. anorg. Chem.* **263,** 112 (1950).
45. DÖNGES E. *Z. anorg. Chem.* **263,** 280 (1950).
46. FISCHER G. Private communication (1957).

*J. Phys. Chem. Solids* Pergamon Press 1958. Vol. 7. pp. 78–89.

# THEORY OF IMPURITY PHOTO-IONIZATION SPECTRUM OF SEMICONDUCTORS IN MAGNETIC FIELDS

**R. F. WALLIS* and H. J. BOWLDEN†**

*U.S. Naval Research Laboratory, Washington 25, D.C.

† Wayne State University, Detroit, Michigan, and U.S. Naval Research Laboratory, Washington 25, D.C.; Present address: National Carbon Research Laboratories, National Carbon Company, Division of Union Carbide Corporation, Parma, Ohio.

(*Received* 31 *December* 1957; *revised* 25 *February* 1958)

**Abstract**—The impurity photo-ionization magneto-optic (IPMO) effect is the effect of an external magnetic field on the optical photo-ionization spectrum of impurities in semiconductors. A theory of the IPMO effect has been developed for simple semiconductors. Two cases can be distinguished, depending on whether the impurity ionization energy for zero field is larger or smaller than $\frac{1}{2}\hbar\omega_c = heH/2m^*c$. In the low-field case, the photo-ionization spectrum consists of a series of rather strong peaks corresponding to transitions from bound levels to the various magnetic sub-bands of the continuum. In the high-field case, the photo-ionization spectrum consists of one, or at most two, strong peaks if the temperature is such that only the lowest bound level is appreciably occupied. Detailed calculations are presented of the high-field absorption spectrum for donor impurities in InSb, based on wave functions similar to those of YAFET, KEYES and ADAMS.

## 1. INTRODUCTION

CONSIDERABLE effort has been devoted recently to the study of optical absorption by electrons and holes in semiconductors in external magnetic fields. If the transitions involve energy levels of a single band, the optical absorption is known as cyclotron resonance.[1] If transitions occur between energy levels of different bands, the absorption is known as the interband magneto-optic (IMO) effect.[2] Both cyclotron resonance and the IMO effect provide direct information concerning the effective mass parameters of the band or bands involved. The IMO effect in addition gives rather precise information about the energy gap between bands and its dependence on magnetic field.

A third type of magneto-optic effect in semiconductors concerns optical transitions of an electron or hole in the presence of a magnetic field from a discrete impurity level either to an excited discrete level or to a continuum level. The first case constitutes the Zeeman effect for impurity spectra. The second case will be called the impurity photo-ionization magneto-optic (IPMO) effect.[2] From the details of the spectrum for the IPMO effect, one may expect to obtain information concerning both the effective mass parameters of the band with which the impurity levels are associated and the magnetic field-dependence of the ionization energy of the impurities.

In the present paper a theory is developed for the IPMO effect when the impurity states are associated with a parabolic band having its extremum at $k = 0$ and which is non-degenerate in the absence of spin. Attention is also given to the impurity Zeeman effect for the case of large magnetic fields.

## 2. GENERAL FORMULATION

We consider a semiconductor which contains impurities and which is located in a constant external magnetic field. The Hamiltonian for a charge carrier can be written as

$$\mathscr{H} = \frac{1}{2m}\left(\mathbf{p}+\frac{e}{c}\mathbf{A}_0\right)^2 + V_p(\mathbf{r}) + V_i(\mathbf{r}) + \mu\mathbf{H}_0\cdot\boldsymbol{\sigma} \quad (1)$$

where $\mathbf{A}_0$ is the vector potential for the external magnetic field $\mathbf{H}_0$, $V_p(\mathbf{r})$ is the periodic potential of the lattice, $V_i(\mathbf{r})$ is the impurity potential, $\boldsymbol{\sigma}$ is the Pauli spin operator, and $\mu$ is the Bohr magneton. We shall restrict our attention to those

materials in which the impurity levels are associated with a parabolic band having its extremum at $k = 0$ and which is non-degenerate in the absence of spin. If the effective mass treatment of LUTTINGER and KOHN[3] is applied to the Hamiltonian under the restrictions just mentioned, one finds that the effective mass equation can be written in the form:

$$\left[\frac{1}{2m^*}\left(\mathbf{p}+\frac{e}{c}\mathbf{A}_0\right)^2+V_i(\mathbf{r})\pm\mu\mathbf{H}_0(1-K)\right]F(\mathbf{r}) = EF(\mathbf{r}) \quad (2)$$

where $m^*$ is the effective mass and $K$ is an anti-symmetric constant of the type discussed by KJELDAAS and KOHN.[4] The inclusion of spin leads only to a shift in the energy by a constant amount which may be plus or minus, depending on the spin orientation. Since we shall be concerned only with electric dipole transitions which do not affect the spin, the inclusion of spin does not lead to any observable effects on the absorption spectrum. Accordingly, spin terms will be neglected.

It is convenient to choose the external magnetic field in the $z$-direction with the vector potential specified by

$$\mathbf{A}_0 \rightarrow (-\tfrac{1}{2}y\mathbf{H}_0, \tfrac{1}{2}x\mathbf{H}_0, 0). \quad (3)$$

The impurity potential is chosen to have the Coulomb form

$$V_i(\mathbf{r}) = -\frac{e^2}{Dr} \quad (4)$$

where $D$ is the dielectric constant.

Using equations (3) and (4) and neglecting spin terms, the effective mass equation can be written as

$$\left[-\nabla^2-i\gamma\frac{\partial}{\partial\phi}+\gamma^2\rho^2/4-2/r\right]F(\mathbf{r}) = EF(\mathbf{r}) \quad (5)$$

where $\rho$, $\phi$, $z$ are cylindrical co-ordinates, energy is measured in units of the effective Rydberg $\mathrm{Ry}^* = m^*e^4/2\hbar^2D^2$, length in units of the effective Bohr radius $a_0^* = D\hbar^2/m^*e^2$, $\gamma = \frac{1}{2}\hbar\omega_c/\mathrm{Ry}^*$ and $\omega_c = eH_0/m^*c$. Equation (5) appears to be quite difficult to solve exactly. In discussing approximate solutions to equation (5), it is convenient to distinguish between the cases $\gamma < 1$ and $\gamma > 1$. These cases will be referred to as the low-field and high-field cases, respectively, and are characterized by the impurity ionization energy for zero magnetic field, $E_I$, being greater or less than $\frac{1}{2}\hbar\omega_c$. Our discussion of the low-field case will not, however, include values of $\gamma$ so small that the term $\gamma^2\rho^2/4$ in equation (5) can be completely neglected.

### 3. LOW-FIELD CASE

For $\gamma < 1$ the forces exerted by the magnetic field on the charge carrier are small compared to those exerted by the impurity atom, provided that the carrier is reasonably close to the impurity. For the ground state and the lower excited states, the carrier is localized near the impurity, so that for these states with $\gamma < 1$ one may as a first approximation neglect the terms involving $\gamma$ in equation (5). The effective mass functions $F(\mathbf{r})$ can then be taken to be hydrogen atom wave functions. It turns out to facilitate the mathematical development, however, if the ground-state effective mass function is chosen to be

$$F_g(\mathbf{r}) = N_g \exp(-\beta r^2) \quad (6)$$

rather than the $1s$ hydrogen atom function $(\pi)^{-\frac{1}{2}}e^{-r}$. In equation (6), $N_g$ is a normalization constant and $\beta$ is a variational parameter. The ground-state ionization energy, $E_I$, for zero magnetic field may be evaluated by using equations (5) and (6) with $\gamma = 0$. The best value of $E_I$ is found to be 0·849 $\mathrm{Ry}^*$ with $\beta = 0{\cdot}283$ $(a_0^*)^{-2}$.

For the continuum states, the charge carrier spends very little time near the impurity atom, so that the forces due to the magnetic field may be expected to be large on the average compared to the forces due to the impurity atom. We shall accordingly neglect the effect of the impurity atom on the continuum states in both the low-field and high-field cases. This amounts to using the Born approximation for continuum states.

The solutions to equation (5) with the $2/r$ term omitted have been discussed by DINGLE[5] and may be written as

$$F_c(\mathbf{r}) = c_0 e^{im\phi}\sigma^{\frac{1}{2}|m|}e^{-\frac{1}{2}\sigma}L_{l+|m|}^{|m|}(\sigma)\exp(ik_z z) \quad (7)$$

with

$$c_0^2 = (\gamma/2\pi L_z)l!/[(l+|m|)!]^3. \quad (7a)$$

In equations (7), $\sigma = \gamma\rho^2/2$, $L_{l+|m|}^{|m|}(\sigma)$ is the associated Laguerre polynomial, $k_z$ and $L_z$ are the propagation constant and dimension of the sample

parallel to the magnetic field, $m$ is the quantum number for orbital angular momentum about the magnetic field and may take any integral value, and $l$ is a positive integer or zero. If periodic boundary conditions are employed in the $z$-direction, the permitted values of $k_z$ are $2\pi n_z/L_z$, where $n_z$ is an integer. The corresponding continuum energy levels are given by

$$E_c = \gamma(2l+m+|m|+1)+k_z^2. \tag{8}$$

An energy-level diagram is given in Fig. 1. For

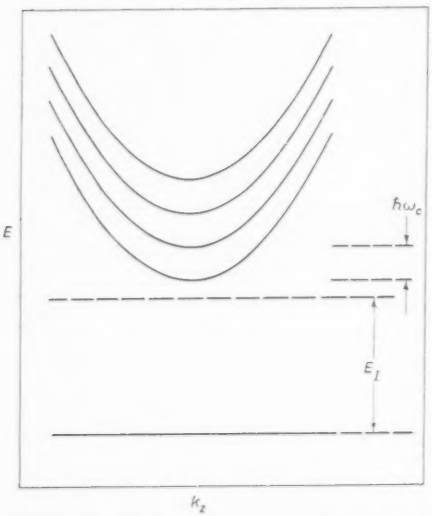


FIG. 1. Energy-level diagram for the low-field case. The parabolas at successively higher energies represent continuum levels corresponding to successively larger integral values of $l+\frac{1}{2}(m+|m|)$.

given $l$ and $m$, the continuum energies form a "magnetic sub-band" or "Landau level". The separation of adjacent sub-bands is equal to $2\gamma$. In general excited discrete impurity levels will exist, but these are omitted from Fig. 1 for simplicity.

The calculations of optical absorption coefficients to be given in the present paper are based on the semiclassical radiation theory generalized to include a constant external magnetic field.[6] Since the Bohr radii of the discrete impurity levels are small compared to the wavelength of the light absorbed, we have employed the dipole approximation in the calculations.

In the absence of broadening, the optical absorption coefficient associated with transitions from an initial state $i$ to various final states $j$ can be written as

$$k(\nu) = 8\pi^3(n/Dhc)N_i \sum_j (E_j-E_i)|Q|^2 \times \times \delta(E_i-E_j+h\nu) \tag{9}$$

where $n$ and $D$ are respectively the refractive index and dielectric constant of the material, $N_i$ is the concentration of impurity atoms in the initial state, $\nu$ is the frequency of the radiation, and $E_i$ and $E_j$ are the energies of initial and final states, respectively. For plane polarized radiation, the quantity $|Q|^2$ is to be taken as $|M_\mu|^2$, where

$$M_\mu = e\int F_i^*(\mathbf{r})\mu F_j(\mathbf{r})\,d\mathbf{r}, \tag{9a}$$

$\mu$ is the co-ordinate in the direction of the electric vector of the radiation, and $F_i(\mathbf{r})$ and $F_j(\mathbf{r})$ are the effective mass functions for the initial and final states. For circularly polarized radiation propagating in the direction of the magnetic field—i.e. with the Poynting vector $\mathbf{S}$ parallel to $\mathbf{H}_0$—the quantity $|Q|^2$ is to be taken as $\frac{1}{2}|M_x-iM_y|^2$ and $\frac{1}{2}|M_x+iM_y|^2$ for right and left circularly polarized light, respectively. We are using the convention for circularly polarized light given by BORN[7] and have chosen the magnetic field in the $z$-direction. It should be noted that the various quantities entering into equation (9) are in ordinary units, not in units of the effective Rydberg and effective Bohr radius.

Collision broadening can be incorporated into the theory by replacing the factor $\delta(E_i-E_j+h\nu)$ in equation (9) by $(1/h)\mathscr{S}(\nu_{ji}, \nu)$ where the Lorentz shape function $\mathscr{S}(\nu_{ji}, \nu)$ is given by

$$\mathscr{S}(\nu_{ji}, \nu) = \frac{1}{\pi}\left[\frac{\Delta\nu}{(\nu_{ji}-\nu)^2+(\Delta\nu)^2}\right] \tag{10}$$

where $h\nu_{ji} = E_j-E_i$ and $\Delta\nu$ is the half-width.

For the low-field case the optical absorption coefficient associated with transitions from the ground state to the various magnetic sub-bands of the continuum has been calculated for circularly polarized light with $\mathbf{S} \parallel \mathbf{H}_0$. Using equations (6), (7), and (9a), the matrix elements $M_x$ and $M_y$ were evaluated with the aid of the following expression for the associated Laguerre polynomials:

$$L_{l+k}^{k}(\sigma) = (-1)^k \Gamma(k+l+1) \sum_{p=0}^{l} (-1)^{l-p} \binom{k+l}{p} \times \frac{}{l} \times \sigma^{l-p}/(l-p)!. \quad (11)$$

One finds that the only allowed transitions between ground and continuum states are to continuum states with $m = -1$ and $m = +1$ for right and left circularly polarized light, respectively. The results for $|Q|^2$ were substituted into equation (9) modified to include collision broadening. The energy difference $E_j - E_l$ was taken to be

$$\hbar\omega_c[l+\tfrac{1}{2}(m+|m|+1)] + (\hbar^2 k_z^2/2m^*) + E_I.$$

The sum over $j$ is equivalent to sums over the quantum numbers $k_z$, $l$, $m$. After replacing the sum over $k_z$ by an integral, the absorption coefficient in ordinary units for right circularly polarized light was found to be

$$k(\omega) = 8(n/D)\alpha N_0(\beta/s^2)(2/1+\epsilon^2)^4 \sum_l (l+1) \times \times [(1-\epsilon^2)/(1+\epsilon^2)]^{2l} \times \times [4\pi g(l)]^{\frac{1}{2}}[K_l(\omega, 0) + K_l(\omega, 2)] \quad (12)$$

where $\alpha$ is the fine structure constant, $\omega$ is the circular frequency,

$$s = (eH_0/\hbar c),\ \epsilon^2 = 4\beta/s,\ g(l) = m^* E_{gl}/\hbar^2\beta$$

and

$$E_{gl} = \hbar\omega_c(l+\tfrac{1}{2}) + E_I.$$

The quantities $K_l(\omega, p)$ are given by

$$K_l(\omega, p) = a \int_{-\infty}^{\infty} x^p [(x^2-b)^2 + a^2]^{-1} \exp[-g(l)x^2]\, dx \quad (12a)$$

where $b = (\hbar\omega/E_{gl}) - 1$, $a = \hbar\Delta\omega/E_{gl}$ and $\Delta\omega = 2\pi\Delta\nu$. The integrals $K_l(\omega, p)$ can be related[6] to certain tabulated integrals which appear in the theory of Doppler broadened spectral lines. The absorption coefficient for left circularly polarized light can be obtained from equation (12) by replacing $l$ by $l+1$ in the quantities $g(l)$, $K_l(\omega, 0)$, and $K_l(\omega, 2)$.

The photo-ionization absorption coefficient for right circularly polarized light has been calculated, using equation (12) with $\gamma = 0{\cdot}125$, $a = 0{\cdot}02$, $\beta = 0{\cdot}283(a_0^*)^{-2}$, $E_I = 0{\cdot}849$ Ry*, and treating the constant factor $8(n/D)\alpha N_0(\beta/s^2)(2/1+\epsilon^2)^4$ as arbitrary. The results are plotted in Fig. 2. The zero-field curve was computed by using the ground-state effective mass function $F_g(\mathbf{r})$ given by equation (6), but using plane waves for $F_c(\mathbf{r})$ given by

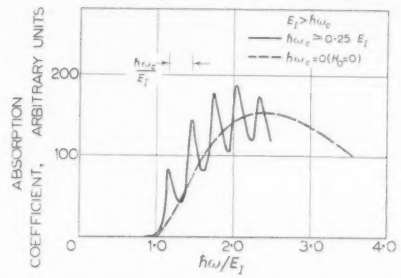


FIG. 2. Photo-ionization absorption spectrum for the low-field case. The radiation is right circularly polarized with the Poynting vector **S** parallel to the external magnetic field $\mathbf{H}_0$.

$$F_c(\mathbf{r}) = (L_x L_y L_z)^{-\frac{1}{2}} \exp i(k_x x + k_y y + k_z z). \quad (13)$$

In general the absorption spectrum should include a series of discrete lines corresponding to transitions to excited bound states. Within the framework of the present theory, these discrete lines would exhibit the familiar Zeeman effect for hydrogen-like atoms and are therefore omitted.

The series of absorption peaks is the most striking feature of the photo-ionization spectrum introduced by an external magnetic field in the low-field case. The peaks arise because the density of states is infinite at the minimum of each magnetic sub-band in the absence of broadening. The spacing between adjacent peaks predicted by the present theory is $\hbar\omega_c$, so that an estimate of the effective mass can be derived from the observed spacing. If the influence of the impurity potential on the continuum wave functions were included in the theory, the predicted spacing of the absorption peaks might not be constant with the value $\hbar\omega_c$. The deviations should be especially prominent in the spacing of the peaks nearest the threshold and should provide a measure of the effect of the impurity potential on the continuum states. The impurity potential may also affect the relative intensities of the peaks. Comparison with the zero-field case[8] indicates that the peaks near threshold

may be enhanced relative to those at higher frequencies.

Another noteworthy feature of the low-field photo-ionization spectrum is the sharp rise in absorption just beyond the threshold. This rise is more abrupt than that for the zero-field case. From the frequency at which the rise occurs, one can determine rather precisely the dependence of the impurity ionization energy on magnetic field and, by extrapolation, the ionization energy at zero field.*

The photo-ionization spectrum for left circularly polarized light is similar to that for right, except that the first peak, starting from the low-frequency side, is missing.

A calculation has also been made of the photo-ionization spectrum in the low-field region for plane polarized light with $\mathbf{E} \parallel \mathbf{H}_0$. Transitions from the ground state are permitted only to magnetic sub-bands with $m = 0$. The IPMO effect is less striking for this case than for $\mathbf{E} \perp \mathbf{H}_0$. Instead of a series of peaks, the spectrum for $E \parallel \mathbf{H}_0$ consists of a series of ripples superposed on a smooth curve similar to the $H_0 = 0$ spectrum. The peaks are washed out because the square of the appropriate matrix element introduces into the absorption coefficient a factor $k_z^2$ which compensates for the infinite state density at $k_z = 0$. It should be noted, however, that the conclusion just mentioned may be modified if the effect of a coulomb impurity potential on the continuum states is included in the theory.

## 4. HIGH-FIELD CASE ($\gamma \gg 1$)

### (a) *Wave Functions and Energies*

Since the Schrödinger equation is not separable, some method of approximation must be used to obtain the wave functions and energy levels. For the continuum states, the free-electron functions

$$F_{lmc}(\sigma, \phi, z) = \Phi_{lm}(\sigma, \phi) \frac{1}{\sqrt{L_z}} \exp(ik_z z) \quad (14)$$

will be used, where $\sigma = \gamma\rho^2/2$ and $\Phi_{lm}$ is displayed in equation (7). This is equivalent to the Born approximation. For the bound states, we will adopt variational functions of the form

$$F_{lm\lambda}(\sigma, \phi, z) = \Phi_{lm}(\sigma, \phi) P_\lambda(z) \exp(-\tfrac{1}{4}\gamma\epsilon^2 z^2), \quad (15)$$

where $P_\lambda(z)$ represents a set of suitably chosen orthogonal polynomials, and the variational parameter $\epsilon$ is set independently for the different states $(lm\lambda)$.

A justification for the use of functions similar to those defined by equation (15) in the high-field limit has been given by YAFET *et al.*,[9] who adopted a function with two variational parameters, one of them corresponding to a replacement of $\sigma$ by $\epsilon_r^2\sigma$ in $\Phi_{lm}$. The result of their calculations for the ground state (000) indicates that, for $\gamma > 10$, the value $\epsilon_r = 1$ is very good. We have therefore adopted this value from the start. The first few polynomials $P_\lambda(z)$ have the form

$$P_0(z) = (\epsilon^2\gamma/2\pi)^{1/4} \quad (16a)$$

$$P_1(z) = (\epsilon^6\gamma^3/2\pi)^{1/4} z \quad (16b)$$

$$P_2(z) = (\epsilon^2\gamma/2\pi)^{1/4} \frac{2\epsilon^2}{(3\epsilon_0^4 + 2\epsilon^2\epsilon_0^2 + 3\epsilon^4)^{\frac{1}{2}}} \left[1 - \frac{\gamma}{2}(\epsilon_0^2 + \epsilon^2) z^2\right]. \quad (16c)$$

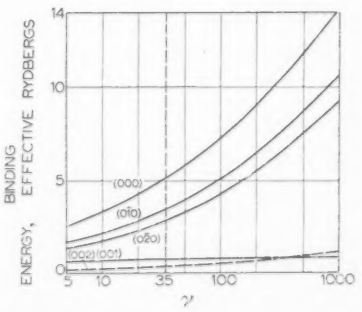


FIG. 3. Binding energy as a function of $\gamma$ for the high-field case. The various states are labeled by the quantum numbers $(lm\lambda)$. The curve for (002) is estimated except at $\gamma = 35$.

* The small absorption in Fig. 2 for $(\hbar\omega/E_I) < 1$ is due to the collision broadening assumed when $H_0 \neq 0$. The curve for $H_0 = 0$ is not corrected for collision broadening.

In $P_2(z)$ the symbol $\epsilon_0$ represents the value of $\epsilon$ obtained for the state with the same $l$ and $m$ values, but with $\lambda = 0$.

The result of the variational calculation in each case presents a relationship between $\gamma$ and $\epsilon$. The results obtained for the levels which have been investigated are shown in the following formulas and the dependence of the binding energy on $\gamma$ is shown in Fig. 3.

(i) $(lm\lambda) = (000)$:

$$E = \gamma(1-\tfrac{1}{4}\epsilon^2+\tfrac{1}{2}\epsilon^4)-2\epsilon\sqrt{\frac{2\gamma}{\pi}}$$

$$\sqrt{\frac{\pi\gamma}{2}} = \frac{2}{\epsilon(1-\epsilon^2)^{3/2}}[\mathscr{L}(\epsilon)-2\sqrt{1-\epsilon^2}]$$

(ii) $(lm\lambda) = (001)$:

$$E = \gamma(1+\tfrac{1}{4}\epsilon^2+\tfrac{1}{2}\epsilon^4)-\frac{4\epsilon}{3}\sqrt{\frac{2\gamma}{\pi}}$$

$$\sqrt{\frac{\pi\gamma}{2}} = \frac{2\epsilon}{(1-\epsilon^2)^{5/2}}\left[\frac{2(1+2\epsilon^2)}{3\epsilon^2}\sqrt{1-\epsilon^2}-\mathscr{L}(\epsilon)\right]$$

(iii) $(lm\lambda) = (0\bar{1}0)$:

$$E = \gamma\left[1-\frac{\epsilon^2(2-7\epsilon^2+2\epsilon^4)}{4(2+\epsilon^2)}\right]-\frac{4\epsilon}{2+\epsilon^2}\sqrt{\frac{2\gamma}{\pi}}$$

$$\sqrt{\frac{\pi\gamma}{2}} = \frac{2+\epsilon^2}{\epsilon(1-\epsilon^2)^{5/2}}\left[\mathscr{L}(\epsilon)-\frac{6\sqrt{1-\epsilon^2}}{2+\epsilon^2}\right]$$

(iv) $(lm\lambda) = (0\bar{1}1)$:

$$E = \gamma\left[1+\frac{\epsilon^2(4+13\epsilon^2-2\epsilon^4)}{4(4+\epsilon^2)}\right]-\frac{16\epsilon}{3(4+\epsilon^2)}\sqrt{\frac{2\gamma}{\pi}}$$

$$\sqrt{\frac{\pi\gamma}{2}} = \frac{\epsilon(4+\epsilon^2)}{(1-\epsilon^2)^{7/2}}\left[\frac{2(2+13\epsilon^2)}{3\epsilon^2(4+\epsilon^2)}\sqrt{1-\epsilon^2}-\mathscr{L}(\epsilon)\right]$$

(v) $(lm\lambda) = (100)$:

$$E = \gamma\left[3+\tfrac{1}{4}\epsilon^2-\frac{\epsilon^2(1-\epsilon^2)(4-4\epsilon^2+3\epsilon^4)}{2(4+4\epsilon^2+7\epsilon^4)}\right]-$$
$$-\frac{2\epsilon(4+4\epsilon^2+3\epsilon^4)}{4+4\epsilon^2+7\epsilon^4}\sqrt{\frac{2\gamma}{\pi}}$$

$$\sqrt{\frac{\pi\gamma}{2}} = \frac{4+4\epsilon^2+7\epsilon^4}{2\epsilon(1-\epsilon^2)^{7/2}}\left[\mathscr{L}(\epsilon)-\left(\frac{6+5\epsilon^2+4\epsilon^4}{4+4\epsilon^2+7\epsilon^4}\right)\cdot 2\sqrt{1-\epsilon^2}\right]$$

(vi) $(lm\lambda) = (\bar{1}10)$:

$$E = \gamma\left[3 - \frac{\epsilon^2(16-104\epsilon^2+54\epsilon^4-85\epsilon^6+14\epsilon^8)}{4(16+24\epsilon^2+54\epsilon^4+11\epsilon^6)}\right]$$

$$-\frac{8\epsilon(4+4\epsilon^2+7\epsilon^4)}{16+24\epsilon^2+54\epsilon^4+11\epsilon^6}\sqrt{\frac{2\gamma}{\pi}}$$

$$\sqrt{\frac{\pi\gamma}{2}} = \frac{16+24\epsilon^2+54\epsilon^4+11\epsilon^6}{8\epsilon(1-\epsilon^2)^{9/2}}\left[\mathscr{L}(\epsilon) - \left(\frac{28+24\epsilon^2+53\epsilon^4}{16+24\epsilon^2+54\epsilon^4+11\epsilon^6}\right)\cdot 2\sqrt{1-\epsilon^2}\right]$$

(vii) $(lm\lambda) = (101)$:

$$E = \gamma\left[3+\frac{3}{4}\epsilon^2 - \frac{3\epsilon^2(1-\epsilon^2)(4+\epsilon^4)}{2(12+16\epsilon^2+7\epsilon^4)}\right] - \frac{4\epsilon(4+4\epsilon^2+\epsilon^4)}{12+16\epsilon^2+7\epsilon^4}\sqrt{\frac{2\gamma}{\pi}}$$

$$\sqrt{\frac{\pi\gamma}{2}} = \frac{\epsilon(12+16\epsilon^2+7\epsilon^4)}{2(1-\epsilon^2)^{9/2}}\left[\frac{4+50\epsilon^2+43\epsilon^4+8\epsilon^6}{3\epsilon^2(12+16\epsilon^2+7\epsilon^4)}\cdot 2\sqrt{1-\epsilon^2} - \mathscr{L}(\epsilon)\right]$$

(viii) $(lm\lambda) = (\bar{0}20)$:

$$E = \gamma\left[1+\frac{1}{4}\epsilon^2 - \frac{\epsilon^2(1-\epsilon^2)(8-8\epsilon^2+3\epsilon^4)}{2(8+8\epsilon^2-\epsilon^4)}\right] - \frac{16\epsilon}{8+8\epsilon^2-\epsilon^4}\sqrt{\frac{2\gamma}{\pi}}$$

$$\sqrt{\frac{\pi\gamma}{2}} = \frac{8+8\epsilon^2-\epsilon^4}{4\epsilon(1-\epsilon^2)^{7/2}}\left[\mathscr{L}(\epsilon) - \left(\frac{14+\epsilon^2}{8+8\epsilon^2-\epsilon^4}\right)\cdot 2\sqrt{1-\epsilon^2}\right].$$

In the above expressions,

$$\mathscr{L}(\epsilon) = \ln\frac{1+\sqrt{1-\epsilon^2}}{1-\sqrt{1-\epsilon^2}}.$$

For $\lambda = 2$, the situation is mathematically more complicated. In these cases, rather than an analytical variation, a numerical evaluation was carried out for the single value $\gamma = 35$. The formulas below give the energy in terms of $\gamma$ and the $\epsilon$ parameters.

$(lm\lambda) = (002)$:

$$E = \gamma + \frac{c^2}{2\epsilon^3}\left[\frac{7}{4}(1-\epsilon^2)^2q^2+\epsilon^2(1-\epsilon^2)q+\epsilon^4\right]\sqrt{\frac{\pi\gamma}{2}} -$$

$$-2c^2\left\{\frac{2-5\epsilon^2}{2\epsilon^4}q^2 - \frac{2}{\epsilon^2}q + \left[1+q+\frac{3}{4}q^2\right]\frac{1}{\sqrt{1-\epsilon^2}}\mathscr{L}(\epsilon)\right\}$$

$(lm\lambda)=(\bar{0}12)$:

$$E=\gamma+\frac{c^2}{2\epsilon^3}\left[\frac{7}{4}(1-\epsilon^2)^2q^2+\epsilon^2(1-\epsilon^2)q+\epsilon^4\right]\sqrt{\frac{\pi\gamma}{2}}+$$
$$+\frac{c^2}{1-\epsilon^2}\left\{2+\frac{2(2+\epsilon^2)}{\epsilon^2}q-\frac{4-16\epsilon^2-3\epsilon^4}{2\epsilon^4}q^2-\right.$$
$$\left.-[2-\epsilon^2+(4-\epsilon^2)q+\tfrac{3}{4}(6-\epsilon^2)q^2]\frac{1}{\sqrt{1-\epsilon^2}}\mathscr{L}(\epsilon)\right\}.$$

In these expressions

$$c^2=\frac{\epsilon^5}{\epsilon^4-(\epsilon_0^2+\epsilon^2)\epsilon^2+\frac{3}{4}(\epsilon_0^2+\epsilon^2)^2}\sqrt{\frac{\gamma}{2\pi}},\quad q=\frac{\epsilon_0^2+\epsilon^2}{1-\epsilon^2}.$$

It will be noted in Fig. 3 that levels corresponding to eigenfunctions which are odd in $z$ ($\lambda$ odd) tend to finite binding energies as $\gamma\to\infty$, while the functions even in $z$ ($\lambda$ even) tend to infinite binding energies. This division according to $z$-parity is not invalidated by the form of the perturbing term.

Fig. 4 shows an energy-level diagram for the case $\gamma=35$. In $n$-type InSb, this corresponds to a field of about 55,000 G, and the energy scale in this case is in units of 0·00069 eV. We have included states (010), (011), and (012). These differ in energy from the corresponding states with $m=-1$ only by the constant difference $2\gamma$. Table 1 lists the values of $\epsilon$ and the binding energy $E_B$ obtained for each of the levels listed for $\gamma=35$. It will be noted here that the bound states for $l+\frac{1}{2}(m+|m|)>0$ lie in the region of the $l+\frac{1}{2}(m+|m|)=0$ continuum. This leads to some interesting effects which are discussed in the Appendix.

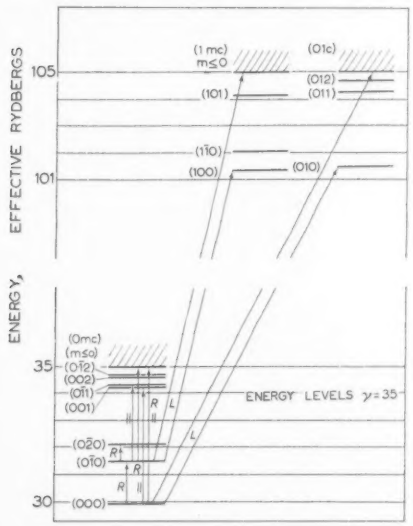


FIG. 4. Energy-level diagram in the high-field region for $\gamma=35$. The arrows show some allowed optical transitions. The symbols $R$ and $L$ refer to right and left circularly polarized radiation. The symbol $\|$ refers to radiation with electric vector $\mathbf{E}$ parallel to $\mathbf{H}_0$.

*Table* 1. *Variational parameter* $\epsilon$ *and binding energy* $E_B$ *for* $\gamma=35$

| $lm\lambda$ | $\epsilon$ | $E_B$ |
|---|---|---|
| 000 | 0·42918 | 5·070 |
| 001 | 0·16172 | 0·777 |
| 010 | 0·32840 | 3·510 |
| 011 | 0·15191 | 0·735 |
| 002 | 0·12 | 0·39 |
| 012 | 0·10 | 0·36 |
| 100 | 0·34640 | 3·617 |
| 110 | 0·29648 | 2·961 |
| 020 | 0·28586 | 2·900 |

### (b) *Absorption Coefficients*

In the high-field case we have investigated the optical absorption coefficient for transitions from various discrete levels to both higher discrete levels and continuum levels. The quantity $|Q|^2$ in equation (9) was evaluated, using the effective mass

functions given in equations (15) and (16). For absorptive transitions between two discrete levels, the following selection rules were obtained in the limit $\mathbf{H}_0 \to \infty$. If the light is right circularly polarized with $\mathbf{S} \parallel \mathbf{H}_0$, then $\Delta l = \pm 1, 0$; $\Delta m = -1$; $\Delta\lambda$ even. If the light is left circularly polarized with $\mathbf{S} \parallel \mathbf{H}_0$, then $\Delta l = \pm 1, 0$; $\Delta m = +1$; $\Delta\lambda$ even. If the light is plane polarized with $\mathbf{E} \parallel \mathbf{H}_0$, then $\Delta l = 0$; $\Delta m = 0$; $\Delta\lambda$ odd.

For an arbitrary large magnetic field, the exact effective mass functions do not have the forms of the functions specified by equations (15) and (16), but can be expressed as linear combinations of such functions. The quantum number $m$ is still a good quantum number, and the effective mass functions can still be classified as either even or odd with respect to replacing $z$ by $-z$. The above quoted selection rules for $m$ and $\lambda$ are accordingly still valid for arbitrary fields. However, the mixing of the high-field limit functions at arbitrary fields makes possible absorptive transitions from any given state to any higher energy state with the proper $m$ and $\lambda$ values regardless of the $l$ value.

The selection rules for absorptive transitions from discrete levels to continuum levels are the same for quantum numbers $l$ and $m$ as in the case of transitions involving two discrete levels. Transitions are permitted from any $\lambda$ value to any value of $k_z$.

Some of the more important absorptive transitions satisfying the selection rules for the limit $\mathbf{H}_0 \to \infty$ are indicated by arrows in Fig. 4.

The optical absorption coefficient for transitions between two discrete levels $i$ and $j$ with collision broadening included can be written as

$$k(\omega) = 8\pi^2(n/Dhc)N_i|Q|^2a/(a^2+b^2) \tag{17}$$

where

$$a = \hbar\Delta\omega/(E_j - E_i) \text{ and } b = (\hbar\omega/E_j - E_i) - 1.$$

For transitions from a discrete level $i$ to various continuum levels specified by quantum numbers $l$, $m$, $k_z$, the absorption coefficient including broadening can be evaluated in a manner similar to that employed to derive equation (12) for the low-field case. Using the effective mass functions given by equations (7), (15), and (16) to evaluate the proper form of $|Q|^2$, one finds that the resulting absorption coefficient can be expressed in terms of the integrals $K_l(\omega, p)$ defined by equation (12a). The quantity $E_{gl}$ entering into $K_l(\omega, p)$ is to be replaced, however, by the energy difference of the magnetic subband at $k_z = 0$ and the particular discrete level under consideration.

Since the high-field theory developed in the present paper is particularly applicable to InSb containing donor impurities, we have made calculations of the absorption spectrum for this material for various types of polarized light. The value of $\gamma$ was chosen to be 35, which corresponds to a magnetic field of about 55,000 G. The calculations were carried out for a temperature of 4·2°K (liquid-helium temperature) and a donor concentration of $10^{14}\text{cm}^{-3}$. The dielectric constant $D$ was taken to be 16, while the effective mass $m^*$ for conduction electrons was taken to be 0·013 $m$.[10] The broadening parameter $a$ is 0·02 in all cases. The impurity atoms were assumed to be distributed among their energy states according to a Boltzmann distribution.

In Fig. 5 the absorption spectrum for plane

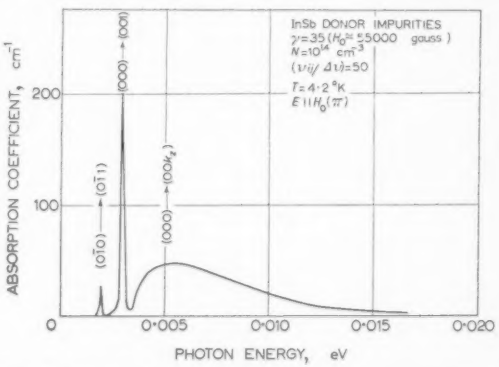


FIG. 5. Optical absorption spectrum of donor impurities in InSb at $\gamma = 35$. The electric vector $\mathbf{E}$ of the radiation is parallel to $\mathbf{H}_0$.

polarized light having $\mathbf{E} \parallel \mathbf{H}_0$ is plotted. The spectrum consists of several discrete lines and a rather broad photo-ionization continuum. At the particular magnetic field chosen, the region of absorption lies in the rather inaccessible 200–600 $\mu$ range.

The absorption spectrum for right circularly polarized light with $\mathbf{S} \parallel \mathbf{H}_0$ is shown in Fig. 6. The photo-ionization spectrum again lies in the inaccessible 200–600 $\mu$ region. The two discrete lines shown occur at wavelengths of about 1 and 3 mm. The difference in intensity of the two discrete lines

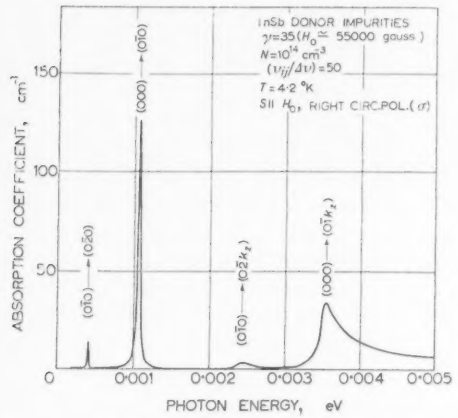


FIG. 6. Optical absorption spectrum of donor impurities in InSb at $\gamma = 35$ for right circularly polarized light.

in both Fig. 5 and Fig. 6 is due primarily to the difference in occupancy of the (000) and $(0\bar{1}0)$ levels.

The absorption spectrum for left circularly polarized light with $\mathbf{S} \parallel \mathbf{H}_0$ is plotted in Fig. 7. The spectrum is made up primarily of four peaks,

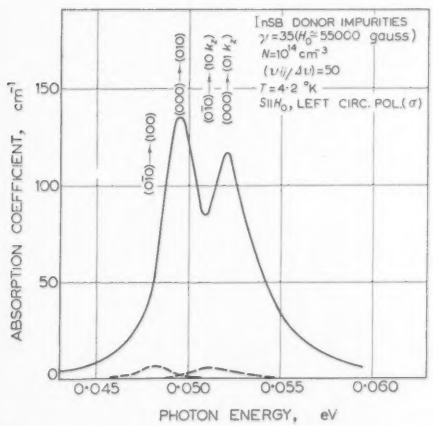


FIG. 7. Optical absorption spectrum of donor impurities in InSb at $\gamma = 35$ for left circularly polarized light.

two being quite strong and two rather weak. Since the weaker peaks are not evident in the total absorption (solid line), their contribution is indicated by the dotted lines. The region of absorption in Fig. 7 is near the cyclotron resonance frequency for conduction electrons. In fact the maximum of the weak peak corresponding to the $(0\bar{1}0) \rightarrow (100)$ transition falls almost exactly at the cyclotron resonance frequency for $m^* = 0{\cdot}013\, m$ and $\mathbf{H}_0 = 55{,}000$ G. It is clear that the absorption in Fig. 7 occurs at much higher frequencies than that of either Fig. 5 or Fig. 6. The absorption spectrum in Fig. 7 shows two strong peaks, one corresponding to a transition between discrete levels and one corresponding to photo-ionization.

The absorption coefficient for the maximum of the strong peak at about 0·049 eV is on the same order of magnitude as that to be expected for the cyclotron resonance absorption associated with $10^{14}$ free conduction electrons at 4·2° K. At higher temperatures the maximum absorption due to cyclotron resonance should decrease (at fixed carrier concentration) both because of increased broadening and because of effects arising from the non-parabolic nature of the conduction band.

Recently BOYLE and BRAILSFORD[11] have reported measurements of the optical absorption of InSb as a function of magnetic field at liquid-helium temperatures and a wavelength of 87 microns. Their data show a strong absorption maximum with a shoulder on the high-field side. They ascribe the absorption at the maximum to transitions which we call $(000) \rightarrow (010)$ and $(000) \rightarrow (1\bar{1}0)$ and ascribe the shoulder to the $(0\bar{1}0) \rightarrow (100)$ transition and to other transitions having excited initial states. The strong photo-ionization peak in our theoretical absorption spectrum in Fig. 7 is not at all evident in the data of BOYLE and BRAILSFORD. The reason for this apparent discrepancy is not clear to us at the moment. We believe, however, that the interpretation of the experimental data will be facilitated if the experiments are done as a function of frequency with a fixed magnetic field of 50–60 kG, so that the freeze-out of carriers will be relatively complete, as indicated by the work of KEYES and SLADEK,[12] and will not vary during a given experiment.

## 5. DISCUSSION

The theory developed in this paper is restricted to impurity states associated with a non-degenerate parabolic band having its extremum at $k = 0$. If one accepts the results of HERMAN[13] on the band structure of various semiconductors, then it appears that the present theory is applicable to donor impurities in the semiconductors gray tin, indium antimonide, and cadmium telluride. There also

appears to be some evidence[14] that indium phosphide containing donor impurities may satisfy the assumptions of the present theory. The theory as it stands is clearly not applicable to donor impurities in silicon or germanium, since these semiconductors have conduction bands with minima away from $k = 0$. Furthermore, the theory is not applicable to acceptor impurities in practically all semiconductors, because most materials have valence bands which are degenerate at $k = 0$.

No corrections for induced emission have been made in the calculations of the optical absorption coefficients. The populations of the excited states are sufficiently small, under the conditions for which detailed calculations have been made, that the corrections for induced emission are not very important.

It has been found[6] that fourth-order terms in the expansion of the conduction band energy in powers of $k$ lead to observable effects on the cyclotron resonance absorption of conduction electrons in indium antimonide. Although the fourth-order terms may lead to observable effects in the present problem, it is felt that these effects are small, at least for indium antimonide with magnetic fields up to 60 kG, and have not been included in the theory.

It is interesting to compare the photo-ionization spectra for the low- and high-field cases. The low-field spectrum has a number of peaks of appreciable magnitude. As the magnetic field increases, the peaks at the higher frequencies decrease in intensity until finally in the high-field limit only one peak remains (or at most two peaks if plane polarized light with $\mathbf{E} \perp \mathbf{H}_0$ is used).

The decline of the high-frequency absorption peaks as the magnetic field is increased is related to the fact that in the high-field limit the motion of the electron in a plane perpendicular to the magnetic field is determined mainly by the magnetic field and not by the impurity potential. The transverse motion of the electron in both bound and continuum states is accordingly described by single functions of the type $\Phi_{lm}(\sigma, \phi)$ and the resulting selection rules $\Delta l = 0, \pm 1$ and $\Delta m = 0, \pm 1$ lead to the existence of only one or two peaks in the high-field photo-ionization spectrum. In the low-field region, however, a given bound state is described by a linear combination of $\Phi_{lm}(\sigma, \phi)$ rather than a single $\Phi_{lm}(\sigma, \phi)$ and the corresponding photo-ionization spectrum involves more peaks than in the high-field region.

A comment should be made about the use of the effective mass equation (equation (2)) in the high-field case. If the magnetic field is small enough (even though $\gamma \gg 1$) so that two criteria are satisfied, then the use of the effective mass equation appears justified. First, the separation between magnetic sub-bands, $\hbar\omega_c$, should be small compared to the energy gap between valence and conduction bands at zero magnetic field, $E_G$. Second, the characteristic length, $s^{-\frac{1}{2}}$, should be large compared to a lattice spacing. For InSb at 4·2°K and $\gamma = 35$, $\hbar\omega_c = 0{\cdot}048$ eV, which is less than $E_G = 0{\cdot}23$ eV, while $s^{-\frac{1}{2}} \simeq 100$ Å, which is considerably greater than the lattice spacing.

Our treatment has neglected interactions between impurity centers. This assumption appears justified if the concentration of impurities is small enough so that the average distance between impurity centers is large compared to the effective Bohr radius $a_0^*$. For donor impurities in InSb the upper limit of concentration giving essentially independent centers is on the order of $10^{14}$ cm$^{-3}$, as has been pointed out by KEYES and SLADEK.[12]

*Acknowledgements*—We wish to thank ELIAS BURSTEIN for providing the stimulation to undertake this problem and for helpful discussions. We are indebted to R. J. ELLIOTT, who pointed out the possibility of Auger-type processes in the high-field case. Finally, we thank M. C. WALLIS for carrying out some of the numerical calculations.

## APPENDIX: AN AUGER EFFECT IN SEMICONDUCTORS

A study of Fig. 4 reveals that the "bound" states for $l + \frac{1}{2}(m + |m|) > 0$ lie in the range of the continuum of $l + \frac{1}{2}(m + |m|) = 0$. Under these conditions an autoionization process or Auger effect[15] can occur. The theory of such processes is not in very good condition, but the fact that this is a one-electron system, whereas previously treated Auger processes involve more than one electron, makes it possible to estimate the effect of this process. Several approaches are possible; we have studied the effect by a perturbation-type calculation of the transition probability from the discrete state (100) to the continuum states ($00k_z$), with a deduction of the resulting line broadening.

For this procedure, we observe that, although our adopted wave functions for the above-mentioned states are not all eigenfunctions of the magnetic-field free-particle Hamiltonian, yet they are not mixed by it, so that this is a suitable choice for $\mathscr{H}_0$. $\mathscr{H}'$ is then just the

Coulomb term $2/r$. The resulting matrix element cannot be evaluated in closed form, but an appropriate numerical evaluation for $\gamma = 35$ gives a line width of $\hbar\Gamma \sim 0{\cdot}1$ Rydberg. This is much smaller than the value assumed for collision broadening in Section IV(b) in calculating the absorption coefficient for transitions to the state (100). It should be noted that the state (010), which is involved in the transition having the most intense absorption in Fig. 7, is not broadened by interaction with the continuum states having $l+\frac{1}{2}(m+|m|) = 0$ because the $m$ values are different.

## REFERENCES


1. Lax B., Zeiger H., Dexter R. and Rosenblum E. *Phys. Rev.* **93,** 1418 (1954).
   Dresselhaus G., Kip A. F. and Kittel C. *Phys. Rev.* **98,** 368 (1955).
   Burstein E., Picus G. and Gebbie H. *Phys. Rev.* **103,** 185 (1956).
2. Burstein E. and Picus G. *Bull. Amer. Phys. Soc.* **2.** 57 (1957).
3. Luttinger J. and Kohn W. *Phys. Rev.* **97,** 869 (1955).
4. Kjeldaas T. and Kohn W. *Phys. Rev.* **105,** 806 (1957).
5. Dingle R. B. *Proc. Roy. Soc.* A**211,** 500 (1952).
6. Wallis R. F. *J. Phys. Chem. Solids* **4,** 101 (1958).
7. Born M. *Optik* p. 24 Julius Springer, Berlin (1933).
8. Burstein E., Picus G., Henvis B. and Wallis R. *J. Phys. Chem. Solids* **1,** 69 (1956).
9. Yafet Y., Keyes R. W. and Adams E. N. *J. Phys. Chem. Solids* **1,** 137 (1956).
10. Dresselhaus G., Kip A. F., Kittel C. and Wagoner G. *Phys. Rev.* **98,** 556 (1955).
11. Boyle W. S. and Brailsford A. D. *Phys. Rev.* **107,** 903 (1957).
12. Keyes R. W. and Sladek R. J. *J. Phys. Chem. Solids* **1,** 143 (1956).
13. Herman F. *J. Electronics* **1,** 103 (1955).
14. Kane E. O. Private communication.
15. Condon E. U. and Shortley G. H. *The Theory of Atomic Spectra* pp. 369 ff. Cambridge University Press (1953).

*J. Phys. Chem. Solids* Pergamon Press 1958. Vol. 7. pp. 90–93.

# L'EFFET DES ELEMENTS DE LA PREMIÈRE LONGUE PÉRIODE SUR LA RÉSISTIVITÉ DU CUIVRE ET DE L'ALUMINIUM

**C. R. VASSEL**

Institut de Recherche des Métaux Non-Ferreux, Budapest

(*Received* March 11, 1958)

VOL
7
195

**Abstract**—The residual resistivity of various impurities of the First Long Period has been measured in copper (K, Ca, Ti, V, Cr, Mn, Fe, Co, Ni, Zn, Ga, As, Se) and in aluminium (Ca, Ti, Cr, Mn, Fe, Cu, Zn). These measurements are compared with those of other workers and with the theoretical conclusions of MOTT and of FRIEDEL.

**Résumé**—La résistivité résiduelle de diverses impuretés de la première longue période a été mesurée dans le cuivre (K, Ca, Ti, V, Cr, Mn, Fe, Co, Ni, Zn, Ga, As, Se) et dans l'aluminium (Ca, Ti, Cr, Mn, Fe, Cu, Zn). Ces mesures sont comparées à celles d'autres expérimentateurs et aux considérations théoriques de MOTT et de FRIEDEL.

## 1. INTRODUCTION

L'EFFET de divers éléments en solution sur la résistivité du cuivre et d'autres métaux bons conducteurs a été étudié par divers expérimentateurs, tels que NORBURY,[1] LINDE,[2] GULYAEV,[3] HIBBARD,[4] PAWLEK,[5,6] LIEBERTZ[7] et ZOLLER.[8,9] Nous avons nous-mêmes fait des mesures dans ce domaine,[10] que nous allons présenter et comparer à celles des autres expérimentateurs. Nous montrerons qu'elles sont en accord satisfaisant avec les considérations théoriques de FRIEDEL.[11]

## 2. RESULTATS EXPERIMENTAUX

Nous avons utilisé un cuivre électrolytique de pureté 99,95 pour-cent, un aluminium raffiné de pureté 99,99 pour-cent et des éléments d'addition de pureté comparable.[10] L'analyse de ces métaux a été faite par diverses méthodes chimiques et, physico-chimiques. La résistivité a été mesurée par différentes méthodes et dans différents états—moulé, filé, étiré et recristallisé—ainsi que pour différentes compositions. Les résultats, donnés dans les tableaux 1 et 2, représentent, suivant le procédé usuel, l'augmentation de la résistivité pour 1 pour-cent atomique, c'est-à-dire $\Delta\rho/c$ en $\mu\Omega$cm/pour-cent. Les signes $>$ et $<$ signifient que nous pensons nos mesures respectivement trop faibles ou trop fortes.

Seuls LINDE[2] et PAWLEK,[5] pour le cuivre, et LIEBERTZ,[7] pour l'aluminium, ont analysé en détails leurs propres mesures. NORBURY, GULYAEV, HIBBARD et ZOLLER ont seulement fait quelques mesures non-systématiques, ou analysé les mesures d'autres expérimentateurs. La Fig. 1 contient les

*Tableau* 1. *Alliages de cuivre*—$\Delta\rho/c$ *en* $\mu\Omega$cm/*pour-cent*

| K | Ca | Sc | Ti | V | Cr | Mn | Fe | Co | Ni | Zn | Ga | Ge | As | Se |
|---|---|---|---|---|---|---|---|---|---|---|---|---|---|---|
| $< 0{,}3$ | 1,0 | — | $> 7{,}0$ | 9,7 | 4,1 | 3,0 | $> 6{,}2$ | 3,2 | 1,7 | 0,6 | — | 3,6 | 8,3 | $> 3{,}0$ |

*Tableau 2. Alliages d'aluminium—*$\Delta\rho/c$ *en* $\mu\Omega$cm/*pour-cent*

| K | Ca | Sc | Ti | V | Cr | Mn | Fe | Co | Ni | Cu | Zn | Ga | Ge | As |
|---|---|---|---|---|---|---|---|---|---|---|---|---|---|---|
| — | > 4,5 | — | > 4,5 | > 5,3 | 6,3 | 7,3 | — | — | — | 0,8 | 0,35 | — | — | — |

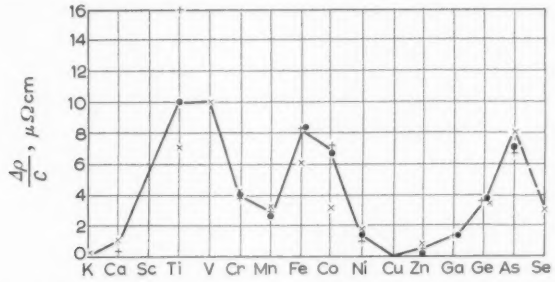


FIG. 1. Résistivités résiduelles dans le cuivre. $\Delta\rho/c$ en $\mu\Omega$cm/pour-cent atomique. · LINDE;[2] + PAWLEK;[5,6] × VASSEL.[10] Trait continu : valeurs réelles probables.

résultats de LINDE, PAWLEK et nous-mêmes pour le cuivre; la Fig. 2 contient ceux de LIEBERTZ, ZOLLER et nous-mêmes pour l'aluminium.

### 3. DISCUSSION DES RESULTATS

Dans la Fig. 1, les résultats des différents auteurs sont comparables, sauf pour le titane et le cobalt. Cette différence pourrait être due, pour le titane, à une forte affinité de ce métal pour d'autres impuretés. Il peut en être de même du cobalt, qui est peu soluble dans le cuivre.

Dans la Fig. 2, les résultats concordent de même, sauf pour le titane et le vanadium. Ces métaux sont très peu solubles dans l'aluminium. Des expériences nous ont ainsi montré que le titane se dissout à moins de 0,002 pour-cent atomique dans l'aluminium. Ceci veut dire que le titane a une forte tendance à former des composés avec l'aluminium, et sans doute aussi avec les autres impuretés. Ce fait est en parfait accord avec les faits connus de la métallurgie chimique.

En ce qui concerne les éléments à droite du cuivre, dans le cuivre comme dans l'aluminium, nous trouvons que la loi de NORBURY–LINDE est généralement bien suivie: la résistivité augmente à peu près comme $|\Delta Z|^2$. $Z$ est ici le nombre d'électrons de valence, ou le numéro de la colonne dans le tableau de Mendeleief; $\Delta Z$, la différence de ces

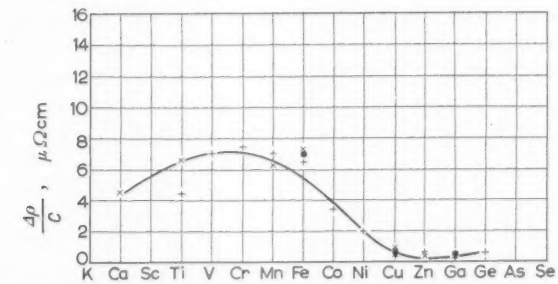


FIG. 2. Résistivités résiduelles dans l'aluminium. $\Delta\rho/c$ en $\mu\Omega$cm/pour-cent atomique. · ZOLLER;[8,9] + LIEBERTZ;[7] × VASSEL.[10] Trait continu : valeurs réelles probables.

nombres pour l'impureté et pour la matrice. On sait qu'une telle loi a été expliquée d'abord par MOTT,[12] puis plus exactement par FRIEDEL[11] et d'autres auteurs, en traitant les électrons de conductibilité de la matrice comme des électrons libres diffusés par les atomes d'impureté.

Pour le selenium dans le cuivre, la loi en $|\Delta Z|^2$ ne semble plus être valable. Nous pensons que, dans ce cas, il faut considérer que le selenium n'a pas un nombre d'électrons de valence $Z = +6$, mais un nombre $Z' = -2$ : ce sont les deux électrons qui lui manquent pour remplir sa couche $p$. Ce point de vue est en accord avec les faits de la chimie; l'oxygène a également une valence $Z' = -2$. Si ce point de vue est adopté, $|\Delta Z| = 3$, comme pour le Cu–Ge. Pour Cu–As au contraire, $|\Delta Z| = 4$, que l'on prenne pour l'arsenic $Z = +5$ ou $Z' = -3$. Ces considérations expliquent donc bien le pic de résistivité très symétrique observé pour Cu–As (Fig. 1).

On peut présenter le raisonnement qui précède d'un point de vue un peu différent, qui nous a été suggéré par Monsieur FRIEDEL. La série des éléments Zn, Ga, Ge, As, Se a des couronnes $4s$ et $4p$ de plus en plus stables et qui se remplissent donc progressivement du Zn au Se, quand ces éléments sont dissous dans le cuivre. D'après les considérations de FRIEDEL,[11] on s'attend à une résistivité résiduelle maxima pour l'impureté dont la couronne $4p$ est à moitié plaine,* c'est-à-dire pour l'As. La résistivité maxima est donnée approximativement par la formule suivante :[13] †

$$\left(\frac{\Delta\rho}{c}\right)_{\text{max.}} \simeq \frac{4\pi\alpha}{pk_M}(2l+1)\cdot 0{,}24\mu\Omega\text{cm/pour-cent} \quad (1)$$

Dans cette formule, $p$ est nombre d'électrons de valence par atome de la matrice, $k_M$ leur quantité de mouvement au niveau de Fermi, exprimée en unités atomiques ($e = m = h = 1$); $l$ est le nombre quantique de la couronne à moitié pleine de l'impureté. Enfin $\alpha$ est une constante égale ici à l'unité. Pour les alliages de cuivre ici considérés, $l = 1$, $p = 1$, $k_M = 0{,}725$. D'où $(\Delta\rho/c)_{\text{max.}} \simeq$ $\simeq 12\mu\Omega$cm/pour-cent, en assez bon accord avec le pic de 8,3 pour-cent mesuré par nous pour Cu–As.

En ce qui concerne les éléments allant de K au Ni, nous observons une différence considérable d'allure pour le cuivre et l'aluminium. Dans le cas du cuivre, nous observons deux pics assez forts, l'un pour Ti–V, l'autre pour Fe; dans le cas de l'aluminium, nous trouvons un seul pic, plus faible et plus étalé. Ces résultats sont en accord avec ceux des autres expérimentateurs. Notre valeur plus faible pour le Cu–Ti suggère que les deux pics du cuivre sont assez semblables.

On sait que FRIEDEL[11] a proposé d'expliquer ces pics de résistivité par le même mécanisme de résonance invoqué plus haut pour les éléments Cu, Zn, Ga, Ge, As, Se. Le pic de l'aluminium serait dû à la résonance de ses électrons de conductibilité avec la couronne $d$ à moitié pleine des impuretés de transition. Dans ce cas, $p = 3$, $k_M = 1{,}02$, $l = 2$ et $\alpha = 1$; la formule (1) prédit un pic $(\Delta\rho/c)_{\text{max.}} \simeq 4{,}7\mu\Omega$cm/pour-cent, en bon accord avec les mesures.

Le fait que l'on observe deux pics dans le cuivre serait dû à ce que la règle de Hund s'appliquerait dans ce cas et conduirait les impuretés à vider une demi-couronne $3d^5$, d'une direction de spin, avant l'autre. Ainsi, par exemple, le Fe aurait une demi-couronne $3d^5$ pleine qui diffuserait peu les électrons; et la demi-couronne de spin opposé à moitié pleine, diffusant donc fortement les électrons. Chaque atome d'impureté ne diffuserait donc fortement qu'une moitié des électrons de conductibilité. Il faut ainsi introduire un facteur $\alpha = \frac{1}{2}$ dans la formule (1). Avec $p = 1$, $k_M = 0{,}72$ et $l = 2$, celle-ci donne pour les deux pics $(\Delta\rho/c)_{\text{max.}} \simeq$ $\simeq 10{,}5\mu\Omega$cm/pour-cent, en accord satisfaisant avec les valeurs de la Fig. 1.

En conclusion, la loi de NORBURY en $|\Delta Z|^2$ s'applique raisonnablement bien aux impuretés «normales» (Cu à Se) dissoutes dans le cuivre et l'aluminium, à condition de prendre toujours la plus petite valeur possible pour $|\Delta Z|$. Cette loi s'applique aussi aux impuretés de transition selon notre systématisation,[14] laquelle est en parfait accord avec les faits connus de la chimie, physique et métallurgie chimique. Dans tous les cas, les pics de résistivité observés ont des positions et des valeurs en bon accord avec les considérations théoriques de FRIEDEL.

* La couronne $4s$ est trop élargie par résonance avec les électrons de conductibilité pour donner un pic de résistivité.[11]

† Cette formule se déduit de la formule générale donnée par FRIEDEL[11] en faisant $\eta_l = (\pi/2)$ et tous les autres déphasages égaux à zéro ou à des multiples de $\pi$.

## REFERENCES


1. NORBURY A. L. *Trans. Faraday Soc.* **16,** 570 (1921).
2. LINDE J. O. *Ann. Phys., Lpz.* **15,** 219 (1932).
3. GULYAEV A. P. et TRUSOVA E. F. *Zh. tekh. fiz.* **20,** 66 (1950).
4. HIBBARD W. R. *Trans. Amer. Inst. Min. (Metall). Engrs.* **200,** 594 (1954).
5. PAWLEK F. et REICHEL K. *Z. Metallk.* **47,** 347 (1956).
6. KAYSER O., PAWLEK F. et REICHEL K. *Metall.* **8,** 532 (1954).
7. LIEBERTZ J. Diplom Arbeit, non-publié (1956).
8. ZOLLER H. *Metall.* **10,** 203 (1956).
9. ZOLLER H. *Metall.* **11,** 378 (1957).
10. VASSEL C. R. *Bergakad.* **9,** 306 (1957); *Aluminium* **33,** 781 (1957).
11. FRIEDEL J. *Canad. J. Phys.* **34,** 1190 (1956).
12. MOTT N. F. et JONES H. *The Theory of the Properties of Metals and Alloys.* Clarendon Press, Oxford (1936).
13. FRIEDEL J. *Nuovo Cim.* sous-presse (Ecole d'été de Varenna 1956).
14. VASSEL C. R. *Z. Metallk.* **49,** sous-presse (1958).


VOL.
7
1958

## Electrical resistance of some noble-metal alloys at liquid-helium temperatures

(*Received* 21 *March* 1958)

IN the following letter the results are given of an investigation of the electrical resistivity in the liquid-helium temperature region of some alloys with a noble-metal base and various other elements as solutes. The measurements constitute a continuation of an investigation earlier made by J. O. LINDE in co-operation with the Kamerlingh Onnes Laboratory, Leiden.[1] Some of the results from the Institute here have been reported[2] at the Fifth International Low-Temperature Conference, Madison, 1957. The results given in the present ve not been published previously.

The alloys were prepared from spectroscopically pure materials supplied by Johnson, Matthey and Co. Ltd., London, by melting the components in evacuated silica tubes in a high-frequency furnace (in some cases in a wire-wound furnace). After slight rolling, the ingots were homogenized by annealing at 800–900°C for about 2 hr. The alloys were then drawn to wires of about 0·2 mm diameter. Small pieces of the wires (3–7 cm) were used for the measurements. They were welded to short wires of the same material. Copper wires were soldered to the "H-shaped" specimens as leads for

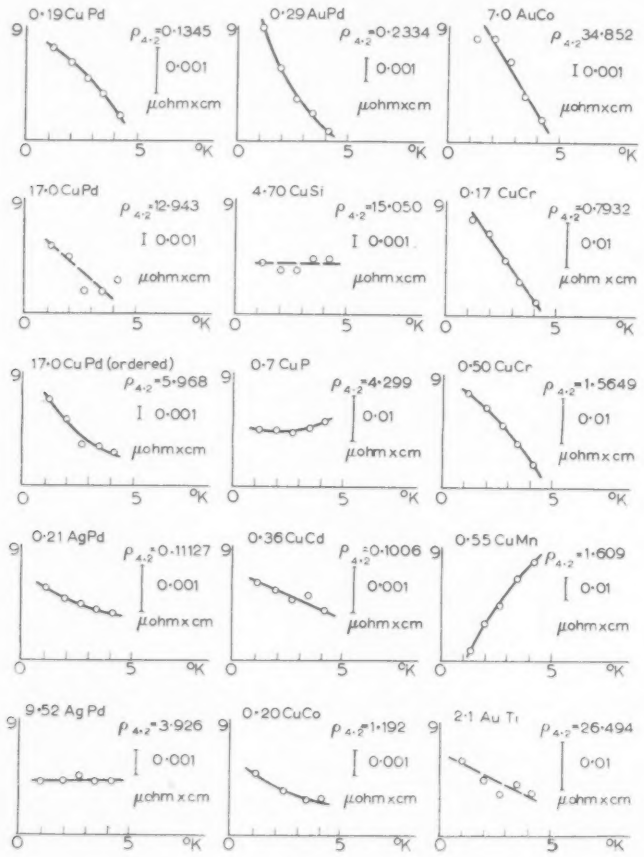


FIG. 1.

the current and connections to an electrical potentiometer. The samples were as a rule annealed at about 500°C prior to the measurements (when quenching from higher temperatures was not necessary).

The measurements were generally carried out at five different temperatures in the range 4·2–1·2°K, in which the fixed temperatures were determined with a carbon resistance thermometer, calibrated with the aid of a helium gas thermometer. By combining these measurements with a measurement of the resistivity of the samples at room temperature, the resistance values at the different temperatures could be converted to resistivity values.

The diagrams show the values of the resistivity $\rho$ in $\mu\Omega$cm as a function of the temperature in °K. The notation for the alloys consists of the atomic percentage of the solute and the chemical symbols of the basis metal and the solute, given in that order. The scales used and the resistivity at 4·2°K for the different samples are also noted in the diagrams.

From the diagrams it is apparent that the resistivity–temperature derivative is negative in the liquid-helium region for most of the dilute alloys studied. This implies that the curves will display a resistivity minimum at some higher temperature. An exception to this behavior is found for the alloy 0·55 CuMn, which belongs to the group of alloys for which the resistance minimum is followed by a maximum at still lower temperatures[1], further for the alloys 0·7 Cu P, 9·52 Ag Pd, and 4·70 Cu Si. For the last-mentioned alloys, which are characterized by a fairly high concentration of solute, the change of resistivity with temperature is rather small. The measurements are in these cases not accurate enough to enable us to decide whether a minimum exists or not in the resistivity-temperature curves. This is to be tested by further measurements.

Of the alloy 17·0 Cu Pd, two samples were made, one of which was annealed in the temperature range below 400°C to produce an ordered state of the specimen and the other quenched from 600°C, both being homogenized prior to these treatments. In the samples of 7·0 Au Co and 0·17 Cu Cr a slight degree of precipitation may have occured during the quenching process. Results of measurements on samples of these alloys in the cold-worked state have been reported earlier from this Institute.[2]

*Acknowledgements*—I am much indebted to Dr. J. O. LINDE for putting the alloys at my disposal and for valuable discussions. The work has been granted by Statens Tekniska Forskningsråd, Stockholm.

*Department of Physics* NILS BÄCKLUND
*Royal Institute of Technology*
*Stockholm* 70, *Sweden.*

## REFERENCES

1. GERRITSEN A. N. and LINDE J. O., *Physica* **17,** 573 584 (1951); **18,** 877 (1952).
2. LINDE J. O., *Proc. Fifth Internat. Conf. on Low-Temp. Phys. and Chem.* (*Madison*) 1957 (in the press).

---

## $Pt^{195}$ nuclear magnetic resonance in metallic platinum

(*Received* 5 *May* 1958; *in revised form* 3 *June* 1958)

A NUCLEAR magnetic resonance, definitely associated with $Pt^{195}$, has been located in platinum metal. Heretofore, the nuclear resonance of $Pt^{195}$ has been observed in aqueous solutions of chloroplatinic acid only[1] and the presently accepted value of its magnetic moment is based on that work. The purpose of this letter is to point out that the moment so determined may be in error by several per cent and also that the character of the metallic platinum resonance is quite unusual.

The resonance associated with $Pt^{195}$ in the metal at 25°C is shifted to *lower* frequency by $3{\cdot}52 \pm 0{\cdot}01$ per cent relative to the resonance of the same isotope in a one-molar aqueous chloroplatinic acid solution in the same external magnetic field. Our data on the solution are in agreement with those of PROCTOR and YU. This rather large shift is in the opposite sense to that observed for any other metallic shift reported in the literature[2]; however, this behavior may be representative of other heavy transition metals as yet unreported. The usual paramagnetic (Knight) shift toward *higher* frequency in the metal is satisfactorily explained[2] on the basis of hyperfine interaction between the nuclear magnetic moments and the conduction

electrons in the *s*-state; existing theories, however, do not account for the present observations.

The position and width of the resonance in platinum metal were observed over a wide range of temperature and magnetic field. Both the relative shift and line width were found to be independent of external magnetic field over the range 2·37 to 11·00 kG at room temperature. The shape of the absorption was closely Lorentzian, the peak-to-peak width of the derivative curve, corrected for slight modulation and field inhomogeneity broadening being 2·54 G, with a probable error of 0·06 G. The theoretical second moment for the absorption in the metal is 0·165 $G^2$ (using $\gamma = 0{\cdot}551 \cdot 10^4\ G^{-1}\ sec^{-1}$); this would correspond to a peak-to-peak width of 0·81 G for a Gaussian curve and should be a reasonable estimate of the true width in this case since no quadrupole or spin exchange interactions are to be expected. (Pt 195, which is 33·7 per cent abundant, is the only isotope with non-zero spin; its spin is one-half.) The Lorentzian shape and excessive width indicate a relaxation-time broadening. This was investigated by measuring the width at 78°K, and it was found to have decreased to $1{\cdot}24 \pm 0{\cdot}06$ G. Using the relationship

$$1/T_2 = (2/\pi)^{1/2}(1/T_2') + (1/2T_1), \qquad (1)$$

first suggested by BLOEMBERGEN, PURCELL, and POUND,[3] it was possible to derive an approximate value for $T_1$, the spin-lattice relaxation time, on the assumption that no motional narrowing was occurring (i.e., $T_2'' = T_2'$ in the notation of Reference 3, which is used throughout this discussion) and that the limiting line shapes are Gaussian (at 0°K) and Lorentzian (at high temperatures). $T_2$ was obtained by integrating the experimental curves, using the relationships $T_2 \gtrsim T_2^* = \frac{1}{2}g(\nu)_{max}$ and $\int_0^\infty g(\nu)d\nu = 1$. Using $(T_2'')^{-1} = 2{\cdot}24 \cdot 10^3\ sec^{-1}$, $T_1$ was calculated to be $7{\cdot}5 \times 10^{-5}$ sec at 298°K, and $21 \times 10^{-5}$ sec at 78°K. This change in $T_1$ was accompanied by a rather large change in the resonance position described by Fig. 1. The ordinate $\delta(\Delta H/H)$ is $(H_{78} - H_T)/H_{78}$ where $H_{78}$ and $H_T$ are the external magnetic field values required for resonance at a constant frequency and a sample temperature of 78°K and T°K, respectively. The total relative shift observed over the temperature range investigated is 0·65 per cent, about ten times that observed for any other metal.[4] The measured value of $[\nu(\text{metal}, 78°K) - \nu(\text{sol})]/\nu(\text{metal}, 78°K)$ is $-4{\cdot}154 \pm 0{\cdot}001$ per cent. The reason for stating $\Delta H/H$ one time and $\Delta\nu/\nu$ the next reflects the experimental method used to obtain the data.

It is possible to interpret these results qualitatively using only the electron–nuclear interactions known from the study of non-transition metals if we assume that the cause of the negative shift is an

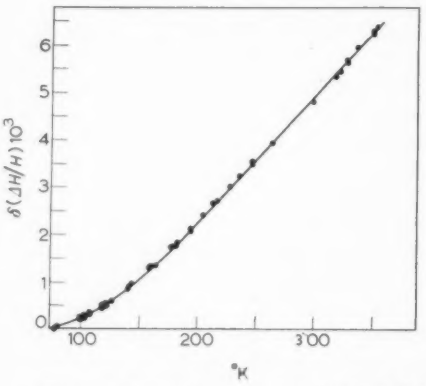


FIG. 1. Plot of change in resonance field of $Pt^{195}$ in platinum metal as a function of temperature at a constant frequency of 7·6606 mc/sec. The resonance field decreases from a value $8717{\cdot}0 \pm 0{\cdot}3$ G at 78°K.

exceptionally large paramagnetic chemical shift[5] for the $[PtCl_6]^{2-}$ complex and that a hypothetical non-paramagnetic compound has a resonance at a frequency less than that of the metal in a fixed magnetic field. Large chemical shifts which may be of a similar nature have been observed for some cobalt complexes.[6]

By using the Korringa relation[7] and the above hypothesis, an approximate figure for the Knight shift has been derived from the $T_1$ data presented above. This appears in Table 1. Even if the use of the revised Korringa relation given by PINES were straightforward, it is doubtful whether it would represent an improvement in the present case since it does not include non-*s* relaxation processes.

Although these computed shifts raise additional questions to be discussed below, the Knight shift will be assumed to be 1·8 per cent. After taking

*Table* 1. *Relaxation time and Knight shift for metallic* $Pt^{195}$

| $T$°K | $T_2$ | $T_1$ | $T_1T$ | $(\Delta H/H)_{\text{Korr.}}$ |
|---|---|---|---|---|
| 298 | $1{\cdot}18 \cdot 10^{-4}$ | $7{\cdot}5 \cdot 10^{-5}$ | $2{\cdot}2 \cdot 10^{-2}$ | $1{\cdot}7 \cdot 10^{-2}$ |
| 78 | $2{\cdot}4 \cdot 10^{-4}$ | $21{\cdot}0 \cdot 10^{-5}$ | $1{\cdot}6 \cdot 10^{-2}$ | $1{\cdot}9 \cdot 10^{-2}$ |

into account the core diamagnetism, amounting to about 0·9 per cent,[8] the moment of $Pt^{195}$ is found to be about 5·0 per cent lower than the value 0·6005 n.m.[1]. The latter value does not include the diamagnetic correction.

The fact that the derived Knight shifts stated in Table 1 differ by about ten per cent of their value is not considered significant in view of the difficulty of measuring $T_2$ and considering the approximate nature of equation (1). A point deserving emphasis, however, is that the Korringa relation predicts only a slight temperature dependence of the Knight shift, and if anything, a small *increase* with decreasing temperature, while the observed fact is that the resonance has shifted to higher field (by 0·5 per cent, 50 G in 10 kG) in going from room temperature to 78°K. The latter statement is equivalent to saying that if the relative Knight shift has the value $K$ per cent at room temperature its value is $(K-0{\cdot}5)$ per cent at 78°K and thus the Knight shift *decreases* rapidly with decreasing temperature.

It is not possible to bring the observed decrease in $(\Delta H/H)$ into agreement with the $T_1$ values given above by using the theoretical expressions for relaxation time and Knight shift based on the hyperfine interaction alone without making assumptions concerning changes in mean probability density of a conduction electron at the nucleus averaged over the top of the Fermi distribution, $P_F$; the density of electronic states per unit energy at the top of the Fermi distribution $\rho(E_0)$; or the spin susceptibility per unit volume, $\chi_s$, which are incredible when compared with the results of specific heat and magnetic susceptibility measurements.[9,10] Estimates of the change in core diamagnetism based on the volume change of platinum on cooling (about 0·6 per cent over the region 78°K to 298°K) amount to only 0·4 per cent of the total diamagnetic contribution to the susceptibility and are negligible when compared to the shifts reported here.

Two possible conclusions from this discussion follow. A relatively fast change in the mixture of states forming the wave function in the solid may occur as a function of temperature. The proportions of the configurations $5d^86s^2$, $5d^96s^1$, and $5d^{10}$ would have to change in such a way that $P_F$, the total $s$-state contribution at the nucleus, averaged over the top of the Fermi distribution, would decrease with temperature. The low-temperature ground state configuration would have the least $s$-state contribution. The difficulty in applying even the revised Korringa relation[7] under these conditions of rapidly changing $s$-character is obvious. Relaxation processes involving $d$ electrons would be required to account for the shortness of the observed relaxation time at low temperature. This argument is consistent with the 10 per cent increase in magnetic susceptibility in going from 298 to 78°K[10] and would probably not influence the linearity of the electronic specific heat curves in the temperature region used to gather such data.

Despite the plausibility of the above argument, it is not necessarily the only one consistent with the data; one might, for instance, regard the negative shift as real in the sense that there is no platinum compound (even hypothetical) from which platinum metal is shifted by an ordinary (positive) Knight shift. One might then inquire into configuration interactions with higher $s$-states which apparently can cause the hyperfine coupling constant to be negative.[11] The temperature dependence of the shift and line width could perhaps be equally well explained by this mechanism.

Work on the pressure dependence of the Knight shift would be very valuable in determining whether the suggested rapid electronic change is a volume effect. Also, a direct measurement of $T_1$ vs. temperature would aid in isolating the effects of the factors entering theoretical $T_1$ and $(\Delta H/H)$ expressions.

*Acknowledgements*—The author is grateful to Professor H. Brooks for a discussion of these results, and to Dr. L. E. Orgel.

*Metals Research Laboratories* T. J. Rowland
*Electro Metallurgical Company*
*Division of Union Carbide Corporation*
*Niagara Falls, New York*

REFERENCES

1. PROCTOR W. G. and YU F. C. *Phys. Rev.* **81,** 20 (1951).
2. KNIGHT W. D. *Solid State Physics* **2,** 93. Academic Press, Inc., New York (1956).
3. BLOEMBERGEN N., PURCELL E. M. and POUND R. V. *Phys. Rev.* **73,** 679 (1948).
4. MCGARVEY B. R. and GUTOWSKY H. S. *J. Chem. Phys.* **21,** 2114 (1953).
5. GRIFFITH J. S. and ORGEL L. E. *Trans. Faraday Soc.* **53,** 601 (1957). In a private communication Dr. Orgel stated that a paramagnetic shielding term for $Pt^{4+}$ of over 2 per cent would be rather surprising unless spin-orbit effects are very large.
6. FREEMAN R., MURRAY G. R. and RICHARDS R. E. *Proc. Roy. Soc.* A **242,** 455 (1957).
7. A good discussion may be found in the article by D. PINES *Solid State Physics* **1,** 420. Academic Press, Inc., New York (1955).
8. DICKINSON W. C. *Phys. Rev.* **80,** 567 (1950).
9. KOK J. A. and KEESOM W. H. *Physica* **3,** 1035 (1936).
10. HOARE F. E. and MATTHEWS J. C. *Proc. Roy. Soc.* A **212,** 137 (1952).
11. ABRAGAM A. and PRYCE M. H. L. *Proc. Roy. Soc.* A **206,** 164 (1951).


## Superconductivity of rhenium nitride

(*Received* 12 *June* 1958)

THE existence of rhenium nitride is reported by HAHN and KONRAD.[1] The compound was investigated because of the considerable line width of its X-ray diffraction powder pattern, as described in their paper. Strain was rather improbable, since the synthesis was carried out by decomposing $NH_4ReO_4$ at approximately 300°C in an ammonia atmosphere and annealing at this temperature did not change the extreme line width. This broadening was therefore presumably due to the extremely small crystallite size.

Rhenium nitrides of the approximate composition $ReN_{0.34}$ were prepared and their X-ray powder pattern corresponded to that described above. They became superconducting between 4 and 5°K. A rise in the transition temperature of rhenium powder of over 1°K above that of the cast rhenium ingot had first been observed by HULM and GOODMAN.[2] Decomposition of $NH_4ReO_4$ at lower temperatures produced samples whose line widths were so broad that no lines could be distinguished. They were not superconducting above 1°K. If the decomposition was carried out at approximately 700°C, the lines in the X-ray powder pattern were sharper and corresponded to those of rhenium metal. Simultaneously the superconducting transition temperature began to approach that of rhenium metal.[2]

$ReN_{0.34}$ is of interest as a superconductor, for the size of the crystallites is very small. We determined the crystallite size of the samples which were superconducting above 4°K and found a crystallite size range between 20 and 26 Å. This size agrees quite well with the results of BUCKEL[3] and RÜHL,[4] who investigated the crystalline state of superconducting metal films condensed at low temperatures. They found a cessation of superconductivity for crystallite sizes in the neighborhood of 20 Å. In their case two dimensions of the films were, however, macroscopic. 20 Å is at least one order of magnitude below the penetration depth of superconductors.

The fact that we observe superconductivity by our magnetic method in a material of crystallite size between 20 and 26 Å suggests that, barring the unlikely possibility of a very large change in penetration depth, the particles are in effective electrical contact and exclude the field by their infinite conductivity rather than by a Meissner effect. To check this we looked for a true Meissner effect and found less than 5 per cent of that expected. This shows that the contacts are at least not so effective as to make the material act like bulk superconductor, and puts an upper limit of the order of 2–300 Å on the "effective" size of the aggregates of crystallites.

*Acknowledgement*—We would like to thank P. W. ANDERSON for some helpful discussions.

*Bell Telephone Laboratories Inc.* B. T. MATTHIAS
*Murray Hill, New Jersey*

*Department of Physics* W. H. ZACHARIASEN
*University of Chicago*
*Chicago, Ill.*


REFERENCES

1. HAHN H. and KONRAD A., *Z. anorg. allgem. Chem.* **264,** 178 (1951).
2. HULM J. K. and GOODMAN B. B., *Phys. Rev.* **106,** 659 (1957).
3. BUCKEL W., *Z. Phys.* **138,** 136 (1954).
4. RÜHL W., *Z. Phys.* **138,** 121 (1954).

# CONTENTS LISTS OF VOLUME 5, NOS. 1-4

## Volume 5 Nos. 1/2


page

B. V. Derjaguin et I. I. Abrikossova:
Mesure directe de l'attraction moléculaire dans les solides . . . . . 1

S. I. Pekar:
Théorie des ondes électro-magnétiques dans un cristal avec excitons . . . . . 11

R. W. Soshea, A. J. Dekker et J. P. Sturtz:
Centres colorés produits par les rayons X dans MgO . . . . . 23

Jiro Yamashita et Tatumi Kurosawa:
Sur le courant électronique dans NiO . . . . . 34

Walter A. Harrison:
Résistivité due aux dislocations dans le cuivre . . . . . 44

T. W. Hickmott et Gert Ehrlich:
Adsorption chimique sensible à la structure: le mécanisme de désorption du tungstène . 47

P. Kisliuk:
Les probabilités de fixation des gaz absorbés chimiquement à la surface des solides—2e partie . . . . . 78

F. J. Low et C. F. Squire:
Résonance magnétique nucléaire dans LiF . . . . . 85

William Paul et D. M. Warschauer:
Propriétés optiques des semi-conducteurs sous pression hydrostatique—I Germanium . 89

William Paul et D. M. Warschauer:
Propriétés optiques des semi-conducteurs sous pression hydrostatique—II Silicium . 102

J. B. Goodenough, D. G. Wickham et W. J. Croft:
Quelques propriétés cristallographiques et magnétiques du système $Li_x^+ Ni_{1\ 2x}^{+\ +} Ni_x^{+\ +\ +} O$ . 107

W. L. Gordon, C. H. Shaw et J. G. Daunt:
Distribution atomique radiale dans l'hélium 4 liquide par diffusion des rayons X . . 117

J. Hornstra:
Dislocations dans les réseau du diamant . . . . . 129

J. R. Drabble et C. H. L. Goodman:
Liaison chimique du tellurure de bismuth . . . . . 142

Lettres aux Redacteurs:

R. E. Behringer: Note sur "La structure de bande de l'aluminium: un calcul self-consistent" . . . . . 145

A. S. Nowick: Défense de la méthode de traitement par l'énergie de déformation pour les petits atomes dissous . . . . . 147


## Volume 5 No. 3


R. J. Sladek:
Bandes d'impuretés induites magnétiquement dans InSb de type *n* . . . . . 157

page

H. M. Bath et M. Cutler:
Mesure de vitesse de recombinaison de surface dans le silicium par photoconductibilité stationnaire . . . . . 171

H. A. Gersch et W. C. Koehler:
Modèles de configurations ordonnées magnétiquement sur des réseaux simples . . 180

J. W. Nielsen et E. F. Dearborn:
La croissance des monocristaux des grenats magnétiques . . . . . 202

F. A. Kröger et H. J. Vink:
Relations entre les concentrations des imperfections dans les solides . . . . . 208

D. S. Tannhauser:
Autodiffusion du brome dans le bromure d'argent . . . . . 224

Revues des livres . . . . . 236

VOL
7
195

## Volume 5 No. 4

G. B. Benedek et T. Kushida:
L'influence de la pression sur l'effet Knight dans les métaux alcalins et le cuivre . . 241

Hazimu Kawamura:
Le potentiel de déformation du chlorure de potassium . . . . . 256

D. F. C. Morris:
L'énergie de réseau et la chaleur de formation du monosulfure de lithium . . . 264

Truman O. Woodruff et Werner Känzig:
Absorption par résonance paramagnétique d'un centre V dans LiF . . . . . 268

James C. Phillips et Herbert B. Rosenstock:
Méthodes topologiques de localisation des points critiques . . . . . 288

T. J. Swoboda, R. C. Toole et J. D. Vaughan:
Nouveaux composés magnetiques de la structure du type du ilmenite . . . . 293

R. M. Bozorth et Dorothy E. Walsh:
Moment ferromagnétique de $CoMnO_3$ . . . . . 299

D. B. Fischbach et A. S. Nowick:
Quelques effets électriques transitoires de la déformation plastique dans les cristaux de NaCl . . . . . 302

A. David Pearson:
Etudes sur les oxydes inférieurs du titane . . . . . 316

W. G. Maisch et H. G. Drickamer:
L'effet de la pression sur les centres colorés dans les cristaux d'halogénures alcalins . . 328

D. Saint-James:
Determination des lois de force dans les cristaux de type du diamant . . . . 337

## Volume 5 Nos. 1/2

*page*

Б. В. Дерягин и И. И. Абрикосова:
Прямые измерения молекулярного притяжения между твердыми телами . . 1

С. И. Пекар:
Теория электромагнитных волн в кристалле с экситонами . . . . . 11

Р. Сошеа, А. Деккер и Дж. Щтурц:
Центры окраски в MgO, индуцированные X-лучами . . . . . 23

И. Ямашита и Т. Куросава:
Об электронном токе в NiO . . . . . 34

В. А. Гаррисон:
Сопротивление меди, обусловленное дислокациями . . . . . 44

Т. Хикмотт и Г. Эрлих:
Структурно-чувствительная хемисорбция: механизм десорбции с вольфрама . 47

П. Кислюк:
Вероятности прилипания газов при хемисорбции с твердых поверхностей. Часть II 78

Ф. Лоу и К. Скуайр:
Ядерный магнитный резонанс в LiF . . . . . 85

В. Паул и Д. Варшауер:
Оптические свойства полупроводников под гидростатическим давлением:
I. Германий . . . . . 89

В. Паул и Д. Варшауер:
Оптические свойства полупроводников под гидростатическим давлением:
II. Кремний . . . . . 102

Дж. Гуденаф, Д. Викхам и В. Крофт:
Некоторые магнитные и кристаллографические свойства системы $Li_x^+ Ni_{1-2x}^{++} Ni_x^{+++} O$ 107

В. Л. Гордон, К. Шоу, Дж. Доунт:
Радиальная функция распределения атомов в жидком гелии 4 по данным рассеяния X-лучей . . . . . 117

Дж. Хорнстра:
Дислокации в решетке алмаза . . . . . 129

Дж. Драббл и К. Гудман:
Химическая связь в теллуриде висмута . . . . . 142

Письма в Редакцию

Р. Берингер:
Замечание о зонной структуре алюминия при самосогласованном вычислении 145

А. С. Новик:
В защиту энергетического подхода к атомам в твердом растворе . . 147

## Volume 5 No. 3

Р. Сладек:
Образование магнитно-индуцированных примесных полос в *n*-InSb. . . . 157

page

Г. Бат и М. Кутлер:
Измерение скорости поверхностной рекомбинации в кремнии при стационарной фотопроводимости . . . . . 171

Г. А. Герш и В. Келер:
Типы магнитно упорядоченных конфигураций в простых решетках . . 180

Дж. Нильсен и Е. Ф. Дирборн:
Рост монокристаллов магнитных гранатов . . . . . 202

Ф. Крегер и Г. Винк:
Соотношения между концентрациями пефектов в твердых телах . . . 208

Д. С. Таннгаузер:
Самодиффузия брома в бромиде серебра . . . . . 224

Резцензии книг . . . . . 236

VOL
7
195

## Volume 5 No. 4

Г. Бенедек и Т. Кушида:
Зависимость эффекта Найта в щелочных металлах и в меди от давления . . 241

Х. Кавамура:
Деформационный потенциал хлорида калия . . . . . 256

Д. Ф. Моррис:
Решеточная энергия и теплота образования моносульфида лития . . . 264

Т. Вудрефф и В. Кенциг:
Парамагнитное резонанское поглощение V-центра в LiF . . . . . 268

Дж. Филлипс и Г. Розеншток:
Топологические методы локализации критических точек . . . . . 288

Т. Свобода, Р. Туул и Дж. Воган:
Новые магнитные совединения типа ильменита . . . . . 293

В. Р. М. Бозорт и Д. Валш:
Ферромагнитный момент $CoMnO_3$ . . . . . 299

Д. Фишбах и А. С. Новик:
Некоторые переходные электрические эффекты при пластическом деформировании кристаллов NaCl . . . . . 302

А. Д. Пирсон:
Исследования низших окислов титана . . . . . 316

В. Майш и Г. Дрикамер:
Эффект давление на центры окраски в кристаллах галогенидов щелочных металлов . . . . . 328

Д. Сен-Джемс:
Определение закона взаимодействия в кристаллах типа алмаза . . . . 337

## Volume 5 Nos. 1/2

page

B. V. DERJAGUIN und I. I. ABRIKOSSOVA:
Direkte Messungen der Anziehung zwischen Molekülen in Festkörpern . . . . 1

S. I. PEKAR:
Die Theorie elektromagnetischer Wellen in einem Kristall mit Exzitonen . . . . 11

R. W. SOSHEA, A. J. DEKKER und J. P. STURTZ:
Durch Röntgenstrahlen erzeugte Farbzentren in MgO . . . . . 23

JIRO YAMASHITA und TATUMI KUROSAWA:
Über elektronische Stromleitung in NiO . . . . . 34

WALTER A. HARRISON:
Der elektrische Widerstand von Versetzungen in Kupfer . . . . . 44

T. W. HICKMOTT und GERT EHRLICH:
Strukturempfindliche Chemisorption. Der Mechanismus der Desorption von Wolfram . 47

P. KISLIUK:
Die Haftwahrscheinlichkeit von Gasen die an Oberflächen von Festkörpern chemisorbiert wurden—II . . . . . 78

F. J. LOW und C. F. SQUIRE:
Kernmagnetische Resonanz in LiF . . . . . 85

WILLIAM PAUL und D. M. WARSCHAUER:
Optische Eigenschaften von Halbleitern unter hydrostatischem Druck—I Germanium . 89

WILLIAM PAUL und D. M. WARSCHAUER:
Optische Eigenschaften von Halbleitern unter hydrostatischem Druck—II Silizium . . 102

J. B. GOODENOUGH, D. G. WICKHAM und W. J. CROFT:
Einige magnetische und kristallographische Eigenschaften des Systems $Li_z^+Ni_{1-2z}^{++}Ni_z^{+++}O$ 107

W. L. GORDON, C. H. SHAW und J. G. DAUNT:
Die radiale Atomverteilung in flüssigem Helium 4 auf Grund der Streuung von Röntgenstrahlen . . . . . 117

J. HORNSTRA:
Versetzungen im Diamantgitter . . . . . 129

J. R. DRABBLE, und C. H. L. GOODMAN:
Die chemische Bindung in Wismuttellurid . . . . . 142

Briefe an die Herausgeber:

ROBERT E. BEHRINGER: Bemerkungen zur Bandstruktur des Aluminiums: Eine selbstkonsistente Berechnung . . . . . 145

A. S. NOWICK: Eine Verteidigung der Methode der Spannungsenergie bei kleinen, gelösten Atomen . . . . . 147

## Volume 5 No. 3

R. J. SLADEK:
Magnetisch hervorgerufene Störbandbildung in *n*-InSb . . . . . 157

page

H. M. Bath und M. Cutler:
Messung der Rekombinationsgeschwindigkeit an der Oberfläche von Silizium durch stationäre Photoleitfähigkeit . . . . . 171

H. A. Gersch und W. C. Koehler:
Magnetisch geordnete Konfigurationen bei einfachen Gittern . . . . . 180

J. W. Nielsen und E. F. Dearborn:
Das Wachstum von magnetischen Granateinkristallen . . . . . 202

F. A. Kröger und H. J. Vink:
Beziehungen zwsichen den Konzentrationen von Fehlstellen in Festkörpern . . . 208

D. S. Tannhauser:
Selbstdiffusion von Brom in Silberbromid . . . . . 224

Buch Rezension . . . . . 236

VOL
7
195

Volume 5 No. 4

G. B. Benedek und T. Kushida:
Die Druckabhängigkeit der Knight-Shift bei den Alkalimetallen und Kupfer. . . 241

Hazimu Kawamura:
Das Deformationspotential von Kaliumchlorid . . . . . 256

D. F. C. Morris:
Die Gitterenergie und Bildungswärme von Lithiummonosulfid . . . . . 264

Truman O. Woodruff und Werner Känzig:
Paramagnetische Resonanzabsorption eines V-Zentrums in LiF . . . . . 268

James C. Phillips und Herbert B. Rosenstock:
Topologische Methoden zur Festlegung kritischer Punkte . . . . . 288

T. J. Swoboda, R. C. Toole und J. D. Vaughan:
Neue magnetische Verbindungen mit Ilmenittyp-Struktur . . . . . 293

R. M. Bozorth und Dorothy E. Walsh:
Das ferromagnetische Moment von $CoMnO_3$ . . . . . 299

D. B. Fischbach und A. S. Nowick:
Einige vorübergehende elektrische Wirkungen der plastischen Verformung von NaCl-Kristallen . . . . . 302

A. David Pearson:
Untersuchungen der niederen Oxyde von Titan . . . . . 316

W. G. Maisch und H. G. Drickamer:
Der Einfluss von Druck auf die Farbzentren in Alkalihalogenidkristallen . . . . 328

D. Saint-James:
Die Bestimmung der Kraftgesetze in Kristallen vom Diamanttyp . . . . . 337

*J. Phys. Chem. Solids* Pergamon Press 1958. Vol. 7. pp. 105–117.

# THE QUANTUM THEORY OF THE HIGH FREQUENCY SURFACE IMPEDANCE OF A METAL*

M. YA. AZBEL'

Physical Technical Institute, Ukrainian Academy of Science.

(*Received* 2 *January* 1958; *in revised form* 19 *May* 1958)

**Abstract**—A quantum-mechanical formula is derived for the high-frequency surface impedance of a metal in a constant magnetic field of arbitrary direction. No special assumptions are made about the dispersion law of the conduction electrons. It is shown that in general, the relative amplitude of the quantised resistance oscillations is considerably greater than at zero frequency. In principle, an experimental determination of the magnetic field dependence of the impedance would be sufficient to determine the shape of the Fermi surface and the velocities of the electrons thereon.

## 1. INTRODUCTION

In a conventional calculation of metallic resistance, the quantisation of the energy levels of the conduction electrons may be safely ignored, and semiclassical considerations used throughout with a high degree of accuracy. This is because in any practical case the level separation $\Delta\epsilon$ is everywhere far smaller than the Fermi energy $\epsilon_0$. A level splitting of the order of $\epsilon_0$ would correspond to a specimen thickness as little as $d \sim \hbar/(2m^*\epsilon_0)^{\frac{1}{2}} \sim 10^{-8}$ cm or to the application of a magnetic field $H \sim \epsilon_0/\mu \sim 10^9$ oersted. In these expressions $m^* \sim 10^{-27}$ gm is the effective mass of an electron and $\epsilon_0 \sim 10^{-11}$ erg the Fermi energy; $\mu = |e|\hbar/m^*c$.

There are, however, two limitations to this semiclassical approach. Firstly, it makes no reference to the purely quantum-mechanical oscillation of the conductivity, a phenomenon absent from a classical model but nevertheless of great significance. Secondly, interest attaches not only to the resistance $R$ but also to its magnetic field derivative $dR/dH$, which can be measured directly; and as the period of the quantum oscillations is extremely small, their contribution to $dR/dH$ can be of the same order as, or even greater than, the classical contribution. At zero frequency the quantum-mechanical part is generally not so important;[1] but in calculating the derivative of the resistance at high frequencies a consideration of the quantum effects is essential.

The study of these oscillation phenomena is particularly important in that it holds out the possibility of deriving the shape of the Fermi surface directly from experimental data.[1,2] The usual procedure for establishing the Fermi surface involves an elaborate harmonic analysis of a complicated curve; however, it will be seen in Section 6 that a study of $R(H)$ at high frequencies using thin foils allows this difficulty to be circumvented.

Hitherto, diamagnetic oscillations of conductivity have been discussed only in the case of bulk metal in a static field. In this treatment, given by Lifshitz and Kosevich,[1] it was assumed that the current density within the metal was uniform, so that a static operator having no explicit dependence on co-ordinates could be employed. A non-uniform current density is less easily dealt with, especially as it is an essential part of the problem to consider a specimen of limited size. Moreover, it is not clear at the present time how to discuss quantum-mechanically the energy spectrum and the matrix elements corresponding in classical terms to the diffuse reflection of electrons from the metal surface. Notwithstanding this complication a solution may be obtained; for it can be shown that in the most interesting case of the anomalous

* Translated by R. D. Lowde.

skin-effect,* a significant contribution to the quantum-mechanical increment $\Delta j^q$ added to the classical current density is made only by those electrons which do not encounter the surface. In consequence a determination of metallic impedance does not involve establishing even the energy spectrum of the electrons which hit the surface.

In a classical discussion, on the other hand, the electrons which impinge upon the surface play an essential part in the process; and for this reason the boundary condition imposed at the surface of the metal on the electron distribution function must be examined carefully.[3,4]

## 2. THE COMPLETE SYSTEM OF EQUATIONS FOR THE IMPEDANCE

The surface impedance of a metal is governed by Maxwell's equations:

$$\text{curl } E = -\frac{1}{c}\frac{\partial H}{\partial t}; \quad \text{curl } H = \frac{1}{c}4\pi j; \quad (2.1)$$

the kinetic equation for the statistical operator $\hat{f}$:

$$\frac{\partial \hat{f}}{\partial t} + \frac{i}{\hbar}[\hat{\mathscr{H}}, \hat{f}] + \tilde{W}\hat{f}/t_0 = 0; \quad (2.2)$$

and the formula relating $\hat{f}$ to the current density, in quasiclassical approximation

$$\boldsymbol{j}(\boldsymbol{R}) = eSp\{\hat{f}\hat{\boldsymbol{v}}\delta(\boldsymbol{R}-\hat{\boldsymbol{r}})\}; \quad (2.3)$$

$$\boldsymbol{v} = \nabla_p \epsilon(\boldsymbol{p}). \quad (2.4)$$

Here $E$ and $H$ are the electric and magnetic field strengths, $j$ is the current density, and $\hat{\mathscr{H}}$ the Hamiltonian. $\tilde{W}\hat{f}/t_0$ describes the change in the statistical operator resulting from collision processes, with $t_0$ the relaxation time. $R$ is a radius vector, considered as a $C$-number in contrast to the operator $\hat{r} = (\hbar/i)(\partial/\partial P)$, $P$ being a generalized momentum. $\hat{v}$ is the velocity operator; $\epsilon = \epsilon(\hat{p}) \equiv \epsilon[P-(e/c)A]$ is a function giving the dispersion law of the conduction electrons, and $\delta$ is the delta-function. The order in which $\hat{v}$ and $\delta(R-\hat{r})$ are taken in (2.3) is immaterial, since in the quasiclassical approximation a hermitian operator is uniquely determined by its classical counterpart, and within an error $\sim \hbar^2$ any symmetrization procedure must lead to the same result. (This statement is easily verified if one recalls that to order $\hbar^2$, $[\hat{a}, \hat{b}] = (\hbar/i)[a, b]$, with $[a, b]$ the classical Poisson bracket). In what follows, the one-to-one correspondence between a hermitian operator in a quasiclassical representation and the appropriate classical quantity will be made use of frequently.

We now proceed to transform (2.2). We first make it linear in the RF field by putting

$$\hat{f} = f^0(\hat{E}) + \hat{f}', \quad (2.5)$$

where $\hat{E} = \epsilon(\hat{p}) + \mathscr{U} = \hat{\mathscr{H}} - e\phi$. $\phi$ is the scalar potential, $\hat{p}$ the kinematic momentum; $\mathscr{U}$ is the potential energy, which if emission phenomena are ignored is zero in the deep interior of the metal and infinite outside. Then in an approximation linear in the electric field

$$\frac{\partial \hat{f}'}{\partial t} + \frac{i}{\hbar}[\hat{E}^0, \hat{f}'] + \tilde{W}\hat{f}'/t_0 = -\frac{d}{dt}f^0(\hat{E});$$

$$\hat{\mathscr{H}} = \hat{E}^0 + \hat{\mathscr{H}}';$$

or, expressed in matrix elements

$$\frac{\partial f'_{kk'}}{\partial t} + \frac{i}{\hbar}(\epsilon_k - \epsilon_{k'})f'_{kk'} + (\tilde{W}\hat{f}')_{kk'}/t_0 = -\frac{df_{kk'}{}^0(\hat{E})}{dt}. \quad (2.6)$$

$\hat{E}^0$ and $\epsilon_k$ are respectively the Hamiltonian and the set of energy levels in the absence of a variable field; $k$ is a running integer representing the quantum numbers.

To deal with the right-hand side of equation (2.6) we note that all classical magnitudes except $f^0(E)$ depend smoothly on energy, so that their matrix elements may be calculated quasiclassically; the matrix elements of $f^0(\hat{E}^0)$ are known. It is clear that the non-linear effects ignored in the present treatment will always be negligible in a practical case; and so retaining the quasiclassical linear approximation, we may write ($\phi = 0$, for simplicity)

$$\frac{df^0{}_{kk'}(\hat{E})}{dt} = \frac{\partial}{\partial t}\{f^0(\hat{E}) - f^0(\hat{E}^0)\}_{kk'}$$

$$= \frac{\partial}{\partial t}\frac{1}{\epsilon_k - \epsilon_{k'}}[\hat{E}^0, f^0(\hat{E}) - f^0(\hat{E}^0)]_{kk'}$$

* The anomalous skin effect occurs when the skin depth $\delta$ is small in comparison with the Larmer radius $r$ and the electron mean free path $l$; at liquid helium temperatures this is true even for $\lambda \sim 1$ m.

$$= \frac{1}{\epsilon_k - \epsilon_{k'}} \frac{\partial}{\partial t}[\hat{E}, f^0(\hat{E}) - f^0(\hat{E}^0)]_{kk'}$$

$$= \frac{1}{\epsilon_k - \epsilon_{k'}} \frac{\partial}{\partial t}[f^0(\hat{E}^0), \hat{E}]_{kk'}$$

$$= \frac{f^0(\epsilon_k) - f^0(\epsilon_{k'})}{\epsilon_k - \epsilon_{k'}} \left(\frac{d\hat{E}}{dt}\right)_{kk'}$$

$$= \frac{f^0(\epsilon_k) - f^0(\epsilon_{k'})}{\epsilon_k - \epsilon_{k'}} (e\boldsymbol{v}\boldsymbol{E})_{kk'}.$$

The system of equations for monochromatic waves of frequency $\omega$ thereupon becomes

$$\text{curl } \boldsymbol{E} = -\frac{i\omega}{c}\boldsymbol{H}; \quad \text{curl } \boldsymbol{H} = \frac{4\pi}{c}\boldsymbol{j}; \tag{2.1}$$

$$i\left(\omega + \frac{1}{\hbar}\frac{\partial \epsilon}{\partial k}k'\right) f'_{k'}(k) + (\tilde{W}f')_{k'}/t_0$$

$$= \frac{f^0\left(\epsilon_k + \dfrac{\partial \epsilon}{\partial k}k'\right) - f^0(\epsilon_k)}{\dfrac{\partial \epsilon}{\partial k}k'} (e\boldsymbol{v}\boldsymbol{E})_{k'}; \tag{2.7}$$

$$\boldsymbol{j}(\boldsymbol{R}) = ef'_{k'}[\hat{\boldsymbol{v}}\delta(\boldsymbol{R} - \hat{\boldsymbol{r}})]_{-k'}. \tag{2.8}$$

Here we write $\phi_{kk'}$ for $\phi_{k-k'(k)}$; in the quasi-classical approximation the only significant cases have $|k-k'| \ll |k|$.

It now appears that the quantum-mechanical increment to the classical current density is given by different formulae according to whether or not the constant magnetic field is strictly parallel to the metallic surface. These two cases will therefore be treated separately. We take two coordinate systems, $xyz$ and $x\zeta\xi$. The $z$ axis is along the direction of the constant magnetic field, the $x$ axis in the plane of the surface of the metal; $\zeta$ is measured normal to the surface.

### 3. QUANTUM-MECHANICAL INCREMENT TO THE CLASSICAL CURRENT DENSITY IN A MAGNETIC FIELD PARALLEL TO THE SURFACE OF THE METAL

As pointed out in the introduction, the problem is materially simplified by the fact that electrons hitting the surface of the metal do not contribute significantly to $\Delta j^q$. This circumstance is most easily understood in the case where the magnetic field is parallel to the metal surface; the electrons corresponding to the closed section $\epsilon(p) = \epsilon_0$, $p_z = \text{const.}$ of the Fermi surface do not enter the deeper layers of the material; $\overline{v_y} \sim \overline{dp_x}/dt = 0$. In these expressions and subsequently, a bar implies that an average has been taken over the time of revolution of the electron in its orbit. It is therefore quite straightforward to separate the electrons into two groups which respectively do and do not encounter the surface. For the latter group, in a slab bounded by $y = 0$, $\mathscr{D}$;

$$0 \leqslant y(t) \leqslant \mathscr{D} \text{ and } y(t) = \frac{P_x - p_x(t)}{|eH/c|} \tag{3.1}$$

throughout the motion, so that

$$\left|\frac{eH}{c}\right| \mathscr{D} + p_x^{\min} \geqslant P_x \geqslant p_x^{\max}; \tag{3.2}$$

the extrema are taken with respect to the time $t$ defining the phase in the orbit. It is assumed that the magnetic field is not too small, and that

$$\left|\frac{eH}{c}\right| \mathscr{D} \geqslant p_x^{\max} - p_x^{\min}. \tag{3.3}$$

The energy spectrum of these electrons is naturally independent of the position of the classical centre of the orbit, which is determined by $P_x$; it is infinitely degenerate in $P_x$:

$$\epsilon = \epsilon(n, p_z), \tag{3.4}$$

where the function $\epsilon$ can be found[5] from

$$S(\epsilon, p_z) = \left|\frac{ehH}{c}\right| (n+\gamma), \quad \gamma < 1, \tag{3.5}$$

and where $n$ is integral. $S$ is the area of the section $\epsilon(p) = \epsilon$, $p_z = \text{const.}$

For electrons hitting the surface the degeneracy in $P_x$ is obviously removed, since the fraction of the orbit which is executed between collisions with the surface depends on the position of the orbit centre. It follows that in the evaluation of $\Delta j^q$, for electrons not hitting the surface the summation is taken only over $n$ and $p_z$, while for electrons which do hit the surface there is a further summation over $P_x$. The integration over $P_x$ which results in the

latter case gives rise to a factor $(\mu H/\epsilon_0)^{\frac{1}{2}} \ll 1$ in $\Delta j^q$.

The foregoing may be illustrated by the example of specular reflexion. In this case the energy spectrum of the electrons which collide with the surface is again determined[6] by (3.5), with $S(\epsilon, p_z, P_x)$ the area of the section

$$\epsilon(\boldsymbol{p}) = \epsilon;\ p_z = \text{const};\ P_x - \left|\frac{eH}{c}\right| \mathscr{D} \leqslant p_x \leqslant P_x, \tag{3.6}$$

so that

$$\epsilon = \epsilon(n, p_z, P_x). \tag{3.7}$$

Equations (2.7) and (2.8) now take on the form

$$i(\omega + l\Omega) f_l' + (\tilde{W} f')_l / t_0 = -\frac{f^0(\epsilon_{n p_z P_x} + l\hbar\Omega) - f^0(\epsilon_{n p_z P_x})}{l\hbar\Omega} (e\boldsymbol{v}\boldsymbol{E})_l; \tag{3.8}$$

$$\Omega = \frac{\partial\epsilon}{\partial n} = \frac{ehH}{c\partial S/\partial\epsilon} = \frac{2\pi}{T};\quad (e\boldsymbol{v}\boldsymbol{E})_l = \frac{1}{T}\int_0^T e^{-it\Omega l t} e\boldsymbol{v}(t)\boldsymbol{E}\left(\frac{P_x - p_x(t)}{|eH/c|}\right) dt;$$

$$\boldsymbol{j}(y) = \frac{2e}{h^2}\int_{-\infty}^{\infty} dP_x \sum_{n=0}^{\infty}\sum_{l=-\infty}^{\infty} f_l'\left[\boldsymbol{v}(t)\delta\left(y - \frac{P_x - p_x(t)}{|eH/c|}\right)\right]_{-l}. \tag{3.8a}$$

In (3.8a) the coefficient $2/h^2$ is found by reference to the correspondence principle.

To extract the oscillating part of $\Delta j^q$ from (3.8a) we make use of Poisson's formula

$$\Delta\boldsymbol{j}^q(y) = \frac{4e}{h^2}\sum_{s=1}^{\infty}\int_{-\infty}^{\infty} dP_x \int_0^{\infty} e^{2\pi i n s} \times$$

$$\times\, dn \sum_{l=-\infty}^{\infty} f_l'\left[\boldsymbol{v}\delta\left(y - \frac{P_x - p_x(t)}{|eH/c|}\right)\right]_{-l}. \tag{3.8b}$$

(see, for example, COURANT and HILBERT[7]). It may now be shown from (3.8), using a procedure similar to that of LIFSHITZ,[1] that only $f_0'$ makes a significant contribution, due to the appearance of $\partial f^0/\partial\epsilon_{n,p_z,P_x}$ on the right-hand side. Supposing for simplicity that the essential factor is the collision of electrons with impurities, one may write

$$f_0' = -\frac{\partial f^0}{\partial\epsilon_{n p_z P_x}} e\Psi_0, \tag{3.9}$$

where $\Psi$ satisfies the classical equation

$$v_y\frac{\partial\Psi}{\partial y} + \frac{\partial\Psi}{\partial t} + \frac{\Psi}{t_0^*} = vE;\quad \frac{1}{t_0^*} = \frac{1}{t_0} + i\omega. \tag{3.10}$$

(3.10) implies that the time $t_0(p)$ of free flight can always be introduced into a classical discussion of the anomalous skin-effect at any temperature. (On this point we see the work of AZBEL' and KANER.[4]) From (3.10),

$$\Psi = \int_{\alpha}^{\infty} \exp\left(-\frac{t-t'}{t_0^*}\right)\boldsymbol{v}(t')\boldsymbol{E}\left(y + \frac{\bar{p}_x(t) - \bar{\bar{p}}_x(t')}{|eH/c|}\right) dt'. \tag{3.11}$$

Here $\alpha(y, t)$ is the next root below $t$ of the equation

$$p_x(\alpha) = p_x(t) + \left|\frac{c}{eH}\right| y. \tag{3.12}$$

If there is no such root, corresponding to the fact that the electrons have

$$y \geqslant \frac{p_x^{\max} - p_x^{\min}}{|eH/c|}$$

and do not encounter the surface of the metal, one must put

$$\alpha = -\infty. \tag{3.13}$$

(3.11) gives the solution of (3.10) which is periodic in $t$ and goes to zero for the reflected electrons at $y = 0$. The latter condition is that for the diffuse reflexion of electrons from the surface in a classical discussion; the distribution function of the reflected electrons is that for the equilibrium state, $\Psi = 0$. From (3.8b), (3.9), (3.4) and (3.7),

VOL 7 195

$$\Delta j^q(y) = -\frac{4e^2}{h^2}\sum_{s=1}^{\infty}\int_0^{\infty} dn\cdot e^{2\pi i n s}\left\{\frac{\partial f^0}{\partial \epsilon_{np_z}}\int_{p_x^{\max}}^{\left|\frac{eH\mathscr{D}}{c}\right|+p_x^{\min}} \Psi_0\left[\nu\delta\left(y-\frac{P_x-p_x(t)}{|eH/c|}\right)\right]_0 dP_x + \right.$$

$$\left. + \int_{-\infty}^{p_x^{\max}} + \int_{\left|\frac{eH\mathscr{D}}{c}\right|+p_x^{\min}}^{\infty} \frac{\partial f^0}{\partial \epsilon_{np_xP_z}}\Psi_0\left[\nu\delta\left(y-\frac{P_x-p_x(t)}{|eH/c|}\right)\right] dP_x\right\}. \tag{3.14}$$

Carrying out the integrals by the methods of LIFSHITZ and KOSEVICH,[6] it may be shown that the second and third components of the right-hand side are—under the condition (3.3)—of substantially smaller magnitude than the first. Thus only those electrons which do not collide with the surface are important.

Turning attention to the first integral, we obtain

$$\Delta j_i^q(y) = \sum \frac{h^3}{2\pi} H^2 \chi_i \times$$

$$\times \left(\frac{d\ln S}{d\epsilon}\right)^2 \frac{\partial \Delta \mathscr{M}_z}{\partial H}\Bigg|_{\epsilon=\zeta_{\rm ch},\, p_z = p_z^{\rm ext}}. \tag{3.15}$$

$\Delta\mathscr{M}_z$ having been evaluated by LIFSHITZ and KOSEVICH.[5] The sum is taken over all extremal sections, and

$$\chi_i(y) = \frac{4\pi e^2}{h^3 \bar{t}_0^{*-1}} v_i(t) s\left(y-\frac{p_x^{\max}-p_x(t)}{|eH/c|}\right) s\left(\mathscr{D}-y-\frac{p_x(t)-p_x^{\min}}{|eH/c|}\right) \overline{v_j(t') E_j\left(y+\frac{p_x(t)-p_x(t')}{|eH/c|}\right)}. \tag{3.16}$$

$$s(w) = \begin{cases} 1 (w>0) \\ 0 (w<0). \end{cases}$$

In (3.16) the averaging is performed over $t$ and $t'$ for a period of revolution of the electron.

As the calculation has been carried through for variable $H$ and variable chemical potential $\zeta_{\rm ch}$, and as the total number of electrons is physically conserved rather than $\zeta_{\rm ch}$, it would follow that ideally the oscillations $\Delta\zeta_{\rm ch}{}^q$ of chemical potential should be allowed for. However, they may be ignored because[5,1] $\Delta\zeta_{\rm ch}{}^q \sim (\mu H/\epsilon_0)^{\frac{1}{2}}$, whereas $\Delta j_i{}^q \sim (\mu H/\epsilon_0)^{\frac{1}{2}}$. It will become evident below that this is also true in all the other cases to be considered (sections 4 and 5) since the amplitude of the oscillations $\Delta j_i{}^q$ always substantially exceeds the amplitudes $\Delta\zeta_{\rm ch}{}^q$.

## 4. QUANTUM-MECHANICAL INCREMENT TO THE CLASSICAL CURRENT DENSITY IN AN OBLIQUE MAGNETIC FIELD

For simplicity we shall deal only with the most straightforward case, which is at the same time the most interesting one; that of a strong magnetic field with

$$\Omega \gg \omega,\ 1/t_0;\ \frac{v}{\delta_{\rm eff}}\left(\frac{\mu H}{\epsilon_0}\right)^{\frac{1}{2}}. \tag{4.1}$$

$\delta_{\rm eff}$ being the effective depth of the skin layer. If we consider plane sections of the Fermi surface normal to the $z$-axis, the main contribution to $\Delta j^q$ will come only from electrons near the central section which do not collide with the surface. Indeed, it is not difficult to see that $\Delta j^q$ is then always determined by electrons which are near to those sections $\epsilon(p) = \epsilon_0$, $p_z = p_z^{\rm ext}$ of the Fermi surface whose area is an extremum. This is connected with the fact that events involving large values of $n \sim \sim \epsilon_0/\mu H \gg 1$ play a prominent part, and because where $n$ is close to the limiting value of $\epsilon$, $\partial n/\partial\epsilon \sim \sim \partial S/\partial\epsilon = 0$, so that $|p_z - p_z^{\rm ext}| \sim (2m^*\epsilon_0)^{\frac{1}{2}}(\mu H/\epsilon_0)^{\frac{1}{2}}$ is considerable (LIFSHITZ and KOSEVICH[1,5,6]).

Assuming that the angle $\Phi$ of inclination of the constant magnetic field to the surface is of order unity, then for all extremal sections of the Fermi surface except the central one the average velocity of an electron in the depths of the metal is $\bar{v}_\xi \sim \bar{v}_z \sim (\epsilon_0/m^*)^{\frac{1}{2}}$. Such electrons depart into the body of the specimen and do not return to the

skin layer. On the central section, in contrast, $\bar{v}_z = 0$; but electrons in the neighbourhood of such a section return repeatedly to the skin layer (according to (4.1), $\delta_{\text{eff}}/\bar{v}_z T \sim (\epsilon_0/\mu H)^{\frac{1}{3}}\delta_{\text{eff}}/r \gg 1$). Since $\Omega \gg \omega,\ 1/t_0$, they acquire a much larger directed velocity than electrons not lying near the central section. It follows that $\Delta j^q$ is essentially due to the electrons with $\bar{v}_z \doteqdot 0$. For the same reason the electrons which are scattered diffusely by the surface and consequently pass through the skin layer only once between collisions do not affect $\Delta j^q$. In the subsequent calculation, therefore, it will be sufficient to consider only electrons of a central section which do not encounter the surface and which, accordingly, have a spectrum given by (3.4).

With an inclined field $E$ depends on $\zeta$, i.e. on $y$ and $z$. $\hat{f}'$ is therefore non-diagonal in $p_z$ as well as in $n$. Since $\epsilon(n+l, p_z+p_z') - \epsilon(n, p_z) = l\hbar\Omega + \bar{v}_z p_z'$, equation (2.7) may be written for the "lower" electrons in the form

$$i\left(\omega + l\Omega + \frac{1}{\hbar}\bar{v}_z p_z'\right) f'_{lp_z'} + (\tilde{W}\hat{f}')_{lp_z'}/t_0 = -\frac{f^0(\epsilon_{np_z} + l\hbar\Omega + \bar{v}_z p_z') - f^0(\epsilon_{np_z})}{l\hbar\Omega + v_z p_z'}(e\boldsymbol{v}\boldsymbol{E})_{lp_z'}.$$

Just as when the field is parallel to the surface, under condition (4.1) only the case $l = 0$ is important on the central section. The right-hand side can therefore be written $\partial f^0/\partial\epsilon_{np_z}$. Supposing as in section 3 that

$$f'_{0p_z'} = -e\frac{\partial f^0}{\partial\epsilon_{np_z}}\Psi_{0p_z'}, \tag{4.2}$$

we arrive at a classical equation for $\Psi$:

$$v_\zeta\frac{\partial\Psi}{\partial\zeta} + \frac{\partial\Psi}{\partial t} + \frac{\Psi}{t_0^*} = vE. \tag{4.3}$$

It remains to isolate those electrons which do not strike the surface (remembering that the discussion concerns only electrons near a central section, for which $\bar{v}_\zeta = 0$). This is a simple matter if we recall that only the case $l = 0$ is significant in a classical situation satisfying (4.1). For $\Delta j^q$ is formally derived from the classical formula for current density merely by substituting $\partial f^0/\partial\epsilon$ for $\partial f^0/\partial\epsilon_{np_z}$ and replacing an integration over $\epsilon$ by the summation over $n$. It will be understood that the formula thus obtained gives $\Delta j^q$ and not the classical $j$, if only because the electrons having $\bar{v}_\zeta T \ll \delta_{\text{eff}}$ contribute no more than a trifling amount to the current density classically. Thus the electrons on a central section not hitting the surface can conveniently be separated out by this single device. (Even this device could be avoided, using equation (4.4), for those electrons hitting the surface after being allotted to a narrow region near the extremal section by the condition $\epsilon_0/\hbar\Omega \gg 1$, make no contribution for the purely classical reason given above).

Let us write the classical formula for the current density in the form

$$\boldsymbol{j} = -\frac{2|e|^3 H}{ch^3}\int\frac{\partial f^0}{\partial\epsilon}\boldsymbol{v}\Psi\, d\epsilon dp_z dt$$

$$= -\frac{2|e|^3 H}{ch^3}\int d\epsilon dp_z \cdot \frac{\partial f^0}{\partial\epsilon}\int_0^T dt\int_{-\infty}^{\infty} d\zeta_0 \times$$

$$\times\,\delta(\zeta - \zeta_0 - \zeta_1(t))\Psi(\zeta_0, \epsilon, p_z, t). \tag{4.4}$$

where $\Psi$ is a solution of

$$\frac{d\Psi}{dt} + \frac{\Psi}{t_0^*} = \boldsymbol{v}\boldsymbol{E}(\zeta_0 + \zeta_1(t)),$$

$$\zeta_1(t) = \int_{t_0'}^{t} v_\zeta\, dt_1. \tag{4.5}$$

If we now choose for $t_0'$ the point where $\zeta_1(t)$ has a minimum, so that

$$v_\zeta(t_0') = 0,\ v_\zeta'(t_0') > 0;\ t_0' = t_0'(\epsilon, p_z), \tag{4.6}$$

then given that $\bar{v}_\zeta = 0$, $\zeta_0$ will be the coordinate describing the top of the trajectory. Electrons not hitting the surface $\zeta = 0$ will then have $\zeta_0 > 0$. The diameter of an orbit corresponding to the central section in the direction $\zeta$ is obviously

$$\int_{t_0'}^{t_0''} v_\zeta\, dt_1,$$

in which $t_0''$ is the point of maximum $\zeta(t)$ and

$$v(t_0'') = 0;\ v_\zeta'(t_0'') < 0;\ t_0'' = t_0''(\epsilon, p_z);\ (4.6)_\zeta$$

VOL 7 195

thus electrons not encountering the surface $\zeta = \mathscr{D}$ will have

$$\zeta_0 + \int_{t_0'}^{t_0''} v_\zeta\, dt_1 \leqslant \mathscr{D};\quad \zeta_0 \leqslant \mathscr{D} - \int_{t_0'}^{t_0''} v_\zeta\, dt_1. \tag{4.7}$$

(It is assumed that

$$\mathscr{D} \geqslant \int_{t_0'}^{t_0''} v_\zeta\, dt_1).$$

Using $\partial(\epsilon, p_z)/\partial(n, p_z) = \hbar\Omega$, it follows that the correct value for $\Delta j^q$ is to be taken from the formula

$$\boldsymbol{j} = -\frac{2|e|^3 H}{ch^3}\int dp_z \sum_{n=0}^{\infty} \frac{\partial f^0}{\partial \epsilon_{np_z}} \hbar\Omega \int_0^T dt \int_0^{\mathscr{D} - \int_{t_0'}^{t_0''} v_\zeta\, dt_1} \times d\zeta_0 \delta(\zeta - \zeta_0 - \zeta_1(t)) \Psi(\zeta_0, t, \epsilon_{np_z}, p_z);$$

$$t_0' = t_0'(\epsilon_{np_z}, p_z);\quad t_0'' = t_0''(\epsilon_{np_z}, p_z); \tag{4.8}$$

$$\Psi(\zeta_0, \epsilon, p_z, t) = \int_{-\infty}^{t} \exp\left(-\frac{t-t'}{t_0^*}\right) \boldsymbol{v}(t') E(\zeta_0 + \zeta_1(t'))\, dt'.$$

(Naturally a finite solution of (4.5) must be taken that is periodic in $t$). $\Delta j^q$ can now be obtained by use of Poisson's formula, with the result:

$$\Delta j_i^q = -\frac{4|e|^3 H}{ch^2} \sum_{s=1}^{\infty} \int_0^{\infty} e^{2\pi i s n}\, dn \cdot \int_{-\infty}^{\infty} dp_z \cdot \frac{\partial f^0}{\partial \epsilon_{np_z}} \times \tag{4.9}$$

$$\times v_i(t) s\left(\zeta - \int_{t_0'}^{t} v_\zeta\, dt_1\right) s\left(\mathscr{D} - \zeta - \int_{t}^{t_0''} v_\zeta\, dt_1\right) \int_{-\infty}^{t} \exp\left(-\frac{t-t'}{t_0^*}\right) v_j(t') E_j\left(\zeta - \int_{t_0'}^{t} v_\zeta\, dt_1\right) dt' = -\frac{4|e|^3 H}{ch^2}$$

$$\sum_{s=1}^{\infty} \int_0^{\infty} e^{2\pi i s n}\, dn \int_{-\infty}^{\infty} dp_z \frac{\partial f^0}{\partial \epsilon_{np_z}} \left(\frac{\bar{1}}{t_0^*}\right)^{-1} v_i(t) s\left(\zeta - \int_{t'}^{t} v_\zeta\, dt_1\right) s\left(\mathscr{D} - \zeta - \int_{t}^{t_0''} v_\zeta\, dt_1\right) v_j(t') E_j\left(\zeta - \int_{t'}^{t} v_\zeta\, dt_1\right)$$

Hence

$$\Delta j_i^q = \sum \frac{h^3}{2\pi} H^2 \chi_i \left(\frac{d \ln S}{d\epsilon}\right)^2 \frac{\partial \Delta \mathscr{M}_z}{\partial H}\Bigg|_{\epsilon = \epsilon_0,\, p_z = 0}, \tag{4.10}$$

where the summation is to be taken *only over the central sections*, and

$$\chi_i = \frac{4\pi e^2}{h^3 t_0^{*-1}} v_i(t) s\left(\zeta - \int_{t_0'}^{t} v_\zeta\, dt_1\right) s\left(\mathscr{D} - \zeta - \int_{t}^{t_0''} v_\zeta\, dt_1\right) v_j(t') E_j\left(\zeta - \int_{t'}^{t} v_\zeta\, dt_1\right). \tag{4.11}$$

These formulae have the same form as (3.15) and (3.16), but are of considerably more restricted application due to the condition (4.1).

(4.10) and (4.11) can be said to give $\Delta j^q$ correctly in a magnetic field of any inclination, subject to the following rule: if the magnetic field is parallel to the surface of the metal ($\pi/2 - \phi \ll \delta_{\text{eff}}/l$) the sum in (4.10) is to be taken over *all* extremal sections $p_z = p_z^{\text{ext}}$; in an oblique field ($\pi/2 - \phi \gg \delta_{\text{eff}}/r$) it runs over *only the central sections*.

## 5. THE TOTAL SURFACE IMPEDANCE

A calculation of the total surface impedance requires the solution of Maxwell's equations, which in the present instance reduce to

$$E_\alpha''(\zeta) = \frac{4\pi i\omega}{c^2} j_x(\zeta);\quad (\alpha = x, \xi) \tag{5.1}$$

$$j_\xi(\zeta) = 0 \tag{5.2}$$

together with the relation which has been established between the current density and the electric

field intensity:

$$j_i(\zeta) = j_i^{cl}(\zeta) + \Delta j_i^{q}(\zeta). \tag{5.3}$$

In (5.1), $\xi$ refers to a direction in the plane in the metal surface perpendicular to $x$.

Consider first a half-space. Following the procedure of AZBEL', KAGANOV and KANER,[3,4] we write $j_i(\zeta)$ in the form $j_i(|\zeta|)$ and continue $Ej(\zeta)$ into the region $\zeta < 0$ in an even fashion. We now take the Fourier transform of both sides of (5.1) and (5.2), getting

$$-k^2\epsilon_\alpha(k) - 2E_\alpha'(0) = \frac{4\pi i\omega}{c^2}\{j_\alpha^{cl}(k) + \Delta j_z^{q}(k)\}; \tag{5.4}$$

$$j_\zeta^{cl}(k) + \Delta j_\zeta^{q}(k) = 0. \tag{5.5}$$

$j_i^{cl}(k)$ was determined explicitly in an earlier paper[4] which contains a number of conclusions we shall call upon below. For a half-space, $\Delta j_i^{q}(k)$ has the form

Only[4] large values of $k$ and $k'$ contribute significantly to the anomalous skin-effect; by the method of steepest descents,

$$\chi_i \approx \frac{8\pi^2 e^2}{h^3 t_0^{*-1}} \frac{v_i v_j}{|v_\zeta'(t)|\, T^2} \frac{1}{k}\left\{\epsilon_j(k) - \frac{1}{\pi}\int_0^\infty \frac{\sqrt{k}\,\epsilon_j(k')\,dk'}{\sqrt{k'}(k+k')}\right\}\Bigg|_{\substack{\epsilon=\epsilon_0 \\ p_z = p_z^{\mathrm{ext}},\,0 \\ v_\zeta = 0}} \tag{5.8}$$

Evidently in this approximation $\chi_\zeta(\zeta)$ goes to zero with $k$, because $v_\zeta = 0$. The same is true of $j_\zeta^{cl}(k) \sim v_\zeta$; the explanation lies in the fact that only electrons that are travelling almost parallel to the metal surface are important in the anomalous skin effect. For this reason the term in $\epsilon_\zeta(k)$ drops out of the formulae for $j_\alpha(k)$, and it is sufficient to take the summation only over two indices, $x$ and $\xi$, of $j$.

This being the case, (5.5) is satisfied automatically, and it remains only to solve (5.4). When the magnetic field is parallel to the metal surface, the asymptotic dependence of $j_\alpha^{cl}(k)$ on $k$ has the form[4]

$$\Delta j_i^{q}(k) = \sum \frac{h^3}{2\pi} H^2 \chi_i(k)\left(\frac{d\ln S}{d\epsilon}\right)^2 \frac{\partial \Delta \mathcal{M}_z}{\partial H}\Bigg|_{\epsilon=\epsilon_0,\, p_z = p_z^{\mathrm{ext}},\, 0}; \tag{5.6}$$

$$\chi_i(k) = \frac{4\pi e^2}{h^3 t_0^{*-1}}\left\{v_i(t)v_j(t')\cos\left(\frac{kc}{eH}\int_t^{t'} v_\zeta\,dt_1\right)\epsilon_j(k) - \right. \tag{5.7}$$

$$\left. -\frac{1}{\pi}v_i(t)v_j(t')\int_{-\infty}^{\infty}\frac{\sin\left|\frac{c}{eH}\right|\left(k\int_{t_0'}^{t} v_\zeta\,dt_1 + k'\int_{t_0'}^{t'} v_\zeta\,dt_1\right)}{k+k'}\epsilon_j(k')\,dk'\right\};$$

$$\epsilon_j(-k) = \epsilon_j(k) = 2\int_0^\infty E_j(\zeta)\cos k\zeta\,d\zeta;\quad j_i(k) = 2\int_0^\infty j_i(\zeta)\cos k\zeta\,d\zeta.$$

$$j_\alpha^{cl}(k)=\frac{3\pi}{4}\frac{1}{k}\left\{\mathscr{A}_{\alpha\beta}^{cl}\epsilon_\beta(k)-\frac{2}{\pi^2}C_{\alpha\beta}^{cl}\int_0^\infty\frac{k\ln k/k'\epsilon_\beta(k')\,dk'}{k^2-k'^2}-\right.$$

$$\left.-\frac{1}{\pi}(\mathscr{A}_{\alpha\beta}^{cl}-C_{\alpha\beta}^{cl})\int_0^\infty\frac{\sqrt{k}\epsilon_\beta(k')\,dk'}{\sqrt{k'}(k+k')}\right\}; \tag{5.9}$$

$$\mathscr{A}_{\alpha\beta}^{cl}=\frac{8e^2}{3h^3}\int_0^{2\pi}\frac{n_\alpha n_\beta}{k}\frac{d\phi}{1-\exp\left(-2\pi i\frac{\omega}{\Omega}-\frac{\overline{2\pi}}{\Omega t_0}\right)};\quad C_{\alpha\beta}^{cl}=B_{\alpha\beta}^{cl}-\frac{2e^2}{3h^3}\int_0^{2\pi}\frac{n_\alpha n_\beta}{K}\left[1-\exp\left(-2\pi i\frac{\omega}{\Omega}-\frac{\overline{2\pi}}{\Omega t_0}\right)\right]d\phi; \tag{5.10}$$

$$B_{\alpha\beta}^{cl}=\frac{8e^2}{3h^3}\int_0^{2\pi}\frac{n_\alpha n_\beta}{K}\,d\phi;$$

$$\mathbf{n}=\boldsymbol{v}/v=(n_x,n_\zeta,n_\xi)=(\sin\theta\cdot\sin\phi,\ \cos\theta,\ \sin\theta\cos\phi);$$

All quantities are to be taken at $\epsilon=\epsilon_0$, $\theta=(\pi/2)$, $(v_y=0)$. $K$ is the gaussian curvature at the appropriate point, and $1/t_0$ is averaged over the time of revolution of an electron in its orbit.

The situations of greatest importance are those of a strong magnetic field ($\Omega\gg\omega$, $\overline{1/t_0}$) and of resonance ($\omega\doteq\pm\Omega,\pm2\Omega,\ldots$). To discuss these it will be sufficient to leave only the terms in $A_{\alpha\beta}$. It will be apparent from equations (5, 6), (5.8) and (5.9) that the quantum increment affects only $A_{\alpha\beta}$:

$$j_\alpha(k)=\frac{3\pi}{4}\mathscr{A}_{\alpha\beta}\frac{1}{k}\left\{\epsilon_\beta(k)-\frac{1}{\pi}\int_0^\infty\frac{\sqrt{k'}\epsilon_\beta(k')\,dk'}{\sqrt{k'}(k+k')}\right\}; \tag{5.11}$$

$$\mathscr{A}_{\alpha\beta}=\mathscr{A}_{\alpha\beta}^{cl}+\Delta\mathscr{A}_{\alpha\beta}{}^q;\ \Delta\mathscr{A}_{\alpha\beta}{}^q=\sum\frac{16}{3}\frac{e^2}{t_0{}^{*-1}}H^2\frac{v_\alpha v_\beta}{|v_y'(t)|\,T^2}\left(\frac{d\ln S}{d\epsilon}\right)^2\frac{\partial\Delta\mathscr{M}_z}{\partial H}\Big|_{\epsilon=\epsilon_0,p_z=p_z{}^{\text{ext}},v_y=0} \tag{5.12}$$

In the previous paper[4] referred to above, it was shown how to derive the total surface impedance $Z_{\alpha\beta}$ from $A_{\alpha\beta}$. $Z_{\alpha\beta}$ is determined by

$$E_\alpha(0)=Z_{\alpha\beta}\mathscr{J}_\beta, \tag{5.13}$$

$\mathscr{J}_\beta=(c^2/4\pi i\omega)E_\beta'(0)$ being the total current flowing in the direction $\beta$. In the particular case when the complex tensor $A_{\alpha\beta}$ is reduced to its principal axes, the principal values of $Z_\alpha$ may be expressed in terms of the principal values of $A_\alpha$:

$$Z_\alpha\doteq\frac{16}{9}\left(\frac{\sqrt{3}\pi\omega^2}{c^4}\right)^{\frac{1}{3}}e^{i(\pi/3)}\mathscr{A}_\alpha{}^{-\frac{1}{3}}. \tag{5.14}$$

In general, for a constant magnetic field of arbitrary magnitude and direction, the accurate formula for $j_\alpha(k)$ is extremely unwieldy. Nevertheless, $j_\alpha(k)$ can be written in the following form with an error of only a few per cent in the numerical factor for the impedance:

$$j_\alpha(k)=\frac{3}{4}\pi a_{\alpha\beta}\frac{1}{k};\quad a_{\alpha\beta}=a_{\alpha\beta}^{cl}+\Delta a_{\alpha\beta}{}^q, \tag{5.15}$$

where $\Delta a_{\alpha\beta}{}^q$ is given by (5.12) with $v_\zeta$ in place of

$v_y$; and where $a^{l}_{\alpha\beta}$, $p_z{}^{\text{ext}}$ coincides with $A^{q}_{\alpha\beta}$ $p_z{}^{\text{ext}}$ (see equation 5.10) if $(\pi/2)-\phi \ll \delta_{\text{eff}}/l$, but with $B^{q}_{\alpha\beta}$, 0 if $(\pi/2)-\phi \gg \delta_{\text{eff}}/r$. The impedance, is now easily expressed in terms of $a_{\alpha\beta}$:

$$Z_{xx,\xi\xi} \approx \frac{16}{9}\left(\frac{\sqrt{3}\pi\omega^2}{c^4}\right)^{\frac{1}{3}} e^{i(\pi/3)}\frac{(x_1+x_2)x_1x_2+a_{\xi\xi,xx}}{x_1x_2(x_1{}^2+x_1x_2+x_2{}^2)};$$

$$Z_{x\xi} = Z_{\xi x} \approx -\frac{16}{9}\left(\frac{\sqrt{3}\pi\omega^2}{c^4}\right)^{\frac{1}{3}} e^{i(\pi/3)}\frac{a_{x\xi}}{x_1x_2(x_1{}^2+x_1x_2+x_2{}^2)}; \tag{5.16}$$

$$x_{1,2} = \{\tfrac{1}{2}(a_{xx}+a_{\xi\xi}) \pm \sqrt{\tfrac{1}{4}(a_{xx}-a_{\xi\xi})^2+a_{x\xi}{}^2}\}^{\frac{1}{3}}.$$

The cube root to be taken is the one whose argument lies in the interval $[-(\pi/6), (\pi/6)]$.

According to these formulae, the situation where the numbers of electrons and holes are the same ($N_1 = N_2$) is not a special one, as with the classical part of the high-frequency $Z_{\alpha\beta}$ but in contrast to the static case. The formulae give the impedance in the zeroth and first approximation in $(\mu H/\epsilon_0)^{\frac{1}{3}}$, and the zero order approximation in $\delta_{\text{eff}}/r$. It is an approximation which reduces to zero only in exceptional cases for which $v_x$ or $v_\xi$ are zero at the point $\epsilon = \epsilon_0$, $p_z = p_z{}^{\text{ext}}$, $v_\zeta = 0$; an example is the case of an isotropic quadratic dispersion law when the constant magnetic field is parallel to the surface and coincides in direction with the electric field. Equation (5.15) is, moreover, inapplicable if the equations $p_z = p_z{}^{\text{ext}}$ and $v_\zeta = 0$ reduce to the same, so that $\epsilon = \epsilon_0$, $p_z = p_z{}^{\text{ext}}$, $v_\zeta = 0$ together determine a line rather than a single point. This occurs, for instance, when the magnetic field is perpendicular to the surface and the dispersion law is isotropic. Since electrons with $p_z = 0$ remain in the skin-layer throughout, the skin effect for them is normal, and $\bar{v}_x = 0$, $\bar{v}_y = 0$. The impedance, as given by the zero order approximation in $(\mu H/\epsilon_0)^{\frac{1}{3}}$, becomes zero; to have obtained a finite result, terms with $l \neq 0$ would have had to be included in the sums.

Electrons with (conserved) $v_z = 0$ do not in general arrive at the surface of the metal and therefore in this particular exceptional case the calculation can be carried through. The skin effect is "normal" for the electrons responsible for the quantum oscillations and "anomalous" for the remainder, and so the magnitude of the quantum oscillations is relatively greater than in the static case.

For a quadratic dispersion law a calculation shows

$$\Delta j_\pm{}^q = -\frac{2H}{\epsilon_0 N}\sigma_\pm \Delta\mathscr{M}_z E_\pm(z);$$

$$E_\pm = E_x \pm iE_y, j_\pm = j_x \pm ij_y;$$

$$\sigma_\pm = \frac{Ne^2t_\pm}{m};\ \frac{1}{t_\pm} = \frac{1}{t_0} + i(\omega \mp \Omega).$$

Here $N$ stands for the electron density. The surface impedance comes to

$$Z_\pm = -\frac{4\pi i\omega}{c^2}\frac{E_\pm(0)}{E_\pm{}'(0)} \approx Z(0)\times$$

$$\times\left\{1-e^{-i(\pi/3)}\frac{28\sqrt{3}\sigma_\pm}{c^2\epsilon_0 N}\omega H(2\delta^2 l/3\pi)^{2/3}\Delta\mathscr{M}_z\right\};$$

$$Z(0) = (\sqrt{3}\pi\omega^2 l/c^4\sigma)^{\frac{1}{3}}e^{i(\pi/3)}.$$

Thus in a zero order approximation in $l/\delta$ the quantum-mechanical increment to the surface impedance is purely real, and with $kT < \hbar\Omega$ its relative amplitude is of the order $(\hbar\Omega/\epsilon_0)^{\frac{1}{3}}(l/\delta)^{\frac{1}{3}}$.

Finally it may be added that all the above formulae apply to the situation where electromagnetic radiation is incident on one side of a thin metallic foil, so long as $\mathscr{D} > d$. Since the skin-effect is anomalous, only electrons with $\bar{v}_\zeta = 0$ are of importance for $\Delta j_t{}^q$; however, those whose paths do not lie in the skin layer make no contribution to $\Delta j_t{}^q$ and consequently the rear surface of the foil has no influence on $\Delta j_t{}^q$. If, on the other hand, the foil thickness $\mathscr{D} < d$, then in our approximation the amplitude of the quantum oscillations of appropriate period will be zero because $\chi_t = 0$. (See

equation 4.11.) It is therefore possible to determine the $d$ and the $S_{ext}$ corresponding to a given oscillation period by studying $Z_{\alpha\beta}(H)$ in a foil of thickness $\mathscr{D} < l$ and observing the magnetic field strength at which the amplitude of the quantum oscillations having that period suffers a sharp increase.

### 6. PRINCIPLES OF AN EXPERIMENTAL MEASUREMENT OF THE FERMI SURFACE

LIFSHITZ and POGORELOV have shown[2] that a study of the quantum-mechanical oscillations provides a convenient method of determining the shape of the Fermi surface experimentally. The period $\Delta(1/H) = eh/cS_{ext}(\epsilon_0)$ gives directly the extremal areas $S_{ext}$ of sections of that surface, and if $S_{ext}$ is known for various different directions, $\epsilon(p) = \epsilon_0$ can be deduced. For this purpose the study of quantum oscillations in the high-frequency conductivity is particularly suitable for two reasons.

Firstly, the conductivity oscillations are in general $\epsilon_0/\mu H \gg 1$ times greater than in the static case. In particular it may easily be shown from (5.15) that if $Z = R+iX$, the directly measured oscillation amplitudes $dR/dH$, $dX/dH$ are $(\epsilon_0/\mu H)^{\frac{1}{2}} \gg 1$ times greater than their classical counterparts. Secondly, use can be made of the fact that in an oblique magnetic field the oscillations do not give all extremal sections, as in the static case or with a parallel magnetic field, but depend only on the central section. Thus if measurements are taken at various angles of inclination of the magnetic field the analysis of the data will be materially simpler than in the static case, where a large number of harmonics with different periodicities are observed in superposition.

Measurements on foils of thickness $\mathscr{D} < l$ will be particularly valuable, for (as further discussed in other papers[8]) a determination of $Z_{\alpha\beta}(H)$ in this case permits all the extremal areas to be derived *without harmonic analysis*. To achieve this one would perform the experiments with an increasing magnetic field. The different oscillation periods would come into prominence successively, and one would note the field strengths at which the amplitude of an oscillation of some definite period became abruptly enlarged. At the same time, $d$ is determined directly; and a knowledge of $d$ for all directions by itself gives the shape of the Fermi surface, at least if it is non-reentrant. In particular, on the central section in a parallel field (the special features of which are easily isolated by the additional use of an inclined field) $d = |(2c/eH)\, p_x^{\max}|$ the maximum being taken in relation to $t$; and so by rotating $H$ in the plane of the surface, the shape of the section $\epsilon(p) = \epsilon_0$, $v_y = 0$ can be established. If foils could be used whose surfaces had a variety of different, but definite orientations with respect to the crystal axes, $\epsilon(p) = \epsilon_0$ could be constructed directly.

To determine the electron velocities at the Fermi surface, a knowledge of the extremal effective mass $(1/2\pi)(\partial S/\partial\epsilon)_{ext}$ is required.[2] This may in principle be determined from the amplitude of the quantum oscillations of magnetic susceptibility.[2] However, in practice this amplitude is excessively sensitive to the influence of a number of incidental factors such as the mosaic structure of the crystals, and in consequence the method of quantum oscillations is unsatisfactory. $(\partial S/\partial\epsilon)_{ext}$ may be determined far more accurately from the classical variation in the impedance in a magnetic field strictly parallel to the metal surface. The extremal masses are given directly[4] by the resonant frequencies of the cyclotron resonance phenomenon:

$$\left(\frac{\partial S}{\partial \epsilon}\right)_{ext} = \frac{2\pi e H_{res}}{\omega c}.$$

It is unquestionably much easier to interpret a curve of superposed resonances than to decipher a superposition of quantum-mechanical harmonics.

Separation of the classical from the quantum-mechanical variation in $Z_{\alpha\beta}$ presents no special problem. Both amplitude and period differ;

$$|\Delta Z^q| \ll |\Delta Z^c \quad \left|\frac{d\Delta Z^q}{dH}\right| \gg \left|\frac{dZ^c}{dH}\right|,$$

while as a rule the quantum period is much less than the classical one. In an intense magnetic field ($\Omega \gg \omega$) the classical oscillations (cyclotron resonance) generally vanish, while the quantum ones of course remain. Again, in an oblique magnetic field *only* those quantum oscillations are preserved which correspond to the *central sections*. The appropriate quantity to measure is $dZ/dH$, because in the next higher approximation (i.e. taking account of the departure from the most extreme form

of the anomalous conditions), cyclotron resonance does in fact occur even in an inclined field.[4] Finally, measurements with a varying frequency of the h.f. field will also allow the desired separation. The period of the quantum oscillations will be practically unaltered, while the periods of cyclotron resonance vary in proportion to $\omega$.

Speaking generally, the most valuable procedure is to measure $dZ/dH$ in strong magnetic fields with $\Omega \gg \omega$.

by the properties of all the extremal sections $p_z = p_z^{\text{ext}}$ of the Fermi surface $\epsilon(p) = \epsilon_0$, thus:

$$\Delta\left(\frac{1}{H}\right) = \frac{eh}{cS(\epsilon_0, p_z^{\text{ext}})}.$$

On the other hand in an oblique magnetic field ($\pi/2-\phi \gg \delta_{\text{eff}}/r$) only the central sections $p_z = 0$, $\epsilon(p) = \epsilon_0$ exert an effect.

(4) According to equation (5.16) the tensor impedance of the surface may be expressed in terms of the tensor $a_{\alpha\beta} = a^{cl}_{\alpha\beta} + \Delta a^{q}_{\alpha\beta}$, where

$$a^{cl}_{\alpha\beta} = \begin{cases} \dfrac{8e^2}{3h^3}\displaystyle\int_0^{2\pi} \frac{n_\alpha n_\beta}{K} \frac{d\phi}{1-\exp\left(-2\pi i\dfrac{\omega}{\Omega} - \dfrac{2\pi}{\Omega t_0}\right)}; & \left(\dfrac{\pi}{2}-\phi \ll \dfrac{\delta_{\text{eff}}}{l}\right) \\ \dfrac{8e^2}{3h^3}\displaystyle\int_0^{2\pi} \frac{n_\alpha n_\beta}{K} d\phi; & \left(\dfrac{\pi}{2}-\phi \gg \dfrac{\delta_{\text{eff}}}{r}\right) \end{cases}$$

$$\Omega = \frac{2\pi}{T} = \frac{2\pi eH}{c\partial S/\partial\epsilon}.$$

## 7. CONCLUSIONS

(1) Quantum-mechanical oscillations of the high-frequency conductivity are predicted whose amplitude relative to the corresponding classical quantity is in general $\epsilon_0/\mu H \gg 1$ times greater than the same relative amplitude of quantum-mechanical oscillations of the static conductivity.

(2) The amplitude of the quantum oscillations in $dR/dH$ and $dX/dH$ is $(\epsilon_0/\mu H)^{\frac{1}{2}}$ times greater than the classical values of $dR/dH$, $dX/dH$.

(3) In an applied magnetic field strictly parallel to the surface of the metal ($\pi/2-\phi \ll \delta_{\text{eff}}/l$), the period of the quantum oscillations is determined

All magnitudes here are taken at $v_\zeta = 0$. $n = v/v$; $\phi$ is reckoned along the curve $\epsilon(p) = \epsilon_0$, $v_\zeta = 0$, $K$ is the gaussian curvature of the Fermi surface; $S$ is the area of the section $\epsilon(p) = \epsilon_0$, $p_z = \text{const}$; $t_0(p)$ is the mean free flight time that may always be introduced in a discussion of the anomalous skin-effect, and

$$\Delta a^{q}_{\alpha\beta} = \sum \frac{16}{3} \frac{e^2}{t_0^{*-1}} H^2 \frac{v_\alpha v_\beta}{|v_\zeta'| T^2} \left(\frac{d\ln S}{d\epsilon}\right)^2 \frac{\partial \Delta \mathcal{M}_z}{\partial H}\bigg|_{\epsilon=\epsilon_0, p_z=p_z^s, v_\zeta=0}$$

$$p_z^s = \begin{cases} p_z^{\text{ext}} & \left(\dfrac{\pi}{2}-\phi \ll \delta_{\text{eff}}/l\right) \\ 0 & \left(\dfrac{\pi}{2}-\phi \gg \delta_{\text{eff}}/r\right). \end{cases}$$

(5) By determining the periods (in applied magnetic field) of both the classical and quantum-mechanical oscillations of surface impedance, both $S_{\text{ext}}$ and $(\partial S/\partial\epsilon)_{\text{ext}}$ may be found. The former is derived from the quantum period and the latter from the resonant frequencies for cyclotron resonances. In principle a knowledge of these two

magnitudes for a number of different directions of the magnetic field would lead to a complete derivation of the shape of the Fermi surface and of the electron velocities on it. A series of measurements of $Z_{\alpha\beta}(H)$ with monocrystalline foils will give, firstly, $S_{\text{ext}}$ without the necessity for a complicated harmonic analysis; and secondly, will allow the Fermi surface to be plotted directly.

A further communication[8] is published separately, containing rigorous proofs of some of the propositions put forward in this paper, together with a more detailed derivation of the equations and a discussion of certain additional topics. I am greatly indebted to Profs. I. M. LIFSHITZ and L. D. LANDAU for valuable discussions.

*Note added in proof* (April 16, 1958), "We shall make two more remarks.

1. The essential increase in the quantum oscillations takes place at the very low frequencies corresponding to the normal skin effect ($\delta \gg r, l$; $\omega\tau_0 \ll 1$)

$$\Delta j_i^{q}(t) = \Delta\sigma_{ik}\, E_k(t) - a_{ik}\frac{\partial E_k}{\partial t};$$

$$a_{ik} = -\sum_s \frac{8\pi e^2 a}{c^2 t_0^{-1}} H^2 \left(\frac{d\ln S}{d\epsilon}\right)^2 \frac{\partial \Delta M^z}{\partial H} v_i(t_1) \int_0^{t_1} v_\zeta\, dt_2 \cdot v_k(t_1') \int_0^{t_1'} v_\zeta\, dt_2 \Bigg|_{\substack{\epsilon=\epsilon_0 \\ p_z = p_z^s}}$$

where $\Delta\sigma_{ik}(H)$ = the quantum oscillating part of the static conductivity (see LIFSHITZ I. M. and LIFSHITZ I. M. and KOSEVICH A. M.[1]) and $a$ is the positive root of the determinant $\mathrm{Det}|\sigma_{ik}(H) - a\delta_{ik}| = 0$ ($\sigma_{ik}$ is obtained in reference 9).

If $r \gg \delta$, the ratio of the second term to the first is of order $(\epsilon_0/\mu H)(\delta^2/r^2)$.

2. One can see that in the oblique magnetic field there occurs the cyclotron resonance (see reference 4) on the quantum oscillation amplitude. The resonant part of the amplitude predominates if

$$\left(\frac{r}{\delta}\right)\left(\frac{\mu H}{\epsilon_0}\right)^{\frac{1}{3}} \cos\Phi < 1 < \left(\frac{l}{\delta}\right)\left(\frac{\mu H}{\epsilon_0}\right)^{\frac{1}{2}} \cos\Phi.$$

Thanks to this, the cyclotron resonance frequencies (and therefore $(\partial S/\partial\epsilon)_{\text{ext}}$) can be measured on one sample at all the orientations of $H$. The investigation of one single crystal film ($d \simeq 10^{-3}$ to $10^{-4}$ cm) allows one to obtain one by one all the $(\partial S/\partial\epsilon)_{\text{ext}}$ and $S_{\text{ext}}$ without additional harmonic analysis.

Thus the experimental measurements of $Z(H)$ on one single crystal film sample gives the principal possibility of establishing the shape of the Fermi surface (knowing the periods of the quantum oscillations) and the velocities of the electrons thereon (knowing the cyclotron resonance frequencies)."

## REFERENCES


1. LIFSHITZ I. M. *Zh. eksp. teor. fiz.* **30,** 814, 1956; **32,** 1509 (1957).
   LIFSHITZ I. M. and KOSEVICH A. M. *Zh. eksp. teor. fiz.* **33,** 88 (1957).
2. LIFSHITZ I. M. and POGORELOV A. V. *Dokl. Akad. Nauk. SSSR* **96,** 1143 (1954).
3. AZBEL' M. YA and KAGANOV M. I. *Dokl. Akad. Nauk.* **94,** 41 (1954).
   AZBEL' M. YA. *Dokl. Akad. Nauk.* **100,** 437 (1955).
4. AZBEL' M. YA. and KANER E. A. *Zh. eksp. teor. fiz.* **30,** 811, 1956; *ibid.* **32,** 896 (1957); *J. Phys. Chem. Solids,* **6,** 2/3 (1958).
5. LIFSHITZ I. M. and KOSEVICH A. M. *Dokl. Akad. Nauk.* **96,** 963 (1954).
6. LIFSHITZ I. M. and KOSEVICH A. M. *Zh. eksp. teor. fiz.* **29,** 743 (1955).
7. COURANT R. and HILBERT D. *Methods of Mathematical Physics* Vol. 1. Interscience, New York (1955).
8. AZBEL' M. YA. *Zh. eksp. teor. fiz.* **34,** No. 3, 4, 5 (1958).
9. LIFSHITZ I. M., AZBEL' M. YA. and KAGANOV M. T. *Zh. eksp. teor. fiz.* **30,** 220 (1956).

*J. Phys. Chem. Solids* Pergamon Press 1958. Vol. 7. pp. 118–126.

# THEORETICAL CALCULATION OF DISTRIBUTION COEFFICIENTS OF IMPURITIES IN GERMANIUM AND SILICON, HEATS OF SOLID SOLUTION

KURT WEISER

RCA Laboratories Princeton, N.J.*

(*Received* 25 *March* 1958; *revised* 17 *April* 1958)

**Abstract**—The distribution coefficients of Groups III, IV and V impurities in germanium and silicon were calculated, and very satisfactory agreement with experimental values was obtained. The method of calculation consisted in estimating the change in energy involved in transferring the impurity atoms from a crystalline reservoir to the solid and molten host material respectively. The binding energy of an impurity in the host lattice and the strain energy which it introduces were estimated. The change in vibrational entropy is believed to be negligible.

VOL
7
195

## 1. INTRODUCTION

THE distribution coefficient, or segregation constant, of an impurity is defined as the ratio of the concentration of the impurity in the solid to that in the molten host substance at equilibrium. Since a knowledge of segregation constants is of great importance for purification and doping of semiconductors, considerable research has been devoted to the task of determining their values for many impurities in germanium and silicon.[1–6] No attempts have been made, however, to calculate segregation constants theoretically.

A few years ago THURMOND and STRUTHERS[1] derived a general equation for the segregation constant of an impurity from thermodynamical considerations. It follows from the equation that the segregation constant can be calculated from a knowledge of the differences in enthalpy and entropy between the impurity in the solid and in the molten host substance. In this paper these differences will be estimated by means of a simple physical model for most Group III, IV and V impurities in germanium and silicon. The segregation constants will then be calculated and compared to experimental values.

* (Now at I.B.M. Research Center, Poughkeepsie, N.Y.).

## 2. DILUTE SOLUTION MODEL

The equation derived by THURMOND and STRUTHERS was obtained in the following manner: The reference state of the impurity was taken as the solid impurity at its melting point. The change in chemical potential in terms of enthalpy and entropy differences was then expressed for the transfer of impurity atoms to the host crystal to a concentration $c^s$ on the one hand, and into the molten host material to a concentration $c^l$ on the other hand. By setting the chemical potentials of the impurity in the host crystal and in the melt equal to each other it was possible to solve the equation for the ratio $c^s/c^l$, which, by definition, is equal to the distribution coefficient $k$. In this manner the authors arrived at the following expression:

$$\ln k = \frac{\Delta H^f - \Delta H^s}{RT} + \frac{\sigma - \Delta S^f}{R} + \ln \gamma. \qquad (1)$$

In this equation, $k$ stands for the distribution coefficient, $\Delta H^f$ is the heat of fusion, taken as independent of temperature between the melting point of the impurity and that of the host crystal, and $\Delta S^f$ the entropy of fusion of the impurity at its melting point. $\Delta H^s$ is the differential heat of solution of the impurity in the solid host crystal, or

the energy necessary to transfer the impurity from its own lattice to that of the host crystal. $\sigma$ is the change in vibrational entropy as a result of this transfer, and $\gamma$ is an "activity coefficient" which expresses the departure of the melt from ideal solution behavior.*

In this paper the terms of equation (1) will be evaluated, assuming the following conditions to prevail: (a) The concentration of the impurity in both the solid and the molten host substance is very dilute so that the melting point of the host crystal is virtually unchanged, and interactions between impurity atoms can be neglected. (b) Ionizable impurities, i.e., those of Groups III and V, are fully ionized in the solid. Thus, all impurity atoms form two-electron bonds with each of the four surrounding host atoms. (c) Impurities other than the one under consideration are present only in negligible quantities in order to avoid the mass action effects described by Reiss and co-workers.[8]

Since heats and entropies of fusion can be obtained from literature data, a theoretical calculation of $k$ depends on the estimation of the heats and entropies of solution, $\Delta H^s$, $\sigma$ and $\gamma$.

## 3. EVALUATION OF HEATS AND ENTROPIES OF SOLUTION

### 3.1. *Heat of solution in the solid*, $\Delta H^s$

3.1.1. *Energy cycle.* We can redefine $\Delta H^s$ as the energy necessary to replace one gram atom of the host crystal by one gram atom of the impurity taken from a reservoir of the crystalline impurity. To estimate this energy we postulate the following process: We first create one gram atom of vacancies in the host crystal, spaced far apart since we are dealing with very dilute solutions; we then condense the atoms taken from the bulk of the crystal on its surface. One gram atom of impurity is then evaporated from the solid crystalline reservoir and condensed in the vacancies. The total energy for the process is given by:

$$\Delta H^s = 4\epsilon_H - H_H + H_A - H_{A-H}. \qquad (2)$$

where $\epsilon_H$ is the bond energy of the host crystal, in which each atom is surrounded by four neighbors, and $H_H{}^V$ is its heat of sublimation to a monatomic gas. $H_A{}^V$ is the heat of sublimation of the impurity to a monatomic gas at the same temperature, and $H_{A-H}{}^V$ is the energy released by the impurity atom upon condensation in the vacancy. The temperature for which we compute this process is not very important since the value for $\Delta H^s$ at a given temperature $T$ should differ from that calculated at the melting point of the host crystal $T_H$ at most by $\int_T^{T_H} \Delta C_p dT$ where $\Delta C_p$ is the difference in heat capacity between the host crystal and the impurity crystal. For any reasonable temperature $T$, such as the melting points of the impurities considered here, this correction is negligible. For the sake of simplicity, the temperature was chosen as that of the melting point of the host crystal. The heats of sublimation of the impurities considered here, all of which have melting points below those of germanium and silicon, were taken as the heat of vaporization of the molten impurities plus the heat of fusion.†

Since, in the case of the diamond lattice, the heat of sublimation is just twice the bond energy between atoms,[9], we can rewrite equation (2) in the form:

$$\Delta H^s = H_H{}^V + H_A{}^V - H_{A-H}^V. \qquad (3)$$

We shall assume that $H_{A-H}{}^V$ can be broken into two components, a bonding energy $E^b$, and a strain energy $E^{st}$, so that equation (3) becomes:

$$\Delta H^s = H_H{}^V + H_A{}^V - E^b + E^{st}. \qquad (4)$$

The bonding energy represents the heat liberated as a result of the formation of chemical bonds by the impurity to its four neighboring host atoms. The strain energy represents heat which must be supplied if the impurity atom differs in size from the host atom, and thus introduces strain into the lattice. We shall assign a positive sign to both $E^b$ and $E^{st}$.

3.1.2. *Strain energy.* When a host atom is replaced by an impurity atom whose normal tetrahedral radius[9] differs from that of the host atom by $\Delta r$, the four nearest neighbors move out radially

* Two substances are said to form an ideal solution if there are neither heat effects nor volume changes upon mixing. The entropy of mixing can then be calculated on the assumption of complete randomness in the occupation of the available sites. Such solutions obey Raoult's Law.[7]

† In the case of arsenic no value was available for the heat of vaporization of molten arsenic; an extrapolated value was used instead.

by an amount $\Delta r_1$, which is less than $\Delta r$ because of the compression of the impurity-host atom bonds.* The displacement of the four nearest neighbors of the first shell will push the atoms of the second shell outward by an amount $\Delta r_2$, which in turn will displace the atoms of the third shell by $\Delta r_3$, and so forth. Because of the resistance of the atoms to displacement from their normal positions, $\Delta r_1 > \Delta r_2 > \Delta r_3 \ldots$ so that the disturbance dies out rapidly.

To simplify our calculations we shall ignore the atomistic nature of the displacements beyond the shell comprising the four nearest neighbors, and approximate the host material beyond this shell by a continuous medium of macroscopic elastic properties (Fig. 1). Assuming Hooke's Law and

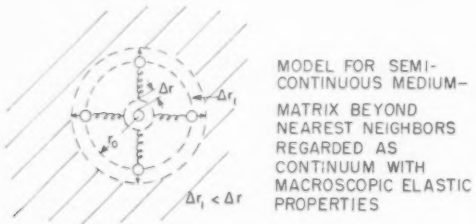


FIG. 1. Strain due to impurity atom.

classical elasticity theory, the strain energy can then be expressed by:

$$E^{st} = 4 \times \tfrac{1}{2} g K_c (\Delta r - \Delta r_1)^2 + 8\pi G r_0 (\Delta r_1)^2. \quad (5)$$

The first term represents the compression of the four impurity-host atom bonds, and would equal zero if these bonds were incompressible so that the four nearest neighbors move out by an amount $\Delta r$. The stiffness constant of these bonds is written as $gK_c$, where $K_c$ is the force constant between two host atoms, and $g$ is a dimensionless parameter of the order of unity. The second term represents the energy stored in the surrounding matrix by the expansion of a cavity of radius $r_0$ (i.e. the interatomic distance in the host crystal) by an amount $\Delta r_1$ (see for example ref. 10). $G$ represents the shear modulus of elasticity of the host crystal.

* In the following argument it will be assumed that the impurity atom is larger than the host atom, which is the case for the majority of the impurities considered here. The treatment for smaller impurity atoms does not, however, differ substantially from the one presented here.

We can eliminate $\Delta r_1$ from equation (5) by the requirement

$$\frac{dE^{st}}{d(\Delta r_1)} = 0.$$

$$\frac{dE^{st}}{d(\Delta r_1)} = 4gK_c(\Delta r - \Delta r_1) + 16\pi G r_0 \Delta r_1 = 0 \quad (6a)$$

$$\frac{\Delta r_1}{\Delta r} = \frac{2gK_c}{2gK_c + 8\pi G r_0}. \quad (6b)$$

In the absence of a generally agreed upon value for the stiffness constant $K_c$ of germanium or silicon bonds we shall proceed as follows: In the case of a simple, monatomic cubic lattice with only nearest neighbor forces of importance, KITTEL has shown[11] that the stiffness constant of the bonds is equal to the lattice constant multiplied by one of the elastic stiffness constants of the lattice, $c_{11}$. For this particular case ($c_{12} = 0$), $c_{11}$ equals the inverse of the linear compressibility, which for cubic crystals equals $c_{11} + 2c_{12}$ (see for example ref. 12). We shall therefore assume that, in general for a cubic crystal, the stiffness constant is proportional to the inverse of the linear compressibility, the proportionality constant being approximately equal to the lattice constant:

$$K_c = ma(c_{11} + 2c_{12}) \quad (7)$$

where $a$ is the lattice constant, and $c_{11}$ and $c_{12}$ are elastic stiffness constants; $m$ is a dimensionless proportionality factor of the order of unity.† Substituting equation (7) into equation (6b) we thus

† The following argument, due to R. N. HALL of the General Electric Research Laboratory, suggests that $m$ is identically equal to unity: The bulk compressibility $B$ of a cubic crystal equals $1/3\ (c_{11} + 2c_{12})$, provided only nearest neighbor forces are considered.[11] Let the interatomic distances in a unit cell of volume $V$ change by $r$, resulting in a volume change $\Delta V$. Now, $\Delta V/V \propto \Delta r/r$, and the energy $W$ required for this volume change is given by $W = 1/2BV(\Delta V/V)^2 = 9/2BV(\Delta r/r)^2$. In the diamond lattice the interatomic distance $r$ is equal to $\sqrt{3}/4a$, where $a$ is the lattice constant. The energy $W$ can therefore be rewritten as $W = 24Ba(\Delta r)^2$. A unit cell contains eight atoms and sixteen bonds. The energy required to compress these bonds is equal to $W = 1/2 \times 16K_c(\Delta r)^2$. Equating these values for $W$ we find that $K_c = 3aB = a(c_{11} + 2c_{12})$, which is identical with equation (7) for $m = 1+$.

obtain:

$$\frac{\Delta r_1}{\Delta r} = \frac{2gm(ac_{11}+2ac_{12})}{2gm(ac_{11}+2ac_{12})+8\pi G r_0} = \frac{2g'(ac_{11}+2ac_{12})}{2g'(ac_{11}+2ac_{12})+8\pi G r_0} \quad (8)$$

where we have combined the constants $g$ and $m$ into $g'$. The ratio $\Delta r_1/\Delta r$ can thus be evaluated from values of the elastic stiffness constants of the crystal $c_{11}$ and $c_{12}$, the shear modulus $G$, the interatomic distance $r_0$, and the lattice constant $a$. Table 1 lists values for these parameters in c.g.s. units at room temperature.

Substituting these values into equation (8) we obtain:

$$\frac{\Delta r_1}{\Delta r} = \frac{25{\cdot}4g'}{25{\cdot}4g'+41} = \frac{g'}{1{\cdot}6+g'} \text{ for Ge} \qquad = \frac{32{\cdot}2g'}{32{\cdot}2+47} = \frac{g'}{1{\cdot}5+g'} \text{ for Si.} \quad (9)$$

It is clear that a weak impurity-host atom stiffness constant causes the difference in atomic radii to be taken up largely by the compression of the impurity-host atom bonds ($\Delta r_1 \ll \Delta r$) while a strong stiffness constant leads to increasing absorption by the lattice ($\Delta r_1 \to \Delta r$). Finally, substituting equation (9) into equation (5) and usir g the appropriate values for $G$ and $r_0$, we can express the strain energy function of $\Delta r$:

$$E^{st} = \left[25\times10^4 g'\left(1-\frac{g'}{1{\cdot}6+g'}\right)^2 + 41\times10^4\left(\frac{g'}{1{\cdot}6+g'}\right)^2\right]\Delta r^2 \text{ for Ge}$$

$$= \left[32\times10^4 g'\left(1-\frac{g'}{1{\cdot}5+g'}\right)^2 + 47\times10^4\left(\frac{g'}{1{\cdot}5+g'}\right)^2\right]\Delta r^2 \text{ for Si.} \quad (10)$$

The value of the strain energy thus depends on the choice of the empirical parameter $g'$ which we require to be of the order of unity. The value of $g'$ which gave the best overall agreement of calculated and experimental values of the distribution coefficient was $g' = 0{\cdot}7$. Thus, the strain energy was computed from:

$$E^{st} = 12\times10^4\Delta r^2(\text{ergs/atom}) = 17\times10^{20}\Delta r^2(\text{cals/g atom}) \text{ for Ge} \qquad = 15\times10^4\Delta r^2(\text{ergs/atom}) = 22\times10^{20}\Delta r^2(\text{cals/g atom}) \text{ for Si.} \quad (11)$$

*Table* 1

(all values in c.g.s. units)

| | $c_{11}^{(11)}$ | $c_{12}^{(11)}$ | $G^{(13)}$ | $r_0^{(11)}$ | $a^{(11)}$ |
|---|---|---|---|---|---|
| Ge | $1{\cdot}29\times10^{12}$ | $0{\cdot}48\times10^{12}$ | $6{\cdot}7\times10^{11}$ | $2{\cdot}44\times10^{-8}$ | $5{\cdot}65\times10^{-8}$ |
| Si | $1{\cdot}66\times10^{12}$ | $0{\cdot}64\times10^{12}$ | $8{\cdot}0\times10^{11}$ | $2{\cdot}35\times10^{-8}$ | $5{\cdot}43\times10^{-8}$ |

3.1.3. *Bonding energy*. To calculate the bonding energy $E^b$ of equation (4) we shall find it convenient to treat the case of Group IV impurities separately from that of the ionizable impurities of Group III and V. For Group IV impurities, $E^b$ is simply equal to the energy of four impurity-host atom bonds. This energy will be estimated on the basis of a rule recently suggested by ALLEN,[14] according to which the energy of a bond, $\epsilon_{AH}$, between atoms $A$ and $H$ is given by:

$$\frac{1}{\epsilon_{AH}} = \frac{1}{2}\left(\frac{1}{\epsilon_{AA}}+\frac{1}{\epsilon_{HH}}\right) \quad (12)$$

where $\epsilon_{AA}$ and $\epsilon_{HH}$ are the energies of the bonds between atoms A and A, and H and H respectively. This rule combines the observation of the additivity of covalent radii, and the rule that bond energies for a series of diatomic molecules involving analogous electronic configurations (e.g.,

$S_2$, $Se_2$, $Te_2$) are inversely proportional to the interatomic distance.

The bond energies of Group IV elements in the diamond lattice configuration are equal to one half the heat of sublimation.[9] The heat of vaporization of grey tin is not known, but can be taken as equal to that of white tin, since the heat of transformation, about 500 calories,[15] is negligible compared to the heat of sublimation, 71,900 calories, at the transformation temperature.[16] By analogy, we shall assume that the heat of transformation from lead to a hypothetical "grey" lead is also negligible compared to the heat of vaporization. We shall therefore take as the bond energy for all Group IV elements one half the heat of vaporization of the elements at their melting point:

$$\epsilon_{AA} = \tfrac{1}{2} H_A^{v}. \tag{13}$$

From equations (12) and (13) we can thus write the following expression for the bonding energy $E^{b}$:

$$E^{b} = 4\epsilon_{AH} = \left[\frac{1}{4}\left(\frac{1}{H_H^{v}} + \frac{1}{H_A^{v}}\right)\right]^{-1}. \tag{14}$$

In the case of Group III and V elements, equation (13) is no longer true, and furthermore the impurities must undergo considerable changes during the transfer from their own lattice to the host lattice, since their electronic configurations must be altered in order to be tetrahedrally bonded to their nearest neighbors. In addition, the impurity acquires an electrical charge either by releasing an electron to the conduction band of the host crystal (donors), or by acquiring an electron from the valence band (acceptor). Nevertheless, it was found that equation (14) gave satisfactory results for the ionizable impurities of Groups III and V as well as for Group IV impurities.

We finally incorporate equation (14) into equation (4), and obtain for the heat of solid solution:

$$\Delta H^{s} = H_H^{v} + H_A^{v} - \left[\frac{1}{4}\left(\frac{1}{H_H^{v}} + \frac{1}{H_A^{v}}\right)\right]^{-1} + E^{st} \tag{15a}$$

$$= \frac{(H_H^{v} - H_A^{v})^2}{H_H^{v} + H_A^{v}} + E^{st} \tag{15b}$$

$$= E^{\Delta b} + E^{st} \tag{15c}$$

where $E^{\Delta b}$ equals $(H_H^{v} - H_A^{v})^2/H_H^{v} + H_A^{v}$.

We have introduced a new symbol, $E^{\Delta b}$, which stands for that part of the heat of solid solution which is due to a difference in bond energies in the host crystal and in the impurity crystal.

### 3.2. *Change in vibrational entropy*

The term $\sigma$ of equation (1) represents the change in vibrational entropy of the system as the impurity is transferred from its own lattice at the melting point $T_A$ to that of the host lattice at the melting point $T_H$. We can estimate the magnitude of $\sigma$ from the following argument: At temperatures considerably above the Debye temperature of a crystal the vibrational entropy per atom $S^{vibr.}$ can be expressed by:[17]

$$S^{vibr.} = 4k + 3k \ln kT/h\nu^{m} \tag{16}$$

provided that the crystal has zero entropy at the absolute zero. In this equation, $k$ is Boltzmann's constant, $h$ is Planck's constant, and $\nu^{m}$ is the frequency of the highest vibrational mode of the crystal.

If we make the reasonable assumption that the vibrational spectrum of the host crystal will remain virtually unchanged by the introduction of a few impurity atoms, the change in vibrational entropy accompanying the transfer of the impurity atom will be given by:

$$\begin{aligned}\Delta S^{vibr.} &= (4k + 3k \ln kT_H/h\nu_H^{m}) - \\ &\quad - (4k + 3k \ln kT_A/h\nu_A^{m}) \\ &= 3k \ln \frac{T_H \nu_A^{m}}{T_A \nu_H^{m}}\end{aligned} \tag{17}$$

where the symbols have been defined above, and the subscripts A and H stand for impurity crystal and host crystal respectively. Substituting $k\theta$ for $h\nu^{m}$[17], where $\theta$ is the Debye temperature, we finally obtain:

$$\sigma = \Delta S^{vibr.} = 3k \ln \frac{T_H \theta_A}{T_A \theta_H}. \tag{18}$$

An examination of the Debye temperatures and melting points of germanium and silicon and of the impurities considered here, indicates that the ratio $T_H\theta_A/T_A\theta_H$ is of the order of unity. We shall therefore neglect $\sigma$ in our calculations.

### 3.3. *Heat of solution and excess entropy of solution in the melt*

The activity coefficient of the impurity in the melt, $\gamma$, represents a heat of solution and an excess entropy of solution;[18] for ideal solutions $\gamma$ equals one. From an examination of the liquidus curves of germanium and silicon with the impurities of Groups III, IV and V considered here, THURMOND[19] concluded that these solutions exhibit "regular solution" behavior, i.e. that they show an ideal entropy of mixing but exhibit heat of mixing. The activity coefficient of the impurity could thus be expressed by an "interaction parameter" $b$:

$$\ln \gamma = (1-x^2)b/RT. \qquad (19)$$

The impurity atom fraction, $x$, is negligible compared to unity for the very dilute solutions considered here, and $T$ is essentially the melting point of the host crystal, $T_H$, so that:

$$\ln \gamma = b/RT_H \cdot x \ll 1. \qquad (20)$$

THURMOND has tabulated the values of $b$ for the various impurities in germanium and silicon so that $\gamma$ can be computed from equation (20).

## 4. RESULTS OF CALCULATIONS

It is now possible to evaluate all the terms appearing in equation (1). $\Delta H^f$ and $\Delta S^f$ were obtained from the compilation of thermodynamic data by STULL and SIMKE.[20] $\Delta H^s$ was computed from equation (15) using equation (11) to evaluate the strain energy. The heats of sublimation used to calculate $E^{\Delta b}$ were taken from STULL and SIMKE[20] $\sigma$ was neglected, as explained in Section 3.2, and ln $\gamma$ was computed from equation (20).

Table 2 lists the experimentally determined values of $b$, and the calculated values for $E^{\Delta b}$ and $E^{st}$, as well as the total heat of solution, $\Delta H^s$. Also listed are the values of $\Delta r$, the difference in tetrahedral covalent radii between the host atom and the impurity atom.[9] Table 3 gives the calculated and experimental values for the distribution coefficients.

An examination of Table 3 reveals that agreement between calculated and experimental values of the distribution coefficients is quite good for most impurities. In all but three of the fifteen cases calculated the agreement is better than half an order of magnitude. In almost half the cases the agreement is better than a factor of two. The values

*Table 2. Experimental values of b. Calculated values of the heat of solution due to difference in bond strengths ($E^{\Delta b}$), strain energy ($E^{st}$) and total heat of solution ($\Delta H^s$) in* kcal/g *atom of impurity; $\Delta r$ is difference in atomic radii of host atom and impurity atom*

| | | Sn | Pb | As | Sb | Bi | Al | Ga | In | Tl |
|---|---|---|---|---|---|---|---|---|---|---|
| (a) Impurity in Ge | $\Delta r$(Å) | 0·18 | 0·24 | −0·04 | 0·14 | 0·24 | 0·04 | 0·04 | 0·22 | 0·25 |
| | $b$(kcal) | 0·72 | 4·0 | −1·5 | 0·87 | 3·6 | −2·5 | −0·56 | 0·72 | 3·6 |
| | $E^{\Delta b}$(kcal) | 2·3 | 15·0 | 3·3 | 5·7 | 14·9 | 1·3 | 4·3 | 8·1 | 18·5 |
| | $E^{st}$(kcal) | 5·7 | 10·2 | 0·3 | 3·5 | 10·2 | 0·3 | 0·3 | 8·6 | 11·0 |
| | $\Delta H^s$(kcal) | 8·0 | 25·2 | 3·6 | 9·2 | 25·1 | 1·6 | 4·6 | 16·7 | 29·5 |
| (b) Impurity in Si | $\Delta r$(Å) | 0·23 | | 0·01 | 0·19 | | 0·09 | 0·09 | 0·27 | |
| | $b$(kcal) | 5·2 | | −3·5 | 4·7 | | −2·3 | 1·6 | 5·8 | |
| | $E^{\Delta b}$(kcal) | 6·0 | | 8·0 | 11·7 | | 4·6 | 9·4 | 14·3 | |
| | $E^{st}$(kcal) | 11·6 | | 0·1 | 7·9 | | 1·8 | 1·8 | 16·0 | |
| | $\Delta H^s$(kcal) | 17·6 | | 8·1 | 19·6 | | 6·4 | 11·2 | 30·3 | |

*Table 3. Calculated and experimental values of distribution coefficients*

| | | Sn[3,5] | Pb[6] | As[21,2,4] | Sb[1,2,3] | Bi[8] | Al[2,3] | Ga[2,3] | In[2,3] | Tl[3] |
|---|---|---|---|---|---|---|---|---|---|---|
| (a) Impurity in Ge | $k_{calc.}$ | 0·02 | 0·0001 | 0·10 | 0·020 | 0·00004 | 0·10 | 0·02 | 0·0008 | 0·00001 |
| | $k_{exp.}$ | 0·02 | 0·0004 | 0·02, 0·05, 0·10 | 0·003 | 0·00004 | 0·10 | 0·10 | 0·0010 | 0·00004 |
| (b) Impurity in Si | $k_{calc.}$ | 0·008 | | 0·01 | 0·003 | | 0·040 | 0·01 | 0·0003 | |
| | $k_{exp.}$ | 0·020 | | 0·09, 0·30 | 0·010 | | 0·001 | 0·01 | 0·0005 | |

range over five orders of magnitude. The disagreement in the three exceptions, antimony in germanium and aluminum and arsenic in silicon, is up to one and a half orders of magnitude.

No results were listed for boron, phosphorus and germanium–silicon system because the values of $b$ were not known. Calculations were, nevertheless, carried out with assumed values of $b$. In the case of phosphorus, $b$'s equal to those for arsenic were chosen, and good agreement with experiment was found in both germanium and silicon. In the case of germanium–silicon system, the assumption was made that the melt behaves ideally, i.e. $b = 0$, and with this assumption good agreement was also obtained. On the other hand, the distribution coefficients calculated for boron both in germanium and silicon were too low by approximately two orders of magnitude, with an assumed value of $b = 0$. It is probably that the strain energy for boron was overestimated with the use of equation (11) since the difference in atomic radii, e.g. 0·34 Å in germanium, is so large that anharmonic terms may become important: this factor alone would not, however, suffice to explain the large disagreement with experiment.

## 5. DISCUSSION

An examination of the terms entering into the calculation of $k$, (equation (1)) reveals that the heat of solid solution, $\Delta H^s$, is by far the dominant term. In the model chosen, a calculation of $\Delta H^s$ depends on an evaluation of $E^{\Delta b}$ and $E^{st}$, and it is of interest to compare their values for various impurities. Table 2 shows that $E^{st}$ increases as the square of $\Delta r$ (equation (11)) and that $E^{\Delta b}$ also increases with increasing $\Delta r$. Thus the total heat of solution increases with increasing $\Delta r$, leading to smaller values of $k$. The increase in $E^{\Delta b}$ with increasing $\Delta r$ is the result of the decrease in the heat of sublimation of elements as their atomic radii increase; from equation (14) it is seen that this results in a smaller bonding energy. We also note from Table 2 that the strain energy reaches a maximum of about three quarters of the total heat of solid solution for tin in germanium.

It is surprising that the method used to calculate the bonding energy for Group IV impurities could be applied without change to those of Group III and V. The role of the excess electron or hole, and the effect of the impurity charge remain to be investigated.

The use of equation (11) for the calculation of the strain energy involves the use of an empirical parameter $g'$ which we required to be of the order of unity. To give an idea of the sensitivity of the results to the choice of $g'$, it can be pointed out that the distribution coefficient of thallium in germanium (maximum $\Delta r$) would be approximately one half an order of magnitude smaller if the strain energy had been calculated with $g'$ equal to unity. The fact that the same value of $g'$ could be used for all the impurities in germanium and silicon indicates that the stiffness constant of the impurity-host atom bond is essentially equal to that between two host atoms, i.e., $g \approx 1$.

Data of the temperature dependence of $k$ close to the melting point of the host crystal would yield heats and entropies of solution in the very dilute solution range considered here, and would thus constitute a sensitive test of the theory. In the

original publication of THURMOND and STRUTHERS[1] the temperature dependence of the distribution coefficient of antimony in germanium was investigated. Two conflicting values for the heat of solid solution were given (55,400 cal and 23,100 cal), both of which are much higher than the one calculated here, namely 9200 cal. This disagreement is, of course, in line with the disagreement between experimental and theoretical values for the distribution coefficient itself. The data on various impurities in germanium which were obtained by THURMOND, TRUMBORE and KOWALCHIK[6] were generally taken well below 900°C and then extrapolated to the melting point; the calculation of heats of solution near the melting point does not therefore seem justified. The distribution coefficient of tin in germanium was investigated near the melting point by TRUMBORE[5] but the scatter of points obscures any temperature dependence of $k$. From both investigations it appears that the rate of decrease of $k$ with temperature decreases with decreasing temperature, in some cases even leading to a flat $\log k$ vs. $1/T$ at low temperatures. These phenomena, dealing with more concentrated solutions, are outside the scope of the model developed here. For other impurities than the ones considered here, however, e.g. Ag, Ni, Cu, HALL[21] found from an examination of the literature that $\log k$ plotted against $1/T$ does give straight lines over a fairly wide concentration range.

In conclusion, it should be pointed out that the approach of breaking up the heat of solid solution of an impurity into an electronic component and strain component has been used by other authors in treating metallic systems.[22] What distinguishes the case of impurities in a diamond lattice is the existence of well defined, localized bonds between the host atoms and the impurity. As a result, the compression of these bonds must be considered in calculating strain energies, and the bonding energy of the impurity atom can be calculated from simple empirical rules governing the strength of covalent chemical bonds.

## SUMMARY

The values for the distribution coefficients of Group III, IV, and V impurities in germanium and silicon have been calculated on the basis of a simple model. The crystalline impurity was chosen as the reference state, and the change in enthalpy and entropy was estimated for the transfer of impurity atoms to the solid and the molten host substance respectively. The major factor which determines the value of the distribution coefficient was found to be the heat of solid solution. This could be estimated by postulating a stepwise process for the transfer of an impurity atom from its own lattice to the host lattice, and by calculating the energy needed for each step. It was necessary to estimate the bonding energy of the impurity atom in the host crystal, and the strain energy which it introduces by virtue of a difference in size. The change in vibrational entropy of the impurity atom for the transfer from its own lattice to the host lattice is believed to be negligible.

Agreement between calculated and experimental values was very satisfactory.

*Acknowledgements*—The author acknowledges with gratitude the help and advice extended to him by Dr. B. ABELES and Dr. F. HERMAN of this Laboratory in the course of many discussions.

## REFERENCES

1. THURMOND C. D. and STRUTHERS J. D. *J. Phys. Chem.* **57,** 831 (1953).
2. HALL R. N. *J. Phys. Chem.* **57,** 836 (1953).
3. BURTON J. A., PRIM R. C. and SLICHTER W. P. *J. Chem. Phys.* **21,** 1991 (1953).
4. BURTON J. A. *Physica* **20,** 845 (1954).
5. TRUMBORE F. A. *J. Electrochem. Soc.* **103,** 579 (1956).
6. THURMOND C. D., TRUMBORE F. A. and KOWALCHIK M. *J. Chem. Phys.* **25,** 799 (1956).
7. GUGGENHEIM E. A. *Mixtures.* Oxford University Press (1952).
8. REISS H., FULLER C. S. and MORIN F. J. *Bell Syst. Tech. J.* **35,** 535 (1956).
9. PAULING L. *Nature of the Chemical Bond* (2nd Edn.) Cornell University Press (1948).
10. FRENKEL J. *Kinetic Theory of Liquids* Chap 1. Oxford University Press (1946).
11. KITTEL C. *Introduction to Solid State Physics* (2nd Edn.) Wiley, New York (1956).
12. SMITH H. M. J. *Phil. Trans. Roy. Soc.* **A241,** 105 (1948).
13. MCSKIMMIN H. J. *J. Appl. Phys.* **24,** 988 (1953).
14. ALLEN T. L. *J. Chem. Phys.* **27,** 810 (1957).
15. STEINER L. E. *Introduction to Chemical Thermodynamics* Chap. 15. McGraw Hill, New York (1948).
16. SEARCY A. W. and FREEMAN R. D. *J. Amer. Chem. Soc.* **76,** 5229 (1954).

17. TOLMAN R. C. *Principles of Statistical Mechanics.* Oxford University Press (1938).
18. HILDEBRAND J. H. and SCOTT R. L. *Solubility of Non-electrolytes* (3rd Edn.) Reinhold Publishing Company, New York (1950).
19. THURMOND C. D. *J. Phys. Chem.* **57,** 827 (1953).
20. STULL D. R. and SIMKE G. C. *Thermodynamic Properties of the Elements* Advances in Chemistry Series No. 18. American Chemical Society (1956).
21. HALL R. N. *J. Phys. Chem. Solids* **3,** 63 (1957).
22. ORIANI R. A. *J. Phys. Chem. Solids* **2,** 327 (1957).

VOL
7
195

*J. Phys. Chem. Solids* Pergamon Press 1958. Vol. 7. pp. 127–140.

# A QUADRATIC PHOTOELECTROMAGNETIC EFFECT IN GERMANIUM*

MANUEL CARDONA† and WILLIAM PAUL

Division of Engineering and Applied Physics, Harvard University, Cambridge, Massachusetts

(*Received* 7 *April* 1958)

**Abstract**—The quadratic photoelectromagnetic (P.E.M.) effect observed by KIKOIN and NOSKOV in cuprite has been observed in germanium and silicon. The effect occurs when the magnetic field $B$ is rotated an angle $\phi$ about an axis lying in the illuminated face and perpendicular to the primitive direction of $B$. The linear effect is produced by the component $B\cos\phi$ of $B$, while the quadratic effect is produced by the action of $B\sin\phi$ on the electric current generated by $B\cos\phi$. From this elementary argument the quadratic P.E.M. effect should be proportional to $B^2\sin\phi\cos\phi$. A part of the effect is produced by the action of a magnetic field on a current produced by the action of a magnetic field on the diffusion current of the injected carriers. Calculating this term, one finds the same type of average of the collision time as appears in the magnetoresistance coefficients. Consequently, the effect becomes anisotropic and, instead of being proportional to $B^2\sin 2\phi$, is proportional to $B^2[\sin(2\phi+\Delta)+g]$, where $\Delta$ and $g$ are functions of the constants of the semiconductor and the orientation of the sample. For certain simple orientations (such as the crystallographic axes) $\Delta = 0$ and $g = 0$. The ratio of the quadratic to the linear P.E.M. fields is, for small light intensities, a function only of the Hall angles, the magnetoresistance coefficients of electrons and holes, the impurity concentration, and the magnetic field. Agreement between theory and experiment is satisfactory.

## 1. INTRODUCTION

THE photoelectromagnetic or P.E.M. effect was discovered by KIKOIN and NOSKOV[1] in 1934, and its theoretical interpretation given by FRENKEL[2] in the same year. The discovery of KIKOIN and NOSKOV was made on cuprite at liquid-air temperature; the effect was not observable at room temperature. Since 1953 the effect has been studied in germanium[3–6,15] and in other semiconductors.[7,8] The effect can be applied to the measurement of the recombination times and the surface recombination velocities of injected carriers in semiconductors.[4,5,10,11,12,17] Recently the theory of the first-order P.E.M. effect has been developed with great generality[12,13] and experimentally verified.[14] The P.E.M. effect can be defined as the transverse electric field produced by the action of a magnetic field on a diffusion current of holes and electrons generated by the absorption of light at one face of a semiconductor. If the magnetic field is perpendicular to the diffusion currents, one obtains the effect called in this article the first-order or linear P.E.M. effect. When the magnetic field is not perpendicular to the diffusion currents, there is an additional effect proportional to the square of the magnetic field for small values of the magnetic field. We shall call this the second-order or quadratic P.E.M. effect. The theory and experimental observation of the quadratic P.E.M. effect in germanium, silicon, and indium antimonide are the subject of this paper.

## 2. THE FIRST-ORDER P.E.M. EFFECT

In this section we shall limit ourselves to a few remarks which will be useful for our further development of the theory of the second-order P.E.M. effect. The geometry and experimental configuration used for the measurement of the first-order

* This work was supported in part by the Office of Naval Research, under contract with Harvard University.

† M.C. gratefully acknowledges financial support from the Institute of International Education during the summer of 1957.

P.E.M. effect are shown in Fig. 1. In developing the theory of the P.E.M. effect, it is assumed that we have an infinite slab of thickness $t$, that the illumination of the semiconductor is predominantly with wavelengths lying within the fundamental absorption band (so that the light is absorbed almost completely in the surface of the

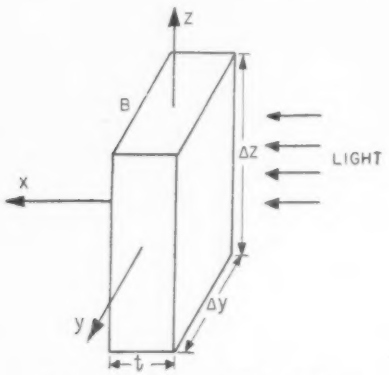


FIG. 1. The linear P.E.M. effect.

semiconductor), that the magnetic field is small (so that the conditions for a linear Hall effect are satisfied), and that the condition of charge neutrality is satisfied.

In the literature it is also implicitly assumed that diffusion currents, derived from concentration gradients, and drift currents, derived from applied electric fields, behave in the same way under the action of a magnetic field. This is not a trivial assumption, especially since it is not evident how to justify it, if one starts by considering the effect of the magnetic field on individual current carriers. However, the equivalence of the two currents, under the action of a magnetic field, can be demonstrated in a straightforward fashion if one follows the usual development of the theory of transport from the Boltzmann equation. The concentration gradient produces the same current as an electric field given by

$$E_{\text{dif}} = \frac{kT}{en} \nabla_r n$$

and the diffusion current is equivalent to a drift current

$$I_{\text{dif}} = -eD_e \nabla_r n$$

where the diffusion coefficient $D_e$ is related to the mobility $\mu_e$ by the Einstein relation $D_e = \mu_e kT/e$.

Under the conditions mentioned, the first-order P.E.M. field is given by

$$E_y = \frac{(\mu_{eH}+\mu_{hH})B\int_0^t I_x\,dx}{\sigma_0 t + e(\mu_e+\mu_h)\int_0^t (n-n_0)\,dx} \qquad (1)$$

where $\mu_e$ and $\mu_h$ are the electron and hole conduction mobilities and $\mu_{eH}$, $\mu_{hH}$ are the electron and hole Hall mobilities, respectively. $I_x$ is the component of the hole current density along $x$. Both $I_x$ and $(n-n_0)$ are proportional to the illumination $U$, as can be seen from the solution of the diffusion equation in the $x$ direction. Hence,

$$E_y = \frac{\alpha U}{U+\beta} B \qquad (2)$$

where $\alpha$ and $\beta$ depend on the physical constants of the semiconductor. When $U$ is small, $E_y \propto UB$. When $U$ is large, $E_y = \alpha B$. From $\alpha B$ we can obtain the recombination time, provided the thickness $t$ is much larger than the diffusion length $L$. If, on the other hand, $t \ll L$, we can obtain the surface recombination velocity $s$.

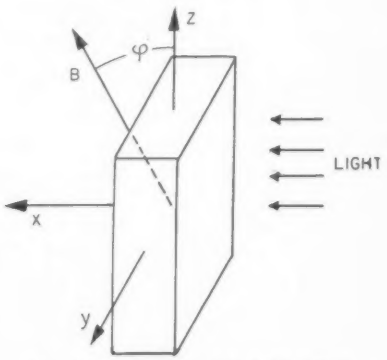


FIG. 2. The quadratic P.E.M. effect.

### 3. THE QUADRATIC P.E.M. EFFECT

(a) *General*

We next assume that the magnetic field $B$ is turned in the $xz$ plane to form an angle $\phi$ with the $z$ axis (Fig. 2). An elementary treatment[2,4] simply demonstrates that there exists a quadratic P.E.M. field[1,2,4] between the faces of the semiconductor perpendicular to the $z$ axis which is proportional to

$B^2 \sin\phi \cos\phi$. Our treatment will show that this proportionality is an approximation which is sometimes quite poor.

A field similarly quadratic in $B$ always exists between the illuminated and non-illuminated faces of the semiconductor, in addition to the Dember field.* This field is caused by the action of $B_z$ on $I_y$.

(b) *Theory of the quadratic P.E.M. effect*

In our theory of the quadratic P.E.M. effect, we shall assume $U$ small, so that the injected carrier density is small compared with the equilibrium majority carrier density and the first-order P.E.M. field is linear in $U$. This condition is always satisfied in our experimental work on the strongly $n$- and $p$-type samples. The generalization of the theory for the case in which this condition is not satisfied has been carried out by the authors, but the formulae become extremely complicated without adding any physical insight to the phenomenon.

We shall also assume that the first-order P.E.M. effect is linear in $B$. Under these conditions equation (1) reduces to

$$E_y = \frac{B\cos\phi(\mu_{eH}+\mu_{hH})}{\sigma_0 \cdot t}\int_0^t I_x(x)\,dx. \qquad (3)$$

The electron current density along $y$ is

$$I_{ye} = -I_x(x)B\cos\phi\,\mu_{eH} + E_y e\mu_e n$$

and the hole current density

$$I_{yh} = -I_x(x)B\cos\phi\,\mu_{hH} + E_y e\mu_h p.$$

Using equation (3),

$$I_{ye} = -B\cos\phi\left[I_x(x)\mu_{eH} - \frac{\mu_{eH}+\mu_{hH}}{\sigma_0 \cdot t} e\mu_e n\int_0^t I_x(x)\,dx\right]$$

and

$$I_{yh} = -B\cos\phi\left[I_x(x)\mu_{hH} - \frac{\mu_{eh}+\mu_{hH}}{\sigma_0 \cdot t} e\mu_h p\int_0^t I_x(x)\,dx\right].$$

* The Dember voltage is the voltage that appears between the illuminated and non-illuminated (opposite) faces of a slab of semiconductor.[23]

Each of these currents produces a Hall effect under the action of the $x$ component of the magnetic field $B\sin\phi$. The Hall current density along $z$ is found by multiplying the electron and hole current densities along $y$ by the Hall angles $\mu_{eH}B\sin\phi$ and $\mu_{hH}B\sin\phi$. This is rigorously true for the fractions of $I_y$ produced by the action of the electric field along $y$ on the free carriers existing in the sample, but, as we shall see, it is not true for the fraction $I_y$ produced when $B$ deviates the current along $x$. To take into account this fact, which we shall study in detail later, we shall write $\mu'_H$ instead of $\mu_H$ in the contribution to the quadratic P.E.M. effect of the injected carriers that are deviated twice by the magnetic field. The current density along $z$ will be given by

$$I_z = B^2\cos\phi\sin\phi\left[I_x(\mu_{hH}'^2 - \mu_{eH}'^2) + \frac{(\mu_{eH}+\mu_{hH})e(n\mu_{e}\mu_{eH} - p\mu_h\mu_{hH})}{\sigma_0 \cdot t}\times \times\int_0^t I_x(x)\,dx\right] + E_z\sigma_0.$$

Imposing the condition $\int_0^t I_z dx = 0$, together with $\partial E_z/\partial x = 0$, we obtain

$$E_z = -\frac{B^2\cos\phi\sin\phi}{\sigma_0 \cdot t}\int_0^t I_x(x)\,dx \times \times\left[\mu_{hH}'^2 - \mu_{eH}'^2 + \frac{(\mu_{eH}+\mu_{hH})e(n\mu_{e}\mu_{eH} - p\mu_h\mu_{hH})}{\sigma_0 \cdot t}\right]. \qquad (4)$$

We can then write the ratio of the second-order to the first-order P.E.M. voltages as

$$\frac{V_z}{V_y} = -\frac{B\Delta z\sin\phi}{\Delta y}\times \times\left[\frac{\mu_{hH}'^2 - \mu_{eH}'^2}{\mu_{eH}+\mu_{hH}} + \frac{e(n\mu_{e}\mu_{eH} - p\mu_h\mu_{hH})}{\sigma_0}\right], \qquad (5)$$

where $\Delta y$ and $\Delta z$ are the dimensions of the semiconductor in the $y$ and $z$ directions, respectively. If we now assume $\mu'_{eH} = \mu_{eH}$ and $\mu'_{hH} = \mu_{hH}$[5] reduces to

$$\frac{V_z}{V_y}=-\frac{B\Delta z\sin\phi}{\Delta y}\times$$
$$\times\left[\mu_{hH}-\mu_{eH}+\frac{e(n\mu_e\mu_{eH}-p\mu_h\mu_{hH})}{\sigma_0}\right]. \quad (6)$$

If the sample is strongly extrinsic, for instance $n$-type, then equation (6) reduces to

$$\frac{V_z}{V_y}=-\frac{B\Delta z\sin\phi}{\Delta y}\mu_{hH}. \quad (7)$$

However, we find experimentally that the value of $\mu_{hH}$ determined in this way is quite different from the value obtained directly from Hall effect and conductivity measurements. The reason is that our hypothesis $\mu_{hH}=\mu'_{hH}$ and $\mu_{eH}=\mu'_{eH}$ is wrong.

(c) *The planar Hall effect*

We shall now study the planar Hall effect, which is the analogue of the quadratic P.E.M. effect, with a conduction current in the $x$ direction substituted for the diffusion current. The first-order Hall effect is along the $y$ direction and the planar or second-order Hall effect along the $z$ direction. The current along the $y$ direction due to the first-order Hall effect is composed of two parts. One is produced by the action of the magnetic field on the current along $x$ and the other by the action of the electric field along $y$ on the free carriers inside our sample. The sum of the currents must be zero. If the current produced by the action of the magnetic field behaves under the action of the component along $x$ of the magnetic field in the same way as an electric current, then there can be no net Hall effect along the $z$ direction. In fact, we find a second-order Hall effect along the $z$ direction.[18] Now, according to the phenomenological interpretation we have given of the second-order P.E.M. effect, the current produced by the action of the $x$-component of the magnetic field on the current along $y$ produced by the action of the $z$ component of the magnetic field on the current along $x$, will be proportional to $\mu_H'^2$, while the current produced by the action of the $x$-component of the magnetic field on the current along $y$ produced by the action of the electric field along $y$ on the free carriers will be proportional to $\mu_H^2$. In order to give an intuitive picture of why $\mu_H'$ is not equal to $\mu_H$, we calculate the planar Hall effect, using the pictorial kinetic method[19] in the appendix. This analysis shows that

$$\mu_H'^2-\mu_H^2=\frac{e^2\langle\tau^2\rangle^2}{m^2\langle\tau\rangle^2}\left[\frac{\langle\tau\rangle\langle\tau^3\rangle}{\langle\tau^2\rangle^2}-1\right]$$
$$=\frac{e^2\langle\tau^2\rangle^2\xi}{m^2\langle\tau\rangle^2}=\mu_H^2\xi \quad (8)$$

where $\xi$ is the transverse magnetoresistance coefficient given by

$$\xi=\frac{\langle\tau\rangle\langle\tau^3\rangle}{\langle\tau^2\rangle^2}-1.$$

$\mu_H^2$ and $\mu_H'^2$ contain different averages of the relaxation time $\tau$ of the carriers. The quadratic P.E.M. effect is closely related to the planar Hall effect and the magnetoresistance. If we assume that the scattering is due only to collisions with longitudinal acoustical phonons, equation (8) gives

$$\mu_H'^2-\mu_H^2=\mu^2\left(\frac{9\pi}{16}\right)\left(1-\frac{\pi}{4}\right).$$

Use of this formula also incorrectly predicts the observed quadratic P.E.M. field; the predicted values of the magnetoresistance and planar Hall effect, similarly, do not agree with experiment. The discrepancy is understandable if we remember that the assumptions underlying the last formula do not apply to germanium, which has a non-isotropic electron mass and two types of holes. In view of the difficulties involved in interpreting the magnetoresistance of $p$-type germanium in terms of its band structure and the carrier scattering mechanisms, we have decided instead to try to interpret the P.E.M. results in terms of the phenomenological theory of magnetoresistance and the experimental values of the magnetoresistance coefficients.

(d) *Phenomenological theory of the magnetoresistance, the planar Hall effect, and the quadratic P.E.M. effect*

The electric current density in a cubic semiconductor under the action of an electric and magnetic field is given by[20]

$$\boldsymbol{I}=\sigma_0\boldsymbol{E}+\alpha\boldsymbol{E}\times\boldsymbol{B}+\beta\boldsymbol{E}B^2+\gamma\boldsymbol{B}(\boldsymbol{E}\cdot\boldsymbol{B})+\delta[B^2]\boldsymbol{E},$$

VOL. 7 195

where $[B^2]$ is a second-order tensor whose components with respect to the crystallographic axes are

$$[B^2]=\begin{bmatrix} B_1^2 & 0 & 0 \\ 0 & B_2^2 & 0 \\ 0 & 0 & B_3^2 \end{bmatrix}.$$

Assuming $E$ and $B$ to be small, so that powers of $E$ greater than the first and of $B$ greater than the second can be neglected, we find

$$\boldsymbol{E}=\rho_0[\boldsymbol{I}+a(\boldsymbol{I}\times\boldsymbol{B})+bIB^2+c\boldsymbol{B}(\boldsymbol{I}\cdot\boldsymbol{B})+dIB^2]$$

where

$$a=-\alpha\rho \qquad d=-\delta\rho_0$$
$$b=-(\beta+\rho_0\alpha^2)\rho_0 \qquad \rho_0=1/\sigma_0.$$
$$c=(\gamma-\rho_0\alpha^2)\rho_0$$

Referring the last equation to any system of orthogonal axes, we obtain

$$\boldsymbol{E}_s=\rho_0[\boldsymbol{I}_s+a(\boldsymbol{I}\times\boldsymbol{B})_s+bI_sB^2+cB_s(\boldsymbol{I}\cdot B)+ +d\sum_{rs's''s'''} I_{s'}a_{rs}a_{rs'}a_{rs''}a_{rs'''}B_{s''}B_{s'''}]$$

where $a_{rs}$ are the direction cosines of the new axes with respect to the crystallographic axes of the semiconductor. For the configuration of the planar Hall effect, we have

$$I=I_x \quad B_y=0 \quad B_x/B_z=\tan\phi.$$

The electric field along $z$ is given by

$$E_z=\rho_0cI_xB_xB_z+\rho_0dI_x[(\Sigma_s a_{sx}{}^3a_{sz})B_x{}^2+ +(\Sigma_s a_{sx}a_{sz}{}^3)B_y{}^2+2B_xB_z(\Sigma_s a_{sx}{}^2a_{sz}{}^2)]$$

that is

$$E_z=I_xB^2[G\sin(2\phi+\Delta)+g] \qquad (9)$$

where

$$G=\rho_0\{[\tfrac{1}{2}c+d\Sigma_s(a_{sx}{}^2a_{sz}{}^2)]^2+ +\tfrac{1}{4}d^2[\Sigma_s a_{sx}{}^3a_{sz}-a_{sz}{}^3a_{sx}]^2\}^{\frac{1}{2}}$$
$$g=\tfrac{1}{2}d\rho_0[\Sigma_s(a_{sx}{}^3a_{sz}+a_{sx}a_{sz}{}^3)]$$
$$\tan\Delta=\frac{\Sigma_s(a_{sx}{}^3a_{sz}-a_{sx}a_{sz}{}^3)}{[\tfrac{1}{2}c+d\Sigma_s a_{sx}{}^2a_{sz}{}^2]}.$$

Comparing (8) and (9), we see that

$$\mu_H{}'^2-\mu_H{}^2=-2\sigma_0G\frac{\sin(2\phi+\Delta)+g/G}{\sin 2\phi}$$

i.e. $\mu_H'$ is a function of $\phi$. When the axes are in particularly simple directions with respect to the applied fields, simplification of the formula results; this is shown in Table 1. The ratio of the

*Table* 1

| Axes | Formula | $G$ |
|---|---|---|
| $x=(100)$ | $E_z=I_xB^2G\sin 2\phi$ | $\frac{c\rho_0}{2}$ |
| $z=(100)$ | $E_z=I_xB^2G\sin 2\phi$ | $\frac{c\rho_0}{2}$ |
| $x=(110)$, $y=(001)$, $z=(1\text{–}10)$ | $E_z=I_xB^2G\sin 2\phi$ | $\frac{(c+d)\rho_0}{2}$ |
| $x=(111)$, $y=(11\text{–}2)$, $z=(-110)$ | $E_z=I_xB^2G\sin 2\phi$ | $\frac{(c+\frac{2}{3}d)\rho_0}{2}$ |

second-order P.E.M. voltage to the first-order voltage is given by

$$-\frac{V_z}{V_y}=\frac{B\Delta z\sin\phi}{\Delta y}\,\frac{(\mu_{hH}{}^2-\mu_{eH}{}^2)-2(G_h-G_e)\sigma_0}{\mu_{eH}+\mu_{hH}}+ +\frac{e(n\mu_e\mu_{eH}-p\mu_h\mu_{hH})}{\sigma_0}. \qquad (10)$$

If the semiconductor is strongly $n$-type,

$$-\frac{V_z}{V_y}=\frac{B\Delta z\sin\phi}{\Delta y}\left[\mu_{hH}-\frac{2(G_h-G_e)\sigma_0}{\mu_{eH}+\mu_{hH}}\right] \qquad (11)$$

and if strongly $p$-type,

$$-\frac{V_z}{V_y}=\frac{B\Delta z\sin\phi}{\Delta y}\left[-\mu_{eH}-\frac{2(G_h-G_e)\sigma_0}{\mu_{eH}+\mu_{hH}}\right]. \qquad (12)$$

In this way we obtain for $V_z$ the sum of a term proportional to $\sin 2\phi$ another proportional to $\sin(2\phi+\Delta_e)+g_e$ and another proportional to

$\sin(2\phi+\Delta_h)+g_h$. The overall effect can be written in the form

$$V_z = A[\sin(2\phi+\Delta)+g]B^2 \qquad (13)$$

and in general $V_z/V_y$ is not proportional to $\sin 2\phi$. The relation (13) has been observed, but the expression of $g$ and $G$ as a function of the constants of the semiconductor is too complicated to attempt to obtain any information from the experimentally determined values of $g$ and $\Delta$.

## 4. EXPERIMENT

### (a) *Experimental apparatus*

The first- and second-order P.E.M. effects have been determined by a d.c. potentiometric method. The experimental apparatus was simple: a tungsten bulb as light source; a water cell of cut-off wavelength $1{\cdot}2\ \mu$ to ensure non-penetrating radiation for germanium; a sample-holder permitting rotation of the sample inside the magnetic field; and a graduated disk attached to the sample-holder to allow measurement of the angle between sample and magnetic field to $\pm 0{\cdot}5^\circ$.

### (b) *Experimental method*

The first- and second-order P.E.M. effects were determined for several oriented and non-oriented samples of germanium and silicon at temperatures between 26° and 28°C; the temperature increment changes $V_z/V_y$, whose experimental and theoretical values we shall be comparing, by only 1 per cent and is therefore disregarded.

It was necessary to eliminate or correct for the effects of thermovoltages and photovoltages at the contacts to the semiconductor especially when dealing with very impure samples, for then they were of the same order of magnitude as the linear P.E.M. effect. Blackpainting and masking the contacts considerably reduced the undesired voltages, but introduced errors into the determination of the area of the illuminated surface. The thermovoltages and photovoltages can be corrected for as follows: suppose the first-order effect is measured for both directions of magnetic field. Then

$$\begin{aligned} V_y^+ &= V_t(0)+V_t(B)+V_t(B^2)+V_y(B)+V_y(B^2) \\ V_y^- &= V_t(0)-V_t(B)+V_t(B^2)-V_y(B)+V_y(B^2) \end{aligned} \qquad (14)$$

$V_y^+$ and $V_y^-$ are the measured voltages; $V_t(0)$ is the sum of the thermo- and photovoltages when $B = 0$; $V_t(B)$ and $V_t(B^2)$ are the linear and quadratic terms in $B$ of these voltages; $V_y(B)$ and $V_y(B^2)$ are the linear and quadratic terms in the first-order P.E.M. effect. From equation (14) we obtain

$$V_y(B)+V_t(B) = \frac{V_y^+ - V_y^-}{2}.$$

Since $V_t(0)$ is at most of the order of $V_y(B)$, we expect that $V_t(B)$ is of the order of $V_y(B^2)$, that is negligible. Therefore:

$$V_y(B) = \frac{V_y^+ - V_y^-}{2}.$$

Similarly, for the quadratic effect:

$$\begin{aligned} V_z^+ &= V_t(0)+V_t(B)+V_t(B^2)+V_z(B)+V_z(B^2) \\ V_z^- &= V_t(0)-V_t(B)+V_t(B^2)-V_z(B)+V_z(B^2) \end{aligned}$$

where $V_z(B)$ is the voltage between the quadratic effect contacts produced by the linear P.E.M. effect as they are not on an equipotential of the first-order effect. By an analogous argument, $V_t(B^2)$ can be neglected and we have:

$$V_z(B^2) = \frac{V_z^+ + V_z^-}{2} - V_t(0).$$

The determination of $V_z$ and $V_y$ therefore requires five voltage measurements. The values obtained by this method and by masking the sample coincide within the experimental error, which tends to confirm our hypothesis that $V_t(B)$ is negligible compared with $V_y(B)$, and $V_t(B^2)$ negligible compared with $V_z(B^2)$. Further confirmation comes from the work of M. C. STEELE, who showed, in an article[21] published after the beginning of our experimental work, that $V_t(B) = 0$, and $V_t(B^2)/V_t(0) < 0{\cdot}005$.

In the measurement of $V_y$ and $V_z$ as a function of the angle $\phi$, the origin of $\phi$ was fixed by determining the position of the sample-holder and graduated disk that made $V_y$ equal to zero ($\phi = \pi/2$). The condition of linearity of $V_y$ and $V_z$ with respect to the light intensity $U$ was checked by determining $V_y$ and $V_z$ as a function of $U$, where $U$ was measured with a photocell. The linearity was also checked by measuring whether the photoconductivity was negligible. The dimensions of

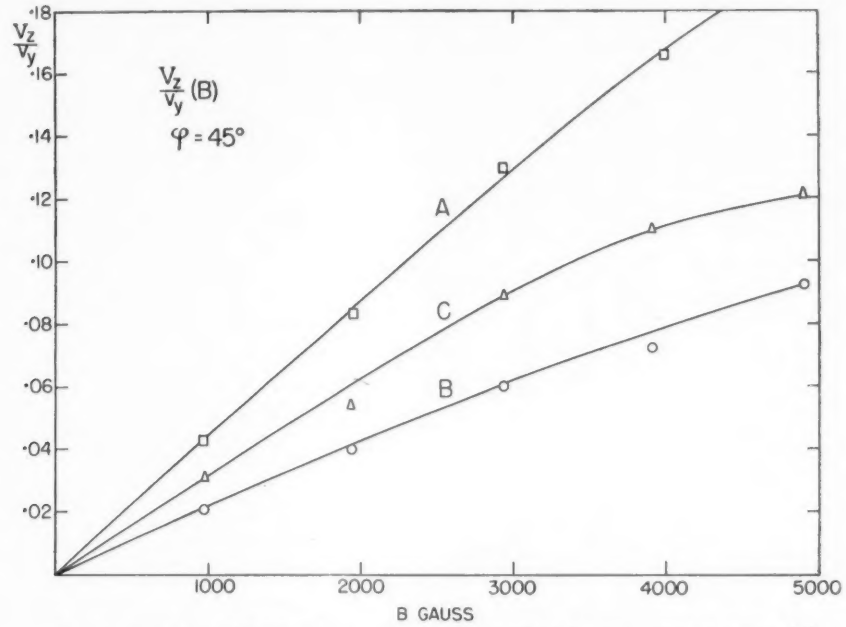


FIG. 3. Quadratic P.E.M. voltage versus magnetic field for non-oriented *n*-type (*A*), intrinsic (*B*), and *p*-type (*C*) germanium.

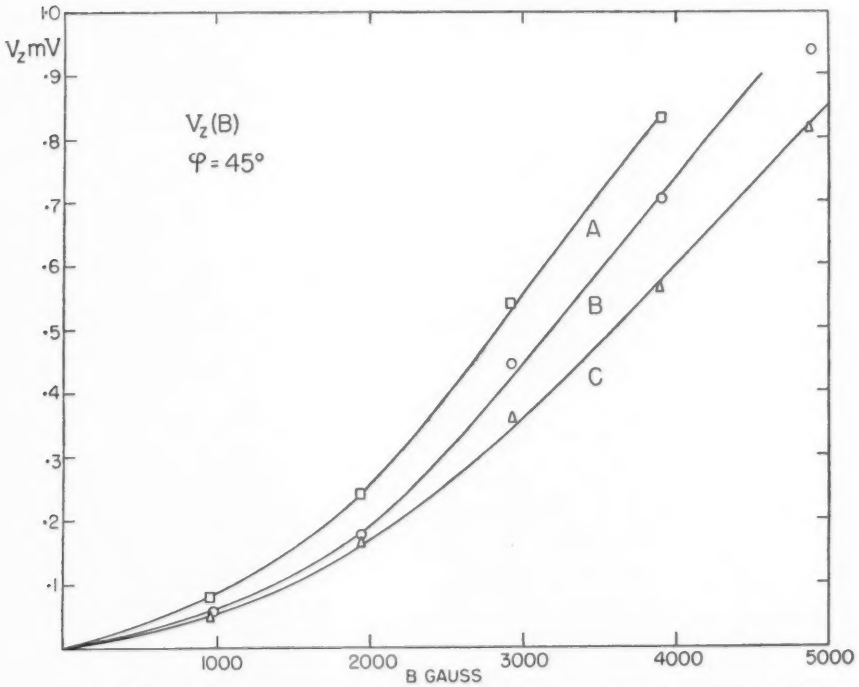


FIG. 4. Ratio of the quadratic to the linear P.E.M. voltage versus magnetic field for non-oriented *n*-type (*A*), intrinsic (*B*), and *p*-type (*C*) germanium.

most of the samples were $1\times1$ cm$\times1$ mm. The ratio $E_z/E_y$ was shown to be independent of the dimensions of the sample by measuring it in two samples of $n$- and $p$-type germanium of different dimensions, but of the same resistivity and orientation. The contacts were soldered to the centers of each of the side faces of the sample. The use of "$n$-type" solder for $n$-type samples prevented the possible formation of $p$–$n$ junctions in the contacts, which would have increased the size of the photo- and thermo-voltages. $p$-type samples were similarly treated.

## 5. RESULTS AND DISCUSSION

(a) *Dependence of $V_y$ and $V_z$ on $B$*

The dependence of $V_z$ and $V_z/V_y$ on $B$, at low light intensity, is shown for samples $A$, $B$, and $C$ in Figs. 3 and 4. $A$ and $C$ were non-oriented samples, $n$- and $p$-type respectively, of approximately 5 $\omega$-cm resistivity, i.e. large enough for the formulae for extrinsic samples to be applicable. The accuracy obtained for these samples in the measurement of the second-order P.E.M. voltage is 3 per cent. $B$ was an intrinsic sample at room temperature. We find that $V_z/V_y$ is negative for all three samples, and proportional to $B$ for fields less than 4000 G, within the experimental error. This agrees with our theory; however, we also note that $V_z/V_y$ is smallest for the intrinsic sample $B$, whereas the following formulae, at first glance, imply that it should be largest there:

$$\frac{-V_z}{V_y}=\frac{B\sin\phi\Delta z}{\Delta y}\times$$

$$\times\left[\frac{\mu_{hH}{}'^2-\mu_{eH}{}'^2}{\mu_{hH}+\mu_{eH}}+e\frac{n\mu_e\mu_{eH}-p\mu_h\mu_{hH}}{\sigma_0}\right]$$

(Sample $B$)

should be larger than for sample $C$ in which

$$\frac{-V_z}{V_y}=\frac{B\sin\phi\Delta z}{\Delta y}\left[\frac{\mu_{hH}{}'^2-\mu_{eH}{}'^2}{\mu_{eH}+\mu_{hH}}-\mu_{hH}\right].$$

(Sample $C$)

The "discrepancy" is explained by the difference in orientation of these samples, which causes $\mu_{eH}{}'$ and $\mu_{hH}{}'$ to be different in each.

(b) *Dependence of $V_z/V_y$ on the shape of the sample*

Measurements of $V_z/V_y$ on samples of the same resistivity and orientation, but of different dimensions, are given in Table 2. They demonstrate the absence of any shape effect.

(c) *Dependence of $V_z$, $V_y$, and $V_z/V_y$ on $\phi$*

Fig. 5 demonstrates the functional dependence of $V_z$ on $\phi$ for sample $C$: $V_z=0{\cdot}54\sin(2\phi+2^\circ)+$ $+0{\cdot}17$, in good agreement with the theory (cf. equation (13)). Fig. 6 demonstrates that the same functional dependence describes samples $A$, $B$, and

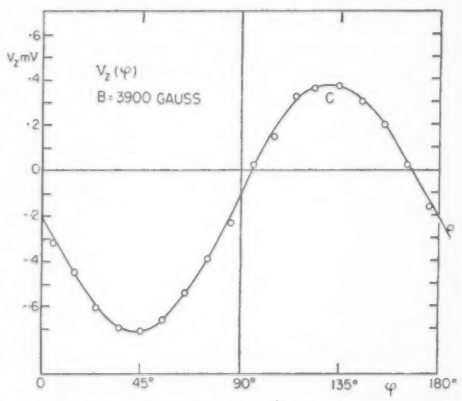


FIG. 5. Quadratic P.E.M. voltage versus angle $\phi$ for $p$-type germanium ($C$).

*Table 2*

| Sample | $\Delta y$(cm) | $\Delta z$(mm) | $t$(mm) | $V_z/V_y$(cm²/V-sec) | Ratio $V_z/V_y$ | Ratio $\Delta z$ |
|---|---|---|---|---|---|---|
| (1) $n$-type | 2 | 5 | 2 | 3400 | 2 : 1 | 2 : 1 |
| $n$-type | 2 | 10 | 2 | 6800 | | |
| (2) $p$-type | 2 | 5 | 2 | 850 | 1·9 : 1 | 2 : 1 |
| $p$-type | 2 | 10 | 2 | 1600 | | |

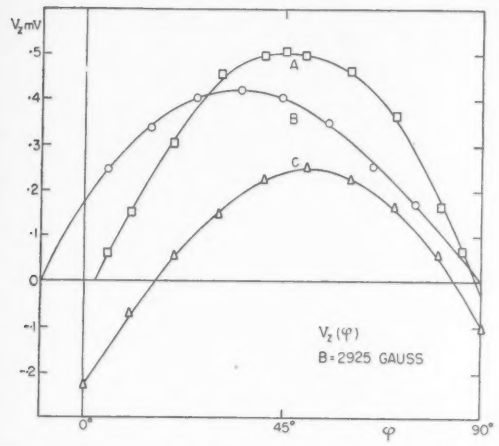


FIG. 6. Quadratic P.E.M. voltage versus angle $\phi$ for non-oriented $n$-type ($A$) intrinsic ($B$), and $p$-type ($C$) germanium.

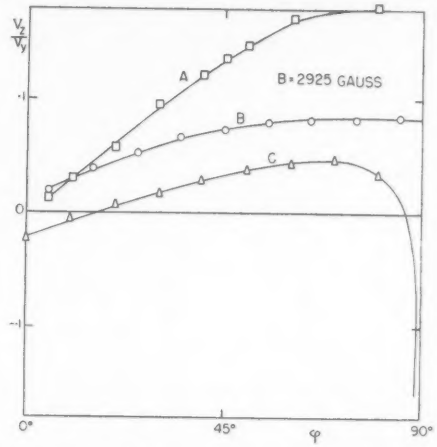


FIG. 8. Ratio of the quadratic to the linear P.E.M. voltages versus angle $\phi$ for non-oriented $n$-type ($A$) intrinsic ($B$), and $p$-type ($C$) germanium.

$C$. Fig. 7 shows $V_y(\phi)$ between 0° and 180° for sample $C$. The voltage $V_y$ is proportional to $\cos\phi$, in agreement with the theory leading to equation (8). In Fig. 8 we show the dependence of $V_z/V_y$ on $\phi$ for samples $A$, $B$, and $C$. For sample $A$ this ratio is, within experimental error, proportional to $\sin\phi$, as the terms proportional to $\sin\phi$:

$$\left[\frac{e(n\mu_e\mu_{eH}-p\mu_h\mu_{hH})}{\sigma_0}+(\mu_{eH}-\mu_{hH})\right]\frac{B\sin\phi\Delta z}{\Delta y}$$

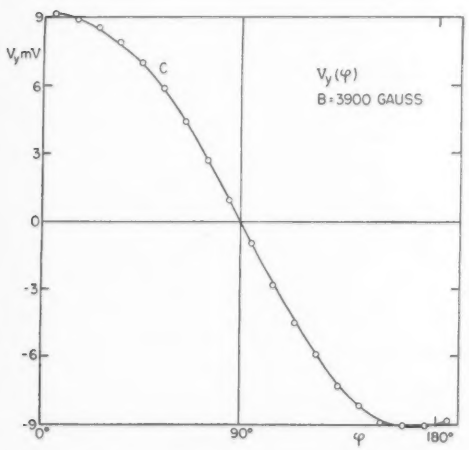


FIG. 7. Linear P.E.M. voltage versus angle $\phi$ for $p$-type, germanium ($C$).

are much larger than the ones of the form

$$\frac{2(G_h-G_e)\sigma_0}{\mu_{eH}+\mu_{hH}}\,\frac{B\Delta z\sin\phi}{\Delta y}.$$

The sum of the terms proportional to $\sin\phi$ is smaller for an extrinsic $p$-type sample. This explains the greater relative deviation of the curve for sample $C$, but a quantitative explanation is impossible for this arbitrarily oriented sample.

(d) *Dependence of $V_z/V_y$ on $U$*

The ratio of $V_z/V_y$ will depend on $U$, since the ratio of electrons to holes in the samples is being altered. Fig. 9 shows this dependence for $n$- and $p$-type oriented samples $R$ and $Q$. Since $V_z/V_y$ will decrease in any sample if the relative number of electrons is increased, the directions of the changes observed are correct. Fig. 10 shows the variation of $V_z/V_y$ with $U$ for two $p$-type samples $Q'$ and $P$ of different orientations. Again we find a decrease in $V_z/V_y$ with increasing $U$, different for the two different orientations. The relative variation of $V_z/V_y$ is large for $Q'$ and $P$, but is of the same absolute magnitude as in samples $R$ and $Q$.

(e) *Dependence of $V_z$ and $V_z/V_y$ on $\phi$ for chosen oriented samples*

Figs. 11 and 12 show the variation of $V_z/V_y$ and $V_z$ with $\phi$ between 0° and 90°, for the same $p$-type

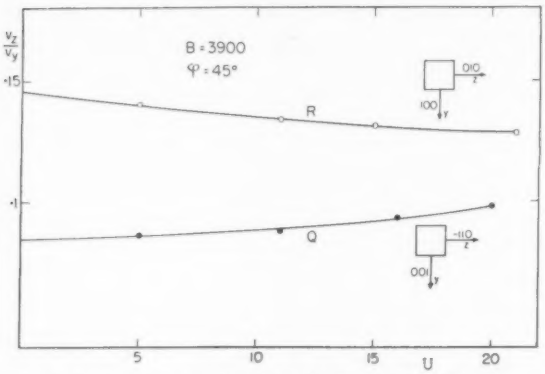


FIG. 9. Ratio of the quadratic to the linear P.E.M. voltages versus light intensity for oriented $p$-type ($Q$) and $n$-type ($R$) germanium.

sample in two different orientations. According to the theory, $V_z/V_y$ is proportional to $\sin\phi$, and $V_z$ to $\sin 2\phi$. The terms $\Delta$ and $g$ of equation (13) are zero. Clearly the experiments confirm the theoretical predictions.

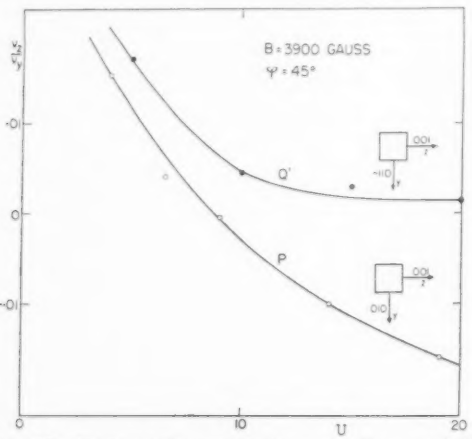


FIG. 10. Ratio of the quadratic to the linear P.E.M. voltages versus light intensity for oriented $p$-type germanium ($P$) and ($Q'$).

(f) *Quantitative interpretation*

So far we have confirmed the functional dependences of $V_z$ and $V_z/V_y$ on $B$, $U$, and $\phi$ in a general fashion. We shall now examine the theoretical and experimental magnitudes of the ratio

$$\frac{V_z}{V_y B \sin\phi} \cdot \frac{\Delta y}{\Delta z}$$

for sample orientations that make $\Delta = g = 0$.

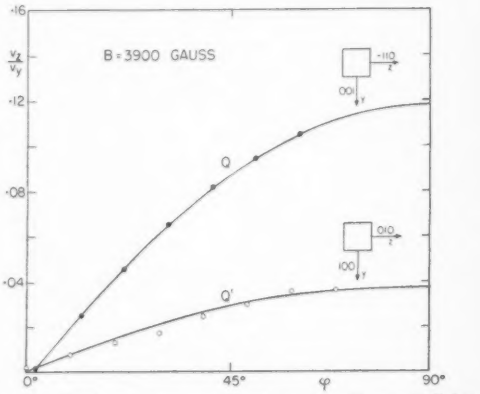


FIG. 11. Ratio of the quadratic to the linear P.E.M. voltages versus angle $\phi$ for oriented $p$-type germanium ($P$) and ($Q'$).

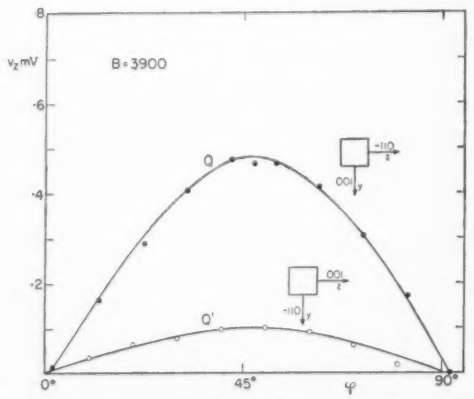


FIG. 12. Quadratic P.E.M. voltage versus angle $\phi$ for oriented $p$-type germanium ($Q$) and ($Q'$).

*Table* 3

| Sample | Material | Resistivity (Ω-cm) | Orientation | | | Temp (°K) | Magnetoresistance coeff. ($10^7$cm$^4$/V$^2$sec$^2$) | | | | | | $-\frac{V_z}{V_y B \sin\phi}\frac{\Delta y}{\Delta z}$ Theoret. expression | cm²/V-sec | |
|---|---|---|---|---|---|---|---|---|---|---|---|---|---|---|---|
| | | | $x$ | $y$ | $z$ | | $b_e$ | $c_e$ | $d_e$ | $b_h$ | $c_h$ | $d_h$ | | Calculated | Experimental |
| $R$ | $n$-Ge | 5 | 100 | 010 | 001 | 300 | 1 | −0·6 | 2·4 | 2·8 | −2·1 | −0·2 | $\frac{\mu_h H^2-\mu_e H^2-c_h+c_e}{\mu_e H+\mu_h H}+\mu_e H$ | 4800 | 5200 |
| $S$ | $n$-Ge | 5 | 110 | 1–10 | 001 | 300 | 1 | −0·6 | 2·4 | 2·8 | −2·1 | −0·2 | $\frac{\mu_h H^2-\mu_e H^2-c_h+c_e}{\mu_e H+\mu_h H}+\mu_e H$ | 4800 | 4700 |
| $S'$ | $n$-Ge | 5 | 110 | 001 | −110 | 300 | 1 | −0·6 | 2·4 | 2·8 | −2·1 | −0·2 | $\frac{\mu_h H^2-\mu_e H^2-c_h+c_e+d_e-d_h}{\mu_e H+\mu_h H}+\mu_e H$ | 9000 | 8500 |
| $P$ | $p$-Ge | 5 | 110 | 010 | 001 | 300 | 1 | −0·6 | 2·4 | 2·8 | −2·1 | −0·2 | $\frac{\mu_h H^2-\mu_e H^2-c_h+c_e}{\mu_e H+\mu_h H}-\mu_h H$ | −600 | −850 |
| $Q$ | $p$-Ge | 5 | 110 | 1–10 | 001 | 300 | 1 | −0·6 | 2·4 | 2·8 | −2·1 | −0·2 | $\frac{\mu_h H^2-\mu_e H^2-c_h+c_e}{\mu_e H+\mu_h H}-\mu_h H$ | −600 | −850 |
| $Q'$ | $p$-Ge | 5 | 110 | 001 | −110 | 300 | 1 | −0·6 | 2·4 | 2·8 | −2·1 | −0·2 | $\frac{\mu_h H^2-\mu_e H^2-c_h+c_e+d_e-d_h}{\mu_e H+\mu_h H}-\mu_h H$ | 2800 | 3300 |
| α | $n$-Si | 5 | 111 | 11–2 | 1–10 | 300 | | | | | | | $\frac{\mu_h H^2-\mu_e H^2-2(G_h-G_e)\sigma_0}{\mu_e H+\mu_h H}+\mu_e H$ | | 3500 |
| α′ | $n$-Si | 5 | 111 | 1–10 | 11–2 | 300 | | | | | | | $\frac{\mu_h H^2-\mu_e H^2-2(G_h-G_e')\sigma_0}{\mu_e H+\mu_h H}+\mu_e H$ | | 1700 |
| β | $p$-Si | 5 | 111 | 11–2 | 1–10 | 300 | | | | | | | $\frac{\mu_h H^2-\mu_e H^2-2(G_h-G_e)\sigma_0}{\mu_e H+\mu_h H}-\mu_h H$ | | 0 |
| β′ | $p$-Si | 5 | 111 | 110 | 112 | 300 | | | | | | | $\frac{\mu_h H^2-\mu_e H^2-2(G_h-G_e)\sigma_0}{\mu_e H+\mu_h H}-\mu_h H$ | | −1800 |

The samples $P$, $Q$, $Q'$, $R$, $S$, $S'$ were used in the orientations marked in Table 3. The magnetoresistance coefficients $b$, $c$, and $d$ were also measured. The magnetoresistance coefficients for electrons were assumed to be the same in $n$- and $p$-type samples; similar assumptions were made for holes. These assumptions will certainly be justified if the relaxation times are mainly determined by lattice scattering; the consistency of our results will confirm this, at least at room temperature. In Table 3 are listed the predicted values for $V_z/V_yB\sin\phi \cdot \Delta y/\Delta z$, using the measured magnetoresistance coefficients and the experimental values of the same quantity at room temperature. The agreement is adequate to demonstrate the validity of our attempt to explain the photoelectromagnetic effects in terms of the magnetoresistance coefficients.

(g) *Other measurements*

The linear and quadratic P.E.M. effects have been observed at room temperature in $n$- and $p$-type oriented silicon samples at 5 ω-cm resistivity. Due to the small recombination time of these samples, the first-order effect is very small, and the second-order effect is observable for $B \sim 5000$ G with an accuracy of only 20 per cent. The results are listed in Table 3.

The linear and quadratic P.E.M. effects have also been observed for the oriented germanium samples at 260 and 160°K. Results are listed in Table 4. The magnetoresistance coefficients were not measured for the experiments mentioned in this section. However, the agreement between theory and experiment can be partially confirmed by means of the following symmetry relations

VOL. 7 1958

*Table* 4

| Sample | Material | Resistivity (Ω-cm) | Orientation | | | Temp (°K) | $-\frac{V_z}{V_yB\sin\phi}\frac{\Delta y}{\Delta z}$ Theoret. expression | cm²/V-sec Experimental |
|---|---|---|---|---|---|---|---|---|
| | | | $x$ | $y$ | $z$ | | | |
| $R$ | $n$-Ge | 5 | 100 | 010 | 001 | 160 | $\frac{\mu_hH^2-\mu_eH^2-c_h+c_e}{\mu_eH+\mu_hH}+\mu_eH$ | 14,000 |
| $R$ | $n$-Ge | 5 | 100 | 010 | 001 | 260 | ,, | 6800 |
| $S$ | $n$-Ge | 5 | 110 | 1–10 | 001 | 160 | ,, | 16,000 |
| $S$ | $n$-Ge | 5 | 110 | 1–10 | 001 | 260 | ,, | 6800 |
| $S'$ | $n$-Ge | 5 | 110 | 001 | −110 | 160 | ,, | 18,600 |
| $S'$ | $n$-Ge | 5 | 110 | 001 | −110 | 260 | ,, | 12,800 |
| $P$ | $p$-Ge | 5 | 100 | 010 | 001 | 160 | $\frac{\mu_hH^2-\mu_eH^2-c_h+c_e}{\mu_eH+\mu_hH}-\mu_hH$ | 0 |
| $P$ | $p$-Ge | 5 | 100 | 010 | 001 | 260 | ,, | 0 |
| $Q$ | $p$-Ge | 5 | 110 | 1–10 | 001 | 160 | ,, | 0 |
| $Q$ | $p$-Ge | 5 | 110 | 1–10 | 001 | 260 | ,, | 0 |
| $Q'$ | $p$-Ge | 5 | 110 | 001 | −110 | 160 | ,, | 4900 |
| $Q'$ | $p$-Ge | 5 | 110 | 001 | −110 | 260 | ,, | 5200 |

$$\left[-\frac{V_z\Delta y}{V_yB\sin\phi\Delta z}\right]_{RS}-\left[-\frac{V_z\Delta y}{V_yB\sin\phi\Delta z}\right]_{S'}=\frac{d_h-d_e}{\mu_{eH}+\mu_{hH}}=\left[-\frac{V_z\Delta y}{V_yB\sin\phi\Delta z}\right]_{PQ}-\left[-\frac{V_z\Delta y}{V_yB\sin\phi\Delta z}\right]_{Q'}$$

$$\left[-\frac{V_z}{V_yB\sin\phi\Delta z}\right]_{RS}-\left[-\frac{V_z\Delta y}{V_yB\sin\phi\Delta z}\right]_{PQ}=\mu_{hH}+\mu_{eH}=\left[-\frac{V_z\Delta y}{V_yB\sin\phi\Delta z}\right]_{S'}-\left[-\frac{V_z\Delta y}{V_yB\sin\phi\Delta z}\right]_{Q'}.$$

The quadratic P.E.M. effect has also been observed in InSb.

## APPENDIX

In order to give an intuitive picture of why $\mu_H'$ is not equal to $\mu_H$, we shall calculate the planar Hall effect using the pictorial kinetic method.[19] The equations of motion for a carrier in the configuration we have described are (sub-section 3c)

$$\left.\begin{aligned}\frac{dV_x}{dt}&=\frac{e}{m}E_x+\omega_0V_y\cos\phi\\ \frac{dV_y}{dt}&=\frac{e}{m}E_y-\omega_0V_x\cos\phi+\omega_0V_z\sin\phi\\ \frac{dV_z}{dt}&=\frac{e}{m}E_z-\omega_0V_y\sin\phi\end{aligned}\right\}\qquad\text{(A-1)}$$

where $V$ is the velocity acquired by a particle under the action of the fields $E$ and $B$, and $\omega_0$ is the cyclotron resonance frequency $eB/m$. In these equations we assume that we have only one type of carrier and that the effective mass is isotropic. The third term in the second equation is, as we shall see, of second degree in $B$, and therefore can be neglected in comparison to the other two terms, which are of first degree. By doing this and integrating these equations, we find

$$V_x+iV_y=\frac{ie}{\omega m}[E_x+iE_y](e^{-i\omega t}-1),$$

$$\text{where } \omega=\omega_0\cos\phi,$$

which gives us for the velocity along $y$

$$V_y=\frac{e}{\omega m}E_x(\cos\omega t-1)+\frac{e}{\omega m}E_y\sin\omega t.$$

Substituting this in the last of equations (A-1), we find:

$$V_z=\frac{e}{m}E_zt-\left[\frac{e}{m}E_x\left(\frac{\sin\omega t}{\omega}-t\right)-\frac{e}{m}E_y\left(\frac{\cos\omega t-1}{\omega}\right)\right]\sin\phi.$$

Using the averaging function

$$\frac{1}{\tau(E)}e^{-t/\tau}\,dt,$$

we find for the average acquired velocity $V_z$ of all particles of initial energy $E$:

$$\bar{V}_z=\frac{e}{m}E_z\tau+\frac{e}{m}\left[E_x\tau-\frac{\tau}{1+\omega^2\tau^2}E_x-E_y\left(\frac{1}{\omega(1+\omega^2\tau^2)}-\frac{1}{\omega}\right)\right]\sin\phi$$

$$=\frac{e}{m}\left[E_z\tau-\left(E_x\frac{\omega^2\tau^3}{1+\omega^2\tau^2}-E_y\frac{\omega\tau^2}{1+\omega^2\tau^2}\right)\sin\phi\right].$$

Averaging this expression for particles of all energies between zero and infinite, we find, writing down the condition that the current along $z$ must be zero:

$$0=E_z\langle\tau\rangle+\left\{\left\langle\frac{\tau^3\omega^2}{1+\omega^2\tau^2}\right\rangle\times E_x-\left\langle\frac{\omega\tau^2}{1+\omega^2\tau^2}\right\rangle E_y\right\}\sin\phi$$

that is

$$E_z=\left\{E_y\omega\frac{\left\langle\frac{\tau^2}{1+\omega^2\tau^2}\right\rangle}{\langle\tau\rangle}-E_x\omega^2\frac{\left\langle\frac{\tau^3}{1+\omega^2\tau^2}\right\rangle}{\langle\tau\rangle}\right\}\sin\phi$$

and substituting the value of the first-order Hall effect

$$E_y=\Theta_HE_x=\left\langle\frac{\tau^2}{1+\omega^2\tau^2}\right\rangle\frac{Be}{m\langle\tau\rangle}E_x\cos\phi$$

we finally find

$$E_z=\frac{e^2}{m^2}E_x\left\{\frac{\left\langle\frac{\tau^2}{1+\omega^2\tau^2}\right\rangle^2}{\langle\tau\rangle^2}-\frac{\left\langle\frac{\tau^3}{1+\omega^2\tau^2}\right\rangle}{\langle\tau\rangle}\right\}B^2\sin\phi\cos\phi.$$

Assuming that the magnetic field is small, we find

$$E_z = \frac{E_x e^2}{m^2}\left[\frac{\langle\tau^2\rangle^2}{\langle\tau\rangle^2} - \frac{\langle\tau^3\rangle}{\langle\tau\rangle}\right]B^2\frac{\sin 2\phi}{2}.$$

In this expression,

$$\frac{e^2}{m^2}E_x\frac{\langle\tau^2\rangle^2}{\langle\tau\rangle^2}B^2\frac{\sin 2\phi}{2}$$

is the fraction of the effect due to the current produced directly by the electric field along $y$, while the fraction:

$$\frac{e^2}{m^2}E_x\frac{\langle\tau^3\rangle}{\langle\tau\rangle}B_2\frac{\sin 2\phi}{2}$$

is due to the current along $x$ deviated twice by the magnetic field. Considering that the effect can be written in a phenomenological way:

$$E_z = -E_x[\mu_H{}'^2 - \mu_H{}^2]B^2\frac{\sin 2\phi}{2} \qquad \text{(A-2)}$$

where the mobilities $\mu_H'$ are the same ones previously defined, we find that

$$\mu_H = \frac{e}{m}\frac{\langle\tau^2\rangle}{\langle\tau\rangle}\mu_H{}' = \frac{e}{m}\left[\frac{\langle\tau\rangle^3}{\langle\tau\rangle}\right]^{\frac{1}{2}}\frac{e}{m}\left[\frac{\langle\tau^3\rangle}{\langle\tau\rangle}\right]^{\frac{1}{2}}$$

or

$$\mu_H{}'^2 - \mu_H{}^2 = \frac{e^2}{m^2}\frac{\langle\tau^2\rangle^2}{\langle\tau\rangle^2}\left[\frac{\langle\tau\rangle\langle\tau^3\rangle}{\langle\tau^2\rangle^2} - 1\right]$$

$$= \frac{e^2}{m^2}\frac{\langle\tau^2\rangle^2}{\langle\tau\rangle^2}\xi = \mu_H{}^2\xi \qquad \text{(A-3)}$$

where $\xi$ is the transverse magnetoresistance coefficient given by

$$\xi = \frac{\langle\tau\rangle\langle\tau^3\rangle}{\langle\tau^2\rangle^2} - 1.*$$

*Acknowledgements*—Grateful acknowledgement is made of helpful discussions on the observation and interpretation of the P.E.M. effects, with Professors Harvey Brooks and José Balta and Drs. M. G. Holland, M. I. Nathan, A. C. Smith, and D. M. Warschauer. The performance of these experiments would not have been possible without the considerable aid given by Lincoln Laboratory in providing suitable oriented samples of germanium.

* After this work was completed our attention was drawn to publications by Kikoin and Bykovsky[24] dealing with several aspects of the same phenomena.

## REFERENCES

1. Kikoin I. K. and Noskov M. M. *Phys. Z. Sowjet.* **5,** 586 (1934); **6,** 478 (1934).
2. Frenkel J. *Phys. Z. Sowjet.* **5,** 597 (1934); **8,** 185 (1935).
3. Aigrain P. and Bulliard H. *C.R. Acad. Sci., Paris* **236,** 595, 672 (1953).
4. Bulliard H. *Ann. Phys., Paris* **15,** 52 (1954).
5. Moss T. S., Pincherle L. and Woodward A. M. *Proc. Phys. Soc.* **B66,** 743 (1953).
6. Oberly J. J. *Phys. Rev.* **93,** 911 (1954).
7. Moss T. S. *Proc. Phys. Soc.* **B66,** 993 (1954); *Physica* **20,** 989 (1954).
8. Kurnik S. W., Strauss A. J. and Zitter R. N. *Phys. Rev.* **94,** 1791 (1954).
9. Bulliard H. *Phys. Rev.* **94,** 1564 (1954).
10. Grossvalet G. *Ann. Radioélect.* **9,** 360 (1954).
11. Aigrain P. *Ann. Radioélect.* **9,** 219 (1954).
12. van Roosbroeck W. *Phys. Rev.* **101,** 1713 (1956).
13. Anselm A. I. *Zh. tekh. fiz.* **24,** 2064 (1954).
14. Buck T. M. and McKim F. S. *Phys. Rev.* **106,** 904 (1957).
15. Aigrain P. and Garretta O. *C.R. Acad. Sci., Paris* **238,** 1573 (1954).
16. Pincherle L. *Photoconductivity Conference* (Ed. R. G. Breckenridge, B. R. Russell and E. E. Hahn) p. 307. Wiley, New York (1956).
17. Garreta O. and Grosvalet J. *Progress in Semiconductors* (Ed. A. F. Gibson, P. Aigrain and R. E. Burgess) Vol. 1, p. 167. Wiley, New York (1956).
18. Goldberg C., Adams E. and Davis R. *Phys. Rev.* **105,** 865 (1956).
19. Dingle R. B. *Physica* **22,** 671 (1956).
    Brooks H. *Advances in Electronics and Electron Physics* Vol. 7 (1955).
20. Seitz F. *Phys. Rev.* **79,** 372 (1950).
21. Steele M. C. *Phys. Rev.* **107,** 81 (1957).
22. Pearson G. L. and Suhl H. *Phys. Rev.* **83,** 768 (1951).
23. Dember H. *Phys. Z.* **32,** 557, 856 (1931); **33,** 207 (1932).
    Grozinger G. and Aron J. *Phys. Rev.* **100,** 978 (1955).
24. Kikoin I. K. and Yu. A. Bykovsky *Dokl. Akad. Nauk. SSSR* **109,** 735 (1956); **116,** 381 (1957).

*J. Phys. Chem. Solids* Pergamon Press 1958. Vol. 7. pp. 141–145.

# COMPARISON OF RADIO-COPPER AND HOLE CONCENTRATIONS IN GERMANIUM

**KATHERINE WOLFSTIRN and C. S. FULLER**

Bell Telephone Laboratories, Incorporated Murray Hill, New Jersey

(*Received* 7 *April* 1958; *in revised form* 12 *May* 1958)

VOL. 7 1958

**Abstract**—The changes in carrier concentration which occur when $^{64}Cu$ is introduced into $p$- and $n$-type germanium containing known concentrations of gallium and arsenic have been determined by resistivity measurements. The results for four different $^{64}Cu$ concentrations indicate the presence of three ionization levels. Although the precise positions of the levels cannot be determined, graphical solutions employing the level scheme of WOODBURY and TYLER[1] are shown to be reasonably consistent with the results.

## INTRODUCTION

WOODBURY and TYLER[1] report three acceptor energy levels for copper in germanium at 0·04 0·32, and 0·44 eV above the valence band.* The positions of these ionization levels determine the change in carrier concentration when Cu is introduced into Ge containing known concentrations of acceptor or donor elements. In this work the changes in carrier concentration for four $^{64}Cu$ concentrations, as determined by radiochemical analysis, were measured in both gallium-doped Ge and in arsenic-doped Ge by means of resistivity measurements. The results are found to be in reasonable agreement with calculations based on the published[1] values for the ionization energy levels for copper in Ge.

## PROCEDURE AND RESULTS

Two series of germanium specimens ($1·5\times0·1\times\times0·4$ cm$^3$) were prepared. One series contained 3·7 to $3·9\times10^{16}$ cm$^{-3}$ Ga and the other series 2·7 to $3·3\times10^{16}$ cm$^{-3}$ As (see Table 1). All specimens were first lapped on No. 400 Aloxite abrasive paper. A visible plate of $^{64}Cu$ was next applied to two opposite faces. One copper-plated gallium-doped and one copper-plated arsenic-doped specimen were placed in each of eight quartz tubes under about $10^{-3}$ atm. air pressure. Two tubes were placed in each of four furnaces maintained at 904°, 857°, 780° and 726°C and heated for 2 hr, 16¼ hr, 16¼ hr, and 16¼ hr, respectively. These times were calculated to ensure saturation at the respective temperatures. After a fast quench, the samples were removed from the tubes and cleaned of excess surface copper. Resistivities were determined at 25°C by the two-point probe method both before and after the heating.

The carrier concentration ($n$ or $p$) was derived from the relations: $1/\rho_n = qn\mu_n$ and $1/\rho_p = qp\mu_p$ where $\rho_n$ and $\rho_p$ are resistivities (25°C) in ohm cm, $q = 1·6\times10^{-19}$ coulombs, $n$ and $p$ are the number of electrons or holes per cm$^3$, and $\mu_n$ and $\mu_p$ are the mobilities[2] of the electrons and holes in cm$^2$/volt sec corrected for ionized impurity scattering. Table 1, column 11 lists the values of $\Delta c$, the total change in carrier concentration, for each specimen after saturation with Cu. In the case of specimens 4 and 8 of Table 1, an additional correction for the scattering by the multiply-charged copper ions was introduced.†

After the resistivity measurements were completed, each specimen was crushed and the total copper concentration measured by counting the radioactive $^{64}Cu$ by the usual techniques.[3] The results are given in Table 1, column 6.

* An energy gap value of 0·70 eV has been assumed.

† Such a correction in the cases of the other specimens can be neglected.

The average error in the resistivity measurements is about $\pm 1$ per cent. Because of the uncertainties in the mobilities of the carriers, the error in the carrier concentrations is estimated as $\pm 5$ per cent. Individual determinations of radio-copper concentration are precise to $\pm 5$ per cent. Variations in dislocation densities from specimen to specimen in the crystal introduce additional errors which are difficult to estimate. However, the fact that the resistivity and radio-copper determinations are made on the same specimens minimizes errors from this source. The crystals employed had etch pit densities between 20–40 per mm$^2$. Because the ratio of the change in carrier concentration to the radio-copper concentration involves both a difference between two carrier concentrations as well as the radio-copper concentration, it is subject to larger error. A maximum error of $\pm 15$ per cent in this ratio (next to last column Table 1), could exist.

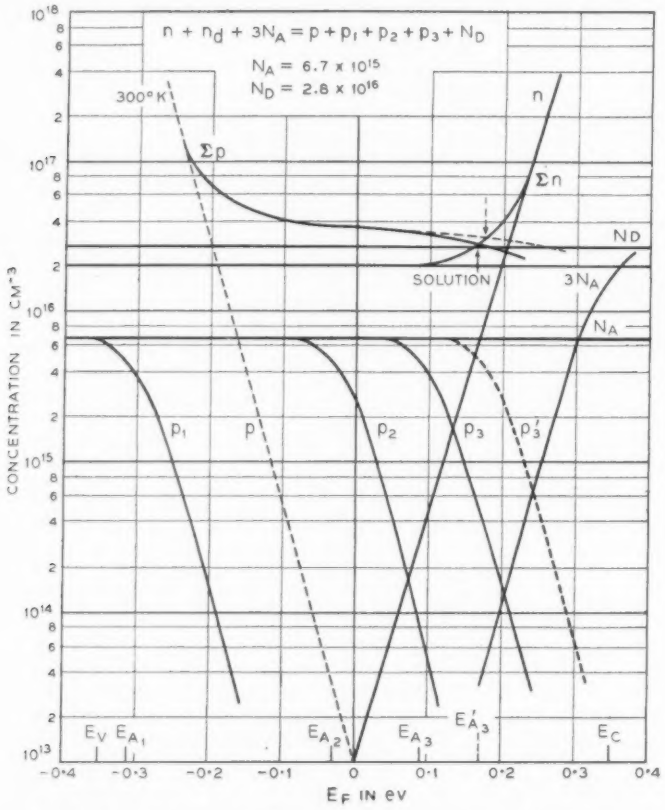


FIG. 1. Graphical solution for the Fermi level position for specimens No. 4 and No. 8 (averaged) in Table 1. Full lines show solution based on ref. (1). Dashed lines and arrow shows solution which is in better agreement with present results.

## DISCUSSION OF RESULTS

In Table 1, columns 6 and 11, the total copper as determined by radiochemical analysis and the change in carrier concentration, $\Delta c$, from electrical measurements agree within experimental error for all specimens which are $p$-type after copper saturation. This is shown by column 12, Table 1, which gives the ratio of $\Delta c$ to $^{64}$Cu concentration,

VOL. 7 1958

*Table* 1

| Crystal | Doping | Specimen number | Time (hr) | Temp. (°C) | Total $^{64}$Cu atoms/cm$^3$ | Orig. type | Orig. carrier conc. (cm$^{-3}$) | Final type | Final carrier conc. (cm$^{-3}$) | Change in carrier conc. $\Delta c$ | Av. ratio $\Delta c$ to $^{64}$Cu | Change in carrier conc. $\Delta c$ (cm$^{-3}$) (calc.)† |
|---|---|---|---|---|---|---|---|---|---|---|---|---|
| Ge IV–779 | As | 1 | 2 | 904 | $3{\cdot}4\times10^{16}$ | N | $2{\cdot}8\times10^{16}$ | P | $6{\cdot}6\times10^{15}$ | $3{\cdot}5\times10^{16}$ | | |
| | | 5 | | | 3·3 | N | 2·8 | P | 5·6 | 3·4 | 1·0 | |
| Ge VIII–950 D | Ga | 9 | | | 3·6 | P | 3·9 | P | $6{\cdot}9\times10^{16}$ | 3·0 | | |
| | | 13 | | | 3·3 | P | 3·9 | P | 7·1 | 3·2 | 0·9 | |
| Ge IV–779 | As | 2 | $16^{1/4}$ | 857 | $3{\cdot}4\times10^{16}$ | N | $2{\cdot}8\times10^{16}$ | P | $5{\cdot}4\times10^{15}$ | $3{\cdot}3\times10^{16}$ | | |
| | | 6 | | | 3·3 | N | 3·3 | P | 4·6 | 3·8 | 1·1 | |
| Ge VIII–950 D | Ga | 10 | | | 3·1 | P | 3·8 | P | $6{\cdot}9\times10^{16}$ | 3·1 | | |
| | | 14 | | | 3·2 | P | 3·7 | P | 7·1 | 3·4 | 1·0 | |
| Ge IV–779 | As | 3 | $16^{1/4}$ | 780 | $1{\cdot}7\times10^{16}$ | N | $2{\cdot}8\times10^{16}$ | N | $1{\cdot}3\times10^{14}$ | $2{\cdot}8\times10^{16}$ | 1·7 | $2{\cdot}95\times10^{16}$ |
| | | 7 | | | 1·4 | N | 2·7 | N | 1·9 | 2·7 | 1·8 | 2·62 |
| Ge VIII–950 D | Ga | 11 | | | 1·4 | P | 3·8 | P | $5{\cdot}0\times10^{16}$ | 1·20 | | |
| | | 15 | | | 1·3 | P | 3·7 | P | 4·9 | 1·20 | 0·9 | |
| Ge IV–779 | As | 4 | $16^{1/4}$ | 726 | $7{\cdot}2\times10^{15}$ | N | $2{\cdot}7\times10^{16}$ | N | $1{\cdot}2\times10^{16}$ | $1{\cdot}5\times10^{16}$ | 2·1 | $1{\cdot}94\times10^{16}$ |
| | | 8 | | | 6·2 | N | 2·8 | N | 1·2 | 1·6 | 2·6 | |
| Ge VIII–950 D | Ga | 12 | | | 6·6 | P | 4·0 | P | $4{\cdot}3\times10^{16}$ | 0·3* | | |
| | | 16 | | | 7·0 | P | 3·9 | P | 4·6 | 0·7 | 1·0 | |

* This run does not appear in average.

† Based on WOODBURY and TYLER[1].

averaged for each pair of specimens. The average of this ratio for all of the $p$-type specimens is 1·0.

The closeness of the agreement (within an average error of $\pm 10$ per cent) between the number of copper atoms and the number of holes indicates that the concentrations of interstitial copper at equilibrium is fairly low in Ge compared to the substitutional copper. Previous work[4] showed that under transient conditions, considerably more radio-copper than acceptor-copper is present. However, the distribution of copper under these conditions is quite non-uniform and a reliable comparison is difficult. TWEET,[5] on the basis of precipitation experiments, finds a substitutional-interstitial ratio of approximately 6 at 715°C. The present results would suggest a ratio of at least 20.

In the case of specimens No. 4 and No. 8, which are strongly $n$-type, approximately 2·5 holes are produced per Cu atom added, corresponding to the presence of both doubly and triply-charged copper ions. Thus at least three acceptor energy levels are introduced into germanium by copper. Taking the average results for specimens No. 4 and No. 8, we have made a graphical solution for the Fermi level according to the method of SHOCKLEY.[6] This is shown in Fig. 1, in which the positions of the three acceptor levels of WOODBURY and TYLER[1] (0·04 eV and 0·32 eV from the valence band and 0·26 eV from the conduction band) have been inserted. The solution employing those levels predicts a somewhat higher value for the change in carrier concentration ($1{\cdot}94 \times 10^{16}$

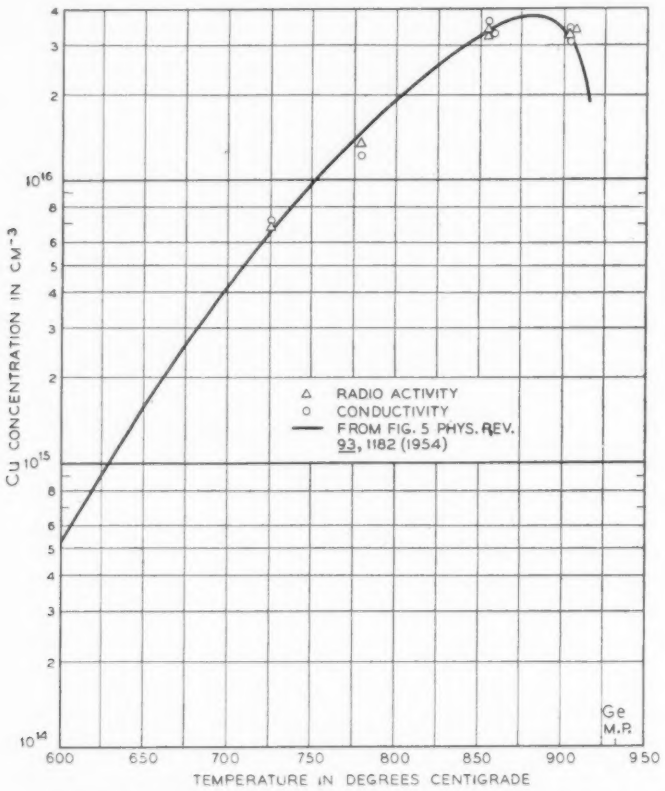


FIG. 2. Comparison of the radio-copper determinations (triangles) and the resistivity determinations (open circles) of the solubility of Cu with previously published results[7] as shown by solid curve.

cm$^{-3}$) than is observed ($1{\cdot}58\times10^{16}$ cm$^{-3}$). Agreement with experiment can be obtained if the highest level is shifted upward to a position 0·18 eV from the conduction band. It is interesting that WOODBURY and TYLER[1] likewise observed a level approximately in this position in some *n*-type specimens. The calculated results are shown in the last column of Table 1 and are to be compared with the second from the last column.

Similar graphical solutions (not shown) have been carried out for specimens No. 3 and No. 7 shown in Table 1. From the position of the Fermi level in each case, the number of occupied states is calculated to be $2{\cdot}95\times10^{16}$ cm$^{-3}$ and $2{\cdot}62\times10^{16}$ cm$^{-3}$, respectively for No. 3 and No. 7. These figures are in good agreement with the $\Delta c$ values of $2{\cdot}8\times10^{16}$ cm$^{-3}$ and $2{\cdot}7\times10^{16}$ cm$^{-3}$ determined electrically as shown in Table 1. In this case, because of the lower position assumed by the Fermi level, only singly and doubly charged copper ions are present. Again the observed carrier change imposes restrictions on the level positions. Thus the middle and upper levels cannot be shifted downwards very far, nor can the middle level be moved upwards appreciably without also shifting similarly the upper level. The latter can of course be shifted independently upwards, but not appreciably beyond the position 0·18 eV from the conduction band mentioned above for specimens No. 4 and No. 8.

The results of Table 1 are therefore consistent with three acceptor levels for copper in germanium at approximately the positions stated by WOODBURY and TYLER.[1] Shifts of the second level greater than about $-0{\cdot}1$ or $+0{\cdot}05$ eV from the 0·32 eV assignment[1] would be inconsistent with the present results. Also a position for the upper level within about $\pm0{\cdot}025$ eV of 0·18 eV from the conduction band fits the data of Table 1 better than the assignment of 0·28 eV.[1]

Fig. 2 is a plot of the number of copper atoms, per cm$^3$ against temperature in °C as determined both by resistivity measurements and by the radiochemical method. Only the *p*-type specimens of Table 1 are represented. These data are seen to be in agreement with previous solubility values of copper in germanium in the temperature range 725–900°C.[7]

As indicated previously, the purpose of the present work was not to attempt to determine the ionization energy levels of copper in germanium. This is best done by other methods. However, because the number of copper atoms is here measured by the radiochemical method, the results do provide a useful and independent way of testing the predictions of energy level schemes determined by these other methods. Except for the possibility that the upper copper ionization level may require a shift of about 0·1 eV closer to the conduction band, the present results are in agreement with the published level positions.[1] However, it should be emphasized that this latter requirement involves the assumption of the presence of multiply-charged scattering ions. Such increased scattering, over singly charged or neutral impurities, would not occur if a pairing of ions of opposite signs takes place. Although such a possibility seems unlikely in the present case, its occurrence cannot be excluded.

*Acknowledgement*—The authors are indebted to their colleagues at Bell Laboratories for useful comments and to the reviewer for calling attention to some needed mobility corrections in the calculations of the carrier concentrations.

## REFERENCES

1. WOODBURY H. H. and TYLER W. W. *Phys. Rev.* **105,** 84 (1957).
2. PRINCE M. *Phys. Rev.* **92,** 631 (1953).
3. HOFFMAN R. E. *Atom Movements* p. 51. Amer. Soc. Metals, Cleveland, Ohio (1951).
4. FULLER C. S. and DITZENBERGER J. A. *J. Appl. Phys.* **28,** 40 (1957).
5. TWEET A. G. *Phys. Rev.* **106,** 221 (1957).
6. SHOCKLEY W. *Electrons and Holes in Semiconductors* p. 465. van Nostrand, New York (1950).
7. FULLER C. S., STRUTHERS J. D., DITZENBERGER J. A. and WOLFSTIRN K. B., *Phys. Rev.* **93,** 1182 (1954).

*J. Phys. Chem. Solids* Pergamon Press 1958. Vol. 7. pp. 146–152.

# ENERGY TRANSFER IN ZnS:Cu:Cl PHOSPHORS

**N. T. MELAMED**

Westinghouse Research Laboratories, Pittsburgh 35, Pennsylvania

(*Received* 19 *February* 1958; *in revised form* 1 *April* 1958)

**Abstract**—The transfer of energy from blue to green emitting centers has been studied in ZnS : Cu : Cl phosphors. It appears that energy can be transported even at low temperatures and low impurity concentrations. An estimate of the energy transfer expected from a resonance process through electric dipole–dipole interaction, yields values for energy transfer which are much lower than these observed. Several possible transfer mechanisms are discussed.

VOL
7
195

## 1. INTRODUCTION

Of considerable interest in the understanding of luminescence is a knowledge of those processes by which energy is transported within a phosphor from one activator to another. In the non-photoconducting phosphors, energy transport is mainly regarded as due to a resonance process. In the photoconducting phosphors, on the other hand, particularly in the sulfides of zinc and cadmium, the transport of energy has usually been described by means of an energy-band model in terms of the motion of free electrons and holes.

Despite the success of the band model, and its applications by Schön,[1] Klasens[2, 16] and others in interpreting many of the observed features of photoconducting phosphors, the possibility exists that other transfer mechanisms may play a role. This possibility has been recognized by Shionoya and by Shionoya and Amano.[3] In two recent publications, these authors have presented what they believe to be evidence for a resonance transfer process in ZnS containing copper or lead with manganese. They arrived at their conclusions by observing that when a phosphor was irradiated in the excitation band of copper or lead, an emission characteristic of manganese could be obtained.

The present paper describes a study of energy transfer between the blue and green emitting centers of ZnS : Cu : Cl. The blue centers are believed to consist of zinc vacancies, while the green centers have been attributed to substitutional copper impurities.[4,5] The study is confined to a region of low impurity concentrations, and covers a range of temperature from room temperature to 4°K. We find that transfer occurs at very low concentrations and at low temperatures. In the ZnS : Cu : Cl phosphor, we do not think transfer is due to a resonance process.

## 2. ENERGY-TRANSFER PROCESSES

(a) *Photoconductive transfer*

In Fig. 1 is shown an often-used energy-level diagram for the blue and green centers in ZnS : Cu : Cl, in which details such as traps and non-radiative centers have been omitted. Without reference to a particular mathematical treatment

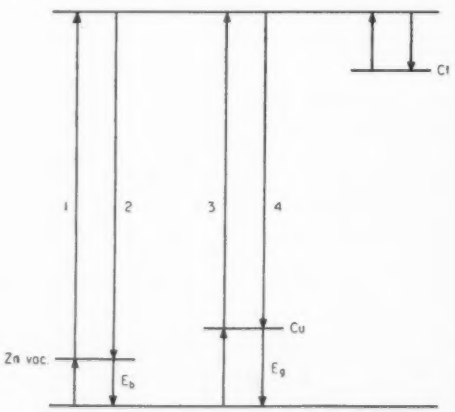


Fig. 1. Simplified energy-level diagram for the blue- and green-emitting ZnS : Cu : Cl phosphor. Transitions 1 and 3 refer to excitation, 2 and 4 to emission.

based on this diagram, the transfer process with which we are concerned may be described as follows: Absorption of radiation in blue centers results in the creation of free electrons, and of holes trapped at the blue impurity levels. Recombination of free electrons with the bound holes results in blue emission. At room temperature, however, we may expect a number of bound holes to be thermally excited into the valence band, wherein they may diffuse towards other blue centers or be captured by green centers. The creation of free electrons and holes at blue centers, and their recombination at green centers results in a transfer of energy.

The relative efficiency of the photoconductive transfer process will depend principally on the relative concentrations of blue and green centers, increasing with an increase in the ratio of green to blue centers, and on the temperature. In particular, we expect that the effectiveness of the electron–hole transfer mechanism will decrease rapidly with decreasing temperatures, since at temperatures such that $kT \ll E_B$, virtually no free holes will be created by direct irradiation into the blue excitation band.

(b) *Resonance transfer*

By resonance transfer we refer to a process whereby energy is transferred from one impurity to a nearby impurity through the interaction of their electric or magnetic dipole or quadrupole fields. The description which follows is based on a theoretical treatment by DEXTER.[6] The transfer of energy occurs by means of the following steps: (1) excitation of a center through the absorption of a photon, (2) relaxation of the lattice about the excited center, (3) transfer of the excitation energy to a nearby center through the electric dipole or quadrupole field, resulting in the excitation of the second center, (4) relaxation about the first center to a state similar to its initially unexcited state, and (5) emission of a photon from the second center. The transfer probability, $P_{bg}$, for a dipole–dipole interaction, is given by DEXTER as

$$P_{bg} = \frac{3\hbar^4 c^4 Q_g}{4\pi R^6 n^4 \tau_b} \left( \frac{\mathscr{E}}{\kappa^{\frac{1}{2}} \mathscr{E}_c} \right)^4 \int \frac{f_b(E) F_g(E)}{E^4} dE \quad (1)$$

where $\tau_b$ is the lifetime of an excited blue center, $n$ is the refractive index, $(\mathscr{E}/\mathscr{E}_c)$ is the ratio of the electric field in an impurity atom to that in the crystal, and $\kappa$ is the dielectric constant. $f_b(E)$ is the relative number of quanta of blue emitted as a function of energy in electron volts, and $F_g(E)$ is the analogous function for the green absorption. The integral, $\int f_b(E) F_g(E)\, dE$, is therefore the energy overlap between the green absorption and blue emission bands, normalized under the conditions that $\int f_b(E)\, dE = 1$ and $\int F_g(E)\, dE = 1$. $Q_g = \int \sigma_g(E)\, dE$, and is measured as the area under the absorption curve, with $\sigma_g(E)$, the absorption cross-section of an impurity atom, measured as the ratio of the absorption coefficient to the number of impurity centers per unit volume. The separation distance between centers is $R$.

The efficiency of a dipole–dipole transfer process depends, among other variables, on the overlap between the emission band of the activator which absorbs the primary photon and the absorption band of the impurity to which transfer takes place, and on the optical absorption cross-section of the externally excited activator. It follows from the $1/R^6$ term in equation (1) that the transfer yield will also be strongly dependent on the distance between near-neighbor impurity atoms. Because of the absence in equation (1) of a term for temperature, the transfer probability is to a first approximation temperature-independent; the primary source of temperature-dependence lies in a thermal shift and broadening of the absorption and emission bands. For the ZnS : Cu : Cl phosphors, we expect little or no temperature-dependence for transfer due to resonance, since the emission and absorption bands are virtually unchanged from room temperature to 4°K. This temperature-insensitivity is in marked contrast to the behavior expected for a photoconductive transfer mechanism based on Fig. 1, and may therefore be used as an experimental means for distinguishing between the two mechanisms.

(c) *Cascade transfer*

A cascade process refers to the emission of a photon from one center and its absorption by a second center before it has escaped the phosphor. It will therefore depend on the overlap between the emission and absorption bands of the respective centers. The transfer yield is given by[6]

$$\eta = Av \int f_b(E)[1 - \exp\{-N_g \sigma_g(E) l\}] \quad (2)$$

where the average is performed over the linear dimensions of the crystal. $f_B(E)$ and $\sigma_g(E)$ retain the meaning they had in equation (1); $N_g$ is the number of green centers/cm$^3$.

Transfer by a cascade process will be nearly temperature-independent in ZnS : Cu : Cl for the reasons that apply to resonance transfer. The concentration dependence will be determined by the value of the absorption factor, $[1-\exp(-N_g\sigma_g(E)l)]$. The transfer yield can be estimated from the dimensions of the particle, the shapes of emission and absorption bands, and the absorption cross-section of the green centers.

### 3. EXPERIMENTAL PROCEDURES

The procedure for studying energy transfer consists in optically irradiating into the excitation band of the blue centers and observing the appearance of a green emission. The presence of a green emission implies that energy transport takes place. The ratio of the intensities of the blue and green emissions is a measure of the energy transported.

The phosphors were prepared as powders, in a manner previously described,[5] using luminescence-grade ZnS, Cu $(NO_3)_2$, and a large excess of $NH_4Cl$. The copper concentration was varied between 0 and 0·005 molar per cent.

The apparatus used to obtain the excitation and emission spectra is shown in Fig. 2. The excitation spectra were obtained by irradiating the phosphor

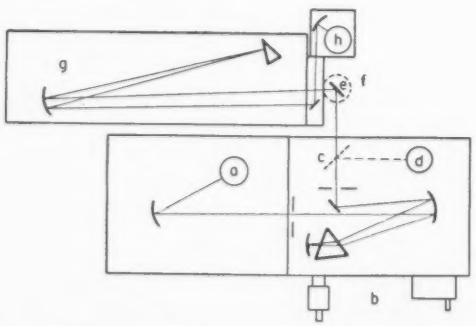


FIG. 2. Apparatus for obtaining excitation and emission spectra. (a) U.V. lamp (H-6); (b) monochromator for excitation (Perkin–Elmer model 98); (c) mirror for alternately exciting and monitoring; (d) thermocouple for measuring excitation intensity; (e) phosphor; (f) dewar; (g) monochromator for measuring emission (Beckman model DU); (h) 1P21 photomultiplier.

with a particular excitation wavelength, and measuring the intensities of the resulting blue and green emission bands at their emission peaks. These intensities were then corrected for the contribution made by one band to the intensity maximum of the other. This process was performed for various wavelengths in the region between 2500 and 4500 Å. Figs. 3, 4, and 5 show the results of such measurements.

The excitation intensity at each wavelength was maintained constant in the number of quanta emitted per second by monitoring the radiation with a bismuth/silver thermocouple. The band width at half intensity-maximum of the excitation radiation varied with wavelength in a manner which depended on the intensity distribution of the ultraviolet source; except for a few points, however, it did not exceed 50 Å.

The emission bands were detected with the aid of a Beckman monochromator whose slit width corresponded to a band width of 6 Å or less over the visible range. The photomultiplier used to measure the emission intensity had previously been calibrated for its spectral response in the visible and near ultraviolet region.

For low-temperature measurements the specimens were inserted into a dewar vessel equipped with transparent fused-silica appendages. To insure accurate temperature control, the samples were immersed in the refrigerant.

### 4. EXPERIMENTAL RESULTS

In Fig. 3 is shown for two temperatures the excitation spectrum of ZnS : Cl. Since this phosphor did not contain copper, only the blue emission was observed. In the long-wavelength region there appears to be an excitation band with a maximum at about 3450 Å, which we attribute to direct excitation of blue centers (transition 1 of Fig. 1). At somewhat shorter wavelengths, in the region of 3200 Å, some structure is present, consisting of one or more relatively narrow bands. The origin of this structure is not certain; similar structure has been observed in a number of semiconductors, for example, CdS,[7] and has been attributed by some to the creation of excitons. Wavelengths below 3200 Å produce transitions across the band gap.[8] For these wavelengths the intensity of the blue emission was only moderately dependent on the excitation wavelength.

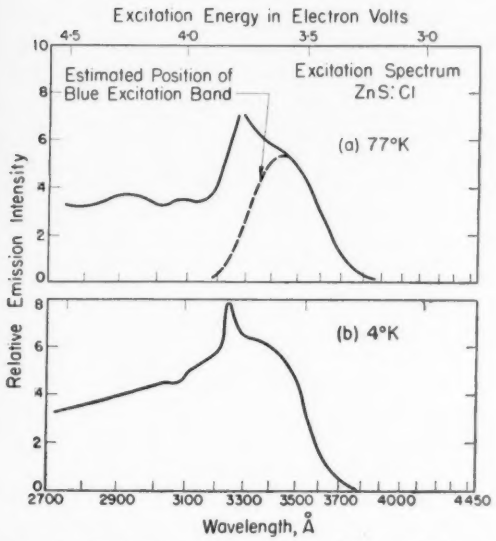


FIG. 3. Excitation spectrum for blue emission of ZnS : Cl.

In Figs. 4 and 5 are shown the excitation spectra of two specimens of ZnS : Cu : Cl containing 0·0001 and 0·001 molar per cent copper, respectively.

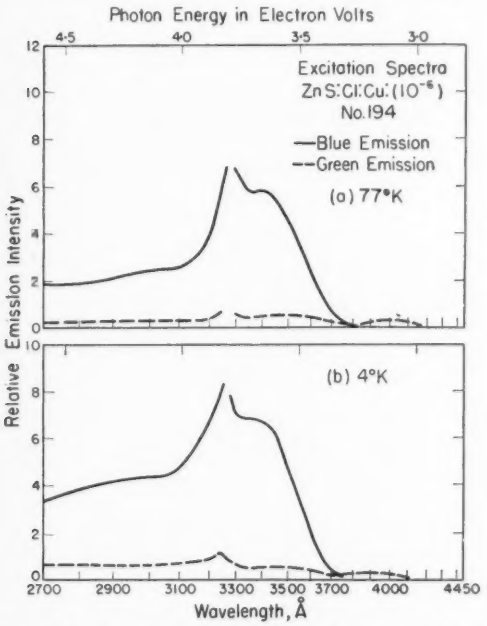


FIG. 4. Excitation spectra for blue and green emissions of ZnS : Cu($10^{-6}$) : Cl.

The incorporation of copper produced a green emission band with a maximum at 5200 Å. The excitation spectrum for the green emission contains two excitation bands in the long-wavelength region. One of these has a maximum at 3900 Å and originates from direct excitation into copper impurity

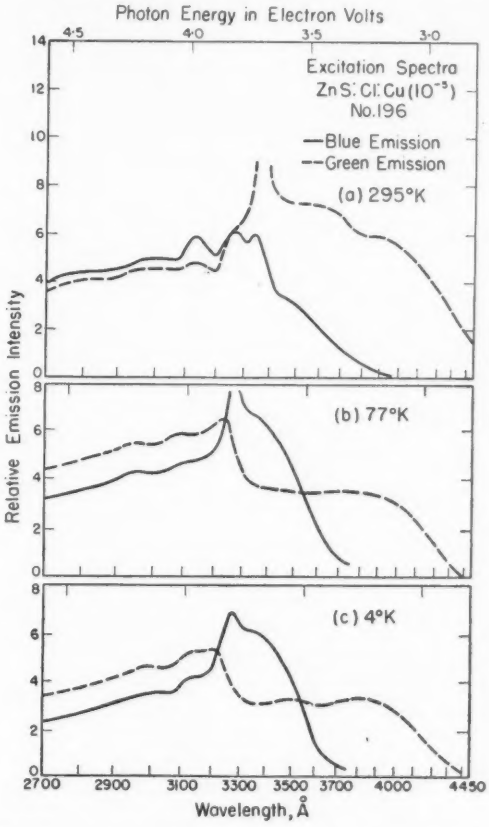


FIG. 5. Excitation spectra for blue and green emissions of ZnS : Cu($10^{-5}$) : Cl.

centers (transition 3 of Fig. 1). The second band has a maximum at 3450 Å, and coincides with the 3450 Å excitation band for the blue emission. We believe the 3450 Å excitation band for the green emission results from absorption of energy by blue centers, with subsequent transfer to green centers. We conclude from these results that energy transfer from blue to green centers takes place in the 3450 Å excitation band.

The temperature-dependence of the transfer

process may be seen by comparing for a given specimen, the ratio of the green to blue emission obtained at several temperatures by 3450 Å excitation. These are shown in Table 1 for specimens

*Table* 1. *Ratio of intensities of green to blue emissions for* 3450 Å *excitation*

| Copper concn. (molar) | $T = 300°K$ | $T = 77°K$ | $T = 4°K$ |
|---|---|---|---|
| $10^{-6}$ | 0·4 | 0·078 | 0·076 |
| $5\times10^{-6}$ | 1 | 0·29 | 0·29 |
| $10^{-5}$ | 1·6 | 0·59 | 0·53 |

having different copper concentrations. It is seen that the intensity of the green emission decreases relative to the blue between room temperature and 77°K, but remains constant from 77 to 4°K. Despite this initial decrease in the green intensity, transfer takes place to a significant extent at low temperatures.

The sensitivity of the transfer process to temperature is much less than can be expected from the energy-level diagram of Fig. 1. Fig. 1 predicts some photoconductive transfer at room temperature. At 77°K, however, the rate at which holes are thermally released from the blue impurity levels should be smaller by a factor of $\exp E_b/k(1/T_1 - 1/T_2)$. At 4°K the thermal release of holes from blue centers should be truly negligible and so, therefore, should be the transfer yield. That this is not so is seen in Table 1. A photoconductive transfer process based on the energy-level diagram of Fig. 1 does not, therefore, account for the observed results.

A resonance transfer process is consistent with the temperature-independence observed at low temperatures, but is not likely at such low copper concentrations provided that the impurities are randomly distributed. Using the expression derived by DEXTER for the transfer probability by dipole–dipole interaction and substituting values appropriate to ZnS : Cu : Cl phosphors, we can calculate the separation distance for which resonance transfer is to be expected.

For ZnS, the refractive index, $n$, is 2·37. In Fig. 6 are shown the blue and green emission and excitation bands normalized to unity at their maxima. The shapes of the emission bands were obtained by direct measurement. The positions of the excitation bands were obtained from the excitation spectra, and are assumed to coincide with the absorption bands for these centers. The value of the

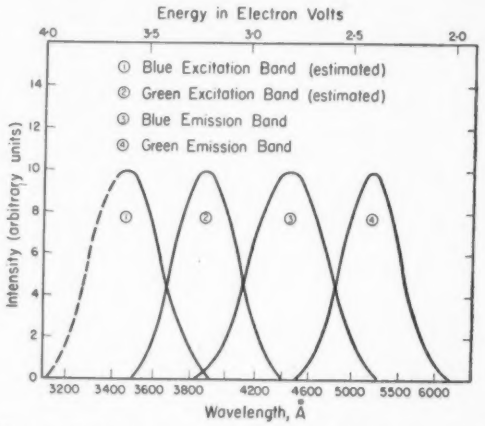


FIG. 6. Emission and excitation bands for the blue and green emissions of ZnS : Cu : Cl normalized to unity at their maxima.

overlap integral, obtained graphically from the blue emission and the green absorption bands, is $\sim 1/20\ \text{eV}^{-1}$, with $E \sim 3$ eV. DEXTER takes $(\mathscr{E}/\kappa^{\frac{1}{2}}\mathscr{E}_c)^4$ to be unity, since the ratio of the average strength of the electric field within the crystal, to that of an isolated atom, $(\mathscr{E}_c/\mathscr{E}) = 1/\kappa^{\frac{1}{2}}$.

It remains to evaluate $Q_g$. Since $Q_g$

$$= \int \sigma_g(E)\,dE = \int \frac{\alpha_g(E)}{N_g}$$

where $N_g$ is the number of green centers per cm$^3$ and $\alpha_g$ is the absorption coefficient of the green absorption band, $Q_g$ can be obtained graphically from the value of the absorption coefficient of the green centers plotted against wavelength energy in electron volts.

The absorption curve for green centers in a specimen containing $2{\cdot}5\times10^{18}$ copper centers/cm$^3$ is shown in Fig. 7. $\alpha_g$ was computed from diffuse reflectance measurements on a powder specimen, using a method developed by JOHNSON.[9] The value of $Q_g$ obtained in this manner is $1{\cdot}2\times10^{-16}$ cm$^2$ eV.

In order for appreciable transfer to take place,

$P_{bg}\tau_b \geqslant 1$. Substituting the above values into DEXTER's expression, one obtains:

$$P_{bg}\tau_b = \left(\frac{21{\cdot}0}{R}\right)^6.$$

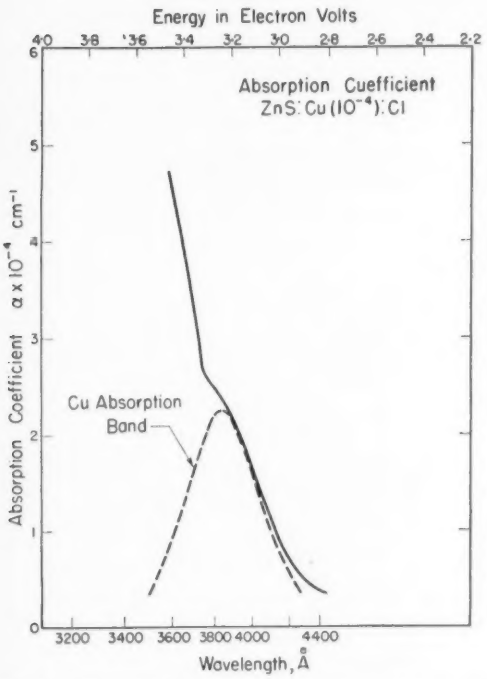
Energy in Electron Volts
4·0 3·8 3·6 3·4 3·2 3·0 2·8 2·6 2·4 2·2
Absorption Cuefficient
ZnS: Cu (10⁻⁴): Cl
Absorption Coefficient α x 10⁻⁴ cm⁻¹
Cu Absorption Band
0 1 2 3 4 5 6
3200 3400 3600 3800 4000 4400
Wavelength, Å

FIG. 7. Absorption band for green emitting centers.

For transfer to take place, therefore, $R \sim 21$ Å, or the blue and green centers must lie about 4 lattice units apart.

The ratio of emitted green to blue quanta resulting from resonance transfer is given by

$$\frac{I_g}{I_b} = \frac{\beta N_g}{1-\beta N_g} \qquad (3)$$

where $\beta = (4/3)\pi R^3 = 3{\cdot}9\times10^{-20}\text{cm}^3$, the volume sensitized by a single blue center. For the specimen shown in Fig. 5 with $N_g = 2{\cdot}5\times10^{17}$ centers/cm$^3$, the green to blue ratio calculated from equation (3) is $I_g/I_b = 0{\cdot}01$. This figure is smaller by a factor of 50 than the ratio of 0·53 observed at the low temperatures.

It is evident, that for randomly distributed impurities, energy transfer by resonance cannot account for the large transfer observed at these concentrations.

## 5. DISCUSSION

The failure of the photoconductive and resonance transfer mechanisms, in the simplest set of circumstances, to account for the observed transfer leaves the cascade process as the remaining possibility. A calculation of the transfer expected by cascade involves considerable difficulties in the case of powders. In particular, it requires a detailed description of the internal and external reflections. While this can be done in principle, by extending JOHNSON's treatment[9] for the reflectance of powder samples to the case where the light originates in the powder itself,[10] the results would still be subject to considerable uncertainty. It is felt therefore that a cascade process remains as a possible transfer mechanism.

There are, however, a number of reasonable complicating elements which make other transfer mechanisms possible. One possibility is that the blue and green centers are not randomly distributed. PRENER and WILLIAMS[11] have suggested that the green centers consist of associated copper and chlorine impurities at next-nearest neighbor sites. Without referring to their particular model, it is clear that a close association between the blue and green centers could require a major revision of some of the foregoing conclusions. For example, dipole or multipole interaction could play a dominant role at low concentrations and be virtually concentration-independent. Furthermore, direct electronic transitions between centers could take place at low temperatures.

Other possibilities exist. It may be that copper produces, in addition to the 3900 Å excitation band, a band with a maximum at 3450 Å, which coincides with the blue excitation band, or that an exciton band may exist, which extends into the blue excitation band. It has also been suggested that the blue and green emissions originate in the same center.[12] Since there is no clear evidence with which to decide among these possibilities, they too must remain uncertain.

Finally, the transfer may be photoconductive, even at low temperatures. Photoconductive transfer can take place if irradiation into the 3450 Å band creates both free electrons and holes. We can imagine at least two ways in which this can happen.

One possibility is that the excitation band for the blue emission consists of two superimposed excitation bands arising from (*a*) transitions from the impurity levels of zinc vacancies to the conduction band and (*b*) transitions from the valence band to the chlorine levels (Fig. 8). The thermal trap

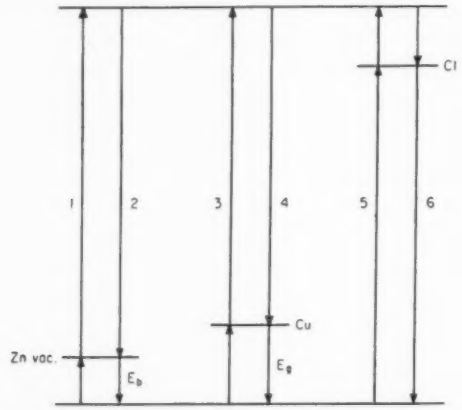


FIG. 8. Modified energy-level diagram of Fig. 1, showing transitions 5 and 6 between valence band and chlorine impurities.

depth for chlorine, 0·25 eV below the conduction band edge,[13] leads us to expect that an excitation band for chlorine, if it exists, will have its maximum in the region of 3400 Å. Furthermore, the appreciably greater band width of the blue emission of ZnS : Cl, as compared with those of silver or copper in ZnS, suggests that the converse process of emission may also consist of two superimposed bands.

An important feature of such a process is that it predicts an eventual depletion of one of the two blue centers. The failure to observe this effect may have been due to insufficient excitation intensity ($\sim 4\times10^{13}$ photons/sec) during the course of the measurement. While this does not eliminate the possibility that exhaustion may occur, it reduces the likelihood that such a process is the dominant factor in a photoconductive mechanism.

An alternative photoconductive process is possible, which does not require the superposition of two excitation bands, and predicts no depletion of centers. Such a process can occur, if in chlorine, for example, 3450 Å radiation not only promotes electrons from the valence band to the chlorine levels, but also excites electrons from chlorine levels to higher states in the conduction band. A process of this kind has been proposed to explain the increased absorption at 4500 Å which results from excitation in ZnS : Cu : Co.[14] Similar explanations have been also used by SMITH and TURKEVICH[15] to account for emptying of traps by visible and near ultraviolet radiation in copper-activated ZnS, and by HOOGENSTRAATEN and KLASENS[16] to explain the intensity-dependence of the light sum of ZnS : Cu : Co under 3650 Å excitation. In view of this evidence, we are of the opinion that a photoconductive mechanism based on the latter process, is the most likely transfer mechanism.

*Acknowledgements*—The author wishes to thank Dr. E. N. ADAMS, II, for his very useful comments and suggestions during the course of this work, and Miss SALLY WARNER for her assistance in taking the measurements.

## REFERENCES

1. SCHÖN M. *Z. Phys.* **119,** 463 (1942); *Tech.-wiss. Abhandl. Osram-Ges.* **6,** 49 (1953).
2. KLASENS H. A. *Nature, Lond.* **158,** 306 (1946). KLASENS H. A., RAMSDEN W. and QUANTIE C. *J. Opt. Soc. Amer.* **38,** 60 (1948).
3. SHIONOYA S. *J. Chem. Phys.* **23,** 1173 (1955). SHIONOYA S. and AMANO K. *Ibid* **25,** 380 (1956).
4. KRÖGER F. A. and DIKHOFF J. *Physica* **16,** 297 (1950). KRÖGER F. A. and VINK H. J. *J. Chem. Phys.* **22,** 250 (1954).
5. BOWERS R. and MELAMED N. T. *Phys. Rev.* **99,** 1781 (1955).
6. DEXTER D. L. *J. Chem. Phys.* **21,** 836 (1953).
7. GROSS E. F., KAPLIANSKII A. A. and NOVIKOV B. V. *Soviet Phys. (Dokl.)* **1,** 582 (1956). See also: LAMBE J. J., KLICK C. C. and DEXTER D. L. *Phys. Rev.* **103,** 1715 (1956). KLICK C. C. *Phys. Rev.* **89,** 274 (1953).
8. VAN DOORN C. Z. *Physica* **20,** 1155 (1954). PIPER W. W. *Phys. Rev.* **92,** 23 (1953).
9. JOHNSON P. *J. Opt. Soc. Amer.* **42,** 978 (1952).
10. CLAFFY E. W. and KLICK C. C. *J. Electrochem. Soc.* **104,** 445 (1957).
11. PRENER J. S. and WILLIAMS F. E. *J. Electrochem. Soc.* **103,** 342 (1956); *J. Chem. Phys.* **25,** 361 (1956).
12. BROWNE P. F. *J. Electronics* **2,** 2 (1956).
13. KRÖGER F. A. *Physica* **22,** 637 (1956).
14. ANTONOV-ROMANOVSKII A. A. and SHCHUKIN I. P. *Dokl. Akad. Nauk SSSR* **71,** 445 (1950).
15. SMITH A. W. and TURKEVITCH J. *Phys. Rev.* **87,** 306 (1952).
16. HOOGENSTRAATEN W. and KLASENS H. A. *J. Electrochem. Soc.* **100,** 366 (1953).

VOL 7 195

*J. Phys. Chem. Solids* Pergamon Press 1958. Vol. 7. pp. 153–158.

# INFRARED FLUORESCENCE OF COPPER-ACTIVATED ZINC SULPHIDE PHOSPHORS

G. MEIJER

Philips Research Laboratories, N.V. Philips' Gloeilampenfabrieken, Eindhoven, Netherlands

(*Received* 28 *March* 1958)

**Abstract**—An infrared fluorescence was observed for ZnS : Cu, Al and ZnS : Cu, Ga at 1·57$\mu$ and 1·72$\mu$. This emission appeared to be excited at low temperatures by radiation of 1·38$\mu$ and between 0·5$\mu$ and 0·8$\mu$, provided that the phosphor was excited by 3650 Å. The infrared quenching of the visible fluorescence and an infrared stimulation of the visible phosphorescence show a spectrum analogous to the infrared excitation spectrum, and seem to be connected with the same transitions.

## 1. INTRODUCTION

THE influence of infrared absorption on the visible luminescence of zinc sulphide phosphors has been investigated by various authors. For copper-activated ZnS GARLICK and MASON[1] observed at low temperatures a stimulation of the phosphorescence by irradiation with infrared of 1·2$\mu$ wavelength. Other stimulation peaks were found by FONDA[2] at about 0·8$\mu$ and 1·35$\mu$, by DALY[3] at 1·26$\mu$, 2·08$\mu$, and 2·7$\mu$, and by BROWNE[4] at 1·2$\mu$, 1·37$\mu$, and 2·55$\mu$.

Infrared quenching of the fluorescence was found by MELAMED[5] and by VINOKUROV[6] at 0·8$\mu$ and 1·3$\mu$, and by BROWNE[4] at 0·7$\mu$ and 1·3$\mu$. ANTONOV–ROMANOVSKII and SHCHUKIN[7] observed an enhancement of the infrared absorption for ZnS : Cu, Co by ultraviolet excitation with maxima at 0·8$\mu$ and 1·3$\mu$.

An infrared luminescence was found by DUMBLETON and GARLICK[8] at 1·5$\mu$ and 1·65$\mu$, and by BROWNE[4] at 1·475$\mu$, 1·645$\mu$, and 1·79$\mu$, which was excited by 0·76$\mu$ and 1·35$\mu$ irradiation.

The present paper deals with an investigation of the infrared fluorescence for well-defined copper-activated ZnS phosphors and the correlation of this phenomenon with the infrared quenching and one particular infrared stimulation of the visible luminescence.

## 2. PREPARATION OF THE PHOSPHORS*

Zinc sulphide of fluorescence quality was obtained by precipitation from a zinc sulphate solution. The ZnS powder was activated in the usual way and fired at 1200°C in an $H_2S$ atmosphere for 3 hr. The $H_2S$ was purified by washing with a KHS solution and dried with $P_2O_5$.

* The phosphors were prepared in our laboratory under the supervision of Mr. W. VAN GOOL.

## 3. APPARATUS

The measurements were made with a Leiss monochromator. The radiation was modulated by a rotating chopper and detected by a lead sulphide cell. The signal was amplified, rectified, and fed to a d.c. voltmeter. In the quenching and stimulation experiments, a photomultiplier was used. The phosphor was mounted in a Dewar vessel, in which it could be cooled to 80°K.

## 4. MEASUREMENTS

In all experiments the phosphor was excited by ultraviolet radiation of 3650 Å wavelength. The fluorescence of ZnS : Cu, Al is green, whereas the phosphors with a copper content higher than the aluminium content show in addition a blue emission band. The excitation and stimulation spectra reported in the following sub-sections have been corrected so that they represent the intensity of the emitted radiation for the same number of incident quanta at each wavelength. The peaks in the spectra obtained are listed in Table 1. The second column gives the activator and coactivator contents of the samples in gram-atoms per mole ZnS.

### (a) *Infrared fluorescence*

At low temperatures an infrared emission was observed which was excited by infrared radiation with simultaneous or previous irradiation with 3650 Å. The emission spectrum (Fig. 1) consists of

*Table* 1. *Experimental data.*

| Sample | Activator and coactivator content ($10^{-4}$g atom/mole ZnS) | Infrared emission at 80°K (Wavelength in $\mu$) | Infrared excitation (Wavelength in $\mu$) | Quenching of the fluorescence at 300°K (Wavelength in $\mu$) | Stimulation of the phosphorescence (Wavelength in $\mu$) |
|---|---|---|---|---|---|
| 1 | 0·8 Cu<br>1·0 Al | 1·57<br>1·72 | < 0·8<br>1·40 | < 0·8<br>1·4 (weak) | 1·17<br>~ 2·25(weak) green (80°K) |
| 2 | 1·0 Cu<br>1·0 Al | 1·57<br>1·73 | < 0·8<br>1·36 | < 0·8<br>1·4 (weak) | 1·22<br>~ 2·25(weak) green (80°K) |
| 3 | 1·2 Cu<br>1·0 Al | 1·57<br>1·73 | < 0·8<br>1·40 | < 0·8<br>1·4 | 1·18<br>~ 2·25(weak) green and blue (80°K)<br>< 0·8 green<br>1·35 green (~ 250°K) |
| 4 | 3·0 Cu<br>1·0 Al | ~ 1·6<br>~ 1·7 (weak) | < 0·8<br>1·4 | < 0·8<br>1·4 | 1·18<br>2·12<br>2·38 (weak) green and blue (80°K)<br>< 0·8 green<br>1·36 green (~ 250°K) |
| 5 | 1·0 Cu<br>1·0 Al<br>0·1 Co | 1·57<br>1·72 | < 0·8<br>1·38 | < 0·8<br>1·4 (strong) | 0·93<br>1·03<br>1·26 green (80°K) |
| 6 | 1·0 Cu<br>1·0 Ga | 1·57<br>1·72 | < 0·8<br>1·40 | — | 1·21<br>~ 2·25(weak) green and yellow (80–150°K)<br>< 0·8 yellow<br>1·36 yellow (~ 250°K) |

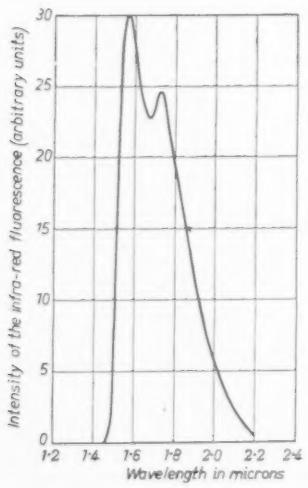


FIG. 1. Infrared fluorescence spectrum at 80°K of ZnS : Cu, Al; ZnS : Cu, Al, Co; and ZnS : Cu, Ga.

two bands at 1·57$\mu$ and 1·72$\mu$, respectively. The excitation spectrum (Fig. 2) shows one peak at 1·38$\mu$, whereas another excitation band begins at about 0·8$\mu$, having a very broad maximum in the visible. The measurement of the short-wavelength region of the excitation spectrum was rather difficult owing to the low intensity of the light source at those wavelengths. Therefore beyond 0·5$\mu$ the detection of any infrared emission was impossible. The 1·72$\mu$ emission was found to be excited by irradiation in both excitation bands, whereas the 1·57$\mu$ emission was excited only by irradiation in the broad band. The emission intensity decreased with increasing temperature; at room temperature only a very weak infrared luminescence was found. On removing the 3650 Å irradiation at 80°K, the infrared emission fell very slowly.

When the phosphor was excited by 2537 Å, i.e. beyond the fundamental absorption edge, without simultaneous irradiation at longer wavelength, a

weak infrared emission was obtained in the 1·6$\mu$ region. For silver-activated ZnS phosphors, no infrared fluorescence was observed at wavelengths below 3$\mu$.

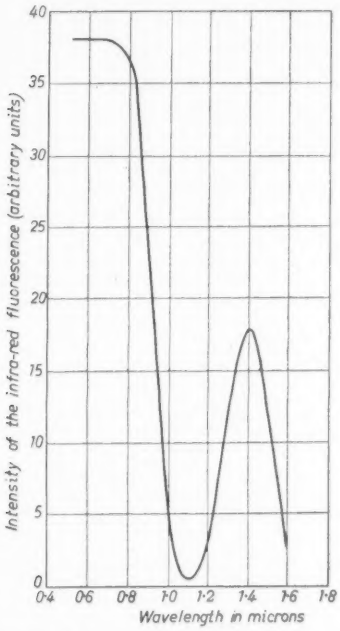


FIG. 2. Infrared excitation spectrum for the fluorescence shown by Fig. 1. The total infrared emission intensity is plotted against the wavelength of the exciting radiation.

(b) *Infrared quenching of the visible fluorescence*

For ZnS : Cu, Al the visible fluorescence may be quenched by infrared irradiation at room temperature. The quenching spectrum (Fig. 3) consists of a peak at about 1·4$\mu$ and a broad band starting at about 0·8$\mu$. For the samples 1 and 2 ([Cu] $\leqslant$ [Al]), the quenching was less pronounced than for the samples 3 and 4 ([Cu] $>$ [Al]). A very marked quenching effect occurred when the phosphor also contained cobalt (sample 5). On cooling the phosphor to about 200°K, the 1·4$\mu$ quenching fell to zero.

(c) *Infrared stimulation of the visible phosphorescence*

At 80°K the phosphorescence was stimulated by infrared irradiation of suitable wavelength (Fig. 4). The stimulated emission was green for the samples 1, 2, and 5. and also contained blue for the samples 3 and 4. A yellow emission was stimulated in sample 6. On increasing the temperature the intensity of the stimulated emission fell rapidly to zero.

In the case of copper contents higher than the aluminium content (sample 3 and 4), yet another quite different stimulation was observed at 1·36$\mu$ and at wavelengths shorter than 0·8$\mu$ (Fig. 5), which was found to depend on the temperature in

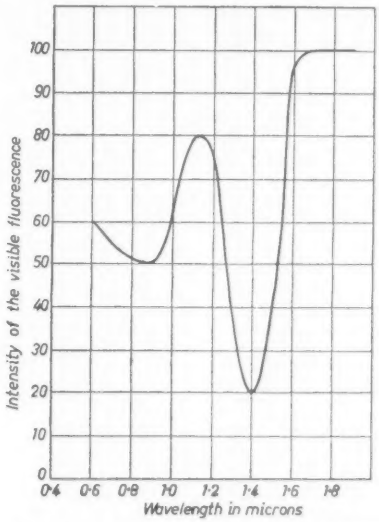


FIG. 3. Infrared quenching spectrum at 300°K of the visible fluorescence of ZnS : Cu, Al and ZnS : Cu, Al, Co (uncorrected).

the same way as the quenching of the fluorescence. The stimulated light was green, in contrast with the stimulated emission at 1·2$\mu$.

For ZnS : Cu, Ga (sample 6) a yellow stimulation was found at the same wavelengths and with the same temperature-dependence.

## 5. DISCUSSION

Table 2 gives the wavelengths obtained and the corresponding energy values. The stimulation of the phosphorescence at about 1·2$\mu$, 2·25$\mu$, 0·9$\mu$, and 1·0$\mu$, mentioned in the first part of sub-section 4(c), is probably connected with electron traps,[1] and will not be discussed here.

The remarkable similarity of the infrared excitation spectrum, the quenching spectrum, and the green and yellow stimulation spectrum for the samples 3 and 4, and sample 6, respectively,

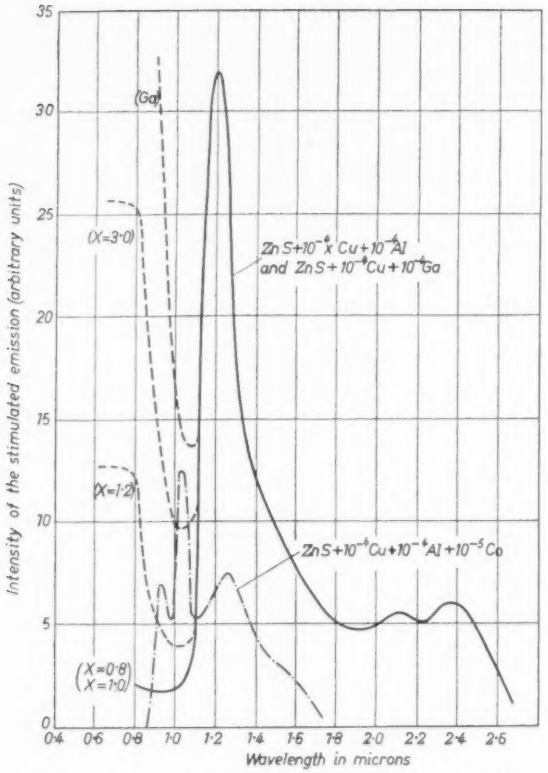


FIG. 4. Infrared stimulation of the visible phosphorescence at 80°K.

*Table 2. Summary of the experimental results*

| | $\lambda(\mu)$ | $\Delta E$(eV) |
|---|---|---|
| Infrared fluorescence: emission | 1·57<br>1·72 | 0·79<br>0·72 |
| Infrared fluorescence: excitation | < 0·8<br>1·38 | > 1·5<br>0·90 |
| Visible fluorescence: infrared quenching | < 0·8<br>1·4 | > 1·5<br>0·9 |
| Visible phosphorescence: infrared stimulation | < 0·8<br>1·36<br><br>1·2<br>2·1<br>2·4<br>0·93 (Co)<br>1·03 (Co) | > 1·5<br>0·91<br><br>1·0<br>0·6<br>0·5<br>1·3<br>1·2 |

leads us to suppose that all three processes mentioned in sub-sections 4(a), 4(b), and the second part of 4(c) are governed by the same transitions. In discussing these processes we shall use the band scheme given by Fig. 6. Excitation of a copper-activated ZnS phosphor with 3650 Å lifts an electron from an occupied copper level into the conduction band (transition 1). A free electron may recombine with an empty activator level (transition 2) under emission of light, or may be trapped. The quenching of the fluorescence may, according to KLASENS[9] and BROWNE,[4] be attributed to the transition of a positive hole from an "empty" copper level into the valence band, i.e. an electron is lifted from the valence band into the empty level. The free hole may recombine without radiation with a trapped electron. Cobalt incorporated in the phosphor causes deep electron traps and radiationless recombination (killer). The bands in the

quenching spectrum may be attributed to transition 3 (0·9 eV) of the hole from the ground state into the first excited state, and to transition 5 ($\geqslant$ 1·5 eV)

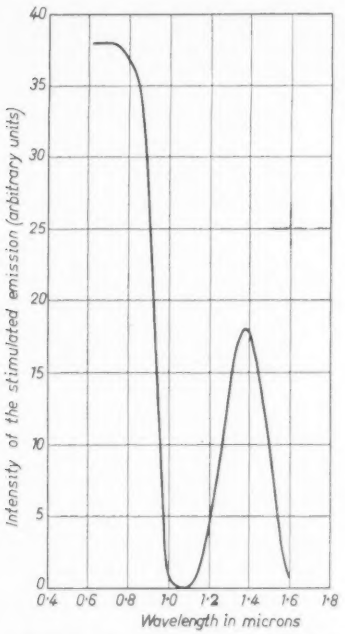


FIG. 5. Infrared stimulation at about 250°K of the phosphorescence for ZnS+1·2×10$^{-4}$Cu+10$^{-4}$Al, ZnS+3·0×10$^{-4}$Cu+10$^{-4}$Al and ZnS+10$^{-4}$Cu+10$^{-4}$Ga.

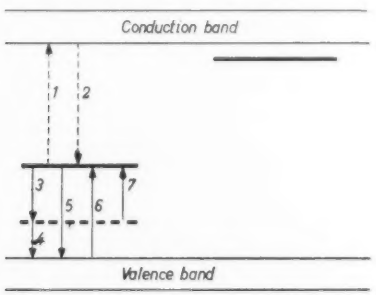


FIG. 6. Level scheme for ZnS : Cu, Al. 1 and 2 indicate transitions of an electron, 3–7 are transitions of a positive hole.

which is an ionization. At low temperatures transition 3 causes no quenching, but at higher temperatures the excited hole is lifted to the valence band thermally (transition 4), and then quenching is made possible.

On the other hand, an excited hole may fall back to the ground state, and also a free hole may be captured by an "occupied" copper centre. As the quenching spectrum and the infrared excitation spectrum show the same maxima, we are led to believe that the emission peaks correspond to the transitions 6 and 7 (0·79 and 0·72 eV, respectively). At lower temperatures more free electrons will be trapped, and thus a higher concentration of "empty" copper centres will result. Therefore, we expect: (1) that the infrared fluorescence intensity will increase with decreasing temperature, (2) that an excitation corresponding to transition 3 alone will cause only an emission corresponding to transition 7, and (3) that with 2537 Å excitation, assuming that it produces free holes and electrons, infrared emission will occur without the necessity of excitation with infrared. This is in full agreement with the experimental results. The proposed model gives rise to a FRANCK–CONDON shift of 0·2 eV for the emission and excitation corresponding to the first excited state, and 0·7 eV in the case of an ionization. The stimulation mentioned in the second part of sub-section 4 (c) also seems to be connected with the transitions 5, and 3 followed by 4. In the case of ZnS : Cu, Ga, we suggest that the yellow emission is stimulated owing to the fact that free holes recombine with electrons trapped by the gallium centres. Although the infrared stimulation is not yet completely understood, the striking analogy between the observed processes suggests the following interpretation of the green stimulation of the ZnS : Cu, Al samples 3 and 4: When more copper than aluminium is incorporated, new centres are formed (e.g. *S* vacancies). We suppose that these centres introduce electron energy levels near the conduction band. When a free hole recombines without radiation with an electron trapped in such a centre, the energy is transferred directly to a green copper centre by resonance. Excitation of a blue copper centre by resonance transfer appears to be impossible.

Our model of the copper centre in ZnS supports the idea[9] that copper at a zinc site of the ZnS lattice can be described as an effective negative charge to which, in the case of an "empty" centre, a positive hole is bound. One might therefore expect a complete series of energy levels. This supposition might be corroborated by more detailed experiments.

## REFERENCES


1. GARLICK G. F. J. and MASON D. E. *J. Electrochem. Soc.* **96,** 90 (1949).
2. FONDA G. R. *J. Opt. Soc. Amer.* **36,** 382 (1946).
3. DALY E. F. *Proc. Roy. Soc.* A**196,** 554 (1949).
4. BROWNE P. F. *J. Electronics* **2,** 1 (1956).
5. MELAMED N. T. *J. Electrochem. Soc.* **97,** 33 (1950).
6. VINOKUROV L. A. *Dokl. Akad. Nauk SSSR* **85,** 529 (1952).
7. ANTONOV-ROMANOVSKII V. V. and SHCHUKIN I. P. *Dokl. Akad. Nauk SSSR* **71,** 445 (1950).
8. DUMBLETON M. J. and GARLICK G. F. J. *Proc. Phys. Soc.* B**67,** 442 (1954).
9. KLASENS H. A. *J. Electrochem. Soc.* **100,** 72 (1953).


VOL
7
195

*J. Phys. Chem. Solids* Pergamon Press 1958. Vol. 7. pp. 159–164.

# THE ANTIFERROMAGNETICISM OF $CuCl_2.2H_2O$

**W. MARSHALL***

Atomic Energy Research Establishment, Harwell, Berks., England

(*Received* 8 *April* 1958)

**Abstract**—A simple explanation is given of the unusual behavior of $CuCl_2 \cdot 2H_2O$, which has a Néel temperature of 4·33°K but a broad maximum in the magnetic susceptibility at about 4·8°K. The explanation is based upon the fact that in $CuCl_2 \cdot 2H_2O$ the strongest interaction exists only in linear chains, and hence it is not as effective in determining the long-range order as it is in determining the short-range order.

VOL. 7 1958

$CuCl_2 \cdot 2H_2O$ is an antiferromagnet with a Néel temperature of 4·33°K.[1] The specific heat has been measured by FRIEDBERG,[2] who found a curve of typical shape but with a rather larger "tail" than is usual above the Néel temperature. The magnetic susceptibility has been measured by GORTER *et al.*,[3] who found a normal behavior below the Néel temperature; but above the Néel temperature the susceptibility continues to rise with temperature and goes through a broad maximum at about 4·8°K. GORTER also points out that the magnitude of the susceptibility is rather smaller than one would expect. The purpose of the present paper is to suggest a simple explanation for these three departures from the usual behavior of antiferromagnets.

The physics of the explanation can be summarized very easily after studying the structure of the crystal. $CuCl_2 \cdot 2H_2O$ is a crystal of the rhombic bi-pyramidal class with a unit cell, shown in Fig. 1, of dimensions 7·38, 8·04, and 3·72 Å for *a*, *b*, and *c*, respectively. In the unit cell there are two copper atoms at (0, 0, 0) and ($\frac{1}{2}$, $\frac{1}{2}$, 0); four oxygen atoms at (0, 0·25, 0), (0, —0·25, 0), (0·5, 0·75, 0), (0·5, 0·25, 0); four chlorine atoms at (0·25, 0, 0·37), (—0·25, 0, —0·37), (0·25, 0·5, 0·37), (0·75, 0·5, —0·37). The hydrogen positions are unknown. From Fig. 1 we therefore see that each copper atom has two nearest neighbors, vertically above and below along the *c*-axis and four next-nearest neighbors in the *a*–*b* plane. From nuclear-magnetic-resonance studies, POULIS and HARDEMAN[1] conclude that all the electron spins in an *a*–*b* plane are parallel to one another and antiparallel to the electrons in the *a*–*b* planes vertically above and below. The magnetic studies of GORTER *et al.* support this conclusion and show that the "easy direction" for the spins is along the *a* axis. This arrangement of spins is shown in Fig. 1.

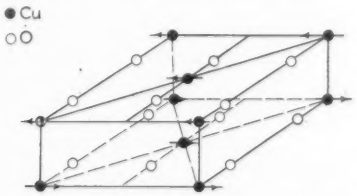


FIG. 1. The unit cell of $CuCl_2 \cdot 2H_2O$. Only copper atoms and oxygen atoms are shown.

We now postulate that this spin arrangement is due to an antiferromagnetic coupling between the nearest neighbors along the short *c*-axis and a ferromagnetic coupling between the next-nearest neighbors in the *a*–*b* plane. This is certainly the most obvious coupling scheme which would give rise to the observed spin arrangements. Actually the following argument would not be affected if there were additional ferromagnetic couplings in the *a*–*b* plane, but it is essential that the antiferromagnetic coupling from one plane to another should exist only between the nearest neighbors along the *c*-axis. Thus, for example, it is essential for the argument that any coupling between two copper atoms such as (0, 0, 0) and ($\frac{1}{2}$, $\frac{1}{2}$, 1) should be negligible.

* Present address: Department of Physics, University of California, Berkeley 4, Calif.

Let the antiferromagnetic coupling along the $c$-axis be of magnitude $J$ and the ferromagnetic coupling in the $a$–$b$ plane be of magnitude $J'$. Then we can understand the behavior of $CuCl_2 \cdot 2H_2O$ if we accept the second postulate that

$$J' < J. \tag{1}$$

The explicit calculations to be described later give a best fit with a value of 0·165 for the ratio $J'/J$.

We now notice that the Néel temperature is chiefly determined by the magnitude of $J'$ because the stronger antiferromagnetic coupling exists in only one dimension. Thus, for example, if $J'$ were zero, we would be left with a set of unconnected linear chains running along the $c$-axis, and hence $T_c$ would be zero because a linear chain cannot support long-range order no matter how strong the antiferromagnetic coupling is. Hence if $J'$ is small $T_c$ is also small. Now consider the short-range order in the crystal. Roughly speaking, this is determined by the Boltzmann factors $\exp(-J/kT)$ for vertical pairs and $\exp(-J'/kT)$ for horizontal pairs. Since $T_c$ is small (roughly $\approx J'/k$) even at this Néel temperature, the first factor, which becomes $\exp(-J/kT_c)$, can be very small, i.e. there can be a great deal of short-range antiferromagnetic order along the $c$-axis. Thus the spins will still be "locked in" antiparallel and so the susceptibility will continue to rise with temperature until thermal agitation gradually breaks down this coupling and the susceptibility will then go through a broad maximum.

This simple explanation accounts for the other unusual features of $CuCl_2 \cdot 2H_2O$ also. Because there is an exceptionally large amount of short-range order along the $c$-axis, the tail to the specific-heat wave must be larger, and the absolute magnitude of the susceptibility must be smaller, than we would normally expect at any particular value of $T/T_c$.

For explicit calculations we use the simple Ising model and solve the order–disorder problem by using the Bethe–Peierls method. We divide the lattice into two sub-lattices, $p$ and $m$, each one consisting of alternate $a$–$b$ planes. Thus each atom has two nearest neighbors vertically above and below along the $c$-axis which are on the other sub-lattice and to which it is coupled antiferromagnetically, and four next-nearest neighbors lying in the same $a$–$b$ plane and hence the same sub-lattice to which it is coupled ferromagnetically. For complete order all the spins on the $p$ sub-lattice are + and all those on the $m$ sub-lattice are −; in this case we say the spins are all "right" and any deviations we call "wrong".

In the usual way we must consider a cluster of atoms consisting of a central atom and the surrounding shell of atoms to which it is coupled. Because the outside atoms will have different effects on the shell atoms, depending upon whether the latter lie in the same $a$–$b$ plane or not, i.e. on the same sub-lattice or not, we must use two long-range-order parameters for the cluster. Furthermore, in the presence of a magnetic field clusters centered on a $p$ sub-lattice atom are not equivalent to those centered on an $m$ sub-lattice atom, so that we must consider these two types of cluster separately and use a pair of long-range-order parameters for each.

First consider a cluster centered on a $p$ sub-lattice atom. The relative probability of any arrangement of spins over this cluster of seven atoms can be written down immediately by using the following factors:

$t = \exp(-J/kT)$ for every (++) or (−−) pair along the $c$-axis (i.e. between sub-lattices)
$r = \exp(-J'/kT)$ for every (+−) pair in the $a$–$b$ plane (i.e. in the same sub-lattice)
$s = \exp(-2\mu H/kT)$ if the central atom is (−)
$\lambda_1$ for each nearest neighbor in the shell which is (+), i.e. "wrong"
$\phi_1$ for each next-nearest neighbor in the shell which is (−), i.e. "wrong". (2)

Here $\lambda_1$ and $\phi_1$ are long-range-order parameters introduced in the usual way.

Then we can sum over all those distributions with the central atom (+), i.e. "right" to give the total relative probability of this atom being "right" as

$$R_p = (1+t\lambda_1)^2(1+r\phi_1)^4. \tag{3}$$

the sub-script $p$ being introduced to signify this refers to a $p$ sub-lattice atom. Similarly the total relative probability of the central atom being (−) i.e. "wrong" is

$$W_p = s(t+\lambda_1)^2(r+\phi_1)^4. \tag{4}$$

Then, if $P_p$ and $M_p$ are the real probabilities of a spin on the $p$ sub-lattice being (+) and (−) respectively,

$$P_p = R_p/(R_p+W_p), \quad M_p = W_p/(R_p+W_p). \tag{5}$$

But from the rules given by equation (2) we can also write down an alternative expression for $P_p$ by asking for the probability that one of the shell atoms belonging to $p$ be (+). This probability is the sum of two terms: the probability the center atom is (+) times the probability the shell atom is (+) given that the former is (+), plus the probability that the center atom is (−) times the probability the shell atom is (+) given that the former is (−), i.e.

$$P_p = P_p/(1+r\phi_1)+M_p r/(r+\phi_1) \tag{6}$$

that is,

$$P_p\phi/(1+r\phi_1) = M_p/(r+\phi_1). \tag{7}$$

Similarly from this same cluster we can write down the probability that an $m$ sub-lattice spin be (−) as

$$M_m = P_p/(1+t\lambda_1)+M_p t/(t+\lambda_1). \tag{8}$$

Now consider a cluster centered on an atom of the $m$ sub-lattice. We can write down the relative probability of any arrangements of spins over this cluster using the factors:

$t = \exp(-J/kT)$ for every (++) or (−−) pair along the $c$-axis (i.e. between sub-lattices)
$r = \exp(-J'/kT)$ for every (+−) pair in the $a$–$b$ plane (i.e. in the same sub-lattice)
$s = \exp(-2\mu H/kT)$ if the central atom is (−)
$\lambda_2$ for each nearest neighbor in the shell which is (−), i.e. "wrong"
$\phi_2$ for each nearest neighbor in the shell which is (+), i.e. "wrong". (9)

$\lambda_2$ and $\phi_2$ are also long-range-order parameters. The total relative probability that the center atom be (−), i.e. "right", is

$$R_m = s(1+t\lambda_2)^2(1+r\phi_2)^4 \tag{10}$$

and the total relative probability it be (+), i.e. "wrong", is

$$W_m = (t+\lambda_2)^2(r+\phi_2)^4. \tag{11}$$

Hence from this cluster we obtain the real probabilities that a spin of the $m$ sub-lattice be (−) or (+) as $M_m$ or $P_m$ respectively where

$$M_m = R_m/(R_m+W_m); \quad P_m = W_m/(R_m+W_m). \tag{12}$$

An alternative expression for $M_m$, derived in just the same way as (6), is

$$M_m = M_m/(1+r\phi_2)+P_m r/(r+\phi_2), \tag{13}$$

that is

$$M_m\phi_2/(1+r\phi_2) = P_m/(r+\phi_2). \tag{14}$$

Finally from this cluster we can write down the probability that a $p$ sub-lattice spin be (+) as

$$P_p = M_m/(1+t\lambda_2)+P_m t/(t+\lambda_2). \tag{15}$$

From these expressions we must find four consistency equations to solve for the four parameters $\lambda_1, \phi_1, \lambda_2, \phi_2$. Two such equations are given already by equations (7) and (14); two more come from equating the expressions for $P_p$ given by (5) and (15) and by equating those for $M_m$ given by (8) and (12). The problem is now solved in principle. These four equations are solved for the unknowns $\lambda_1, \phi_1, \lambda_2, \phi_2$ and then we can write down the magnetic moment as

$$M = \tfrac{1}{2}N\mu[P_p-M_p+P_m-M_m] = N\mu[P_p-M_m]. \tag{16}$$

The problem is greatly simplified because we need only the susceptibility in small fields $H$. We therefore expand

$$s = 1-\epsilon \tag{17}$$

where $\epsilon = 2\mu H/kT$

is small. We first solve the equations for $\epsilon$ equal to zero and then compute the corrections to first order when $\epsilon$ is small but non-zero.

When $\epsilon$ is zero, the equations are satisfied identically by

$$\lambda_1 = \lambda_2 = \lambda, \qquad \phi_1 = \phi_2 = \phi. \tag{18}$$

Hence

$$R_p = R_m = R = (1+t\lambda)^2(1+r\phi)^4,$$
$$W_p = W_m = W = (t+\lambda)^2(r+\phi)^4, \tag{19}$$

and (7) becomes

$$\phi(r+\phi)R = (1+r\phi)W. \tag{20}$$

Equating (8) to (12) gives

$$\lambda(t+\lambda)R = (1+t\lambda)W. \tag{21}$$

From (20) and (21) we deduce

$$\phi^2(1+t\lambda)+\phi r(1-\lambda^2)-\lambda(t+\lambda) = 0. \tag{22}$$

From this equation we notice that $\phi$ and $\lambda$ become unity together and one solution is always the disordered solution

$$\lambda = 1 = \phi. \tag{23}$$

From an examination of (20) and (22) we deduce that below a certain critical value of $T$ there exists another solution with $\lambda$ and $\phi$ unequal and smaller than one. This is the ordered solution. We determine the critical point in the following way. Let

$$\lambda = 1-\delta_1, \quad \phi = 1-\delta_2, \tag{24}$$

where $\delta_1$ and $\delta_2$ are small. Then (22) gives

$$\delta_2 = \frac{1+r}{1+t}\delta_1 \tag{25}$$

whereas (20) gives

$$\delta_2 = \frac{(1-t)(1+r)}{(1+t)(2r-1)}\delta_1. \tag{26}$$

The solutions of these equations are $\delta_1$ and $\delta_2$ zero or

$$r = 1-t/2, \tag{27}$$

which is an equation to give the critical point. Define $\alpha$ by

$$J' = \alpha J \tag{28}$$

then

$$r = t^\alpha \tag{29}$$

and (27) becomes

$$t_c{}^\alpha = 1-t_c/2, \tag{30}$$

where $t_c$ is the critical value of $t$. As $\alpha$ becomes small, $t_c$ tends to zero, i.e. $T_c$ tends to zero. This confirms the qualitative argument given earlier that $T_c$ is chiefly dependent on the value of $J'$ and goes to zero as $J'$ goes to zero. Above the critical value of $t$ the only solution is the disordered solution given by equation (23); below $t_c$ equations (20) and (22) must be solved simultaneously for $\lambda$ and $\phi$, using numerical methods. Assuming this to be done, we now solve the equations in the more general case when $\epsilon$ is not zero. Working throughout just to first order in $\epsilon$, we put

$$\lambda_1 = \lambda+c_1\epsilon, \qquad \phi_1 = \phi+d_1\epsilon,$$
$$\lambda_2 = \lambda+c_2\epsilon, \qquad \phi_2 = \phi+d_2\epsilon, \tag{31}$$

where $\lambda$ and $\phi$ are the solutions for zero $\epsilon$.

Solving for $c_1, c_2, d_1$, and $d_2$, a great deal of tedious algebra gives eventually

$$A\phi(1+r\phi)(r+\phi) = -d_1(r+2\phi+r\phi^2),$$
$$B\phi(1+r\phi)(r+\phi) = d_2(r+2\phi+r\phi^2), \tag{32}$$

$$A+\frac{B\lambda(1-t^2)}{(1+t\lambda)(t+\lambda)} = \frac{-c_2t(t+2\lambda+t\lambda^2)(1+2t\lambda+\lambda^2)}{\lambda(1+t\lambda)^2(t+\lambda)^2},$$

$$B+\frac{A\lambda(1-t^2)}{(1+t\lambda)(t+\lambda)} = \frac{c_1t(t+2\lambda+t\lambda^2)(1+2t\lambda+\lambda^2)}{\lambda(1+t\lambda)^2(t+\lambda)^2},$$

where we have introduced

$$A = 1+\frac{2c_1t}{(1+t\lambda)}-\frac{2c_1}{(t+\lambda)}+\frac{4d_1r}{(1+r\phi)}-\frac{4d_1}{r+\phi},$$
$$B = 1-\frac{2c_2t}{(1+t\lambda)}+\frac{2c_2}{t+\lambda}-\frac{4d_2r}{1+r\phi}+\frac{4d_2}{r+\phi}. \tag{33}$$

In terms of these quantities the susceptibility from equation (16) is given by

$$\chi = M/H = \frac{2\mu^2H}{kT}\,\frac{\lambda(t+\lambda)(1+t\lambda)}{(1+2t\lambda+\lambda^2)^2}(A+B) \tag{34}$$

which, solving (32) and (33) for $(A+B)$, gives

$$\chi = \frac{4\mu^2N}{kT}\,\frac{\lambda(t+\lambda)(1+t\lambda)}{(1+2t\lambda+\lambda^2)^2}\times$$
$$\times\left[1+\frac{2\lambda(1-t^2)}{t(1+2t\lambda+\lambda^2)}-\frac{4\phi(1-r^2)}{(r+2\phi+r\phi^2)}\right]^{-1}. \tag{35}$$

In the disordered region this expression for $\chi$ simplifies to

$$\chi = \frac{\mu^2 N}{2kT_c}\frac{T_c}{T}\frac{2t}{1-2t(1-r)}. \qquad (36)$$

This expression has been plotted, for various values of $\alpha$, against $T/T_c$ in Fig. 2 using the relation obtained from equation (2) that

$$\frac{T}{T_c} = \frac{\log t_c}{\log t}, \qquad (37)$$

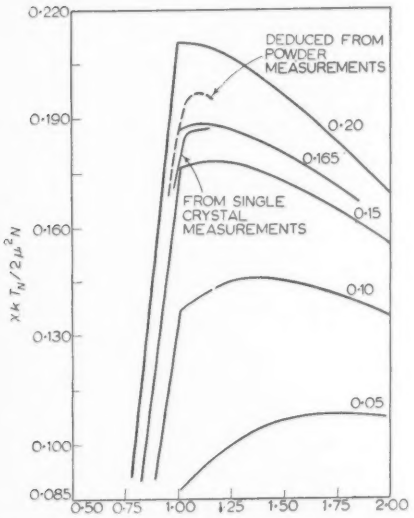


FIG. 2. The magnetic susceptibility of $CuCl_2 \cdot 2H_2O$ for various values of $\alpha$. The heavy curve is the experimental curve as determined with a single crystal. The dashed curve is the experimental value deduced from powder measurements.

and for each value of $\alpha$ solving equation (30) to give $t_c$. From Fig. 2 we see that the susceptibility has a broad maximum above the Néel temperature for all values of $\alpha$ smaller than 0·21. We also show the susceptibility below the Néel temperature which is obtained by solving for $\lambda$ and $\phi$ numerically and substituting into equation (35). From the experimental curve given in Fig. 2, we see that $\alpha \approx 0{\cdot}165$ gives a good fit between theory and experiment. The precise value of $\alpha$ to take depends upon which of the two experimental curves is chosen.

The theory shows that there is an abrupt change of slope in the susceptibility curves at the Néel temperature, whereas both the experimental curves seem to show an abrupt change slightly above $T_c$. It seem likely that this is not a real effect.

According to GORTER the susceptibility maximum occurs at about 4·8°. Now from equation (36) it is possible to plot the position of the maximum as a function of $\alpha$. Determining $\alpha$ by this method gives

$$\alpha = 0{\cdot}165. \qquad (38)$$

We can also compute the specific heat and compare to experiment. We find eventually

$$C_v/Nk = 2t[\log t]^2 \times$$
$$\times \frac{d}{dt}\left\{\frac{(1+\lambda t)}{(1+2t\lambda+\lambda^2)}\left[\frac{\lambda t}{(1+\lambda t)}+2\alpha\frac{\phi r}{(1+\phi r)}\right]\right\}, \qquad (39)$$

which is plotted for various values of $\alpha$ in Fig. 3.

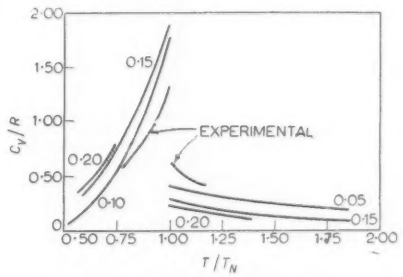


FIG. 3. The specific heat of $CuCl_2 \cdot 2H_2O$.

We see from this figure that the agreement with experiment is very poor, but this is only to be expected because we have used the Ising model to describe the interactions, and this is a very crude model especially for calculating the specific heat. We can see this very easily by computing the partition function at high temperatures and evaluating the susceptibility and the specific heat. The leading terms of a series in powers of $1/kT$ are

$$\chi = \frac{4\mu^2}{kT}\overline{S_z^2}, \qquad C_v/R = \frac{1}{k^2T^2N}\overline{\mathscr{H}^2} \qquad (40)$$

where $S_z$ is the total $z$ component of spin and $\mathscr{H}$ is the Hamiltonian. Now $\overline{S_z^2}$ is just $N/4$, and so the leading term for the susceptibility is the same for Ising and Heisenberg models. But $\overline{\mathscr{H}^2}$ for the Heisenberg model is exactly three times that for the Ising model. At high temperatures therefore, because we have used the Ising model, we should

expect to get the correct result for $\chi$ but a result only one-third of the experimental specific heat. Furthermore because the total amount of entropy associated with the specific-heat curve is the same on either model, i.e.

$$\int_0^\infty \frac{C_v}{T} dT = R \log 2,$$

it follows that, since the Ising model gives low values for $C_v$ at high temperatures, it must give high values at low temperatures. From Fig. 3 it can be seen that this is just the behavior found.

From this argument we may expect to get reasonable agreement with the magnetic-susceptibility curve, but we must not expect to get any agreement with the specific-heat curve. The difference between theory and experiment in Fig. 3 is therefore only to be expected. In the near future it is planned to reconsider this problem using the correct Hamiltonian, and then we would expect good agreement with experiment for both susceptibility and specific heat.

*Acknowledgement*—I would like to thank Professor C. J. GORTER for bringing this problem to my notice and for his interest in the calculation.

*Note added in proof*: Since this paper was written, Dr. H. M. Gijsman has kindly informed me of some details of the measurements of $\chi_a$ made by him and VAN DEN HANDEL. These measurements were briefly reported by VAN DER MAREL *et al.*[3] From their measurements VAN DEN HANDEL and GIJSMAN conclude that the maximum in $\chi_a$ for small applied fields probably occurs at a temperature a little higher than 5·0°K. (Unfortunately this temperature range cannot be examined carefully.) If we take the position of the maximum to be about 5·2°K instead of the 4·8°K deduced by VAN DER MAREL *et al.*[3] and use this result to determine $\alpha$, we obtain a result of $\alpha \approx \cdot 138$. I am grateful to Dr. GIJSMAN for communicating this information before publication and for a correspondence on this point.

VOL 7 195

## REFERENCES

1. POULIS N. J. and HARDEMAN G. E. G. *Physica* **18,** 207 (1952).
2. FRIEDBERG S. A. *Physica* **18,** 714 (1952).
3. VAN DER MAREL L. C., VAN DEN BROCK, WASSCHER J. D. and GORTER C. J. *Physica* **21,** 685 (1955).

*J. Phys. Chem. Solids* Pergamon Press 1958. Vol. 7. pp. 165–169.

# RÉSONANCE NUCLÉAIRE DES PROTONS DANS L'ACIDE TRICHLORACÉTIQUE

**MAURICE GOLDMAN**

G.E.N. de Saclay, Gif-sur-Yvette (Seine et Oise), France

(*Received* 14 *April* 1958)

**Résumé**—Le spectre de résonance magnétique des protons de l'acide trichloracétique a été observé dans une poudre ainsi que dans les monocristaux pour plusieurs orientations de ceux-ci dans le champ magnétique. Cette étude a montré que l'acide trichloracétique est dimérisé. La distance entre les protons d'un dimère est égale à 2,56±0,02 Å. Il existe dans le cristal deux orientations des axes proton–proton faisant entre elles un angle de 31°±30′.

**Abstract**—Proton magnetic resonance spectra have been observed for both monocrystalline and polycrystalline samples of trichloracetic acid. They provide evidence that the acid is a dimer with a proton–proton distance of 2·56±0·02 Å.

The spectrum of the single crystal was studied as a function of orientation in the magnetic field and indicates the presence of two orientations of the proton–proton vector in the crystal, inclined at an angle of 31°±30′.

A $\gamma$-irradiated polycrystalline sample was investigated at room temperature and the temperature of liquid nitrogen, and a comparison of the spin-lattice relaxation times suggests that the—C—$Cl_3$ groups are rotating at room temperature.

## 1. INTRODUCTION

L'EXISTENCE de groupes relativement isolés de spins identiques dans un cristal conduit à une structure de leur raie de résonance nucléaire. PAKE[1] a étudié le cas de paires de protons et a montré que le couplage magnétique dipolaire entre les deux spins d'une paire déplace leurs niveaux d'énergie dans le champ magnétique appliqué et donne naissance à deux raies de résonance dont l'écartement est :

$$\Delta H = \frac{3\mu}{r^3}(3\cos^2\theta - 1)$$

où $\mu$ est le moment magnétique du proton, $r$ la distance entre les protons de la paire et $\theta$ l'angle de 'axe proton–proton et du champ magnétique.

Ces deux raies présentent une certaine largeur causée par l'intéraction dipolaire des protons avec les spins extérieurs à la paire considérée.

Lorsqu'on a affaire à une poudre cristalline, les directions des axes proton–proton sont réparties au hasard et la courbe de résonance présente deux maxima distants de $3\mu/r^3$ approximativement, et d'autant plus accusés que la largeur des raies de résonance de chaque microcristal de la poudre est plus faible.

Une étude de la résonance nucléaire des protons permet donc de déterminer la distance entre les protons de chaque paire ainsi que l'orientation des différentes paires existant dans le cristal. Cette étude a été effectuée dans le cas de l'acide trichloracétique.

## 2. MODE OPÉRATOIRE

L'observation des courbes d'absorption nucléaire des protons a été effectuée au moyen d'un spectromètre à bobines croisées à une fréquence de 16 MHz. Le signal était détecté par un amplificateur (« Lock-in ») et l'on enregistrait la dérivée de la courbe d'absorption. La mesure du temps de relaxation $T_1$ des protons a été effectuée par passage rapide du champ magnétique à travers la valeur de résonance, le spectromètre étant réglé sur le mode dispersion.[2]

Des mesures ont été réalisées avec des poudres cristallines ainsi qu'avec des monocristaux.

La fabrication des monocristaux a été réalisée en faisant lentement descendre dans un four à gradient de température un tube contenant de l'acide trichloracétique fondu, comportant à sa base une pointe capillaire. La cristallisation s'effectuait en une dizaine d'heures et l'on obtenait des monocristaux de plusieurs centimètres cubes, contenant souvent des bulles d'air occluses.

Des enregistrements de résonance sur des échantillons fondus puis cristallisés rapidement ont fait apparaître des pics latéraux sur la courbe d'absorption, d'autant plus importants que la cristallisation était plus brutale. Ce phénomène, qui nous a gêné longtemps, a pu être expliqué par une orientation préférentielle des cristaux sur les parois du tube lors d'une cristallisation rapide. En effet, tous les échantillons donnaient des courbes identiques après avoir été réduits en pourdre. Il n'est donc pas possible, pour enregistrer une courbe de résonance de pourdre, de fondre l'acide trichloracétique pour augmenter le coefficient de remplissage.

Il n'a, d'autre part, pas été possible d'observer l'absorption nucléaire à la température de l'azote liquide avec des échantillons ordinaires; le temps de relaxation spin-réseau des protons augmente alors considérablement et l'on ne peut éviter de saturer le signal par le champ de radio-fréquence. Il est possible de diminuer ce temps de relaxation en irradiant l'échantillon par des rayons—$\gamma$. Une irradiation de $10^7$r par une source de cobalt 60, a fait passer, dans notre échantillon le temps de

FIG. 1. Dérivée du signal d'absorption nucléaire des protons dans un monocristal d'acide trichloracétique. Le pic du milieu correspond à l'eau résiduelle.

relaxation $T_1$, dans l'azote liquide, de 220 à 15 sec et a permis l'enregistrement du signal.

Toutes les manipulations d'acide trichloracétique ont dû être effectuées dans une boîte à gants à atmosphère désséchée, car ce produit est très hygroscopique. On n'a pu cependant éviter la présence de traces d'eau résiduelle qui donnaient un petit pic étroit au centre des raies de résonance.

### 3. RÉSULTATS EXPÉRIMENTAUX

(a) *Courbes de monocristal*

Nous avons réalisé des séries d'enregistrements de courbes de résonance nucléaire de protons dans des monocristaux d'acide trichloracétique à la température ordinaire. Entre chaque enregistrement le cristal subissait une rotation de 6° autour d'un axe perpendiculaire au champ magnétique. Des mesures ont été effectuées pour trois orientations différentes de l'axe de rotation par rapport aux axes cristallins. Chaque enregistrement comporte deux doublets dont l'écartement varie sinusoïdalement en fonction de l'angle de rotation du cristal, avec une période égale à $\pi$ ainsi qu'il est prévu par la théorie. Ces courbes indiquent donc la présence de deux directions des axes proton–proton dans le cristal. La Fig. 1 reproduit un enregistrement réalisé dans un monocristal. La Fig. 2 montre la variation de la distance entre les raies de chaque doublet avec l'angle de rotation du cristal dans le champ magnétique.

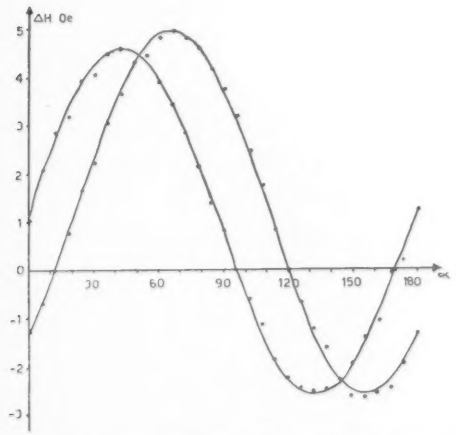


FIG. 2. Variation de la distance entre les raies de chaque doublet de resonance des protons en fonction de l'angle de rotation du cristal dans le champ magnétique.

La largeur des raies individuelles, entre extrêma de leur dérivée, varie entre 0,4 et 0,6 Oe suivant l'orientation du cristal dans le champ magnétique. Cette faible largeur provient de ce que l'encombrement stérique des groupes $-C-Cl_3$ impose une distance assez grande entre les paires de protons de dimères voisins. Quant aux moments magnétiques nucléaires des chlores, ils sont trop petits pour élargir notablement les raies de résonance des protons.

En prouvant l'existénce de paires de protons isolées, ces résultats montrent qu'à l'état cristallisé, l'acide trichloracétique est dimérisé par liaison hydrogène, contrairement à l'acide acétique, qui est polymérisé en longues chaînes.[3]

Le facteur de séparation des raies, égal à :

$$\frac{3\mu}{r^2} = 2{,}56 \pm 0{,}06 \text{ Oe}$$

correspond à une distance entre les protons du dimère de :

$$d = 2{,}56 \pm 0{,}02 \text{ Å}.$$

Cette valeur est en bon accord avec la valeur déduite des distances interatomiques déterminées par diffraction électronique pour les dimères de l'acide acétique et de l'acide trifluoracétique,[4] en admettant dans les groupes oxhydriles, une distance O–H de 0,96 Å.

L'angle que forment entre elles les deux directions des axes proton–proton existant dans les cristal est égal à :

$$\alpha = 31° \pm 30'.$$

(b) *Courbes de poudres*

Nous avons observé la résonance des protons dans des échantillons polycristallins d'acide trichloracétique, à la température ordinaire avec un échantillon ordinaire et à la température de l'azote liquide avec un échantillon irradié par des rayons—$\gamma$.

Ces courbes présentent des maxima très accusés ainsi que l'on peut le prévoir d'après la faible largeur des raies individuelles dans un monocristal. La Fig. 3 reproduit un enregistrement réalisé à température ordinaire et la Fig. 4 la courbe de résonance intégrée, que l'on compare à la courbe théorique d'une paire isolée. La distance entre les maxima augmente d'environ 10 pour cent

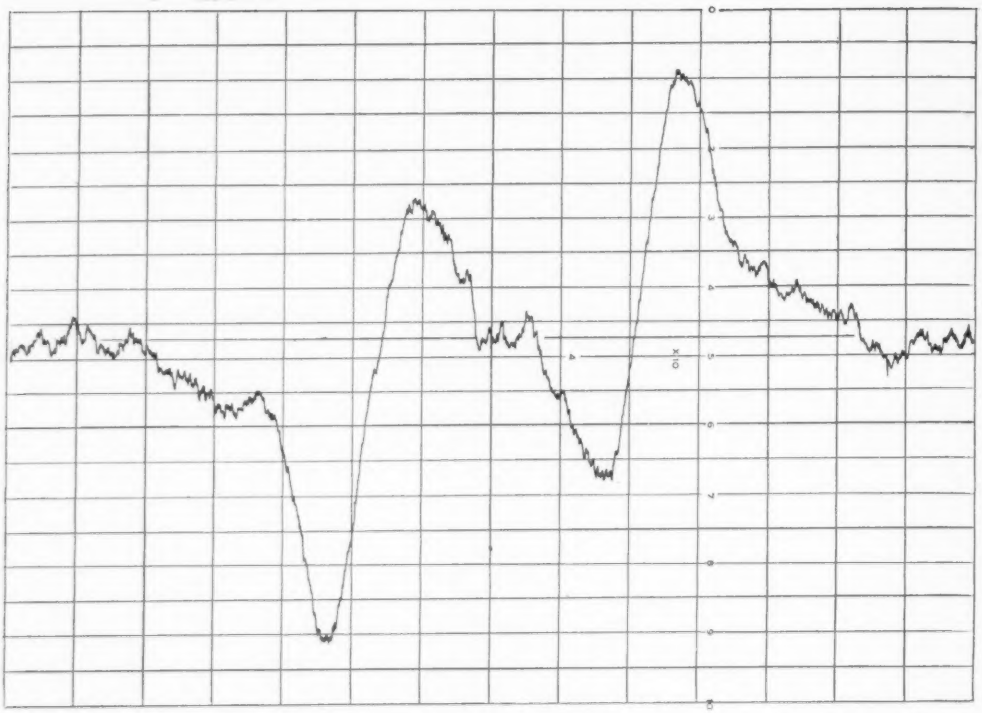

FIG. 3. Dérivée du signal d'absorption nucléaire des protons d'une poudre d'acide trichloracétique à température ordinaire.

à la température de l'azote liquide, ce qui correspond à une diminution de la distance entre les protons d'une paire d'environ 3 pour cent.

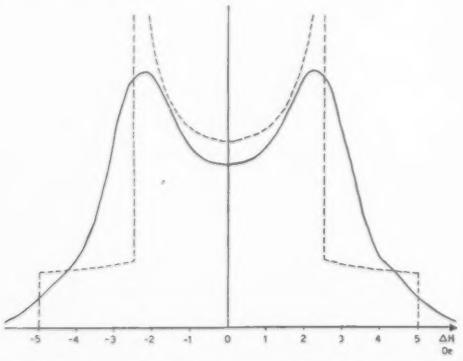


FIG. 4. Courbe d'absorption nucléaire des protons de la poudre obtenue par intégration de la courbe de la Fig 3. La courbe pointillée est la courbe d'absorption théorique d'un ensemble de paires de protons distants de 2,56 Å et d'orientations réparties au hasard.

Il ne semble pas déraisonnable que la longueur des liaisons hydrogènes puisse varier dans cette proportion, compte tenu de la faible énergie de ces intéractions.

(c) *Temps de relaxation des protons*

Le temps de relaxation spin-réseau des protons a été mesuré dans des échantillons de poudre à la température ordinaire et à la température de l'azote liquide.

Dans nos échantillons, il était de :

1,7 sec à 300°K

220 sec à 77°K.

Une telle variation est difficilement explicable si l'on admet que la relaxation des protons est dûe à la présence d'impuretés paramagnétiques. Elle pourrait être interprétée par la rotation des groupes —C—$Cl_3$, rotation suggérée par BUYLE-BODIN[5]

pour expliquer la disparition des raies de résonance quadrupolaire des chlores vers 110°K.

*Remerciements*—Je remercie M. A. ABRAGAM pour ses conseils et ses suggestions ainsi que toute la section de résonance magnétique du C.E.N.S. pour l'aide que j'y ai trouvée. Je remercie également M. SUTTON, chef du groupe de Chimie sous Radiation, qui a réalisé l'irradiation des échantillons.

OL.
7
958

## BIBLIOGRAPHIE

1. PAKE G. E. *J. Chem. Phys.* **16,** 327 (1948).
2. CHIAROTTI G., CRISTIANI G., GIULOTTO L. and LANZI G. *Nuovo Cim.* **12,** 519 (1954).
3. JONES R. E. *Université de Californie Rapport* UCRL —3641 (1956).
4. BROCKWAY L. O. *J. Amer. Chem. Soc.* **66,** 574 (1944).
5. BUYLE-BODIN M. Thèse, Paris (1955). Thèse de l'Université de Paris (1955) Masson et C^ie^, editeurs.

*J. Phys. Chem. Solids* Pergamon Press 1958. Vol. 7. pp. 170–174.

# POLARIZED LUMINESCENT EMISSION FROM KCl : Tl AT LOW TEMPERATURES

CLIFFORD C. KLICK and W. DALE COMPTON

U.S. Naval Research Laboratory, Washington, D.C.

(*Received* 16 *May* 1958)

**Abstract**—At temperatures near that of liquid helium, polarized emission is observed from isolated thallium centers in KCl with a polarization $P = 0{\cdot}2$. The center responsible for this effect has its maximum emission along the cubic axis. The polarization does not appear at liquid nitrogen temperatures and it is not dependent on the concentration of thallium. Arguments are given which make it seem unlikely that this effect is due to crystal strain or the proximity of the luminescent center to other imperfections. It is possible that there is a splitting of the levels of the excited state of thallium due to the Jahn–Teller effect. Comparison is made of the experimental results with the theory of the Jahn–Teller effect developed by VAN VLECK and by ÖPIK and PRYCE. Difficulties with this interpretation are discussed. In contrast to the thallium center, polarization is not found for luminescent emission from *F*-centers in KCl at temperatures near liquid helium.

VOL
7
195

## INTRODUCTION

POLARIZED luminescence has been observed in a number of cases in which the center is not symmetrical and is a useful tool for ascertaining the symmetry of the center.[1–4] It is of interest to inquire whether there are processes by which a symmetrical center can yield polarized emission.

For the investigation of such an effect there are two obvious choices of simple and reasonably well-understood centers. One is the *F*-center in alkali halides[5] and the other is thallium in potassium chloride.[6] The first excited state of the thallium ion is a $^3P_1$ state for ions in a gas and the same designation has been fruitful in describing the ion in the KCl lattice. It was at one time suggested that the crystalline electric field would remove the degeneracy of the thallium in its excited state,[7] but it is now generally concluded that this will not occur in crystals of cubic symmetry.[8,9]

A theorem due to JAHN and TELLER[10,11] argues, however, that for a wide variety of types of centers the spatial degeneracy of the center will be removed if it is placed in a crystal lattice. VAN VLECK[12] and, more recently, ÖPIK and PRYCE[13] have investigated this effect theoretically in a detailed way for a number of centers including those with properties similar to the *F*-center and the thallium ion. It seemed worthwhile, therefore, to look for this effect experimentally since it does not seem to have been observed in luminescence.

## EXPERIMENTAL ARRANGEMENT

The thallium ion in KCl has an absorption band at 2500 Å and a main emission band at 3000 Å; a weaker emission band is found at 4750 Å in samples with high concentrations of thallium. The arrangement of the experiment is shown schematically in Fig. 1. Samples, about 1 cm by 1 cm by 2 mm, were mounted in a helium dewar which has previously been described[14] but which has been modified by the addition of a quartz window placed so that the luminescent emission from the sample could be observed at right angles to the direction of the incident exciting light. Two sample orientations were used. In each case the exciting light fell on the (100) face of the crystal; in one case the emitted light was observed at right angles from the (010) face, and in the other case at right angles from a cut and polished (110) face. The samples were held against a brass block cooled with liquid helium or liquid nitrogen and conduction to the block was increased by placing a thin layer of vacuum grease between the sample and its support where possible. However, illumination of the two

large faces and one edge of the crystal by room temperature radiation at the windows resulted in some heating of the sample. This heating would tend to be more pronounced at liquid-helium temperature; no attempt was made to measure it.

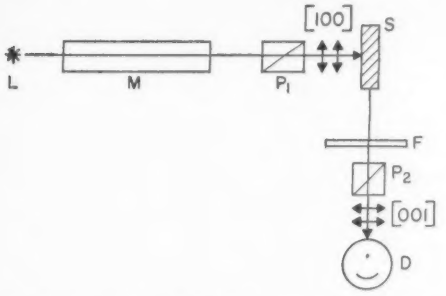


FIG. 1. Schematic drawing of the experimental arrangement. L is the light source; M is a monochromator; $P_1$ is a polarizing prism; S is the sample with the exciting light entering a cube face and the emission leaving a cube face. F is a filter to transmit the luminescent emission from S; $P_2$ is a polarizing prism used as an analyzer; and D is the detector. The electric vector of the exciting light is drawn for the case when it is in the [100] direction. The electric vector for the luminescent emission is drawn for polarization along the [001] direction. Experiments were also performed in which the luminescent emission was observed through a (110) face.

A linear arrangement of source, sample, and detector was also used successfully, but the right angle method of Fig. 1 was preferred since it effectively eliminated the problem of polarized stray light from the monochromator falling on the detector. The source was a hydrogen lamp giving a continuous ultraviolet emission spectrum in the wavelength region of interest. A grating monochromator was used to monochromatize the exciting light with a band pass of about 150 Å. Ultraviolet transmitting prisms were used to polarize the exciting light and to analyze the emission. A 1P28 photomultiplier was the detector and its output was amplified by a d.c. amplifier and recorded on a strip chart recorder.

For the investigation of the *F*-center in KCl a different wavelength region is involved. The absorption peaks at 5450Å and the emission occurs at 10,100Å. This emission is found, however, only if *M* and *R* centers are absent[2,3] so that special techniques of coloration are required. In this investigation the sample was held in the dewar, cooled to liquid-helium temperatures, and then X-rayed for an hour at 50KVP and 20 mA through a beryllium window. The exciting source was a tungsten ribbon filament lamp; its output passed through the monochromator and then was chopped at 10 c/s. The first polarizer was a standard polaroid film and the second one was a special infra-red polaroid film. A lead sulfide detector was used and the output was amplified by a 10 cycle amplifier.

## RESULTS

Crystals of KCl were measured with two different concentrations of thallium: 20 and 1000 parts

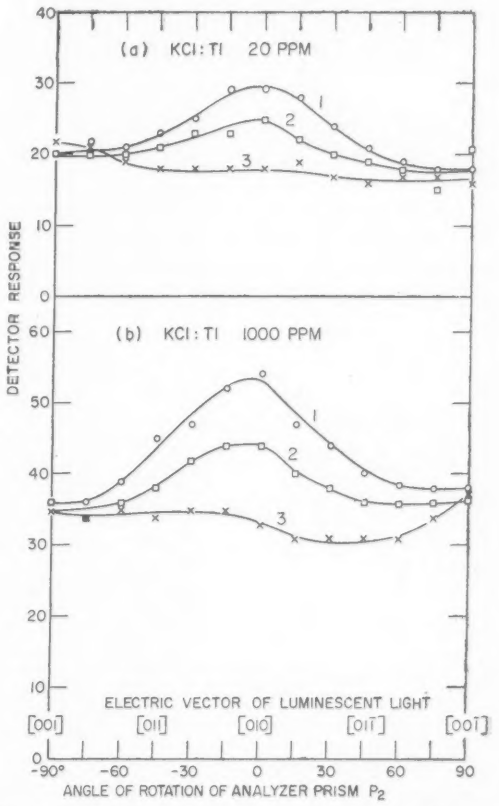
(a) KCl:Tl 20 PPM
(b) KCl:Tl 1000 PPM
DETECTOR RESPONSE
ELECTRIC VECTOR OF LUMINESCENT LIGHT
[001] [011] [010] [01T] [00T]
ANGLE OF ROTATION OF ANALYZER PRISM P2

FIG. 2. Variation of detector response as the analyzing prism, $P_2$, is rotated using the experimental arrangement of Fig. 1. The upper set of curves is for a sample with 20 p.p.m. of Tl in KCl and the lower set for 1000 p.p.m. In each case curve 1 corresponds to excitation with polarized light with the electric vector along [010]; curve 2 is for the electric vector along [110]; curve 3 is for the electric vector along [100].

per million (p.p.m.). The results of measurements on the 3000 Å emission from these crystals at liquid-helium temperatures are given in Fig. 2 for emission from the (100) face. Polarizer $P_1$ (see Fig. 1) was set in each of three positions and the detector signal measured as the analyzer, $P_2$, was rotated. Curve 1 corresponds to the case where the electric vector of the exciting light was in the [010] direction of Fig. 1. This corresponds to a direction at right angles to the plane of the drawing. It is seen that the maximum signal is observed when the electric vector of the luminescent light transmitted by the analyzer is [010] which is parallel to that of the exciting light, and is a minimum for emitted light polarized in the [001] direction. Curve 2 is similar data for $P_1$ transmitting light with its electric vector in the [110] direction; curve 3 corresponds to the [100] direction. In this last case, the electric vector of the luminescent light is always at right angles to that of the exciting light so that it might be expected that there is no variation of the detector output with angle of rotation of $P_2$. The variation which is found in both samples is not the same, it is relatively small, and it is not regular. It seems very likely that this is due to a small misalignment of $P_2$ such that the light transmitted is refracted slightly and falls on different parts of the 1P28 photosurface as $P_2$ is rotated. The well-known variation of photosensitivity of these devices across the cathode surface could then account for the observed shapes of the curves marked (3). Rearrangement of the equipment between runs made on the two samples would account for the fact that the two curves marked (3) are not of the same shape.

The polarization $P$ of luminescent light may be defined as

$$P=\frac{I_{\parallel}-I_{\perp}}{I_{\parallel}+I_{\perp}} \qquad (1)$$

where $I_{\parallel}$ and $I_{\perp}$ are the intensities of the emitted light polarized in directions parallel and perpendicular to the direction of polarization of the exciting light. For the KCl : Tl sample with 20 p.p.m. of thallium and excited with light polarized along [010], $P = 0{\cdot}21$ at liquid-helium temperatures; for the sample with 1000 p.p.m. $P = 0{\cdot}18$. These results appear to be the same within experimental error and the maximum polarization may be taken as $P = 0{\cdot}2$. In the case where the emission was through the (110) face, the observed polarization was $P = 0{\cdot}1$ and was independent of the orientation of the polarizing prism.

* *Note added in proof*: The polarization was found to be constant as the exciting light was varied from the peak of the absorption band at 2465 Å to points on either side of the band at 2370 Å and 2590 Å. An investigation of the emission spectrum failed to show any dependence (within 0·01 eV) of the spectrum on the degree of polarization of the emission.

At liquid-nitrogen temperature and at room temperature there appeared to be no polarization in any sample of KCl : Tl.

By variation of the filter F of Fig. 1 it was possible to look at the weak 4750 Å emission which appears in samples of high thallium concentration. No polarization of this emission was found even at liquid-helium temperatures when observed through the (010) face.

No polarization was found in the emission of the *F*-center in KCl through the (010) face at liquid-helium temperatures. The minimum measureable polarization was about $P = 0{\cdot}05$ in this case.

## DISCUSSION

An analysis was made of the polarization characteristics to be expected for the various experimental arrangements used here and for simple dipoles oriented along the ⟨100⟩, ⟨110⟩, or ⟨111⟩ directions in the crystal. All of the low temperature observations are in quantitative agreement with a model which proposes that one out of every three thallium centers absorbs and emits like a simple dipole along a ⟨100⟩ direction and the other two give unpolarized emission.

The observed polarization of emission could be due to a basic lack of symmetry in the center which might occur if the thallium ions were clustered, if negative ion vacancies were next to the thallium ions, or if there were crystal strains which distorted a symmetrical center. These possibilities will be discussed briefly.

Clustering of the thallium ions seems an unlikely explanation for several reasons. First, no important difference in polarization is found for crystals with thallium concentrations differing by a factor of 50. Second, the closest approach of two thallium ions would be along the ⟨110⟩ direction.

The observed polarization is for centers distorted along the ⟨100⟩ directions. Finally, the disappearance of the effect at liquid-nitrogen temperatures would mean the breaking apart of such clusters at low temperatures. This could only happen by the diffusion of positive ion vacancies. From the known activation energies for diffusion of these vacancies it may be shown that the jump frequency is only 1 in $10^{25}$ seconds at 100°K.[5] This would appear to be much too small to cause this effect.

If negative ion vacancies were next to the thallium ions the correct polarization would occur. Here, however, there is again the difficulty that these ions would have to diffuse away to eliminate polarization at liquid-nitrogen temperatures. Because of their increased size, negative ion vacancies are even less mobile than positive ion vacancies, as has been shown by transport measurements at high temperatures. An attempt was made to find experimental evidence for association of negative ion vacancies with thallium centers by X-raying KCl : Tl crystals at liquid-helium temperatures and looking for changes in the *F*-absorption band which might arise from electrons trapped at negative ion vacancies that are associated with thallium ions. For a crystal with 10 p.p.m. of Tl which was X-rayed for an hour to a density of 1p.p.m. of *F*-centers, the energy of the peak position decreased by 0·3 per cent and the width at half maximum of the curve decreased by 1 per cent from values measured for a pure crystal. This variation appears to be within the accuracy of measurement. For a crystal with 1000 p.p.m. of Tl, the peak of the band decreased by 1 per cent in energy and the width increased 4 per cent. No changes were found in the emission spectrum of the *F*-center under these conditions. Since no change was observed in the polarization of thallium luminescence as a function of thallium concentration, the effect on the *F*-band of large thallium concentration is probably not connected with polarization at all but may reflect a general lattice distortion.

Mechanical strain may occur either as a uniform long range macroscopic strain or as a randomly distributed short range strain as might be found near dislocations. For luminescent centers distorted by a uniform strain, the polarization observed should be independent of the polarization, or lack of it, of the exciting light. This is not observed. For the randomly distributed strains only a rather minor variation in polarization would be expected between liquid-helium and liquid-nitrogen temperatures since strains should not be relieved in this temperature region.

It seems likely, then, that the observed polarization arises in thallium ions at normal lattice positions. Since the Jahn–Teller effect offers an explanation which might account for these observations, it will be profitable to examine the applicability of the effect in this instance. ÖPIK and PRYCE treat KCl : Tl specifically and conclude that the Jahn–Teller effect would result in a center polarized along the ⟨111⟩ direction. The observed luminescence appears to be from centers oriented along the ⟨100⟩ direction.

A crude estimate may be made for the jump activation energy, *E*, if the Jahn–Teller effect is the cause of polarization. Assume that the frequency (*P*) of jumping from one orientation to another is given by

$$P = S\exp(-E/kT) \qquad (2)$$

and that *S* is a frequency approximately that of lattice vibrations. If luminescence is allowed and occurs in approximately $10^{-7}$ seconds, *P* must be at least $10^7$ for polarization to be removed. We take *S* as $4\times10^{12}$ which is the vibrational frequency in the neighborhood of the thallium ion.[6] Equation (2) then gives a value of about 0·1 for *E* if *T* is taken as 100°K. This would be an upper limit since the true quenching temperature is less than 100°K. An activation energy of this amount is consistent with the values calculated by VAN VLECK in several cases.

A serious difficulty does arise in understanding this process for the case of KCl : Tl. A configuration coordinate curve model has been used to describe the optical processes in this system and this description assumes strong local interactions of the ion with its neighbors. The quantitative curves that have been proposed show that immediately after absorption of light the center is above the minimum of the excited state by about 40 vibrational quanta.[15] This high local temperature may be dissipated quickly—possibly in 40 vibrations of the center, but the problem is whether the center becomes randomly oriented in this time or not. Qualitative arguments would seem to indicate that randomization would occur, although no careful

analysis of the jump frequency has been made for these conditions.

A very different view of optical processes from that of the strong local interaction was formulated by PEKAR[16] and by HUANG and RHYS.[17] In this view the optical transition is accompanied by the simultaneous creation of many phonons throughout the lattice. If this were the correct mode for lattice interactions, no serious problem of local heating would arise and the Jahn–Teller effect might be expected. However, the simplest form of this theory ignores any relaxation of the lattice around the center and it predicts, as a result, that the shapes of the emission and absorption bands are identical. For KCl : Tl it is known that the half-width of the emission band at low temperature is 0·32 eV and that for the absorption band the half-width is 0·11 eV. Also, on the basis of this theory, the center should interact with the longitudinal optical vibrations of the lattice. For KCl these would have a frequency of $6{\cdot}3 \times 10^{12}$ c/s. The observed value of the interaction frequency of the center in its excited state is $4{\cdot}6 \times 10^{12}$ c/s and is deduced from the half width changes with temperature of the emission spectrum.[18] There are also difficulties, then, with accepting the long range interaction mechanism for KCl : Tl. A compromise may be possible between these extreme points of view of the interaction of a center with the lattice.

## CONCLUSION

It is believed that the polarization of the luminescent emission from KCl : Tl, which appears at low temperatures, arises in isolated thallium centers in the pure lattice. It appears consistent in temperature dependence with values expected on the basis of the Jahn–Teller effect. There are unresolved difficulties involving the type of interaction between the center and the lattice. For strong local interactions the center would have high local temperatures for short times which might make the Jahn–Teller effect unobservable; and the interaction frequency and the symmetry of band shapes predicted on the weak local interaction theory are not observed. These results may point to the need for a more careful study of the interaction between center and lattice in this case.

*Acknowledgements*—The authors wish to acknowledge their indebtedness to Professor D. L. DEXTER and Professor M. H. L. PRYCE for detailed discussion of this work.

## REFERENCES

1. FEOFILOV P. P. *Dokl. Akad. Nauk SSSR*, **92**, 743 (1953).
2. LAMBE J. and COMPTON W. D. *Phys. Rev.* **106**, 684 (1957).
3. VAN DOORN C. Z. *Philips Res. Rep.* **12**, 309 (1957).
4. WEST E. J. and COMPTON W. D. *Phys. Rev.* **108**, 576 (1957).
5. For a review of the extensive work in this field see F. SEITZ, *Rev. Mod. Phys.* **26**, 7 (1954).
6. Some of the work on KCl : Tl is summarized in F. SEITZ and D. TURNBULL *Solid State Physics* Vol. 5 p. 97. Academic Press, London, New York (1957).
7. WILLIAMS F. E. *J. Phys. Chem.* **57**, 780 (1953).
8. MEYER H. J. G. Thesis (unpublished) p. 36 University of Amsterdam (1956).
9. KNOX R. S. and DEXTER D. L. *Phys. Rev.* **104**, 1245 (1956).
10. JAHN H. A. and TELLER E. *Proc. Roy. Soc.* A**161**, 220 (1937).
11. JAHN H. A. *Proc. Roy. Soc.* A**164**, 117 (1938).
12. VAN VLECK J. H. *J. Chem. Phys.* **7**, 72 (1939).
13. ÖPIK V. and PRYCE M. H. L. *Proc. Roy. Soc.* A**239**, 425 (1957).
14. RUSSELL G. A. and KLICK C. C. *Phys. Rev.* **101**, 1473 (1956).
15. WILLIAMS F. E. and HEBB M. H. *Phys. Rev.* **84**, 1181 (1951).
16. PEKAR S. I. *Zh. eksp. theor. fiz.* **20**, 510 (1950); *Ibid.* **22**, 641 (1952).
17. HUANG K. and RHYS A. *Proc. Roy. Soc.* A**204**, 406 (1950).
18. PATTERSON D. A. and KLICK C. C. *Phys. Rev.* **105**, 401 (1957).

VOL 7 195

*J. Phys. Chem. Solids* Pergamon Press 1958. Vol. 7. pp. 175–200.

# THE INTENSITY-DEPENDENCE OF PHOTOCONDUCTION AND LUMINESCENCE OF PHOTOCONDUCTORS IN THE STATIONARY STATE

H. A. KLASENS

Philips Research Laboratories, N.V. Philips' Gloeilampenfabrieken, Eindhoven, Netherlands

(*Received* 24 *January*, 1958; *revised* 4 *April* 1958)

VOL. 7 1958

**Abstract**—The properties of photoconductors and photoconducting phosphors are determined by states in the forbidden zone. Two models are considered for discussing the intensity-dependence of photoconduction and luminescence photoconductors. In each model two recombination processes between electrons and holes are competing. It is shown that the one-state model, where direct recombination may take place between free electrons and free holes or via one impurity state, is generally not adequate.

The two-state model with two discrete states having different capture cross-sections for capturing electrons and holes, can explain satisfactorily many aspects of photoconductors quantitatively, such as superlinearity of luminescence and photoconduction, changes in power from 1 to 0·5 in the conductivity versus intensity curves, activation and killing of phosphors, saturation, etc.

DUBOC's method of considering all possible combinations between simplified versions of the equations describing the stationary state was applied successfully to the mathematical solution of the two-state model. Although there are 128 such combinations, all of which may occur under appropriate conditions, only a few occur in each individual case when only the intensity of excitation is varied. Others may appear when the temperature is varied.

A few practical cases are analysed and the correct combinations of approximations determined. In particular, two examples of superlinearity are studied in detail. It appears that the general features of the curves can in both cases be described adequately in terms of the model with two discrete states, without having to introduce energy distributions of "ground states", as proposed by ROSE. However, a problem remains in that the range of light intensity over which superlinearity occurs is much greater than is predicted by the simple model; it is possible that this can be explained e.g. by the spatial distribution of photoconductive excitation through the sample, due to the absorption of the incident radiation.

## INTRODUCTION

WHEN materials such as ZnS, CdS, PbO, etc., are exposed to radiation which is strongly absorbed by these materials, free carriers, electrons, and holes are created. A stationary state will be reached after a certain period, at which the rate of formation of free carriers is equalled by the rate of recombination.

This recombination may take place in various ways. Direct recombination between free electrons and holes has been found in a number of materials such as germanium,[1] silicon,[1] InSb,[2] CdTe,[3] and CdS.[4] It is possible that an exciton is formed first.[5,6] This will be treated here as essentially a one-step process.

More often recombination takes place after one of the carriers has been captured by discrete states in the forbidden zone. These states are due to imperfections in the lattice, such as impurities, vacancies, or dislocations. If the impurity state is so far below the Fermi level in the dark that it is occupied by an electron, it must first capture a hole before recombination can occur between a free electron and the captured hole. One or possibly both of the two steps in this recombination process may proceed with emission of light.

If both steps are "radiationless," the whole of the absorbed energy is converted into heat.

After an electron or hole has been captured by a discrete state, it may be thermally re-emitted into

the conduction or filled band respectively. The lifetimes of free and trapped carriers are therefore determined not only by a number of capture cross-sections but also by the positions of the impurity levels and by the temperature. The rate of excitation itself is also an important factor in determining the occupation of the various discrete levels, the concentrations of free carriers and the paths along which most of the recombination takes place. It has often been observed, for example, in fluorescent photoconductors that at low excitation densities recombination takes place via one centre and at higher excitation densities via another. If both are accompanied by light emission, a change in the colour of fluorescence will then be observed.[7,8] If the first process is radiationless, the fluorescence intensity increases superlinearly with the excitation intensity, whereas if the second process is radiationless, the increase will be sublinear in the range where the recombination changes from one process to the other.

Fluorescence and photoconduction have many features in common. For example, both are promoted by the incorporation of the same kind of impurities (activators). In ZnS, copper is a well-known activator for producing fluorescence, whereas it turns CdS into a sensitive photoconductor. The same applies to silver.

Both photoconductance and photoluminescence can be quenched by thermal or infrared radiation. Sublinearity and superlinearity of photoconductance as a function of excitation intensity have both been observed.

In the present paper the intensity-dependence of fluorescence and photoconduction will be considered. Before discussing various possible models and laws which can be derived from them, the experimental data in the literature will be reviewed. Examples are drawn only from the field of ZnS- and CdS-type materials.

*Review of experimental data on the intensity-dependence of photoconduction and fluorescence*

Various powers $m$ have been observed in the relation between the photoconduction $\sigma$ and light intensity $U(\sigma \propto U^m)$. Very often, however, these powers are near 1 or near 0·5.[9–16] A transition from $m = 1 \rightarrow m = 0{\cdot}5$ often takes place when the exciting intensity increases within a fairly narrow range.[10,11,13,15]

Depending on the temperature, the photocurrent may increase superlinearly over a limited range of intensities.[13,17–26] In CdSe single crystals the superlinear range was found to shift to higher intensities with increasing temperature and to be intermediate between ranges with a power near unity.[21,22]

In the relation between fluorescence $I$ and excitation intensity $U$, the most common power is unity. At a high exciting intensity, however, "saturation" occurs, the power being less than one.[27] With cathode rays, high excitation densities are easily obtained and saturation fluorescence is often observed with sulphide phosphors.[28–32] Superlinear relations have been observed especially at low intensities, with occasionally powers of 1·5, 2, and $> 2$.[33–43] Incorporation of elements such as nickel and cobalt, known as "killers", shifts the superlinear range to higher intensities. In the (ZnCd)S–Ag, Ni phosphors,[35,37] the superlinear range is intermediate between ranges with a linear relationship. Thus at low intensities a very small, but constant, quantum efficiency is found ($10^{-5}$), which over a narrow range jumps to a higher constant value.

ANTONOV–ROMANOVSKY *et al.*,[41–43] measuring the quantum efficiency of copper-activated ZnS over a wide range, found a "plateau" of constant quantum efficiency near one, sloping down to lower values at low and high intensities.

## POSSIBLE MODELS

The fact that the incorporation of certain impurities (silver, copper, etc.) in ZnS, CdS, CdSe, etc., often enhances the photoconduction and increases or alters the luminescence shows that these impurities are the seats of new recombination processes which did not exist before. Since electrons and holes also recombined before activation, there must at least be two possible ways for electrons and holes to recombine in an "activated" material. Two possible models illustrating such competitive processes are shown in Figs. 1(a) and (b). In both cases free carriers are produced optically by raising electrons from the occupied into the conduction band (process $U$). In Fig. 1(a) direct recombination takes place between free carriers (process $F$) before activation. Activation has produced a new level $A$ and has opened up a new two-step process $I \rightarrow C$. In Fig. 1(b) it has been

assumed that recombination in the unactivated material occurs via a level $H$. Such a level may be associated, for example, with a vacancy or dislocation or it may be a surface level. Another possibility is that during activation two new levels of the type $A$ and $H$ are introduced simultaneously.

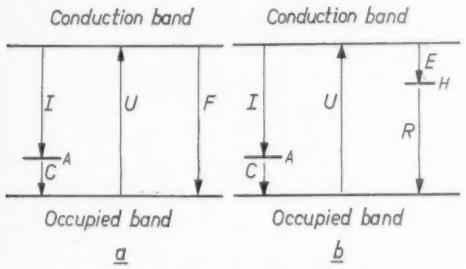


FIG. 1. Possible competitive recombination processes: (*a*) one-state model; (*b*) two-state model.

The model most often chosen in the literature, when discussing the properties of photoconductors and photoconducting phosphors, is that of Fig. 1(b).

Although such models are relatively simple and often perhaps too simple, the complete solution of the stationary state under excitation is already very complex. Even with simplifying assumptions such as the free-carrier densities being small compared to the concentration of trapped carriers, etc.—assumptions which may be valid over a limited range of intensities—the complete solution may still occupy half a page of print.[44] Moreover the physics of the problem is not easily revealed by such a solution. To obtain more simple solutions further assumptions are then often made to explain a certain behaviour of the material. Such assumptions are more usually based on intuition than on experimental facts, and one may be misled easily in this way and draw conclusions which are not really justified.

On the other hand new and complicating assumptions have sometimes been introduced which are not always necessary to explain a certain behaviour.

For example, to explain the constant efficiency of (ZnCd)S–Ag, Ni at low intensities, ROBERTS and WILLIAMS[45] assumed that the activator gave rise to two states in the forbidden zone: the ground state $A$ and a second or "waiting" state above it in which an electron arrives from the conduction band and from which it may either be re-excited thermally or fall to the ground state. SCHÖN[44] has shown that this additional assumption is not necessary and that the constant low efficiency can be explained with the two-level model of Fig. 1(b). A superlinear photoconductance can also be explained with this model without having to resort to a two-step excitation, as TOLSTOI[26] did.

ANTONOV–ROMANOVSKY *et al.*[41–43] introduced as a new factor the optical liberation of electrons from traps, with the additional assumption that electrons liberated optically behave differently from electrons released thermally, in order to explain the plateau in the efficiency versus intensity curve.

BUBE[46] assumed the presence of three discrete levels in the forbidden zone in order to explain the superlinear behaviour of his CdSe single crystals.

ROSE[47,48] went even further by assuming a quasi-continuous distribution of bound states in the forbidden zone of a photo-conductor. With this model fractional powers between 0·5 and 1·0 for the current/light curves of a photoconductor can easily be explained with suitably chosen energy distributions of the discrete states. The phenomena of activation, superlinearity, and infrared quenching of photoconductance, however, led to the assumption of two classes of recombination centers, both classes giving rise to levels distributed through the forbidden gap. A few aspects of ROSE's model will be discussed at the end of this paper.

In our opinion, the authors mentioned above have discarded the more simple models of Figs. 1(a) and (b) prematurely, without realizing their versatility.

It is the purpose of the present paper, therefore, first to put these simple models to a full test, to see which of them can most accurately account for the observed facts and which conclusions can safely be drawn regarding the various parameters involved in the recombination processes, before allowing for additional factors such as, for example, possible energy distributions of the impurity states.

In analysing the kinetics of the stationary state, a procedure first used by DUBOC[49] proved to be most fruitful. A similar procedure was applied by BROUWER[50] to find an easy way of solving KRÖGER and VINK's[51] set of equations describing the interdependence between imperfections in a crystal

which is in equilibrium with a vapour. Following KRÖGER and VINK, a simple graphical method of representation will be used.

According to DUBOC's method, the group of equations describing the stationary state is replaced by groups of simpler equations, each group being valid under appropriate conditions. Solutions of all possible combinations of the simple equations are considered. It will be shown that all possible combinations can in fact occur, depending on the choice of parameters, but that, once the parameters are chosen, the material passes through only a limited number of combinations when the intensity of excitation is varied from extremely low to extremely high values. The procedure will first be illustrated by the more simple model of Fig. 1(a).

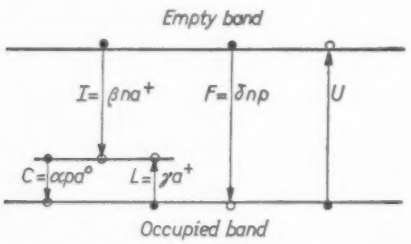


FIG. 2. Schematic drawing showing electronic transitions which are considered in discussing the equilibrium condition for a one-state model.

## THE ONE-STATE MODEL

In describing the stationary condition during excitation, the following symbols will be used (see also Fig. 2):

$a$ = total density of recombination centers ($A$). The levels are below the dark Fermi level.
$a^0$ = density of occupied $A$ levels
$a^+$ = density of empty $A$ levels*
$n$ = density of free electrons in the conduction band
$p$ = density of free holes in the occupied band
$F = \delta np$ = rate of direct recombination between free carriers
$I = \beta n a^+$ = rate of recombination between electrons and holes trapped by $A$
$C = \alpha p a^\circ$ = rate of capture of free holes by occupied $A$ centres
$L = \gamma a^+$ = rate of thermal release of holes from empty $A$ centres
$U$ = rate of excitation of free carriers. Between $\gamma$ and $\alpha$ there exists the relationship

$$\gamma = \alpha N_p \exp(-E_A/kT), \tag{1}$$

where $E_A$ is the distance between $A$ and the top of the occupied band and $N_p$ is the effective density of states in the occupied band ($\sim 10^{19}$).

The stationary state is described by the following equations:

$$a = a^0 + a^+ \tag{2}$$

$$n = a^+ + p \tag{3}$$

$$U = I + F \tag{4}$$

$$C = L + I \tag{5}$$

In order to keep the calculation as simple as possible, it has been assumed that the band gap is so large and the dark Fermi level so far below the empty band and so far above $A$ and the full band that for $U = 0$, $a_0{}^0 = a$, while $n_0$ and $p_0$ can be neglected. The analysis given below could easily be extended to a more general set of equations. Such an extension will be discussed in more detail below.

Other factors such as a thermal generation of electrons from $A$ can also easily be included by adding the appropriate term to equations (4) and (5).

The complete solution of equations (2)–(5), giving the relation between $n$, $p$, $a^+$, and $U$, is:

$$\left.\begin{aligned} U &= \frac{(Pn+Qn^2)-\{(Pn+Qn^2)^2-4\alpha(Rn^3+Sn^4)\}^{\frac{1}{2}}}{2\alpha} \\ p &= \frac{U-\beta n^2}{(\delta-\beta)n};\quad a^+ = n-p \end{aligned}\right\} \tag{6}$$

with
$$P = (\alpha a+\gamma)(\beta-\delta)$$
$$Q = \beta(\beta+\alpha)-\delta(\beta-\alpha)$$
$$R = (\alpha\beta a+\beta\delta-\gamma\delta)(\beta-\delta)$$
$$S = \alpha\beta\delta.$$

* It is not our intention to indicate the effective charges of the centres in this way. By $a^+$ is meant a centre which has lost an electron.

Although this solution is still relatively simple, one gets little insight in the total behaviour of $n$ and $p$ as a function of $U$ with various values of the parameters.

Using DUBOC's procedure, we shall now make all possible combinations of the simplest form of equations (2)–(5) by neglecting in turn one of the two terms on the right-hand side of each equation. We thus have the following set of simplified equations:

$$\left.\begin{array}{l}(1)\ a=a^0\quad(1)\ n=a^+\quad(1)\ U=I\quad(1)\ C=L\\(2)\ a=a^+\quad(2)\ n=p\quad(2)\ U=F\quad(2)\ C=I\end{array}\right\}\qquad(7)$$

A particular situation can in general be described approximately by one particular combination of four simplified equations, one out of each

*Table* 1. *Solutions of all quantities involved in the equilibrium kinetics of the one-state model for all the possible combinations of Duboc's approximations*

| Code | $a^0$ | $a^+$ | $p$ | $n$ | $C$ | $L$ | $I$ | $F$ |
|---|---|---|---|---|---|---|---|---|
| 1111 | $a$ | $\frac{U^{\frac12}}{\beta^{\frac12}}$ | $\frac{\gamma U}{\alpha\beta^{\frac12}a}$ | $\frac{U^{\frac12}}{\beta^{\frac12}}$ | $\frac{\gamma U^{\frac12}}{\beta^{\frac12}}$ | $\frac{\gamma U^{\frac12}}{\beta^{\frac12}}$ | $U$ | $\frac{\delta\gamma U}{\alpha\beta a}$ |
| 1112 | $a$ | $\frac{U^{\frac12}}{\beta^{\frac12}}$ | $\frac{U}{\alpha a}$ | $\frac{U^{\frac12}}{\beta^{\frac12}}$ | $U$ | $\frac{\gamma U^{\frac12}}{\beta^{\frac12}}$ | $U$ | $\frac{\delta U^{\frac12}}{\alpha\beta^{\frac12}a}$ |
| 1121 | $a$ | $\frac{\alpha^{\frac12}a^{\frac12}U^{\frac12}}{\delta^{\frac12}\gamma^{\frac12}}$ | $\frac{\gamma^{\frac12}U^{\frac12}}{\delta^{\frac12}\alpha^{\frac12}a^{\frac12}}$ | $\frac{\alpha^{\frac12}a^{\frac12}U^{\frac12}}{\delta^{\frac12}\gamma^{\frac12}}$ | $\frac{\gamma^{\frac12}\alpha^{\frac12}a^{\frac12}U^{\frac12}}{\delta^{\frac12}}$ | $\frac{\gamma^{\frac12}\alpha^{\frac12}a^{\frac12}U^{\frac12}}{\delta^{\frac12}}$ | $\frac{\alpha\beta aU}{\delta\gamma}$ | $U$ |
| 1122 | $a$ | $\frac{\alpha^{\frac12}a^{\frac12}U^{\frac12}}{\delta^{\frac12}\beta^{\frac12}}$ | $\frac{\beta^{\frac12}U^{\frac12}}{\delta^{\frac12}\alpha^{\frac12}a^{\frac12}}$ | $\frac{\alpha^{\frac12}a^{\frac12}U^{\frac12}}{\delta^{\frac12}\beta^{\frac12}}$ | $\frac{\beta^{\frac12}\alpha^{\frac12}a^{\frac12}U^{\frac12}}{\delta^{\frac12}}$ | $\frac{\gamma\alpha^{\frac12}a^{\frac12}U^{\frac12}}{\delta^{\frac12}\beta^{\frac12}}$ | $\frac{\beta^{\frac12}\alpha^{\frac12}a^{\frac12}U^{\frac12}}{\delta^{\frac12}}$ | $U$ |
| 1211 | $a$ | $\frac{\alpha^{\frac12}a^{\frac12}U^{\frac12}}{\beta^{\frac12}\gamma^{\frac12}}$ | $\frac{\gamma^{\frac12}U^{\frac12}}{\alpha^{\frac12}\beta^{\frac12}a^{\frac12}}$ | $\frac{\gamma^{\frac12}U^{\frac12}}{\alpha^{\frac12}\beta^{\frac12}a^{\frac12}}$ | $\frac{\gamma^{\frac12}\alpha^{\frac12}a^{\frac12}U^{\frac12}}{\beta^{\frac12}}$ | $\frac{\gamma^{\frac12}\alpha^{\frac12}a^{\frac12}U^{\frac12}}{\beta^{\frac12}}$ | $U$ | $\frac{\delta\gamma U}{\alpha\beta a}$ |
| 1212 | $a$ | $\frac{\alpha a}{\beta}$ | $\frac{U}{\alpha a}$ | $\frac{U}{\alpha a}$ | $U$ | $\frac{\alpha\gamma a}{\beta}$ | $U$ | $\frac{\delta U^2}{\alpha^2a^2}$ |
| 1221 | $a$ | $\frac{\alpha aU^{\frac12}}{\gamma\delta^{\frac12}}$ | $\frac{U^{\frac12}}{\delta^{\frac12}}$ | $\frac{U^{\frac12}}{\delta^{\frac12}}$ | $\frac{\alpha aU^{\frac12}}{\delta^{\frac12}}$ | $\frac{\alpha aU^{\frac12}}{\delta^{\frac12}}$ | $\frac{\alpha\beta aU}{\delta\gamma}$ | $U$ |
| 1222 | $a$ | $\frac{\alpha a}{\beta}$ | $\frac{U^{\frac12}}{\delta^{\frac12}}$ | $\frac{U^{\frac12}}{\delta^{\frac12}}$ | $\frac{\alpha aU^{\frac12}}{\delta^{\frac12}}$ | $\frac{\gamma\alpha a}{\beta}$ | $\frac{\alpha aU^{\frac12}}{\delta^{\frac12}}$ | $U$ |
| 2111 | $pa^0=\frac{\gamma a}{\alpha}$ | $a$ | indefinite | $a$ | $\gamma a$ | $\gamma a$ | $\beta a^2$ | indefinite |
| 2112 | $pa^0=\frac{\beta a^2}{\alpha}$ | $a$ | indefinite | $a$ | $\beta a^2$ | $\gamma a$ | $\beta a^2$ | indefinite |
| 2121 | $\frac{\delta\gamma a^2}{\alpha U}$ | $a$ | $\frac{U}{\delta a}$ | $a$ | $\gamma a$ | $\gamma a$ | $\beta a^2$ | $U$ |
| 2122 | $\frac{\delta\beta a^3}{\alpha U}$ | $a$ | $\frac{U}{\delta a}$ | $a$ | $\beta a^2$ | $\gamma a$ | $\beta a^2$ | $U$ |
| 2211 | $\frac{\gamma\beta a^2}{\alpha U}$ | $a$ | $\frac{U}{\beta a}$ | $\frac{U}{\beta a}$ | $\gamma a$ | $\gamma a$ | $U$ | $\frac{\delta U^2}{\beta^2a^2}$ |
| 2212 | $\frac{\beta a}{\alpha}$ | $a$ | $\frac{U}{\beta a}$ | $\frac{U}{\beta a}$ | $U$ | $\gamma a$ | $U$ | $\frac{\delta U^2}{\beta^2a^2}$ |
| 2221 | $\frac{\delta^{\frac12}\gamma a}{\alpha U^{\frac12}}$ | $a$ | $\frac{U^{\frac12}}{\delta^{\frac12}}$ | $\frac{U^{\frac12}}{\delta^{\frac12}}$ | $\gamma a$ | $\gamma a$ | $\frac{\beta aU^{\frac12}}{\delta^{\frac12}}$ | $U$ |
| 2222 | $\frac{\beta a}{\alpha}$ | $a$ | $\frac{U^{\frac12}}{\delta^{\frac12}}$ | $\frac{U^{\frac12}}{\delta^{\frac12}}$ | $\frac{\beta aU^{\frac12}}{\delta^{\frac12}}$ | $\gamma a$ | $\frac{\beta aU^{\frac12}}{\delta^{\frac12}}$ | $U$ |

column. There are thus $2^4 = 16$ such border-line cases. In referring to these combinations, it was found most practical to introduce a code system. Instead of mentioning each time the set of four equations which describes a given situation most faithfully, a particular combination of equations will be designated by a code number consisting of 4 digits, each digit indicating which of the two equations of each column has been chosen. For example, a situation indicated by the code number 1122 means:

$a = a^\circ$, which in fact means that $a^+ \ll a$
$n = a^+$, or $p \ll a^+$
$U = F$, or the bulk of the recombination is between free electrons and free holes
$C = I$, or the thermal release of holes can be neglected.

The solutions of $n$, $p$, $I$, $F$, $C$, and $L$ as functions of $U$ for the 16 situations are shown in Table 1.

The same table can be used for a system in which there is one recombination level far enough above the dark Fermi level to be completely empty when not excited and nearer to the conduction band, simply by substituting $n$ for $p$ and vice versa, and by realizing that $a^+$ then means a level occupied by an electron and $a^0$ an empty one.

Two combinations indicated by code numbers 2111 and 2112 are remarkable because the values of $p$, $a^0$, and $F$ are indefinite. The two situations have in common the approximations $U = I = \beta n a^+$; $a^+ = a$ and $n = a^+$, or $U = \beta a^2$. At this singular value of $U$ only the product of $pa^0$ is defined. This is a case where $p$, $a^0$, and $F$ show a discontinuity. It will be shown in an example below that at this singular value of $U$, $p$ and $F$ increase with an infinite power of $U$ in our first approximation.

We shall now follow systematically those situations which may arise when, starting from very low values, $U$ is increased.

At extremely low values of $U$, $a^0$ always equals $a$ and $C = L$ (thermal equilibrium). One thus has, at low intensities: $\gamma a^+ = \alpha p a$. It depends on the value of $\gamma/\alpha a = N_p[\exp(-E_a/kT)]/a$, whether $p$ is larger or smaller than $a^+$ for $U \to 0$.

$$\text{Now } F/I = \delta n p/\beta n a^+ = \delta\gamma/\alpha\beta a. \tag{8}$$

This ratio therefore determines whether $I$ is smaller or larger than $F$ for $U \to 0$. Consequently there are four possible initial conditions, depending on the values of the parameters:

| $\frac{\gamma}{\alpha a}$ | $\frac{\delta\gamma}{\alpha\beta a}$ | Initial situation |
|---|---|---|
| $<1$ | $<1$ | 1111 |
| $>1$ | $<1$ | 1211 |
| $<1$ | $>1$ | 1121 |
| $>1$ | $>1$ | 1221 |

(9)

The condition 1111 is favoured by low temperatures, a large number of activators, and a high value of $\beta/\delta$. Having chosen the parameters such

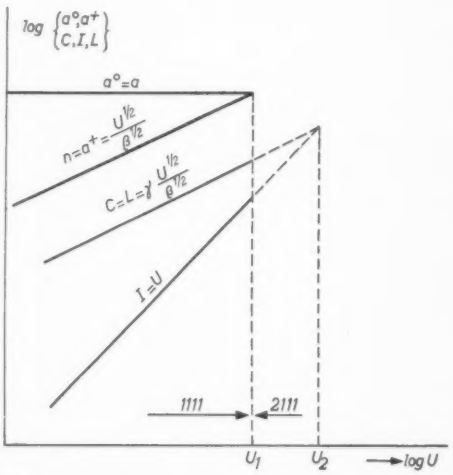


FIG. 3. Diagram illustrating a change in situation from 1111 to 2111 at $U = U_1$. The transition 1111 → 1112 which would occur at $U_2$ where $I$ and $C$ meet (dashed lines), cannot take place because $U_2 > U_1$.

that this situation really occurs at very low intensities, one can easily ascertain what will happen when $U$ is increased. No change will take place in the second or third digit in the code number initially, since $F$ and $I$ both increase linearly with $U$, whereas $p$ and $n$ are both proportional to $U^{\frac{1}{2}}$. What will happen is that either $a^+$ becomes equal to $a$ (the centres are becoming saturated) or $I$ draws level with $C$. In the first case the code number changes to 2111, in the second case to 1112. What actually happens depends on the values of the parameters. If the transition 1111 → 2111

occurs at all, it will occur at that value of $U$ at which $a^+ = U^{\frac{1}{2}}/\beta^{\frac{1}{2}} = a$ (Fig. 3) or $U = U_1 = \beta a^2$.

On the other hand, a change to 1112 might take place and that would happen at $U = U_2$ where $C = \gamma U^{\frac{1}{2}}/\beta^{\frac{1}{2}} = I = U$ or $U_2 = \gamma^2/\beta$.

Thus if $\beta a^2 < \gamma^2/\beta$ or $\beta a < \gamma$, $U_1$ is smaller than $U_2$ and the first transition will occur; if $U_1 > U_2$, the second occurs.

When arriving at the situation characterized by the code number 2111, $p$ has just reached the value $p_1 = \gamma/\alpha$ and $F = F_1 = \delta\gamma a/\alpha$ (Fig. 4). In the

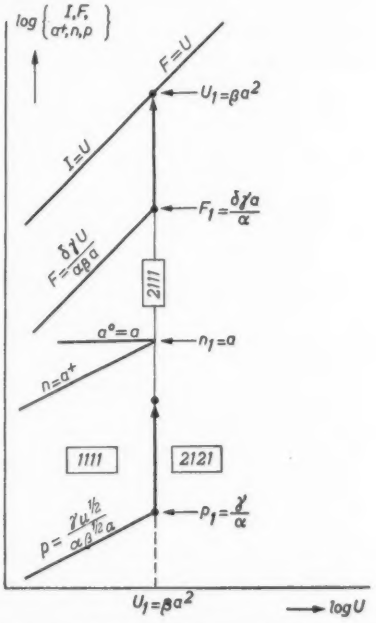


FIG. 4. Diagram illustrating the vertical jumps of $p$ and $F$ in the situation 2111 at $U_1 = \beta a^2$. $F$ jumps from $F_1$ to $U_1$ and $p$ jumps by the same amount.

situation 2111 itself, $p$, $a^0$, and $F$ are indefinite and only the product $pa^0$ is defined ($= \gamma a/\alpha$). Since $a^0$ can only become smaller than $a$, $p$ can grow in a vertical direction (in our first approximation $U$ remains constant) until again a change in code number takes place. This can occur not only if $p$ overtakes $n$ but also, since $F$ grows at the same rate as $p(F = \delta np)$, if $F$ catches up with $U$.

In the first case $p$ and also $F$ would increase by a factor $a/p_1 = \alpha a/\gamma$. In the second case both would increase by a factor $U_1/F_1 = \alpha\beta a/\gamma\delta$. It depends on the ratio of these two factors which transition actually occurs. In the situation shown in Fig. 4, $F$ has caught up with $U$ before $p$ has drawn level with $n$, and the code number changes from 2111 to 2121.

Thus if $\alpha\beta a/\gamma\delta < \alpha a/\gamma$, or $\beta < \delta$, the transition will be $2111 \rightarrow 2121$; but if $\beta > \delta$, the next code number is 2211. In this way one can follow systematically which situations arise successively when starting from one of the four possible initial conditions until no further changes can take place. The final situations are either 1222 or 2222. Since in both cases $n = p$ and $I = C$, one has $a^+/a^0 = \alpha/\beta$. Thus the majority of the recombination centres will be occupied if $\alpha \ll \beta$ (1222) or empty if $\alpha \gg \beta$ (2222).

There are 14 possible ways of arriving at one of these situations from one of the initial situations. These 14 possibilities can be read from Fig. 5, where all possible transitions are given, with the

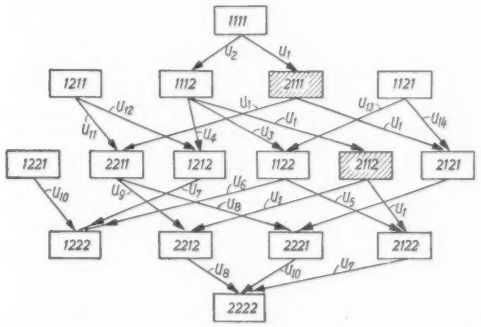


FIG. 5. Showing the relation between all possible equilibrium situations in a one-state model. The arrows indicate transitions which can occur when the excitation density is increased.

The shaded areas indicate situations where superlinearity occurs

$$U_1 = \beta a^2;\ U_2 = \frac{\gamma^2}{\beta};\ U_3 = \frac{\alpha^2\beta a^2}{\delta^2};\ U_4 = \frac{\alpha^2 a^2}{\beta};$$

$$U_5 = \frac{\beta\delta a^2}{\alpha};\ U_6 = \frac{\alpha^2\delta a^2}{\beta^2};\ U_7 = \delta a^2;\ U_8 = \frac{\beta^2 a^2}{\delta};$$

$$U_9 = \gamma a;\ U_{10} = \frac{\delta\gamma^2}{\beta^2};\ U_{11} = \frac{\beta\gamma a}{\alpha};\ U_{12} = \frac{\alpha\gamma a}{\beta};$$

$$U_{13} = \frac{\delta\gamma^3}{\alpha\beta^2 a};\ U_{14} = \frac{\delta\gamma a}{\alpha}.$$

values of $U$ at which they take place. This figure shows that with our code the digits of the code numbers can increase only when $U$ is raised.

In the manner described above, the conditions can be specified under which one obtains a particular sequence of situations. It can easily be shown, for example, that to proceed according to $1111 \rightarrow 1112 \rightarrow 2112 \rightarrow 2122 \rightarrow 2222$ the following relations must exist between the parameters: $\gamma/a < \beta < \delta < \alpha$.

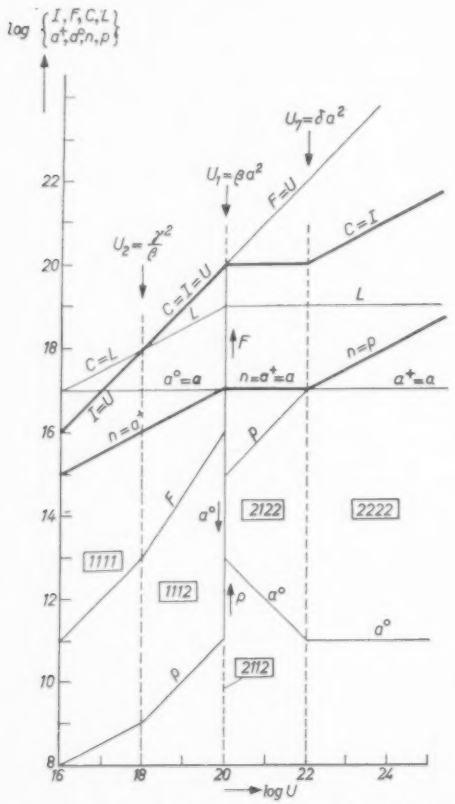


FIG. 6. Behaviour diagram showing, to a first approximation, the effect of $U$ for a material with $10^{17}$ recombination centres and with

$$\gamma = 10^{2},\ \alpha = 10^{-8},\ \beta = 10^{-14},\ \text{and}\ \delta = 10^{-12}.$$

These conditions are satisfied, for example, by: $a = 10^{17}$ cm$^{-3}$, $\gamma = 10^{2}$ sec$^{-1}$, $\alpha = 10^{-8}$ cm$^{3}$ sec$^{-1}$, $\beta = 10^{-14}$ cm$^{3}$ sec$^{-1}$, $\delta = 10^{-12}$ cm$^{3}$ sec$^{-1}$.

With the aid of Table 1, the behaviour of our model can easily be followed by using a graphical representation as shown in Fig. 6. The initial condition is 1111, since $\gamma < \alpha a$ and $\delta\gamma/\alpha\beta a$. At, e.g., $U = 10^{16}$ cm$^{-3}$ sec$^{-1}$, this situation still prevails with $I = U = 10^{16}$,* $C = L = 10^{17}$, $n = a^{+} = 10^{15}$, $p = 10^{8}$, $F = 10^{11}$.

The slopes on a log scale with log $U$ as abscissa can immediately be read from Table 1. At $U = 10^{18}$ $I = C = L$ and the code number changes to 1112. One notices that at lower intensities practically all recombinations occur through $A$, although, with $L = C$, the level is in thermal equilibrium with the occupied band and therefore a "shallow trapping state". In Fig. 7 the values of $F$ and $I$ calculated

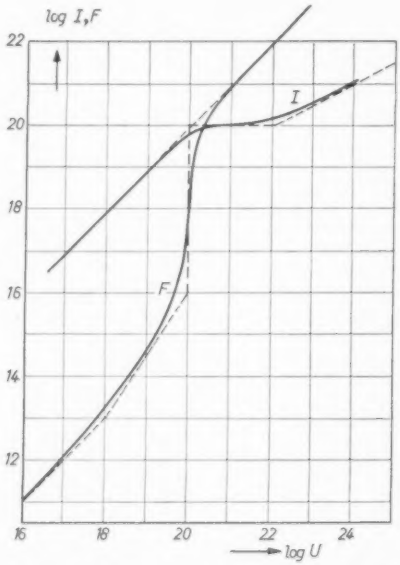


FIG. 7. Comparison between the exact values of $F$ and $I$ with the approximate values of Fig. 6 (dashed lines).

from equation (6) are compared with the approximate values of Fig. 6. The transition region between 1111 and 1112 would, under the chosen conditions, produce a power near 1·2 for the relation between $F$ and $U$ over a substantial range of approximately three orders of magnitude.

A sharp rise such as is found for $F$ and $p$ near $U = 10^{20}$ would in practice be less steep. When a crystal is exposed to exciting light, the latter is absorbed within a layer of a certain depth, depending

* The dimensions will be omitted from this point onwards for the sake of simplicity.

on the absorption coefficient. The density of excitation drops exponentially, and layers near the surface will reach the superlinear range at a lower intensity of the exciting light than layers further removed from the surface. This causes the superlinear range to be spread out in practice over a larger range than that indicated in Fig. 7. The influence of the exponential drop in excitation density is counterbalanced to some extent by the interdiffusion of free carriers between volume elements. Measurements of the photo-electromagnetic (P.E.M.) effect have shown, however, that the ambipolar diffusion length in sulphide photoconductors is very small ($\sim 0{\cdot}1\mu$).[60]

At first sight the one-state model seems to account for a number of experimental facts. Activation of a phosphor and also sensitization or desensitization of a photoconductor can obviously be explained. In Fig. 6, for example, with $U < 10^{20}$, $n$ is 10 times higher than it would have been without $A$. Moreover, infrared quenching of $I$ and $n$ can be explained if one assumes that the infrared absorption lifts electrons from the occupied band into empty $A$ levels. In that case exposure to infrared has the same effect as increasing the temperature. For example, if $\gamma$ is increased to such an extent that $\delta\gamma/\alpha\beta a$ becomes $> 1$, while $\gamma/\alpha a$ remains $< 1$, the code number 1111 changes to 1121, $I$ will be quenched, and the conductivity will be lowered at the same time.

Transitions $n \propto U$ to $n \propto U^{\frac{1}{2}}$ which are frequently observed, would happen at the transitions $2211 \rightarrow 2221$, $2212 \rightarrow 2222$, or $1212 \rightarrow 1222$. In each case $F$ takes over from $I$ in being equal to $U$. At the lower intensities $F$ would in all cases be proportional to $U^2$. This would be in agreement with observations of BROSER and WARMINSKY[10] on both photoconduction and luminescence of a CdS crystal if the emission they observed were indeed due to a band–band transition. This does not seem likely, however, since their crystal was activated with silver and the fluorescence intensity was found to increase with the silver content.[52] Here the one-state model obviously fails.

This model is also apparently too simple in many other respects. Although superlinearity is found (2111 and 2112), it is only for the minority charge carriers, contrary to the observation of, for example, BUBE on CdSe.[22] A superlinear increase of the luminescence via an activator level could never be accounted for with the one-state model. The only emission which could be superlinear is the band–band emission $F$.

It is of interest in this connection to note that DIEMER *et al.*[53] found the so-called "edge emission" in CdS in the region 5100–5500 Å, first observed by KRÖGER[54] and attributed by him to a band–band transition, to be sublinear at high exciting intensities. In other words there must be another transition competing strongly with the edge emission at high excitation rates. If the edge emission were a band–band or exciton transition, this other transition would be via an impurity level. Table 3 shows clearly that such a situation can never arise. This supports the criticism[55,56] that this emission cannot be a band–band transition, but must be connected with a level in the forbidden zone.

Summarizing, we conclude that the one-state model discussed above is useful only if band–band transitions are actually involved, and secondly that the behaviour of common photoconductors, and in particular the superlinearity of photoconduction and fluorescence, cannot be explained on the basis of the one-state model. We must therefore turn to a more complicated model with two states in the forbidden zone.

### THE TWO-STATE MODEL

When considering two types of levels in the forbidden zone, each type with its own parameters, three models can be drawn up, depending on the position of the two levels with respect to the dark Fermi level. Both may be below or above the dark Fermi level or one may be above and the other below it. We have chosen the latter case, but the analysis could easily be extended to include also the other models. We have thus added to the one-state model of Fig. 2 levels $H$ above the dark Fermi level and not occupied by electrons when the substance is not excited and in thermal equilibrium. This level is assumed to be in thermal equilibrium with the conduction band only.

The stationary state is described by:

$$a = a^0 + a^+ \tag{10}$$

$$h = h^0 + h^- \tag{11}$$

$$a^+ + p = h^- + n \tag{12}$$

$$U = I + R \tag{13}$$

$$C = L + I \tag{14}$$

$$E = B + R. \tag{15}$$

The new symbols have the following meaning (see also Fig. 8):

$h$ = total density of $H$ levels
$h^0$ = density of empty $H$ levels
$h^-$ = density of occupied $H$ levels
$R$ = recombination rate via $H$ per unit volume = $\eta p h^-$
$E$ = rate of capture of electrons by empty $H$ levels = $\epsilon n h^0$
$B$ = rate of thermal release of electrons from occupied $H$ levels = $\zeta h^-$.

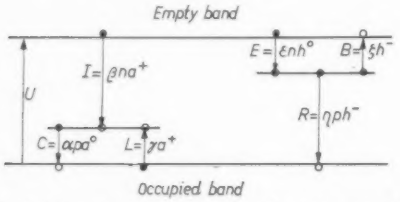


FIG. 8. Schematic drawing indicating the transitions, parameters, and symbols used in discussing the two-state model.

It has been assumed, in formulating the stationary state by the above equations, that the wavelength of excitation is shorter than that corresponding to the band gap. In the examples analysed below, this is indeed the case. Very often, however, excitation takes place with wavelengths at the long-wave side of the absorption edge (for example ZnS phosphors excited with 3650 Å). In that case the exciting radiation is absorbed by the impurity centre itself, resulting e.g. in a free electron and a trapped hole. It is also possible that even with shorter wavelengths a similar process occurs via an exciton, which dissociates at the centre into a free electron and a trapped hole. In that case a slightly different set of equations is to be used. This situation will be discussed in a forthcoming paper.

The code system we shall use is based on the following set of simplified equations:

$$\left.\begin{array}{llll} (1)\ a = a^0 & (2)\ a = a^+ & & \\ (1)\ h = h^0 & (2)\ h = h^- & & \\ (1)\ a^+ = h^- & (2)\ a^+ = n & (3)\ h^- = p & (4)\ n = p \\ (1)\ U = I & (2)\ U = R & & \\ (1)\ C = L & (2)\ C = I & & \\ (1)\ E = B & (2)\ E = R & & \end{array}\right\} \tag{16}$$

All situations which can occur and which are possible combinations of six of the above equations one out of each row, are indicated by a code number, this time consisting of six digits. Each digit corresponds to one row of the set of equations (16) and indicates which equation of the corresponding row is chosen. There are 128 different situations. It may be emphasized again that, in order to keep the calculation as simple as possible, it has been assumed that for $U = 0$, $a_0^0 = a$, $h_0^0 = h$ and that $n_0$ and $p_0$ can be neglected. It has already been pointed out above that DUBOC's analysis can be applied to a more general set of equations in which these assumptions are not made. Such cases will be discussed further below.

The band–band recombination has also been left out in our simple two-level model. We have already seen that this transition does not play an important part under normal conditions, although it may very well exert its influence under abnormal conditions e.g. high exciting densities, extremely low values of $a$ and $h$, etc. In each individual example the magnitude of the band-to-band recombination may be estimated. VAN ROOSBROECK and SHOCKLEY[57] have derived a formula for the capture cross-section of a free hole capturing a free electron. Using this formula, one can make an estimate of $\delta$ in each particular case.* In our model the band-to-band transition is given by the product $\delta np$. By comparing this with the magnitude of $I$ and $R$ as determined from the analysis of a particular example, one can always check whether it is really permissible to neglect the band-to-band transition.

The solutions for 32 of the more important situations are shown in Table 2. All situations with $a^+ = a$, $p = h^-$, and $p = n$—conditions which are not often encountered in the usual sulphide-type photoconductors—have been left out of this table,

* With a band gap of 3·7 eV—as in ZnS—$\delta$ would be of the order of $10^{-12}$ cm$^3$sec$^{-1}$ at room temperature.

*Table* 2

| No. | Code | $a^0$ | $a^+$ | $h^0$ | $h^-$ | $n$ | $p$ | $I = \beta n a^+$ | $R = \eta p h^-$ |
|---|---|---|---|---|---|---|---|---|---|
| 1 | 111111 | $a$ | $\frac{\epsilon^{\frac{1}{2}}h^{\frac{1}{2}}U^{\frac{1}{2}}}{\beta^{\frac{1}{2}}\zeta^{\frac{1}{2}}}$ | $h$ | $\frac{\epsilon^{\frac{1}{2}}h^{\frac{1}{2}}U^{\frac{1}{2}}}{\beta^{\frac{1}{2}}\zeta^{\frac{1}{2}}}$ | $\frac{\zeta^{\frac{1}{2}}U^{\frac{1}{2}}}{\beta^{\frac{1}{2}}\epsilon^{\frac{1}{2}}h^{\frac{1}{2}}}$ | $\frac{\gamma\epsilon^{\frac{1}{2}}h^{\frac{1}{2}}U^{\frac{1}{2}}}{\alpha\beta^{\frac{1}{2}}\zeta^{\frac{1}{2}}a}$ | $U$ | $\frac{\gamma\epsilon\eta hU}{\alpha\beta\zeta a}$ |
| 2 | 111112 | $a$ | $\frac{\alpha^{\frac{1}{3}}\epsilon^{\frac{1}{3}}h^{\frac{1}{3}}a^{\frac{1}{3}}U^{\frac{1}{3}}}{\beta^{\frac{1}{3}}\gamma^{\frac{1}{3}}\eta^{\frac{1}{3}}}$ | $h$ | $\frac{\alpha^{\frac{1}{3}}\epsilon^{\frac{1}{3}}h^{\frac{1}{3}}a^{\frac{1}{3}}U^{\frac{1}{3}}}{\beta^{\frac{1}{3}}\gamma^{\frac{1}{3}}\eta^{\frac{1}{3}}}$ | $\frac{\gamma^{\frac{1}{3}}\eta^{\frac{1}{3}}U^{\frac{1}{3}}}{\alpha^{\frac{1}{3}}\beta^{\frac{1}{3}}\epsilon^{\frac{1}{3}}h^{\frac{1}{3}}a^{\frac{1}{3}}}$ | $\frac{\gamma^{\frac{1}{3}}\epsilon^{\frac{1}{3}}h^{\frac{1}{3}}U^{\frac{1}{3}}}{\alpha^{\frac{1}{3}}\beta^{\frac{1}{3}}\eta^{\frac{1}{3}}a^{\frac{1}{3}}}$ | $U$ | $\frac{\gamma^{\frac{1}{3}}\epsilon^{\frac{1}{3}}\eta^{\frac{1}{3}}h^{\frac{1}{3}}U^{\frac{1}{3}}}{\alpha^{\frac{1}{3}}\beta^{\frac{1}{3}}a^{\frac{1}{3}}}$ |
| 3 | 111121 | $a$ | $\frac{\epsilon^{\frac{1}{2}}h^{\frac{1}{2}}U^{\frac{1}{2}}}{\beta^{\frac{1}{2}}\zeta^{\frac{1}{2}}}$ | $h$ | $\frac{\epsilon^{\frac{1}{2}}h^{\frac{1}{2}}U^{\frac{1}{2}}}{\beta^{\frac{1}{2}}\zeta^{\frac{1}{2}}}$ | $\frac{\zeta^{\frac{1}{2}}U^{\frac{1}{2}}}{\beta^{\frac{1}{2}}\epsilon^{\frac{1}{2}}h^{\frac{1}{2}}}$ | $\frac{U}{\alpha a}$ | $U$ | $\frac{\epsilon^{\frac{1}{2}}\eta h^{\frac{1}{2}}U^{\frac{1}{2}}}{\alpha\beta^{\frac{1}{2}}\zeta^{\frac{1}{2}}a}$ |
| 4 | 111122 | $a$ | $\frac{\alpha^{\frac{1}{2}}\epsilon^{\frac{1}{2}}h^{\frac{1}{2}}a^{\frac{1}{2}}}{\beta^{\frac{1}{2}}\eta^{\frac{1}{2}}}$ | $h$ | $\frac{\alpha^{\frac{1}{2}}\epsilon^{\frac{1}{2}}h^{\frac{1}{2}}a^{\frac{1}{2}}}{\beta^{\frac{1}{2}}\eta^{\frac{1}{2}}}$ | $\frac{\eta^{\frac{1}{2}}U}{\alpha^{\frac{1}{2}}\beta^{\frac{1}{2}}\epsilon^{\frac{1}{2}}h^{\frac{1}{2}}a^{\frac{1}{2}}}$ | $\frac{U}{\alpha a}$ | $U$ | $\frac{\epsilon^{\frac{1}{2}}\eta^{\frac{1}{2}}h^{\frac{1}{2}}U}{\alpha^{\frac{1}{2}}\beta^{\frac{1}{2}}a^{\frac{1}{2}}}$ |
| 5 | 111211 | $a$ | $\frac{\alpha^{\frac{1}{2}}a^{\frac{1}{2}}U^{\frac{1}{2}}}{\gamma^{\frac{1}{2}}\eta^{\frac{1}{2}}}$ | $h$ | $\frac{\alpha^{\frac{1}{2}}a^{\frac{1}{2}}U^{\frac{1}{2}}}{\gamma^{\frac{1}{2}}\eta^{\frac{1}{2}}}$ | $\frac{\alpha^{\frac{1}{2}}\zeta a^{\frac{1}{2}}U^{\frac{1}{2}}}{\gamma^{\frac{1}{2}}\epsilon\eta^{\frac{1}{2}}h}$ | $\frac{\gamma^{\frac{1}{2}}U^{\frac{1}{2}}}{\alpha^{\frac{1}{2}}\eta^{\frac{1}{2}}a^{\frac{1}{2}}}$ | $\frac{\alpha\beta\zeta aU}{\gamma\epsilon\eta h}$ | $U$ |
| 6 | 111212 | $a$ | $\frac{\alpha^{\frac{1}{2}}a^{\frac{1}{2}}U^{\frac{1}{2}}}{\gamma^{\frac{1}{2}}\eta^{\frac{1}{2}}}$ | $h$ | $\frac{\alpha^{\frac{1}{2}}a^{\frac{1}{2}}U^{\frac{1}{2}}}{\gamma^{\frac{1}{2}}\eta^{\frac{1}{2}}}$ | $\frac{U}{\epsilon h}$ | $\frac{\gamma^{\frac{1}{2}}U^{\frac{1}{2}}}{\alpha^{\frac{1}{2}}\eta^{\frac{1}{2}}a^{\frac{1}{2}}}$ | $\frac{\alpha^{\frac{1}{2}}\beta a^{\frac{1}{2}}U^{\frac{3}{2}}}{\gamma^{\frac{1}{2}}\epsilon\eta^{\frac{1}{2}}h}$ | $U$ |
| 7 | 111221 | $a$ | $\frac{\alpha^{\frac{1}{3}}\epsilon^{\frac{1}{3}}a^{\frac{1}{3}}h^{\frac{1}{3}}U^{\frac{1}{3}}}{\beta^{\frac{1}{3}}\eta^{\frac{1}{3}}\zeta^{\frac{1}{3}}}$ | $h$ | $\frac{\alpha^{\frac{1}{3}}\epsilon^{\frac{1}{3}}a^{\frac{1}{3}}h^{\frac{1}{3}}U^{\frac{1}{3}}}{\beta^{\frac{1}{3}}\eta^{\frac{1}{3}}\zeta^{\frac{1}{3}}}$ | $\frac{\alpha^{\frac{1}{3}}\zeta^{\frac{1}{3}}a^{\frac{1}{3}}U^{\frac{1}{3}}}{\beta^{\frac{1}{3}}\epsilon^{\frac{1}{3}}\eta^{\frac{1}{3}}h^{\frac{1}{3}}}$ | $\frac{\beta^{\frac{1}{3}}\zeta^{\frac{1}{3}}U^{\frac{1}{3}}}{\alpha^{\frac{1}{3}}\epsilon^{\frac{1}{3}}\eta^{\frac{1}{3}}h^{\frac{1}{3}}a^{\frac{1}{3}}}$ | $\frac{\alpha^{\frac{1}{3}}\beta^{\frac{1}{3}}\zeta^{\frac{1}{3}}a^{\frac{1}{3}}U^{\frac{1}{3}}}{\epsilon^{\frac{1}{3}}\eta^{\frac{1}{3}}h^{\frac{1}{3}}}$ | $U$ |
| 8 | 111222 | $a$ | $\frac{\alpha^{\frac{1}{2}}\epsilon^{\frac{1}{2}}h^{\frac{1}{2}}a^{\frac{1}{2}}}{\beta^{\frac{1}{2}}\eta^{\frac{1}{2}}}$ | $h$ | $\frac{\alpha\epsilon^{\frac{1}{2}}h^{\frac{1}{2}}a^{\frac{1}{2}}}{\beta^{\frac{1}{2}}\eta^{\frac{1}{2}}}$ | $\frac{U}{\epsilon h}$ | $\frac{\beta^{\frac{1}{2}}U}{\alpha^{\frac{1}{2}}\epsilon^{\frac{1}{2}}\eta^{\frac{1}{2}}h^{\frac{1}{2}}a^{\frac{1}{2}}}$ | $\frac{\alpha^{\frac{1}{2}}\beta^{\frac{1}{2}}a^{\frac{1}{2}}U}{\epsilon^{\frac{1}{2}}\eta^{\frac{1}{2}}h^{\frac{1}{2}}}$ | $U$ |
| 9 | 112111 | $a$ | $\frac{U^{\frac{1}{2}}}{\beta^{\frac{1}{2}}}$ | $h$ | $\frac{\epsilon hU^{\frac{1}{2}}}{\beta^{\frac{1}{2}}\zeta}$ | $\frac{U^{\frac{1}{2}}}{\beta^{\frac{1}{2}}}$ | $\frac{\gamma U^{\frac{1}{2}}}{\alpha\beta^{\frac{1}{2}}a}$ | $U$ | $\frac{\gamma\epsilon\eta hU}{\alpha\beta\zeta a}$ |
| 10 | 112112 | $a$ | $\frac{U^{\frac{1}{2}}}{\beta^{\frac{1}{2}}}$ | $h$ | $\frac{\alpha\epsilon ha}{\gamma\eta}$ | $\frac{U^{\frac{1}{2}}}{\beta^{\frac{1}{2}}}$ | $\frac{\gamma U^{\frac{1}{2}}}{\alpha\beta^{\frac{1}{2}}a}$ | $U$ | $\frac{\epsilon hU^{\frac{1}{2}}}{\beta^{\frac{1}{2}}}$ |
| 11 | 112121 | $a$ | $\frac{U^{\frac{1}{2}}}{\beta^{\frac{1}{2}}}$ | $h$ | $\frac{\epsilon hU^{\frac{1}{2}}}{\beta^{\frac{1}{2}}\zeta}$ | $\frac{U^{\frac{1}{2}}}{\beta^{\frac{1}{2}}}$ | $\frac{U}{\alpha a}$ | $U$ | $\frac{\epsilon\eta hU^{\frac{1}{2}}}{\alpha\beta^{\frac{1}{2}}\zeta a}$ |
| 12 | 112122 | $a$ | $\frac{U^{\frac{1}{2}}}{\beta^{\frac{1}{2}}}$ | $h$ | $\frac{\alpha\epsilon ha}{\beta^{\frac{1}{2}}\eta U^{\frac{1}{2}}}$ | $\frac{U^{\frac{1}{2}}}{\beta^{\frac{1}{2}}}$ | $\frac{U}{\alpha a}$ | $U$ | $\frac{\epsilon hU^{\frac{1}{2}}}{\beta^{\frac{1}{2}}}$ |
| 13 | 112211 | $a$ | $\frac{\alpha^{\frac{1}{2}}\zeta^{\frac{1}{2}}a^{\frac{1}{2}}U^{\frac{1}{2}}}{\epsilon^{\frac{1}{2}}\eta^{\frac{1}{2}}\gamma^{\frac{1}{2}}h^{\frac{1}{2}}}$ | $h$ | $\frac{\alpha^{\frac{1}{2}}\epsilon^{\frac{1}{2}}h^{\frac{1}{2}}a^{\frac{1}{2}}U^{\frac{1}{2}}}{\gamma^{\frac{1}{2}}\zeta^{\frac{1}{2}}\eta^{\frac{1}{2}}}$ | $\frac{\alpha^{\frac{1}{2}}\zeta^{\frac{1}{2}}a^{\frac{1}{2}}U^{\frac{1}{2}}}{\epsilon^{\frac{1}{2}}\eta^{\frac{1}{2}}\gamma^{\frac{1}{2}}h^{\frac{1}{2}}}$ | $\frac{\gamma^{\frac{1}{2}}\zeta^{\frac{1}{2}}U^{\frac{1}{2}}}{\alpha^{\frac{1}{2}}\epsilon^{\frac{1}{2}}\eta^{\frac{1}{2}}h^{\frac{1}{2}}a^{\frac{1}{2}}}$ | $\frac{\alpha\beta\zeta aU}{\gamma\epsilon\eta h}$ | $U$ |
| 14 | 112212 | $a$ | $\frac{U}{\epsilon h}$ | $h$ | $\frac{\alpha\epsilon ha}{\gamma\eta}$ | $\frac{U}{\epsilon h}$ | $\frac{\gamma U}{\alpha\epsilon ha}$ | $\frac{\beta U^2}{\epsilon^2 h^2}$ | $U$ |
| 15 | 112221 | $a$ | $\frac{\alpha^{\frac{1}{3}}\zeta^{\frac{1}{3}}a^{\frac{1}{3}}U^{\frac{1}{3}}}{\beta^{\frac{1}{3}}\eta^{\frac{1}{3}}\epsilon^{\frac{1}{3}}h^{\frac{1}{3}}}$ | $h$ | $\frac{\alpha^{\frac{1}{3}}\epsilon^{\frac{1}{3}}h^{\frac{1}{3}}a^{\frac{1}{3}}U^{\frac{1}{3}}}{\beta^{\frac{1}{3}}\eta^{\frac{1}{3}}\zeta^{\frac{1}{3}}}$ | $\frac{\alpha^{\frac{1}{3}}\zeta^{\frac{1}{3}}a^{\frac{1}{3}}U^{\frac{1}{3}}}{\beta^{\frac{1}{3}}\eta^{\frac{1}{3}}\epsilon^{\frac{1}{3}}h^{\frac{1}{3}}}$ | $\frac{\beta^{\frac{1}{3}}\zeta^{\frac{1}{3}}U^{\frac{1}{3}}}{\alpha^{\frac{1}{3}}\epsilon^{\frac{1}{3}}\eta^{\frac{1}{3}}h^{\frac{1}{3}}a^{\frac{1}{3}}}$ | $\frac{\alpha^{\frac{1}{3}}\beta^{\frac{1}{3}}\zeta^{\frac{1}{3}}a^{\frac{1}{3}}U^{\frac{1}{3}}}{\eta^{\frac{1}{3}}\epsilon^{\frac{1}{3}}h^{\frac{1}{3}}}$ | $U$ |
| 16 | 112222 | $a$ | $\frac{U}{\epsilon h}$ | $h$ | $\frac{\alpha\epsilon^2h^2a}{\beta\eta U}$ | $\frac{U}{\epsilon h}$ | $\frac{\beta U^2}{\alpha\epsilon^2h^2a}$ | $\frac{\beta U^2}{\epsilon^2h^2}$ | $U$ |
| 17 | 121111 | $a$ | $h$ | $\frac{\beta\zeta h^2}{\epsilon U}$ | $h$ | $\frac{U}{\beta h}$ | $\frac{\gamma h}{\alpha a}$ | $U$ | $\frac{\gamma\eta h^2}{\alpha a}$ |
| 18 | 121112 | $a$ | $h$ | $\frac{\beta\gamma\eta h^3}{\alpha\epsilon aU}$ | $h$ | $\frac{U}{\beta h}$ | $\frac{\gamma h}{\alpha a}$ | $U$ | $\frac{\gamma\eta h^2}{\alpha a}$ |
| 19 | 121121 | $a$ | $h$ | $\frac{\beta\zeta h^2}{\epsilon U}$ | $h$ | $\frac{U}{\beta h}$ | $\frac{U}{\alpha a}$ | $U$ | $\frac{\eta hU}{\alpha a}$ |
| 20 | 121122 | $a$ | $h$ | $\frac{\beta\eta h^2}{\alpha\epsilon a}$ | $h$ | $\frac{U}{\beta h}$ | $\frac{U}{\alpha a}$ | $U$ | $\frac{\eta hU}{\alpha a}$ |

VOL. 7 1958

*Table 2*—continued

| No. | Code | $a^0$ | $a^+$ | $h^0$ | $h^-$ | $n$ | $p$ | $I = \beta n a^+$ | $R = \eta p h^-$ |
|---|---|---|---|---|---|---|---|---|---|
| 21 | 121211 | $a$ | $h$ | $nh_0 = \frac{\zeta h}{\epsilon}$ | $h$ | indefinite | $\frac{\gamma h}{\alpha a}$ | indefinite | $\frac{\gamma\eta h^2}{\alpha a}$ |
| 22 | 121212 | $a$ | $h$ | $nh_0 = \frac{\gamma\eta h^2}{\alpha\epsilon a}$ | $h$ | indefinite | $\frac{\gamma h}{\alpha a}$ | indefinite | $\frac{\gamma\eta h^2}{\alpha a}$ |
| 23 | 121221 | $a$ | $h$ | $\frac{\beta\eta\zeta h^3}{\alpha\epsilon a U}$ | $h$ | $\frac{\alpha a U}{\beta\eta h^2}$ | $\frac{U}{\eta h}$ | $\frac{\alpha a U}{\eta h}$ | $U$ |
| 24 | 121222 | $a$ | $h$ | $\frac{\beta\eta h^2}{\alpha\epsilon a}$ | $h$ | $\frac{\alpha a U}{\beta\eta h^2}$ | $\frac{U}{\eta h}$ | $\frac{\alpha a U}{\eta h}$ | $U$ |
| 25 | 122111 | $a$ | $\frac{U^{\frac{1}{2}}}{\beta^{\frac{1}{2}}}$ | $\frac{\beta^{\frac{1}{2}}\zeta h}{\epsilon U^{\frac{1}{2}}}$ | $h$ | $\frac{U^{\frac{1}{2}}}{\beta^{\frac{1}{2}}}$ | $\frac{\gamma U^{\frac{1}{2}}}{\alpha\beta^{\frac{1}{2}}a}$ | $U$ | $\frac{\gamma\eta h U^{\frac{1}{2}}}{\alpha\beta^{\frac{1}{2}}a}$ |
| 26 | 122112 | $a$ | $\frac{U^{\frac{1}{2}}}{\beta^{\frac{1}{2}}}$ | $\frac{\gamma\eta h}{\alpha\epsilon a}$ | $h$ | $\frac{U^{\frac{1}{2}}}{\beta^{\frac{1}{2}}}$ | $\frac{\gamma U^{\frac{1}{2}}}{\alpha\beta^{\frac{1}{2}}a}$ | $U$ | $\frac{\gamma\eta h U^{\frac{1}{2}}}{\alpha\beta^{\frac{1}{2}}a}$ |
| 27 | 122121 | $a$ | $\frac{U^{\frac{1}{2}}}{\beta^{\frac{1}{2}}}$ | $\frac{\beta^{\frac{1}{2}}\zeta h}{\epsilon U^{\frac{1}{2}}}$ | $h$ | $\frac{U^{\frac{1}{2}}}{\beta^{\frac{1}{2}}}$ | $\frac{U}{\alpha a}$ | $U$ | $\frac{\eta h U}{\alpha a}$ |
| 28 | 122122 | $a$ | $\frac{U^{\frac{1}{2}}}{\beta^{\frac{1}{2}}}$ | $\frac{\beta^{\frac{1}{2}}\eta h U^{\frac{1}{2}}}{\alpha\epsilon a}$ | $h$ | $\frac{U^{\frac{1}{2}}}{\beta^{\frac{1}{2}}}$ | $\frac{U}{\alpha a}$ | $U$ | $\frac{\eta h U}{\alpha a}$ |
| 29 | 122211 | $a$ | $\frac{\alpha a U}{\gamma\eta h}$ | $\frac{\eta\gamma\zeta h^2}{\alpha\epsilon a U}$ | $h$ | $\frac{\alpha a U}{\gamma\eta h}$ | $\frac{U}{\eta h}$ | $\frac{\alpha^2\beta a^2 U^2}{\eta^2\gamma^2 h^2}$ | $U$ |
| 30 | 122212 | $a$ | $\frac{\alpha a U}{\gamma\eta h}$ | $\frac{\eta\gamma h}{\alpha\epsilon a}$ | $h$ | $\frac{\alpha a U}{\gamma\eta h}$ | $\frac{U}{\eta h}$ | $\frac{\alpha^2\beta a^2 U^2}{\eta^2\gamma^2 h^2}$ | $U$ |
| 31 | 122221 | $a$ | $\frac{\alpha^{\frac{1}{2}}a^{\frac{1}{2}}U^{\frac{1}{2}}}{\beta^{\frac{1}{2}}\eta^{\frac{1}{2}}h^{\frac{1}{2}}}$ | $\frac{\beta^{\frac{1}{2}}\eta^{\frac{1}{2}}\zeta h^{\frac{1}{2}}}{\alpha^{\frac{1}{2}}\epsilon a^{\frac{1}{2}}U^{\frac{1}{2}}}$ | $h$ | $\frac{a^{\frac{1}{2}}a^{\frac{1}{2}}U^{\frac{1}{2}}}{\beta^{\frac{1}{2}}\eta^{\frac{1}{2}}h^{\frac{1}{2}}}$ | $\frac{U}{\eta h}$ | $\frac{\alpha a U}{\eta h}$ | $U$ |
| 32 | 122222 | $a$ | $\frac{\alpha^{\frac{1}{2}}a^{\frac{1}{2}}U^{\frac{1}{2}}}{\beta^{\frac{1}{2}}\eta^{\frac{1}{2}}h^{\frac{1}{2}}}$ | $\frac{\beta^{\frac{1}{2}}\eta^{\frac{1}{2}}h^{\frac{1}{2}}U^{\frac{1}{2}}}{\alpha^{\frac{1}{2}}\epsilon a^{\frac{1}{2}}}$ | $h$ | $\frac{\alpha^{\frac{1}{2}}a^{\frac{1}{2}}U^{\frac{1}{2}}}{\beta^{\frac{1}{2}}\eta^{\frac{1}{2}}h^{\frac{1}{2}}}$ | $\frac{U}{\eta h}$ | $\frac{\alpha a U}{\eta h}$ | $U$ |

but the powers of $n$, $p$, $I$, and $R$ as functions of $U$ for all situations are given in Table 3. Also the solutions for $C$, $L$, $B$, and $E$ are omitted in Table 2, but they can be derived immediately from the values of $a^0$, $a^+$, $h^0$, $h^-$, $n$, and $p$. One sees immediately from these tables under which conditions the following powers may be found:

$$n, p\text{: } 0, 1/3, 1/2, 2/3, 1, 2, \infty;$$

$$I, R\text{; } 0, 1/2, 2/3, 1, 3/2, 2, \infty.$$

The transition $n \propto U \rightarrow n \propto U^{\frac{1}{2}}$ which could not be explained satisfactorily with the one-state model will now be reconsidered. Tables 2 and 3 show that a great number of situations have a linear relationship between $n$ and $U$. Restricting ourselves to Table 2, there are already 13 of these situations. An analysis of possible transitions as made above for the one-state model shows that there are two situations (111212 and 111222), which cannot, by raising $U$, pass directly into another situation of Table 2 in which $n$ is proportional to $U^{\frac{1}{2}}$. The eleven remaining situations can all show such transitions. The thirteen possible transitions are shown in Fig. 9.

It is sometimes assumed[15] that by measuring $n$ at the transition point, information can be obtained concerning the number of deep traps. This is based on the following argument. If all deep traps are filled during excitation, charge neutrality requires $a^+ = h^- = h$ at low or medium intensities (code 121...). This changes to $n = a^+ > h$ (code 122...) when $n$ becomes of the same order of magnitude as $h$. Such transitions are indeed shown

in Fig. 9 (Nos. 4, 5, 7, 8, 10, and 12), but they are not the only ones possible, and if the other transitions are actually taking place the conclusion that $n = h$ at the transition point is not valid. It is therefore not surprising that BUBE[15] found a large discrepancy between the number of deep traps determined in this way and the number determined from the glow curve.

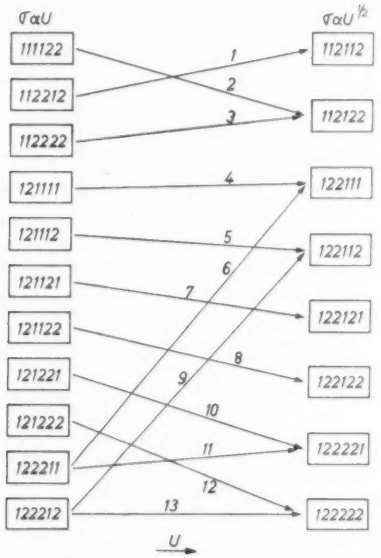


FIG. 9. The arrows indicate all possible transitions between the situations of Table 4 in which $n \propto U$ changes to $n \propto U^{\frac{1}{2}}$ when $U$ is increased.

In order to determine the actual nature of the transition, more properties must be measured on the same crystal such as, for example, the luminescence or the effect of temperature on the transition point or preferably both. BROSER and WARMINSKY,[10] who measured both the conductivity and the luminescence at the transition point, found the latter to change from $I \propto U^2$ to $I \propto U$.

In that case, assuming that the fluorescence they observed is process $I$ of Fig. 8, only four transitions need to be considered:

$$\left.\begin{array}{l}(1)\ 112212 \rightarrow 112112\\ (3)\ 112222 \rightarrow 112122\end{array}\right\} \text{ at } U = \frac{\epsilon^2 h^2}{\beta}$$

$$\left.\begin{array}{l}(6)\ 122211 \rightarrow 122111\\ (9)\ 122212 \rightarrow 122112\end{array}\right\} \text{ at } U = \frac{\gamma^2 \eta^2 h^2}{\alpha^2 \beta a^2}.$$

The difference between (1) and (3) on the one hand and (6) and (9) on the other is that in the first two cases the traps remain partly filled over the transition range, while in the latter two cases they are already completely filled. In all cases the recombination changes in character at the transition point, e.g. from $U = R$ to $U = I$. By studying the effect of temperature, the nature of the transition might be indentified still further. If the transitions were found to move to higher values of $U$ with increasing temperature, an estimate could be made of the distance $E_A$ between the lower impurity level $A$ and the occupied band.

## ACTIVATION

We shall now demonstrate with the aid of a few examples the effect of incorporating impurities which give rise to levels $A$, assuming that there are already a certain number of $H$ levels present in the material before activation.

In order to see which of the 128 situations arise, once a certain combination of parameters has been chosen, we shall use the same graphical method as applied above to the one-state model.

First one needs to know the initial conditions which possibly occur for $U \rightarrow 0$. At very low intensities obviously $a^0 = a$ and $h^0 = h$. Furthermore at very low intensities we always have $C = L$ and $B = E$.

Thus at very low intensities

$$\gamma a^+ = \alpha p a.$$

It depends on the value of $\gamma/\alpha a$ whether $p$ is larger or smaller than $a^+$. Similarly the ratio $\zeta/\epsilon h$ determines the ratio $n/h^-$.

Now

$$\frac{I}{R} = \frac{\beta n a^+}{\eta p h^-} = \frac{\alpha \beta \zeta a}{\epsilon \eta \gamma h}. \qquad (17)$$

$I/R$ can be smaller or larger than unity, depending on the parameters. There are thus 8 initial conditions possible, depending on the parameters as shown in Table 4.

Now

$$\frac{\gamma}{\alpha a} = \frac{N_p \exp(-E_A/kT)}{a}$$

and with $N_p \sim 10^{19}$ and $a$ usually $\lesssim 10^{16}$ (activator content $10^{-7}$), $E_A$ must be smaller than 0·17 eV to

*Table*

| Code | $n$ | $p$ | $I$ | $R$ | Code | $n$ | $p$ | $I$ | $R$ |
|---|---|---|---|---|---|---|---|---|---|
| 111111 | $\frac{1}{2}$ | $\frac{1}{2}$ | 1 | 1 | 113111 | $\frac{1}{2}$ | $\frac{1}{2}$ | 1 | 1 |
| 111112 | $\frac{2}{3}$ | $\frac{1}{3}$ | 1 | $\frac{2}{3}$ | 113112 | $\frac{2}{3}$ | $\frac{1}{3}$ | 1 | $\frac{2}{3}$ |
| 111121 | $\frac{1}{2}$ | 1 | 1 | $\frac{1}{2}$ | 113121 | 1 | 1 | 1 | 2 |
| 111122 | 1 | 1 | 1 | 1 | 113122 | 2 | 1 | 1 | 2 |
| 111211 | $\frac{1}{2}$ | $\frac{1}{2}$ | 1 | 1 | 113211 | $\frac{1}{2}$ | $\frac{1}{2}$ | 1 | 1 |
| 111212 | 1 | $\frac{1}{2}$ | $\frac{3}{2}$ | 1 | 113212 | 1 | $\frac{1}{2}$ | $\frac{3}{2}$ | 1 |
| 111221 | $\frac{1}{3}$ | $\frac{2}{3}$ | $\frac{2}{3}$ | 1 | 113221 | $\frac{1}{2}$ | $\frac{1}{2}$ | $\frac{1}{2}$ | 1 |
| 111222 | 1 | 1 | 1 | 1 | 113222 | 1 | $\frac{1}{2}$ | $\frac{1}{2}$ | 1 |
| 112111 | $\frac{1}{2}$ | $\frac{1}{2}$ | 1 | 1 | 114111 | $\frac{1}{2}$ | $\frac{1}{2}$ | 1 | 1 |
| 112112 | $\frac{1}{2}$ | $\frac{1}{2}$ | 1 | $\frac{1}{2}$ | 114112 | $\frac{1}{2}$ | $\frac{1}{2}$ | 1 | $\frac{1}{2}$ |
| 112121 | $\frac{1}{2}$ | 1 | 1 | $\frac{3}{2}$ | 114121 | 1 | 1 | 1 | 2 |
| 112122 | $\frac{1}{2}$ | 1 | 1 | $\frac{1}{2}$ | 114122 | 1 | 1 | 1 | 1 |
| 112211 | $\frac{1}{2}$ | $\frac{1}{2}$ | 1 | 1 | 114211 | $\frac{1}{2}$ | $\frac{1}{2}$ | 1 | 1 |
| 112212 | 1 | 1 | 2 | 1 | 114212 | 1 | 1 | 2 | 1 |
| 112221 | $\frac{1}{3}$ | $\frac{2}{3}$ | $\frac{2}{3}$ | 1 | 114221 | $\frac{1}{2}$ | $\frac{1}{2}$ | $\frac{1}{2}$ | 1 |
| 112222 | 1 | 2 | 2 | 1 | 114222 | 1 | 1 | 1 | 1 |
| 121111 | 1 | 0 | 1 | 0 | 123111 | 1 | 0 | 1 | 0 |
| 121112 | 1 | 0 | 1 | 0 | 123112 | 1 | 0 | 1 | 0 |
| 121121 | 1 | 1 | 1 | 1 | 123121 | $\infty$ | 0 | 0 | 0 |
| 121122 | 1 | 1 | 1 | 1 | 123122 | $\infty$ | 0 | 0 | 0 |
| 121211 | $\infty$ | 0 | $\infty$ | 0 | 123211 | $\infty$ | 0 | $\infty$ | 0 |
| 121212 | $\infty$ | 0 | $\infty$ | 0 | 123212 | $\infty$ | 0 | $\infty$ | 0 |
| 121221 | 1 | 1 | 1 | 1 | 123221 | $\infty$ | 0 | $\infty$ | 0 |
| 121222 | 1 | 1 | 1 | 1 | 123222 | $\infty$ | 0 | $\infty$ | 0 |
| 122111 | $\frac{1}{2}$ | $\frac{1}{2}$ | 1 | $\frac{1}{2}$ | 124111 | $\frac{1}{2}$ | $\frac{1}{2}$ | 1 | $\frac{1}{2}$ |
| 122112 | $\frac{1}{2}$ | $\frac{1}{2}$ | 1 | $\frac{1}{2}$ | 124112 | $\frac{1}{2}$ | $\frac{1}{2}$ | 1 | $\frac{1}{2}$ |
| 122121 | $\frac{1}{2}$ | 1 | 1 | 1 | 124121 | 1 | 1 | 1 | 1 |
| 122122 | $\frac{1}{2}$ | 1 | 1 | 1 | 124122 | 1 | 1 | 1 | 1 |
| 122211 | 1 | 1 | 2 | 1 | 124211 | 1 | 1 | 2 | 1 |
| 122212 | 1 | 1 | 2 | 1 | 124212 | 1 | 1 | 2 | 1 |
| 122221 | $\frac{1}{2}$ | 1 | 1 | 1 | 124221 | 1 | 1 | 1 | 1 |
| 122222 | $\frac{1}{2}$ | 1 | 1 | 1 | 124222 | 1 | 1 | 1 | 1 |

*Table 4. Initial situations for $U \to 0$*

| Code | $\gamma/\alpha a$ | $\zeta/\epsilon h$ | $\alpha\beta\zeta a/\epsilon\eta\gamma h$ |
|---|---|---|---|
| 111111 | $<1$ | $<1$ | $>1$ |
| 111211 | $<1$ | $<1$ | $<1$ |
| 112111 | $<1$ | $>1$ | $>1$ |
| 112211 | $<1$ | $>1$ | $<1$ |
| 113111 | $>1$ | $<1$ | $>1$ |
| 113211 | $>1$ | $<1$ | $<1$ |
| 114111 | $>1$ | $>1$ | $>1$ |
| 114211 | $>1$ | $>1$ | $<1$ |

make $\gamma/\alpha a > 1$ at room temperature. With more impurities added, the limit of $E_A$ will be even lower.

We shall concern ourselves mainly with deeper levels which are of greater interest, and we shall limit ourselves to the initial conditions 111111 or 111211. Let us assume that the "unactivated" material contains a relatively small number ($h = 10^{16}$) of rather deep traps, 0·7 eV, below the conduction band, and further that these levels have large capture cross-sections both for capturing electrons, when empty, and for capturing holes, when occupied, say $10^{-16}$ and $10^{-15}$, respectively.

Now $\epsilon = 10^{-9}$,* $\eta = 10^{-8}$, and $\zeta = 10^{-2}$ at room temperature. Such a material has a low

* The coefficient $\epsilon$ is the product of the capture cross-section of an empty $H$-centre for capturing an electron and the thermal velocity of free electrons ($\sim 10^7$cm sec$^{-1}$).

3

| Code | $n$ | $p$ | $I$ | $R$ | Code | $n$ | $p$ | $I$ | $R$ |
|---|---|---|---|---|---|---|---|---|---|
| 211111 | 0 | $\infty$ | 0 | $\infty$ | 221111 | 1 | 1 | 1 | 1 |
| 211112 | 1 | 1 | 1 | 1 | 221112 | 1 | $\frac{1}{2}$ | 1 | $\frac{1}{2}$ |
| 211121 | 0 | $\infty$ | 0 | $\infty$ | 221121 | 1 | 2 | 1 | 2 |
| 211122 | 1 | 1 | 1 | 1 | 221122 | 1 | 1 | 1 | 1 |
| 211211 | 0 | 1 | 0 | 1 | 221211 | 1 | 1 | 1 | 1 |
| 211212 | 1 | 1 | 1 | 1 | 221212 | 2 | 1 | 2 | 1 |
| 211221 | 0 | 1 | 0 | 1 | 221221 | $\frac{1}{2}$ | 1 | $\frac{1}{2}$ | 1 |
| 211222 | 1 | 1 | 1 | 1 | 221222 | 1 | 1 | 1 | 1 |
| 212111 | 0 | $\infty$ | 0 | $\infty$ | 222111 | 0 | $\infty$ | 0 | $\infty$ |
| 212112 | 0 | $\infty$ | 0 | 0 | 222112 | 0 | $\infty$ | 0 | $\infty$ |
| 212121 | 0 | $\infty$ | 0 | $\infty$ | 222121 | 0 | $\infty$ | 0 | $\infty$ |
| 212122 | 0 | $\infty$ | 0 | 0 | 222122 | 0 | $\infty$ | 0 | $\infty$ |
| 212211 | 0 | 1 | 0 | 1 | 222211 | 0 | 1 | 0 | 1 |
| 212212 | 0 | $\infty$ | 0 | 0 | 222212 | 0 | 1 | 0 | 1 |
| 212221 | 0 | 1 | 0 | 1 | 222221 | 0 | 1 | 0 | 1 |
| 212222 | 0 | $\infty$ | 0 | 0 | 222222 | 0 | 1 | 0 | 1 |
| 213111 | 1 | 1 | 1 | 2 | 223111 | 1 | 0 | 1 | 0 |
| 213112 | 1 | $\frac{1}{2}$ | 1 | 1 | 223112 | 1 | 0 | 1 | 0 |
| 213121 | 1 | 1 | 1 | 2 | 223121 | 1 | 0 | 1 | 0 |
| 213122 | 1 | $\frac{1}{2}$ | 1 | 1 | 223122 | 1 | 0 | 1 | 0 |
| 213211 | $\frac{1}{2}$ | $\frac{1}{2}$ | $\frac{1}{2}$ | 1 | 223211 | $\infty$ | 0 | $\infty$ | 0 |
| 213212 | 1 | $\frac{1}{2}$ | 1 | 1 | 223212 | $\infty$ | 0 | $\infty$ | 0 |
| 213221 | $\frac{1}{2}$ | $\frac{1}{2}$ | $\frac{1}{2}$ | 1 | 223221 | $\infty$ | 0 | $\infty$ | 0 |
| 213222 | 1 | $\frac{1}{2}$ | 1 | 1 | 223222 | $\infty$ | 0 | $\infty$ | 0 |
| 214111 | 1 | 1 | 1 | 2 | 224111 | 1 | 1 | 1 | 1 |
| 214112 | 1 | 1 | 1 | 1 | 224112 | 1 | 1 | 1 | 1 |
| 214121 | 1 | 1 | 1 | 2 | 224121 | 1 | 1 | 1 | 1 |
| 214122 | 1 | 1 | 1 | 1 | 224122 | 1 | 1 | 1 | 1 |
| 214211 | $\frac{1}{2}$ | $\frac{1}{2}$ | $\frac{1}{2}$ | 1 | 224211 | 1 | 1 | 1 | 1 |
| 214212 | 1 | 1 | 1 | 1 | 224212 | 1 | 1 | 1 | 1 |
| 214221 | $\frac{1}{2}$ | $\frac{1}{2}$ | $\frac{1}{2}$ | 1 | 224221 | 1 | 1 | 1 | 1 |
| 214222 | 1 | 1 | 1 | 1 | 224222 | 1 | 1 | 1 | 1 |

photoconductivity with $n = U/\epsilon h$ over a range of $10^{15}$ in $U$ from $U = 10^{10}$ to $10^{25}$. Rose[47] has pointed out that in order to increase the photoconduction of such a material, a recombination centre must be added with a small capture cross-section for electrons. This will be our level $A$, and we have chosen the following parameters:

$\beta = 10^{-12}$, $\alpha = 10^{-8}$, and $\gamma = 10^{2}(E_A = 0{\cdot}53$ eV).

With the aid of Tables 2 and 3, the behaviour of the activated material can easily be drawn on a log–log scale. With $a = 10^{15}$, for example, the initial condition is 111211, changing to 111212 at $U = 10^{9}$. The behaviour from $U = 10^{10}$ to $10^{25}$ is shown in Fig. 10(a). At $U = 10^{17}$ all $A$ levels are empty (saturation) and there is a change to 211212 followed by 211222 and finally by 214222. This is the final situation with $p = n$. Since in this situation $\alpha p a^0 = \beta n a^+$, $a^0/a^+ = \beta/\alpha$ and similarly, because $\epsilon n h^0 = \eta p h^-$, $h^0/h^- = \eta/\epsilon$. As $\beta > \epsilon$ and $\eta > \epsilon$ the levels $A$ remain practically unoccupied at extremely high excitation densities, whereas only 10 per cent of the traps are filled with electrons independent of $U$. Only at very low values of $U$, where the situation is characterized by the code number 111211, is an increase of $n$ due to $A$ found, but at those low values of $U$, $n < p$. At all other intensities, $n = U/\epsilon h$ and consequently there is no increase of photoconductivity at at all due to the incorporation of $A$.

The situation changes completely with $a > h$. This is illustrated in Fig. 10(b), where the

behaviour of a material is shown with the same parameters as for Fig. 10(a) but with $a = 10^{17}$. The photoconduction now increases suddenly at the moment when all $H$ levels become occupied by electrons. The recombination via these levels becomes blocked and takes an other course via $A$ with a corresponding rise of $n$ from $U/\epsilon h$ to $U/\beta h$, for the first time at a value of $U = \eta\gamma h^2/\alpha a$ ($10^{17}$ in our example). At the same time $I$ increases superlinearly until $I = U$, and as a result 121212 changes to 121112. After a subsequent change to 121122 $n$ finally catches up with $a^+$. The situation changes to 122122 and $n$ now begins to rise more slowly and becomes independent of $U$ when all $A$ levels are emptied. At this point $p$ begins to rise suddenly by a factor of 10. Simultaneously $R$ increases with the same rate as $p$ and takes over again from $I$. This discontinuity of $p$ and $R$ has the code number 222122, which changes to 222222 when $R$ has become equal to $U$ again. From here onwards $n$ remains constant, while $h^0$ increases and becomes of the same order of magnitude as $h$ at $U = 10^{24}$. We are entering a third region of discontinuities (212222), this time of $p$, $h^-$, and $B$. This is at the same time the end of the range of effective activation of the photoconductivity and $p$ jumps to $n = U/\epsilon h$ (code number 214222), the same value as that before activation. It is of some interest to note that the levels $H$ become filled only at medium intensities and lose their electrons at low and at high intensities.

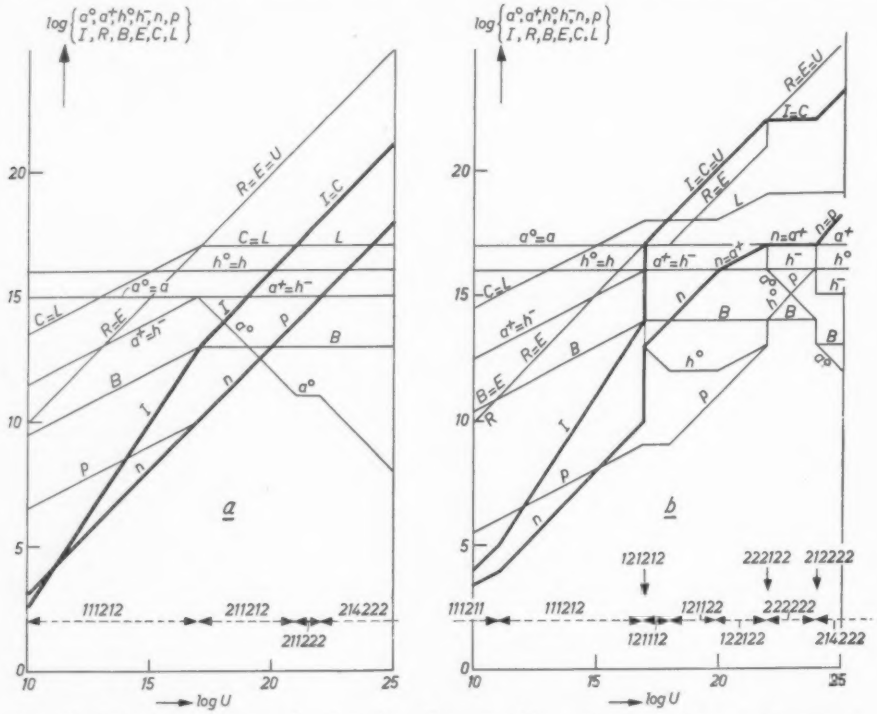


FIG. 10. Behaviour diagram showing the effect of adding $A$ states with a small capture cross-section for electrons to a material containing $10^{16}$ fast $H$ states per cm³: (*a*) $10^{15}$ $A$ states per cm³; (*b*) $10^{17}$ $A$ states per cm³.

Although no further changes would occur in our two-state model, the band–band recombination $F = \delta np$ has now to be considered. At $U = 10^{24}$, $F$ would be $10^{22}$ with $\delta = 10^{-12}$ and still lower than $R$ but, since it increases with $U^2$, it will become the major recombination process for values of $U > > 10^{26}$.

In Fig. 11 the relation between free carrier concentrations and density of excitation is drawn for

six different values of $a$. This figure illustrates clearly the activation of a photoconductor by the addition of recombination centres with low cross-sections for capturing electrons to a material which

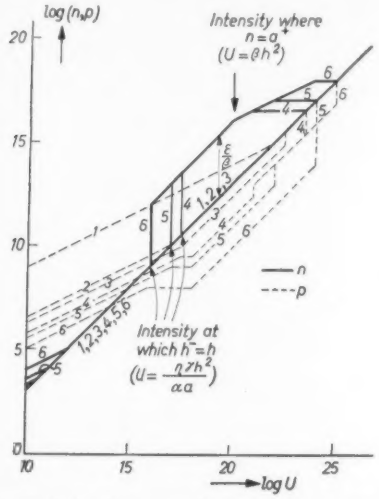


FIG. 11. Relation between the concentrations of free carriers and the excitation density for

$\beta = 10^{-12}$; $\alpha = 10^{-8}$; $\gamma = 10^{2}$;

$\eta = 10^{-8}$; $\epsilon = 10^{-9}$; $\zeta = 10^{-2}$;

$h = 10^{16}$ and $a = 0(1)$, $10^{15}(2)$, $10^{15.5}(3)$, $10^{16.5}(4)$, $10^{17}(5)$ and $10^{18}(6)$

contains a certain number of centres with high cross-sections for capturing electrons and holes in the way as described by ROSE. The activation takes place because electrons from $A$ are transferred to $H(a^{+} = h^{-})$. In order to prevent the "fast" states $H$ from capturing electrons, there must be enough electrons available from $A$ to fill these states completely.

This is not the only condition however. Another condition is that $A$ must be far enough above the filled band to keep the holes trapped. More conditions to obtain superlinearity of $I$ and $n$, and thus effective activation, are further discussed below.

It is also clearly demonstrated that it is not necessary to distribute the $A$ states, as ROSE assumed, over a range of energies in order to obtain superlinearity.

Fig. 10(b) furthermore illustrates how the efficiency of a phosphor may pass through a maximum a phenomenon observed by ANTONOV–ROMANOVSKY.[42] In Fig. 12 the fluorescence efficiency is shown of a phosphor with the parameters of No. 4 of Fig. 11, e.g. with $h = 10^{16}$ and $a = 3 \times 10^{16}$. This figure shows a great resemblance to Fig. 1 of ANTONOV–ROMANOVSKY's paper. By changing the activator content and the temperature ($\gamma$), one could check whether this explanation for a maximum in the efficiency curve is correct.

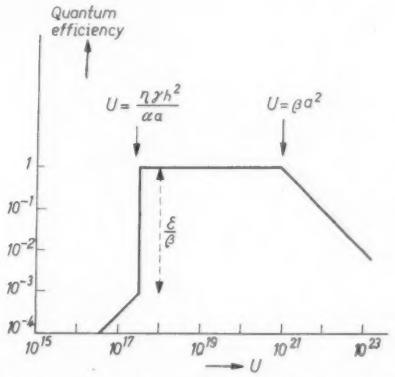


FIG. 12. Quantum efficiency of a phosphor with the same parameters as used for Fig. 11 with $a = 10^{16.5}$. This figure is to be compared with Fig. 1 of ANTONOV-ROMANOVSKY's paper.[42]

The transition from quenching ($U = R$) to fluorescence ($U = I$) need not necessarily take place via a superlinear range. This can occur, for example, by way of $112211 \rightarrow 112212 \rightarrow 112112$. To obtain such a sequence, the $H$ level must be so close to the empty band that even at very low intensities $n > h^{-}$. This situation obtains, for example, with the following parameters:

$a = 10^{16}$; $\alpha = 10^{-12}$; $\gamma = 10^{3}$; $\beta = 10^{-14}$;

$h = 10^{14}$; $\epsilon = 10^{-14}$; $\zeta = 10^{3}$; $\eta = 10^{-8}$.

If $a$ were zero, $n$ would be $\gamma^{\frac{1}{2}}U^{\frac{1}{2}}/\eta^{\frac{1}{2}}\epsilon^{\frac{1}{2}}h^{\frac{1}{2}}$ over the range $U = 0$—$10^{17}$ ($I = 0$).

After activation, fluorescence appears with a quantum efficiency near unity for $U > 10^{14}$, as shown in Fig. 13. The dashed line gives the value of $n$ and $p$ before activation. One notices that the addition of $A$ has increased the photoconductivity over the whole intensity range, despite the fact that the $H$ levels, with their high cross-section for

capturing holes, are never being filled up. Activation is possible here because the $H$ levels have a small cross-section for capturing electrons, of the same order as that of the $A$ levels ($\epsilon = \beta$). In the next section we shall discuss some conditions under which superlinearity will occur.

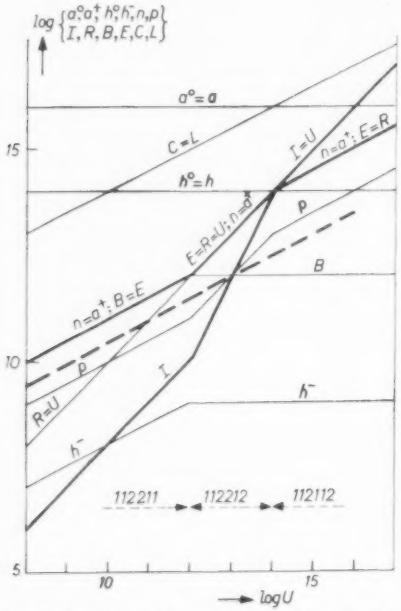


FIG. 13. Behaviour of a material with the following parameters:

$$a = 10^{16},\ \alpha = 10^{-12},\ \gamma = 10^{3},\ \beta = 10^{-14},$$

$$h = 10^{14},\ \epsilon = 10^{-14},\ \zeta = 10^{3},\ \eta = 10^{-8}.$$

## SUPERLINEARITY OF $n$ AND $I$

We see from Table 3 that there are 12 situations showing superlinearity of $n$ and $I$. Of these there are only two (121211 and 121212) where the photoconduction is $n$-type. In all other cases the third digit of the code number is 3, indicating that $n \ll h^-$, $p$ and $p \gg a^+$. Since this is a rare phenomenon in sulphide-type photoconductors, we shall limit ourselves to the situations 121211 and 121212. Fig. 14 shows how these situations can arise from 111211 by raising $U$. The other possible initial situations of Table 4 do not lead to the desired superlinear situations.

The conditions for obtaining superlinearity of $I$ and $n$ in $n$-type photoconductors are therefore:

$$\gamma < \alpha a;\ \zeta < \epsilon h \text{ and } \alpha\beta\zeta a < \epsilon\eta\gamma h$$

in accordance with Table 4 and furthermore, from Fig. 14:

$$U_2 < U_1,\ U_3,\ U_4;$$

or $U_4 < U_1,\ U_2,\ U_3$ with $U_2 < U_1,\ U_5,\ U_6,\ U_7$.

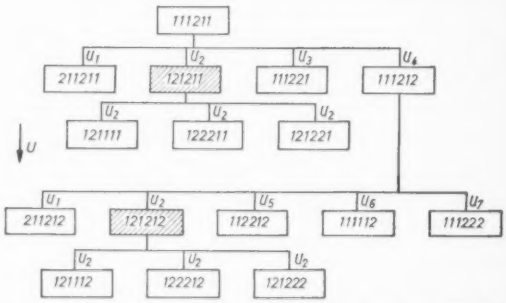


FIG. 14. Pedigree of code numbers indicating possible transitions which may arise when, starting from 111211, the excitation density is increased. The shaded numbers indicate situations with superlinearity of $n$ and $I$.

The values of $U_1$, etc., are easily deduced from Table 2. For example, if 111211 changes into 211211, this happens when $a^+$ becomes equal to $a$ or

$$\frac{\alpha^{\frac{1}{2}} a^{\frac{1}{2}} U_1^{\frac{1}{2}}}{\eta^{\frac{1}{2}}\gamma^{\frac{1}{2}}} = a.$$

In this way one finds:

$$U_1 = \frac{\eta\gamma a}{\alpha};\ U_2 = \frac{\eta\gamma h^2}{\alpha a};\ U_3 = \frac{\gamma^3\eta\epsilon^2 h^2}{\alpha\beta^2\zeta^2 a}$$
$$U_4 = \frac{\zeta^2\alpha a}{\eta\gamma};\ U_5 = \frac{\alpha\epsilon^2 a h^2}{\eta\gamma};\ U_6 = \frac{\epsilon^2\eta\gamma h^2}{\beta^2\alpha a}; \tag{18}$$
$$U_7 = \frac{\epsilon\gamma h}{\beta}.$$

We shall now consider two cases of superlinearity in more detail, namely the superlinear rise of fluorescence in (ZnCd)S–Ag, Ni studied by NAIL *et al.*[37] and the superlinear photoconduction found by BUBE[21,22] in CdSe. These measurements lend themselves very well as test cases for our two-state model, because they were carried out

over a large range of intensities, while in both cases one extra factor was varied, the nickel content in the first case and the temperature in the last.

*Superlinearity of fluorescence in (ZnCd)S–Ag, Ni*

It is well known that nickel has a "poisoning" effect on the fluorescence of most ZnS-type phosphors. Nickel apparently causes a radiationless transition which competes with the fluorescence transition due, for example, to the presence of silver. It is further known that silver produces an occupied level near to the occupied band, whereas nickel gives rise to a rather deep trapping level.[58] The combination Ag+Ni is therefore very suitable for checking the applicability of our model, especially since $a$(Ag) and $h$ (Ni) can be varied independently.

NAIL *et al.*[37] have carried out very extensive measurements of the brightness of a (ZnCd)S–Ag phosphor containing various amounts of nickel. Their results are shown in Fig. 15(a). The efficiencies of the phosphor at very low intensities are a factor $10^5$ lower than in the high-intensity range.

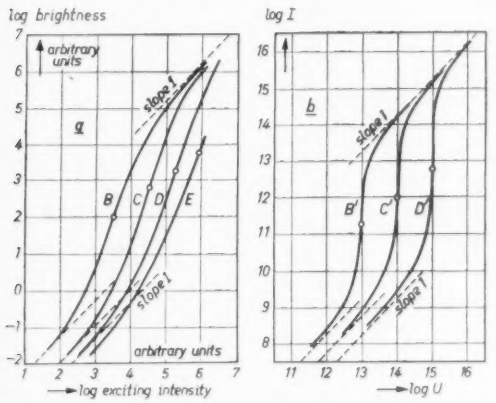


FIG. 15. (*a*) Superlinear dependence of brightness upon excitation intensity at room temperature as observed by NAIL, URBACH and PEARLMAN[37] for a phosphor with the composition ZnS 50, CdS 50 per cent by weight, Ag 400 ppm and Ni 0·3 ppm (curve B), 1 ppm (C), 3 ppm (D), and 5 ppm (E). (*b*) Theoretical curves calculated from the two-state model with: $a = 10^{19}$; $\beta = 10^{-14}$; $\alpha = 10^{-9}$; $\gamma = 10$; $\eta = 10^{-10}$; $\epsilon = 10^{-7}$; $\eta = 1$ and $h = 10^{16}$ (B′) $3 \cdot 10^{16}$ (C′) and $10^{17}$ (D′).

The efficiency increases superlinearly in an intermediate range.

When analysing the superlinearity of this phosphor, a choice has to be made between two possible code numbers: 121211 and 121212. This can be done by looking at the neighbouring ranges. In the pedigree of Fig. 14 we see that 111211 and 111212 are the situations from which they arise. In Fig. 15(a) the superlinear range is bordered at low and high intensities by ranges of linear relations between $I$ and $U$. Since $I$ is proportional to $U^{3/2}$ in 111212, this cannot be the low-intensity situation, and the superlinear condition is thus characterized by the code number 121211. In 111211 the efficiency $I/U = \alpha\beta\zeta a/\gamma\epsilon\eta h$.

One clearly sees in Fig. 15(a) that the curves do not approach the same asymptote at low intensities for different nickel contents. The higher the nickel content, the lower the efficiency becomes at low intensities. The asymptotes are shifted vertically by a factor which is approximately proportional to the nickel content in accordance with 111211.

At higher intensities the situation may change to 122211, 121111, or 121221; 122211 drops out, however, since it would give $I \propto U^2$.

The fact that the curves all seem to have the same asymptote at high intensities, irrespective of the nickel content, points to 121111 rather than 121221.

Support for this model of superlinearity also comes from the horizontal displacement of the curves. It can easily be verified that the exciting intensities corresponding to the points of inflection for curves $B$ to $E$ (indicated by small circles in Fig. 15(a)), are proportional to the square of the nickel content. According to the theory, the sharp rise of $I$ occurs at $U_2$ which is indeed proportional to $h^2$ (see equation 18).

Summarizing, we may conclude that the behaviour of this phosphor can be characterized by the code numbers $111211 \rightarrow 121211 \rightarrow 121111$.

From Table 2 and Fig. 14, a number of relations between the parameters can be deduced, which have to be fulfilled in order to obtain this situation. From Table 4 one sees that the initial condition is 111211 if,

$$\gamma < \alpha a, \ \zeta < \epsilon h \text{ and } \alpha\beta\zeta a < \epsilon\eta\gamma h. \qquad (19)$$

From Fig. 14 we see that $U_2$ must be smaller than $U_1$, $U_3$, and $U_4$ in order to arrive at 121211, or with equation (18)

$$h < a, \ \beta\zeta < \epsilon\gamma, \text{ and } \eta\gamma h < \alpha\zeta a. \qquad (20)$$

When these conditions are all fulfilled, the transition $111211 \rightarrow 121211$ must take place. In this situation there is in our first-order approximations of Table 2 a discontinuity of $I$ which jumps to a higher value. The magnitude of this jump depends on which of the three possible situations 121111, 122211, or 121221 is realized first. In order to arrive at the first situation the corresponding jump must be the smallest, i.e.

$$\frac{\epsilon\eta\gamma h}{\alpha\beta\zeta a} < \frac{\epsilon h}{\zeta} \text{ or } \eta\gamma < \alpha\beta a \tag{21}$$

and

$$\frac{\epsilon\eta\gamma h}{\alpha\beta\zeta a} < \frac{\epsilon\gamma}{\beta\zeta} \text{ or } \eta h < \alpha a.$$

The relations (19), (20), and (21) are not all independent. If $\alpha\beta\zeta a < \epsilon\eta\gamma h$ and $\eta h < \alpha a$ the condition $\beta\zeta < \epsilon\gamma$ is automatically fulfilled. Similarly if $\eta\gamma < \alpha\beta a$ and $\alpha\beta\zeta a < \epsilon\eta\gamma h$: $\zeta$ must be smaller than $\epsilon h$.

We are thus left with the following six conditions which must be fulfilled simultaneously:

$$\begin{aligned} &\gamma < \alpha a;\ \alpha\beta\zeta a < \epsilon\eta\gamma h;\ h < a; \\ &\gamma\eta h < \alpha\zeta a;\ \eta\gamma < \alpha\beta a;\ \eta h < \alpha a. \end{aligned} \tag{22}$$

From the experimental conditions for curve $D$, we know $a \sim 10^{19}$, $h \sim 10^{17}$, and the jump

$$\frac{\epsilon\eta\gamma h}{\alpha\beta\zeta a} \sim 10^5.$$

It is further known that the empty fluorescence centres have a small cross-section of the order of $10^{-21}$ cm$^2$, corresponding to $\beta = 10^{-14}$. After some trial and error the following choice of parameters is found to satisfy the conditions:

$$\begin{aligned} &\beta = 10^{-14};\ \alpha = 10^{-9};\ \gamma = 10; \\ &\eta = 10^{-10};\ \epsilon = 10^{-7};\ \zeta = 1. \end{aligned}$$

Although the magnitudes of these parameters seem quite reasonable, they may still be out by a few orders of magnitude and serve only as an example to illustrate this case of superlinearity. To determine the parameters more accurately, further measurements would have to be carried out. The effect of temperature on the superlinear range would, for example, give information about $E_A$ and determine the ratio $\gamma : \alpha$.

With our choice of parameters and with the aid of Table 2, Fig. 16 can easily be drawn to illustrate

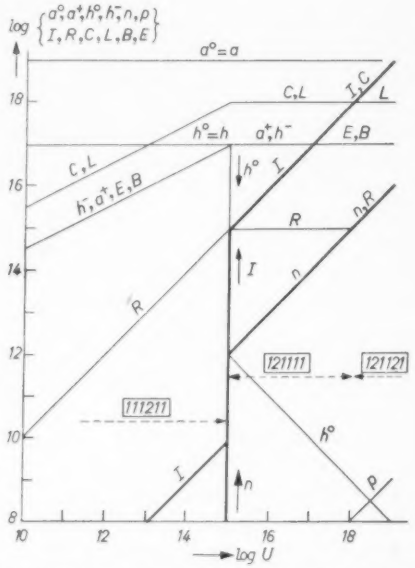


FIG. 16. First approximation behaviour chart of a model with the parameters of Fig. 15(b) and $h = 10^{17}$.

the behaviour of this phosphor to a first approximation over a wide range of intensities. From the figure one sees immediately that $a^+ \ll a^0$; $n$, $p \ll a^+$, $h^-$; $R \ll L$ and $I \ll E$ near the discontinuity and that $I$ can be solved with sufficient accuracy from the equations

$$\begin{aligned} a &= a^0 \\ h &= h^0 + h^- \\ a^+ &= h^- \\ U &= I + R \\ C &= L \\ E &= B. \end{aligned} \tag{23}$$

The result is shown in Fig. 15(b) for $h = 10^{16}$, $3 \times 10^{16}$, and $10^{17}$, respectively. These theoretical curves are to be compared with the experimental curves $B$, $C$ and $D$ of Fig. 15(a).

The practical and theoretical curves differ mainly in this respect that the superlinear range in the actual measurements is stretched out over a wider range of intensities. The main reasons for

this have been mentioned before: the spread of $U$ inside the grains and possibly a small spread of $E_H$ values.

*Superlinearity of the photoconductivity in* CdSe *single crystals*

The photoconductivity of CdSe single crystals has been measured extensively over a wide range of intensities and temperatures by BUBE[21,22]. The intensity-dependence of the photoconduction, and thus of the concentration of free electrons $n$, showed a power of approximately one at low and high temperatures. Superlinearity was observed at intermediate temperatures for low excitation intensities and at high temperatures for high excitation intensities. Since the position of the electron Fermi level was given for one crystal (5A) at the kinks where a change of the slope took place, all the measurements for this crystal could be combined on one graph showing $n$ as a function of the excitation intensity at various temperatures (Fig. 17).

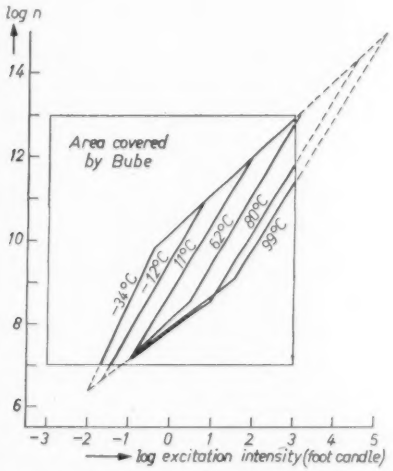


FIG. 17. Dependence of the free electron density upon excitation intensity for a "self-activated" CdSe single crystal at different temperatures as observed by BUBE.[22]

The first conclusion to be drawn from these results is that the low intensity range below the superlinear range cannot be characterized by the code number 111211, since in that case $n$ would be proportional to $U^{\frac{1}{2}}$. With the slope near unity the correct code number must be 111212.

Secondly, the position of the $A$ level can immediately be deduced from the horizontal displacements of the superlinear parts of the curves. Since $U_2 = \eta\gamma h^2/\alpha a$ and $\gamma/\alpha = N_p \exp(-E_A/kT)$, a plot of log $U_2$ versus $T^{-1}$ should give a straight line with slope $-E_A/k$.

The superlinear range is spread out in these measurements even more than in the previous case of superlinear luminescence. This "smoothing" of the curve is no doubt accentuated by the use of an incandescent lamp with its broad emission spectrum as a source of excitation. We have taken the intensity corresponding to the middle of the superlinear part of each curve. Plotting the logarithm of these intensities against $1/T$ indeed gives a straight line with a slope corresponding to $E_A = 0{\cdot}55$ eV (Fig. 18).

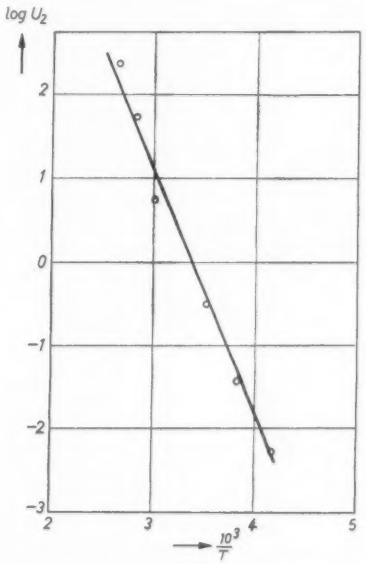


FIG. 18. Plot of log $U_2$ against $1/T$ where $U_2$ corresponds to the middle of the superlinear ranges of Fig. 16.

From 121212 the situation may change into one of three possible situations each showing a linear relation between $n$ and $U$: 121112, 121222, or 122212.

In 111212, $n = U/\epsilon h$ and in 122212, $n = \alpha a U/\gamma\eta h$. The ratio between these two values, being $\alpha\epsilon a/\eta\gamma$, would therefore be a function of temperature if the high intensity range were to be characterized by 122212. As this is not the case,

the high-intensity situation is either 121112 with a jump of $n$ equal to $\epsilon/\beta$ or 121222 with a jump $\alpha\epsilon a/\beta\eta h$.

Not enough evidence is available to make a decision on this point.

Concerning $E_H$ the following can be said: Judging from the conductivity glow curves, also determined by BUBE, the crystal contains traps with a depth of 0·43 eV and less. It is not likely, however, that these traps play an important part in the superlinearity of the photoconduction. At 99°C, for example, the superlinear range starts at $n = 10^9$.

$$\text{Now } \zeta h^- + \eta p h^- = \epsilon n h^0$$

$$\text{or } \frac{h^-}{h^0} = \frac{\epsilon n}{\zeta + \eta p} \leqslant \frac{\epsilon n}{\zeta} = \frac{n}{N_c \exp(-E_H/kT)}.$$

With $n = 10^9$, $N_c = 10^{19}$ and $E_H = 0{\cdot}43$ eV, $h^-/h^0$ would be $\leqslant 10^{-4}$.

We know, however, that superlinearity sets in as soon as the fast recombination centres $H$ get filled up completely. In order to have $h^- \sim h^0$ with $n = 10^9$ at 99°C, these states must be at least 0·75 eV below the conduction band.

When $h^-$ has become equal to $h$, which happens at $U_2 = \eta\gamma h^2/\alpha a$, $n$ has just reached the value $n_2 = U_2/\epsilon h = \eta\gamma h/\epsilon\alpha a$. From Fig. 17 one can read that for −12°C the value of $n_2$ is approximately $10^{7{\cdot}5}$.

Knowing $E_A$, the ratio $\gamma : \alpha$ can be calculated and is found to be $10^{8{\cdot}5}$ at this temperature. From this and from the value of $n$, we know that $\eta h/\epsilon a$ must be of the order of $10^{-1}$.

It is also possible from BUBE's data to make a rough estimate of $U_2$. One foot candle (10 lumens/m²) corresponds to approximately $10^{13}$ light quanta per sec per cm². If 10 per cent is absorbed (the crystal has a sharp cut-off at 7000 Å) and the absorption coefficient is of the order of $10^4$, the excitation density corresponding to 1 foot candle is of the order of $10^{16}$. At −12°C the superlinear range is obtained at approximately 0·1 footcandle or $U_2(-12°\text{C}) = \eta\gamma h^2/\alpha a = 10^{15}$, and since $\gamma/\alpha \sim 10^9$: $\eta h^2/a \sim 10^6$.

Furthermore, to arrive at 121212 from 111211 via 111212, the following conditions must be fulfilled, which are derived from Table 4 and from the fact that $U_4$ must be smaller than $U_1$, $U_2$, and $U_3$, while $U_2$ must be smaller than $U_1$, $U_5$, $U_6$, and $U_7$:

$$h < a;\ \gamma\eta < \alpha\epsilon a;\ \beta\eta h < \alpha\epsilon a;\ \gamma < \alpha a;\ \beta < \epsilon;$$

$$\alpha\beta\zeta^2 a < \epsilon\eta\gamma^2 h;\ \alpha\zeta a < \eta\gamma h.$$

The vertical displacement of the two linear parts of the conductivity curves on the log $n$/log $U$ plot of Fig. 17 is approximately 2. Assuming that 121112 is the next stage after 121212, this would mean that $n_{121112}/n_{111212} = 10^2 = \epsilon/\beta$.

After some trial and error, a set of parameters can be found which satisfies all the above conditions.

Such a set is for example:

$E_A = 0{\cdot}55$ eV; $\alpha = 10^{-8}$; $\beta = 10^{-12}$; $a = 10^{18}$;
$E_H = 0{\cdot}75$ eV; $\epsilon = 10^{-10}$; $\eta = 10^{-10}$; $h = 10^{17}$.

Fig. 19 gives the first approximation of all factors involved in the kinetics as a function of $U$ for $\gamma = 10^2$ and $\zeta = 10^{-3}$ (32°C).

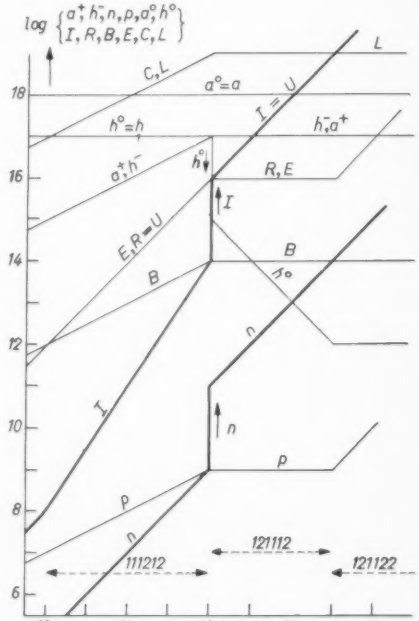


FIG. 19. First approximation behaviour chart of a model with

$a = 10^{18}$, $\alpha = 10^{-8}$, $\beta = 10^{-12}$, $\gamma = 10^2$,
$h = 10^{17}$, $\epsilon = 10^{-1}$, $\eta^0 = 10^{-10}$, $\zeta = 10^{-3}$.

A more accurate calculation of $n$ is obtained by using a less drastic simplification of equations (10)–(15), in fact from the equations:

$$\begin{aligned} a &= a^0 \\ h &= h^0 + h^- \\ a^+ &= h^- \\ U &= I + R \\ C &= L \\ E &= R. \end{aligned} \tag{24}$$

One can easily verify from Fig. 19 that there would be little point in including the other neglected terms in the calculations. The results for $n$ are shown for three different temperatures ($\gamma = 1$, $10^2$, and $10^4$) in Fig. 20. The dotted lines indicate an

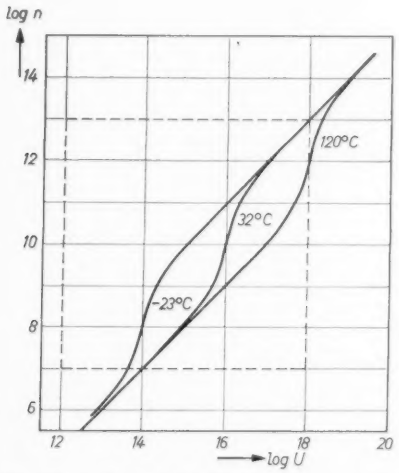


FIG. 20. Theoretical dependence of $n$ upon $U$ for $a = 10^{18}$, $\alpha = 10^{-8}$, $\beta = 10^{-12}$, $h = 10^{17}$, $\epsilon = 10^{-10}$, $\eta = 10^{-19}$, $E_A = 0{\cdot}55$ eV, $E_H = 0{\cdot}75$ eV at three different temperatures. The dotted area is to be compared with the experimental area covered by BUBE (Fig. 17).

area which corresponds to the experimental area of BUBE's measurements. These curves give a reasonable representation of the experimental data considering the fact that the superlinear part should be smoothed out over a larger range. Here also the two-state model seems to be adequate.

## POSSIBLE EXTENSIONS OF THE ANALYTICAL METHOD

In the two-state model discussed above it has been assumed that the Fermi level is so far below $H$ and so far above $A$ when the material is not excited and in equilibrium condition, that $a_0^+$, $h_0^-$, $n_0$, and $p_0$ can be neglected. However, in particular cases these assumptions may not be valid, as for instance when studying the photoconduction of a material with an appreciable dark conductivity. This would mean that $H$ is already partly filled in the dark and that $n_0$ cannot be neglected. To analyse such a case one would have to add to the equations (10)–(15)

$$h^- = h_0^- + \Delta h^- \tag{25}$$

$$n = n_0 + \Delta n \tag{26}$$

and using, instead of (12), the equation

$$a^+ + p = \Delta h^- + \Delta n \tag{12a}$$

where $\Delta(n, h^-)$ indicates the deviations from the equilibrium values in the dark. In certain cases the deviation may be negative. The inclusion of these extra equations would entail the adding of two more columns to equation (16) and the use of a code number with 8 digits. Instead of 128 one would then have 512 different situations.

In the most common phosphors and photoconductors with large band gaps the use of the more simple set of equations seems justified.

A sulphide phosphor is usually made in such way that, together with an activator, a co-activator is incorporated in the lattice in approximately equal molar amounts. For example, a fluorescent zinc sulphide showing a single green emission band is obtained by incorporating equal molar amounts of copper and aluminium. The dark conductivity is low, the copper centre can be described as a $Cu^+$ ion on a $Zn^{2+}$ position, whereas all the aluminium is present as $Al^{3+}$.

It is known that $Al^{3+}$ and other co-activators such as $Cl^-$, $Br^-$, $Ga^{3+}$, etc., give rise to traps.[58] Often these traps are so shallow that they can only be filled at low temperatures and do not play an important part in the kinetics at room temperature. The $H$ levels in our examples below are usually not connected with these co-activators, but with other impurities such as cobalt or nickel or with

lattice vacancies or dislocations which give rise to deeper traps. The co-activators merely serve to incorporate the activators in the proper way, e.g. as $Cu^+$ or $Ag^+$, while other impurities or lattice defects are responsible for superlinear effects, quenching, etc.

If more activator than co-activator is incorporated ([Cu] : [Al] $> 1$ in our example), it is conceivable that part of the copper is present as $Cu^{2+}$, corresponding to a solution of CuS in ZnS. Such a $Cu^{2+}$ centre can be considered as an empty $Cu^+$ centre. In that case $a_0^+$ cannot be neglected, and one should add the equations

$$a^+ = a_0^+ + \Delta a^+ \tag{27}$$

and if the Fermi level were so low that $p$-conductivity was found in the dark also

$$p = p_0 + \Delta p \tag{28}$$

with the neutrality condition

$$\Delta a^+ + \Delta p = h^- + n. \tag{12b}$$

However, experience has shown that no $p$-conductivity is found and that in fact new recombination centres arise when an excess of activator is used. These centres are most likely charged anion vacancies compensating the effective charge of an activator ($Cu^+$ in ZnS has an effective negative charge).

Such a situation with two recombination centres giving rise to two different levels of the type $A$ can be analysed in a way similar to that used in the more simple two-state model described above. The same applies to a photoconductor with more than one trap level.

## DISCUSSION OF ROSE'S MODEL

ROSE assumed the presence of two classes of recombination centres (I and II), both classes giving rise to states distributed through the forbidden gap. Class I centres are supposed to have capture cross-sections for electrons greater than that of class II centres and capture cross-sections for holes equal or less than that of class II centres.

The occupation of the bound states is determined by two steady-state Fermi levels, one for the electrons and one for the holes. In the dark these levels are at the same position and coincide with the normal Fermi level under thermal equilibrium. When the material is exposed to light, the two levels move apart.

ROSE furthermore assumed that levels lying between the two steady-state Fermi levels* and called "ground states" act as recombination levels, whereas those levels outside this region and called "shallow trapping states" are in thermal equilibrium with the nearest allowed band and do not take an appreciable part in the recombination processes.

Superlinearity in particular is explained by putting the majority of the class II levels outside the two steady-state levels at low light intensities. As the light intensity is increased, the steady-state Fermi levels move apart and more of the class II states are turned into ground states. As the capture cross-sections of these ground states are smaller than those of the ground states belonging to class II, the class I states and the life of the free electrons will be increased continuously, thus giving rise to superlinearity.

At least one serious objection, however, may be brought forward against this theory. Superlinearity has been observed of photoconductance and of luminescence with the same activators. If the activator levels were distributed over a considerable range, a change in the spectral distribution would be expected on changing the intensity of the exciting light.

Such a change is not found. Occasionally a change in emission colour is in fact observed, for example in ZnS–Cu, but this is due to the presence of two emission bands, each emission band corresponding to one discrete level. In ZnS phosphors with a single emission band and showing superlinearity, the spectral distribution does not change noticeably in the superlinear range.

Levels near the conduction band, on the other hand, have shown a certain spread in depth. Such a spread was, for example, observed with the cobalt level in ZnS which is about 0·5 eV below

* In fact the actual dividing lines between the two types of states are not the steady-state Fermi levels but so-called "demarcation lines", usually close to the Fermi levels. The demarcation line is so defined that a trapped electron at the demarcation line has an equal probability of being released thermally into the conduction band or of being captured by a free hole in the filled band.

VOL 7 195

the conduction band.[59] Similar observations have been made with other trapping levels. Moreover, a theoretical decay curve is practically never found with the luminescence intensity $I_t$ proportional to $t^{-2}$ after sufficient long periods of decay; instead it is proportional to $t^{-\alpha}$ with $\alpha < 2$, a fact which points strongly to a spread in depths of trapping levels.

Such spreads in depth will undoubtedly have an effect on the intensity-dependence of photoconduction and fluorescence. The spread is usually not very large, judging from the glow curves of well-defined, carefully prepared phosphors.

Whereas, however, ROSE started from one extreme—a uniform distribution for two types of states—we have chosen an approach from the opposite end, namely one definite energy for each of the two recombination centres.

The truth lies probably somewhere between the two, with, for example, a narrow Gaussian distribution for one or both states.

## CONCLUSION

The properties of photoconductors, and in particular the intensity-dependence of photoconduction and luminescence, can be described by a two-state model without having to introduce, in the first instance, an energy distribution of these states. The advantage of such a model is that one can draw definite conclusions about the positions of the states in the forbidden zone and about their cross-sections for capturing free carriers. Despite the apparent simplicity of this model, it can account quantitatively for many complex problems, such as saturation and quenching of luminescence, superlinearity, etc.

Owing to the versatility of the model, since many parameters can be varied independently, one has to be extremely cautious in drawing conclusions from a few experimental data. In general, it is necessary to measure many properties of the same material or to study the effect of small alterations in the chemical composition before the stationary state can be analysed and definite conclusions drawn regarding the parameters involved.

*Acknowledgement*—I want to express my thanks to Dr. G. DIEMER for stimulating discussions and suggestions.

## REFERENCES

1. HAYNES J. R. and BRIGGS H. B. *Phys. Rev.* **86,** 647 (1952).
2. MOSS F. S. and HAWKINS T. H. *J. Phys. Radium* **17,** 712 (1956).
3. VAN DOORN C. Z. and DE NOBEL D. *Physica* **22,** 338 (1956).
4. SMITH R. W. *Phys. Rev.* **105,** 900 (1957).
5. GROSZ E. F. and JACOBSON M. A. *Soviet Phys. Tech. Phys.* **1,** 1340 (1957).
6. GRILLOT E. *J. Phys. Radium* **17,** 822 (1956).
7. GISOLF J. H. and KRÖGER F. A. *Physica* **6,** 1101 (1939).
8. LEVSHIN W. L. *Zh. eksp. teor. fiz.* **17,** 675 (1947).
9. FRERICHS R. *Phys. Rev.* **76,** 1869 (1949).
10. BROSER I. and WARMINSKY R. *Ann. Phys., Lzg.* **7,** 289 (1950).
11. SMITH R. W. *R.C.A. Rev.* **13,** 350 (1951).
12. BUBE R. H. *Phys. Rev.* **83,** 393 (1951).
13. FASSBENDER J. and SERAPHIN B. *Ann. Phys., Lzg.* **10,** 374 (1952).
14. GOBRECHT H., HAHN J. and KÖSEL H. J. *Z. Phys.* **136,** 285 (1953).
15. BUBE R. H. *J. Chem. Phys.* **23,** 18 (1955).
16. BUBE R. H. *J. Appl. Phys.* **27,** 1237 (1956).
17. VEITH W. *C.R. Acad. Sci., Paris* **230,** 947 (1950).
18. KALLMANN H. and KRAMER B. *Phys. Rev.* **87,** 91 (1952).
19. LASHKAREV V. E. and FEDORUS G. A. *Izvest. Akad. Nauk SSSR, Ser. Fiz.* **16,** 81 (1952).
20. WLÉRICK G. and PRÉGERMAIN F. *J. Phys. Radium* **15,** 757, 1954.
21. BUBE R. H. *Photoconductivity Conference (Atlantic City)*, p. 575. Wiley, New York (1955).
22. BUBE, R. H. *Proc. Inst. Radio Engrs.* **43,** 1836 (1955).
23. THOMSEN S. M. and BUBE R. H. *Rev. Sci. Instrum.* **26,** 664 (1955).
24. DIRKSEN H. J. and MEMELINCK O. H. *Appl. Sci. Res.* **4B,** 205 (1955).
25. VEITH W. *Z. angew. Phys.* **7,** 1 (1955).
26. TOLSTOI N. A. *Soviet Phys. J.E.T.P.* **3,** 190 (1956).
27. DE GROOT W. *Physica* **6,** 393 (1939).
28. SCHERER K. and RÜBSAAT R. *Arch. Elektrotech.* **31,** 821 (1937).
29. NOTTINGHAM W. B. *J. Appl. Phys.* **10,** 73 (1939).
30. STRANGE J. W. and HENDERSON S. T. *Proc. Phys. Soc.* **58,** 383 (1956).
31. HEIMANN W. and SCHUH F. *Naturwiss.* **33,** 157 (1946).
32. BRIL A. *Physica* **15,** 361 (1949).
33. RIEHL N. *Z. tech. Phys.* **20,** 152 (1939).
34. KLASENS H. A., RAMSDEN W. and CHOW Q. *J. Opt. Soc. Amer.* **38,** 60, 1948.
35. NAIL N. R., URBACH F. and PEARLMAN D. *Cornell Symposium on Solid Luminescent Materials*, p. 190. Wiley, New York (1948).
36. VERGUNAS F. I. and GAVRILOV F. F. *Dokl. Akad. Nauk SSSR* **59,** 1273 (1948).

37. NAIL N. R., URBACH F. and PEARLMAN D. *J. Opt. Soc. Amer.* **39,** 690 (1949).
38. GARLICK G. F. J. and GIBSON A. F. *J. Opt. Soc. Amer.* **39,** 935 (1949).
39. LITVINOVA P. S. *Zh. eksp. teor. fiz.* **19,** 688 (1949).
40. VERGUNAS F. I. and GAVRILOV F. F. *Zh. eksp. teor. fiz.* **20,** 224 (1950).
41. ALENTSEV M. N., ANTONOV-ROMANOVSKY V. V. and VINOKUROV L. A. *Dokl. Akad. Nauk SSSR* **96,** 1133 (1954).
42. ANTONOV-ROMANOVSKY V. V. *J. Phys. Radium* **17,** 694 (1956).
43. ANTONOV-ROMANOVSKY V. V. and VINOKUROV L. A. *Soviet Phys. J.E.T.P.* **2,** 711 (1956).
44. SCHÖN M. *Tech. Wiss. Abhandl. Osram* **6,** 49 (1953) (equations 32–40); *Physica* **20,** 930 (1954) (equations 23–28).
45. ROBERTS S. and WILLIAMS F. E. *J. Opt. Soc. Amer.* **40,** 516 (1950).
46. BUBE, R. H. *J. Phys. Chem. Solids* **1,** 234 (1957).
47. ROSE A. *Proc. Inst. Radio Engrs.* **43,** 1850 (1955).
48. ROSE A. *Phys. Rev.* **97,** 322 (1955).
49. DUBOC C. A. *Brit. J. Appl. Phys. Suppl.* No. **4,** 107 (1955).
50. BROUWER G. *Philips Res. Rep.* **9,** 366, 1954.
51. KRÖGER F. A. and VINK H. J. *Z. phys. Chem.* **203,** 1 (1954); *Physica* **20,** 950 (1954).
52. BROSER I., KALLMANN H. and WARMINSKY R. *Z. Naturf.* **4a,** 631 (1949).
53. DIEMER G., v. GURP G. J. and MEYER H. J. G. *Physica* **23,** 987 (1957).
54. KRÖGER F. A. *Physica* **7,** 1 (1940).
55. LAMBE J. J., KLICK C. C. and DEXTER D. L. *Phys. Rev.* **103,** 1715 (1956).
56. SMITH R. W. *Phys. Rev.* **105,** 900 (1957).
57. VAN ROOSBROECK W. and SHOCKLEY W. *Phys. Rev.* **94,** 1558 (1954).
58. HOOGENSTRAATEN W. *J. Electrochem. Soc.* **100,** 356 (1953).
59. HOOGENSTRAATEN W. and KLASENS H. A. *J. Electrochem. Soc.* **100,** 366 (1953).
60. DIEMER G. and HOOGENSTRAATEN W. *J. Phys. Chem. Solids* **2,** 119 (1957).

VOL
7
195

*J. Phys. Chem. Solids* Pergamon Press 1958. Vol. 7. pp. 201–206.

# STRUCTURE OF THE METASTABLE STATE OF $Mn^{++}$ AND $Fe^{+++}$

A. M. CLOGSTON

Bell Telephone Laboratories Inc., Murray Hill, New Jersey

(*Received* 3 *June* 1958)

**Abstract**—A discussion is presented of the possibility of performing spin-resonance experiments on various metastable excited states of ions of the configuration $(3d)^n$. There appears to be no reason why such experiments should not be feasible. A special study is made of the ions $Mn^{++}$ and $Fe^{+++}$ with configuration $3d^5$. Observations on the metastable levels of these ions would be particularly useful in understanding the splittings of the ground state $^6S$.

VOL. 7 1958

## 1. INTRODUCTION

MEASUREMENTS of the lifetimes[1–3] of various metastable levels of ions having the configuration $(3d)^n$ and $(4f)^n$ raise the possibility that sufficient populations might be established in these states to make possible paramagnetic-resonance measurements of their structure. Experiments of this sort have been suggested and carried out by HERSHBERGER[4] and BLEANY and LOW,[5] apparently without success. It would appear, however, from the considerations outlined below that there is no fundamental reason for this result. Sufficient interest attaches to the properties of the excited states of the 3*d* and 4*f* shell ions that the experiments should be repeated in various salts with improved experimental conditions. It is the primary purpose of this paper to study the metastable levels of the ions $Mn^{++}$ and $Fe^{+++}$, having the configuration $(3d)^5$, and to show how spin-resonance measurements of the structure of these levels will help in understanding the magnetic behavior of the ions.

The metastable states with which we are concerned here are derived from the ground states of the various ions by the reversal of a spin in the *d* or *f* shell, and lie generally in the optical region of the spectrum. Transitions to these states are forbidden by parity and spin considerations and occur only because of mixing due to vibrations and spin-orbit coupling. The lifetimes of the state are about $10^{-2}$ sec and correspond therefore to about $10^8$ cycles of microwave radiation. Lifetime broadening would therefore not be an important effect. The long lifetimes reported exist only in dilute crystals and are drastically shortened in concentrations greater than 0·1–1 per cent.[7]

It appears to be feasible to absorb at least 100 mW of optical power in a sample of convenient experimental size if the material under consideration has sufficiently strong absorption bands at some energy higher than the metastable level, but within the visible or near ultraviolet.* This situation exists for $Cr^{+++}$, where the Stark splitting of the ground state establishes a set of spin-allowed, parity-forbidden quartet levels in the green region of the visible spectrum, with a set of doublet levels lying at lower energy in the red. For a ruby crystal composed of a few tenths per cent $Cr^{+++}$ ions in $Al_2O_3$, illumination in the green produces a powerful fluorescence in the red. In the case of $Mn^{++}$, the metastable level lies at approximately 18,000 $cm^{-1}$ in most crystals,[8] but there are no strong absorptions much lower than 50,000 $cm^{-1}$.[9] If this should prove to be an experimental obstacle, it may be possible to provide the necessary absorption levels by adding ions of lead, thallium, or cerium to the crystal, as is done with various manganese-activated phosphors.[10]

* This is the experience of S. GESCHWIND, who is examining the feasibility of making experiments of the kind suggested in $Cr^{+++}$.

In the case of $Fe^{+++}$ the metastable level lies lower than for $Mn^{++}$, appearing at about 12,000 $cm^{-1}$.[8] There appears also to be a strong absorption band in the vicinity of 20,000–25,000 $cm^{-1}$.[8,11] $Fe^{+++}$ may therefore be a convenient experimental material. It might be expected that suitable crystals containing $Fe^{+++}$ would fluoresce in the near infrared when illuminated in the violet or near ultraviolet,[12] but this effect does not seem to have been reported.

Experimental investigations of manganese-activated phosphors suggest that optical energy absorbed in a crystal containing $Mn^{++}$ ions is transferred with high efficiency to the metastable levels responsible for the fluorescence.[13,14] If it is assumed that the transfer is only 10 per cent efficient due to loss of energy in various non-radiative processes, one should still be able to obtain 10 mW of power reradiated from the metastable levels. With a lifetime of $10^{-2}$ sec, this implies an excited population of about $10^{14}$ spins. If the resonance lines are not unduly broadened by processes that are not yet anticipated, this population is within the sensitivity range of a good microwave spectrometer.[15]

Paramagnetic-resonance measurements of the metastable levels of these ions will have a high intrinsic interest. It can be expected, for instance, that information would be obtained of importance to the understanding of luminescent processes particularly in regard to the nature of concentration quenching of fluorescence. There may also be revealed possibilities for the creation of maser amplifiers working at very short wavelengths and supplied with energy from the visible range of the spectrum.

We are particularly concerned in this paper with the greater understanding that could be obtained of the ground-state splittings of the important ions $Mn^{++}$ and $Fe^{+++}$. For these ions, the electron configuration is $(3d)^5$. The ground state is $^6S$ and has a very small crystal field splitting of the order of $10^{-3}$ $cm^{-1}$.[16] A set of quartet levels lie in the visible or near-infrared portion of the spectrum. The metastable level has the symmetry $^4T_1$ and is derived from the free-ion term $^4G$. The shift of this level in a cubic crystalline field has been calculated by TANABE and SUGANO,[17] by WATANABE,[18] and by ORGEL.[19] The level is three-fold orbitally degenerate and four-fold spin degenerate. We shall find that the twelve-fold degeneracy is split by spin-orbit coupling into a sextuplet, a quartet, and a doublet, with the sextuplet level lying lowest in octahedral symmetry. Interactions with higher energy states further split the sextuplet into a quartet and a doublet similar to the splitting of the ground-state sextuplet. We shall see that the ground-state splitting is closely related to the splitting of the excited sextuplet. Spin-resonance observations of the latter state can therefore be expected to throw considerable light on the mechanisms responsible for the behavior of the ground-state. We may note here that the structure of the excited sextuplet cannot be observed optically because of the broadening of the absorption lines due to vibrations of the crystal lattice.

## 2. FORMALISM

We have adopted the technique of second quantization in making the following calculation. We shall be concerned with states arising from the configuration $(3d^5)$. We take the five $3d$ orbitals as a basic representation, identifying the orbitals by their $z$-directed angular momentum. The orbitals are further identified by a + or − sign indicating spin direction. This array of one-electron states is arranged in the standard order $2^+2^-1^+1^-0^+0^-$ $-1^+-1^--2^+-2^-$. We indicate a simple state by parentheses enclosing a set of occupied orbitals. For instance, the $^6S$ ground-state for $z$-component $S_z$ of total spin equal to $\frac{5}{2}$ is $(2^+1^+0^+-1^+-2^+)$.

In this scheme, operators are represented by sums over one-electron matrix components multiplied by combinations of creation and destruction operators. A one-electron operator $A$, for instance, becomes $\sum_b (a|A|b)\lambda_a^*\lambda_b$, where $\lambda_b$ is a destruction operator for orbital $b$ and $\lambda_a^*$ a creation operator for orbital $a$ with the usual properties appropriate to Fermi–Dirac statistics. We shall use the following operators:

$$L_- = \sum_m \sqrt{l(l+1)-m(m-1)}(\lambda^*_{m-1-}\lambda_{m-}+\lambda^*_{m-1+}\lambda_{m+}) \qquad (1)$$

$$S_- = \sum_m \lambda^*_{m-}\lambda_{m+} \tag{2}$$

$$K = \frac{\sigma}{2}\sum_m \{m(\lambda^*_{m+}\lambda_{m+} - \lambda^*_{m-}\lambda_{m-}) + \sqrt{l(l+1)-m(m+1)}\,\lambda^*_{m+1-}\lambda_{m^+} +$$

$$+ \sqrt{l(l+1)-m(m-1)}\,\lambda^*_{m-1+}\lambda_{m^-}\}. \tag{3}$$

Here $L_-$ is the operator lowering the orbital angular momentum by $\hbar$, $S_-$ the spin lowering operator, and $K$ the spin-orbit interaction energy proportional to the parameter $\sigma$. The orbits are indicated by $m$, which runs from 2 to $-2$, $l$ is always equal to 2, and $\sigma$ is the spin-orbit coupling parameter.

### 3. WAVE FUNCTIONS FOR THE FREE ION

The configuration $(3d^5)$ gives rise to an array of 504 states comprised of various sextuplets, quartets and doublets. We limit our considerations to the sextuplets and quartets. It is very easy to establish Table 1.

The wave functions corresponding to the terms of the free atom are found as follows: ${}^6S(0, \frac{5}{2})$ and ${}^4G(4, \frac{3}{2})$ are found directly. The terms in parentheses indicate $L_z$ and $S_z$ respectively. By operating on ${}^4G(4, \frac{3}{2})$ with $L_-$, we generate ${}^4G(3, \frac{3}{2})$. The orthogonal combination of simple wave functions gives ${}^4F(3, \frac{3}{2})$. This procedure is continued to find the remaining terms. We may then operate throughout with $S_-$ to generate wave functions for other values of $S_z$. The beginning wave functions for each term are given in Table 2.

### 4. WAVE FUNCTIONS IN CUBIC CRYSTAL FIELD

The terms in Table 2 split, in a cubic-crystal field, into various representations of the octahedral

*Table* 1.

| States | | | Derived from |
|---|---|---|---|
| ${}^6S$ | $L_z = 0$ | $S_z = \frac{5}{2}$ | $(2^+1^+0^+-1^+-2^+)$ |
| ${}^4G$ | $L_z = 4$ | $S_z = \frac{3}{2}$ | $(2^+2^-1^+0^+-1^+)$ |
| ${}^4G{}^4F$ | $L_z = 3$ | $S_z = \frac{3}{2}$ | $(2^+2^-1^+0^+-2^+)$, $(2^+1^+1^-0^+-1^+)$ |
| ${}^4G{}^4F{}^4D$ | $L_z = 2$ | $S_z = \frac{3}{2}$ | $(2^+2^-1^+-1^+-2^+)$, $(2^+1^+1^-0^+-2^+)$, $(2^+1^+0^+0^--1^+)$ |
| ${}^4G{}^4F{}^4D{}^4P$ | $L_z = 1$ | $S_z = \frac{3}{2}$ | $(2^+2^-0^+-1^+-2^+)$, $(2^+1^+1^--1^+-2^+)$, $(2^+1^+0^+0^--2^+)$, $(2^+1^+0^+-1^+-1^-)$ |

*Table* 2.

${}^6S(0, \frac{5}{2}) = (2^+1^+0^+-1^+-2^+)$

${}^4G(4, \frac{3}{2}) = (2^+2^-1^+0^+-1^+)$

${}^4F(3, \frac{3}{2}) = \sqrt{\frac{1}{2}}(2^+1^+1^-0^+-1^+) + \sqrt{\frac{1}{2}}(2^+2^-1^+0^+-2^+)$

${}^4D(2, \frac{3}{2}) = \sqrt{\frac{2}{7}}(2^+1^+0^+0^--1^+) + \sqrt{\frac{3}{7}}(2^+1^+1^-0^+-2^+) + \sqrt{\frac{2}{7}}(2^+2^-1^+1^--2^+)$

${}^4P(1, \frac{3}{2}) = \sqrt{\frac{3}{10}}(2^+1^+0^+-1^+-1^-) + \sqrt{\frac{3}{10}}(2^+1^+0^+0^--2^+) + \sqrt{\frac{3}{10}}(2^+1^+1^--1^+-2^+) + \sqrt{\frac{2}{10}}(2^+2^-0^+-1^+-2^+)$

group. There are no diagonal elements of the crystal field, the splitting arising from off-diagonal elements between components of the same symmetry arising from different terms. The metastable level is a term of symmetry $^4T_1$. The terms of this symmetry arising from each angular momentum state are as given in Table 3.

*Table 3.*

$$
\begin{aligned}
{}^4T_1(4,1,\tfrac{3}{2}) &= \sqrt{\tfrac{1}{8}}\,{}^4G(-3,\tfrac{3}{2})+\sqrt{\tfrac{7}{8}}\,{}^4G(1,\tfrac{3}{2})\\
{}^4T_1(4,0,\tfrac{3}{2}) &= \sqrt{\tfrac{1}{2}}\,{}^4G(4,\tfrac{3}{2})-\sqrt{\tfrac{1}{2}}\,{}^4G(-4,\tfrac{3}{2})\\
{}^4T_1(4,-1,\tfrac{3}{2}) &= \sqrt{\tfrac{1}{2}}\,{}^4G(3,\tfrac{3}{2})+\sqrt{\tfrac{7}{8}}\,{}^4G(-1,\tfrac{3}{2})\\
{}^4T_1(3,1,\tfrac{3}{2}) &= \sqrt{\tfrac{5}{8}}\,{}^4F(-3,\tfrac{3}{2})+\sqrt{\tfrac{3}{8}}\,{}^4F(1,\tfrac{3}{2})\\
{}^4T_1(3,0,\tfrac{3}{2}) &= {}^4F(0,\tfrac{3}{2})\\
{}^4T_1(3,-1,\tfrac{3}{2}) &= \sqrt{\tfrac{5}{8}}\,{}^4F(3,\tfrac{3}{2})+\sqrt{\tfrac{3}{8}}\,{}^4F(-1,\tfrac{3}{2})\\
{}^4T_1(1,1,\tfrac{3}{2}) &= {}^4P(1,\tfrac{3}{2})\\
{}^4T_1(1,0,\tfrac{3}{2}) &= {}^4P(0,\tfrac{3}{2})\\
{}^4T_1(1,-1,\tfrac{3}{2}) &= {}^4P(-1,\tfrac{3}{2})
\end{aligned}
$$

The three quantum numbers labeling $^4T_1$ represent $L$, the particular component of the triplet, and $S_z$ respectively.

The octahedral crystal field is represented by:

$$V=\sum_{m,n} Dq[\tfrac{1}{1\,\overline{2}}(35m^4-155m^2+72)\delta_{mn}+$$

$$+5\delta_{m,n+4}+5\delta_{m,n-4}](\lambda^*_{m+}\lambda_{n+}+\lambda^*_{m-}\lambda_{n-}) \qquad (4)$$

where $D$ is the coefficient of the octahedral potential $(x^4+y^4+z^4-\frac{3}{5}r^4)$ and $q=(\frac{2}{1\,\overline{0}\,5})\langle r^4\rangle$. This perturbation mixes the corresponding members of the three triplets. The matrix components are:

$$
\begin{aligned}
[{}^4T_1(1,1,\tfrac{3}{2})|V|{}^4T_1(4,1,\tfrac{3}{2})] &= \phantom{-}4\sqrt{5}\,Dq\\
[{}^4T_1(3,1,\tfrac{3}{2})|V|{}^4T_1(4,1,\tfrac{3}{2})] &= -2\sqrt{5}\,Dq\\
[{}^4T_1(1,0,\tfrac{3}{2})|V|{}^4T_1(4,0,\tfrac{3}{2})] &= -4\sqrt{5}\,Dq\\
[{}^4T_1(3,0,\tfrac{3}{2})|V|{}^4T_1(4,0,\tfrac{3}{2})] &= -2\sqrt{5}\,Dq\\
[{}^4T_1(1,-1,\tfrac{3}{2})|V|{}^4T_1(4,-1,\tfrac{3}{2})] &= -4\sqrt{5}\,Dq\\
[{}^4T_1(3,-1,\tfrac{3}{2})|V|{}^4T_1(4,-1,\tfrac{3}{2})] &= \phantom{-}2\sqrt{5}\,Dq.
\end{aligned}
$$

These are identical to the matrix elements given by ORGEL,[19] except for certain phase factors which are important in expressing the wave functions. The wave functions are:

$${}^4T_1(1,\tfrac{3}{2})=N\left[{}^4T_1(4,1,\tfrac{3}{2})-\frac{4\sqrt{5}\,Dq}{E({}^4P)-E}{}^4T_1(1,1,\tfrac{3}{2})+\right.$$

$$\left.+\frac{2\sqrt{5}\,Dq}{E({}^4F)-E}{}^4T_1(3,1,\tfrac{3}{2})\right] \qquad (5)$$

$${}^4T_1(0,\tfrac{3}{2})=N\left[{}^4T_1(4,0,\tfrac{3}{2})+\frac{4\sqrt{5}\,Dq}{E({}^4P)-E}{}^4T_1(1,0,\tfrac{3}{2})+\right.$$

$$\left.+\frac{2\sqrt{5}\,Dq}{E({}^4F)-E}{}^4T_1(3,0,\tfrac{3}{2})\right] \qquad (6)$$

$${}^4T_1(-1,\tfrac{3}{2})=N\left[{}^4T_1(4,-1,\tfrac{3}{2})+\right.$$

$$+\frac{4\sqrt{5}\,Dq}{E({}^4P)-E}{}^4T_1(1,-1,\tfrac{3}{2})-$$

$$\left.-\frac{2\sqrt{5}\,Dq}{E({}^4F)-E}{}^4T_1(3,-1,\tfrac{3}{2})\right]. \qquad (7)$$

Here, $E$ is the lowest root of the secular equation. Since we will be concerned only with this state, we have suppressed a quantum number in the above wave functions. Let us define

$$\alpha_P=\frac{4\sqrt{5}\,Dq}{E({}^4P)-E} \qquad \alpha_F=\frac{2\sqrt{5}\,Dq}{E({}^4F)-E}.$$

Then

$$N^2(1+\alpha_P{}^2+\alpha_F{}^2)=1.$$

## 5. SPIN-ORBIT INTERACTION

We may now use the wave functions (5), (6) and (7) to compute the matrix elements of spin-orbit interaction within the lowest triplet. The state is three-fold orbitally degenerate and four-fold spin degenerate. The secular determinant is therefore $12\times12$. The determinant factors, however, and allows an exact diagonalization of the problem, yielding the energies and wave functions given in Table 4.

The twelve-fold degeneracy is thus resolved by spin-orbit coupling into a sextuplet, a quartet, and

*Table* 4.

| $W = a$ | $^4T_1(1, \frac{3}{2})$ | $^4T_1(-1, -\frac{3}{2})$ |
|---|---|---|
| | $-\sqrt{\frac{2}{5}}\,^4T_1(0, \frac{3}{2})+\sqrt{\frac{3}{5}}\,^4T_1(1, \frac{1}{2})$ | $\sqrt{\frac{2}{5}}\,^4T_1(0, -\frac{3}{2})+\sqrt{\frac{3}{5}}\,^4T_1(-1, -\frac{1}{2})$ |
| | $\sqrt{\frac{1}{10}}\,^4T_1(-1, \frac{3}{2})+\sqrt{\frac{6}{10}}\,^4T_1(0, \frac{1}{2})-\sqrt{\frac{3}{10}}\,^4T_1(1, -\frac{1}{2})$ | $-\sqrt{\frac{1}{10}}\,^4T_1(1, -\frac{3}{2})+\sqrt{\frac{6}{10}}\,^4T_1(0, -\frac{1}{2})+\sqrt{\frac{3}{10}}\,^4T_1(-1, \frac{1}{2})$ |
| $W = -(2a/3)$ | $\sqrt{\frac{3}{5}}\,^4T_1(0, \frac{3}{2})+\sqrt{\frac{2}{5}}\,^4T_1(1, \frac{1}{2})$ | $-\sqrt{\frac{3}{5}}\,^4T_1(0, -\frac{3}{2})+\sqrt{\frac{2}{5}}\,^4T_1(-1, -\frac{1}{2})$ |
| | $\sqrt{\frac{6}{15}}\,^4T_1(-1, \frac{3}{2})+\sqrt{\frac{1}{15}}\,^4T_1(0, \frac{1}{2})+\sqrt{\frac{8}{15}}\,^4T_1(1, -\frac{1}{2})$ | $-\sqrt{\frac{6}{15}}\,^4T_1(1, -\frac{3}{2})+\sqrt{\frac{1}{15}}\,^4T_1(0, -\frac{1}{2})-\sqrt{\frac{8}{15}}\,^4T_1(-1, \frac{1}{2})$ |
| $W = -(5a/3)$ | $-\sqrt{\frac{3}{8}}\,^4T_1(-1, \frac{3}{2})+\sqrt{\frac{3}{8}}\,^4T_1(0, \frac{1}{2})+\sqrt{\frac{1}{8}}\,^4T_1(1, -\frac{1}{2})$ | $\sqrt{\frac{3}{8}}\,^4T_1(1, -\frac{3}{2})+\sqrt{\frac{3}{8}}\,^4T_1(0, -\frac{1}{2})-\sqrt{\frac{1}{8}}\,^4T_1(-1, \frac{1}{2})$ |

a doublet. The quantity $a$ is given by:

$$a = -\frac{\sqrt{5}}{2}N^2\alpha_F\sigma. \tag{8}$$

The spin-orbit splitting is proportional to $\sigma$ and to

$$\alpha_F = \frac{2\sqrt{5}\,Dq}{E(^4F)-E}.$$

Since $\sigma$ is positive, $a$ will be negative on a octahedral site with $Dq$ positive. The six-fold level will therefore lie lowest. On a tetrahedral site with $Dq$ negative, the doublet will lie lowest. Choosing a value of $Dq$ appropriate to octahedrally coordinated manganese, we find $a$ approximately equal to $-20$ cm$^{-1}$.

### 6. MAGNETIC FIELD SPLITTING

The wave functions given in Table 4 allow the weak field splitting factors to be easily determined for the sextuplet, quartet, and doublet. A magnetic field $H$ is imposed along the $z$-axis, introducing the Zeeman energy

$$\beta H\sum_m[m(\lambda^*_{m+}\lambda^*_{m+}+\lambda^*_{m-}\lambda^*_{m-})+$$

$$+(\lambda^*_{m+}\lambda_{m+}-\lambda^*_{m-}\lambda_{m-})]$$

where $\beta$ is the Bohr magnetron. We calculate the diagonal value of this perturbation and obtain the following $g$-values

Sextuplet: $g = \frac{8}{5}(1-\mu) = 1{\cdot}4$

Quartet: $g = \frac{2}{15}(13-8\mu) = 1{\cdot}6$

Doublet: $g = \frac{8}{3}(1+\mu) = 2{\cdot}9$

where $\mu = N^2(\frac{1}{8}+\frac{5}{8}\alpha_F{}^2)$. An approximate value of $\mu$ is 0·1, which corresponds to the numerical values of $g$ given above.

### 7. ZERO-FIELD SPLITTING OF THE SEXTUPLET

We wish finally to discuss the zero-field splitting of the sextuplet component of the metastable level and to show how it is related to the ground-state splitting. Let us consider a particular member $m$ of the excited sextuplet. This level will be shifted in energy by second-order spin-orbit interaction with higher levels by an amount

$$\Delta_m = \sum_n \frac{|(m|K|n)|^2}{E_m-E_n}. \tag{9}$$

An investigation of the energy-level diagrams given by ORGEL[19] and TANABE and SUGANO[17] and optical absorption measurements by JORGENSEN[8] indicates that the levels next higher than $^4T_1$ are distant by about 5000 cm$^{-1}$. We may therefore estimate $\Delta_m$ to be between 1 and 10 cm$^{-1}$, and expect that this will be the order of the multiplet splittings. It is possible that a doublet level may lie close to $^4T_1$[17] and it could make an important contribution to the shift of the levels.*

We turn now to the behavior of the ground-state. It may easily be shown that the level $^6S$ can couple by spin-orbit interaction only with $^4P$, and will have therefore spin-orbit matrix elements only with states of symmetry $^4T_1$.[19] The dominant interaction will be with the metastable level, since

* This process is mentioned in Ref. 14 (p. 413) and has also been suggested privately by A. D. LIEHR and C. J. BALLHAUSEN.

it lies closest to the ground state by at least a factor of two in energy. We have calculated the matrix elements of $K$ between the ground-state and metastable level and find that each member of the ground sextuplet couples only to a particular member of the excited sextuplet, and that the matrix elements are all identical with the value $b = \sqrt{5}\sigma N\alpha_P$. If $g$ is a member of the ground multiplet and $m$ is the corresponding member of the excited multiplet, we find that $g$ shifts in energy in fourth-order perturbation[20,21,18] by an amount

$$\Delta_g = \frac{|(g|K|m)|^2}{(E_g - E_m)^2} \sum_m \frac{|(m|K|n)|^2}{E_g - E_n} - \frac{|(g|K|m)|^4}{(E_g - E_m)^3}. \quad (10)$$

We may ignore the final term, which will be the same for all members of the multiplet. If we set $D = E_g - E_m$, we then obtain

$$\Delta_g = \left(\frac{b}{D}\right)^2 \sum_n \frac{|(m|K|n)|^2}{E_g - E_n}. \quad (11)$$

Comparing equation (11) with equation (9), the close relation of the ground-state splitting to that of the excited multiplet becomes apparent. Since $D$ enters to the second power, the connection of $^6S$ to other $^4T_1$ levels will have no more than a 20 per cent effect on this relation. The very small ground-state splittings,[16] compared to the estimated value for the excited state, is consistent with equation (11). It is clear that the ground-state and excited sextuplets will be almost certain to have the same sign for the splitting parameter.

*Acknowledgements*—The author would like to acknowledge many helpful discussions with A. D. LIEHR, C. J. BALLHAUSEN, S. GESCHWIND and J. F. DILLON.

## REFERENCES

1. DICKE G. H. and HALL L. A., *J. Chem. Phys.* **27,** 465 (1957).
2. JOHNSON R. P., *J. Opt. Soc. Amer.* **29,** 283, 387 (1939).
3. RANDALL J. T. and WILKINS M. F., *Proc. Roy. Soc.* A**184,** 347 (1945).
4. HERSHBERGER W. D., *J. Chem. Phys.* **24,** 168 (1956).
5. BLEANEY B. and LOW W., *Proc. Phys. Soc.* A**68,** 55 (1955).
6. MANENKOV A. A., PROKHOROV A. M., TRAPEZNIKOVA and FOK M. V., *Optika i Spectroskopiia* **2,** 470 (1957).
7. DEXTER D. L. and SCHULMAN J. H., *J. Chem. Phys.* **22,** 1063 (1954).
8. JORGENSEN C. K. *Acta Chem. Scand.* **8,** 1502 (1954).
9. HROSTOWSKI H. J. Private communication.
10. SCHULMAN J. H., EVANS L. W., GINTHER R. J. and MURATA K. J., *J. Appl. Phys.* **18,** 732 (1947).
11. DILLON J. F., *J. Appl. Phys.* **29,** 539 (1958).
12. ORGEL L. E., *J. Chem. Phys.* **23,** 1958 (1955).
13. SCHULMAN J. H., *J. Appl. Phys.* **17,** 902 (1946).
14. BOTDEN Th.P J. and KRÖGER F. A., *Physica* **14,** 553 (1948).
15. BLEANEY B. and STEVENS K. W. H., *Rep. Progr. Phys.* **16,** 108 (1953).
16. LOW W., *Phys. Rev.* **105,** 792 (1957).
17. TANABE Y. and SUGANO S., *J. Phys. Soc. Japan* **9,** 766 (1954).
18. WATANABE H., *Progr. Theor. Phys., Osaka* **18,** 405 (1957).
19. ORGEL L. E., *J. Chem. Phys.* **23,** 1004 (1955).
20. VAN VLECK J. H. and PEUVEY W. G., *Phil. Mag.* **19,** 961 (1934).
21. PRYCE M. H. L., *Phys. Rev.* **80,** 1107 (1950).

*J. Phys. Chem. Solids* Pergamon Press 1958. Vol. 7. pp. 207–209.

# THE EFFECT OF PRESSURE ON THE ABSORPTION EDGE IN SILVER HALIDES*

**T. E. SLYKHOUSE and H. G. DRICKAMER**

Department of Chemistry and Chemical Engineering, University of Illinois, Urbana, Illinois

(*Received* 1 *May* 1958; *in revised form* 16 *May* 1958)

VOL. 7 1958

**Abstract**—The absorption edge of AgCl, AgBr and AgI has been measured to over 200,000 atmospheres. The behavior of AgCl and AgBr is quite similar with pressure. There is a small red shift in the low pressure (f.c.c.) phase, a transition at 87,000 (83,000) atmospheres, probably to the simple cubic phase, accompanied by a large red shift, and a further small red shift, at higher pressures. The behavior of AgI is quite different. The atmospheric (wurtzite) phase transforms to the f.c.c. at 2900 atmospheres with a large red shift. The f.c.c. shifts red very strongly with pressure to 112,000 atmospheres, where there is a second phase change accompanied by a large blue shift. There is a further small red shift at high pressures.

A peak which appears at 423 m$\mu$ (428 m$\mu$) in AgI at atmospheric pressure has been attributed by SEITZ to a forbidden internal transition in the $Ag^+$ ion, which is permitted by the symmetry of the wurtzite lattice. The peak disappears in the high pressure phase, which is consistent with SEITZ' theory.

THE effect of pressure on the absorption edge of silver halides has been measured to well over 200,000 atmospheres at $25 \pm 1\frac{1}{2}$°C.

The AgCl used was Harshaw single crystal material. The Ag Br was obtained from A. Miller, Department of Physics, University of Illinois. The AgI was from several batches made in this laboratory by J. C. ZAHNER. The equipment and procedure used was that previously described[1,2] with two minor modifications:

(1) In order better to control extrusion, both on the 50,000 atmosphere and 250,000 atmosphere bombs, one piston was given a 30° bevel 0·035 in. wide and a support ring of Solar steel hardened to 58–60 Rockwell C was placed on the bevel.

(2) The higher pressure apparatus was recalibrated and the calibration extended to lower thicknesses of center pellet using the date of reference (1) plus other shifts including AgCl.

The present best calibration is

$$P_c = P_A\left[1+\frac{10{\cdot}8}{P_A^{0{\cdot}14}}\exp(-0{\cdot}174t_c)\right]$$

where

$P_c$ = pressure in center pellet in thousands of atm.
$P_A$ = applied pressure in thousands of atm.
$t_c$ = thickness of the center pellet in thousandths of an inch.

This calibration applies for values of $t_c$ from 10

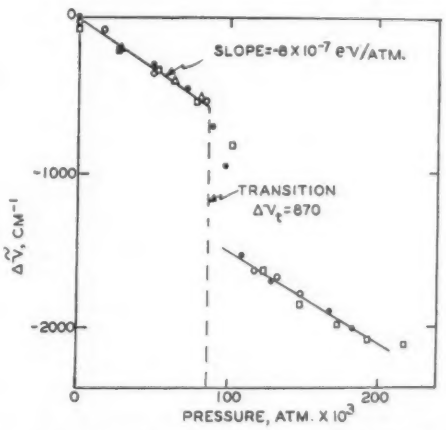


FIG. 1. Shift of silver chloride absorption edge with pressure ($\Delta\tilde{\nu}$ measured from 25,200 cm$^{-1}$).

* This work was supported in part by AEC Contract AT(11-1)-67 Project 5.

to 3 (·010 in–0·003 in). The results for AgCl and AgBr (Figs. 1 and 2) are quite similar. The atmospheric pressure structure is face centered cubic. The shift of the edge with pressure in this phase is quite small. At 87,000 atm for AgCl and 83,000 atm for AgBr there is a phase transition

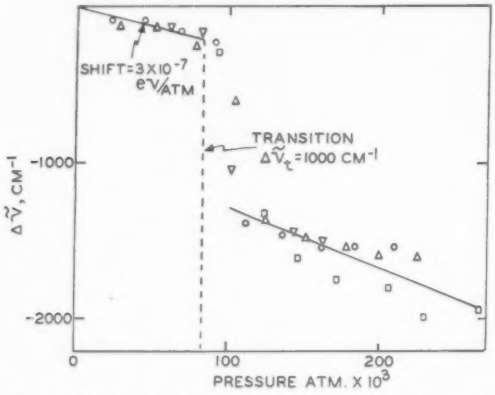


FIG. 2. Shift of silver bromide absorption edge with pressure ($\overline{\Delta\tilde{\nu}}$ measured from 21,980 cm$^{-1}$).

(probably to the simple cubic CsCl structure) accompanied by a large red shift of the order of

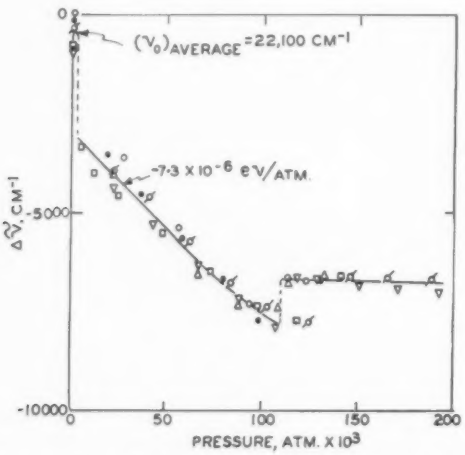


FIG. 3. Shift of silver iodide absorption edge with pressure ($\Delta\tilde{\nu}$ measured from 22,100 cm$^{-1}$).

1000 cm$^{-1}$. Above the transition there is a continuing small red shift.

The behavior of AgI (Fig. 3) is quite different. At room temperature and atmospheric pressure AgI has the wurtzite structure. At 2900 atm it undergoes a transformation to the face centered cubic lattice accompanied by a very large (2760 cm$^{-1}$) red shift in the edge. In the next 100,000 atmosphere the edge shifts to the red 4500 cm$^{-1}$. This is some 10–20 times the shift found for the AgCl and AgBr f.c.c. phases in a similar pressure range. At 112,000 atmospheres there is a second phase transition accompanied by a *blue* shift of 1160 cm$^{-1}$. At higher pressures there is a small red shift with increasing pressure. One would think that the 112,000 atm transition is the f.c.c. → s.c. transition corresponding to similar transitions in AgBr and AgCl discussed above, although the edge shifts blue instead of red. The anomalies in AgI (large red shift for the f.c.c. phase and blue shift at the high pressure transition) are doubtlessly associated with the large size and high polarizability of the iodide ion. At present no completely satisfactory explanation is available. In a previous paper (3) on the spectrum of $Tl^+$ in potassium halides, it was shown that KI gave quite a different effect at the f.c.c. → s.c. phase transition than did KCl or KBr. It would be desirable to study a wide

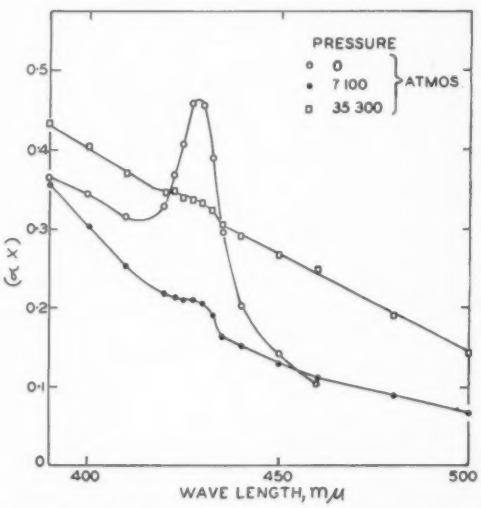


FIG. 4. Effect of pressure on absorption peak of silver iodide.

variety of halides to see how general this difference is.

In the AgI spectrum at one atmosphere there is a peak at 423 mμ (428 mμ) in our apparatus

which SEITZ[4] attributes to an internal transition in silver which is forbidden in the free atom but allowed by lattice symmetry in the wurtzite lattice. By dilution of a sample with NaCl it was possible to study this peak as a function of pressure (Fig. 4). The peak did not shift significantly below the 2900 atm phase transition. Above the transition it

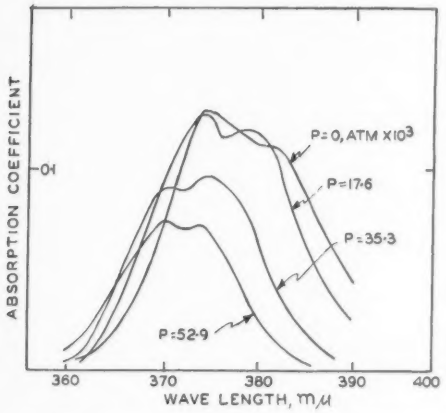


FIG. 5. Shift of absorption peak in cuprous chloride with pressure.

substantially disappeared. These results are entirely consistent with SEITZ' hypothesis. The peak did not reappear above the 110,000 atm phase transition indicating that the high pressure phase is definitely not wurtzite. A similar peak occurs in CuCl and was studied to 50,000 atm (Fig. 5). The shift with pressure was quite small. This is again consistent with SEITZ' theory.

BRIDGMAN[5] has density data for the silver halides to 100,000 atm. When the shifts for AgCl and AgBr were plotted against density the resulting curves showed nothing significant. In Fig. 6 the shift of the edge is plotted vs. density for AgI. At the wurtzite-f.c.c. transition BRIDGMAN finds a discontinuous density increase and our data indicate a discontinuous shift of the edge. When the density is plotted against the shift of the edge, a

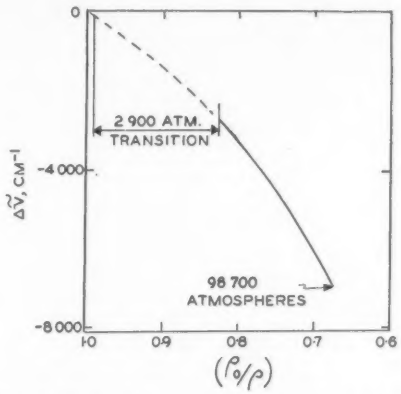


FIG. 6. Shift of silver iodide absorption edge with density to 100,000 atm. ($\Delta\tilde{\nu}$ measured from 22,100 $cm^{-1}$).

continuous curve results. This may be a coincidence, but it may be physically significant.

*Acknowledgements*—The authors wish to thank F. SEITZ and J. BARDEEN for very helpful discussions. T. SLYKHOUSE would like to acknowledge fellowships from the Dow Chemical Company and the Shell Fellowship Committee.

## REFERENCES

1. FITCH R. A., SLYKHOUSE T. E. and DRICKAMER H. G. *J. Opt. Soc. Amer.* **47,** 1015 (1957).
2. PARSONS R. W. and DRICKAMER H. G. *J. Chem. Phys.*—submitted for publication.
3. EPPLER R. A. and DRICKAMER H. G. *J. Phys. Chem. Solids* **6,** 180 (1958).
4. SEITZ F. *Rev. Mod. Phys.* **23,** 328 (1951).
5. BRIDGMAN P. W. *Proc. Amer. Acad. Arts Sci.* **76,** 1 (1945).

*J. Phys. Chem. Solids* Pergamon Press 1958. Vol. 7. pp. 210–213.

# THE EFFECT OF PRESSURE ON THE OPTICAL ABSORPTION EDGE OF GERMANIUM AND SILICON*

**T. E. SLYKHOUSE and H. G. DRICKAMER**

Department of Chemistry and Chemical Engineering, University of Illinois, Urbana, Illinois

(*Received* 26 *May* 1958)

**Abstract**—The shift of the optical absorption edge with pressure has been measured in germanium and silicon to over 100,000 atmospheres. In germanium there is an initial blue shift which reverses at 50,000 atm at $\alpha \cong 20$ cm$^{-1}$ (35,000 atm at $\alpha = 0$). Silicon exhibits a continuous red shift. The data in the low pressure region are consistent with those of other investigators. Evidently the minimum in the conduction band in the $\langle 111 \rangle$ direction shifts to higher energy with increasing pressure, while the minimum in the $\langle 100 \rangle$ direction shifts to lower energies (relative to the valence band). At one atmosphere the minimum in $\langle 111 \rangle$ direction in germanium lies about 0·2 eV above the minimum in the $\langle 100 \rangle$ direction which is consistent with previous estimates.

VOL.
7
1958

ABSORPTION edge measurements have been made on silicon and germanium to over 100,000 atm. pressure. The materials studied were single crystals obtained from Dr. F. Trumbore of Bell Telephone Laboratories. The germanium was *n*-type with resistivity greater than 40 ohm cm. The silicon was *p*-type with a resistivity of 0·08 ohm cm. The apparatus and techniques used have been previously described.[1,2] A Perkin Elmer monochromator with tungsten lamp, quartz or LiF prism, and PbS detector was used. The samples were carefully polished and the reflection correction approached the theoretical as nearly as it could be estimated. The materials are brittle and not particularly strong so that the handling and masking of the very small samples (about 0·005 in. $\times$ 0·005 in. $\times$ 0·050 in. long) was very difficult. There was therefore more scatter in the results than for other more ductile or stronger materials.

The shift with pressure for germanium is shown in Fig. 1 (points and solid curve for $\alpha \cong 20$ cm$^{-1}$). There is an initial blue shift ($8{\cdot}0 \times 10^{-6}$ eV/atm) which compares closely with the results of PAUL and BROOKS[3] ($8{\cdot}9 \times 10^{-6}$ eV/atm). Somewhere near 50,000 atm (at $\alpha = 20$ cm$^{-1}$) the direction of shift reverses and there is a monotonic red shift to the highest pressures studied. The shape of the edge changes somewhat with pressure as can be seen from Fig. 2 where the data are extrapolated to $\alpha = 0$ for one run. The change in slope of the curves represents the beginning of the direct transition. Since this shifts to higher $\alpha$'s with increasing pressure, evidently the gap widens with pressure at $k = 0$. The dotted curve in Fig. 1 represents the shift with pressure extrapolated to $\alpha = 0$ for a number of runs. The initial slope is $5{\cdot}5 \times 10^{-6}$ eV/atm. The reversal takes place at about 35,000 atm which is consistent with the estimates of PAUL and BROOKS.[3]

The results for silicon are shown in Fig. 3 for $2 \cong 25$ cm$^{-1}$. There is a monotonic red shift of the edge at all pressures, the slope being about $-2{\cdot}0 \times 10^{-6}$ eV/atm which is again consistent with the work at Harvard.[3] The edge in germanium is generally attributed to an indirect transition to a minimum of the conduction band in the $\langle 111 \rangle$ direction with symmetry $\Lambda_1$. In silicon the edge probably represents an indirect transition to a minimum in the $\langle 100 \rangle$ direction with symmetry $\Delta_1$. The direct transition at $k = 0$ is to an excited state having the symmetry $\Gamma_2'$. Evidently bands with symmetry states $\Lambda_1$ and $\Gamma_2'$ shift to higher energies with increasing pressure, while the band with symmetry $\Delta_1$ shifts to lower energies. The change in direction of the pressure shift in

* This work was supported in part by AEC Contract AT(11-1)-67 Project 5.

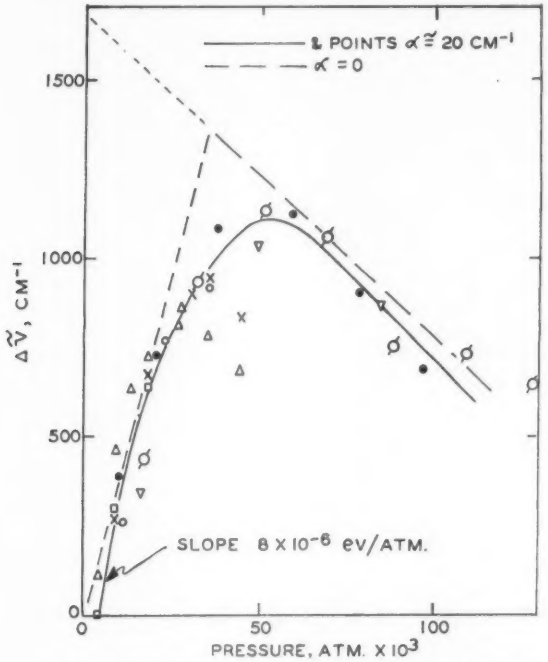


FIG. 1. Shift of germanium absorptions edge with pressure.

germanium at 35,000 atm indicates the point at which the indirect transition in the ⟨100⟩ direction becomes of lower energy than the one in the ⟨111⟩ direction. Fig. 4 is a plot of $E$ vs. $k$ as developed by HERMAN[5] and indicates the shifts of various bands with pressure. If the red shift at high pressures in germanium is extrapolated to atmospheric pressure (Fig. 1) it is seen that at one atmosphere the minimum in the ⟨100⟩ direction is about 1600 cm$^{-1}$ (0·2 eV) above the minimum in

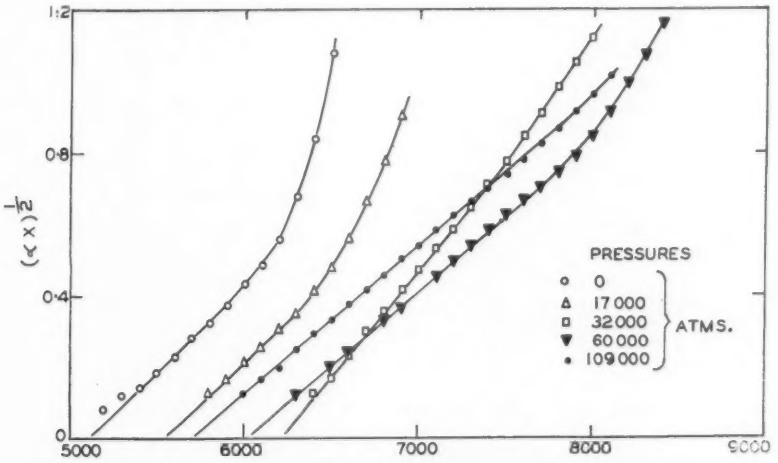


FIG. 2. Extrapolation of a germanium run to $\alpha = 0$.

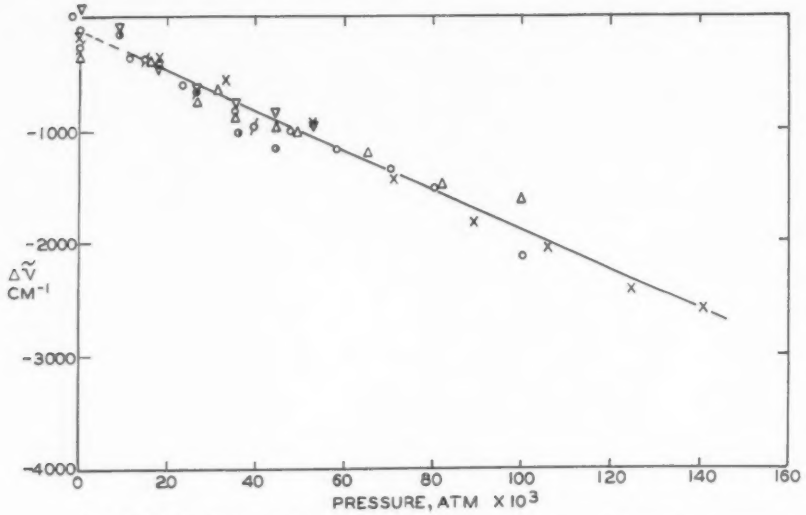


FIG. 3. Shift of silicon absorption edge with pressure ($\alpha = 25$ cm$^{-1}$, $\Delta\tilde{\nu}$ measured from 10,000 cm$^{-1}$).

the $\langle 111 \rangle$ direction. This is consistent with the estimate of HERMAN[5] and of BARDEEN, BLATT and HALL.[6]

The effect of pressure and the difference between silicon and germanium can also be illustrated on a plot if $E$ vs. $d$ (interatomic distance). Fig. 5 represents such a plot as calculated for diamond by KIMBALL[7] who calculated levels arising from the $s$ and $p$ bands of the atoms. If one considers also the effect of $d$ levels, another band will

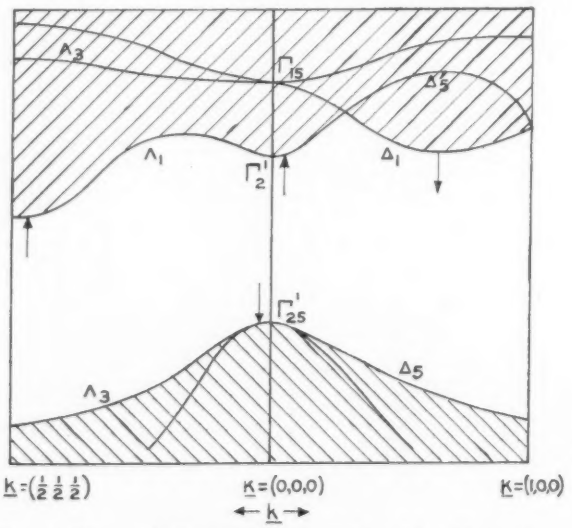


FIG. 4. $E(k)$ vs. $k$ diagram for germanium (after Herman). Arrows indicate probable direction of shift with increasing pressure.

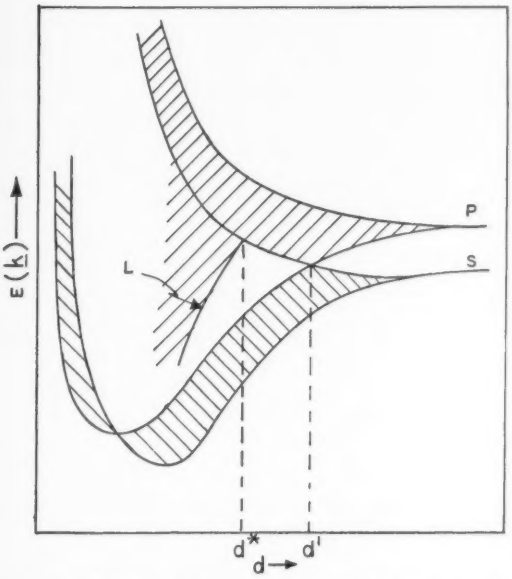


FIG. 5. General $E(K)$ vs. $d$ diagram for the diamond lattice.

come in approximately as shown. Whether a red or a blue shift will be obtained with compression will depend on whether the equilibrium interatomic distance ($d$) is greater than or less than $d^*$. Evidently $d$ is just greater than $d^*$ for germanium at one atmosphere and less than $d^*$ for silicon. One would anticipate a red shift with increasing pressure for diamond.

*Acknowledgements*—The authors wish to acknowledge the very helpful discussions with F. SEITZ and J. BARDEEN. T. E. SLYKHOUSE would like to acknowledge fellowship support from the Dow Chemical Co. and from the Shell Fellowship Committee.

## REFERENCES

1. FITCH R. A., SLYKHOUSE T. E. and DRICKAMER H. G. *J. Opt. Soc. Amer.* **47,** 1015 (1957).
2. SLYKHOUSE T. E. and DRICKAMER H. G. *J. Phys. Chem. Solids* **7,** 207 (1958).
3. PAUL W. and BROOKS H. *Phys. Rev.* **94,** 1128 (1954).
4. PAUL W. (Private communication).
5. HERMAN F. *Phys. Rev.* **95,** 847 (1954).
6. BARDEEN J., BLATT F. J. and HALL L. H. Photoconductivity Conference. Wiley and Sons, New York (1956).
7. KIMBALL G. E. *J. Chem. Phys.* **3,** 560 (1935).

*J. Phys. Chem. Solids* Pergamon Press 1958. Vol. 7. pp. 214–217.

# THE INSTABILITY OF SOME DIHALIDES OF COPPER AND SILVER

**D. F. C. MORRIS**

Department of Chemistry, Brunel College of Technology, London, W.3

(*Received* 23 *January* 1958)

**Abstract**—The instability of crystalline dihalides $CuI_2$, $AgCl_2$, $AgBr_2$, and $AgI_2$ is considered in the light of ionization potentials and polarizabilities. The standard free energies of formation of the dihalides have been estimated, and it is shown that the non-existence of the solid compounds at 25°C is in agreement with thermodynamic data.

VOL
7
195

## INTRODUCTION

ELSEWHERE,[1,2] the differences in the bond character and structure of simple inorganic crystalline compounds have been discussed in relation to ionization potentials. The treatment used has assumed that a hypothetical stage occurs in the formation of crystals of inorganic compounds, which involves interaction of the constituents as ions, whatever the nature of the chemical bonding in the resulting compound.

When ions are brought closely together to form a crystal, the attraction of the cations for the electron clouds of the anions and the simultaneous repulsion of the nuclei of the anions tend to lead to deformation or polarization of the anions. The cations may be similarly polarized, but usually to a much lesser extent.

The result of slight ion polarization is a decrease of polar character, although the ions may maintain their original quantum configurations (e.g. see RITTNER[3]). If the polarization is more extensive, electron sharing occurs, the bonding in the crystal assumes a covalent character, and the constituents no longer possess their original quantum configurations. In extreme cases, polarization of the anions may be so great that complete transfer of an electron from anion to cation may be expected, with the result that the crystal is unstable.

Ion polarization is favoured by a number of factors. In the case of crystals regarded as formed through the interaction of cations of the same formal charge and similar (crystal) radius with a common anion, the ionization potentials $I$ (first ionization potential for univalent cations, second for divalent cations, &c.) may be employed as a relative measure of the polarizing power of cations for anions.[4,5] According to the ionic-interaction approach to crystal formation therefore, instability due to electron transfer from the electronegative to the electropositive constituent is most likely to occur in cases where $I$ is very high and the polarizability of the anion is considerable. This may be illustrated by considering the instability of halides of elements which form medium-sized divalent cations (radii $r = 0{\cdot}64$–$0{\cdot}90$ Å).

## INSTABILITY OF SOME COPPER (II) AND SILVER (II) HALIDES

Table 1 shows medium-sized divalent cations arranged in order of increasing second ionization potential of the corresponding atoms, together with their crystal radii. The polarizabilities of halide ions are listed in Table 2.

The divalent cations where $I$ is extreme are $Cu^{2+}$ and $Ag^{2+}$; instability due to electron transfer from anion to cation is most to be expected, therefore, in the case of halides of copper (II) and silver (II), especially when the electronegative constituent as an anion is very polarizable. It is well known that cupric iodide is unstable, and attempts to prepare this compound yield cuprous iodide and iodine. This case of instability has been discussed by FAJANS.[12] According to the ionic-interaction

*Table* 1. *Medium-sized divalent cations* ($r = 0{\cdot}6$–$0{\cdot}9$ Å): *ionization potentials and crystal radii*

| | $Mg^{2+}$ | $Mn^{2+}$ | $Fe^{2+}$ | $Co^{2+}$ | $Zn^{2+}$ | $Ni^{2+}$ | $Pt^{2+}$ | $Pd^{2+}$ | $Cu^{2+}$ | $Ag^{2+}$ |
|---|---|---|---|---|---|---|---|---|---|---|
| $I$*(eV) | 15·03 | 15·64 | 16·18 | 17·05 | 17·96 | 18·15 | 18·54 | 19·42 | 20·29 | 21·48 |
| $r$†(Å) | 0·64 | 0·80 | 0·74 | 0·72 | 0·69 | 0·69 | 0·80 | 0·80 | 0·70 | 0·89 |

$I$ increases ——————→

* Ionization potentials are from FINKELNBURG and HUMBACH.[6]

† Ionic radii are from AHRENS[7] as modified, with additions, after PAULING[8] and AHRENS.[9]

*Table* 2. *Electronic polarizabilities* ($\alpha$) *of halide ions* (*values in* Å$^3$)

| | $F^-$ | $Cl^-$ | $Br^-$ | $I^-$ |
|---|---|---|---|---|
| FAJANS and JOOS[10] | 0·98 | 3·53 | 4·97 | 7·55 |
| PAULING[11] | 1·04 | 3·66 | 4·77 | 7·10 |

approach to compound formation, since $Cu^{2+}$ has a very high $I$ value and $I^-$ has a large polarizability, the instability may be represented in terms of an electron-transfer change:

$$Cu^{2+} + 2I^- = \underbrace{Cu^+ + I^-} + I.$$

Moreover, since $I$ corresponding to $Cu^+$ is considerable for a univalent cation, the resulting cuprous iodide is essentially covalent in character.

The fact that compounds such as

$$[Cu\ en_2]\ I_2.\quad 1 \text{ or } 2H_2O^*$$

are stable[13] may be correlated with the screening of the electrostatic field of $Cu^{2+}$ by co-ordinating groups.

In the case of silver (II) halides, since the ionization potential corresponding to $Ag^{2+}$ is even greater than for $Cu^{2+}$, from the ionic-interaction standpoint instability may be expected for compounds where the anionic constituent is less polarizable than iodide. This is in agreement with the non-existence of argentic chloride, bromide, and iodide. The fluoride $AgF_2$ is the only stable simple argentic halide, and complete electron transfer does not occur in this case, owing to the small polarizability of the fluoride ion. Fluoride ions, however, are likely to be considerably polarized by argentic ions in crystal formation, and argentic fluoride does not possess the properties of an essentially ionic compound.†

* en is used to represent an ethylene diamine bidentate co-ordinating group.

*Thermodynamic considerations*

The criterion of stability of dihalides $MX_2$ in relation to decomposition to monohalides MX is that the free energy of formation of $MX_2$ does not exceed that of MX.

The standard molar free energies of formation of hypothetical solid compounds such as $CuI_2$, $AgCl_2$, $AgBr_2$, and $AgI_2$ at 25°C can be estimated. The standard free energy of formation of a compound $MX_2$ at 25°C is related to the standard enthalpy of formation $\Delta H^0$ and the standard entropies $S^0$, by the expression

$$\Delta F^0(MX_2) = \Delta H^0(MX_2) - 298{\cdot}16\ [S^0(MX_2) - S^0(M) - S^0(X_2)]; \qquad (1)$$

all the quantities refer to substances in their standard states. A knowledge of the requisite heat content and entropy data will therefore permit the evaluation of the standard free energy of formation of the compound.

The standard enthalpy of formation $\Delta H^0(MX_2)$ may be derived by making use of the expression

$$\Delta H^0(MX_2, c) = \Delta H^0(M^{2+}, g) + 2\Delta H^0(X^-, g) - U, \qquad (2)$$

where $U$ is the lattice energy (enthalpy) of $MX_2$.

† It may be noted from the considerations of this section that the diastatides of copper and silver may be expected to be chemically unstable.

For solid compounds $CuI_2$, $AgCl_2$, $AgBr_2$, and $AgI_2$, all the data necessary for the calculation of $\Delta H^0(MX_2,c)$ from equation (2) are available,[14,15] except for values of lattice energy. KAPUSTINSKII[16] has derived various expressions for the calculation of the lattice energies of ionic compounds of which the lattice constants are unknown; but, as the experimental lattice energies of transition-metal dihalides often differ considerably from theoretical values calculated assuming ionic character,[17] the use of such expressions does not appear to be suitable in the present case. A satisfactory estimate of the lattice energies of hypothetical copper and silver dihalides may be made, however, by use of a procedure due to KARAPET'YANTS.[18] This worker has shown that various linear relationships exist between the experimental lattice energies of dihalides. Thus from graphs of the types shown in Figs. 1 and 2, unknown lattice energies may be determined by interpolation.

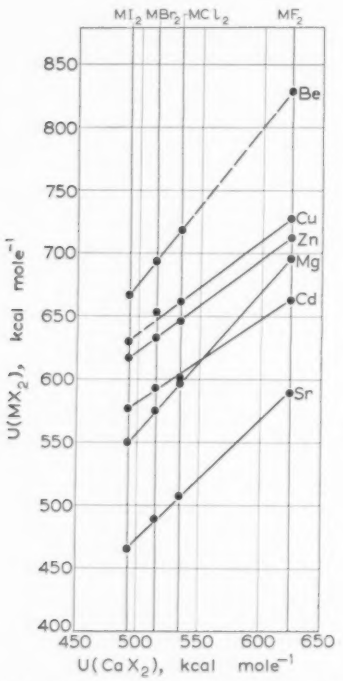


FIG. 1. Experimental lattice energies of dihalides plotted against lattice energies of calcium dihalides.

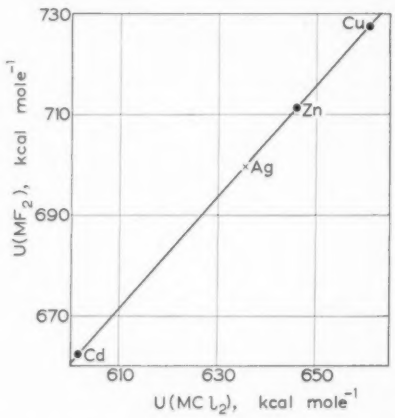


FIG. 2. Lattice energies of difluorides plotted against lattice energies of corresponding dichlorides.

Values of estimated lattice energies and heats of formation $\Delta H^0(MX_2, c)$, together with other relevant data, are quoted in Table 3. The value for the heat of formation of cupric iodide differs only slightly from the value (−1·7 kcal/mole) calculated by ROSSINI *et al.*[14]

In order to derive the standard free energies from equation (1), it remains necessary to know the requisite standard entropies. Where experimental

*Table 3. Estimated standard heats of formation of solid dihalides*

Data are enthalpies in kcal/mole (298°K)

| Compound | $\Delta H^0(M^{2+}, g)$ | $\Delta H^0(X^-, g)$ | $U$ | $\Delta H^0(MX_2, c)$ |
|---|---|---|---|---|
| $CuI_2$ | 730·1 | −49·1 | 630 | 2 |
| $AgCl_2$ | 740·7 | −59·2 | 636 | −13 |
| $AgBr_2$ | 740·7 | −54·9 | 624 | 7 |
| $AgI_2$ | 740·7 | −49·1 | 607 | 36 |

standard entropies are not available in the literature,[14] values have been estimated by the method of LATIMER.[19] The estimated standard entropies and standard free energies of formation are shown in Table 4.

*Table 4. Estimated standard molar entropies and standard free energies of formation*

Data refer to 298°K

| Compound | $S^0(MX_2, c)$ (E.U.) | $\Delta F^0(MX_2, c)$ (kcal/mole) |
|---|---|---|
| $CuI_2$ | 38·0 | 1 |
| $AgCl_2$ | 29·0 | −3 |
| $AgBr_2$ | 34·6 | 11 |
| $AgI_2$ | 40·0 | 36 |

*Table 5. Standard free-energy changes for the decomposition of dihalides of copper and silver to monohalide and halogen**

Data refer to 298°K

| | $\Delta F^0$(kcal) |
|---|---|
| $CuF_2(c) = CuF(c) + \frac{1}{2}F_2(g)$ | 60 |
| $CuCl_2(c) = CuCl(c) + \frac{1}{2}Cl_2(g)$ | 11 |
| $CuBr_2(c) = CuBr(c) + \frac{1}{2}Br_2(l)$ | 6 |
| $CuI_2(c) = CuI(c) + \frac{1}{2}I_2(c)$ | −18 |
| $AgF_2(c) = AgF(c) + \frac{1}{2}F_2(g)$ | 33 |
| $AgCl_2(c) = AgCl(c) + \frac{1}{2}Cl_2(g)$ | −23 |
| $AgBr_2(c) = AgBr(c) + \frac{1}{2}Br_2(l)$ | −34 |
| $AgI_2(c) = AgI(c) + \frac{1}{2}I_2(c)$ | −52 |

* Free energies of formation from ROSSINI *et al.*[14] have been used in computing the $\Delta F^0$ magnitudes. Where only the heat of formation of a compound is quoted in that compilation, the free energy of formation has been derived by using entropy values estimated by the method of LATIMER.[19] The value used for $\Delta F^0$ $CuF_2$ (*c*) has been taken from GLASSNER.[20]

In Table 5 are shown the standard free-energy changes $\Delta F^0$ for decomposition reactions of copper and silver dihalides. The thermodynamic data correspond with the fact that, of the copper and silver dihalides listed, solid $CuI_2$, $AgCl_2$, $AgBr_2$ and $AgI_2$ are unstable with respect to decomposition to monohalide at 25°C.

## REFERENCES


1. MORRIS D. F. C. and AHRENS L. H. *J. Inorg. Nucl. Chem.* **3,** 263 (1956).
2. AHRENS L. H. and MORRIS D. F. C. *J. Inorg. Nucl. Chem.* **3,** 270 (1956).
3. RITTNER E. S. *J. Chem. Phys.* **19,** 1030 (1951).
4. FAJANS K. *Z. Krist.* **66,** 347 (1928).
5. AHRENS L. H. *Geochim. Cosochim. Acta* **3,** 1 (1953).
6. FINKELNBURG W. and HUMBACH W. *Naturwiss.* **42,** 35 (1955).
7. AHRENS L. H. Unpublished data (1955).
8. PAULING L. *The Nature of the Chemical Bond* 2nd Edn. Cornell University Press (1940).
9. AHRENS L. H. *Geochim. Cosmochim. Acta* **2,** 155 (1952).
10. FAJANS K. and JOOS G. *Z. Phys.* **23,** 388 (1924).
11. PAULING L. *Proc. Roy. Soc.* **A114,** 191 (1927).
12. FAJANS K. *Ceramic Age* **54,** 288 (1949); mimeographed sheet, University of Michigan.
13. MORGAN G. T. and BURSTALL F. H. *J. Chem. Soc.* 2018, 2027 (1926); 1259 (1927).
14. ROSSINI F. D., WAGMAN D. D., EVANS W. H., LEVINE S. and JAFFE I. *Selected Values of Chemical Thermodynamic Properties.* Circular of National Bureau of Standards No. 500 (1952).
15. PRITCHARD H. O. *Chem. Rev.* **52,** 529 (1953).
16. KAPUSTINSKII A. F. *Quart. Rev.* **10,** 283 (1956).
17. MORRIS D. F. C. *J. Inorg. Nucl. Chem.* **4,** 8 (1957).
18. KARAPET'YANTS M. K. *Zh. Fiz. Khim.* **28,** 1136 (1954).
19. LATIMER W. M. *J. Amer. Chem. Soc.* **73,** 1480 (1951).
20. GLASSNER A. *Argonne Nat. Lab. Rep.* ANL-5107 (1953).


VOL. 7 1958

*J. Phys. Chem. Solids* Pergamon Press 1958. Vol. 7. pp. 218–227.

# AUTODIFFUSION DES IONS DANS LES HALOGENURES ALCALINS POLYCRISTALLINS

**J. F. LAURENT et J. BÉNARD**

Laboratoire de Chimie Minérale B, 11, rue Pierre Curie, Paris, France.

(*Received* 9 *May*, 1958)

**Resumé**—L'étude de l'autodiffusion des ions dans les halogénures alcalins polycristallins constitués de grains de différentes grosseurs a été réalisée en fonction de la température. Dans tous les cas, l'énergie d'activation d'autodiffusion des ions est la même, que la migration s'effectue dans des monocristaux ou dans des polycristaux. Dans tous les composés, à l'exclusion des sels de césium, la vitesse de diffusion du cation est la même, que l'on opère sur des mono-ou des polycristaux; par contre, celle de l'anion s'accroit et cet accroissement est d'autant plus important que la dimension moyenne des cristaux constituant les agrégats polycristallins est plus petite. Cependant, dans le cas des sels de césium, la vitesse de diffusion du cation est également influencée par la présence des surfaces intercristallines. Il est possible de relier cet accroissement de vitesse de diffusion à la polarisation des ions. Plus l'ion est polarisé, plus l'influence des surfaces intercristallines est importante et ceci quelle que soit la polarité de l'ion diffusant. Une étude autoradiographique confirme ces résultats.

**Abstract**—A study of self-diffusion of ions in polycrystalline alkali halides of different particle size has been made as a function of temperature. In every case, the activation energy for self-diffusion of the ions is the same whether migration takes place in single crystals or polycrystals. For all compounds, with the exception of the salts of cesium, the speed of diffusion of the cation is the same for single or polycrystals. By contrast, the migration rate of the anions increases as the mean dimensions of the crystals comprising the polycrystalline agregates become smaller. However, in the case of the cesium salts the speed of diffusion of the cation is equally influenced by the presence of intercrystalline boundaries. It is possible to connect this increase in the speed of diffusion with the polarization of the ions. The more the ion is polarized, the greater the influence of the intercrystalline surfaces, irrespective of the polarity of the diffusion ion. An autoradiographic study confirms these conclusions.

De nombreuses recherches ont déjà été effectuées en vue de comparer la vitesse d'autodiffusion dans les métaux monocristallins et polycristallins. Ces études sont d'une importance fondamentale pour la connaissance précise de la structure du joint des cristaux constituant les solides. Il ne semble pas, cependant, que des recherches de ce genre aient été entreprises sur des composés ioniques. C'est pourquoi, nous nous sommes proposés d'examiner dans quelle mesure les résultats que nous avions obtenus et publiés récemment dans ce journal[1] sur l'autodiffusion des ions dans les halogénures alcalins monocristallins pourraient se trouver modifiés pour les expériences concernant les échantillons polycristallins. La présente étude a porté comme la précédente sur deux séries d'halogénures alcalins: halogénures de potassium: KF, KCl, KBr, KI; chlorures alcalins: NaCl, KCl CsCl et aussi sur le fluorure de césium CsF. Dans chaque cas, on a étudié l'autodiffusion de l'anion et celle du cation dans des échantillons polycristallins constitués de cristaux de différentes dimensions, et comparé les résultats ainsi obtenus à ceux relatifs aux échantillons monocristallins.

## PARTIE 1

### 1 RAPPEL DE LA METHODE EXPERIMENTALE

La méthode expérimentale employée a été décrite en détail dans notre précédent article.[1] On utilise les isotopes radioactifs correspondant aux différents ions diffusants. Les coefficients

d'autodiffusion à une température donnée et dans un composé donné sont obtenus en calculant la pente de la droite représentant la fonction : log $A = f(x^2)$, $A$ étant la radioactivité de l'élément diffusant à une distance $x$ de l'interface origine. Cette formule est en effet toujours valable ici, car comme nous le verrons par la suite, on ne peut faire intervenir les équations de FISHER[2] et WHIPPLE.[3]

Les échantillons polycristallins ont été préparés à partir de produits («Merck pour analyse») à l'exclusion du chlorure de césium de haute pureté qui nous a été fourni par Monsieur le Professeur Hackspill, Membre de l'Institut de France à qui nous adressons nos vifs remerciements, et du fluorure de césium préparé au laboratoire à partir du chlorure.

Les échantillons sont préparés par frittage de poudres des différents halogénures; les expériences ont été effectuées en général sur quatre grosseurs de cristaux dépendant de la préparation de la poudre de départ :

(a) *Grains très fins*. Précipitation du sel par un refroidissement rapide de la solution aqueuse saturée chaude.

(b) *Grains fins*. Broyage au mortier d'agate des cristaux d'origine.

(c et d) *Grains moyens et gros grains*. Clivage des monocristaux.

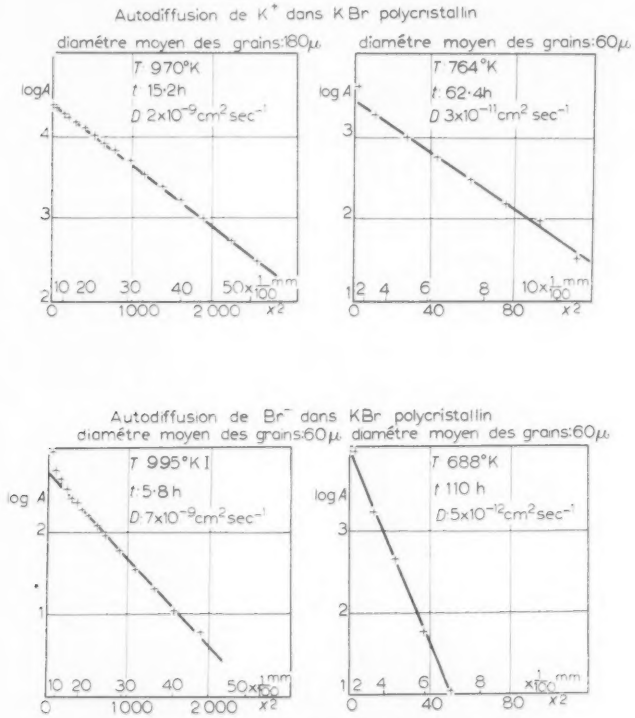


FIG. 1. Exemples de courbes de pénétration par autodiffusion des ions dans le bromure de potassium polycristallin.

Pour ces deux dernières catégories, les monocristaux de départ sont préparés au laboratoire, soit par fusion et refroidissement lent des différents halogénures, soit par clivage direct des blocs monocristallins employés dans notre précédente étude.[1]

Dans chaque cas, la poudre est séchée à 150°–200°C et comprimée dans des moules en acier spécial à haute résistance de façon à obtenir des pastilles cylindriques de 5 mm de hauteur et 1,5

cm² de section. Pour chaque halogénure, on a déterminé la pression de compression minimum qui permet d'obtenir des agrégats de densité maximum[1] et pour chaque composé des pressions supérieures de 4000 à 5000 Kg/cm² à cette pression minimum ont été employées. Les pastilles polycristallines sont ensuite chauffées pendant une centaine d'heures à 20°–30°C au—dessous de la température de fusion de chaque composé, avec montée et baisse de température très lentes. Les pastilles frittées sont ensuite polies comme les monocristaux.[1]

*Détermination de la dimension moyenne des cristaux*

Après frittage, les échantillons sont légèrement polis de façon à éliminer la couche supérieure qui pourrait donner des indications erronnées sur la dimension des cristaux. Le contour des grains est révélé en frottant très légèrement la pastille sur une peau de chamois humide. L'examen au microscope s'effectue avec un oculaire gradué, le diamètre moyen des grains est obtenu en effectuant la moyenne d'une trentaine de mesures. Dans le cas du fluorure de césium qui est très hygroscopique, il n'est pas possible de déterminer la dimension moyenne des cristaux, ce composé s'hydratant très rapidement à l'air.

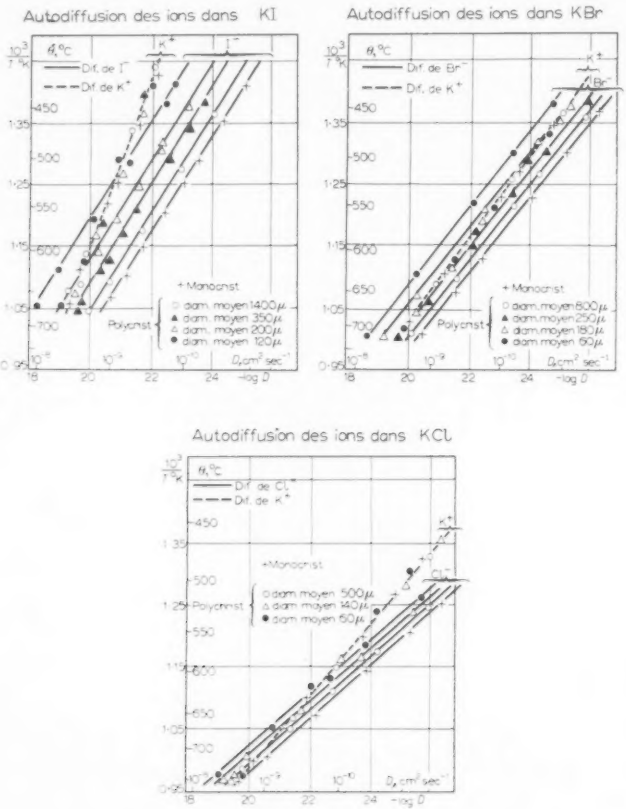


FIG. 2.

## 2 CALCUL DU COEFFICIENT DE DIFFUSION

Les courbes log $A = f(x^2)$ permettent de calculer le coefficient de diffusion. La Fig. 1 donne quelques exemples de courbes relatives à l'autodiffusion des ions dans le bromure de potassium polycristallin. Les deux courbes supérieures

sont relatives à l'autodiffusion de l'ion potassium et les deux courbes inférieures à celles de l'ion bromure. Dans chaque cas, et dans toutes les expériences que nous avons effectuées, les points expérimentaux permettent toujours de définir parfaitement la droite représentant la fonction log $A = f(x^2)$ et de calculer ainsi le coefficient de diffusion correspondant. Ces courbes ne présentent aucune anomalie spéciale même pour les valeurs de $x$ importantes et ceci quelle que soit la

Sur les Fig. 2 et 3 on a représenté l'ensemble de nos résultats expérimentaux. Sur chaque graphique, nous avons aussi indiqué les résultats obtenus dans des échantillons monocristallins. Dans le cas du fluorure de potassium et de césium, nous n'avons pu effectuer la mesure de la vitesse de migration de l'ion fluorure par suite de l'inexistence d'un isotope de cet élément de période suffisamment longue. Seuls les résultats relatifs à la structure cubique à faces centrées du chlorure de césium

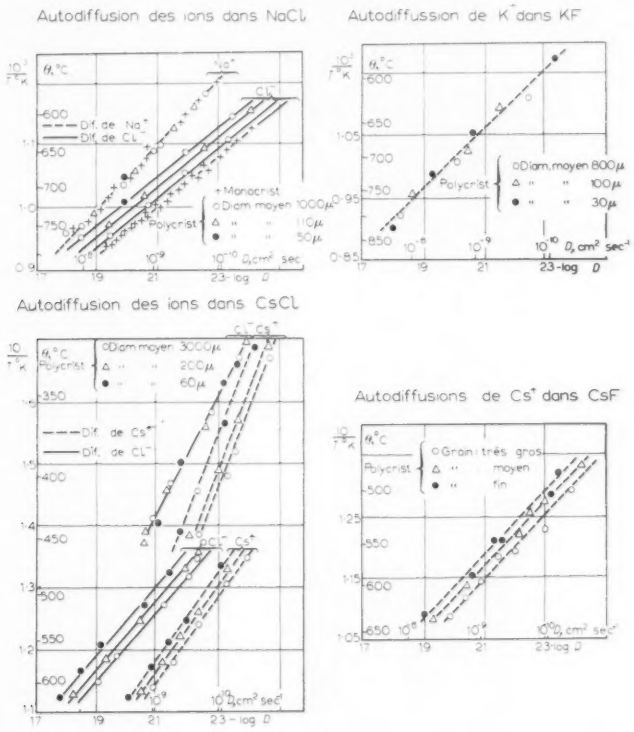


FIG. 3.

grosseur des cristaux constituant les agrégats polycristallins. D'après ces résultats, on voit que les équations de FISHER[2] et de WHIPPLE[3] ne sont pas applicables dans notre cas.

### 3 CALCUL DE L'ENERGIE D'ACTIVATION

Connaissant les coefficients d'autodiffusion des différents ions en fonction de la température et pour différents échantillons, il est facile de déterminer les énergies d'activation correspondantes en calculant la pente des courbes Log $D = f(1/T°\mathrm{K})$.

seront pris en considération, cette structure étant analogue à celle des autres composés étudiés.

### PARTIE 2

L'examen des Fig. 2 et 3 dans lesquelles sont rassemblés tous les résultats expérimentaux permet de faire les observations suivantes :

(1) Dans le domaine de température étudié et pour tous les ions, *les énergies d'activation d'autodiffusion sont les mêmes que l'on opère en mono- ou en polycristaux*. En effet pour un ion donné

et dans un composé donné, les courbes Log $D = f(1/T)$ sont parallèles ou confondues quelle que soit la grosseur des cristaux constituant l'échantillon étudié. Ce résultat indique que le mécanisme de diffusion est certainement le même dans les cristaux uniques et dans les zones intercristallines. Il en résulte que toutes les conséquences relatives aux énergies d'activation que nous avions déduites de notre première étude[1] sont également valables dans le cas des polycristaux; nous ne redonnerons pas le tableau des énergies d'activation, qui serait identique à celui de la précédente étude. Nous indiquerons uniquement la valeur de l'énergie d'activation d'autodiffusion de l'ion césium dans le fluorure de césium qui n'avait pas été déterminée précédemment :

$$Q^{Cs^+}_{CsF} = 38{,}5 \pm 2{,}5 \text{ Kcal/ion.}$$

(2) La présence des surfaces intercristallines se manifeste uniquement par un accroissement du terme de fréquence $D_0$. *Donc dans un composé donné, l'accroissement de la vitesse d'autodiffusion d'un ion pour une grosseur de grain donnée est indépendant de la température.*

(3) *Dans le domaine de température envisagé et dans tous les composés studiés, à l'exclusion des sels de césium, seule la vitesse de diffusion de l'anion est accrue par la présence des surfaces intercristallines; celle du cation reste la même que l'on opère en mono- ou en polycristaux.* Dans le cas du chlorure et du fluorure de césium, la vitesse de diffusion du cation est, elle aussi, augmentée par la présence de surfaces intercristallines, peu il est vrai, par rapport aux autres cas, mais suffisamment cependant pour montrer que *ce phénomène n'est pas une propriété spécifique des anions.*

(4) Dans tous les halogénures, à l'exception de ceux de césium, la vitesse de diffusion du cation reste constante et celle de l'anion s'accroit lorsque la diffusion a lieu dans des agrégats constitués par des cristaux de plus en plus petits. Il en résulte qu'à une certaine température, *le coefficient d'autodiffusion de l'anion peut égaler celui du cation et même le dépasser pour des grains suffisamment petits.* En examinant les diagrammes des Fig. 2 et 3, on peut repérer la température minimum ($\theta$°C min.) au-dessus de laquelle la vitesse de diffusion de l'anion est plus grande que celle du cation. Dans le Tableau 1 sont indiquées les valeurs de $\theta$°C min. correspondant aux échantillons constitués par les cristaux les plus petits que nous ayons étudiés.

*Tableau* 1

| Halogénure | NaCl 50$\mu$ | KCl 60$\mu$ | KBr 60$\mu$ | KI 120$\mu$ |
|---|---|---|---|---|
| $\theta$°C min. | / | 640°C | <400°C | 510°C |

Pour le chlorure de sodium, l'ion sodium diffuse toujours plus vite que l'ion chlorure, même dans des agrégats constitués de grains de 50 $\mu$. Par contre, dans le domaine de température étudié, l'ion bromure diffuse toujours plus vite que l'ion potassium dans des agrégats de bromure de potassium formés de grains de 60 $\mu$. Dans le chlorure et l'iodure de potassium, l'ordre des vitesses d'autodiffusion des deux ions peut être inversé suivant que l'on considère la migration dans un monocristal ou dans un échantillon polycristallin. *Ces résultats infirment nettement l'idée souvent émise, selon laquelle les cations diffuseraient toujours plus vite que les anions.* C'est pourquoi, dans l'interprétation des phénomènes de frittage des poudres de composés ioniques notamment, il semble qu'il faille tenir compte pour une large part de la diffusion des ions dans les régions voisines des joints intercristallins.[4]

Pour un ion donné, et dans un composé donné, les courbes Log $D = f(1/T)$ relatives à différentes grosseurs de grains étant parallèles entre elles, il en résulte que l'accroissement de la vitesse de diffusion pour une grosseur de grain donnée est, par rapport au monocristal, indépendante de la température. On peut donc définir *un coefficient d'accroissement* $D_a$ correspondant à une grosseur de grains donnée. Il est ainsi possible de dresser le Tableau 2.

Dans le cas du chlorure de césium, seules les valeurs relatives à la structure cubique à faces centrées ont été prises en considération. On suppose de plus, dans le cas de KF, CsF et CsCl, que la vitesse de diffusion des ions dans des polycristaux dont les grains mesurent 2 à 3 mm est la même que dans un monocristal.

Si l'on cherche à exprimer l'accroissement de la vitesse de diffusion, non plus en fonction du diamètre moyen des grains, mais en fonction de

VOL. 7 1958

*Tableau* 2

| Halogénure | Diam. moyen des grains en microns | $D_a$ | |
|---|---|---|---|
| | | cation | anion |
| KF | 800 | 1 | / |
| | 100 | 1 | |
| | 30 | 1 | |
| KCl | 500 | 1 | 1,1 |
| | 140 | 1 | 1,5 |
| | 60 | 1 | 2,2 |
| KBr | 800 | 1 | 1,3 |
| | 250 | 1 | 2 |
| | 180 | 1 | 2,7 |
| | 60 | 1 | 5 |
| KI | 1400 | 1 | 1,5 |
| | 350 | 1 | 3 |
| | 200 | 1 | 5 |
| | 120 | 1 | 8,5 |
| NaCl | 1000 | 1 | 1,2 |
| | 110 | 1 | 1,8 |
| | 50 | 1 | 3 |
| CsCl | 200 | 1,1 | 1,25 |
| | 60 | 1,4 | 1,7 |
| CsF | moyen | 1,5 | / |
| | fin | 2,5 | |

l'étendue des surfaces intercristallines, qui apparait comme la seule variable significative, on obtient le faisceau de droites de la Fig. 4. Sur ce graphique, on a représenté le coefficient d'accroissement $D_a$ en fonction de la surface totales des cristaux contenus dans 1 cm³ de l'agrégat polycristallin; cette surface est proportionnelle à $1/d$, $d$ étant le diamètre moyen des grains. Toutes les droites convergent au même point : $D_a = 1$; $S = 0$, qui correspond au monocristal. L'examen de la Fig. 4 montre que dans le domaine de dimension de grain étudié, *l'augmentation de la vitesse de diffusion est proportionnelle à la surface totale de ceux-ci.*

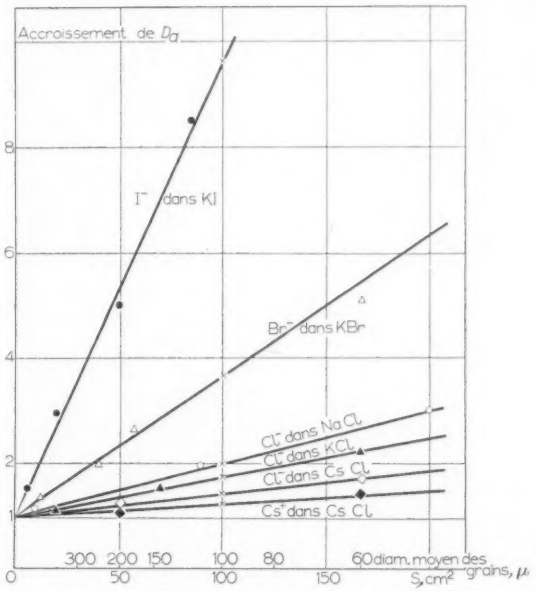


FIG. 4. Accroissement du coefficient d'autodiffusion des ions dans les différents composés, par suite de l'existence de surfaces intercristallines, en fonction de la surface de celles-ci.

Afin de comparer les différents halogénures entre eux, on a repéré sur cette figure, les valeurs du coefficient d'accroissement $D_a$ correspondant à des grains de 100 microns. Ces valeurs sont groupées dans le Tableau 3.

L'examen de ce tableau montre que l'influence de la limite des cristaux sur la vitesse d'autodiffusion des ions dans les agrégats polycristallins varie beaucoup d'un composé à l'autre.

*Tableau* 3

| Halogénures | KI | | KBr | | KCl | | KF | | NaCl | | CsCl | | CsF |
|---|---|---|---|---|---|---|---|---|---|---|---|---|---|
| | $K^+$ | $I^-$ | $K^+$ | $Br^-$ | $K^+$ | $Cl^+$ | $K^+$ | $F^-$ | $Na^+$ | $Cl^-$ | $Cs^+$ | $Cl^-$ | $Cs^+$ |
| $D_a$ | 1 | 9,5 | 1 | 3,7 | 1 | 1,65 | 1 | / | 1 | 2 | 1,3 | 1,45 | 1,5<br>1,7 |

## PARTIE 3

L'ensemble des résultats précédents fait apparaitre, dans la plupart des cas, une différence essentielle de comportement des anions et des cations à l'égard de l'autodiffusion intercristalline, différence qui n'avait jamais été signalée jusqu'ici, à notre connaissance. Nous avons pensé, qu'il serait intéressant de chercher *à établir une relation entre ces observations et les phénomènes de polarisation ionique* qui prennent une importance particulière dans le comportement des ions superficiels, par suite du caractère disymétrique des forces auxquelles ils sont soumis. Des tentatives analogues ont en effet été faites récemment avec succès par différents auteurs et en particulier par WEYL[5] pour expliquer certains phénomènes spécifiques des surfaces. Nous envisagerons donc l'étude de nos résultats expérimentaux en fonction de la possibilité de déformation des ions constituant les différents halogénures étudiés. Il faut noter que dans un halogénure alcalin donné, un ion est d'autant plus polarisé que sa polarisabilité propre et que le pouvoir polarisant de l'ion antagoniste sont plus grands. Nous examinerons tout d'abord les halogénures de potassium, puis les chlorures alcalins et enfin les halogénures de césium.

### 1 ETUDE DES HALOGENURES DE POTASSIUM

Cette étude a porté sur le fluorure, le chlorure, le bromure et l'iodure de potassium. Dans cette série, la vitesse d'autodiffusion du cation commun $K^+$ qui est très peu polarisable, est la même dans des échantillons mono-et polycristallins. Par contre, celle des différents anions ($Cl^-$, $Br^-$, $I^-$) s'accroit lorsque l'on passe du monocristal à des agrégats polycristallins constitués de grains de plus en plus petits. Il est intéressant de rappeler que cet accroissement de la vitesse de diffusion n'entraine aucune variation notable de l'énergie d'activation d'autodiffusion. L'examen du Tableau 3, où sont rassemblées les différentes valeurs de l'accroissement du coefficient d'autodiffusion des ions lorsque l'on passe du monocristal à des agrégats constitués par des grains de 100 microns, montre que cet accroissement est plus important pour l'iodure que pour le bromure et le chlorure. On peut remarquer qu'il suit les variations de polarisabilité des anions dont les valeurs sont groupées dans le Tableau 4.

*Tableau* 4

| Halogénure | KF | KCl | KBr | KI |
|---|---|---|---|---|
| Polarisabilité de l'anion[6] | 0,99 | 3,05 | 4,17 | 6,28 |
| $D_a$ | / | 1,65 | 3,7 | 9,5 |

Dans cette série, la variation de la possibilité de déformation des anions dépend uniquement des différences de polarisabilité, le pouvoir polarisant du cation restant le même. Aussi, on a représenté sur un diagramme (Fig. 5) les variations de l'augmentation du coefficient d'autodiffusion des différents anions (voir tableau 3) en fonction de la polarisabilité de ces ions. L'examen de cette figure montre que *l'accroissement de la vitesse de*

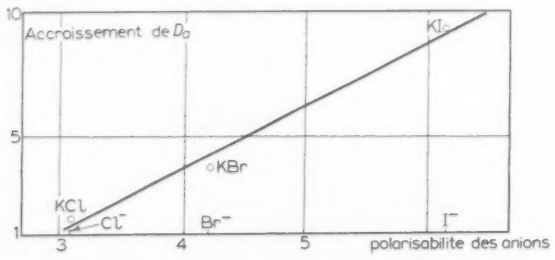


FIG. 5. Variation de l'accroissement du coefficient d'autodiffusion des anions dans les halogénures de potassium polycristallins en fonction de la polarisabilité de ces anions.

*diffusion dû aux surfaces intercristallines est proportionnel à la polarisabilité de l'anion considéré.*

Dans le cas du fluorure de potassium, où la polarisabilité de l'ion fluorure est très petite, il est fort probable que les surfaces intercristallines sont sans influence sur la migration de cet anion; d'ailleurs la valeur de sa polarisabilité ne figure pas sur le graphique, car elle est repoussée bien à gauche sur l'abcisse.

## 2 ETUDE DES CHLORURES ALCALINS

Cette étude a porté sur le chlorure de sodium, le chlorure de potassium et le chlorure de césium. Ici encore, on ne considèrera que la structure cubique à faces centrées du chlorure de césium. Dans cette série, la vitesse d'autodiffusion du cation $Na^+$ dans NaCl et du cation $K^+$ dans KCl est la même dans des mono- ou dans des polycristaux.

*Tableau* 5

| Halogénure | NaCl | KCl | RbCl | CsCl |
|---|---|---|---|---|
| Pouvoir polarisant du cation[7] | 1,04 | 0,57 | 0,45 | 0,37 |
| $D_a$ | 2,0 | 1,65 | / | 1,45 |

Dans cette série, la variation de la possibilité de déformation de l'anion commun $Cl^-$ qui voit sa vitesse de migration s'accroitre par suite de la présence des surfaces intercristallines, dépend uniquement du pouvoir polarisant des différents cations. On a donc représenté sur un graphique (Fig. 6) les variations de l'augmentation de l'accroissement de la vitesse de diffusion de l'anion

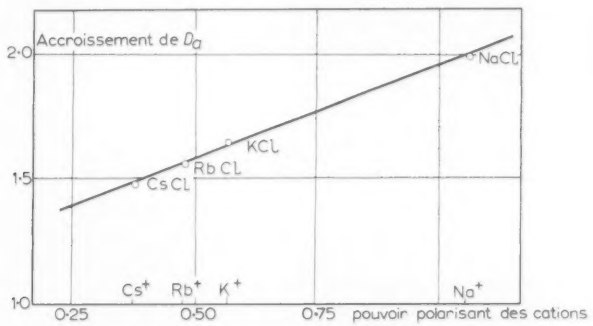


FIG. 6. Variation de l'accroissement du coefficient d'autodiffusion des anions dans les chlorures alcalins polycristallins en fonction du pouvoir polarisant du cation antagoniste.

Par contre, celle de l'anion commun $Cl^-$ et du cation $Cs^+$ s'accroit dans CsCl lorsque l'on passe du monocristal à des agrégats constitués de grains de plus en plus petits. On peut rappeler toutefois que ces accroissements n'entrainent aucune variation notable de l'énergie d'activation d'autodiffusion. L'examen du Tableau 3 montre que l'accroissement de la vitesse d'autodiffusion de l'anion commun $Cl^-$, dû aux surfaces intercristallines, s'accroit lorsqu'on passe du chlorure de césium au chlorure de potassium et au chlorure de sodium. Cet accroissement suit les variations du pouvoir polarisant des différents cations, dont les valeurs sont rassemblées dans les Tableau 5.

dû aux surfaces intercristallines (Tableau 3) en fonction du pouvoir polarisant du cation antagoniste.

L'examen de cette figure montre que *l'accroissement de la vitesse d'autodiffusion de l'anion dû aux surfaces intercristallines est proportionnel au pouvoir polarisant des différents cations antagonistes.*

D'après ce graphique, on peut présumer que le coefficient d'autodiffusion de l'ion chlorure dans le chlorure de rubidium polycristallin est peu différent de celui obtenu dans un monocristal; ainsi dans un échantillon constitué de grains de 100 microns, l'accroissement de ce coefficient doit être de l'ordre de 1,55.

## 3 ETUDE DES HALOGENURES DE CESIUM

Cette étude a porté uniquement sur le chlorure et le fluorure de césium, les autres halogénures ayant une structure cristalline différente des composés précédemment étudiés. Dans cette série, la vitesse d'autodiffusion du cation césium s'accroit lorsque la dimension des grains constituant les agrégats polycristallins dans lesquels ils diffusent, diminue. Cet accroissement n'entraine toutefois aucune variation notable de l'énergie d'activation d'autodiffusion.

L'influence des surfaces intercristallines sur la vitesse d'autodiffusion de l'ion césium dans le fluorure et le chlorure de césium suit aussi les variations du pouvoir polarisant de l'anion : Tableau 6.

*Tableau* 6

| Halogénure | CsCl | CsF |
|---|---|---|
| Pouvoir polarisant de l'anion(7) | 0,30 | 0,57 |
| $D_a$ | 1,30 | 1,5 à 1,7 |

* * *

L'étude des halogénures de potassium et du chlorure de sodium pourrait nous porter à croire que seule la vitesse de diffusion des anions est accrue par la présence de surfaces intercristallines, celle des cations étant indépendante du milieu de diffusion. L'étude des halogénures de césium montre qu'en réalité l'influence des surfaces intercristallines sur la vitesse d'autodiffusion des ions n'est pas une propriété exclusive des anions. *Le facteur essentiel parait être l'aptitude de l'ion à se déformer dans les champs de forces asymétriques qui règnent à la limite des domaines cristallins.* Quelques exemples montrent en particulier qu'à polarisabilité égale et placés dans des conditions équivalentes, les cations ont la même sensibilité aux surfaces intercristallines que les anions.

## 4 COMPARAISONS

### (1) *Chlorure de potassium et fluorure de césium*

L'ion potassium et l'ion fluorure ont des pouvoirs polarisants égaux (0,57); ils possèdent respectivement comme partenaire dans ces deux composés, l'ion chlorure et l'ion césium dont les polarisabilités sont voisines (3,05 pour $Cl^-$ et 2,79 pour $Cs^+$). Ces derniers se trouvent donc placés dans des conditions de polarisation presque équivalentes et il est à prévoir que, de ce fait, leur sensibilité à l'égard des surfaces intercristallines seront voisines, ce que nos expériences vérifient. ($D_a$ pour $Cl^-$ dans KCl : 1,65; $D_a$ pour $Cs^+$ dans CsF : 1,5à 1,7).

### (2) *Chlorure de césium*

Cet halogénure est particulièrement intéressant, car les deux ions qui le constituent ont des polarisabilités voisines et suffisamment élevées pour qu'ils soient sensibles tous deux à l'influence des surfaces intercristallines. Cette sensibilité sera donc d'autant plus importante que le pouvoir polarisant de l'ion antagoniste à l'ion considéré sera plus grand. L'ion césium a un pouvoir polarisant de 0,37 et l'ion chlorure de 0,30, en conséquence l'influence des surfaces intercristallines doit être plus forte pour l'ion chlorure que pour l'ion césium; nos expériences le vérifient parfaitement. ($D_a$ pour $Cs^+$ dans CsCl : 1,30; $D_a$ pour $Cl^-$ dans CsCl : 1,45).

## ETUDE AUTORADIOGRAPHIQUE

Afin de rendre tangible cette diffusion intercristalline, dont l'ensemble de nos expériences nous a amené à admettre l'existence, nous avons suivi par autoradiographie les progrès de l'autodiffusion dans des agrégats polycristallins. Les mesures ont eu lieu sur la diffusion de l'ion iodure dans des échantillons d'iodure de potassium polycristallins dont les grains avaient environ 1 mm de côté. Bien que les essais aient eu lieu à différentes températures, nous ne présenterons qu'une étude relative à une température de diffusion intermédiaire : 580°C. La préparation des échantillons est identique à celle déjà décrite; on opère avec deux pastilles, dont l'une sert à tracer la courbe de pénétration de l'ion radioactif, et l'autre est utilisée pour les autoradiographies.

Le diagramme supérieur de la Fig. 7 représente la variation de l'activité des différentes tranches en fonction de la profondeur de pénétration. Le diagramme inférieur représente la courbe log $A = f(x^2)$, qui permet le calcul du coefficient de diffusion. Le temps de diffusion a été de 82 h, la température de 580°C, le coefficient de diffusion est de

VOL. 7 1958

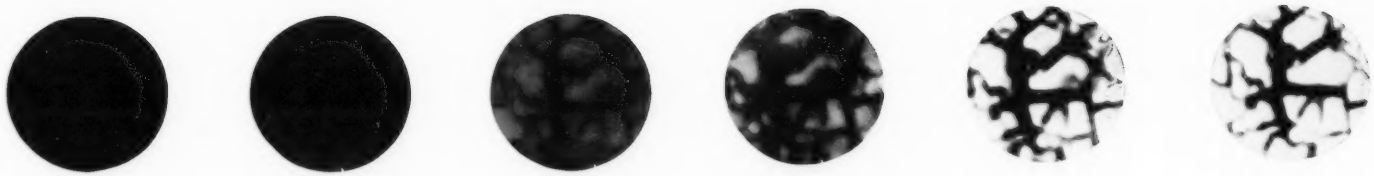

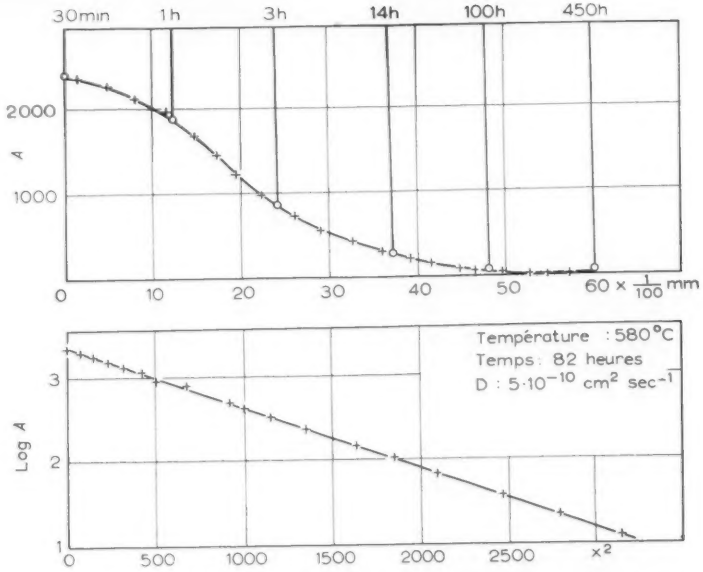


FIG. 7. Autoradiographies montrant l'influence des surfaces intercristallines sur l'autodiffusion de l'ion odure dans l'iodure de potassium polycristallin.

[Facing p. 226

VOL
7
195

$5.10^{-10}cm^2sec^{-1}$. Il faut noter qu'une expérience effectuée à la même température sur un monocristal donne un coefficient de diffusion légèrement inférieur soit: $3,5.10^{-10}cm^2sec^{-1}$. Les autoradiographies représentées en haut des graphiques sont agrandies 1,3 fois environ; elles ont été faites sur du film Kodak, «Kodaline». Les différents temps de pose indiqués sur le diagramme du haut ont été calculés de façon qu'un nombre égal de particules impressionne le film dans chacun des différents essais. Le temps de pose de la première autoradiographie a été déterminé par tâtonnement de façon à obtenir un noir franc sur le négatif. Les autres valeurs du temps de pose sont calculées en prenant cette première valeur comme référence et en considérant l'activité qui reste dans l'échantillon après chaque découpage de 12/100 mm. La radioactivité restante est égale à $\int_{x_1}^{x\infty} y dx$, $y$ étant la fonction $A = f(x)$ qui représente l'activité de l'ion diffusant en fonction de la profondeur de pénétration et $x_1$ la distance de l'interface origine au plan où va être effectuée l'autoradiographie. Cette intégrale n'étant pas calculable, on détermine l'aire comprise sous la courbe $A = f(x)$ entre les plans $x_1$ et $x$, $x$ correspondant à la dernière valeur de $A$ mesurable (cette courbe est déjà déterminée par un autre échantillon traité dans les mêmes conditions). On a ainsi *trés approximativement* le temps de pose correspondant.

Les deux premières autoradiographies ne permettent pas de distinguer la présence des surfaces intercristallines, mais à mesure que l'on pénètre dans le solide, les joints des grains se révèlent de plus en plus et dans le dernier cliché ils apparaissent seuls; aucun noircissement n'est décelable au centre des cristaux. Il faut remarquer que la «quantité» de noircissement devant rester la même sur toutes les autoradiographies, les joints apparaissent très noirs. Cet exemple montre que, comme nous l'avions prévu, la diffusion de l'ion iodure est grandement influencée par la présence de surfaces intercristallines.

Des études identiques ont été effectuées sur la diffusion de l'ion potassium $K^+$ radioactif; dans ce cas, les images autoradiographiques sont toutes les mêmes, quelle que soit la profondeur de pénétration, le film est uniformément noirci. Les joints des grains ne se révèlent absolument pas et n'ont par conséquent aucune influence sur la vitesse de diffusion. Ce dernier résultat est parfaitement en accord avec les mesures des coefficients d'autodiffusion de l'ion potassium, qui d'après nos expériences antérieures ne sont nullement influencées par la présence de surfaces intercristallines.

## CONCLUSION

L'ensemble de ces résultats montre qu'il existe une relation simple entre la possibilité de déformation des ions (anions ou cations) et leur sensibilité aux surfaces intercristallines lors de leur diffusion. Plus l'ion est polarisé, c'est à dire plus sa polarisabilité propre est grande et plus le pouvoir polarisant de l'ion antagoniste est élevé, plus l'influence des surfaces intercristallines est importante lors de sa migration dans des agrégats polycristallins. Il semble donc, que toutes tentatives d'explication théorique de ces phénomènes devra s'effectuer en prenant pour base les propriétés de polarisation des ions.

Cette étude montre de plus que l'énergie d'activation du processus d'autodiffusion des ions dans les halogénures alcalins mono- et polycristallins étant la même, le mécanisme de migration des ions dans les zônes marginales des cristaux et dans la masse même de ceux-ci doit être de même nature.

## BIBLIOGRAPHIE


1. Laurent J. F. et Bénard J., *J. Phys. Chem. Solids* **3**, 112, 7 (1957).
2. Fischer J. C., *J. Appl. Phys.* **22**, 74 (1951).
3. Whipple R. T. P., *Phil. Mag.* **45**, 1225 (1954).
4. Laurent J. F. *Trans. Farad. Soc.* **23**, 165 (1957).
5. Weyl, W. A. *A New Approach to Surface Chemistry and to Heterogeneous Catalysis*. The Pennsylvania State College (1951).
6. Born M. et Heisenberg W. *Z. Phys.* **23**, 388 (1924).
7. Goldschmidt V. *Naturwiss.* **14**, 477 (1926).


VOL. 7 1958

*J. Phys. Chem. Solids* Pergamon Press 1958. Vol. 7. pp. 228–235.

# PREPARATION AND ELECTRICAL PROPERTIES OF MERCURY TELLURIDE*

T. C. HARMAN, M. J. LOGAN and H. L. GOERING

Battelle Memorial Institute

(*Received* 14 *May* 1958)

**Abstract**—Mercury telluride has been prepared by direct reaction of mercury vapor with liquid tellurium. The compound was zone melted and annealed in mercury vapor under various pressures of mercury. It was found that the composition near stoichiometry could be altered by the anneal. Hall coefficient and resistivity were measured as a function of temperature. Analysis of the results gave 0·02 eV for the energy gap at 0°K and a hole to electron mobility ratio of 0·01. The Hall mobility was 17,000 cm²/Vsec at 300°K and 25,000 cm²/Vsec at 143°K.

VOL
7
195

## INTRODUCTION

FOR the past several years, there has been considerable interest in semiconducting compounds. In this paper, results of studies on the preparation and electrical properties of mercury telluride are given. The electrical properties were markedly changed by annealing in mercury vapor. The preparation, zone melting, annealing, and electrical properties of HgTe are described.

## PREPARATION OF MERCURY TELLURIDE

Mercury with an estimated purity of 99·99+ per cent and tellurium which had been sublimed twice in a stream of hydrogen at approximately 800°C were used to prepare the compound. The purification technique for tellurium has been described previously.[1] The elements were placed in a Vycor boat (1·9 cm × 20 cm) and sealed in an evacuated quartz tube (2·2 cm × 56 cm).

The compound was prepared by the two-zone-furnace technique which provided a uniform high-temperature zone for melting and casting the ingot, and a low-temperature zone, which could be varied independently of the other zone, for controlling the vapor pressure of mercury in the system. The material was maintained at the melting point (~ 670°C) for a period of 4 hr or longer; the vapor pressure of mercury was maintained at about 15 atm. In cooling the system, the mercury vapor pressure was always kept equal to or greater than the upper limit of the dissociation pressure of the compound. The upper limit of this pressure at temperatures below the melting point was assumed to be half the vapor pressure of pure mercury at the same temperature.

Under a mercury vapor pressure of about 15 atmospheres, the melting point of the compound was established to be 670±5°C, which is the value quoted in the literature.[2]

## ZONE MELTING OF MERCURY TELLURIDE

The early zone-melting experiments were carried out under 5 and 10 atm of mercury and resulted in extremely polycrystalline HgTe. From zone-melting work with other compounds, it is known that extremely polycrystalline material usually results if the ambient pressure of the volatile constituent is maintained considerably below the dissociation pressure of the compound. (The dissociation pressure may be thought of as the vapor pressure of the volatile constituent in equilibrium with the compound at a specific temperature.) Additional experiments were carried out under a mercury pressure of 15 atm. It was found that if the ingot temperature is too low, the carefully crystallized solid melts because of alloying, and the subsequent rapid nondirectional freeze results in extremely polycrystalline material. This

* This research was supported by Engineer Research and Development Laboratory, Fort Belvoir, under Contract No. DA-44-009-Eng-3199.

alloying phenomena was also observed in annealing experiments. It is concluded that to zone melt HgTe successfully, there must be three carefully controlled temperature zones which have the following limitations. One temperature zone, $T_1$, is for the molten zone (see Fig. 2) which is, of course, at the melting point of the compound. A second zone, $T_2$, is for the solidified ingot and cannot be too high in temperature or too low in temperature. A temperature appreciably higher than the allowable range for $T_2$ would prevent formation of a sufficient temperature gradient for recrystallization, while a temperature appreciably lower would favor alloying and consequent melting of the compound. The third temperature zone, $T_3$, controls the mercury pressure. It can be neither too high in temperature because of the possibility of alloying, nor too low in temperature because of resulting loss of mercury from the liquid zone due to dissociation of the compound. After several experiments, it was found that satisfactory conditions for zone melting HgTe are achieved with the ingot temperature at 620°C (approximately 50°C below the melting point of the compound) and the temperature controlling the mercury pressure at about 560°C, corresponding to a mercury pressure of approximately 15 atm. As shown in Fig. 1, the zone-melting apparatus for HgTe is similar to the

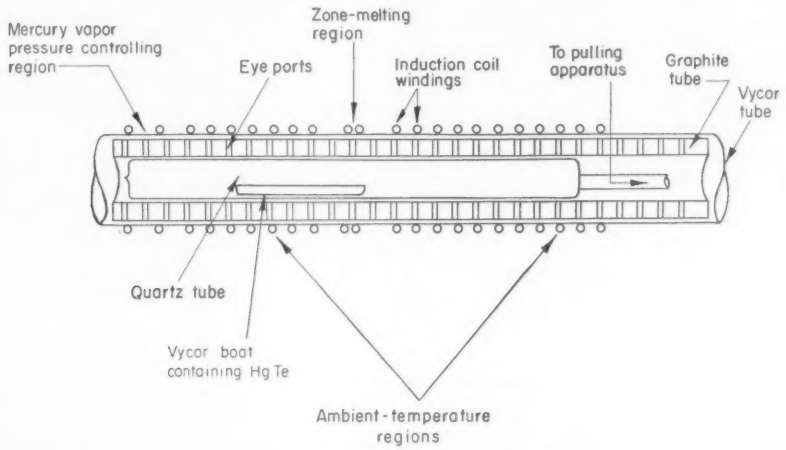


FIG. 1. Apparatus for zone melting.

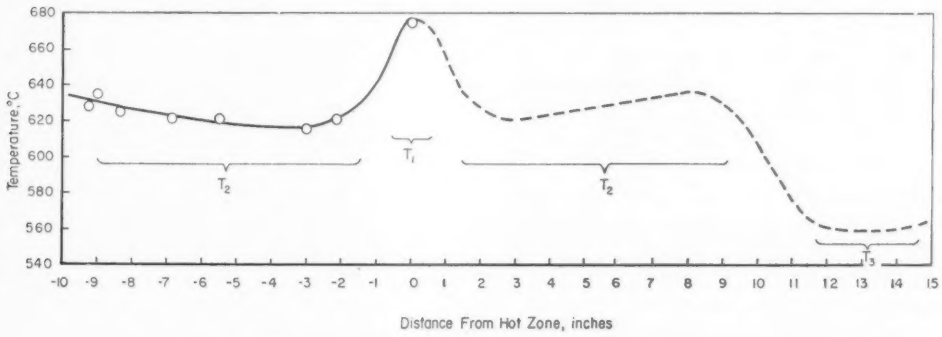


FIG. 2. Temperature distribution along graphite tube used for zone melting HgTe.

one described in reference (1). However, the number of eye ports was increased to allow visual observation of the entire tube. Thus, alloying and condensation of mercury could be observed directly. The temperature distribution along the graphite tube in Fig. 1 is shown in Fig. 2.

The temperature minima in zones $T_2$ and $T_3$ must not deviate more than 10°C from the values shown in Fig. 2. Zone-melt passes at a recrystallization velocity of 1·2 cm/hr were carried out. Specimens removed from the ingots for annealing experiments and investigation of electrical properties possessed several crystallites and were believed to be of sufficient quality to obtain accurate information on energy gap and mobilities of the compound. It is concluded that nearly single-crystal specimens of HgTe can be cut from ingots of HgTe zone melted under the temperature conditions shown in Fig. 2 and at recrystallization rates of about 1·0 cm/hr. The effectiveness of removing foreign impurities from HgTe by the zone-melt technique has been discussed by BLACK *et al.*[3]

## ANNEALING OF HgTe IN MERCURY VAPOR

Studies[4] on CdTe have shown that annealing the compound in cadmium vapor at pressures above the dissociation pressure of the compound results in *n*-type CdTe, while annealing the compound in cadmium vapor at pressures below the dissociation pressure of the compound results in *p*-type CdTe. It was anticipated that the same techniques could be used for altering the composition near stoichiometry of HgTe.

Specimens (12 mm×4 mm×2 mm) were removed from the zone-melted ingot and annealed at 630°C under various pressures of mercury for 10 days. Two furnaces were used, one of which controlled the mercury pressure and the other of which provided the annealing temperature of the sample. Initially, specimens were quenched in water from the annealing temperature. However, it was observed that blisters appeared on the surface and small holes extended throughout the bulk of quenched specimens. One possible explanation of these observations is that weakly bonded mercury in the specimen explodes out of the specimen as a result of the severe pressure change occurring at the specimen surface upon quenching. This hypothesis was shown to be correct by subsequent experiments. The specimens of HgTe were cooled slowly from temperature under the condition that the vapor pressure of mercury over the specimen be equal to half the vapor pressure of mercury at the specimen temperature. With these cooling conditions, annealed specimens do not possess surface blisters or small pores.

As shown in the next section, the samples annealed under a pressure of 10 atmospheres of mercury were *p*-type. As the mercury pressure was increased to 15·5 atm, extrinsic hole density decreased. The results show quite conclusively that the composition near stoichiometry of HgTe can be controlled by annealing in mercury vapor.

## ELECTRICAL PROPERTIES OF MERCURY TELLURIDE

The Hall coefficient as a function of temperature of an unannealed, zone-melted specimen and three annealed specimens is shown in Fig. 3. From the measured Hall coefficient in the extrinsic region, $R_{ext}$, and the Hall maximum, $R_{max}$, on Specimen 5F, the average actual hole to electron mobility ratio, $b$, was determined to be 0·01 using the equation, $R_{max}/R_{ext} = (1-b)^2/4b$. Using this mobility ratio and the conditions that $n_e = n_h b$ at the Hall maximum and $n_e = n_h b^2$ at the Hall null, where $n_e$ and $n_h$ are the electron and hole concentrations, respectively, an energy gap of approximately 0·01 eV is calculated. However, the assumption that the actual electron mobility is always one hundred times greater than the actual hole mobility between the temperature of the Hall crossover, 75°K, and the temperature of the Hall maximum, 250°K, could be in considerable error. Hence, the validity of this method for determining the energy gap of HgTe is uncertain.

In Fig. 4, the resistivity as a function of temperature is given for several specimens of HgTe. Specimens 3A and 5C, which were *n*-type over the measured temperature range, have considerably lower resistivities than the *p*-type Specimens 5E and 5F. The behavior is consistent with the low value of the hole-to-electron mobility ratio. From the data on resistivity as a function of temperature for *p*-type Specimen 5F, a value for the energy gap, $\Delta E$, of 0·08 eV was obtained by use of the equation $1/\rho = Ae^{-\Delta E/2kT}$. This value is identical to that given in early Russian literature.[2] However, since the electron mobility does

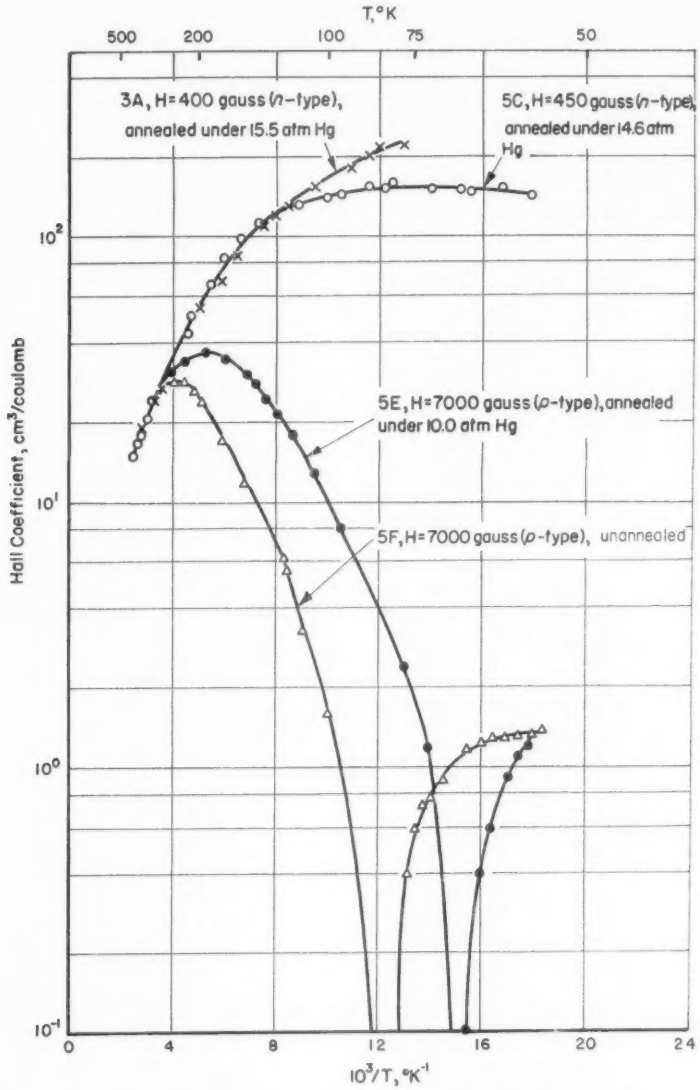


FIG. 3. Hall coefficient as a function of reciprocal temperature for two $n$-type and two $p$-type specimens of HgTe.

not vary as $T^{-3/2}$ in the measured temperature interval, the above equation leads to an erroneous energy gap value.

In Fig. 5, the Hall mobility as a function of temperature is shown for the four specimens of HgTe. It is seen that the mobility varies as $T^{-\alpha}$ from 350°K to 55°K where $\alpha \leqslant 1$. Also, the electron mobility is quite high. A value of 17,000 cm²/Vsec at room temperature and a value of 25,000 cm²/Vsec at 143°K were obtained for the $n$-type specimens. The ratio of $R/\rho$ for the $p$-type specimen, 5F, decreases as the temperature decreases due to hole as well as electron conduction playing a role. For the $n$-type specimens above

200°K, the ratio of $R/\rho$ represents the electron mobility because, although the number of holes and electrons are equal, the hole conductivity is negligible compared to the electron conductivity due to the small value of $b$. It also follows that since $b$ is small, the density of intrinsic carriers, $n_i$, is given by $n_i = 1/R_i e$ and since $n_i/T^{3/2} = Be^{-\Delta E/2kT}$, a plot of $\ln 1/R_i T^{3/2}$ vs. $1/T$ should be linear and yield an accurate value of the energy gap.

Fig. 6 shows $1/R_i T^{3/2}$ vs. $10^3/T°K$ for the semiconductor appears to explain qualitatively the dependence of Hall coefficient on magnetic field from the highest temperature at which measurements were carried out to a temperature of about 140°K. The variation of Hall coefficient with magnetic field at lower temperatures is not understood.

Fig. 8 shows the Hall coefficient as a function of temperature for two $p$-type specimens of HgTe. At the Hall maximum for specimen 5F, it is seen

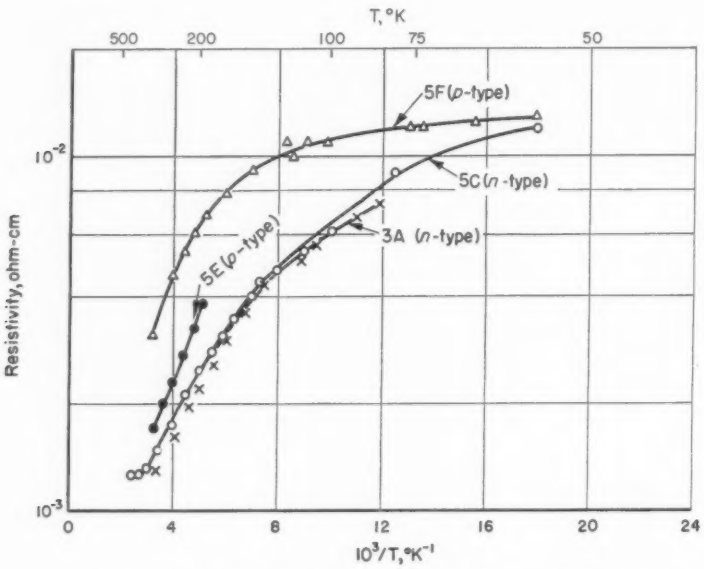


FIG. 4. Resistivity as a function of reciprocal temperature for two $n$-type and two $p$-type specimens of HgTe.

specimens 3A and 5C. From the straight line portion of the curve, an energy gap of 0·02 eV was calculated. This value is in good agreement with the value of 0·025 eV given by TSIDILKOVSKII.[5] The work of CARLSON[6] and BLACK *et al.*[3] also yields an energy gap of 0·025 eV. The deviation from the straight line below 200°K is believed to be due to the onset of extrinsic conduction while the deviation above room temperature is indicative of degeneracy.

Fig. 7 shows the Hall coefficient as a function of temperature for specimens 3A and 5C measured at magnetic fields of approximately 400 gauss and 7000 gauss. The two-band model of an intrinsic that the Hall coefficient increases from 28 cm³/coulomb at 7000 gauss to 32 cm³/coulomb as the magnetic field is decreased to 400 gauss. Also, from the figure it is seen that the temperature of the Hall crossover increases as the magnetic field is increased. This behavior is analogous to that found in $p$-type InSb[7] but opposite to that observed in $p$-type germanium.[8] The InSb data is consistent with results due to contributions from one high-mobility electron and one or more holes of lower mobility, while the explanation of the germanium behavior[8] requires a high-mobility hole, an intermediate-mobility electron and a low-mobility hole.

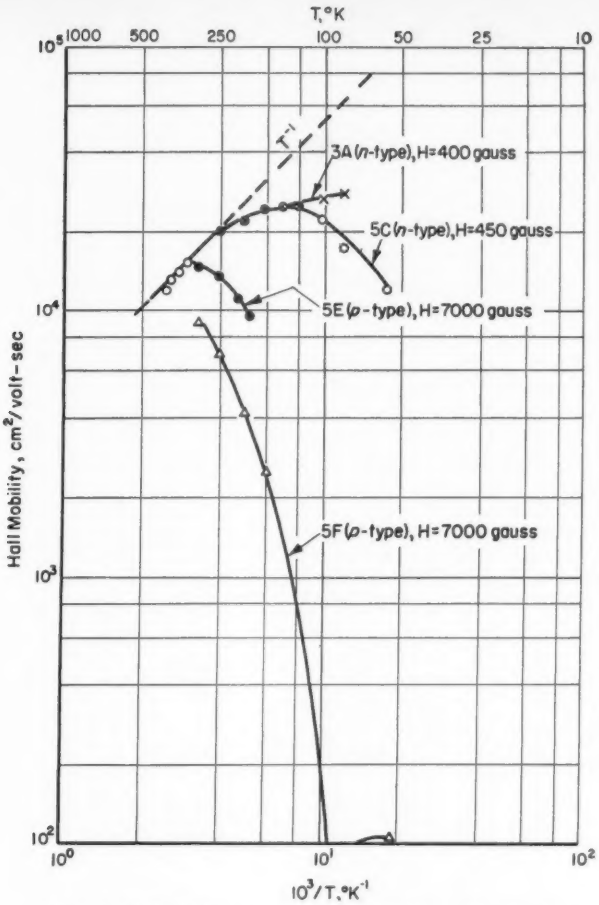


FIG. 5. Hall mobility as a function of reciprocal temperature for two *n*-type and two *p*-type specimens of HgTe.

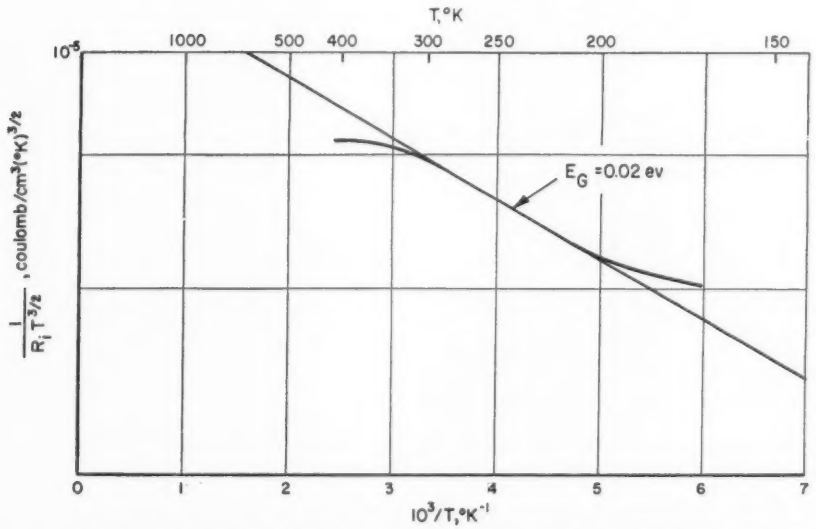


FIG. 6. Reciprocal of the product of temperature to the three-halves power and Hall coefficient as a function of reciprocal temperature for the *n*-type specimens of HgTe.

VOL. 7 1958

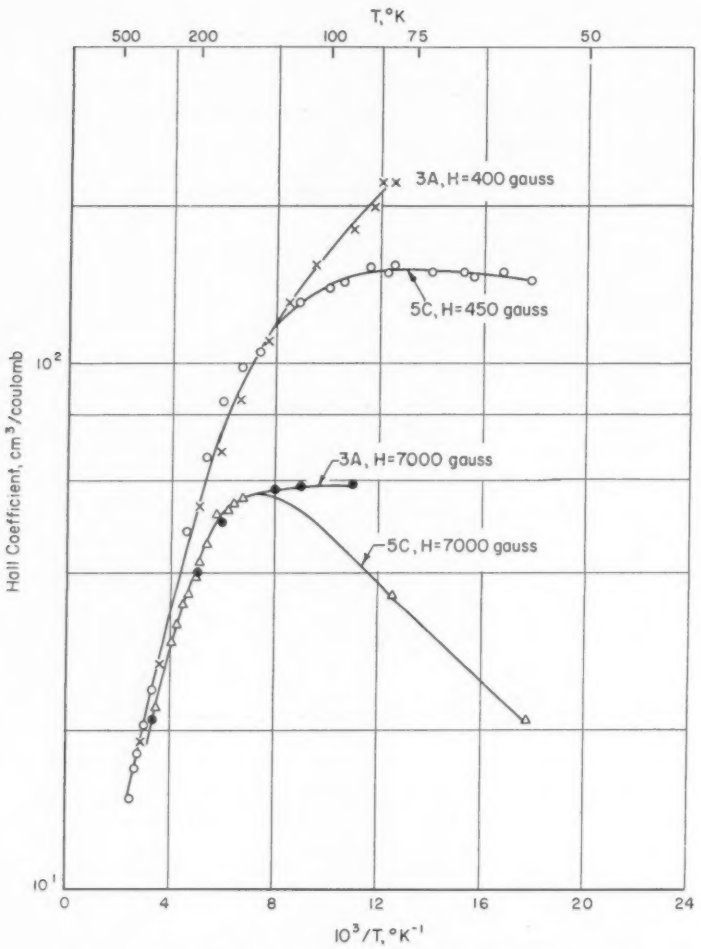


FIG. 7. Hall coefficient as a function of reciprocal temperature for two *n*-type specimens of HgTe at magnetic fields of approximately 400 gauss and 7000 gauss.

## CONCLUSIONS

The compound HgTe can be prepared by direct reaction of liquid tellurium with mercury vapor. By means of a three-temperature-zone apparatus the compound was zone melted. By annealing in mercury vapor the composition of the specimen near stoichiometry can be altered.

It is concluded that the actual hole to electron mobility ratio in HgTe is very small, perhaps the order of 0·01. The energy gap at 0°K is also very small, approximately 0·02 eV. Electron mobilities of 17,000 cm²/Vsec at room temperature and 25,000 cm²/Vsec at 143°K have been achieved.

*Acknowledgements*—The authors gratefully acknowledge helpful discussions with Dr. A. C. BEER. The assistance of Mr. J. I. GENCO in preparing samples is greatly appreciated.

VOL.
7
1958

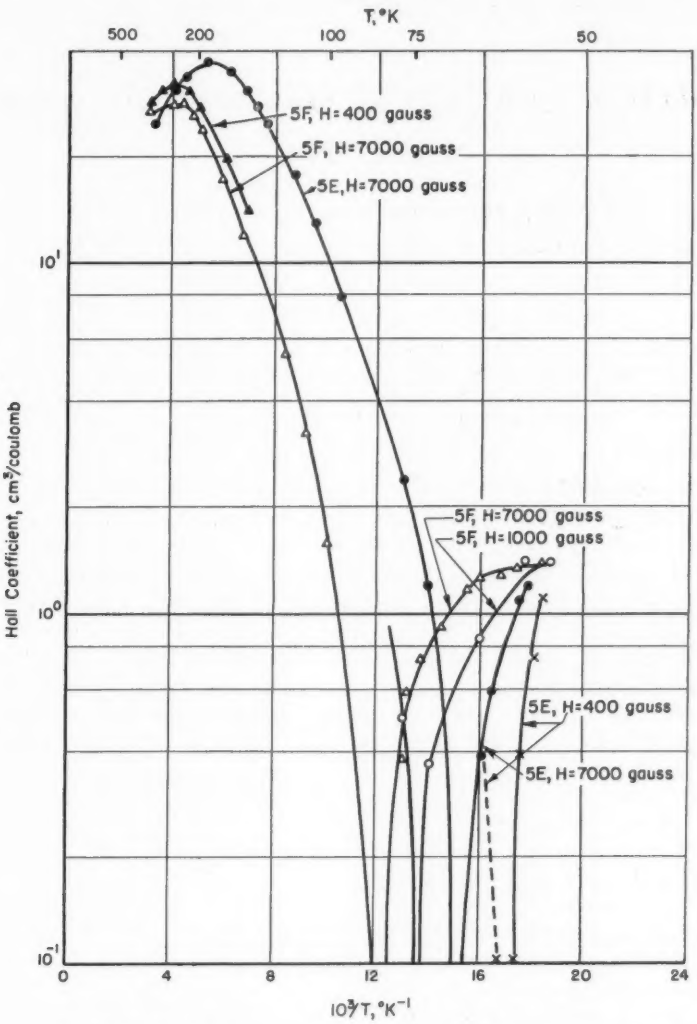


FIG. 8. Hall coefficient as a function of reciprocal temperature for two *p*-type specimens of HgTe for weak magnetic fields and for 7000 gauss.

## REFERENCES

1. HARMAN T. C., PARIS B., MILLER S. E. and GOERING H. L. *J. Phys. Chem. Solids* **2,** 181 (1957).
2. MOKROVSKII N. P. and REGEL A. R. *Zh. tech. fiz. USSR* **22,** 8, 1281 (1952).
3. BLACK J., KU S. and MINDEN H. *J. Electrochem. Soc.* To be published.
4. KROGER F. A. and DENOBEL D. *J. Electronics* **1,** 190 (1955).
5. TSIDILKOVSKII I. M. *Zh. tech. fiz. USSR* **27,** 1744 (1957).
6. CARLSON R. O. To be published.
7. HARMAN T. C., WILLARDSON R. K. and BEER A. C. *Phys. Rev.* **95,** 699 (1954).
8. WILLARDSON R. K., HARMAN T. C. and BEER A. C. *Phys. Rev.* **96,** 1512 (1954).

*J. Phys. Chem. Solids* Pergamon Press 1958. Vol. 7. pp. 236–239.

# ABSORPTION SPECTRUM OF ARSENIC DOPED SILICON

**HENRY J. HROSTOWSKI and R. H. KAISER**

Bell Telephone Laboratories, Incorporated Murray Hill, New Jersey

(*Received* 23 *May* 1958)

**Abstract**—The absorption spectrum of arsenic doped silicon has been obtained and is in good agreement with that calculated from the effective mass theory. Bands which do not obey the calculated term scheme are shown to arise from other donor impurities. Optical and thermal ionization energies appear to be very similar for Group III and Group V impurities.

VOL
7
195

## INTRODUCTION

It has been shown[1] that the effective mass approximation qualitatively accounts for the infrared spectra of Group III acceptors in silicon. For Group V donors one expects better agreement between theory and experiment[2] since the structure of the conduction band of silicon is less complicated and much better known than the valence band structure. However, the reported spectra of phosphorus, arsenic, antimony[3] and bismuth[4] are quite dissimilar. Although all donor spectra were originally interpreted using the Kohn–Luttinger[5] term scheme, Picus, Henvis and Burstein[6] have recently reported for arsenic-doped silicon that two absorptions at about 316 $cm^{-1}$ and 274 $cm^{-1}$ can be attributed to electronic transitions of the neutral arsenic atom, and that the resultant spectrum is no longer consistent with the calculated effective mass term scheme. Our present results for arsenic show a band at $316{\cdot}4 \pm 0{\cdot}2$ $cm^{-1}$ in agreement with Picus *et al.* At higher energies we also observe several bands not previously resolved by other investigators. However, the excited states we attribute to the arsenic atom are in essentially quantitative agreement with theory. Any deviation of the observed spectrum from theoretical predictions can be associated with other donors present as impurities.

## EXPERIMENTAL RESULTS

The samples were prepared by doping a pulled crystal. Measurements were taken in a manner described previously.[1] The 4·2°K transmission spectrum of an arsenic doped sample with a net donor density of $1{\cdot}5 \times 10^{15}/cm^3$ is shown in Fig. 1. The approximate spectral resolution is also indicated. For comparison this figure also gives the spectrum of bismuth doped silicon. We note a band occurring at $316{\cdot}4 \pm 0{\cdot}2$ $cm^{-1}$ in both spectra. Neglecting this absorption, whose origin is discussed below, the patterns for arsenic and bismuth are almost identical. The energies and assignments of the observed arsenic bands are listed in Table 1, using the notation of Kohn and Luttinger.[5]

*Table* 1. *Observed transitions of arsenic in silicon*

| Transition | Assignment | Energy in $eV \times 10^3$ |
|---|---|---|
| I | $1s \rightarrow 2p,\ m = 0$ | $42{\cdot}27 \pm 0{\cdot}04$ |
| II | $1s(1) \rightarrow 2s(5)$* | $\sim 44{\cdot}66$ |
| III | $1s \rightarrow 2p,\ m = \pm 1$ | $47{\cdot}47 \pm 0{\cdot}04$ |
| IV | $1s \rightarrow 3p,\ m = 0$ | $48{\cdot}35 \pm 0{\cdot}04$ |
| V | $1s \rightarrow ?$ | $49{\cdot}87 \pm 0{\cdot}04$ |
| VI | $1s \rightarrow 3p,\ m = \pm 1$ | $50{\cdot}72 \pm 0{\cdot}04$ |
| VII | $1s \rightarrow ?$ | $52{\cdot}47 \pm 0{\cdot}3$ |

*The parenthetical numbers give the degeneracy of these states.

## DISCUSSION

Our spectra[7] indicate that most *n*-type silicon samples have more than one donor present in detectable quantities. In antimony doped silicon

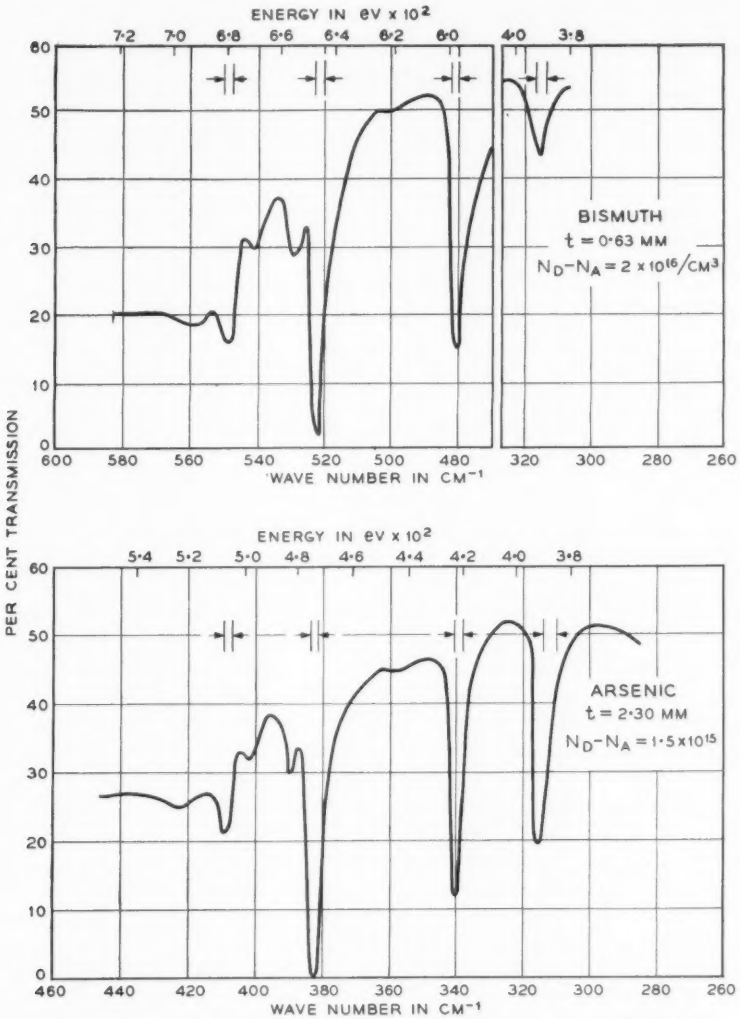


FIG. 1. Electronic spectra of arsenic and bismuth in silicon at 4·2°K. Note the break in energy scale at $5{\cdot}8 \times 10^{-3}$ eV. Approximate effective slit widths are shown.

there is a prominent band at $316{\cdot}4 \pm 0{\cdot}2$ cm$^{-1}$.[3,7] The exact frequency coincidence of this band and those shown in Fig. 1 suggests that the 316·4 cm$^{-1}$ absorption arises from antimony contamination. The 274 cm$^{-1}$ absorption reported by PICUS[6] *et al.* coincides with an intense phosphorus absorption and can correspondingly be attributed to phosphorus contamination. With this interpretation the spectra for arsenic and bismuth are very similar. This result is in accord with the theoretical expectation of a common term scheme[5] for donors and the observation that Group III acceptor spectra are not markedly different from each other.[1]

The known values of the distribution coefficients are consistent with the contamination of bismuth doped samples with antimony and antimony doped samples with arsenic provided

*Table 2. Spacings of excited states; energy difference in* eV$\times 10^3$

| State | Theory[5] | Arsenic | Bismuth[4] |
|---|---|---|---|
| $(2p, m = \pm 1)-(2p, m = 0)$ | $5{\cdot}0 \pm 0{\cdot}3$ | $5{\cdot}20 \pm 0{\cdot}06$ | $5{\cdot}07 \pm 0{\cdot}06$ |
| $(3p, m = 0)-(2p, m = \pm 1)$ | $0{\cdot}2 \pm 0{\cdot}7$ | $0{\cdot}88 \pm 0{\cdot}08$ | $0{\cdot}905 \pm 0{\cdot}075$ |
| $(3p, m = \pm 1)-(2p, m = \pm 1)$ | $3{\cdot}0 \pm 0{\cdot}15$ | $3{\cdot}25 \pm 0{\cdot}08$ | $3{\cdot}45 \pm 0{\cdot}075$ |
| $2s(5)-(2p, m = 0)$ | $\sim 2$ | $\sim 2{\cdot}4$ | $2{\cdot}69 \pm 0{\cdot}06$ |
| ? $-(2p, m = \pm 1)$ | Not calculated | $2{\cdot}40 \pm 0{\cdot}08$ | $2{\cdot}565 \pm 0{\cdot}075$ |
| ? $-(3p, m = 0)$ | Not calculated | $1{\cdot}75 \pm 0{\cdot}4$ | $1{\cdot}10 \pm 0{\cdot}16$ |

antimony and arsenic are impurities present in the bismuth and antimony used for doping purposes. It is difficult however to explain the presence of large amounts of antimony in arsenic doped crystals. It is likely that because of the extremely high vapor pressure of arsenic at the melting point of silicon much of the arsenic volatilizes during the doping process. Since antimony is a common impurity in arsenic, the relative concentration of antimony may be greatly increased as a result of this process.

Experimental energy level spacings for arsenic and bismuth are compared in Table 2 with those calculated by KOHN and LUTTINGER. For arsenic the separations are within the combined limits of error for the states which have been calculated. The $(1s)$–$(3p, m = 0)$ transition is also clearly resolved for arsenic. Resolution of this transition is further evidence of the accuracy of the effective mass theory. The relative intensity and position of this band were predicted theoretically[5] before it was first resolved[4] in bismuth doped silicon. The agreement between the arsenic spectrum and the KOHN–LUTTINGER term scheme is excellent. Furthermore, the observed energy level separations are almost identical for arsenic and bismuth. Within the limits of experimental error the average difference is less than two percent. From the observed energies of transitions I, III, and VI and the calculated separations of the corresponding $p$-states from the conduction band, we get an optical ionization energy, $E_0$ of $53{\cdot}4 \pm 0{\cdot}2 \times 10^{-3}$ eV for arsenic. This is somewhat higher than the accepted thermal value,[8] $E_T$, of $49 \times 10^{-3}$ eV. However, the optical detection of antimony as an impurity and the probability that antimony is inadvertently introduced during the doping process suggest that the reported $E_T$ may be somewhat lower than the true value. The Hall effect measurements of MORIN and MAITA[8] show $E_T$ ranging from $46 \times 10^{-3}$ eV to $56 \times 10^{-3}$ eV. Values of $55 \pm 1 \times 10^{-3}$ have also been obtained several times with highly compensated samples.[9] In this situation any donor levels closer to the conduction band such as antimony are ionized over the whole temperature range investigated and the true value of $E_T$ is observed. These results indicate very little difference between $E_T$ and $E_0$ for arsenic. Previous work has shown that $E_T \approx E_0$ for both phosphorous[3] and bismuth.[4] We therefore expect no substantial difference for antimony. The fact that the reported $E_T$ is less than $E_0$ in this case may result from improper identification of the antimony absorptions.

Similar discrepancies between $E_T$ and $E_0$ have been observed for Group III acceptors where there is agreement for boron and indium but not for aluminum and gallium. BURSTEIN *et al.*[10] have suggested that uncompensated boron centers might account for the differences. In view of the results presented here their suggestion seems correct. We therefore conclude that $E_0 \approx E_T$ for both donors and acceptors.

There is an indication of a very weak arsenic absorption at about 360 cm$^{-1}$. A similar band in the bismuth spectrum was interpreted[4] as the transition from the non-degenerate ground state to the fivefold approximately degenerate $2s$ states. This interpretation suggests that a transition from the ground state to the degenerate $1s$ states should also be observed at lower energies. No evidence of the $1s(1)$ to $1s(5)$ band has been obtained at energies above $36 \times 10^{-3}$ eV. However this transition is expected to be much less intense than the

allowed transitions and may be masked by antimony in the bismuth spectrum. Our measurements of arsenic doped silicon have not yet been extended to sufficiently low energies to detect this absorption.

## CONCLUSIONS

When proper care is taken to eliminate bands associated with donors present unintentionally, the spectrum of arsenic in silicon is very well described by the effective mass theory. The remarkable similarity between the electronic transitions of arsenic and bismuth is consistent with the theoretical prediction of a common term scheme for the excited states of Group V donors in silicon. Present results indicate that $E_T \approx E_0$ for Group V donors and Group III acceptors.

VOL. 7 1958

## REFERENCES

1. Hrostowski H. J. and Kaiser R. H. *J. Phys. Chem. Solids* **4,** 148 (1958).
2. Kohn W. *Solid State Physics* Vol. 5, p. 297. Academic Press, New York (1957).
3. Picus G., Burstein E. and Henvis B. *J. Phys. Chem. Solids* **1,** 75 (1956).
4. Hrostowski H. J. and Kaiser R. H. *J. Phys. Chem. Solids* **4,** 315 (1958).
5. Kohn W. and Luttinger J. M. *Phys. Rev.* **98,** 915 (1955).
6. Picus G. S., Henvis B. W. and Burstein E. *Bull. Amer. Phys. Soc.* Series II, Vol. 3, p. 129 (1958).
7. Hrostowski H. J. Unpublished results.
8. Morin F. J. and Maita J. P. *Phys. Rev.* **96,** 28 (1954).
9. Morin F. J. Private communication.
10. Burstein E., Picus G., Henvis B. and Wallis R. *J. Phys. Chem. Solids* **1,** 65 (1956).

*J. Phys. Chem. Solids* Pergamon Press 1958. Vol. 7. pp. 240–248.

# CONSTITUTION OF THE $AgSbSe_2$–$AgSbTe_2$–$AgBiSe_2$–$AgBiTe_2$ SYSTEM

**J. H. WERNICK, S. GELLER and K. E. BENSON**

Bell Telephone Laboratories, Inc., Murray Hill, New Jersey

(*Received* 30 *June* 1958)

**Abstract**—The six pseudo-binary phase diagrams in the semiconducting system $AgSbSe_2$–$AgSbTe_2$–$AgBiSe_2$–$AgBiTe_2$ have been determined. Complete series of solid solutions with the cubic structure exist in this pseudo-quaternary system. The locus of temperatures and compositions for the order–disorder transition has been determined. Lattice constants as a function of composition for the cubic phase and thermoelectric-power data for some of the solid solutions are presented.

VOL
7
195

## INTRODUCTION

It has recently been shown[1,2] that the high-temperature form of $AgBiSe_2$ (and confirmed for $AgBiS_2$[3]) has a disordered NaCl-type structure. For the compounds $AgSbSe_2$ and $AgSbTe_2$ this structure persists down to room temperature.[1,2] In the case of $AgBiSe_2$, however, there is a transition at 287°C to an ordered rhombohedral structure[2] (space-group $R\bar{3}m$), which on further cooling to 120°C transforms to a hexagonal structure[2] (space-group $P\bar{3}ml$) that results from additional slight displacements of the atoms. The latter transition is easily reversible and is probably higher than first order.[2]

In the present work, we have found that the high-temperature form of $AgBiTe_2$ also has the disordered cubic structure. However, at room temperature a thermodynamically stable modification with formula $AgBiTe_2$ does not exist. Furthermore, it has been shown by others that in the $AgSbS_2$–$AgBiS_2$ system a new compound occurs at the composition $AgSb_{0.833}Bi_{0.167}S_2$.[4] Because these ternary compounds with a structure related to that of NaCl appear to be of significant scientific and also potential practical interest, it was decided to investigate the six pseudo-binary systems shown in Fig. 1 with the purpose of learning more about the thermodynamic and crystallographic relationships among the different phases, the effects of atomic size and metallic nature of the atoms upon the structures, and the possible formation of new phases in these systems.

## EXPERIMENTAL AND DISCUSSION

Each specimen was prepared by mixing the proper amounts of the constituent elements, placing the mixture in a fused silica tube, evacuating, sealing off, and then heating to 1000°C. Differential thermal analyses were made to determine the liquidus, solidus, and solid-state transformation temperatures.

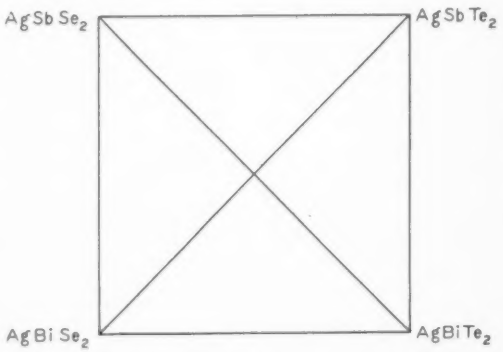


FIG. 1. The six pseudo-binary systems studied.

X-ray powder photographs (Cu$K$ radiation, Norelco Straumanis-type cameras of 114·6 mm diameter) were taken of all samples. In the tables of X-ray data, unless otherwise noted, the data refer to as-cast samples.

Samples that were water-quenched from high temperatures were sealed in evacuated Pyrex tubes. A quench was considered sufficiently rapid

when the tube shattered upon quenching. Annealing experiments were also carried out on samples sealed in evacuated Pyrex tubes.

For the sake of clarity, each binary system will be discussed separately.

(a) *The* $AgSbSe_2$–$AgSbTe_2$ *system*

The phase diagram of this system* (Fig. 2) contains a complete series of solid solutions with the

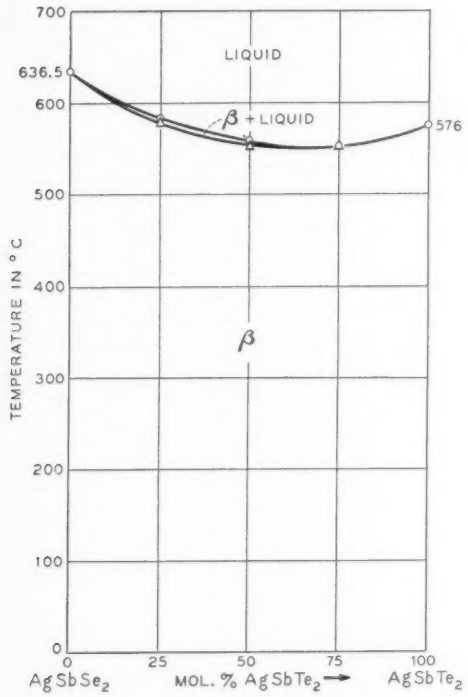


FIG. 2. The $AgSbSe_2$–$AgSbTe_2$ system.

disordered NaCl-type structure, hereafter designated the $\beta$ phase. The liquidus and solidus curves show a tendency toward eutectic formation or separation of phases. The separation between the two curves is less than 10°C, indicating that the distribution coefficient of tellurium is not greatly different from unity.† The plot of lattice constant versus composition (Table 1 and Fig. 3) indicates that these solutions very nearly follow Vegard's law. The small positive deviation from Vegard's law is probably caused by a change in the nature

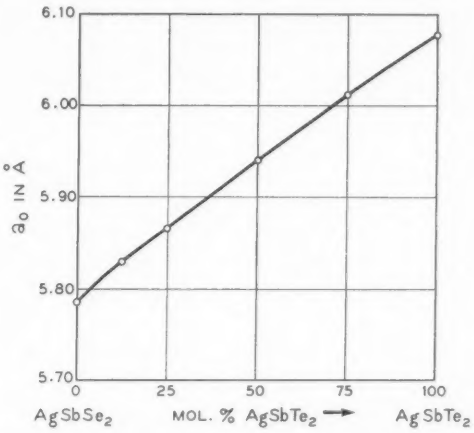


FIG. 3. Lattice constants at 25°C for the cubic $\beta$ phase in the $AgSbSe_2$–$AgSbTe_2$ system.

*Table 1. Lattice constants at 25°C for the cubic* $\beta$ *phase in the* $AgSbSe_2$–$AgSbTe_2$ *system*

| Composition (mol. per cent) | $a_0$ (Å($\pm$0·003)) |
|---|---|
| $AgSbSe_2$ | 5·786 |
| 87·5 $AgSbSe_2$–12·5 $AgSbTe_2$ | 5·831* |
| 75 $AgSbSe_2$–25 $AgSbTe_2$ | 5·865* |
| 50 $AgSbSe_2$–50 $AgSbTe_2$ | 5·940* |
| 25 $AgSbSe_2$–75 $AgSbTe_2$ | 6·013 |
| $AgSbTe_2$ | 6·078 |

* The X-ray samples were annealed at 410°C for 8 days to sharpen the high-angle lines.

* We have previously reported[5] the melting points 610° and 555°C for the two compounds respectively. These values, obtained by an ordinary thermal-analysis technique, are low because of supercooling.

† The solidus temperatures were determined by comparing the differential-analysis data with those of the ternary compounds, which, within experimental error, freeze isothermally. The high-angle line widths on X-ray patterns of some as-cast samples (Tables 4, 5, and 6) are consistent with the amount of separation between liquidus and solidus curves. (This observation was made by C. D. THURMOND.) The heats of fusion appear to be of the same order of magnitude as metals. There appear to be no phase equilibrium data available concerning the $Ag_2Se$–$Sb_2Se_3$, $Ag_2Se$–$Bi_2Se_3$, $Ag_2Te$–$Sb_2Te_3$, and $Ag_2Te$–$Bi_2Te_3$ pseudo-binary systems. Our zone-refining and X-ray data to date indicate that the 1 : 1 compositions in the first three systems are stoichiometric compounds.

of the bonding when the more-metallic tellurium is added to $AgSbSe_2$ or the less-metallic selenium is added to $AgSbTe_2$.

As expected, no evidence of ordering above room temperature was observed. However, in determinations of the thermal e.m.f. of single-crystal samples of $AgSbTe_2$, $AgSbSe_{0.5}Te_{1.5}$, and AgSbSeTe from $-170°$ to 127°C, a heat effect was observed at $-40°$C which may be indicative of an ordering process.

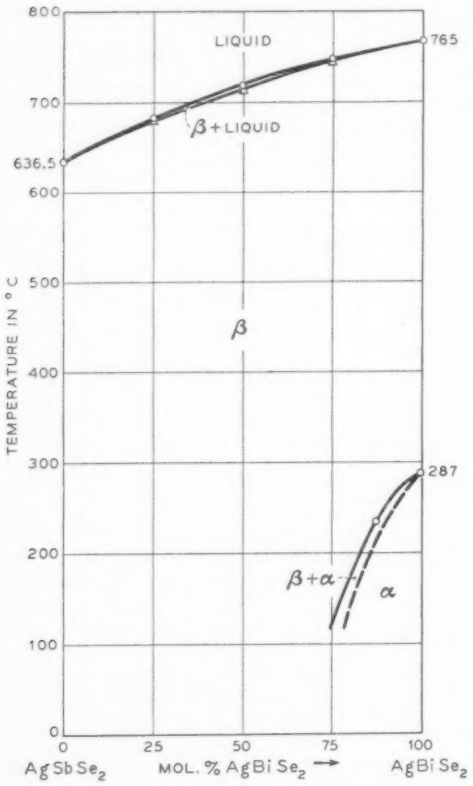


FIG. 4. The $AgSbSe_2$–$AgBiSe_2$ system.

(b) *The* $AgSbSe_2$–$AgBiSe_2$ *system*

A complete series of solid solutions having the NaCl-type disordered structure exists in this system also (Fig. 4). In cooling from the high-temperature (cubic) form of $AgBiSe_2$, there is one thermal arrest at 287°C. At this temperature the transition is to an ordered rhombohedral structure[2] (space-group $R\bar{3}m$), which at about 120°C transforms to a hexagonal structure (space-group $P\bar{3}ml$), hereafter referred to as the $\alpha$ phase. The latter transition is almost surely of higher than first order; no heat effect is observed and the low-temperature form is derived from the intermediate form by only slight additional atomic displacements.[2]

The replacement of some bismuth by antimony stabilizes the high-temperature phase ($\beta$) of $AgBiSe_2$. This may be attributed to a difference in atomic sizes[2] and/or to difference in the metallic nature, and therefore the bonding, of the atoms. Although the locus of temperatures which show the end of transformation of the solid solutions has not been determined, the two-phase area is probably small because the elapsed time, and therefore the temperature range over which the thermal arrest occurs, is small.

The curve of lattice constants versus composition for this system (Table 2 and Fig. 5) also deviates slightly from Vegard's law, as is the case for

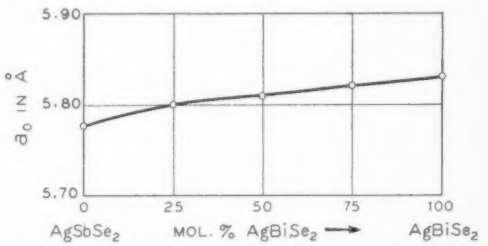


FIG. 5. Lattice constants at 25°C for the cubic $\beta$ phase in the $AgSbSe_2$–$AgBiSe_2$ system.

*Table 2. Lattice constants at 25°C for the cubic* $\beta$ *phase in the* $AgSbSe_2$–$AgBiSe_2$ *system*

| Composition (mol. per cent) | $a_0$ (Å($\pm$0·003)) |
|---|---|
| $AgSbSe_2$ | 5·786 |
| 75 $AgSbSe_2$–25 $AgBiSe_2$ | 5·801 |
| 50 $AgSbSe_2$–50 $AgBiSe_2$ | 5·810* |
| 25 $AgSbSe_2$–75 $AgBiSe_2$ | 5·882 |
| $AgBiSe_2$ | 5·833† |

* The X-ray sample was annealed at 184°C for 11½ days to sharpen the high-angle lines.

† The $a_0$ value reported here was obtained by extrapolation of the other data contained in this table. Samples quenched to obtain the high-temperature form showed broad high-angle lines. A lattice constant of 5·82 $\pm$ 0·02 Å was obtained from such data.

the $AgSbSe_2$–$AgSbTe_2$ system, and probably for similar reasons. The small differences in lattice constant show that the antimony and bismuth atomic sizes do not differ very much (see also Ref. 2).

(c) *The* $AgSbTe_2$–$AgBiTe_2$ *system*

The phase diagram of this system is shown in Fig. 6. Within experimental error, the liquidus and solidus curves coincide. The studies of this and the following ($AgSbSe_2$–$AgBiTe_2$) system have shown that there is no thermodynamically stable modification of $AgBiTe_2$ which exists below the transition temperature. The transition temperature represents the point of decomposition of the high-temperature modification into $Bi_2Te_3$ with some dissolved silver and probably a modification of $Ag_2Te$ or some Ag–Te phase with perhaps some bismuth dissolved in it.* Thus, $\gamma$ designates a two-phase region.‡

If a $AgBiTe_2$ sample is subjected to a sufficiently rapid quench from above the transition temperature (Fig. 6), the disordered NaCl-type phase is obtained. In this case, however, the lines are very broad, indicating that the disordered phase tends to transform rapidly below the transition temperature. If the quench is not rapid enough, the trigonal $AgBiSe_2$-type phase is obtained (lattice constants: $a = 4{\cdot}37 \pm 0{\cdot}01$ Å, $c = 20{\cdot}76 \pm 0{\cdot}05$ Å). In this system, this phase appears to be a transitory non equilibrium one, as shown by the following experiments. A sample of $AgBiTe_2$ (decomposition products) was held at 400°C for 3 hr and quenched in ice water. The quenched sample contained the original room-temperature phases. Another sample was held at 500°C for 4 hr, furnace cooled to 400°C, held at this temperature for 1 hr, and then quenched in ice water. The powder photograph of this sample indicated the presence of the decomposition products. It appears, therefore, that the transitory phase is the route through which the decomposition occurs, though it is not itself an equilibrium phase on this phase diagram. A heat effect should be observed in the decomposition of the trigonal phase. Thus, the transitory phase results from the arresting of the decomposition.†

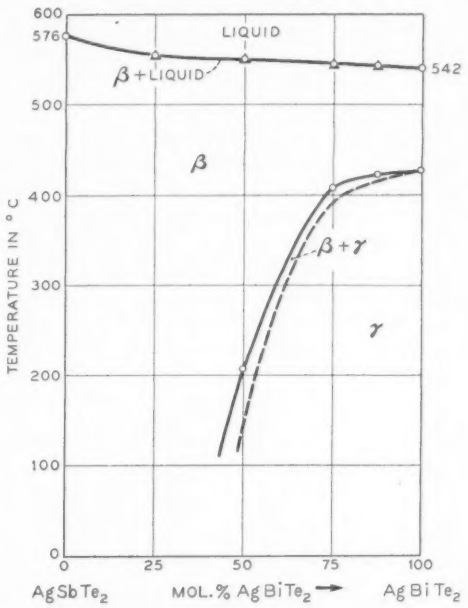


FIG. 6. The $AgSbTe_2$–$AgBiTe_2$ system.

The X-ray photograph of an as-cast sample of $AgSb_{0{\cdot}125}Bi_{0{\cdot}875}Te_2$ indicated that this material was also two-phase. The $Bi_2Te_3$ phase probably contained both silver and antimony dissolved in it. The X-ray photograph of a sample of $AgSb_{0{\cdot}25}Bi_{0{\cdot}75}Te_2$ indicated the presence of some of the transitory phase along with the decomposition phases ($\gamma$). Annealing the latter for 6 days at 340°C resulted in complete decomposition; the $Bi_2Te_3$ phase in this case had smaller spacings than the same phase in the $AgBiTe_2$ decomposition products, indicating the solution of antimony. The X-ray pattern of a furnace-cooled sample of

* Only in the zone-refined samples was the Ag–Te phase identified as the low-temperature modification of $Ag_2Te$. The Ag–Te phase in as-cast samples was not identifiable. However, it has been reported that there are probably at least three $Ag_2Te$ phases.[6]

† Strictly speaking, because of this decomposition, one cannot at present refer to binary cuts involving $AgBiTe_2$ as truly pseudo-binary systems. A detailed study of the pseudo-binary $Bi_2Te_3$–$Ag_2Te$ system is necessary in order to determine the relationship of $AgBiTe_2$ to its end members, $Bi_2Te_3$ and $Ag_2Te$. For the sake of simplicity we shall continue to refer to these systems as pseudo-binaries and the complete system as a pseudo-quaternary system.

‡ It is, of course, possible that this phase is thermodynamically stable over a very narrow temperature range.

$AgSb_{0.5}Bi_{0.5}Te_2$ indicated only the presence of the $\alpha$ phase. Because of the comparatively low temperature at which the transition occurs for this composition, it may be that equilibrium is difficult to attain. Three months' annealing of this sample at 152°C did not result in any decomposition. For this composition the $AgBiSe_2$-type phase appears to be stable. The replacement of half the bismuth with the somewhat smaller antimony atom has resulted in the formation of a single phase, similar to the stabilization of the cubic phase with even greater amounts of antimony. The composition limits of the $\alpha$ phase on this cut have not been determined, and no notation has been placed on the diagram.

For the cubic phase, the lattice constant versus composition curve follows Vegard's law (Table 3 and Fig. 7). Thus, in the high-temperature phase it is seen that the tellurium atoms are dominant in determining bonding, i.e. the distortion of the $[SbTe_6]$ octahedra is probably not significantly greater than that of the $[BiTe_6]$ octahedra. This may be seen in another way. The sesquitellurides of antimony and bismuth are isostructural, whereas the sesquiselenides are not. Thus, the electronic and size differences of antimony and bismuth are dominant in determining bonding in the latter compounds.* It is noteworthy, however, that at room temperature $AgSbTe_2$ prefers the cubic disordered configuration, whereas $AgBiTe_2$ does not form a thermodynamically stable phase. Thus, it appears that at lower temperatures, the electronic differences of the antimony and bismuth atoms play an important role in determining the stability of the two structures.

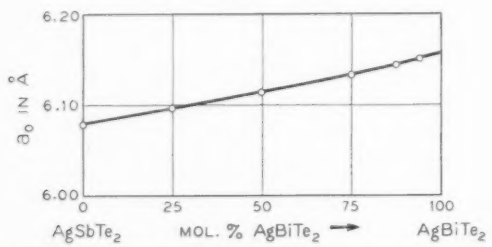


FIG. 7. Lattice constants at 25°C for the cubic $\beta$ phase in the $AgSbTe_2$–$AgBiTe_2$ system.

*Table 3. Lattice constants at 25°C for the cubic $\beta$ phase in the $AgSbTe_2$–$AgBiTe_2$ system*

| Composition (mol. per cent) | $a_0$ (Å($\pm$0·003)) |
|---|---|
| $AgSbTe_2$ | 6·078 |
| 75 $AgSbTe_2$–25 $AgBiTe_2$ | 6·094 |
| 75 $AgSbTe_2$–25 $AgBiTe_2$ | 6·097* |
| 50 $AgSbTe_2$–50 $AgBiTe_2$ | 6·118* |
| 25 $AgSbTe_2$–75 $AgBiTe_2$ | 6·134* |
| 12·50 $AgSbTe_2$–87·50 $AgBiTe_2$ | 6·144* |
| 6·25 $AgSbTe_2$–93·75 $AgBiTe_2$ | 6·150* |
| $AgBiTe_2$ | 6·155† |

* Quenched from 500°C; high-angle lines sharp.
† Extrapolated value obtained from these data.

The lattice constant of the quenched cubic phase of $AgBiTe_2$ is in some doubt. The value obtained by extrapolation in this system is 6·155 Å. In all attempts to quench this phase, either a poor specimen was obtained giving the broad lines of the $\beta$ phase and some of the $\alpha$ phase lines or a poor $\alpha$ phase with broad high-angle lines. It may be assumed that the quenching was not rapid enough. However, a sample annealed for 5 hr at 500°C under a vapor pressure of tellurium of 7$\mu$, when rapidly quenched, gave the pure cubic phase with rather sharp lines out to high angles (some $K\alpha_1$, $K\alpha_2$ resolution was observed). The pattern gave a lattice constant of 6·115 Å, which is 0·040 Å smaller than the value 6·155 Å obtained by extrapolation of the $AgSbTe_2$–$AgBiTe_2$ solid-solution data. However, the lattice constant of the 93·75 mol. per cent $AgBiTe_2$–6·25 mol. per cent $AgSbTe_2$ sample gave a powder photograph with sharp high-angle lines and a lattice constant of 6·150 Å (Table 3). Also, the $AgSbSe_2$–$AgBiTe_2$ and $AgBiSe_2$–$AgBiTe_2$ systems indicate that the 6·155Å value should be more nearly the correct value.

### (d) *The* $AgSbSe_2$–$AgBiTe_2$ *system*

The diagram for this system is shown in Fig. 8. An X-ray photograph of a furnace-cooled sample of $AgSb_{0.25}Bi_{0.75}Se_{0.5}Te_{1.5}$ showed the presence mainly of the $\beta$ phase. Annealing of this sample for 6 days at 300°C resulted in the complete conversion to the phases represented by $\gamma$ on the phase diagram. Based on the observed lattice constants of

* The sesquisulfides of antimony and bismuth are isostructural, and it appears that sulfur is dominant in determining bonding in these compounds.

the two phases, the $Bi_2Te_3$ phase appears to contain selenium and antimony in solid solution and the $Ag_2Te$ phase primarily selenium in solid solution.

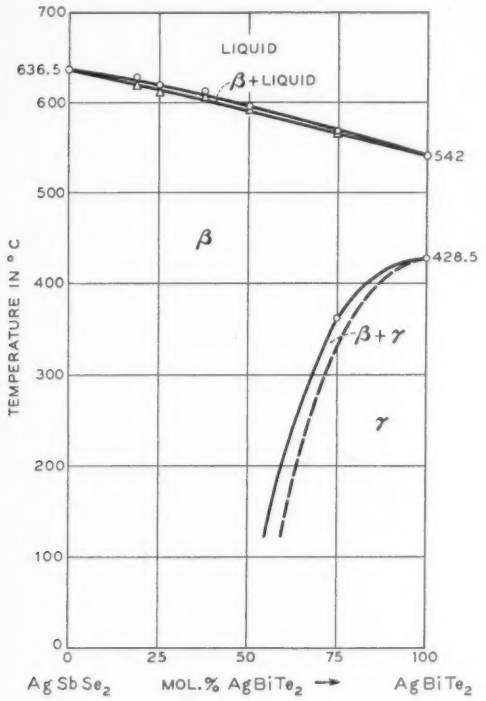


FIG. 8. The $AgSbSe_2$–$AgBiTe_2$ system.

*Table 4. Lattice constants at 25°C for the cubic β phase in the* $AgSbSe_2$–$AgBiTe_2$ *system*

| Composition (mol. per cent) | Lattice constant (Å) |
|---|---|
| 100 $AgSbSe_2$ | 5·786 ± 0·003 |
| 75 $AgSbSe_2$–25 $AgBiTe_2$ | 5·90 ± 0·02* |
| 75 $AgSbSe_2$–25 $AgBiTe_2$ | 5·883 ± 0·003† |
| 50 $AgSbSe_2$–50 $AgBiTe_2$ | 5·97 ± 0·02‡ |
| 50 $AgSbSe_2$–50 $AgBiTe_2$ | 5·98 ± 0·02§ |
| 25 $AgSbSe_2$–75 $AgBiTe_2$ | 6·06 ± 0·02§ |
| $AgBiTe_2$ | 6·155 ± 0·003 (See Table 3) |

* As-cast sample; high-angle lines broad. This point not plotted.

† Annealed 5 days at 575°C.

‡ High-angle lines broad. These limits are based on the line breadth.

§ Quenched from 500°C; high-angle lines broad.

The lattice constants versus composition of the cubic β phase (Table 4 and Fig. 9) are not too accurate because the high-angle lines on some of the photographs were quite broad. Presumably

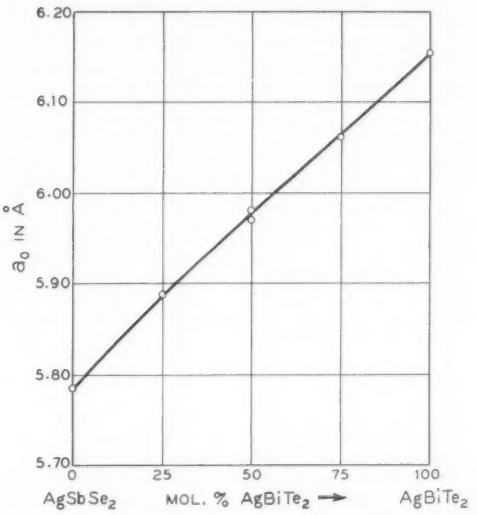


FIG. 9. Lattice constants at 25°C for the cubic β phase in the $AgSbSe_2$–$AgBiTe_2$ system.

long-time annealing of the X-ray samples before furnace cooling or prior to quenching would result in sharpening the high-angle lines by removing inhomogeneities, as was the case for those samples intentionally treated in this manner.

*Table 5. Lattice constants at 25°C for the cubic β phase in the* $AgSbTe_2$–$AgBiSe_2$ *system*

| Composition (mol. per cent) | Lattice constant (Å) |
|---|---|
| $AgSbTe_2$ | 6·078 ± 0·003 |
| 75 $AgSbTe_2$–25 $AgBiSe_2$ | 6·032 ± 0·003 |
| 75 $AgSbTe_2$–25 $AgBiSe_2$ | 6·034 ± 0·003* |
| 75 $AgSbTe_2$–25 $AgBiSe_2$ | 6·034 ± 0·003† |
| 50 $AgSbTe_2$–50 $AgBiSe_2$ | 5·97 ± 0·02‡ |
| 50 $AgSbTe_2$–50 $AgBiSe_2$ | 5·98 ± 0·02§ |
| 25 $AgSbTe_2$–75 $AgBiSe_2$ | 5·90 ± 0·02§ |
| $AgBiSe_2$ | 5·833 ± 0·003 |

* Quenched from 500°C; high-angle lines sharp.

† Annealed 21 days at 152°C.

‡ High-angle lines broad.

§ Quenched from 500°C; high-angle lines broad.

(e) *The* $AgSbTe_2$–$AgBiSe_2$ *system*

The phase diagram for this system (Fig. 10) shows a minimum in the liquidus and solidus curves, indicating a tendency toward eutectic formation. The α phase is a solid solution of $AgSbTe_2$ in $AgBiSe_2$. For this system also, some

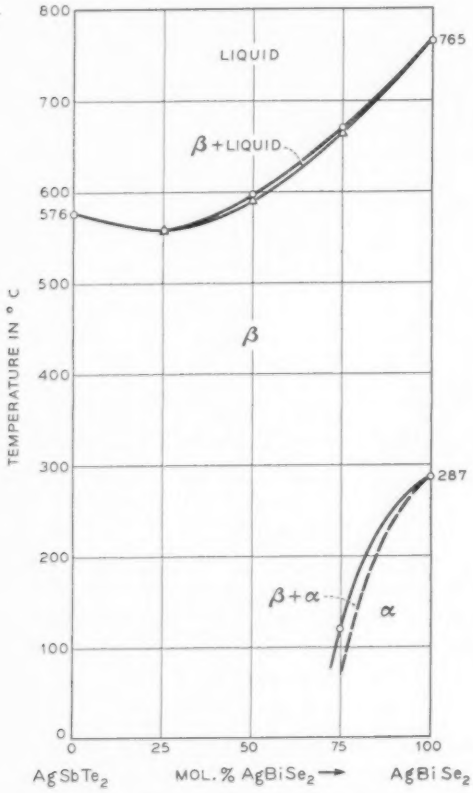


FIG. 10. The $AgSbTe_2$–$AgBiSe_2$ system.

of the X-ray data for the cubic phase (Table 5 and Fig. 11) are not very accurate because of the line broadness.

(f) *The* $AgBiSe_2$–$AgBiTe_2$ *system*

The phase diagram for this system is shown in Fig. 12. X-ray photographs of all furnace-cooled ingots containing less than 50 mol. per cent $AgBiTe_2$ showed the presence only of α solid solutions. Furnace-cooled samples of AgBiSeTe and $AgBiSe_{0.938}Te_{1.062}$ showed the α solid solution in addition to $Bi_2Te_3$-type and $Ag_xTe$-type phases.

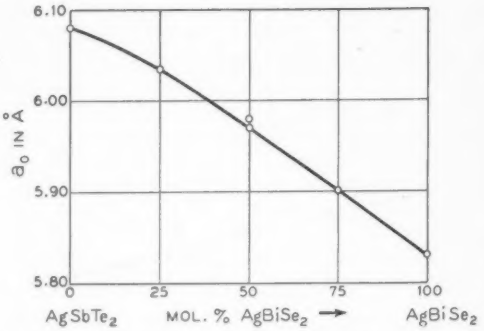


FIG. 11. Lattice constants at 25°C for the cubic β phase in the $AgSbTe_2$–$AgBiSe_2$ system.

Annealing of the latter sample for 6 days at 200°C did not convert any of the phases.

X-ray photographs of all furnace-cooled ingots, the compositions of which were 56·25 mol. per cent $AgBiTe_2$ or greater, showed only the decomposition products solid solutions. Thus, the three-phase (α+γ) region exists only over a narrow range of composition.

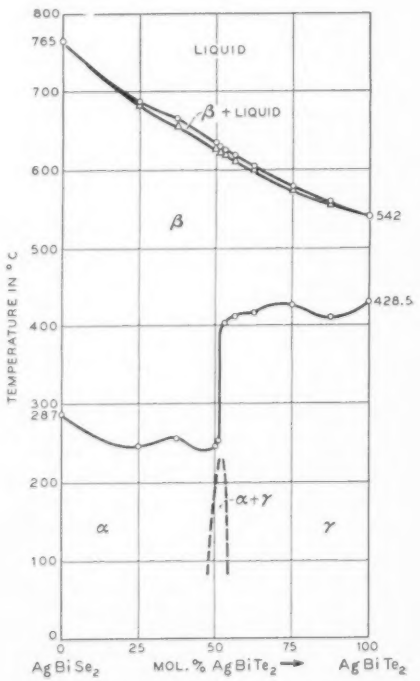


FIG. 12. The $AgBiSe_2$–$AgBiTe_2$ system.

Lattice constant versus composition data for the $\beta$ phase solid solutions are given in Table 6 and

*Table 6. Lattice constants at 25°C for the cubic $\beta$ phase in the $AgBiSe_2$–$AgBiTe_2$ system*

| Composition (mol. per cent) | $a_0$ (Å) |
|---|---|
| $AgBiSe_2$ | 5·833 ± 0·003 |
| 75 $AgBiSe_2$–25 $AgBiTe_2$ | 5·91 ± 0·02* |
| 50 $AgBiSe_2$–50 $AgBiTe_2$ | 6·00 ± 0·02* |
| 48·45 $AgBiSe_2$–51·55 $AgBiTe_2$ | 6·004 ± 0·003† |
| 46·85 $AgBiSe_2$–53·15 $AgBiTe_2$ | 6·00 ± 0·02* |
| 43·75 $AgBiSe_2$–56·25 $AgBiTe_2$ | 6·01 ± 0·02* |
| 25 $AgBiSe_2$–75 $AgBiTe_2$ | 6·09 ± 0·02* |
| 12·5 $AgBiSe_2$–87·5 $AgBiTe_2$ | 6·12 ± 0·02* |
| $AgBiTe_2$ | 6·155 (See Table 3) |

* Quenched from 500°C; high-angle lines broad.

† Quenched from 500°C; high-angle lines sharp.

Fig. 13. The lattice constants should not be considered to be of high accuracy because the high-angle lines on most of the photographs were broad.

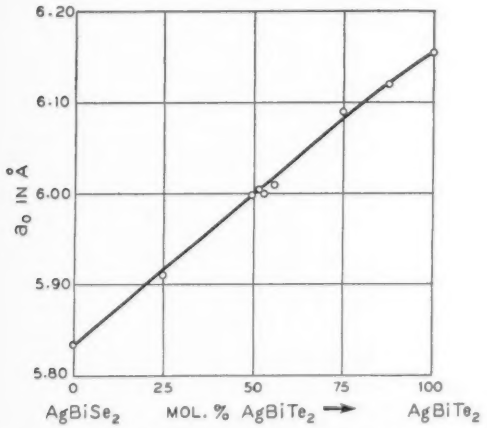


FIG. 13. Lattice constants at 25°C for the cubic $\beta$ phase in the $AgBiSe_2$–$AgBiTe_2$ system.

## FURTHER DISCUSSION

The three-dimensional representation of the pseudoquaternary system is shown in Fig. 14. A wide range of single-phase solid solutions is possible. Solid solutions are desirable for thermoelectric-device applications because of the possibility of lower thermal conductivities,[7] provided that resistivities and thermoelectric powers are not altered significantly. Some of these multicomponent solid solutions have an ordered structure. Thus, various degrees of ordering and local elastic strains may be induced by suitable heat treatment.

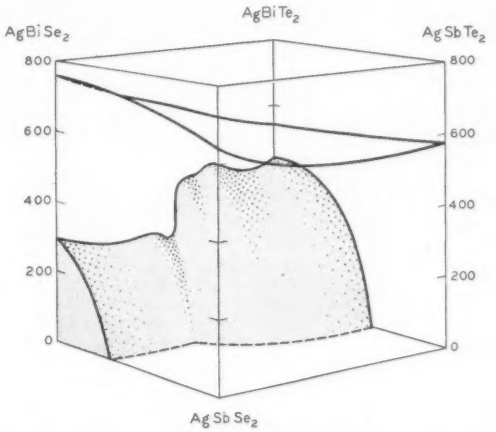


FIG. 14. The $AgSbSe_2$–$AgSbTe_2$–$AgBiSe_2$–$AgBiTe_2$ system.

We have determined thermoelectric powers against copper of a few *p*-type samples in the $AgSbSe_2$–$AgSbTe_2$ system in the range of −170 to 127°C. The thermoelectric powers are essentially constant in this temperature range and in excess of 200 $\mu$V/°C They are therefore comparable with the values obtained for the conventional thermoelectric materials $Bi_2Te_3$ and PbTe.

No new quaternary phases have been found, as in the case of the $AgSbS_2$–$AgBiS_2$ system. The results throughout are in accord with the conclusions of our structural investigations.[2] Further fundamental investigations of these new compounds—thermal, electrical, and structural—are continuing.

*Acknowledgement*—The authors wish to thank C. E. MILLER for taking the X-ray powder photographs.

## REFERENCES

1. WERNICK J. H., GELLER S. and BENSON K. E., *J. Phys. Chem. Solids* **4**, 154 (1958).

2. GELLER S. and WERNICK J. H. *Acta Cryst.*, in press.
3. RAMDOHR P., *S.B. Preuss. Akad. Wiss. Phys. Math. Kl.* **6,** 71 (1938).
See also GRAHAM A. R., *Amer. Min.* **36,** 436 (1951).
4. YARDLEY K., *Min. Mag.* **21,** 163 (1926).
5. WERNICK J. H. and BENSON K. E., *J. Phys. Chem. Solids* **3,** (1/2), 157 (1957).
6. ROWLAND J. F. and BERRY C. G., *Amer. Min.* **36,** 471 (1951).
7. IOFFE A., *J. Phys. Radium* **18,** (4) 209 (1957).

VOL
7
195

*J. Phys. Chem. Solids* Pergamon Press 1958. Vol. 7. pp. 249–251.

# THERMODYNAMICS OF THE Au–Pt SYSTEM

**R. J. WEISS and K. J. TAUER**

Materials Research Laboratory, Ordnance Materials Research Office, Watertown, Massachusetts

(*Received* 12 *February* 1958)

**Abstract**—The electronic, lattice, and mixing free energies are separated for the Au–Pt system, and it is shown that the asymmetric segregation in this system can be ascribed to the filling of the *d* band at ~ 30 per cent gold. The value of the segregation potential $6R(V_{AA}+V_{BB}-2V_{AB})/k$ is derived as ~ 6090 cal/mole.

VOL. 7 1958

In a series of papers[1–5] the authors have shown that the specific heat of many solids is separable into its component parts—lattice, electronic, magnetic, and order–disorder—and that certain of these terms dominate in determining phase boundaries. In some recent work at this laboratory on segregation in the Cu–Ni alloy system, the thermodynamics of such a system was considered and in particular that of the complementary system Au–Pt, which shows marked segregation. It is the purpose of this note to consider the component parts of the thermodynamics of the Au–Pt system.

Fig. 1 is the observed phase diagram.[6] The important features are the segregation of the two

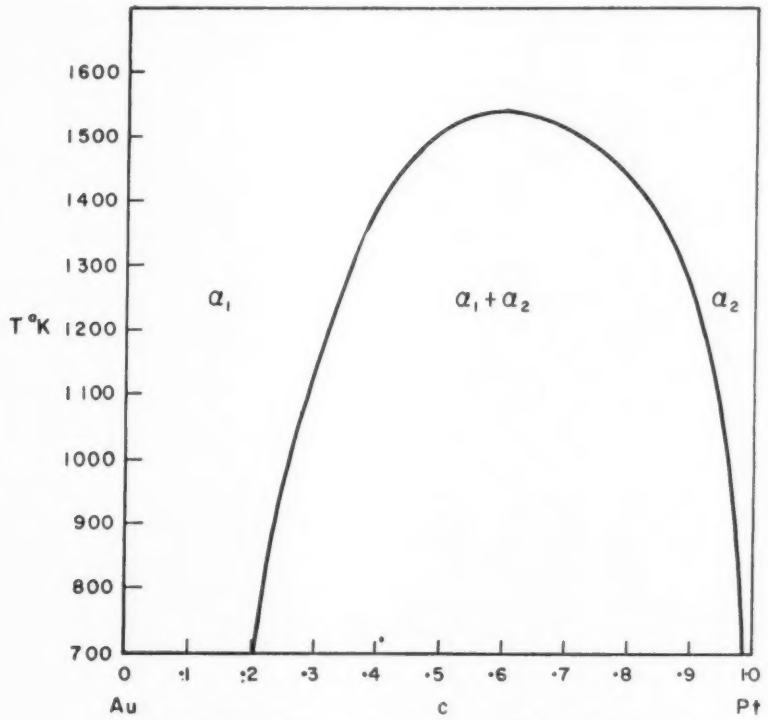


FIG. 1. Phase diagram of Pt–Au system.[6] Both phases are f.c.c.

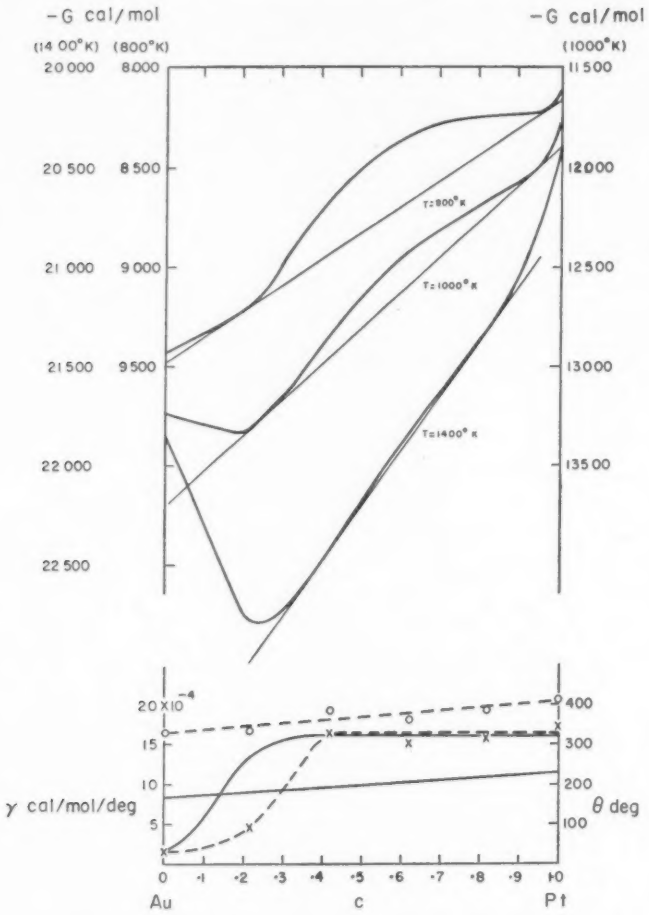


FIG. 2. Free energy per mole versus concentration for the Au–Pt system at 800, 1000, and 1400°K. The common tangents determine the phase boundaries. Included are the variation of $\theta$ and $\gamma$ with concentration (solid lines) as well as the observed variation of $\theta$ and $\gamma$ for Cu–Ni (broken lines).

face-centered cubic phases and in particular the asymmetric segregation. The total free energy, $G$, of a homogeneous alloy system is taken as

$$G(c,T) = -\frac{5{\cdot}11T}{\chi(c)+0{\cdot}221}+\frac{9}{8}R\theta(c)-\frac{\gamma(c)T^2}{2}+$$
$$+RT\{c\ln c+(1-c)\ln(1-c)\}+$$
$$+c(1-c)6R(V_{AA}+V_{BB}-2V_{AB})/k-$$
$$-RA\{[3T/2-\theta(c)]^2+(3/4)T^2\}$$

where $c$ is the concentration (in this case platinum); $\theta$ the Debye temperature; $\gamma$ the electronic specific heat coefficient; $V_{AA}$, $V_{BB}$, and $V_{AB}$ the nearest-neighbor potentials, assumed independent of $c$, and $\chi = \theta/T$. The first term above is an analytic Debye free-energy expression valid to within 1 per cent from $\chi = 0{\cdot}1$ to $0{\cdot}5$, the second term arises from the zero point oscillations, the third term is the electronic contribution, the fourth term divided by $T$ the entropy of mixing, the fifth term the

total heat of mixing,* and the sixth term is a correction of the Debye free-energy due to lattice expansion ($A = 10^{-4}$). For this alloy system no data are available on the variation with concentration of $\theta$, $\gamma$, and the enthalpy of mixing, and we have proceeded as follows. Firstly, as in the Cu–Ni system,[7] we assumed $\theta$ to vary linearly from gold ($\theta = 164$) to platinum ($\theta = 233$) (Fig. 2). The $\theta$ values of copper and gold and of platinum and nickel are inversely proportional to the square root of their masses, indicating similar force constants. Secondly (as in the Cu–Ni system)[7] we assumed $\gamma$ to be constant from $c = 0{\cdot}4$ to $1{\cdot}0$ and equal to the measured value for pure platinum $16{\cdot}2\times10^{-4}$ cal/mole/deg. At the maxima of the segregation region in the phase diagram, we expect $\partial^2G/\partial c^2=0$ ($T=1535$°K and $c=0{\cdot}615$) and this yields a value of $6R(V_{AA}+V_{BB}-2V_{AB})/k = 6087$ cal/mole (positive). In order to determine the value of $\gamma$ from $c = 0$ to $c = 0{\cdot}4$, assuming that it varies smoothly from its value for pure gold ($1{\cdot}67\times10^{-4}$ cal/mole/deg) to the value at $c = 0{\cdot}4$, we plotted the free energy at $T = 1000$°K where the chemical potentials at $c = 0{\cdot}26$; $0{\cdot}97$ are equal and adjusted the $\gamma$ in the range up to $c = 0{\cdot}4$ to yield this. The chosen variation of $\gamma$ with concentration is shown in Fig. 2, together with the measured values of $\gamma$ for Cu–Ni alloys. In both alloys the filling of the $d$ band is clearly shown with the rapid decrease in $\gamma$, but appears to occur at lower concentrations in Au–Pt alloys. With this chosen variation of $\gamma(c)$ the free energies and the common tangents which determine the phase boundaries were determined at 800 and 1400°K. They are shown in Fig. 2 and give good agreement with the observed phase diagram.

From this analysis we have extracted the value of the segregation potential, as well as the necessary variation of $\gamma$ to give agreement with the observed phase diagram. In particular this system owes its asymmetric segregation curve to the filling of the $d$ band.

The Cu–Ni system currently under investigation appears to segregate, but with a much smaller segregation potential.

* The terms linear in $c$ are neglected, since they do not affect the phase boundaries.

## REFERENCES


1. Tauer K. J. and Weiss R. J. *Phys. Rev.* **100,** 1223 (1955).
2. Weiss R. J. and Tauer K. J. *Phys. Rev.* **102,** 1490 (1956).
3. Hofman J. A., Paskin A., Tauer K. J. and Weiss R. J. *J. Phys. Chem. Solids* **1,** 45 (1956).
4. Tauer K. J. and Weiss R. J. *J. Phys. Chem. Solids* **2,** 237 (1957).
5. Weiss R. J. and Tauer K. J. *J. Phys. Chem. Solids* **3,** (1957).
6. Tiedema T. J., Bouman J., and Burgers W. G. *Acta Met.* **5,** 310 (1957).
7. Keesom W. H. and Kurrelmeyer B. *Phys. Rev.* **57,** 1068 (1940).

*J. Phys. Chem. Solids* Pergamon Press 1958. Vol. 7. pp. 252–258.

# DISPERSION THEORY FOR ELECTRONS IN A RANDOM LATTICE WITH APPLICATIONS TO THE ELECTRONIC STRUCTURE OF ALLOYS*

J. KORRINGA

Department of Physics and Astronomy, The Ohio State University, Columbus, Ohio

(*Received* 23 *January* 1958)

VOL. 7 1958

**Abstract**—In a three dimensional atomic lattice, occupied at random by atoms of more than one kind, a complete set of approximate solutions of the one-electron Schrödinger equation is obtained that have the periodicity of a Bloch wave in the average. Equations are given that permit the calculation of their energies, their average behavior, apart from a phase factor, near an atom of any type, and of a damping parameter for each wave. A correspondence is established between a random A–B lattice and a periodic lattice with a complex, energy dependent, potential. The eigenvalue problem in this potential, which can be solved with any of the known methods for a periodic potential, yields the dispersion relation of the system.

## 1. INTRODUCTION

EXISTING theories for electron states in a disordered alloy are very primitive compared to those for a pure metal. The powerful methods, like the Wigner and Seitz method and the orthogonalized plane wave method, cannot be used, because they are based on Bloch's theorem for electron states in a periodic potential. The purpose of this paper is to show that the calculations by means of interference of freely travelling multipole waves and their scattering by the individual atoms,[1] which is known to give exact results for a pure metal,[2] can in a good approximation be applied to alloys when use is made of a statistical generalization of Bloch's theorem.

The new element in our approach, as compared with various known treatments of a random one-dimensional lattice[3] or of diluted alloys[4] is, that an attempt is being made to apply dispersion theory in a medium that is defined in statistical terms.

## 2. QUASI PERIODIC WAVES

Let a simple atomic lattice be occupied by atoms of type A and B in concentrations $c_A$ and $c_B = 1-c_A$ in a random distribution. Let $V(X, Y, Z)$ be the effective potential for an electron in this lattice. We want to find an electron wave that has the symmetry of a Bloch wave with wave vector $\boldsymbol{k}$ in the statistical average, and that is an approximate solution of Schrödinger's equation in this potential.

To this end we divide the lattice into atomic polyhedra, to be called cells in the following. A cell $i$ containing the lattice point $\boldsymbol{R}_i$ will be called an A(B) cell when it is occupied by an A(B) atom. In any cell we will use Cartesian coordinates $\boldsymbol{r}(x, y, z)$ with the corresponding lattice point as origin. The potential in cell $i$ is:

$$V^i(\boldsymbol{r}) = V(\boldsymbol{R}_i+\boldsymbol{r}).$$

For the exact wave function $\psi_k(X, Y, Z)$ we write similarly in cell $i$:

$$\psi_k{}^i(\boldsymbol{r}) = \psi_k(\boldsymbol{R}_i+\boldsymbol{r}).$$

The potential in an A cell is in general quite different from the potential in a B cell. The potentials in two A cells or two B cells show differences also, which are primarily due to differences in the distribution of atoms in the close vicinity.

In a perfect A or B lattice a Bloch wave with wave vector $\boldsymbol{k}$ would satisfy the relation:

$$\psi_k{}^i(\boldsymbol{r}) = \psi_k{}^j(\boldsymbol{r}) \exp i\boldsymbol{k}\cdot(\boldsymbol{R}_j-\boldsymbol{R}_i). \text{ (perfect lattice) (1)}$$

* This research was assisted by the United States Atomic Energy Commission.

In a random A–B lattice the phase factors in (1) as well as the local variations of $\psi$, its norm included, are disturbed. These two effects will tentatively be attributed to distinct properties of the configuration. Besides the large differences in cells of different type, smaller variations between the $\psi^i$ in cells of the same type occur due to differences in the grouping of atoms in the close vicinity. On the other hand, the relation between the phases in different cells is influenced primarily by the grouping of A and B atoms in the region "between" the two cells. With a proper choice of phases $\phi_i$ in the expression

$$\psi_k{}^i(\boldsymbol{r}) = u_k{}^i(\boldsymbol{r}) \exp(-i\boldsymbol{k}\cdot\boldsymbol{R}_i + i\phi_i) \tag{2}$$

one may therefore hope to ensure that the differences between the functions $u^i$, to be called amplitude functions in the following, for cells of the same type, are entirely due to the local groupings of atoms. A mathematical definition of the phases $\phi_i$ in (2) can be attempted from the requirement that the average of $u_k{}^i(\boldsymbol{r})$ over all A cells,

$$u_k{}^{\mathrm{A}}(\boldsymbol{r}) = \frac{1}{Nc_{\mathrm{A}}} \sum_{i\epsilon\mathrm{A}} u_k{}^i(\boldsymbol{r}), \tag{3}$$

is a solution of Schrödinger's equation in the average potential

$$V^{\mathrm{A}}(\boldsymbol{r}) = \frac{1}{Nc_{\mathrm{A}}} \sum_{i\epsilon\mathrm{A}} V^i(\boldsymbol{r}),$$

with an eigenvalue parameter equal to the exact and unknown energy $E(\boldsymbol{k})$ of the state $\psi_k(X, Y, Z)$, and where, as an obvious requirement, the norm of $u_k{}^{\mathrm{A}}(\boldsymbol{r})$ in a cell should be the average of the norms of $u_k{}^i(\boldsymbol{r})$:

$$\int_{\text{cell}} |u_k{}^{\mathrm{A}}|^2 d\boldsymbol{r} = \frac{1}{Nc_{\mathrm{A}}} \sum_{i\epsilon\mathrm{A}} \int_{\text{cell}} |u_k{}^i|^2 d\boldsymbol{r}. \tag{4}$$

Similar relations should hold for the average $u_k{}^{\mathrm{B}}(\boldsymbol{r})$ over all B-cells. We will assume in the following, without proof, that this can be achieved with a high degree of accuracy, but we have to contend with the possibility that the $\phi_i$ may have small imaginary parts. As this is undesirable in the following, we will avoid such imaginary parts in $\phi_i$ by allowing the potential $V^{\mathrm{A}}$, in which $u^{\mathrm{A}}$ must be a solution of Schrödinger's equation, to have the more general average form:

$$V^{\mathrm{A}}(\boldsymbol{r}) = \frac{1}{Nc_{\mathrm{A}}} \sum_{i\epsilon\mathrm{A}} V^i(\boldsymbol{r}) \exp\mu_i, \tag{5}$$

where $\mu_i$ are unknown small real quantities depending on the configuration. A justification of this procedure is given in the next section.

Such a choice of the $\phi_i$ thus enables one to calculate $u^{\mathrm{A}}$ and $u^{\mathrm{B}}$ for given $V^{\mathrm{A}}$ and $V^{\mathrm{B}}$, provided boundary conditions on the cell surface can be specified that are characteristic for the periodicity $\boldsymbol{k}$ and for an "average" distribution of A and B atoms around any one cell. With the potential $V^{\mathrm{A}}$ one can deal, in principle, by starting with the atomic potentials, taking into account an estimated charge transfer, and using the well-known iteration process aiming at self-consistency. The proper boundary conditions, on the other hand, can be obtained from the distribution of phases $\phi_i$ throughout the lattice. This will be shown, in an indirect manner, in Section 4.

### 3. STATISTICAL DISTRIBUTION OF THE PHASES

A basic property of the phases $\phi_i$ introduced in the previous section is that the average of $\phi_i - \phi_j$ over all pairs of A atoms in the lattice with fixed displacement $\boldsymbol{R}_i - \boldsymbol{R}_j = \boldsymbol{R}_{ij}$ is zero:

$$\frac{1}{Nc_{\mathrm{A}}{}^2} \sum_{\substack{i,j\epsilon\mathrm{A} \\ \boldsymbol{R}_i - \boldsymbol{R}_j = \boldsymbol{R}_{ij}}} (\phi_i - \phi_j) = 0 \tag{6}$$

and similarly for B. This property will be used as a definition of the pseudo-periodicity $\boldsymbol{k}$, i.e., as a means to single out a state $\psi_k$ from all other states $\psi_{k'}$. The individual phase differences for fixed $\boldsymbol{R}_{ij}$ will be treated as a random variable, to be described by a statistical distribution function $f_{ij}(\phi)$.

We will now derive an analytical expression for $f_{ij}$ for large $R_{ij}$, without considering in detail all possible atomic distributions. To this end we compare the differences between the phases in three lattice points, $i, j$ and $n$, for which $\boldsymbol{R}_{ij} = \boldsymbol{R}_{jn}$. Obviously one has

$$\phi_i - \phi_n = (\phi_i - \phi_j) + (\phi_j - \phi_n). \tag{7}$$

By moving the point $i$ through the random lattice, both terms in the right-hand side of (7) take on

different values with probabilities described by the distribution function $f_{ij}$. We assume now that the phase differences $\phi_i-\phi_j$ and $\phi_j-\phi_n$ are uncorrelated. This assumption, which is very important for the following, is based on the qualitative notion that the phase differences for two lattice points can be attributed to the deviation of the actual distribution of atoms from that of a superlattice (if $c_A$ and $c_B$ have a simple ratio) in the region "between" the two points. This does not refer to the distribution of atoms on the line between $i$ and $j$, but rather to all atoms between planes through $i$ and $j$ perpendicular to $\boldsymbol{R}_{ij}$. This leads to statistical independence of $\phi_i-\phi_j$ and $\phi_j-\phi_n$ in the case that the points $i, j$ and $n$ are on one line, and in that case only.

From this assumption it follows that the variance $\sigma_{ij}$ of the distribution $f_{ij}$, defined by

$$\sigma_{ij}^2 = \int_{-\infty}^{+\infty} \phi^2 f_{ij}(\phi)\, d\phi, \tag{8}$$

satisfies the relation

$$\sigma_{in}^2 = \sigma_{ij}^2 + \sigma_{jn}^2 \qquad (\boldsymbol{R}_{ij} \| \boldsymbol{R}_{jn}). \tag{9}$$

Consequently, $\sigma_{ij}^2$ is a homogeneous function of the first degree in $|X_i-X_j|$, $|Y_i-Y_j|$, $|Z_i-Z_j|$. Limiting ourselves to crystals with a high degree of symmetry, such as an FCC, BCC or HCP lattice, the possibility that $\sigma_{ij}^2$ depends on the orientation of $\boldsymbol{R}_{ij}$ with respect to the crystalline axis can be disregarded. This leads to:

$$\sigma_{ij}^2 = \alpha R_{ij} F(\theta), \tag{10}$$

where $\theta$ is the angle between the vectors $\boldsymbol{k}$ and $\boldsymbol{R}_{ij}$. From simple considerations about the scattering of a plane wave at randomly distributed scattering centers one can see that the errors in phase in a direction parallel and perpendicular to the wave are of the same order of magnitude, i.e.,

$$F(\pi/2)/F(0) = \mathcal{O}(1). \tag{11}$$

As we have not solved the statistical problem of finding $F(\theta)$, and an analytic expression for $\sigma_{ij}^2$ is required in the following, we will simply take as a reasonable approximation $F(\theta) \equiv 1$, so that we obtain

$$\sigma_{ij}^2 = \alpha R_{ij}, \tag{12}$$

where $\alpha$ is an unknown positive parameter which depends on the wave vector $\boldsymbol{k}$, the nature and the concentration of atoms A and B and on the lattice structure.

According to equation (12) the random variations in $\phi_i-\phi_j$ increase indefinitely with increasing $\boldsymbol{R}_{ij}$, but still they become small compared to the leading phase term $\boldsymbol{k}\cdot\boldsymbol{R}_{ij}$. Therefore the overall character of the wave is preserved, and a corresponding preferred direction, characterized by $\boldsymbol{k}$, prevails approximately in all cells. This result is consistent with our assumption that the variations in the $u^i$ from cell to cell are small and local.

Finally, using the Central Limit theorem of probability, one finds that for $R_{ij}$ large compared with the lattice constant $a$, $\phi_j-\phi_i$, being the sum of a large number of statistically independent random variables, approaches asymptotically a normal distribution:

$$f_{ij}(\phi) = \frac{1}{\sigma_{ij}\sqrt{2\pi}} \exp(-\phi^2/2\sigma_{ij}^2) \,.\, (R_{ij}/a \gg 1). \tag{13}$$

As a reasonable approximation we will, in the following, apply equation (13) for all distances $R_{ij}$ in the lattice.

In contrast with this statistical distribution of $\phi_i-\phi_j$, which has a variance that increases as the square root of the distance, the quantities $\mu_i$ introduced in equation (5) will have only small fluctuations around the average value $\langle\mu_i\rangle = 0$, and the distribution function of $\mu_i-\mu_j$ is independent of the distance. $\mu_i-\mu_j$ represents the logarithmic ratio of the normalization constants of $\psi$ in different cells, and large statistical variations with the distance would imply that the average probability density of $\psi$ over many cells could show large variations throughout the lattice, an extremely unlikely situation in a random system. This supports our argument that the normalization constants are primarily connected with the grouping of atoms in the vicinity. Thus, the quantities $\mu_i-\mu_j$ can be considered as being statistically independent of the phases $\phi_i-\phi_j$, and as having a distribution function independent of $R_{ij}$. This is the reason why they can be used to eliminate possible imaginary parts in the $\phi_i$.

### 4. MULTIPOLE EXPANSION OF $\psi$

In order to calculate the energy $E(\boldsymbol{k})$, the statistical parameter $\alpha(\boldsymbol{k})$ and the average wave function

$u_k^{\mathrm{A}}(\boldsymbol{r})$ and $u_k^{\mathrm{B}}(\boldsymbol{r})$, we will now transform the exact Schrödinger equation by means of a multipole wave expansion. To this end we consider each atom $i$ in the lattice as a center of outgoing multipole waves, travelling freely in a constant potential $V_0$, and having a fixed wave number $k_0$ and corresponding energy

$$E=\frac{\hbar^2}{2m}k_0^2+V_0. \tag{14}$$

Let $\boldsymbol{a}^i \equiv a_{lm}{}^i$ be the coefficient for the angular quantum numbers $l$ and $m$ of atom $i$ in this expansion. We use a vector notation for these coefficients. The superposition, near an atom $j$, of these waves emerging from all other atoms can be expanded in free non-singular multipole waves with respect to this lattice point. The coefficients in this expansion, $\boldsymbol{b}^j \equiv b^j{}_{l'm'}$, are linear combinations of the $\boldsymbol{a}^i$.

$$\boldsymbol{b}^j=\sum_{i\neq j}\Gamma^{ji}\boldsymbol{a}^i \tag{15}$$

where the elements $\Gamma_{l'm'lm}{}^{ji}$ of the matrix $\Gamma^{ji}$ depend on $\boldsymbol{R}_j-\boldsymbol{R}_i$ and on $E$. A second set of linear relations between the $\boldsymbol{a}^j$ and $\boldsymbol{b}^j$, with fixed $j$, is obtained from the condition that the wave going out from atom $j$ and the non-singular wave arriving at $j$ satisfy the scattering problem of an electron with energy $E$ at a potential field equal to the lattice potential in the polyhedron $j$ and embedded in the constant potential $V_0$. This leads, in general, to relations of the form:

$$\boldsymbol{a}^j=U^j\boldsymbol{b}^j \tag{16}$$

where the matrix $U^j$ depends on the shape of the cell, on the lattice potential inside the cell and on $E$. The requirement that the linear homogeneous equations

$$\sum_i(\Gamma^{ji}-(U^j)^{-1}\delta_{ij})\boldsymbol{a}^i=0 \tag{17}$$

have a solution, yields the energy $E$ of all the stationary states.

The correctness of this procedure, for an arbitrary but fixed array of atoms, can best be seen from a limiting procedure.[1] We separate all the polyhedra by a simply connected region $\Omega$ in which there is a constant potential $V_0$. A solution $(\boldsymbol{a}^i, \boldsymbol{b}^i, E)$ of the above equations is analytic in $\Omega$, and its continuation inside all the cells satisfies Schrödinger's equation. Subsequently we let $\Omega$ go to zero.

The equations (17) are of course quite useless unless there is a high degree of order. For a perfect atomic lattice solutions of the form

$$\boldsymbol{a}^i=\boldsymbol{a}^j\exp i\boldsymbol{k}\cdot(\boldsymbol{R}_j-\boldsymbol{R}_i) \tag{18}$$

exist, for which the equation (17) for all $j$ become equivalent. The lattice sums can be evaluated readily in this case, but even then a simplification of the scattering problem is highly desirable. It is customary to approximate the scattering potential by one of spherical symmetry, for which $U$ becomes a diagonal matrix.

For the random A–B lattice we take an average of (17), for the A and B atoms respectively, seeking a solution with quasi periodicity $\boldsymbol{k}$. Writing

$$\boldsymbol{a}^j=\hat{\boldsymbol{a}}^j\exp(-i\boldsymbol{k}\cdot\boldsymbol{R}_j+i\phi_j) \tag{19}$$

and summing over the A and B cells respectively, we obtain:

$$\frac{1}{Nc_{\mathrm{A}}}\sum_{j\in\mathrm{A}}(U^j)^{-1}\hat{\boldsymbol{a}}^j=\frac{1}{Nc_{\mathrm{A}}}\left(\sum_{\substack{i,j\in\mathrm{A}\\ i\neq j}}+\sum_{\substack{j\in\mathrm{A}\\ i\in\mathrm{B}}}\right)\Gamma^{ji}\times$$

$$\times\exp i[\boldsymbol{k}\cdot(\boldsymbol{R}_j-\boldsymbol{R}_i)+\phi_i-\phi_j]\hat{\boldsymbol{a}}^i \tag{20}$$

and a similar equation for B.

When the phases $\phi_i$ are chosen as stipulated earlier, we have:

$$\frac{1}{Nc_{\mathrm{A}}}\sum_{j\in\mathrm{A}}(U^j)^{-1}\hat{\boldsymbol{a}}^j=(U^{\mathrm{A}})^{-1}\hat{\boldsymbol{a}}^{\mathrm{A}} \tag{21}$$

where $U^{\mathrm{A}}$ is the scattering matrix of the average A cell with a potential $V^{\mathrm{A}}$ given by equation (5), and where $\hat{\boldsymbol{a}}^{\mathrm{A}}$ are the multipole coefficients belonging to the average amplitude function of $\psi_{\boldsymbol{k}}$ in an A cell. In the right-hand member of (20), since $\Gamma^{ji}$ is a function of $\boldsymbol{R}_j-\boldsymbol{R}_i$, the double sums can be carried out for fixed $\boldsymbol{R}_j-\boldsymbol{R}_i$ first. Then we have:

$$\frac{1}{Nc_{\mathrm{A}}}\sum_{\substack{i,j\in\mathrm{A}\\ \boldsymbol{R}_i-\boldsymbol{R}_j-\boldsymbol{R}_n\neq 0}}\exp i(\phi_i-\phi_j)\hat{\boldsymbol{a}}^i$$

$$=c_{\mathrm{A}}\langle\exp i(\phi_i-\phi_j)\rangle_{\mathrm{av}}\hat{\boldsymbol{a}}^{\mathrm{A}}, \tag{22}$$

because, as was discussed in Section 3, the variations in $\phi_i-\phi_j$ are statistically independent of the

variations in $\hat{\boldsymbol{a}}^t$, the latter reflecting variations in the wave functions due to the local grouping of atoms. From (13) we obtain:

$$\langle \exp i(\phi_i - \phi_j) \rangle_{\mathrm{av}} = \exp -\alpha R_{ij}. \tag{23}$$

Inserting (21)–(23), equation (20) becomes:

$$(U^{\mathrm{A}})^{-1}\hat{\boldsymbol{a}}^{\mathrm{A}} = \sum_{R_n \neq 0} \Gamma^n \exp(-i\boldsymbol{k}\cdot\boldsymbol{R}_n - \alpha R_n) \times \times (c_{\mathrm{A}}\hat{\boldsymbol{a}}^{\mathrm{A}} + c_B\hat{\boldsymbol{a}}^{\mathrm{B}}), \tag{24}$$

where the sum now extends over all lattice points except $\boldsymbol{R}_n = 0$. In the corresponding equation for $\hat{\boldsymbol{a}}^{\mathrm{B}}$ the right-hand member is identical with that in equation (24). From this we obtain:

$$(U^{\mathrm{A}})^{-1}\hat{\boldsymbol{a}}^{\mathrm{A}} = (U^{\mathrm{B}})^{-1}\hat{\boldsymbol{a}}^{\mathrm{B}} \tag{25}$$

or

$$\hat{\boldsymbol{b}}^{\mathrm{A}} = \hat{\boldsymbol{b}}^{\mathrm{B}}, \tag{26}$$

and, writing

$$\boldsymbol{\gamma} = c_{\mathrm{A}}\hat{\boldsymbol{a}}^{\mathrm{A}} + c_{\mathrm{B}}\hat{\boldsymbol{a}}^{\mathrm{B}} \tag{27}$$

we find:

$$(c_{\mathrm{A}}U^{\mathrm{A}} + c_B U^{\mathrm{B}})^{-1}\boldsymbol{\gamma} = \left[\sum_{R_n \neq 0} \Gamma^n \exp(-i\boldsymbol{k}\cdot\boldsymbol{R}_n - \alpha R_n)\right]\boldsymbol{\gamma}. \tag{28}$$

Equations (25)–(28) are our final general equations. The difference between (28) and the corresponding equation for a perfect lattice is twofold; the scattering matrix $U$ has been replaced by its average for the two types of atoms, and the summand in the right-hand side has an extra factor $\exp -\alpha R_n$. It is significant that these changes occur in combination, because with $\alpha = 0$ the determinant $\mathscr{D}$ of equation (28) would no longer have zero points for real values of the energy $E$ or wave number $k_0$. In fact, from the equation $\mathscr{D} = 0$ one can calculate, for given $U^{\mathrm{A}}$ and $U^{\mathrm{B}}$, both real parameters $E(\boldsymbol{k})$ and $\alpha(\boldsymbol{k})$. By varying $\boldsymbol{k}$, equation (28) thus gives the energy in each band, together with, for every state, the parameter $\alpha$, which represents obviously a kind of damping of the wave. As stated before, the potentials $V^{\mathrm{A}}$ and $V^{\mathrm{B}}$, and thereby the scattering matrices $U^{\mathrm{A}}$ and $U^{\mathrm{B}}$, can be obtained in principle from a self-consistency requirement, although this is a very involved procedure. This is the reason that the random variables $\mu_t$, introduced with equation (5), no longer appear in our final equations.

The orthogonality of states $\psi_k$ with different $\boldsymbol{k}$ is obvious. Different states with the same $\boldsymbol{k}$ correspond to different bands in the solid. Small non-orthogonality terms between them may have been produced by our approximations. We have not verified this point.

## 5. APPROXIMATE EVALUATION OF THE LATTICE SUMS

As is well known, the lattice sums appearing in equation (28) can be obtained from the sum

$$S(x, y, z) = \sum_{R_n \neq 0} \left[\frac{\exp(-i\boldsymbol{k}\cdot\boldsymbol{R}_n - \alpha R_n - ik_0|\boldsymbol{R}_n - \boldsymbol{r}|)}{ik_0|\boldsymbol{R}_n - \boldsymbol{r}|}\right]. \tag{29}$$

We have indeed (cf. Ref. 1):

$$\sum_{R_n \neq 0} \Gamma^{n}{}_{l'm'lm} \exp(-i\boldsymbol{k}\cdot\boldsymbol{R}_n - \alpha R_n) = (-1)^m(2l+1)\epsilon_m \frac{(l-|m|)!}{(l+|m|)!} \times \times [(P_l^{|m|}Q_m P_{l'}^{|m'|}Q_{m'})_{\mathrm{op}} S(\boldsymbol{r})]_{\boldsymbol{r}=0} \tag{30}$$

where $\epsilon_0 = 1$, $\epsilon_m = 2 (m \neq 0)$, and where

$$(P_l^{|m|})_{\mathrm{op}} = P_l^{|m|}\left(\frac{\partial}{\partial ik_0 z}\right),$$

$$(Q_m)_{\mathrm{op}} = Q_m\left(\frac{\partial}{\partial ik_0 x}, \frac{\partial}{\partial ik_0 y}\right). \tag{31}$$

$P_l^m(\alpha)$ is the associated Legendre polynomial:

$$P_l^{|m|}(q) = \frac{d^{|m|}}{dq^{|m|}} P_l(q), \tag{32}$$

and

$$Q_m(p, q) = \mathrm{Re}(p+iq)^m \quad (m \geqslant 0)$$
$$Q_m(p, q) = \mathrm{Im}(p+iq)^{|m|} \quad (m \leqslant 0). \tag{33}$$

The methods by means of which $S(\alpha = 0)$ can be transformed into a rapidly converging sum are

not easily generalized to the case $\alpha \neq 0$. Therefore we will resort to the approximation:

$$S \approx S_1 = \frac{\kappa}{k_0} \sum_{R_n \neq 0} \frac{\exp[-i\boldsymbol{k} \cdot \boldsymbol{R}_n - i\kappa|\boldsymbol{R}_n - \boldsymbol{r}|]}{i\kappa|\boldsymbol{R}_n - \boldsymbol{r}|}, \quad (34)$$

where

$$\kappa = k_0 - i\alpha. \quad (35)$$

This gives correctly the contributions for large $R_n$, for all $l'm'lm$. The terms for smaller $R_n$, in which errors occur which are small if $\alpha \ll k_0$, were uncertain already due to the approximations in the statistical treatment of the phases. $S_1$ is, apart from the factor $\kappa/k_0$, the same as the sum $S$ for a perfect lattice, with $\kappa$ replacing $k_0$. This result, which could have been anticipated, shows that the randomness in the lattice causes an effective damping of the multipole waves in their transmission through the crystal. Apart from the factor $\kappa/k_0$, the equation $\mathscr{D} = 0$ becomes an eigenvalue equation for a complex "energy".

$$E' = \frac{\hbar^2}{2m}\kappa^2 + V_0, \quad (36)$$

where

$$\mathrm{Im}(E') = -\frac{\hbar^2}{m} k_0 \alpha < 0. \quad (37)$$

Our calculations do not suggest that an exact treatment of the phase differences for smaller distances would substantiate this picture, although this is certainly not excluded.

For actual calculations with equation (28) it will be necessary to simplify the scattering problem, as is also done for pure metals, by taking a spherically symmetrical scattering potential. Then we have (cf. Ref. 1):

$$U^{\mathrm{A}} = \tfrac{1}{2}\{1 - \exp(-2i\eta_l^{\mathrm{A}})\}\delta_{l'l}\delta_{m'm} \quad (38)$$

where $\eta_l^{\mathrm{A}}$ is the "atomic" scattering phase of order $l$ for the average, spherically symmetric potential in an A cell.

## 6. EQUIVALENCE WITH A PERIODIC COMPLEX POTENTIAL

The analogy with a perfect lattice can be pushed further if one constructs a complex potential for an "average" atom for which the scattering matrix is:

$$U_{\mathrm{eff}} = (1 - i\alpha/k_0)(c_{\mathrm{A}}U^{\mathrm{A}} + c_B U^{\mathrm{B}}). \quad (39)$$

With this potential, which is energy dependant, the problem becomes identical with that for a perfect lattice, but with the understanding that the energy is complex. This opens the possibility of returning to the Wigner and Seitz cell method, or to any other method valid for a periodic lattice. For example, applying the well-known cell boundary conditions corresponding to a periodicity $\boldsymbol{k}$, one can derive $E'(\boldsymbol{k})$ from which the energy $E(\boldsymbol{k})$ and $\alpha(\boldsymbol{k})$ follow. For the corresponding wave function, $\chi_k$ we have from (27):

$$\chi_k = c_{\mathrm{A}} u_k^{\mathrm{A}} + c_B u_k^{\mathrm{B}}, \quad (40)$$

but in order to calculate the amplitude functions $u_k^{\mathrm{A}}$ and $u_k^{\mathrm{B}}$ separately, one has to use equation (26), expressing the fact that the regular waves, corresponding to the wave function in an average A and an average B cell, are identical. The normalization follows from:

$$c_{\mathrm{A}} \int_{\mathrm{cell}} |u_k^{\mathrm{A}}|^2 d\boldsymbol{r} + c_B \int_{\mathrm{cell}} |u_k^{\mathrm{B}}|^2 d\boldsymbol{r} = 1. \quad (41)$$

This solves the problem, at least in principle.

It is perhaps of interest to observe that the effective potential $V_{\mathrm{eff}}$ corresponding to (39) becomes real in the Born approximation. One sees this most easily from the spherical approximation: when $\eta_l \ll 1$, (38) gives

$$(1 - i\alpha/k_0)^{-1} U_{\mathrm{eff}} \approx \tfrac{1}{2}[1 - \exp\{-2i(c_{\mathrm{A}}\eta_l^{\mathrm{A}} + c_B\eta_l^{\mathrm{B}})\}] \times \times \delta_{ll'}\delta_{mm'}, \ (\eta_l^{\mathrm{A}} \ll 1, \ \eta_l^{\mathrm{B}} \ll 1). \quad (42)$$

The potential that gives the phases $c_{\mathrm{A}}\eta_l + c_{\mathrm{B}}\eta_l$ is equal to $c_{\mathrm{A}}V^{\mathrm{A}} + c_{\mathrm{B}}V^{\mathrm{B}}$ because, in this approximation, the $\eta_l$ are equal to the matrix elements of the potential with respect to the incoming wave. The parameter $\alpha$ vanishes in this approximation, because with a real potential the equations have a solution $\alpha = 0$.

## 7. DISCUSSION

The relatively simple results which we propose to use for the calculation of electron states in alloys have been obtained at the expense of many assumptions and approximations. It seems to us that the final results, as formulated in Section 6,

justify the means, at least when $c_A$ and $c_B$ are of the same order of magnitude, and that further theoretical work should be aimed at a more rigorous and less intuitive derivation. The vanishing of $\alpha$ in the Born approximation corresponds to the fact that the resistance is proportional to the square of the scattering matrix element. It is obvious that a large value of $\eta$, indicating a resonance, will give a strong "damping" of the wave in proportion to the concentration. The value of $\alpha$ for states near the Fermi level is of course a measure for the resistivity, and so our result corresponds to the well-known fact[5] that a resonance near the Fermi level leads to an anomalously large atomic resistivity increase. The question whether our formulas are valid for very low concentrations of an impurity requires a further investigation. Good approximations are available for this case[6] because the close surroundings of all impurity atoms are identical.

For applications to the calculation of the binding energy of alloys one must keep in mind that we have dealt only with the electronic contributions. All the difficulties connected with the interaction between ionic cores and with lattice strain remain.

Finally, we wish to point out that our results, though derived for electron waves in a lattice, can without difficulty be adapted to the treatment of electromagnetic and neutron waves.

*Acknowledgement*—The author is indebted to Dr. J. O. BETTERTON, of the Oak Ridge National Laboratories, for discussions connected with subcontract 2001 under W-7405-eng-26 of the Union Carbide Nuclear Company, from which this study originated. This work was assisted in part by the United States Atomic Energy Commission through Contract No. AT(11-1)-191 with the Ohio State University Research Foundation.

## REFERENCES

1. KORRINGA J. *Physica* **13,** 392 (1947).
2. KOHN W. and ROSTOKER N. *Phys. Rev.* **94,** 1111 (1954).
3. KERNER E. H. *Proc. Phys. Soc.* A**69,** 234 (1956). SAXON S. D. and HUTNER R. A. Philips Res. Rep. **4,** 82 (1949).
4. PARMENTER R. H. *Phys. Rev.* **97,** 587 (1955).
5. FRIEDEL J. *Canad. J. Phys.* **34,** 1190 (1956).
6. FRIEDEL J. *Advanc. Phys.* **3,** No. 10 446–507 (1954).

*J. Phys. Chem. Solids* Pergamon Press 1958. Vol. 7. pp. 259–267.

# THE ELECTRICAL RESISTIVITY AND SUPERCONDUCTIVITY OF SOME URANIUM ALLOYS AND COMPOUNDS

**B. S. CHANDRASEKHAR and J. K. HULM**

Westinghouse Research Laboratories, Pittsburgh 35, Pennsylvania

(*Received* 2 *May* 1958)

VOL. 7 1958

**Abstract**—The electrical resistivity and superconductivity of a series of α (orthorhombic) and quenched γ (body-centered cubic) binary alloys of uranium with niobium and molybdenum were investigated at temperatures down to 1°K. Anomalous resistivity behavior occurs in both types of structure. The γ- alloys are particularly unusual in possessing a negative temperature coefficient from room temperature down to the superconducting transition point. Both systems exhibit superconducting transitions, the γ-alloys in the vicinity of 2°K and the α-alloys closer to 1°K. Some success was achieved in a qualitative interpretation of the resistive and superconductive properties of the alloys in terms of a hypothetical band structure of uranium.

Ten intermetallic compounds of uranium were also tested for superconductivity down to about 1°K. Four new superconductors were discovered: UCo (1·70°K), $U_6Mn$ (2·32°K), $U_6Fe$ (3·86°K) and $U_6Co$ (2·29°K). The last three compounds are isomorphous and include the first superconducting compounds of manganese and iron.

## 1. INTRODUCTION

THE use of uranium and its alloys as nuclear reactor fuel elements has led to extensive work on the metallurgy of these materials. However, only limited research has been carried out on the electrical properties of the alloys, particularly at low temperatures. Studies of the electrical resistance and superconductivity of uranium itself are reviewed by KATZ and RABINOWITCH.[1] These experiments were hampered by difficulties of purifying the metal and by annealing problems originating in the transformations between various allotropic modifications (Table 1). Superconducting transition temperatures ranging from 1·3°K to 0·68°K were reported by several observers,[2–7] although broad transitions characteristic of non-ideal superconducting behavior were obtained for all the samples investigated.

*Table* 1. *Allotropic modifications of uranium*

| *Phase* | *Temperature range* | *Crystal structure* |
|---|---|---|
| α | Up to 662°C | Orthorhombic |
| β | 662°–769°C | Tetragonal |
| γ | 769°C–1129°C (m.p.) | Body-centered cubic |

The phase diagrams of a large number of binary uranium alloys were described at the Geneva Conference,[8,9] with references to internal reports in which most of the original work appeared. Amongst these alloys there is an important group characterized by extensive solubility at high temperatures, but with no true intermetallic compounds. In this group the second element, for example, titanium, zirconium, niobium or molybdenum, itself possesses a cubic modification. In each alloy system there is a range of composition in which the high temperature cubic or γ-phase may be retained at room temperature by quenching. The β-phase is suppressed for all but the lowest concentrations.

Recently, the effect of neutron irradiation on the electrical resistance of some alloys of this type was studied by BLEIBERG, JONES and LUSTMAN.[10] Apart from irradiation results, these experiments demonstrated that the electrical resistance of the quenched γ-phase in the niobium and molybdenum alloys rises appreciably on cooling from room

temperature to 78°K, an unusual effect for metallic alloys. One of the initial objectives of the present work was to extend measurements on the $\gamma$-phase down to very low temperatures, in order to determine whether the resistivity would continue to rise. Although this proved to be the case over most of the temperature range, the $\gamma$-phase alloys became superconducting in the liquid-helium region, which is somewhat surprising in view of their remarkable resistivity behavior. It will be shown later that some understanding of the electronic structure of both the $\alpha$- and $\gamma$-phase alloys may be obtained by correlating the resistivity and superconductivity data.

Another group of uranium alloys is characterized by the formation of one or more distinct intermetallic compounds, for example with aluminum, manganese, iron, cobalt and nickel. These systems usually exhibit limited solid solubility in each of the terminal phases. In continuation of a general investigation of the occurrence of superconductivity in compounds,[11,12] many of these uranium compounds were tested for superconductivity by a magnetic method down to 1°K. Unfortunately, most of these materials were available only in powder or chip form, which did not permit supporting electrical resistance data to be obtained. However, several interesting new superconductors were discovered, including the first compounds of this type for manganese and iron. In the present paper these results are discussed in the light of certain empirical rules for the existence of superconductivity proposed by MATTHIAS.[13]

## 2. EXPERIMENTAL DETAILS

### 2.1. *Sample preparation*

The alloy samples were in the form of cylindrical rods machined from induction-melted ingots, with the alloy concentration ranging from 0 to 30 at. per cent of niobium or molybdenum. Each of the samples was held at 900°C for 24 hours in an atmosphere of helium gas, and then rapidly quenched in water. This heat treatment homogenizes all the alloys in the $\gamma$-phase. The subsequent quenching produces the following results:

*Uranium–molybdenum alloys*: In the range 0 to about 15 at. per cent Mo, the alloys undergo a martensitic transformation to a base-centered orthorhombic phase which is very similar to $\alpha$-uranium,[8] and for convenience we shall refer to these as the $\alpha$-alloys. Above 15 at. per cent Mo, the $\gamma$-phase is retained on quenching and we shall call these the $\gamma$-alloys.

*Uranium–niobium alloys*: The situation here is exactly similar to that described above, with the $\alpha$–$\gamma$ boundary also in the region of about 15 at. per cent Nb.

It should be pointed out that the above is a simplified description of what actually occurs. In a narrow composition range close to the $\alpha$–$\gamma$ boundary, the quenching will certainly result in a two-phase alloy. But this will not affect our considerations, since we shall not be concerned with the behavior of the alloys in this region, but rather where they are certainly in the $\alpha$- or $\gamma$-phase.

All of the uranium compounds studied in this work were prepared by well-established methods.[1] The intermetallic compounds were mainly supplied by Westinghouse Atomic Power Department as a number of small irregular fragments.

### 2.2. *Electrical resistivity determination*

Resistivities were measured by a conventional current–potential method. Two samples were mounted for this purpose inside a cryostat which permitted their temperature to be held constant at any point between 4·2°K and room temperature. The temperature was measured by a copper-constantan thermocouple, which had been separately calibrated against a standard platinum resistance thermometer.

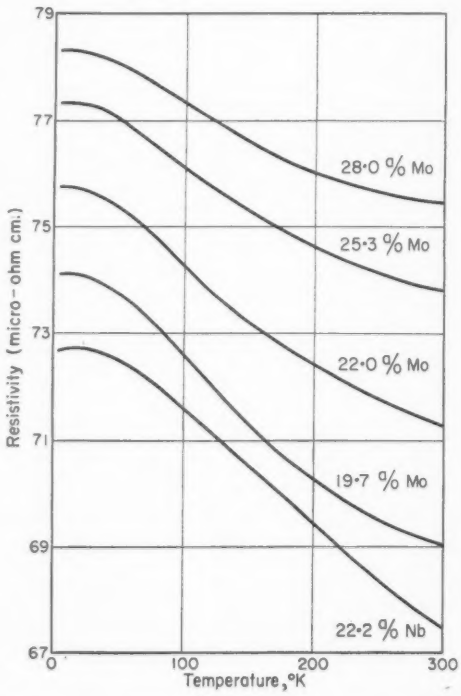


FIG. 1. Resistivity vs. temperature for some typical $\gamma$-phase alloys of uranium. (Each curve is based upon about 30 experimental points.)

*Table 2. Resistivity in μohm cm as a function of temperature for the α-phase alloys*

| Temperature (°K) | Pure U | U+ 9·6% Nb | U+ 14·1% Nb | U+ 2·44% Mo | U+ 7·2% Mo | U+ 11·6% Mo |
|---|---|---|---|---|---|---|
| 298 | 29·09 | 47·72 | 68·22 | 35·58 | 62·03 | 64·98 |
| 77 | 10·11 | 34·68 | 67·26 | 14·53 | 57·94 | 73·90 |
| 4·2 | 3·86 | 26·52 | 65·41 | 7·87 | 56·68 | 71·14 |

### 2.3. *Superconductivity tests*

The samples were tested for superconductivity by a magnetic method using an apparatus which has been described elsewhere.[12] A measuring field of about 5 oersteds was employed and it is believed that the shift in $T_c$ due to the finite field did not exceed 2 per cent (see equation (1), references 12). In most samples this was considerably less than the breadth of the transition due to metallurgical imperfections such as strain and inhomogeneity.

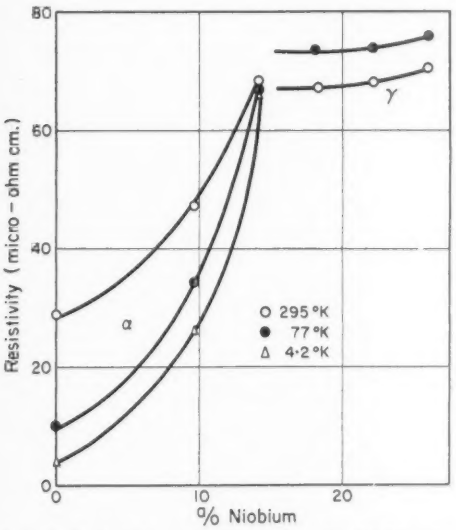


FIG. 2. Resistivity vs. composition for U–Nb alloys at three different temperatures. (The 4·2°K points are essentially coincident with the 77°K points in the γ region and are therefore omitted.)

## 3. RESULTS

### 3.1. *Resistivity data for uranium alloys*

The temperature dependence of the electrical resistivity from room temperature down to 4·2°K for some typical γ-phase alloys in the U–Mo and U–Nb systems is shown in Fig. 1. Results for α-phase samples in the same temperature range are summarized in Table 2. Curves for the change of resistivity with composition at constant temperature are shown in Figs. 2 and 3.

The resistivity curves exhibit a number of striking deviations from the behavior usually found in metallic alloys. The following features are considered significant:

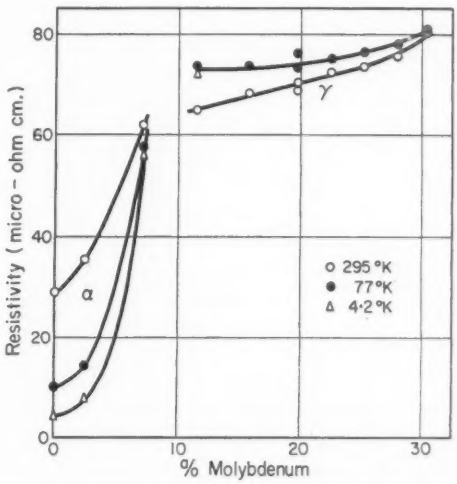


FIG. 3. Resistivity vs. composition for U–Mo alloys at three different temperatures. (Most of the 4·2°K points are essentially coincident with the 77°K points in the γ region and are therefore omitted.)

(1) The resistivities in the γ-phase are high and increase monotonically with decreasing temperature, flattening out as the liquid helium region is approached.

(2) The resistivities in the α-phase show a more normal temperature dependence (Table 2), but the dependence on concentration is anomalous. Thus, Figs. 2 and 3 indicate that $\rho$ is not a linear function

of $c$, as might be expected for a solid-solution alloy at these concentrations.

(3) The transition from the $\alpha$- to the $\gamma$-phase is accompanied by little change in $\rho$, but an abrupt change in $(\partial\rho/\partial c)_T$.

(4) $(\partial\rho/\partial c)$ at 4·2°K for the $\alpha$-molybdenum alloys is appreciably greater than that for the $\alpha$ niobium alloys.

The negative slope of the resistivity–temperature curve confirms the work of BLEIBERG *et al.*[10] and violates the rules of normal alloy behavior. While many examples of a negative temperature coefficient of resistance are reported in the literature,[14] these are usually associated with transitory effects such as the annealing out of imperfections or with crystal structure changes and Curie points. An exception is of course the well-known low temperature resistance minimum in dilute alloys. In the present case the negative slope is definitely associated with a single phase system over the temperature range of the measurements, granting that the system is a quenched, metastable alloy.

Behavior resembling that of the present uranium alloys has been observed in the titanium–niobium system by AMES and MCQUILLAN,[15] in the titanium–vanadium system by BROTZEN *et al.*[16] and in the titanium–molybdenum system by YOSHIDA and TSUYA,[17] although in none of these cases were temperatures below 78°K explored. In the last-mentioned experiments a resistivity maximum was actually observed at certain compositions. For these three systems the negative slope occurs for titanium rich alloys in which a $\beta$- (body-centered cubic) phase is retained by quenching in a fashion similar to the $\gamma$-phase retention procedure for the uranium alloys. It seems likely that the mechanism of the anomalous resistivity has the same origin in both titanium and uranium alloys.

### 3.2. *Superconducting tests on uranium alloys*

Both $\alpha$- and $\gamma$-phase alloys in the uranium–molybdenum and uranium–niobium systems were tested for superconductivity down to temperatures just below 1·0°K. Most of the samples became superconducting, with fairly sharp transitions, even in the case of the quenched $\gamma$-phase samples. A few typical transition curves for $\alpha$- and $\gamma$-U–Mo alloys obtained by measuring the change of induction due to reversal of a field of 5 oersteds are shown in Fig. 4. For these samples the effective permeability in the superconducting state is rather high owing to the large gap between the specimen and the detector coil. However, the permeability values are in all cases consistent with complete superconductivity in the sample material. The transition curves for the $\alpha$- and $\gamma$-U–Nb alloys are very similar to those shown in Fig. 4.

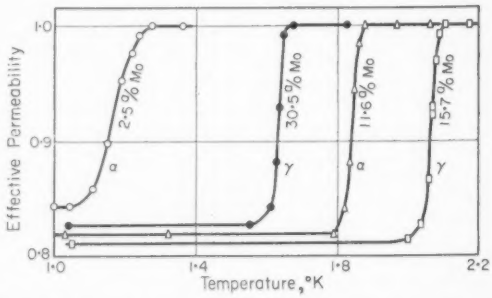


FIG. 4. Effective permeability vs. temperature curves for typical $\alpha$- and $\gamma$-molybdenum alloys, showing the onset of superconductivity (measuring field 5 oersteds).

Efforts were made to obtain critical field data for the samples, since the density of states at the Fermi surface can be derived from the slope of the critical field curve. Unfortunately, all of the samples exhibited quite broad magnetic field transitions, typified by that for the U+28·0 at. per cent molybdenum alloy in Fig. 5, and reliable $H_c$ values could not be obtained. In observations published since our work was done, BERLINCOURT[18] reported that a field of about 30,000 oersteds was required to restore the electrical resistivity of a

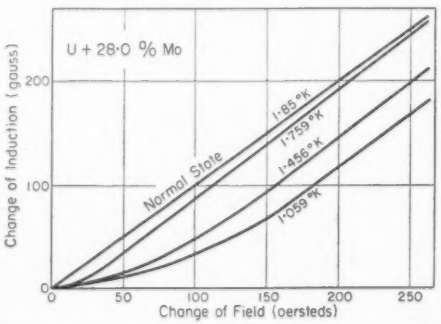


FIG. 5. Change of induction vs. change of field, showing the long drawn out transition to the normal state for U+28·0 at. per cent Mo.

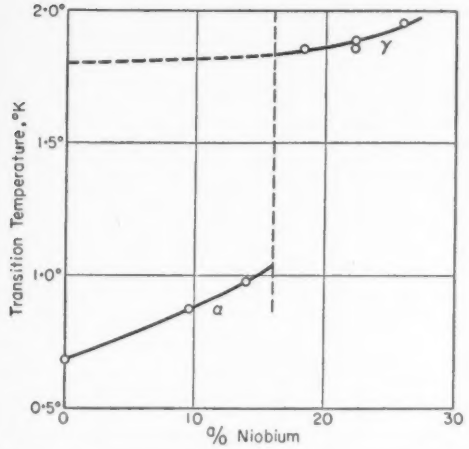


FIG. 6. Superconducting transition temperature vs. composition, U–Nb alloys. (The vertical broken line approximately separates the α and γ regions.)

γ-phase U–Mo alloy at 1·2°K. This high field is probably attributable to the very broad nature of the magnetic field transitions and the well-known alloy behavior that superconducting filaments may exist at fields well above the true critical field.

Figs. 6 and 7 show the variation of transition temperature with composition for both alloy systems. The fairly sharp discontinuity in $T_c$ between the α- and γ-phase regions is well brought out by these curves. A further point of interest is that from Fig. 6 and less unequivocally from Fig. 7 we can get an extrapolated transition temperature for body-centered cubic uranium of about 1·8°K. Pure uranium of course does not exist at low temperatures in the cubic phase, and the value of 1·8°K represents a hypothetical transition temperature belonging to uranium in the body-centered cubic phase. The transition temperature for pure α-uranium can be obtained by extrapolating the curves for the α-alloys below the range of our measurements. This yields a $T_c$ value of 0·7°K, in reasonable agreement with the measurements of HEIN *et al.*[7]

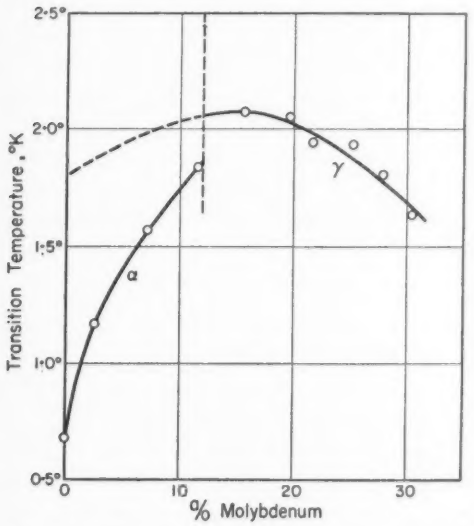


FIG. 7. Superconducting transition temperature vs. composition, U–Mo alloys. (The vertical broken line approximately separates the α and γ regions.)

Figs. 6 and 7 also indicate that the value of $dT_c/dc$, where $T_c$ is the transition temperature and $c$ the concentration of alloying element, is greater for the α-U–Mo alloys than for the α-U–Nb alloys. There is an interesting parallel between this and the behavior of $\partial\rho_0/\partial c$ for these two alloy systems, which was mentioned in the previous section. This similarity in behavior will shortly be discussed in terms of a proposed model of the of the electronic structure of the two alloy systems.

In the uranium–zirconium system it has been reported[19] that a body-centered cubic δ-phase is formed by an ordering reaction upon prolonged annealing. Thus, uranium alloys containing 40, 50, 60, 65, and 70 per cent by weight of zirconium were tested for superconductivity down to 1·08°K. In contrast to the γ-phase alloys, these specimens were normal over the whole range of measurement.

The addition of chromium to uranium tends to stabilize the β-phase,[9] at least for atomic percentages in excess of one. Samples containing 0·3 and 0·6 at. per cent of chromium were tested for superconductivity down to 1·08°K. These samples consisted of mixtures of the α- and β-phases. The lower percentage sample showed a trace of superconductivity (about 20 per cent effect) close to the lowest temperature of measurement, whereas the 0·6 per cent sample was completely normal. It seems probable that the superconductivity behavior was due to the predominant α-phase present in the 0·3 per cent sample.

### 3.3. *Superconducting tests on uranium compounds*

No superconducting compounds of uranium

have previously been reported. In earlier work[12] we tested the compounds UC and UN, which appeared to be favorable to superconductivity on account of their NaCl type structure (isomorphous with NbN). However, both these compounds remained normal down to 1·2°K.

*Table 3. Uranium compounds tested for superconductivity*

| *Compound* | *Structure type* | *Behavior* |
|---|---|---|
| UCo | b.c.c. (distorted CsCl) | S at 1·70°K |
| $U_6Mn$ | b.c. tet. ($U_6Mn$) | S at 2·32°K |
| $U_6Fe$ | b.c. tet. ($U_6Mn$) | S at 3·86°K |
| $U_6Co$ | b.c. tet. ($U_6Mn$) | S at 2·29°K |
| $U_6Ni$ | b.c. tet. ($U_6Mn$) | N to 1·12°K |
| UNi | complex, unknown | N to 1·12°K |
| $UFe_2$ | f.c.c. ($MgCu_2$) | N to 1·06°K |
| $U_2Ti$ | hex. ($AlB_2$) | N to 1·06°K |
| $UAl_2$ | f.c.c. ($MgCu_2$) | N to 1·12°K |
| $U_3Si$ | b.c. tet. | N to 1·10°K |

In the present experiments ten intermetallic compounds were tested for superconductivity down to about 1·1°K, with the results shown in Table 3. The transition curves for the four new superconductors, UCo, $U_6Mn$, $U_6Fe$ and $U_6Co$, are shown in Fig. 8. In some instances the effective

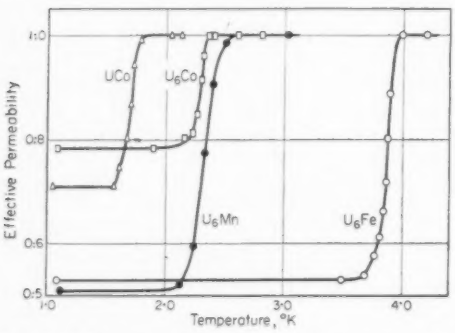


FIG. 8. Effective permeability vs. temperature for four uranium compounds, showing the onset of superconductivity (measuring field 5 oersteds).

permeability in the superconducting region is rather high owing to poor filling of the test coil, but the data obtained for these four samples are consistent with complete superconductivity in the specimen material. For materials of this type the transitions are comparatively sharp and are indicative of fairly good homogeneity of composition.

## 4. DISCUSSION

### 4.1. *The electrical resistivity of the alloys*

The electronic configuration of the free uranium atom has been variously reported[20,21] as $5f^3\ 6d^1\ 7s^2$ and $6d^4\ 7s^2$. In either case, it seems reasonable to assume that the electrons in uranium metal lie in two overlapping bands, after the model for transition metals proposed by MOTT.[22] The Fermi surface would be shared between a low, broad *s*-band and an overlapping band, which we shall for convenience label the *d*-band, with a high density of states $N_d(\zeta)$, where $\zeta$ is the Fermi energy. This certainly is a great simplification of the real state of affairs, but an inspection of the curve of density of states vs. energy for transition metals for which computations have been made, for example tungsten,[23] makes the above model plausible.

The electric current is believed to be carried mainly by the *s*-electrons, since the *d*-electrons are more tightly bound to the ion cores. The *s*-electrons can be scattered into either the *s*-band or the *d*-band, and the relaxation time $\tau_s$ turns out to be determined primarily by the density of states $N_d(\zeta)$ in the *d*-band, and is inversely proportional to it. In a recent discussion of these matters, H. JONES[24] concludes that:

(1) The resistivity is approximately proportional to the density of states in the *d*-band at the Fermi surface, and hence a large value of $N_d(\zeta)$ implies, *ceteris paribus*, a high resistivity.

(2) If, in addition, the slope of the $N_d(E)$ vs. $E$ curve is large at $E = \zeta$, the dependence of Fermi energy on temperature must be taken into account, and it may be shown that the electrical resistivity $\rho$ is given by

$$\rho(\zeta, T) = \rho(\zeta_0, T) \times$$
$$\times \left[1 - \frac{\pi^2 k^2 T^2}{6}\left\{3\left(\frac{1}{N_d}\frac{dN_d}{dE}\right)^2 - \frac{1}{N_d}\frac{d^2N_d}{dE^2}\right\}_{E=\zeta_0}\right], \quad (1)$$

where $\zeta_0$ is the Fermi energy at the absolute zero.

If we assume that uranium has a high density of states at the Fermi surface which also varies rapidly with energy (i.e., large $dN_d/dE$ at $E = \zeta$), then the above equation explains not only the high

VOL. 7 1958

room temperature value of resistivity for pure uranium but also the experimental fact that at higher temperatures the resistivity is not proportional to $T$. Equation (1) predicts resistivity values lower than those which would be expected for simple proportionality to absolute temperatures, and this effect has been observed for several transition metals.

For alloys the resistivity is due to scattering of electrons both by lattice vibrations and by solute atoms. We make the simplifying assumption that these two resistivities are additive, and denote them respectively by $\rho_T$ and $\rho_0$. We note that, in contrast to the behavior of the alloys of the noble metals $\rho_0$ is also dependent on temperature via its dependence on $N_d(\zeta)$; its value should be given by the right-hand side of equation (1) with $\rho_0(\zeta_0)$ substituted for $\rho(\zeta_0, T)$. In this case $\rho_0(\zeta_0)$, the limiting value of $\rho_0(\zeta)$ as $T$ tends to zero, may be represented according to the theory of the resistivity of random solid solutions[25] in the form

$$\rho_0(\zeta_0) \sim N_d(\zeta_0) \cdot c(1-c) \qquad (2)$$

where $c$ is the solute atom concentration. The net result is a total resistivity consisting of a "residual component" $\rho_0$ which decreases with increasing temperature (for a given concentration) and a lattice vibration component $\rho_T$ which increases with increasing temperature, although more slowly than the usual proportionality to $T$.

The above picture allows a qualitative understanding of a number of features of the $\alpha$- and $\gamma$-resistivity curves. One of these is the deviation from Matthiessen's rule in the $\alpha$-region shown by the data of Table 2. Close inspection indicates that the additional resistivity due to a given amount of molybdenum or niobium decreases markedly with increasing temperature, as predicted by equation (1). A second prediction from the model is that for solute concentrations sufficiently large for $\rho_0$ to dominate $\rho_T$, the total resistivity should decrease with increasing temperature, as is found in the $\gamma$-region (Fig. 1). It should be remarked that the application of this model is by no means new, since MOTT[22] has used it to explain the very small temperature coefficient of resistance of constantan, a copper–nickel alloy. The present case, however, appears to provide a test of the theory under a somewhat wider range of conditions.

Considering now the dependence of resistivity on concentration, it is obvious from Figs. 2 and 3 that $\rho_0(\zeta_0)$ measured at 4·2°K is not proportional to $c(1-c)$, as would be expected from proportionality (2) if $N_d(\zeta_0)$ was independent of concentration. Instead the resistivity curve turns upwards quite steeply in the $\alpha$-region and is practically horizontal in the $\gamma$-region. This suggests that with increasing concentration the density of states rises in the $\alpha$-region and falls off again in the $\gamma$-region. Since the $\alpha$-molybdenum resistivity curve climbs more rapidly than the $\alpha$-niobium resistivity curve, evidently there is a more rapid increase of $N_d(\zeta_0)$ in the molybdenum case than in the niobium case. It will shortly be seen that the superconductivity results are also in accord with the density of states variation postulated here.

While the above model seems to provide a consistent picture of the behavior of pure uranium and the $\alpha$- and $\gamma$-alloys,other theoretical proposals have been advanced to explain some of the anomalous resistivity results. According to FRIEDEL,[26] the deviation of the resistivity of $\alpha$-uranium from proportionality to $T$ at high temperatures is due to a weakening of certain covalent bonds in the metal, which permits certain planes of atoms to approach closer and become more strongly bound among themselves. The net result is an increase in the Debye $\Theta$ with increasing temperature. Since $\Theta$ appears in the denominator of the expression for the electrical resistivity, the resistivity is lowered. This model does not appear to explain the anomalous behavior of either the $\alpha$- or $\gamma$-alloys.

COLES[27] has recently suggested that the negative temperature coefficient of resistivity observed for the retained b.c.c. phase in the titanium–niobium system is due to scattering from electron spin disorder. If this is true, the same mechanism would probably operate in the $\gamma$-uranium alloys. However, the theory of this effect has not been worked out in detail.

### 4.2. *The superconducting alloys*

Present theories of superconductivity throw little light on the problem of the influence of crystal structure on superconductivity, even though there is little doubt that for a phenomenon so sensitive to changes of electronic structure, the lattice arrangement plays a vital role. One approach to this problem is to compare the superconducting properties of a material existing in two allotropic

modifications, both of which can be retained at low temperatures. Amongst the elements, only lanthanum exhibits two such modifications which are also superconducting at low temperatures.[28] The f.c.c. phase of lanthanum has a transition at 5·95°K, while the hexagonal phase transition is close to 5·0°K.

For uranium only the α-phase is stable at low temperatures, but the β- and γ-phases may be stabilized by the addition of various other elements. In our experiments, extrapolation to zero impurity content yielded a transition temperature of about 1·8°K for the pure γ-phase, in contrast to 0·68°K for the α-phase.

An empirical formula due to MATTHIAS[13] gives the superconducting transition temperature as

$$T_c \sim C\frac{V^x}{M}T(n),\ 4<x<5, \qquad (3)$$

where $M$ and $V$ are the atomic mass and atomic volume respectively, $T(n)$ is an oscillatory function depending only on the number of valence electrons per atom and $C$ varies over a range of about 20 to 30 per cent for different crystal systems. For comparisons between allotropic forms A and B for a given element we may presume that $M$ and $T(n)$ are unaffected by the change of structure, so that

$$\frac{T_c(\mathrm{A})}{T_c(B)}=\frac{C_\mathrm{A}}{C_B}\left(\frac{V_\mathrm{A}}{V_B}\right)^x. \qquad (4)$$

In lanthanum the f.c.c. form has an atomic volume about one per cent greater than that of the hexagonal modification. The transition temperature of the cubic phase is 19 per cent greater than that of the hexagonal phase. Thus, if we take the volume exponent as 5, the crystal structure factors must differ by 14 per cent which is within the limits set by MATTHIAS.

For uranium the situation is less satisfactory owing to the larger percentage difference in transition temperatures for the α- and γ-phase. Again the atomic volumes differ only by about one per cent, so that we must assume a 264 per cent difference in the crystal structure factors to satisfy equation (4). This is well outside the proposed limits on $C$.

The failure of equation (3) in this instance probably lies in over-simplification of the electronic structure factor $T(n)$. Many workers have emphasized the close connection between $T_c$ and the density of states at the Fermi surface, as determined, for example, from electronic heat capacity measurements. In uranium we have already advocated a steep dependence of $N_d(\zeta)$ on energy at the Fermi surface in order to explain the electrical resistivity behavior. It is not unlikely that with such a steep dependence, the transition from the α- to γ-phase is accompanied by a large change in $N_d(\zeta)$, which in turn causes the observed increase in $T_c$. Confirmation of this point awaits an accurate measurement of the electronic heat capacity coefficient for the α- and γ-alloys.

The actual form of the relationship between $N(\zeta)$ and $T_c$ has recently been discussed by BARDEEN, COOPER and SCHRIEFFER,[29] who propose the formula

$$T_c \sim \exp -\frac{1}{N(\zeta)V_e}, \qquad (5)$$

where $V_e$ is an electron–electron interaction parameter. PINES[30] has argued that for the transition metals $N(\zeta)$ and $V_e$ are decoupled and $V_e$ can be assumed to be approximately independent of $N(\zeta)$. In this case $T_c$ is a monotonically increasing function of $N(\zeta)$.

In our discussion of electrical resistivities it was pointed out that the fact that $\rho_0$ rises more steeply with increasing concentration for the α-uranium–molybdenum alloys than for the α-uranium–niobium alloys (both being non-linear functions of concentration) implies a more rapid increase of $N_d(\zeta)$ with increasing concentration in the first system than in the second system. Combining this with equation (5), we must expect a similar difference in behavior between the $T_c$ vs. composition curves for the two α-alloy systems. This effect is brought out clearly in Figs. 6 and 7.

### 4.3. *The superconducting compounds*

The first superconducting compound containing a ferromagnetic element to be discovered[31] was $CoSi_2$. Superconducting compounds of nickel in the nickel arsenide structure have since been reported.[32,33] The four new superconducting compounds in Table 3 all contain ferromagnetic elements and occur in two structures, distorted CsCl and a new body-centered tetragonal type. It is of special interest that these appear to comprise the first superconducting compounds of manganese

and iron, elements whose presence is usually detrimental to the existence of superconductivity.

The compounds of the $U_6Mn$ type were studied structurally by BAENZIGER *et al.*[34] They have almost identical unit cell volumes and average atomic masses very close to each other, thus forming an almost ideal group to test the valence electron function $T(n)$ in equation (3). In Fig. 9 a plot

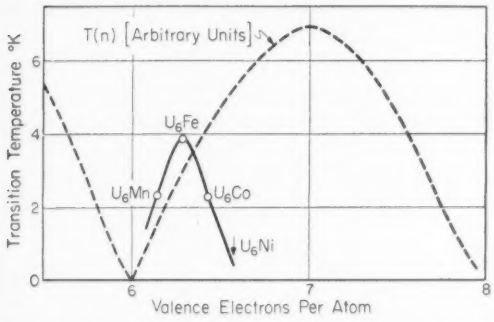


FIG. 9. Superconducting transition temperature as a function of the average number of valence electrons per atom for the $U_6X$ compounds, compared to Matthias' $T(n)$ curve.

of transition temperature vs. the number of valence electrons per atom is compared with the empirical $T(n)$ function proposed by MATTHIAS.

The existence of the maximum in transition temperature confirms the general idea of the oscillatory behavior of $T(n)$. However, the position of the actual maximum is displaced considerably from either of the odd number peaks (5 or 7) proposed by MATTHIAS and in fact lies closer to the proposed minimum in the vicinity of 6. Some modification of equation (3) thus appears to be necessary to attain full agreement with the present results.

*Acknowledgements*—We are grateful to Drs. E. K. HALTEMAN and F. CARD for the loan of the alloy samples, and to Messrs. R. D. BLAUGHER and W. PETRAS for assistance with the experiments.

## REFERENCES

1. KATZ J. J. and RABINOWITCH E. *The Chemistry of Uranium*. McGraw-Hill, New York (1951).
2. ASCHERMANN G. and JUSTI E. *Z. Phys.* **43,** 207 (1942).
3. ALEKSEEVSKII E. and MIGUNOV L. *J. Phys. USSR* **11,** 95 (1947).
4. SHOENBERG D. *Nature, Lond.* **159,** 303 (1947).
5. GOODMAN B. B. and SHOENBERG D. *Nature, Lond.* **165,** 441 (1950).
6. KILPATRICK J. E., HAMMEL E. F. and MAPOTHER D. E. *Phys. Rev.* **97,** 1634 (1955).
7. HEIN R. A., HENRY W. E. and WOLCOTT N. M. *Phys. Rev.* **107,** 1517 (1957).
8. Reactor Technology and Chemical Processing. *Proceedings of the International Conference on the Peaceful Uses of Atomic Energy, Geneva,* 1955, Vol. 9. United Nations, New York (1956).
9. GURINSKY D. H. and DIENES G. J. *Nuclear Fuels*. D. Van Nostrand, New York (1956).
10. BLEIBERG M. L., JONES L. J. and LUSTMAN B. *J. Appl. Phys.* **27,** 1270 (1956).
11. MATTHIAS B. T. and HULM J. K. *Phys. Rev.* **87,** 799 (1952).
12. HARDY G. F. and HULM J. K. *Phys. Rev.* **93,** 1004 (1954).
13. MATTHIAS B. T. *Progress in Low Temperature Physics* Chap. 2. North Holland Publishing Company, Amsterdam (1957).
14. GERRITSEN A. N. *Handbuch der Physik* Vol. 19, page 137. Springer-Verlag, Berlin (1956).
15. AMES S. L. and MCQUILLAN A. D. *Acta Met.* **2,** 831 (1954).
16. BROTZEN F. R., HARMON E. L. and TROIANO A. R. *J. Metals, N.Y.* **203,** 413 (1955).
17. YOSHIDA S. and TSUYA Y. *J. Phys. Soc. Japan* **11,** 1206 (1956).
18. BERLINCOURT T. G. *Proceedings of the International Conference on Low Temperature Physics and Chemistry* Madison, Wis., 1957. To be published (1957).
19. SALLER H. A. and ROUGH F. A. Battelle Memorial Institute Report 1000 A.E.C. (1955).
20. SEABORG G. T. *Nucleonics* **5,** 16 (1949).
21. DAWSON J. K. *Nucleonics* **10,** 39 (1952).
22. MOTT N. F. *Proc. Roy. Soc.* **A153,** 699 (1936).
23. MANNING M. F. and CHODOROW M. I. *Phys. Rev.* **56,** 787 (1939).
24. JONES H. *Handbuch der Physik* Vol. 19, page 227. Springer-Verlag, Berlin (1956).
25. MOTT N. F. and JONES H. *The Theory of the Properties of Metals and Alloys*. Clarendon Press, Oxford (1936).
26. FRIEDEL J. *J. Phys. Chem. Solids* **1,** 175 (1956).
27. COLES B. R. *Advanc. Phys.* **7,** 40 (1958).
28. ANDERSON G. S., LEGVOLD S. and SPEDDING F. H. *Phys. Rev.* **109,** 243 (1958).
29. BARDEEN J., COOPER L. N. and SCHRIEFFER J. R. *Phys. Rev.* **108,** 1175 (1957).
30. PINES D. *Phys. Rev.* **109,** 280 (1958).
31. MATTHIAS B. T. and HULM J. K. *Phys. Rev.* **89,** 439 (1953).
32. MATTHIAS B. T. *Phys. Rev.* **92,** 874 (1953).
33. MATTHIAS B. T. *Phys. Rev.* **97,** 74 (1955).
34. BAENZIGER N. C., RUNDLE R. E., SNOW A. I. and WILSON A. S. *Acta Cryst.* **3,** 34 (1950).

*J. Phys. Chem. Solids* Pergamon Press 1958. Vol. 7. pp. 268–274.

# HEAT CAPACITY OF DILUTE MAGNESIUM–ALUMINUM ALLOYS BELOW 4·2°K

**JOHN RAYNE**

Westinghouse Research Laboratories, Pittsburgh 35, Pennsylvania

(*Received* 2 *May* 1958; *in revised form* 28 *May* 1958)

**Abstract**—Heat capacity measurements below 4·2°K have been made on a series of dilute magnesium–aluminum alloys. The resulting variation of the electronic term with solute concentration suggests that a new overlap across the Brillouin zone is initiated at an electron concentration of about 2·02. The effective mass ratio of these overlap electrons is given approximately by $m^*/m = 0{\cdot}6$, which figure is in reasonable agreement with theoretical estimates. No abrupt change of the Debye temperature with solute concentration is observed.

VOL
7
195

## INTRODUCTION

THERE is considerable interest in the electronic band structure of magnesium and its relation to the variation with solute concentration of the axial ratio in dilute magnesium alloys. The possibility of such a relationship was first advanced by HUME-ROTHERY and RAYNOR[1,2] to explain their X-ray data.

They found that the axial parameter $c$ of such systems, when plotted as a function of solute concentration, exhibited a discontinuity in slope at an electron/atom ratio of 2·0075, whereas the parameter $a$ varied quite smoothly. Following the work of JONES[3] on the variation of the lattice parameters in the $\zeta$ and $\eta$ brasses, they suggested that this behaviour was correlated with the onset of overlap across the $\{000, 2\}$ faces of the Brillouin zone for magnesium. Such an overlap would result in an axial stress tending to expand the lattice along the $c$ axis. This effect, when superimposed on the general trend of the axial parameter to decrease on alloying, would give a break in the slope of the curve giving $c$ as a function of electron concentration. Since the overlap perpendicular to the hexagonal axis has long since been initiated, there would be no break in the corresponding curve for the parameter $a$.

More recently, JONES[4,5] has placed this theory on a quantitative basis, using the rigid band model of an alloy in the approximation of nearly free electrons. Treating the changes in lattice parameters as strains produced by a combination of a uniform pressure and an axial stress, JONES showed that the X-ray data were consistent with a shear strain at constant volume depending only on the electron/atom ratio. With reasonable assumptions about the nature of the zone overlaps and holes, he was able to obtain an analytical expression for this shear, which reproduced its experimental dependence on electron concentration quite well.

GOODENOUGH[6] and MCCLURE,[7] however, have criticized his treatment on the grounds that it neglects contributions to the axial stress arising from sources other than electron overlap. In addition, recent X-ray measurements by VON BATCHELDER and RAEUCHLE,[8] on dilute alloys of aluminum, cadmium and indium in magnesium, failed to confirm the discontinuity in the slope of the curve giving $c$ as a function of electron concentration in the case of aluminum as a solute. It must therefore be concluded that neither the X-ray measurements of the lattice parameters in these systems nor their theoretical interpretation, constitute unequivocal proof of the existence of the overlap in question.

Probably the most conclusive evidence for its existence comes from the measurements of SALKOVITZ, SCHINDLER, and KAMMER[9] on the transport properties of dilute magnesium alloys. They have interpreted their room temperature measurements as indicating an overlap occuring at a concentration of 1·3 at. per cent in the case of

aluminum alloys and at about 2 at. per cent in the case of indium alloys. These figures do not agree very well with those obtained from the X-ray data and it would thus seem desirable to obtain independent evidence regarding the overlap scheme in these systems.

For this reason, low temperature heat capacity measurements were undertaken on a series of dilute magnesium–aluminum alloys. According to the rigid band model, the variation of the electronic contribution with solute concentration in this system should be directly related to the band structure of magnesium beyond the Fermi level. Furthermore the variation of Debye temperature with electron concentration should give some indication of the corresponding variation of elastic constants, thus enabling a comparison to be made with the recent theoretical predictions of REITZ and SMITH.[10]

## EXPERIMENTAL

Measurements were carried out in the same apparatus as described in a previous paper.[11] The specimens employed were 1 in. in diameter, $1\frac{5}{8}$ in. in length and weighed approximately 35·5 g. They were produced by the induction melting of appropriate quantities of Johnson-Matthey 99·99 per cent pure magnesium (Lab. No. 8554) and Alcoa 99·99+ per cent pure aluminum. These were melted under a full atmosphere of helium in an aluminum oxide crucible and were then end poured into a water cooled copper mold. The ingots were homogenized for 24 hr at a temperature 30°C below their melting point in a salt bath of lithium chloride and potassium chloride. Subsequent metallographic examination revealed no coring or indication of a second phase. Finally the ingots were turned to the required size, samples of turnings at each end being analyzed chemically. In no case did the chemical analysis reveal a macroscopic inhomogeneity exceeding 1 per cent of the nominal composition.

## RESULTS

In all cases, it was possible to obtain a good straight line fit to the heat capacity data when plotted as $C/T$ versus $T^2$, a typical graph being shown in Fig. 1. The heat capacity is thus of the usual form

$$C = \gamma T + A(T/\Theta)^3 \qquad (1)$$

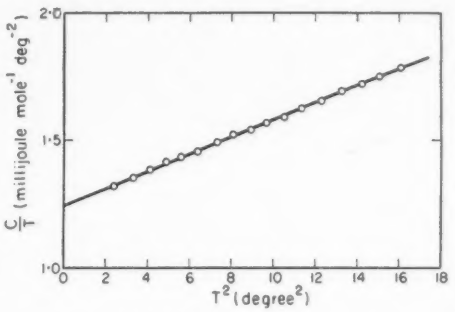


FIG. 1. Heat capacity of Mg–2 per cent Al alloy.

these terms representing the electronic and lattice contributions, respectively. A least squares analysis of the results, in the form $C/T$ versus $T^2$, yields the values of $\gamma$ and $\Theta$ shown in Table 1. The representative uncertainties quoted in this table represent both random errors estimated at the 99 per cent confidence level and systematic errors, which are assumed to be approximately 1/2 per cent. Figs. 2 and 3 show the variation of $\gamma$ and $\Theta$ with solute concentration in graphical form.

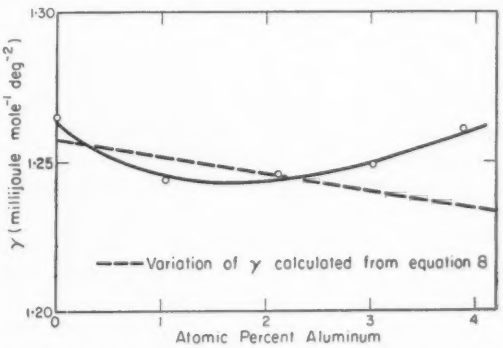


FIG. 2. Variation with solute concentration of electronic heat capacity for Mg–Al alloys.

## DISCUSSION

(a) *Electronic heat capacity*

Reference to Table 1 shows that the $\gamma$ value for pure magnesium agrees reasonably well with the figures obtained by SMITH[12] ($\gamma = 1{\cdot}32$ mJ mole$^{-1}$ deg$^{-2}$) and by LOGAN, CLEMENT and JEFFERS[13] ($\gamma = 1{\cdot}28$ mJ mole$^{-1}$ deg$^{-2}$).

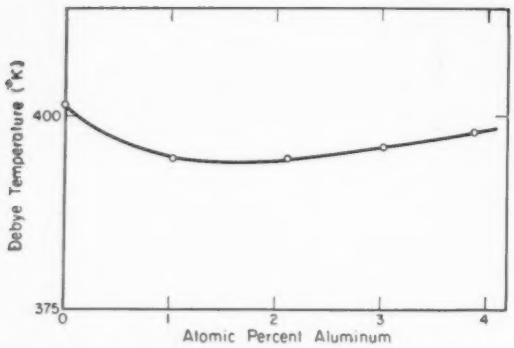


FIG. 3. Variation with solute concentration of Debye temperature for Mg–Al alloys.

*Table* 1. *Values of* $\gamma$ *and* $\Theta$ *in the relation* $C = \gamma T + A(T/\Theta)^3$ *for dilute magnesium alloys*

| Composition (At. per cent) | $\gamma$ $\left(\frac{\text{mJ}}{\text{mole}^{-1}\ \text{deg}^{-2}}\right)$ | $\Theta$ (°K) |
|---|---|---|
| 0 | $1{\cdot}265 \pm 0{\cdot}010$ | $403 \pm 4$ |
| 1·02 | 1·244 | 389 |
| 2·11 | 1·246 | 389 |
| 3·02 | 1·249 | 392 |
| 3·88 | 1·261 | 396 |

In the former case no estimate is available of the specimen purity or of the experimental error, so it is difficult to determine whether or not the residual disagreement with the present work is significant. Owing to the small specimens used in the latter experiment, the estimated error is of the order of 5 per cent so that no great weight can be attached to the close agreement with our figure.

From Figure 2 it can be seen that, with increasing solute concentration, the $\gamma$ value passes through a broad minimum at about 2 at. per cent aluminum. Because of the experimental errors involved, the exact shape of the curve is not known, but the existence of the minimum is fairly well established.

If the present results are interpreted from the standpoint of the rigid band model of binary alloys, the density of states in magnesium beyond the Fermi surface must initially be a decreasing function of energy. This conclusion is at variance with the usual diagrammatic representation of the band structure of magnesium,[14] according to which the density of states beyond the Fermi level increases with energy. In this connection, it is of interest that SALKOVITZ, SCHINDLER and KAMMER[9] have also concluded from their thermoelectric data, that the band shape of magnesium is of the same general form as is indicated by the present work.

To proceed further, it is necessary to consider the zone structure of magnesium in some detail. The form of zone containing two electrons per atom is shown in Fig. 4. Since magnesium is divalent and conducts electricity, there must be

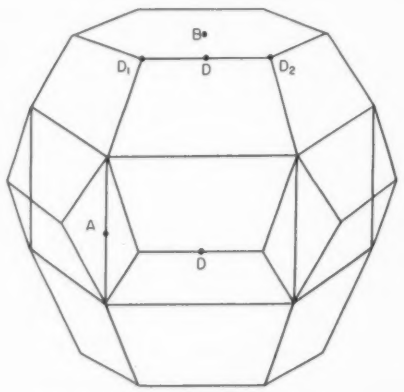


FIG. 4. Brillouin zone for magnesium.

electron overlaps across the zone boundaries. The nature of these overlaps is the subject of some dispute. If we assume a free electron model, then it is easily shown that for magnesium ($c/a = 1{\cdot}62$) $E_A < E_B$. It might thus be assumed, following JONES,[5] that $A$ overlaps have been initiated, while $B$ overlaps are absent. According to REITZ and SMITH,[10] however, considerations of lattice stability require that the opposite situation holds. The present work cannot settle this question, so for simplicity we shall follow JONES and assume that overlaps occur at points such as $A$ and that holes in the first zone appear at points along the line $D_1D_2$, with $D$ the point of highest energy. Under these conditions the holes at $D$ form six simply connected closed surfaces of constant energy, while the overlaps at $A$ form two such regions. We shall further assume that overlap at $B$ can occur at an additional electron concentration $n = n_0$, the overlap in this case forming a single

simply connected region. A schematic representation of the proposed overlap scheme is shown in Fig. 5. With these assumptions it is a simple

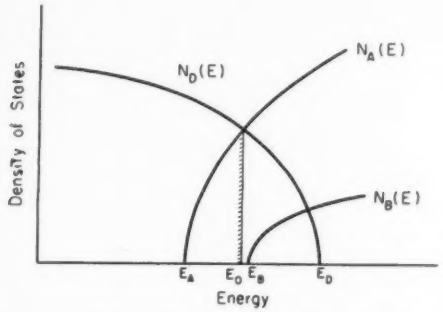


FIG. 5. Schematic diagram for density of states of overlaps and holes in magnesium.

matter to derive the variation of the density of states with electron concentration. Thus we have for $n$ not too large

$$N_A(n) = N_A(0) + \frac{n}{N}\left(\frac{dN_A}{dE}\right) \tag{2}$$

with a similar expression for $N_D(n)$.
Hence, provided there is no $B$ overlap ($n < n_0$),

$$N(n) = 6N_D(n) + 2N_A(n)$$
$$= N(0) + \frac{n}{N}\left(6\frac{dN_D}{dE} + 2\frac{dN_A}{dE}\right)_0. \tag{3}$$

Following JONES,[5] we now assume that, in the energy range being considered, both $N_A$ and $N_D$ are parabolic in shape. If $E_1$ is the energy width of the overlap electrons and $E_2$ that of the holes, then

$$\frac{dN_A}{dE} = \frac{N_A}{2E_1}; \qquad \frac{dN_D}{dE} = -\frac{N_D}{2E_2}, \tag{4}$$

so that (3) can be written

$$N(n) = N(0) + \frac{n}{N}\left(\frac{N_A}{E_1} - \frac{3N_D}{E_2}\right). \tag{5}$$

From (5) it is seen that

$$\frac{dN}{dn} = \frac{1}{N}\left(\frac{N_A}{E_1} - 3\frac{N_D}{E_2}\right) \tag{6}$$

which, if we assume $N_A = N_D$, $E_1 = E_2 = 1$ eV as does JONES, reduces to

$$\frac{dN}{dn} = -\frac{1}{4E_1}. \tag{7}$$

Since $\gamma = \pi^2/3k^2N(E_0)$, this relation can be expressed as

$$\frac{d\gamma}{dn} = -0{\cdot}589 \tag{8}$$

where $\gamma$ is expressed in mJ mole$^{-1}$ deg$^{-2}$ and $E_1$ has been assumed to be 1 eV.

The resulting variation of $\gamma$ with solute concentration is given by the dotted line in Fig. 2, where the zero ordinate has been chosen so as to give the best fit to the experimental points. Clearly, equation (8) is not an adequate representation of the data, no substantial improvement in the fit resulting from any reasonable choice of the parameters in (6). The nature of the deviations of the points from the line strongly suggests that a $B$ type overlap is initiated at about 2 at. per cent aluminum. To investigate whether this is a reasonable assumption, we must calculate the resulting change of $\gamma$; this is simply done as follows.

To sufficient accuracy the change $\Delta E$ in the Fermi energy for an additional electron concentration $n$ is given by

$$\Delta E = \frac{n}{N}. \tag{9}$$

If $n_0$ is the electron concentration at which $B$ overlap is initiated, the corresponding energy width of the $B$ distribution is thus

$$E_3 = \frac{n - n_0}{N}. \tag{10}$$

Hence if $\mathcal{N}_B$ is the number of overlap electrons at B, $m$-* their effective mass and if $V$ is the molar volume, the relevant contribution to $\gamma$ is given by

$$\Delta\gamma = \frac{\pi^2}{2}\mathcal{N}_B\frac{k^2}{E_3} \tag{11}$$

where

$$E_3 = \frac{h^2}{2m}\left(\frac{m}{m^*}\right)_B\left(\frac{3\mathcal{N}_B}{8\pi V}\right)^{2/3} \tag{12}$$

it being assumed that the band is of standard parabolic form.

From (12) we can solve for $\mathcal{N}_B$ to obtain

$$\mathcal{N}_B = \frac{8\pi V}{3}\left[\frac{2m}{h^2}\left(\frac{m^*}{m}\right)_B E_3\right]^{3/2},$$

whence substituting in (11)

$$\Delta\gamma = \frac{\pi^2}{2}\frac{8\pi V}{3}\left[\frac{2m}{h^2}\left(\frac{m^*}{m}\right)_B E_3\right]^{3/2}\frac{k^2}{E_3}$$

$$= \frac{4\pi^3 V}{3}\left[\frac{2m}{h^2}\left(\frac{m^*}{m}\right)_B\right]^{3/2} k^2 E_3^{1/2}. \qquad (13)$$

This equation may be simplified if we introduce the $\gamma$ value for magnesium. Thus if $(m^*/m)_0$ is the effective mass ratio for magnesium, equation (13) may be written as

$$\frac{\Delta\gamma}{\gamma} = \left[\left(\frac{m^*}{m}\right)_B\left(\frac{m}{m^*}\right)_0\right]^{3/2}\left(\frac{E_3}{E_0}\right)^{1/2}. \qquad (14)$$

Substituting the relevant values $(m^*/m)_0 = 1{\cdot}26$, $E_0 = 7{\cdot}05$ eV, this relation becomes

$$\frac{\Delta\gamma}{\gamma} = 0{\cdot}27\left(\frac{m^*}{m}\right)_B^{3/2} E_3^{1/2}. \qquad (15)$$

Using equations (8) and (15), quite a satisfactory fit to the experimental data may be obtained, as can be seen from Fig. 6.* In determining the slope of the straight line portion of this graph, we have taken $E_1 = 0{\cdot}75$ eV. This value seems to be more in accord with the $L_3$ soft X-ray emission data of SKINNER[15] than does JONES' figure of 1 eV. Once having settled on the linear portion of the graph, it is then quite easy to fit the remaining data to equation (15), since from (10) we must have $\Delta\gamma \propto (n-n_0)^{1/2}$ with $n_0 \simeq 0{\cdot}02$.

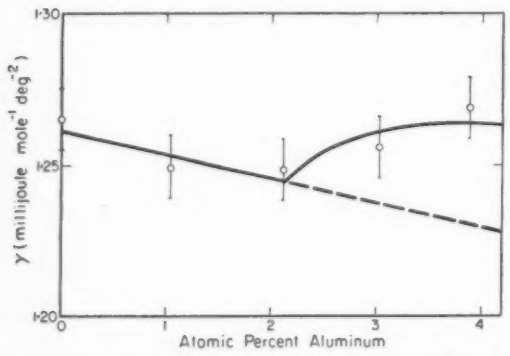


FIG. 6. Fit of experimental data corrected for volume changes to proposed band structure of Mg.

* In this graph the data have been corrected for the volume change on alloying. See reference 11.

It is of interest to compare the value of $(m^*/m)_B$ obtained in this way with theoretical estimates. Thus, from Fig. 6 we find that for $n_0 = 0{\cdot}021$, $n = 0{\cdot}041$

$$E_3 = 0{\cdot}037\text{ eV}; \qquad \frac{\Delta\gamma}{\gamma} = 0{\cdot}027 \qquad (16)$$

whence from (15)

$$\left(\frac{m^*}{m}\right)_B = 0{\cdot}6. \qquad (17)$$

REITZ and SMITH[10] have obtained theoretical estimates of the effective mass ratio for the $B$ overlap in two ways. Using the calculations of TRLIFAJ[16] for the band structure of magnesium and the usual expression for the effective mass ratio in the nearly-free electron approximation, they find $m^*/m = 0{\cdot}4$. On the other hand, from the magnitude of the Hall constant in pure magnesium, a value $m^*/m = 0{\cdot}7$ is obtained. As a compromise they adopt a figure $m^*/m = 0{\cdot}55$, which agrees quite well with that given in equation (17).

Another estimate of the effective mass ratio may be obtained from the theoretical expression, derived by JONES, for the dependence of the effective shear strain at constant volume on the electron concentration $n$. Thus for $n > n_0$

$$\left(\frac{s-s_0}{s_0}\right) = A(n-n_0)^{3/2} + Bn + Cn^2 \qquad (18)$$

where

$$A = \frac{4}{3}\left(\frac{E_0}{\mu V}\right)\frac{\alpha}{N^{3/2}}. \qquad (19)$$

In this expression $\mu = 1/2(c_{11}+c_{12}+2c_{33}-4c_{13})$ and $\alpha$ is defined by the relation

$$N_B = \alpha(E_0 - E_B)^{1/2}$$

so that

$$\alpha = \frac{4\pi}{h^3}(2m)^{3/2}\left(\frac{m^*}{m}\right)^{3/2}. \qquad (20)$$

From a fit of (18) to the experimental data, $A$ is found to be 0·150, which by (19) and (20) gives $(m^*/m)_B = 0{\cdot}49$. Thus, again, there is reasonable agreement with our value.

It may be argued that this agreement is quite fortuitous, in view of the marked discrepancy between our value for $n_0$ and that adopted by JONES. The latter, however, is derived from room temperature X-ray data, while the present figure refers to the overlap near absolute zero. It is quite possible that the alterations in lattice dimensions, on going from 300°K to 0°K, would change the details of the overlap sufficiently to explain the difference in $n_0$. Since the parabolic nature of the associated density of states curve would presumably remain unaltered, the value of $(m^*/m)_B$ would also be constant, thus accounting for the above agreement. It would be of great interest to make X-ray measurements at liquid helium temperatures on suitable magnesium alloys, to see whether or not this hypothesis is true.

Comparison of the per cent work with that of SALKOVITZ, SCHINDLER and KAMMER[9] is somewhat difficult, owing to the fact that their proposed overlap differs for various solutes of the same valency e.g. aluminum, indium and thallium. This could be due to a breakdown in their assumption, that the change due to alloying in the electronic contribution to the thermoelectric power is given by the relation

$$S_{\text{electronic}} = S_{\text{alloy}} - S_{\text{Mg-Cd}} \qquad (21)$$

where $S_{\text{Mg-Cd}}$ is the thermoelectric power of the corresponding magnesium–cadmium alloy. Because of the resulting uncertainty in their analysis, undue significance should not be attached to the disagreement between their work and that obtained from X-ray data. Furthermore, as the work of MACDONALD and PEARSON[17] on copper alloys has shown, the temperature variation of the thermoelectric power of even simple alloys is not at all well understood. Thus the variation of the overlap with temperature as obtained from thermoelectric power measurements must be accepted with caution. It is of interest, however, that the general nature of the temperature dependence of the overlap obtained in this way agrees with our hypothesis regarding its variation with temperature.

(b) *Lattice heat capacity*

Reference to Table 1 shows that the $\Theta$ value for pure magnesium agrees well with those obtained by SMITH[12] ($\Theta = 406 \pm 10$°K) and LOGAN, CLEMENT and JEFFERS[13] ($\Theta = 390 \pm 7$°K). There appears to be a residual discrepancy between the latter result and our value, but this is not believed to be significant, since the results of LOGAN *et al.* were obtained by fitting the heat capacity data in the range 3–13°K to equation (1). It is well known, particularly for hexagonal lattices, that the Debye temperature can change appreciably over this region. Such a variation would give an apparent $\Theta$ which is somewhat lower than $\Theta_0$, the value at 0°K and it is possible that such a situation applies to the data in question.

Recently SLUTSKY and GARLAND[18] have measured the elastic constants of magnesium in the region from 4·2°K to 300°K. By averaging the inverse cube of the elastic wave velocities over all propagation directions and using the usual Debye formula, they were able to compute $\Theta$. Their value of $388 \pm 3$°K is in significant disagreement with our result. No reason can be advanced for this discrepancy.

From Fig. 3 it can be seen that, on alloying, the Debye temperature exhibits a broad minimum at about 2 at. per cent aluminum. According to the calculations of REITZ and SMITH,[10] the onset of a Brillouin zone overlap, such as the one which is presumed to occur in dilute magnesium alloys, should result in an anomalous peak in the variation of the shear constant $C = c_{11} + c_{12} + 2c_{33} - 4c_{13}$ with electron concentration at 0°K. This peak is not found at room temperatures owing to the diffuseness of the Fermi distribution function. At helium temperatures, however, its presence should show as a *maximum* in the variation of Debye temperature with solute concentration. Although the accuracy of the experimental values of $\Theta$ is not very high, there can be no doubt that such a maximum is not present. No reasonable explanation of this result can be adduced and low temperature elastic measurements on dilute magnesium–aluminum alloys are being made to clarify this situation.

## CONCLUSION

From low temperature heat capacity measurements on dilute magnesium alloys it is concluded that an overlap across the {000, 2} faces of the Brillouin zone for magnesium is initiated at an electron concentration of approximately 2·02. The effective mass ratio of these overlap electrons is approximately 0·6. No anomalous behaviour in the variation of Debye temperature with solute concentration is observed.

*Acknowledgements*—It is a pleasure to acknowledge the help of Dr. P. FLINN and Mr. G. MACMANUS in the heat treatment of the specimens used in this work. Thanks are also due to Mr. R. ANDERSON of the Technology Department for his metallographic examination of the alloys.

## REFERENCES

1. HUME-ROTHERY W. and RAYNOR G. V. *Proc. Roy. Soc.* A **177,** 27 (1940).
2. RAYNOR G. V. *Proc. Roy. Soc.* A**174,** 457 (1940).
3. JONES H. *Proc. Roy. Soc.* A**147,** 400 (1934).
4. JONES H. *Physica* **15,** 13 (1949).
5. JONES H. *Phil. Mag.* **41,** 663 (1950).
6. GOODENOUGH J. B. *Phys. Rev.* **89,** 282 (1953).
7. MCCLURE J. W. *Phys. Rev.* **98,** 449 (1955).
8. VON BATCHELDER F. W. and RAEUCHLE R. F. *Phys. Rev.* **105,** 59 (1957).
9. SALKOVITZ E. I., SCHINDLER A. I. and KAMMER E. W. *Phys. Rev.* **105,** 887 (1957).
10. REITZ J. R. and SMITH C. S. *Phys. Rev.* **104,** 1253 (1956).
11. RAYNE J. A. *Phys. Rev.* **108,** 22 (1957).
12. SMITH P. L. *Phil. Mag.* **46,** 744 (1955).
13. LOGAN J. K., CLEMENT J. R. and JEFFERS H. R. *Phys. Rev.* **105,** 1435 (1957).
14. RAYNOR G. V. *Reports on Progress in Physics* **15,** 210. The Physical Society, London (1952).
15. SKINNER H. W. B. *Reports on Progress in Physics* **5,** 257. The Physical Society, London (1938).
16. TRLIFAJ M. *Czech J. Phys.* **1,** 110 (1952).
17. MACDONALD D. K. C. and PEARSON W. B. *Proc. Roy. Soc.* A**219,** 373 (1953).
18. SLUTSKY L. J. and GARLAND C. W. *Phys. Rev.* **107,** 972 (1957).

VOL
7
195

VOL. 7 1958

## The effect of pressure on the absorption edge of sulfur*

(*Received* 12 *June* 1958)

In connection with our studies of the effect of pressure on the structure of solids, the absorption edges of sulfur have been measured. The sulfur was crystallized from the vapor phase on a watch glass held at room temperature. Some specimens were also grown from $CS_2$ solution. The equipment and techniques used have been described previously.[1,2] A Beckman monochromator was used with a tungsten source and 1P21 detector.

The absorption edge was found to shift continuously toward longer wavelengths as far as the data could be obtained. Several runs were taken in both the 50,000- and 250,000-atm cells, and are

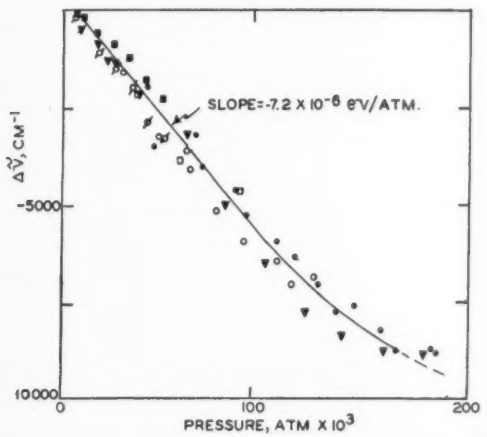


FIG. 1. Shift of sulfur absorption edge with pressure ($\Delta\nu$ measured from 23,250 $cm^{-1}$)

plotted in Fig. 1. This substance could not be observed above 200,000 atm because the shift of 9000 $cm^{-1}$ from the zero value 23,250 $cm^{-1}$ puts the edge into the 14,000 $cm^{-1}$ region where the photomultiplier sensitivity is very low. The linear shift of the edge with pressure below 120,000 atm is an accelerating function of density, as shown in Fig. 2. In this diagram BRIDGMAN's compressibility data[3] were extrapolated to obtain values of $\rho_0/\rho$ between 100,000 and 200,000 atm yielding the dotted portion of the curve. Using a reasonable extrapolation of BRIDGMAN's data, and the rate of

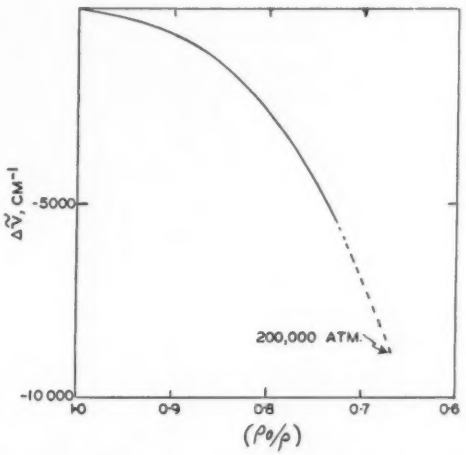


FIG. 2. Shift of sulfur absorption edge with density.

shift observed at the maximum pressure, it is estimated that sulfur will become a metal somewhere in the neighborhood of 400,000–500,000 atm at room temperature.

*Department of Chemistry and Chemical Engineering, University of Urbana, Urbana, Ill.*

T. E. SLYKHOUSE
H. G. DRICKAMER

* This work was supported in part by AEC Contract AT(11-1)-67, Chemical Engineering Project 5.

### REFERENCES

1. FITCH R. A., SLYKHOUSE T. E. and DRICKAMER H. G., *J. Opt. Soc. Amer.* **47,** (11) 1015 (1957).
2. SLYKHOUSE T. E. and DRICKAMER H. G., *J. Phys. Chem. Solids* **7,** 207 (1958).
3. BRIDGMAN P. W., *Proc. Amer. Acad. Arts Sci.* **76,** 1 (1945).

### Lattice distortions due to *d–s* mixing

(*Received* 17 *July* 1958)

WE have shown[1] that the tendency of certain ions, for example $Cu^+$, $Ag^+$, $Au^+$, and $Hg^{++}$, to occur in a linear environment rather than in an environment of higher co-ordination number is correlated with the *d–s* separation in the free atom. If the *d–s* separation is small enough, the loss of electrostatic energy due to the smaller number of neighbours is more than compensated for by the stabilization due to *d–s* mixing in an environment of low symmetry. The relation of these effects to Jahn–Teller distortions was emphasized. Here we point out that a qualitatively similar, but quantitatively less drastic, effect may be responsible for the anomalous X-ray scattering and perhaps for the phase transitions in a variety of halides and sulphides containing $Cu^+$, $Ag^+$, $Hg^{++}$ ions, &c.

HOSHINO has shown[2] that the temperature-dependence of the intensities of X-ray reflections from many halides containing $d^{10}$ ions can only be understood if it is supposed that the metal ion has an extremely large amplitude of vibration or, in some cases, if there exist subsidiary potential-energy minima away from the centre of the co-ordination tetrahedra. Just such effects are to be anticipated if *d–s* mixing is important.

In the group $T_d$ of the environment of a metal atom in a tetrahedral halide, the *d* orbitals transform as $T_1+E$ and the *s* orbital as $A_1$. The stretching vibrations of the tetrahedron transform as $A_1+T_1$. Thus a $T_1$ vibration can mix together the triply degenerate group of *d* orbitals and the *s* orbital. The arguments already presented[1] show that this tends to decrease the force constant of the $T_1$ stretching mode and that if the *d–s* separation is sufficiently small the structure becomes unstable with respect to this mode of distortion. The results on the X-ray scattering from the ordered phases of these halides are consistent with such a mechanism if it is supposed that the correlation between distortions of neighbouring tetrahedra is weak.[3] Similar distortions should occur, for example, in the sulphides of $Cu^+$ and $Ag^+$, and it is probably significant that the compound $Cu_9S_5$ does contain $Cu^+$ ions both slightly displaced from the centre of a tetrahedral environment and in planar trigonal co-ordination.[4] In contrast to the situation for octahedral complexes, *s–p* mixing can lead to similar distortions in tetrahedral compounds of $d^{10}s^2$ ions.[5]

The substances exhibiting anomalous X-ray scattering are also remarkable for very high ionic conductivities and some for the disorder of the metal ions in their high-temperature phases. It may be that the very low barriers to the displacement of metal ions from the centres of their tetrahedra allows the lattice to accommodate interstitial ions more easily than would otherwise be possible.

*Department of Theoretical Chemistry* L. E. ORGEL
*Pembroke Street*
*Cambridge*

VOL
7
195

#### REFERENCES

1. ORGEL L. E. *J. Chem. Soc.* In press.
2. HOSHINO S., *J. Phys. Soc. Japan* **12,** 315 (1957) and references therein.
3. DUNITZ J. D. and ORGEL L. E., *J. Phys. Chem. Solids* **3,** 20 (1957).
4. DONNAY G., DONNAY J. D. H. and KULLERUD G., *Acta Cryst.* **10,** 764 (1957).
5. ORGEL L. E. To be submitted for publication.

---

### On the relation between non-stoichiometry and the formation of donor and acceptor centres in compounds

(*Received* 30 *June* 1958; *in revised form* 29 *July* 1958)

As is generally recognized, non-stoichiometry may give rise to the formation of donor or acceptor centres in semi-conducting compounds. It is often tacitly assumed that each atom present in excess of the stoichiometric composition forms one donor or acceptor centre. As will be shown, this need not always be the case.

If, in a crystalline compound $A_xB_y$, one of the components is present in excess of the concentration required by the simple stoichiometry ratio, the excess atoms can be accommodated in the crystal in three different ways:

(1) at interstitial sites ($A_i$ or $B_i$);

(2) at normal lattice sites with the formation of vacancies:

> $n$ extra $A$ atoms on $A$ sites ($A_A$), giving $n\times y/x$ vacancies on $B$ sites ($V_B$), and similarly $m$

extra $B$ atoms on $B$ sites ($B_B$), giving $m \times x/y$ vacancies on $A$ sites ($V_A$);

(3) at both $A$ and $B$ sites without the formation of vacancies (anti-structure mechanism[1]). Of $n$ extra $A$ atoms, a fraction $n \times x/(x+y)$ is placed at normal sites ($A_A$), the remaining part $n \times y/(x+y)$ being placed at $B$ sites ($A_B$), and similarly for extra $B$.

The electrical consequences of the deviation from stoichiometry differ in the three cases. If $A$ is an electropositive and $B$ an electronegative atom, $A_i$ will act as a donor and $B_i$ as an acceptor. The number of donor or acceptor centres due to the deviation from stoichiometry is thus equal to the number of excess atoms present in case (1).

In case (2) $V_A$ will act as an acceptor and $V_B$ as a donor. The number of donors or acceptors per extra atom is thus equal to the number of vacancies $V_B$ or $V_A$ per extra atom, viz. $y/x$ and $x/y$ respectively.

In case (3), $A_B$ will act as an acceptor and $B_A$ as a donor, the reason being that electropositive atoms have fewer valence electrons than electronegative atoms. The number of donors or acceptors per extra atom is given by the fraction of the extra atoms occupying abnormal positions; it is $y/(x+y)$ (acceptors) for extra $A$ atoms, and $x/(x+y)$ (donors) for extra $B$ atoms. The various cases are summarized in Table 1.

*Table* 1

| Mechanism of incorporation | Number of donors ($d$) or acceptors ($a$) per extra atom | | | | | |
|---|---|---|---|---|---|---|
| | Compound $A_xB_y$ | | Compound $AB$ | | Compound $A_2B_3$ | |
| | $A$ | $B$ | $A$ | $B$ | $A$ | $B$ |
| (1) Interstitial mechanism | 1 ($d$) | 1 ($a$) | 1 ($d$) | 1 ($a$) | 1 ($d$) | 1 ($a$) |
| (2) Vacancy mechanism | $y/x$ ($d$) | $x/y$ ($a$) | 1 ($d$) | 1 ($a$) | $\frac{2}{3}$ ($d$) | $\frac{2}{3}$ ($a$) |
| (3) Anti-structure mechanism | $y/x+y$ ($a$) | $x/x+y$ ($d$) | $\frac{1}{2}$ ($a$) | $\frac{1}{2}$ ($d$) | $\frac{3}{5}$ ($a$) | $\frac{2}{5}$ ($d$) |

It is, of course, also possible that the various mechanisms occur simultaneously, part of the extra atoms being incorporated by one mechanism and the remainder by another. In this case the number of donors or acceptors per extra atom is given by an expression involving factors denoting the extent to which the various mechanisms participate.

Similar complications may arise from the fact that centres of the type formed by extra atoms are also formed by thermal disorder (Frenkel type, Schottky type, or anti-structure type disorder[1]). The effect of disorder is most serious under conditions where the deviation from stoichiometry is small relative to the disorder, i.e. close to the stoichiometric point. In practice it is often difficult to determine with sufficient accuracy the deviation from stoichiometry by chemical means. Then the deviation from stoichiometry is sometimes deduced from electrical measurements, e.g. from the concentration of holes or electrons determined by means of the Hall effect, taking into account the degree of ionization of the donor or acceptor centres and assuming that each centre may give off a certain number of electrons or holes, e.g. one. This has been done for PbS[2] and $Bi_2Te_3$[3]. For PbS case (2) probably applies; since $x = y = 1$, the number of donors or acceptors per extra atom is one. For $Bi_2Te_3$, on the other hand, there are reasons for believing that case (3) applies.[1,4] Therefore here the numbers of donors or acceptors per extra atom are $\frac{2}{5}$ and $\frac{3}{5}$ respectively, and not 1 as assumed in reference (3). In carrying out an analysis of this type, the factors discussed above have obviously to be taken into account.

*Philips Research Laboratories* F. A. KRÖGER
*Eindhoven*
*Netherlands*

**REFERENCES**

1. KRÖGER F. A. and VINK H. J., *Solid State Physics* (Ed. F. SEITZ and D. TURNBULL) Vol. 3, p. 315 and 366. Academic Press, New York (1956).
2. BLOEM J. and KRÖGER F. A., *Z. phys. Chem.* (*Frankfort*) **7,** 1 (1956).
3. SATTERTHWAITE C. B. and URE H. W., *Phys. Rev.* **108,** 1164 (1957).
4. LAGRENAUDIE J., *J. Phys. Radium,* **18,** Suppl. 3, 39A–40A (1957).
   HARMAN T. C., PARIS B., MILLER S. E. and GOERING H. L., *J. Phys. Chem. Solids* **2,** 181 (1957).

VOL
7
195

VOL.
7
1958

## BOOK REVIEW

D. R. HARTREE: **The Calculation of Atomic Structures.** John Wiley & Son, New York, and Chapman & Hall, London, 1957. XIII+181 pp., $5.00.

SHORTLY before his death, the late Professor HARTREE completed a book giving a survey of the most important field of research of his life: the calculation of atomic structures by the self-consistent-field method. The book gives an excellent exposition of the development of this approach during the last three decades, and it contains a great deal of material which has never been collected in this form before, except in a brief review article in *Reports on Progress in Physics* **11**, 113 (1948).

After an introduction about the separable wave-function approximation, there follows a description of the variation principle and a detailed analysis of the energy of the configurations of complete groups. This leads to a derivation of the self-consistent-field equations with and without exchange, and then the numerical procedure for solving these equations is described in detail. After a chapter on configurations comprising incomplete groups, there follows an investigation of the variation of atomic wave functions and fields with atomic number. The following section is devoted to a study of the total energy and, in a chapter of 11 pages, "better approximations" are briefly described.

At the end of the book, there are some useful tables of mean radii, screening numbers, and reduced radial wave functions. The reader would perhaps expect to find a complete list of references to the original self-consistent-field calculations in a book of this type, but the author refers instead to the above-mentioned review article in *Reports on Progress in Physics* and gives only a list of addenda bringing the survey up to date. This slight disadvantage ought to be removed by the publisher before the next printing of this outstanding book, which will certainly become the standard text in this important field.

With this book, the late Professor HARTREE appropriately crowns his life work, and we atomic scientists read it with a deep feeling of admiration and gratitude both for the monograph itself and for the research behind it.

PER-OLOV LÖWDIN

## PAPERS TO BE PUBLISHED IN FUTURE ISSUES

VON O. G. FOLBERTH: Der Gleichgewichtsdamfdruck der Verbindungen InAs, GaAs, InP und GaP am Schmelzpunkt.

G. J. DIENES: The temperature dependence of the elastic moduli of vitreous silica.

D. G. WICKHAM and W. J. CROFT: Crystallographic and magnetic properties of several spinels containing trivalent manganese.

A. MARADUDIN: Screw dislocations and discrete elastic theory.

A. J. COHEN and H. L. SMITH: Ultraviolet and infrared absorption of fused germania.

M. S. WECHSLER and R. H. KERNOHAN: Neutron irradiation effects on copper–aluminum alloys.

G. WEISS and A. MARADUDIN: Thermodynamic properties of a disordered lattice.

P-G. DE GENNES: Sur la relaxation nucleaire dans les cristaux ioniques.

G. A. ALERS, J. R. NEIGHBOURS and H. SATO: Dependence of sound velocity and attenuation of magnetization direction in nickel at high fields.

G. L. PEARSON and W. L. FELDMANN: Powder pattern techniques for delineating ferroelectric domain structures.

D. G. THOMAS: The diffusion and precipitation of indium in zinc oxide.

E. HIRAHARA, M. MURAKAMI and T. HIHARA: Magnetic and electrical anisotropies of the iron sulfide single crystals.

M. J. STEPHEN and A. B. LIDIARD: The Faraday effect in semiconductors.

H. E. FARNSWORTH and J. TUUL: Influence of lattice defect density on the chemisorption and oxide formation on a clean (100) crystal face of nickel as determined by low-energy electron diffraction.

H. E. FARNSWORTH, R. E. SCHLIER and J. TUUL: Tests with low-energy electron diffraction for adsorbed hydrogen and nickel hydroxide formed on the (100) surface of a nickel crystal at 25°C.

F. A. TRUMBORE, C. R. ISENBERG and E. M. PORBANSKY: On the temperature dependence of the distribution coefficient. The solid solubilities of tin in silicon and germanium.

W. KÄNZIG and T. O. WOODRUFF: The electronic structure of an H-Center.

T. RISTE, K. BLINOWSKI and J. JANIK: Spin fluctuation scattering of neutrons in magnetite.

H. C. NASH and C. S. SMITH: Single crystal elastic constants of lithium.

R. I. BATE, R. K. WILLARDSON and A. C. BEER: Transverse magnetoresistance and Hall effect in *N*-type InSb.

N. T. MELAMED: Energy transfer in ZnS : Cu : In phosphors.

A. J. COHEN and E. S. HODGE: Zonal specifity and nonspecifity of certain impurities during growth of synthetic α-quartz.

G. H. JONKER: Analysis of the semiconducting properties of cobalt ferrite.

T. P. HOAR and N. F. MOTT: A mechanism for the formation of porous anodic oxide films on aluminium.

A. WOLD and R. J. ARNOTT: Preparation and crystallographic properties of the systems $LaMn_{1-x}Mn_xO_{3+\lambda}$ and $LaMn_{1-x}Ni_xO_{3+\lambda}$.

R. E. SCHMUNK and C. S. SMITH: Pressure derivatives of the elastic constants of aluminum and magnesium.

H. EHRENREICH: Transport of electrons in intrinsic InSb.



VOL
7
195

*J. Phys. Chem. Solids* Pergamon Press 1958. Vol. 7. pp. 281–289.

# MAGNETIC AND ELECTRICAL ANISOTROPIES OF IRON SULFIDE SINGLE CRYSTALS

**EIJI HIRAHARA* and MIYUKI MURAKAMI***

Department of Physics, Faculty of Engineering, Hiroshima University, Hiroshima, Japan

(*Received* 28 *February* 1958; *revised* 28 *July* 1958)

**Abstract**—Single crystals of iron sulfide of stoichiometric and near-stoichiometric compositions have been prepared by a method similar to the Bridgman technique, and their anisotropies of magnetic susceptibility and electrical conductivity have been observed. Consideration of the experimental results leads to the conclusion that the preferred direction of the antiferromagnetic spins is parallel to the $c$-axis of the crystal below $T_\alpha$ (the temperature of the $\alpha$-transformation) and perpendicular to the $c$-axis above $T_\alpha$. The behavior of the spin orientation in the temperature range between $T_\alpha$ and $T_N$ (the Néel temperature) has been clarified. It appears that the anisotropy of conductivity can be explained qualitatively in terms of the dependence of electron scattering on the spin orientation of each magnetic ion in the crystal. Anomalous behavior of the susceptibility, which appears just below $T_\alpha$ in the cooling process, is reported briefly.

## 1. INTRODUCTION

THE magnetic and other physical properties of the iron sulfide system ($FeS_x$), including the mineral pyrrhotite ($Fe_7S_8$), have been investigated both experimentally and theoretically by many workers. The physical properties, however, seem to be very complicated, because this substance has $\alpha$- and $\gamma$-transformations in addition to $\beta$-transformation which is well known as the transformation between the antiferromagnetic and paramagnetic states.

The magnetic properties have been studied by JUZA and BILTZ,[1] ZIEGLER,[2] HARALDSEN,[3] and MIYAHARA,[4] and their results may be summarized as follows. The susceptibility of stoichiometric iron sulfide ($x = 1{\cdot}00$ in $FeS_x$) is essentially antiferromagnetic, and its $\alpha$- and $\beta$-transformations are observed at temperatures of 138 and 320°C, respectively. With a slight increase of sulfur content the $\alpha$-transformation ($T_\alpha$) shifts to lower temperatures, whereas the temperature of the $\beta$-transformation ($T_N$, or the Néel point) remains almost unchanged at 320°C. As the sulfur content increases to $x = 1{\cdot}06$, the $\gamma$-anomaly makes its appearance in the temperature range between $T_\alpha$ and $T_N$, and the peak of the susceptibility at the $\gamma$-anomaly becomes sharper. When $x$ increases beyond 1·10, the substance becomes ferrimagnetic, showing a large susceptibility. An interpretation of the ferrimagnetic magnetization at the $\gamma$-anomaly has been given by HIRONE and TSUYA,[5] and YOSIDA[6] on the basis of the following model.

The excess sulfur atoms within the lattice are supposed to induce ferric ions in place of ferrous ones. Then, the ferric and ferrous ions are assumed to tend to accumulate on alternate planes perpendicular to the $c$-axis of the crystal, the even planes containing only ferric ions and the odd ones, only ferrous ions. According to this model, the difference between the five Bohr magnetons of a ferric ion and the four Bohr magnetons of a ferrous ion can account for the net magnetic moment of the substance. Recently, LOTGERING[7] has investigated the ferrimagnetic behavior mentioned above, and has attempted to interpret the anomalous behavior, particularly of $FeS_{1.11}$ by the mechanism of the vacancy ordering.

Crystallographic investigations of $FeS_x$ have been carried out by HÄGG and SUCKSDORFF,[8] JUZA and BILTZ,[1] HARALDSEN,[3] UEDA *et al.*[9] and more recently by BERTAUT.[10] Stoichiometric FeS has a hexagonal lattice structure and its

* Now at the Department of Physics, Faculty of Science, Tohoku University, Sendai, Japan.

space-group is $D_{3h}^4-C_{6\bar{3}2c}$. The dimensions of the unit cell are $a_0 = 5{\cdot}968$ Å and $c_0 = 11{\cdot}74$ Å, and a cell contains 12 molecules. This structure is a superstructure of the high temperature-structure, the latter is observed at the temperature above $T_\alpha$ as a simple NiAs-type, and the relations between the unit cells of the two structure types are $a_0 = \sqrt{3}a' = 5{\cdot}96$ Å, and $c_0 = 2c' = 11{\cdot}74$ Å, where $a'$ and $c'$ are the lattice constants of the unit cell for the high-temperature or NiAs-type structure. Stoichiometric FeS contracts at $T_\alpha$ by about 1 per cent along the $c$-axis with increasing temperature. The contraction decreases with increase in sulfur content.

The specific-heat anomaly at $T_\alpha$ and at $T_N$ has been measured by HIRONE *et al.*[11,12] and also by UEDA *et al.*[9] Their results show that the anomalies are about 600 cal/mole at $T_N$ and 550 cal/mole at $T_\alpha$. It should be noted that the anomaly at $T_\alpha$ decreases with the increasing sulfur content and simultaneously $T_\alpha$ shifts to a lower temperature.

Recently, KAMIGAICHI[13] has measured the electrical conductivity of polycrystalline $FeS_x$ ($1{\cdot}00 \leqslant x < 1{\cdot}10$) and observed a large increase at $T_\alpha$. The amount of this increase becomes smaller with increasing sulfur content.

All the measurements mentioned above have been carried out on polycrystalline samples except in the case of the mineral pyrrhotite ($Fe_7S_8$). On this account the detailed nature of the transformations, especially the $\alpha$-transformation, has not yet been clarified. In order to elucidate the mechanism of the various transformations, therefore, the use of single crystals seems to be essential. Such crystals have been successfully prepared in our laboratory, and electrical and magnetic properties have been measured for samples of stoichiometric and near-stoichiometric compositions. In the following sections, we shall describe our experimental procedure and results and shall give some qualitative account of the spin-orientation and its effect on electronic conduction. The latter has been already reported briefly.[14]

## 2. PREPARATION OF SPECIMENS AND EXPERIMENTAL PROCEDURES

The single crystals of $FeS_x$ were prepared in the following way. A pure iron wire (prepared by the Merck Co.) and pure sulfur powder (distilled carefully from a carbon bisulfide solution) were heated in an evacuated terex tube at about 600°C. The compound $FeS_x$, prepared in this way, was ground into powder and sealed in an evacuated, thick silica tube, which was then heated at about 1200°C in a silicon-carbide furnace and slowly cooled by removing the sample gradually from the furnace.

In cooling from high temperatures a single crystal may be produced, but it often breaks the silica tube, since it expands greatly at the $\alpha$-transformation. Hence, a vital point in making a suitable single crystal is to use a thick silica tube.

The composition of the sample was carefully determined by chemical analysis, and the result agreed within 1 per cent with the composition expected from the ratio of iron to sulfur before heat treatment.

The electrical conductivity of the sample was measured by a conventional four-probe method, using a type K–2 potentiometer. The sample and four leads were sealed together into an evacuated terex tube in order to protect the sample from moisture during low-temperature measurements.

The magnetic susceptibility was measured by means of a magnetic balance designed to record automatically a magnetization/temperature curve on a recording chart. The balance, which is placed in an evacuated bell jar with a metal base, is essentially similar to that described by HIRONE *et al.*[15] except for the following point. In order to rotate the sample in an external magnetic field, a small thin disc is attached horizontally to the quartz filament suspending the sample vertically in the field. The disc has scales on its circumference and can be rotated about the vertical axis, which coincides with the quartz filament holding the sample. The disc is rotated by a rod with two small hooks. The rod passes through the metal base of the balance and is able to rotate on its axis without affecting the vacuum in the bell jar.

In the susceptibility measurements it is necessary to keep the sample free from oxidation, for which purpose the sample was sealed into a terex or silica ampule. The external magnetic field for the magnetic balance was about 7000 G for all susceptibility measurements except for the special case.

## 3. EXPERIMENTAL RESULTS

### (a) *Anisotropies of both susceptibility and conductivity*

The results for the temperature variations of magnetic susceptibility and electrical conductivity for a stoichiometric iron sulfide ($FeS_{1.00}$) are shown in Figs. 1 and 2. The temperature range for the measurements extended from liquid-air temperature to 600°C. In Fig. 1 curves 1 and 2 give

the susceptibility results obtained with the external magnetic field parallel and perpendicular to the $c$-axis of the single crystal, respectively. In Fig. 2 curves 1 and 2 show the conductivity results obtained with the electric field parallel and perpendicular to the $c$-axis of the single-crystal sample, respectively. Both Figs. 1 and 2 indicate remarkable anisotropies and, moreover, anomalies appear at 138°C ($\alpha$-transformation) and at 320°C ($\beta$-transformation). Curve 1 appears to indicate a residual susceptibility at absolute zero temperature.

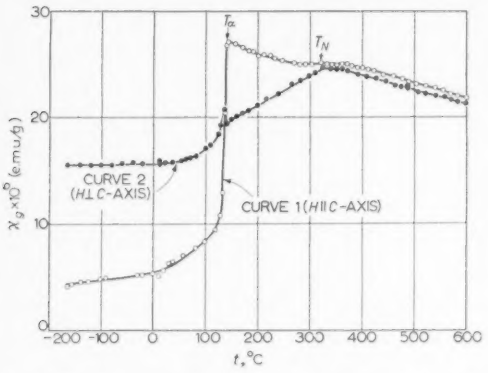


FIG. 1. Temperature variation of the susceptibility of a stoichiometric iron sulfide ($FeS_{1.00}$). The external magnetic field was applied parallel (curve 1) and perpendicular (curve 2) to the $c$-axis.

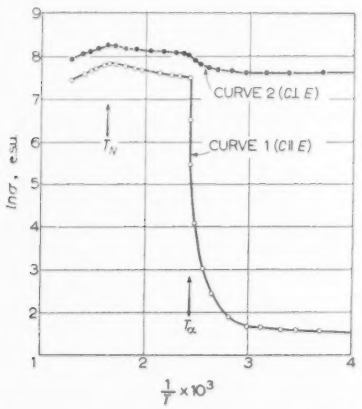


FIG. 2. Temperature variation of the conductivity of a stoichiometric iron sulfide ($FeS_{1.00}$). Abscissa is the reciprocal of the absolute temperature ($T$°K). Curve 1($C \| E$): the electrical field was parallel to the $c$-axis. Curve 2($C \perp E$): the electrical field was perpendicular to the $c$-axis.

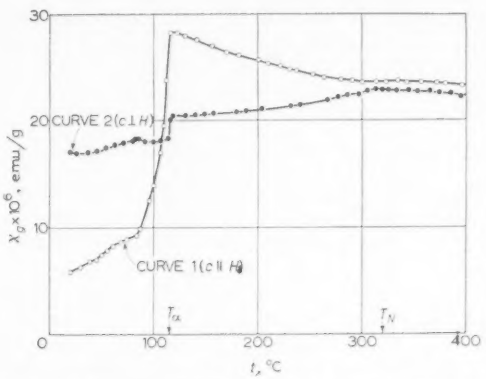


FIG. 3. Temperature variation of the susceptibility of $FeS_{1.04}$. $T_\alpha$ shifts to the lower-temperature side compared with that of the stoichiometric sample, but $T_N$ remains unchanged at 320°C. The anisotropy at $T_\alpha$ is smaller than that of the stoichiometric sample.

Both the anisotropy and the anomaly of $FeS_x$ at $T_\alpha$ have been found to depend sensitively upon the sulfur content ($x$ in $FeS_x$). In fact, with increase of sulfur content, both the anomaly and the anisotropy mentioned above become smaller and finally disappear at $x = 1.09$. Furthermore, $T_\alpha$ itself decreases with the increase of $x$, i.e. $T_\alpha$, which is 138°C for the stoichiometric sample, is observed to fall to 110°C for the sample with $x = 1.04$,

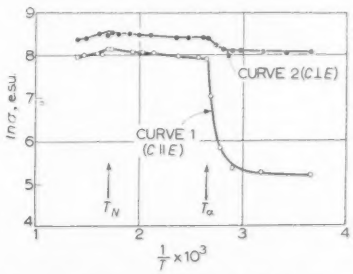


FIG. 4. Temperature variation of the conductivity of $FeS_{1.04}$. $T_\alpha$ shifts to the lower-temperature side compared with that of the stoichiometric sample, but $T_N$ remains unchanged at 320°C. The anisotropy at $T_\alpha$ is smaller than that of the stoichiometric sample, as in the case of the results for susceptibility.

although $T_N$ remains unchanged at 320°C irrespective of $x$, as shown in Figs. 3 and 4. These results are in agreement with previous results on polycrystalline samples.

The interpretation of the anisotropies and anomalies will be attempted in Section 4.

(b) *Anisotropy at the α-transformation*

In order to investigate in more detail the spin orientation of antiferromagnetism in the neighborhood of $T_\alpha$, the following measurements have been carried out. The temperature-dependence of susceptibility has been measured for the various angles between the $c$-axis of the sample and the external magnetic field $H$, and the results are shown in Fig. 5. The curves 1, 2, 3, and 4 show the results

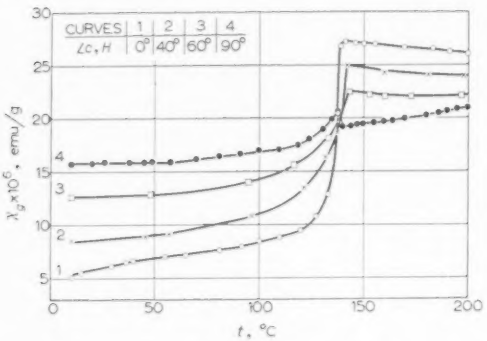


FIG. 5. Anisotropy of susceptibility of $FeS_{1.00}$ at $T_\alpha$ measured for various angles between the external magnetic field and the $c$-axis of the crystal.

corresponding to angles of 0°, 40°, 60°, and 90°, respectively. The sample used in these measurements was the same as that used for Fig. 1.

Rotating measurements of the following type have been made for the same sample. At a temperature below $T_\alpha$ (say at 10°C), the crystal was rotated about axes perpendicular to and then parallel to the $c$-axis of the crystal in an external field perpendicular to the axes of rotation. The results are shown in curves $A$ and $B$ in Fig. 6, respectively. At a temperature above $T_\alpha$ (say at 160°C), the results obtained under similar conditions are shown in curves $A'$ and $B'$ in the same figure. The abscissa in Fig. 6 represents, for curves $A$ and $A'$, the angle between the $c$-axis and the external field $H$, and, for curves $B$ and $B'$, the angle between a certain reference axis in the $c$-plane (perpendicular to the $c$-axis) and $H$. The results for $FeS_{1.04}$ corresponding to those in Figs. 5 and 6 have been already reported.[14]

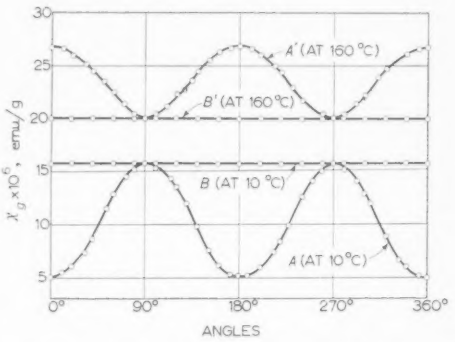


FIG. 6. Anisotropy of susceptibility of $FeS_{1.00}$. Curves $A$ and $A'$: sample rotated about the axis perpendicular to the $c$-axis. Curves $B$ and $B'$: sample rotated about the $c$-axis. Curves $A$ and $B$: results measured at 10°C. Curves $A'$ and $B'$: results measured at 160°C. $T_\alpha$ for the sample is 138°C.

(c) *Measurement of magnetization above $T_\alpha$*

As can be seen in Fig. 1, the susceptibility indicated by curve $1(C \| H)$ has a larger value than that of curve $2(C \perp H)$. It is therefore questionable

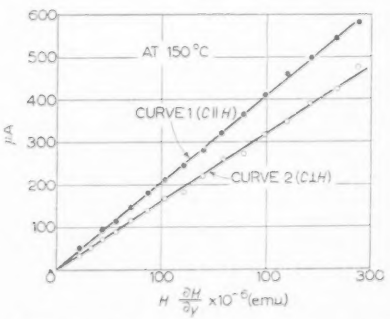


FIG. 7. Magnetic field dependence of the magnetization of $FeS_{1.00}$ above $T_\alpha$ (at 150°C). The ordinate denotes the current ($\mu A$) which counterbalances the force acting on the sample. The abscissa represents a quantity proportional to the square of the magnetic field ($H^2$).

whether the anomalously large susceptibility for $C \| H$ is due to a ferrimagnetic magnetization such as occurs in the $\gamma$-phase. In order to investigate this point in detail the following measurement was

made. A sample was placed in a field gradient $\delta H/\delta y$, and a force $\chi H(\delta H/\delta y)$ induced by the magnetization $\chi H$ was measured by means of the magnetic balance, the direction of $y$ being chosen as the vertical direction. The results obtained at 150°C are shown in Fig. 7, in which the abscissa is $H(\delta H/\delta y)$ and the ordinate is the current counterbalancing the force that acts on the sample. The applied magnetic field ranged from 400 to 7000 G, being parallel (curve 1) and perpendicular (curve 2) to the $c$-axis of the crystal. The experimental points in Fig. 7 are seen to lie on two straight lines which both pass through the origin. Therefore, the magnetization in the above experiment is proportional to the magnetic field, representing two constant susceptibilities for the cases $C \| H$ and $C \perp H$. Thus, the anomalous magnetization mentioned above can hardly be ascribed to the appearance of ferrimagnetism.

(d) *Anisotropy above $T_N$*

Fig. 1 shows distinct anisotropy above $T_N$, the Néel point (320°C). However, it is necessary to determine whether or not this anisotropy is an intrinsic property of the material. To elucidate this

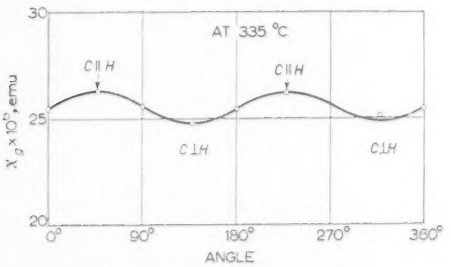


FIG. 8. Anisotropy at temperatures above $T_N$, measured for rotation around the axis perpendicular to the $c$-axis. Maximum and minimum values correspond to $C \| H$ and $C \perp H$, respectively. The abscissa denotes the angle between the external magnetic field and an arbitrary reference line.

point the crystal was rotated, at 335°C, about the axis perpendicular to the $c$-axis of the crystal with the field perpendicular to the axis of rotation. The results are shown in Fig. 8, from which the presence of anisotropy is apparent and may be considered to be characteristic of the substance.

## 4. INTERPRETATION OF RESULTS AND DISCUSSION

These measurements have been made mainly on stoichiometric or near stoichiometric samples. In the following, however, our discussion will be restricted to the stoichiometric samples.

According to the theory[16,17] of antiferromagnetism, the susceptibilities observed with the external field applied parallel and perpendicular to a preferred direction of the elementary magnet, become

$$\chi_{\|} = \frac{3SCB'}{S+1} \Big/ \left[ T + \tfrac{1}{2}(A+\Gamma)C\frac{3SB'}{S+1} \right], \quad (1)$$

and

$$\chi_{\perp} = 1/A, \quad (2)$$

where $S$ is the spin of a magnetic ion, $C$ the Curie constant, $B'$ a derivative of the Brillouin function with respect to its argument, and $T$ the absolute temperature. $\Gamma$ and $A$ are ferromagnetic and antiferromagnetic interaction constants, respectively. Denoting the number of magnetic ions per unit volume by $N$, the Curie constant $C$ is written

$$C = Ng^2 \cdot \mu_B{}^2 \cdot S(S+1)/3k, \quad (3)$$

where $g$, $\mu_B$, and $k$ are the $g$-factor, the Bohr magneton, and Boltzmann's constant, respectively. Furthermore, the Néel point or antiferromagnetic Curie point is given by

$$T_N = \tfrac{1}{2}C(A-\Gamma). \quad (4)$$

Now, $\chi_{\|}$ in equation (1) vanishes at $T = 0$, and increases with temperature. Above the Néel point $\chi_{\|}$ and $\chi_{\perp}$ show paramagnetic behavior, i.e.

$$\chi = C/(T+\theta), \text{ with } \theta = \tfrac{1}{2}C(A+\Gamma). \quad (5)$$

As seen in Fig. 1, the characteristic features of the experimental curves below $T_\alpha$ (138°C) may be well represented by equation (1) and (2), and those above the Néel point $T_N$ (320°C), by equation (5). Therefore, the preferred direction of antiferromagnetic spins below $T_\alpha$ may be reasonably supposed to lie parallel to the $c$-axis of the crystal. This conclusion is further supported by the curves in Fig. 5 and by curves $A$ and $B$ in Fig. 6, as explained below.

Now, the susceptibility observed for the external field $H$ along the direction making an angle $\theta$ with a preferred direction of the spin becomes[18]

$$\chi = \chi_{\parallel} \cdot \cos^2\theta + \chi_{\perp} \cdot \sin^2\theta. \qquad (6)$$

When the preferred direction is parallel to the $c$-axis, $\theta$ in equation (6) is identical with the angle shown on the abscissa of Fig. 6. Then, equation (6) is found to fit exactly the curve $A$ in Fig. 6, representing the spins restricted in parallel with the $c$-axis by a large anisotropy energy.

Next we shall proceed to the detailed discussion of the abrupt jump of both susceptibilities, $\chi_{\parallel}$ and $\chi_{\perp}$, at $T_{\alpha}$, together with the remarkably different magnetic behavior between $T_{\alpha}$ and $T_N$ in comparision with that below $T_{\alpha}$. The abrupt jump at $T_{\alpha}$ of the curve $1(C \parallel H)$ in Fig. 1 cannot be of ferromagnetic origin or due to the parasitic ferromagnetism discussed by NÉEL,[19] since the results in Fig. 7 show that the crystal has no ferromagnetism at this temperature. Looking at the results shown in Fig. 1, the characteristics of $\chi_{\parallel}$ and $\chi_{\perp}$ below $T_{\alpha}$ seem to exchange roles between $T_{\alpha}$ and $T_N$. Furthermore, as pointed out at the beginning of this paper, the $c$-axis of the crystal is observed to contract remarkably at $T_{\alpha}$, a fact which seems to be closely connected with the abrupt change of the susceptibilities. In view of this, we propose the following interpretation for the $\alpha$-transformation, i.e. the abrupt change of the magnetic behavior mentioned above.

In general, we may expect a discontinuous change of both the exchange energy constant $A$ and the anisotropy energy constant, associated with the contraction of the $c$-axis of the crystal at $T_{\alpha}$. On this account the spin direction is supposed to turn down from a direction parallel to the $c$-axis onto the $c$-plane perpendicular to the $c$-axis, and, furthermore, to exchange energy constant $A$ becomes smaller.

According to this assumption, the behavior of curve 1 at and above $T_{\alpha}$ may be represented by an equation similar to (2), and the abrupt increase of the susceptibility can be ascribed to the discontinuous decrease in $A$. Furthermore, the slow decrease with the temperature of curve 1 above $T_{\alpha}$ will be due to the gradual recovery of $A$ through thermal expansion of the crystal lattice. Similar considerations will be found to be valid for curve 2 by using equation (1).

The above explanation is further supported by curves $A'$ and $B'$ in Fig. 6. Curve $A'$ indicates that the spins turned down onto the $c$-plane have so large a resistance that they cannot turn out of the $c$-plane, and the constant value of curve $B'$ suggests two kinds of models for the available spin orientation: one is that the spins take two or more different fixed directions in the $c$-plane, and the other is that the spins in the $c$-plane are able to turn easily to keep themselves always perpendicular to the external magnetic field. However, the former idea is supported by curve 2 ($C \perp H$) in Fig. 1, in which the susceptibility increases with temperature in the temperature range considered and shows the existence of spin components parallel to the external field.

In general, an antiferromagnetic substance such as iron sulfide has two sublattices, in each of which the spins are set antiparallel with each other. On the basis of the model proposed above, each sublattice may be considered to be further divided into two or more minor sublattices, in each of which the spins are parallel. Such spin orientations within the $c$-plane appear to be possible in FeS from considerations of the symmetry of the crystal lattice. However, we are led to the same conclusion as above by a consideration of domain structure or twinning instead of the minor sublattices in each sublattice, the spins in each domain or twin aligning in the same direction.

We shall now compare the present results with previous ones on polycrystalline samples. The susceptibility of polycrystalline samples, $\chi_p$, can be calculated from the observed values of $\chi_{\parallel}$ and $\chi_{\perp}$ for the single crystal as follows:

$$\chi_p = \tfrac{1}{3}\chi_{\parallel} + \tfrac{2}{3}\chi_{\perp}. \qquad (7)$$

Below $T_{\alpha}$, $\chi_p$ may be calculated in a straightforward way from equation (7), but above $T_{\alpha}$ it may be obtained by assuming minor sublattices as follows.

If we assume curve 1 to be given by $\frac{1}{2}\chi_{\perp} + \frac{1}{2}\chi_{\perp}$, and curve 2 to be described by $\frac{1}{2}\chi_{\perp} + \frac{1}{2}\chi_{\parallel}$, and, moreover, $\chi_{\perp}$ is assumed to have the same value in the two cases of the external field $H$ applied along and perpendicular to the $c$-axis, we may get a virtual $\chi_{\parallel}$ curve as shown by the broken line in Fig. 9. Thus, the value of $\chi_p$ in the temperature range may be calculated from equation (7), using both curve 1 and the virtual $\chi_{\parallel}$ curve, and is shown

by the full line in Fig. 9, with the experimental results of HARALDSEN[3] for comparison.

The remarkable anisotropy of electrical conductivity, shown in Fig. 2, cannot be explained completely by the anisotropy of non-magnetic properties, i.e. the anisotropy of the non-spherical and parallel in another direction. Corresponding to the different spin orientations with respect to the directions of the electric current, different values of the electrical conductivity might be expected to appear in the various directions on account of some type of spin-dependent interaction,

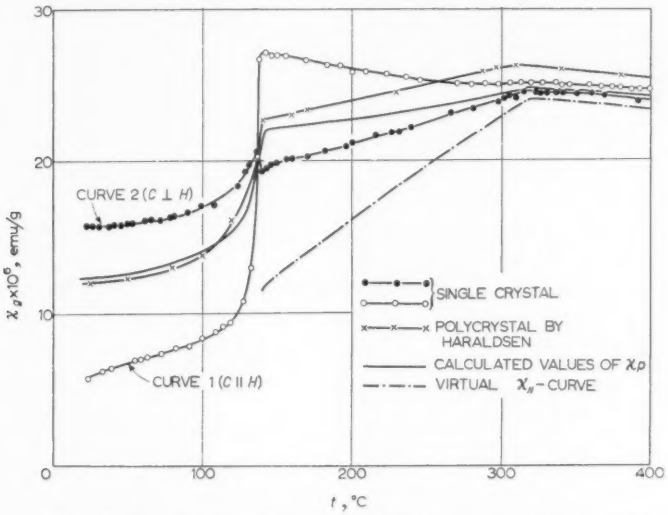


FIG. 9. Comparison of the susceptibilities of our single crystal ($FeS_{1.00}$) with those of HARALDSEN's polycrystalline sample. The calculated susceptibility of the polycrystal $\chi_p$ (full line) was obtained from equation (7). Above $T_\alpha$, Curve 1 was assumed to be $\frac{1}{2}\chi_\perp + \frac{1}{2}\chi_\perp$ and Curve 2 was assumed to be $\frac{1}{2}\chi_\perp + \frac{1}{2}\chi_\parallel$. From the assumption a virtual $\chi_\parallel$ curve (broken line) is drawn.

Fermi surface in momentum space and of scattering, which are mainly governed by crystal structure. Hence, the large anisotropy may be ascribed to the characteristic difference of the spin-orientations of the magnetic ion cores with respect to the direction of the electronic current. As is well known, in crystals containing transition-metal atoms, the conduction electrons are supposed to have, in addition to the usual electrostatic interaction, a spin-dependent interaction with the ion cores. This interaction, i.e. $s$–$d$ interaction, has been discussed in some detail by ZENER[20] and a number of other authors.[21]

For the antiferromagnetic crystal also, the conduction electrons may be considered to have a similar spin-dependent interaction with the magnetic ion cores within the crystal, whose spins are arrayed antiparallel to each other in one direction, although we have no conclusive theory at present.

In view of the above consideration, the observed anisotropies of the electronic conduction in FeS are believed to be caused by the different spin orientions with respect to the direction of an applied electric field.

Thus, at temperatures below $T_\alpha$, the conduction electrons under the influence of an external field along the $c$-axis of a single crystal are forced to travel along the $c$-axis, along which the spins of the magnetic ion cores are antiparallel to each other. Some correlation between such a spin orientation and the spin of a conduction electron might give rise to the hard flow of electric current (curve 1 of Fig. 2) in comparison with the case $E \perp C$, in which the core ions on the plane parallel to $E$ have their spins parallel to each other. For $T > T_\alpha$, the spins of the magnetic ion cores have been supposed

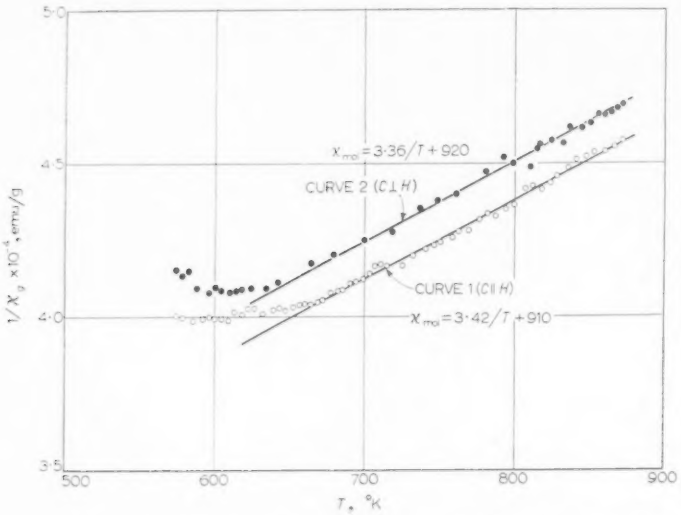


FIG. 10. $1/\chi$ versus $T$ curves at temperatures above $T_N$. From the curves, $C$ and $\theta$ were obtained from equation (5).

to flop down onto the $c$-plane and, furthermore, to become orientated in different directions from one minor sublattice to another. In this case, there is no detectable difference, in comparison with the case of $T < T_\alpha$, between the spin alignments in the directions parallel and perpendicular to the $c$-axis. The corresponding values of the electronic conduction therefore should become of about the same order of magnitude, as is in fact observed. The increase of electrical resistivity above $T_N$ may be understood in a similar way to MOTT's theory[22] of the electronic conduction in ferromagnetic metals, allowing for the random orientations of the spins of magnetic ion cores above $T_N$. Even in this temperature range ($T > T_N$), some minor anisotropy in the electronic conduction is actually observed; this is probably due to the short-range ordering of spin orientation, as seen in Figs. 1 and 8.

## 5. VALUES OF $C$ AND $\theta$, AND A NEW ANOMALY

In order to make an estimate of $C$ and $\theta$ in equation (5), the relation between $1/\chi$ and $T$ is given in Fig. 10, using the observed susceptibility above the Néel point. Two curves for $C \| H$ and $C \perp H$ are found to fit two straight lines, from which we obtain $C_{\text{mol}} = 3{\cdot}42$, $\theta = 910°\text{K}$ for $C \| H$ and $C_{\text{mol}} = 3{\cdot}36$, $\theta = 920°\text{K}$ for $C \perp H$. The mean values are $C_{\text{mol}} = 3{\cdot}38$ and $\theta = 917°\text{K}$, which may be compared with the values $C_{\text{mol}} = 3{\cdot}44$ and $\theta = 857°\text{K}$ for the polycrystalline sample.[17]

The effective number of the Bohr magnetons may be calculated by the equation[23]

$$P_{\text{eff}} = \frac{\sqrt{3RC}}{N \cdot \mu_B} = 2{\cdot}84\sqrt{C}, \qquad (8)$$

which leads to $P_{\text{eff}} = 5{\cdot}22$ for $C_{\text{mol}} = 3{\cdot}38$. On the other hand, if the $d$-orbital of the iron ion is assumed to be completely quenched and the electron spins alone to contribute to the magnetic moment, the effective number of Bohr magnetons is given by

$$P_{\text{eff}} = 2\sqrt{S(S+1)}, \qquad (9)$$

from which we get $P_{\text{eff}} = 4{\cdot}88$ for ferrous ions ($S = 2$), and $P_{\text{eff}} = 5{\cdot}91$ for ferric ions ($S = 5/2$). Comparing these values with the value 5·22 obtained from equation (8), the substance might be considered to contain a large proportion of ferric ions at the expense of ferrous ions. However, the speculation seems to be unreasonable since any ferrimagnetism corresponding to the difference of the magneton numbers between ferric and ferrous

ions has not been observed in a stoichiometric sample. The reasonable interpretation for the effective Bohr magneton number, therefore, will not be given until the nature of an ionic and covalent bonding in the crystal is clear.

From equations (4) and (5), together with the values of $\theta = 917°K$, $C_{mol} = 3{\cdot}38$, and $T_N = 320°C$ $(= 593°K)$, we have $A = 445$/mol and $\Gamma = 95$/mol. On the other hand, we may get $A = 739$/mol from equation (2) and the experimental value of $\chi = 15{\cdot}4 \times 10^{-6}$ emu. The discrepancy between the $A$ values may be reasonable if the temperature variation of $A$ is taken into account.

Finally, brief reference should be made to the anomalous behavior of susceptibility which has been found in the narrow range of temperatures just below $T_\alpha$. When the sample is cooled along the $C \perp H$ curve from the temperature just above $T_\alpha$, an extraordinarily large susceptibility with a temperature width of about 15°C has been observed just below $T_\alpha$. On the other hand, when the sample is cooled along the $C \parallel H$ curve, $T_\alpha$ shifts by about 20°C toward the lower-temperature side in comparison with that in the heating process, and, furthermore, the value of the susceptibility suddenly falls in two steps. These anomalous features have not been observed during the heating process. Although the nature of the anomaly is at present still obscure, it might indicate that in the cooling process the change of the magnitude of exchange energy constant at $T_\alpha$ has a different relaxation time from that of the spin directions (the anisotropy energy constant). However, the details of the anomaly will be further discussed in another paper, since the more detailed experiments are now in progress.

*Acknowledgements*—The authors wish to thank Professor T. MUTŌ, of Tokyo University for his kind advice and valuable discussions, and also Professor T. NAGAMIYA, of Osaka University, for valuable discussion. The authors also wish to thank Mr. TADAMIKI HIHARA for his help in the preparations of the sample and in the measurements in this work.

## REFERENCES

1. JUZA R. and BILTZ W., *Z. anorg. Chem.*, **205,** 273 (1932).
2. ZIEGLER M., Thesis, Zürich (1915).
3. HARALDSEN H., *Z. anorg. Chem.* **231,** 78 (1937); **246** 169, 195 (1941).
4. MIYAHARA S., *Proc. Phys.-Math. Soc. Japan* **22,** 358 (1940).
5. HIRONE T. and TSUYA N., *Phys. Rev.* **83,** 1063 (1951).
6. YOSIDA K., *Progr. Theor. Phys.* **6,** 356 (1956).
7. LOTGERING F. K., *Philips Res. Rep.* **11,** 190 (1956).
8. HÄGG G. and SUCKSDORFF I., *Z. phys. Chem.* B**22,** 444 (1933).
9. UEDA R., ICHINOKAWA T. and MITSUI T., *Busseiron Kenkyū* **33,** 55 (1950).
10. BERTAUT F., *C.R. Acad. Sci. (Paris)* **234,** 1295 (1952); *J. Phys. Radium* **15,** 77 (1954); *Bull. Soc. Franç Minér.* **79,** 276 (1956).
11. HIRONE T., MAEDA S. and TSUYA N., *J. Phys. Soc. Japan* **9,** 503 (1954).
12. HIRONE T., MAEDA S., CHIBA S. and TSUYA N., *J. Phys. Soc. Japan* **9,** 500 (1954).
13. KAMIGAICHI T., *J. Sci. Hiroshima Univ.* A**19,** 499 (1956).
14. KAMIGAICHI T., HIHARA T., TAZAKI H. and HIRAHARA E., *J. Phys. Soc. Japan* **11,** 606, 1123 (1956). HIHARA T., MURAKAMI M. and HIRAHARA E., *J. Phys. Soc. Japan* **12,** 743 (1957).
15. HIRONE T., MAEDA S. and TSUYA T., *Rev. Sci. Instrum.* **25,** 516 (1954).
16. VAN VLECK J. H., *J. Chem. Phys.* **9,** 85 (1941).
17. NAGAMIYA T., YOSIDA K. and KUBO R., *Advanc. Phys.* **4,** 29 (1955).
18. *Ibid.*, p.39.
19. NÉEL L., *Rev. Mod. Phys.* **25,** 58 (1953).
20. ZENER C., *Phys. Rev.* **81,** 440 (1951); **82,** 312 (1951); **83,** 299 (1951); **85,** 318 (1952).
21. MITCHELL A. H. *Phys. Rev.* **105,** 1439 (1957). PRATT G. W., Jr., *Phys. Rev.* **106,** 53 (1957). YOSIDA K., *Phys. Rev.* **106,** 893 (1957); **107,** 396 (1957).
22. MOTT N. F., *Proc. Phys. Soc.* **47,** 571 (1935); *Proc. Roy. Soc.* A**153,** 699 (1936).
23. STONER E. C., *Magnetism and Matter* p. 282. Methuen, London (1934).

*J. Phys. Chem. Solids* Pergamon Press 1958. Vol. 7. pp. 290–294.

# THE TEMPERATURE-DEPENDENCE OF THE ELASTIC MODULI OF VITREOUS SILICA

G. J. DIENES*

Mellon Institute, Pittsburgh, Pennsylvania

(*Received* 21 *March* 1958)

**Abstract**—The temperature-dependence of the elastic moduli of vitreous silica is anomalous in the sense that the moduli of this substance increase with increasing temperature above 60°K. This anomalous behavior is investigated theoretically, and it is shown to be already implied by the very low coefficient of thermal expansion. It is convenient to express the overall temperature coefficient of the modulus as the sum of two terms: the pure volume term (temperature constant) and the pure temperature term (volume constant). The low coefficient of expansion plays a double role in leading to an overall positive temperature coefficient for the moduli: it reduces the pure volume term essentially to zero and it changes the pure temperature term from a negative to a positive one. No conclusions can be drawn about the structure of vitreous silica from the anomalous behavior of its moduli, since this behavior is essentially a reflection of the anomalously low coefficient of thermal expansion. The important unsolved problem is the theoretical elucidation of the thermal expansion of this substance.

## 1. INTRODUCTION

THE anomalous positive temperature coefficients of the elastic moduli of vitreous silica have been studied experimentally in considerable detail in the last few years. The measurements of MARX and SIVERTSEN[1] showed that Young's modulus ($E$) for fused silica increases continuously with increasing temperature ($T$) from —170 to 1000°C. The $E$ versus $T$ curve is essentially linear from 25 to 1000°C. These unusual results were fully confirmed by MCSKIMIN[2] over the temperature range —200 to 40°C. He also showed that the shear modulus as a function of temperature behaves in the same way as Young's modulus. FINE *et al.*[3] extended the measurements to liquid-helium temperature and showed that there is an internal-friction peak in the neighborhood of 35°K at 50–100 kc and a minimum in the moduli near 60°K. Above 60°K the moduli (Young's modulus, shear modulus) and also Poisson's ratio increase continuously with increasing temperature.

It has been suggested[4,5] that this dependence of the elastic moduli of vitreous silica on temperature cannot be reconciled with the current view of its structure, namely the random-network hypothesis of ZACHARIASEN[6] and WARREN.[7] Vitreous silica, however, is anomalous in another important respect, since it has a very low (and at low temperatures negative) coefficient of thermal expansion. Thus, one can ask the following question: should a solid of very low coefficient of thermal expansion possess a positive modulus-temperature coefficient over some temperature range? The purpose of the present note is to examine this problem theoretically. We might anticipate the answer by stating that a very low coefficient of expansion implies a positive modulus-temperature coefficient for a Born–von Kármán-type solid at elevated temperatures. ANDERSON[8] examined this problem independently for a Debye solid and came to the same conclusion. He had to assume, however, that the Debye temperature and Poisson's ratio increase with increasing temperature.

## 2. THEORETICAL FORMULATION

Any modulus, $M$, may be considered as a function of volume and temperature,[9]

$$M = M(V, T). \tag{1}$$

* Permanent address: Brookhaven National Laboratory, Upton, New York.

The temperature-dependence is then given by

$$\frac{dM}{dT}=\left(\frac{\partial M}{\partial V}\right)_T\left(\frac{\partial V}{\partial T}\right)_P+\left(\frac{\partial M}{\partial T}\right)_V. \tag{2}$$

With the use of the coefficient of thermal expansion,

$$\alpha=\frac{1}{V}\left(\frac{\partial V}{\partial T}\right)_P.$$

Equation (2) may be written in the form

$$\frac{dM}{dT}=\alpha V\left(\frac{\partial M}{\partial V}\right)_T+\left(\frac{\partial M}{\partial T}\right)_V. \tag{3}$$

Equation (3) may also be put in the alternative form

$$\frac{dM}{dT}=-K\alpha\left(\frac{\partial M}{\partial P}\right)_T+\left(\frac{\partial M}{\partial T}\right)_V \tag{4}$$

where $K$ is the bulk modulus given by

$$K=-V\left(\frac{\partial P}{\partial V}\right)_T.$$

If $\alpha$ is negligibly small, then it is clear from equation (3) that the sign of $(dM/dT)$ will be governed by the sign of $(\partial M/\partial T)_V$. The purpose of this paper is to evaluate the two partial derivatives in equation (3), with particular emphasis on the $(\partial M/\partial T)_V$ term.

In the following an isotropic solid will be treated for which all elastic properties are defined by two moduli, the bulk modulus, $K$, and the shear modulus, $\mu$. Pure dilatation, $\epsilon_1$, and pure shear, $\epsilon_2$, will be used as the two corresponding strains. If $A$ is the Helmholtz free energy of the system, then the bulk and shear moduli are given by

$$K=\frac{1}{V_0}\frac{\partial^2 A}{\partial\epsilon_1{}^2} \qquad \mu=\frac{1}{V_0}\frac{\partial^2 A}{\partial\epsilon_2{}^2}$$

where $V_0$ is the molar or atomic volume at $T=0$. The Helmholtz free energy is expressed as a function of strain and temperature, in the usual way,[10] by the equation

$$A(\epsilon_1,\epsilon_2,T)=f(\epsilon_1,\epsilon_2)+kT\sum_i \ln(1-e^{-h\nu_i/kT}) \tag{6}$$

where $f$ is a function of the strains only and the $\nu_i$ are functions of the strains but not of the temperature, and where the zero point vibrations have been neglected. At any finite temperature and zero pressure, $\epsilon_1=\epsilon_1{}^0$, where $\epsilon_1{}^0$ represents the dilatation due to thermal expansion. Let the function $f$ be expanded around $\epsilon_1{}^0$ in a power series.* This yields

$$\begin{aligned}f(\epsilon_1,\epsilon_2)=&f(\epsilon_1{}^0,0)+f_1(\epsilon_1{}^0,0)(\epsilon_1-\epsilon_1{}^0)+\\&+f_2(\epsilon_1{}^0,0)\epsilon_2+\tfrac{1}{2}[f_{11}(\epsilon_1{}^0,0)(\epsilon_1-\epsilon_1{}^0)^2+\\&+2f_{12}(\epsilon_1{}^0,0)(\epsilon_1-\epsilon_1{}^0)\epsilon_2+f_{22}(\epsilon_1{}^0,0)\epsilon_2{}^2]+\ldots\end{aligned} \tag{7}$$

where

$$f_1=\frac{\partial f}{\partial\epsilon_1}, \text{ etc.}$$

Then

$$\frac{\partial A}{\partial\epsilon_1}=f_1+f_{11}(\epsilon_1-\epsilon_1{}^0)+f_{12}\epsilon_2+\sum_i Y\frac{\partial\ln\nu_i}{\partial\epsilon_1} \tag{8}$$

where

$$Y=h\nu_i(e^{h\nu_i/kT}-1)^{-1} \tag{9}$$

and $f_1$, $f_{11}$, etc., are functions of $\epsilon_1{}^0$ only. The derivative of $f_1$ with respect to $\epsilon_1$ is zero, and therefore, the bulk modulus is given by

$$K'=KV_0=f_{11}+\sum_i\left[\frac{\partial Y}{\partial\epsilon_1}\frac{\partial\ln\nu_i}{\partial\epsilon_1}+Y\frac{\partial^2\ln\nu_i}{\partial\epsilon_1{}^2}\right] \tag{10}$$

with an identical expression for the shear modulus, $\mu'$, except that $f_{11}$ is replaced by $f_{22}$ and $\epsilon_1$ by $\epsilon_2$. Since

$$\frac{\partial Y}{\partial\epsilon_1}=\left(\frac{\partial\ln\nu_i}{\partial\epsilon_1}\right)Y\left(1-\frac{Y}{kT}e^{h\nu_i/kT}\right) \tag{11}$$

the final expressions for the two moduli are

$$\begin{aligned}K'=&f_{11}(\epsilon_1{}^0,0)+\\&+\sum_i\left[\left(\frac{\partial\ln\nu_i}{\partial\epsilon_1}\right)^2 Y\left(1-\frac{Y}{kT}e^{h\nu_i/kT}\right)+Y\frac{\partial^2\ln\nu_i}{\partial\epsilon_1{}^2}\right]\end{aligned} \tag{12}$$

* This approach was suggested by some work of HUNTINGTON.[11]

$$\mu' = f_{22}(\epsilon_1{}^0, 0) + \\ + \sum_i \left[ \left( \frac{\partial \ln \nu_i}{\partial \epsilon_2} \right)^2 Y \left( 1 - \frac{Y}{kT} e^{h\nu_i/kT} \right) + Y \frac{\partial^2 \ln \nu_i}{\partial \epsilon_2{}^2} \right] \tag{13}$$

At high temperature $h\nu_i/kT \to 0$ and $Y \to kT$ and, therefore, the first term in the brackets of equations (12) and (13) approaches zero. At low temperature the first term dominates and the second term may be neglected. The derivatives with respect to temperature are evaluated next in these two approximations.

(a) *Temperature derivatives at constant volume at low temperature*

At low temperature the derivatives are given by

$$\left( \frac{\partial K'}{\partial T} \right)_{\epsilon_1{}^0} = \sum_i \frac{\gamma^2 Y^2}{kT^2} e^{h\nu_i/kT} \left[ 2 + \frac{h\nu_i}{kT} - \frac{2Y}{kT} e^{h\nu_i/kT} \right] \tag{14}$$

$$\left( \frac{\partial \mu'}{\partial T} \right)_{\epsilon_1{}^0} = \sum_i \frac{\delta^2 Y^2}{kT^2} e^{h\nu_i/kT} \left[ 2 + \frac{h\nu_i}{kT} - \frac{2Y}{kT} e^{h\nu_i/kT} \right] \tag{15}$$

where

$$\frac{\partial \ln \nu_i}{\partial \epsilon_1} = -\gamma$$

$$\frac{\partial \ln \nu_i}{\partial \epsilon_2} = -\delta.$$

The derivatives expressed by equations (14) and (15) are negative and approach zero at absolute zero because $Y \to 0$ as $T \to 0$. Thus, at low temperature the pure temperature terms are negative.

(b) *Temperature derivatives at constant volume at high temperature*

At high temperature the derivatives are given by

$$\left( \frac{\partial K'}{\partial T} \right)_{\epsilon_1{}^0} = k \sum_i \frac{\partial^2 \ln \nu_i}{\epsilon_1{}^2} \tag{16}$$

$$\left( \frac{\partial \mu'}{\partial T} \right)_{\epsilon_1{}^0} = k \sum_i \frac{\partial^2 \ln \nu_i}{\epsilon_2{}^2}. \tag{17}$$

In order to evaluate equations (16) and (17), one must estimate the second derivative of the frequencies with respect to the strains. This may be done as follows on the basis of a one-dimensional model. Let the potential be expanded to fourth term in the distance between the atoms, $x$. Thus,

$$V(x) = a_2(x-x_0)^2 - a_3(x-x_0)^3 + a_4(x-x_0)^4. \tag{18}$$

The force constant is given by the second derivative, namely

$$C(x) = 2a_2 - 6a_3(x-x_0) + 12a_4(x-x_0)^2. \tag{19}$$

In such a Mie–Gruneisen model with nearest-neighbor forces (12), the frequency is proportional to $C^{\frac{1}{2}}$ and, therefore, one may write[12]

$$\frac{d^2 \ln \nu}{d\epsilon_1{}^2} = \frac{1}{2} \frac{d^2 \ln (AC)}{dx^2} \\ = \frac{1}{2A} \frac{d}{dx} \left[ \frac{-6a_3 + 24a_4(x-x_0)}{2a_2 - 6a_3(x-x_0)} \right] \\ = \frac{1}{2A} \left( \frac{-3a_3}{a_2} \right) \frac{d}{dx} \left[ \frac{1 - \frac{4a_4}{a_3}(x-x_0)}{1 - \frac{3a_3}{a_2}(x-x_0)} \right] \\ = \frac{1}{2A} \left( \frac{-3a_3}{a_2} \right) \frac{d}{dx} \left[ 1 - (x-x_0) \left( 4\frac{a_4}{a_3} - 3\frac{a_3}{a_2} \right) \right] \\ = \frac{1}{2A} \left[ 12\frac{a_4}{a_2} - 9\left( \frac{a_3}{a_2} \right)^2 \right]. \tag{20}$$

It is clear from equation (20) that whenever the coefficient of thermal expansion, $a_3$, is small and $a_4 > 0$, the second derivative of the frequency with respect to the strain will be positive. Thus, at high temperature and for small thermal expansion the pure temperature terms are positive.

Several comments concerning this derivation are in order. The results of the one-dimensional model can be extended to the three-dimensional case, although this extension is not fully rigorous because of deformations perpendicular to the bond directions. This correction is generally small.[12] In the argument above $a_4$ was taken to be positive. There is no rigorous proof of this assignment, but a positive value for $a_4$ is probably a rather general one since it is easily shown that $a_4$ is positive for inverse-power and Morse potential functions.

The main result has now been derived. It can be seen from equation (3) that for negligibly small

thermal expansion the second term of that equation, namely the pure temperature term, determines the sign of $dM/dT$. Equation (20) shows that the pure temperature term will be positive at elevated temperature under the same condition, namely, a negligibly small thermal expansion, provided that $a_4$ is positive. It is possible, of course, that $a_4$ is negative for vitreous silica and that, therefore, the above model is not applicable to this substance. The theory strongly suggests, however, that the anomalous temperature-dependence of the moduli and the anomalously low thermal expansion are intimately connected as outlined in this theory.

Although they are not needed for the main point of this paper, the pure volume terms are also given below for the sake of completeness.

(c) *Volume derivatives at constant temperature at low temperature*

At low temperature the volume derivatives are

$$\left(\frac{\partial K'}{\partial \epsilon_1{}^0}\right)_T = \frac{\partial f_{11}}{\partial \epsilon_1{}^0} + \frac{\partial}{\partial \epsilon_1} \sum_i \left[\left(\frac{\partial \ln \nu_i}{\partial \epsilon_1}\right)^2 \times \right.$$

$$\left. \times Y\left(1 - \frac{Y}{kT} e^{h\nu_i/kT}\right)\right]_{\epsilon_1{}^0} \qquad (21)$$

with a similar expression for the shear modulus. Upon carrying out the differentiation, the results are

$$\left(\frac{\partial K'}{\partial \epsilon_1{}^0}\right)_T = \frac{df_{11}}{\partial \epsilon_1{}^0} + \sum_i \left\{\left(\frac{\partial \ln \nu_i}{\partial \epsilon_1}\right)^3 \times \right.$$

$$\left. \times Y\left[1 - e^{h\nu_i/kT}\left(\frac{3Y}{kT} - \frac{2Y^2}{k^2T^2} + \frac{h\nu_i}{k^2T^2}\right)\right]\right\}_{\epsilon_1{}^0} \qquad (22)$$

$$\left(\frac{\partial \mu'}{\partial \epsilon_1{}^0}\right)_T = \frac{\partial f_{22}}{\partial \epsilon_1{}^0} + \sum_i \left\{\left(\frac{\partial \ln \nu_i}{\partial \epsilon_1}\right)\left(\frac{\partial \ln \nu_i}{\partial \epsilon_2}\right)^2 \times \right.$$

$$\left. \times Y\left[1 - e^{h\nu_i/kT}\left(\frac{3Y}{kT} - \frac{2Y^2}{k^2T^2} + \frac{h\nu_i}{k^2T^2}\right)\right]\right\}_{\epsilon_1{}^0} \qquad (23)$$

The term in the brackets is positive, and since $\partial f_{11}/\partial \epsilon_1{}^0$ is expected to be negative the pure volume terms may be either positive or negative at low temperature (this term need not approach zero as $T \to 0$, since it is multiplied by the coefficient of expansion, $\alpha$, in the complete expression for the modulus and $\alpha \to 0$ as $T \to 0$).

(d) *Volume derivatives at constant temperature at high temperature*

At high temperature the expressions for the moduli are

$$K' = f_{11}(\epsilon_1{}^0) + kT \sum_i \frac{\partial^2 \ln \nu_i}{\partial \epsilon_1{}^2} \qquad (24)$$

$$\mu' = f_{22}(\epsilon_1{}^0) + kT \sum_i \frac{\partial^2 \ln \nu_i}{\partial \epsilon_2{}^2}. \qquad (25)$$

Upon differentiation with respect to $\epsilon_1$ one obtains

$$\left(\frac{\partial K'}{\partial \epsilon_1{}^0}\right)_T = \frac{\partial f_{11}}{\partial \epsilon_1{}^0} + kT \sum_i \left(\frac{\partial^3 \ln \nu_i}{\partial \epsilon_1{}^3}\right)_{\epsilon_1{}^0} \qquad (26)$$

$$\left(\frac{\partial \mu'}{\partial \epsilon_1{}^0}\right)_T = \frac{\partial f_{22}}{\partial \epsilon_1{}^0} + kT \sum_i \left(\frac{\partial^3 \ln \nu_i}{\partial \epsilon_2{}^2 \partial \epsilon_1}\right)_{\epsilon_1{}^0}. \qquad (27)$$

The third derivatives of the frequencies with respect to the strains are expected to be small (zero in the approximation of equation (20)). The $\partial f_{11}/\partial \epsilon_1{}^0$ terms are expected to be negative and, therefore, the pure volume terms are probably negative at elevated temperatures.

The final results are summarized in Table 1.

*Table* 1. *The sign of the various terms in the expression for the temperature coefficient of the modulus* (*equation* 3)

| Term | $T = 0°K$ | Low temp. | High temp. | |
|---|---|---|---|---|
| | | | Large $\alpha$ | Small $\alpha$ |
| $\left(\frac{\partial M}{\partial T}\right)_V$ | 0 | − | − | + |
| $\left(\frac{\partial M}{\partial V}\right)_T$ | − or + | − or + | − | − |
| $\frac{dM}{dT}$ | 0 | − | − | + |

$\alpha$ = coefficient of thermal expansion.

$$\frac{dM}{dT} = \alpha V\left(\frac{\partial M}{\partial V}\right)_T + \left(\frac{\partial M}{\partial T}\right)_V.$$

## 3. DISCUSSION

The following points can be made on the basis of the theoretical work of the previous section:

(1) Most solids are characterized by appreciable thermal expansion and, consequently, by a negative temperature coefficient of the moduli. In those cases where the pure volume and pure temperature terms have been investigated[9,11] (by means of variation of moduli with pressure) both terms have been found to be negative ($\alpha$ is large in all these cases).

(2) For an isotropic substance of low thermal expansion, the thermal expansion coefficient plays two important roles in reversing the sign of the temperature coefficient: (a) the smallness of $\alpha$ eliminates the negative volume term and (b) at small $\alpha$ the pure temperature term becomes positive at elevated temperatures.

(3) It is of interest to estimate the pure volume component, since it has been assumed all along that for silica it is very small compared to $dM/dT$. One can do this on the basis of equation (4), using the pressure variation of the modulus. From the data of McSKIMIN,[2] one obtains, for the $-60$ to $40°$C region, for the temperature coefficient of the bulk modulus

$$\frac{dK}{dT} = 12{\cdot}3 \times 10^7 \text{ dynes cm}^{-2}/°\text{C}.$$

From the data of BIRCH and DOW,[13] one can estimate the variation of the bulk modulus with pressure. This dimensionless coefficient is about $-8{\cdot}0$ at 25°C and decreases with increasing temperature. With $\alpha = 2 \times 10^{-6}$ and $K = 3{\cdot}65 \times 10^{11}$, one obtains

$$\alpha V\left(\frac{\partial K}{\partial V}\right)_T = -K\alpha\left(\frac{\partial K}{\partial P}\right)_T$$
$$= 0{\cdot}6 \times 10^7 \text{ dynes cm}^{-2}/°\text{C}$$

which is very small compared to the total $dK/dT$ of $12{\cdot}3 \times 10^7$ dynes cm$^{-2}$/°C, in agreement with the assumptions made in this paper.

(4) The density of vitreous silica can be appreciably increased by reactor irradiation. In some recent work MAYER and GIGON[14] found that there is a corresponding increase in the modulus. Further, preliminary measurements by MAYER[15] indicate that the coefficient of thermal expansion decreases upon irradiation and that there is a corresponding increase in the positive temperature coefficient of Young's modulus. These experimental results are in qualitative agreement with the theory proposed in this paper.

In some ways the results given here are disappointing. The theory indicates that the anomalous modulus-temperature behavior is simply a consequence of the small coefficient of thermal expansion for silica. Consequently, one can conclude nothing about the structure of silica from this anomalous behavior. What is required is an explanation of the thermal expansion behavior of this substance based on first principles, a problem which has not been solved.

*Acknowledgements*—The writer is grateful to H. B. HUNTINGTON and to G. H. VINEYARD for several stimulating discussions, and to O. L. ANDERSON for communicating his results prior to publication.

## REFERENCES

1. MARX J. W. and SIVERTSEN J. M. *J. Appl. Phys.* **24,** 81 (1953).
2. McSKIMIN H. J. *J. Appl. Phys.* **24,** 988 (1953).
3. FINE M. E., VAN DUYNE H. and KENNEY N. T. *J. Appl. Phys.* **25,** 402 (1954).
4. BABCOCK C. L., BARBER S. W. and FAJANS K. *Industr. Engng. Chem.* **46,** 161 (1954).
5. SPINNER S. *J. Amer. Ceram. Soc.* **39,** 113 (1956).
6. ZACHARIASEN W. H. *J. Amer. Chem. Soc.* **54,** 3841 (1932).
7. WARREN B. E. *J. Appl. Phys.* **8,** 645 (1937).
   WARREN B. E., KRUTHER H. and MORNINGSTAR O. *J. Amer. Ceram. Soc.* **21,** 259 (1938) and later papers.
   For a recent review of the physics of the glassy state, see CONDON E. U. *Amer. J. Phys.* **22,** 43, 132, 224, 310 (1954).
8. ANDERSON O. L. To be published.
9. See, for example, LAZARUS D. *Phys. Rev.* **76,** 545 (1949).
10. See, for example BORN M. and HUANG K. *Dynamical Theory of Crystal Lattices* Chap. II. Clarendon Press, Oxford (1954).
11. HUNTINGTON H. B. *Solid State Physics.* (Ed. F. SEITZ and D. TURNBULL). Academic Press, New York (To be published).
12. See, for example, LEIBFRIED G. *Handbuch der Physik,* Vol. VII–1, pp. 274–279. Springer, Berlin (1955).
13. BIRCH F. and DOW R. B. *Bull. Geol. Soc. Amer.* **47,** 1235 (1936).
14. MAYER G. and GIGON J. *J. Phys. Radium* **18,** 109 (1957).
15. MAYER G. Private communication.

*J. Phys. Chem. Solids* Pergamon Press 1958. Vol. 7. pp. 295–300

# ZUR FRAGE DES DAMPFDRUCKS DER VERBINDUNGEN InAs, GaAs, InP UND GaP

O. G. FOLBERTH

Aus dem Forschungslaboratorium der Siemens-Schuckertwerke AG. Erlangen/Deutschland

(*Received* 8 *April* 1958)

**Zusammenfassung** — Es wird eine neue Methode zur Messung des Dampfdruckes einer binären Verbindung an ihrem kongruenten Schmelzpunkt beschrieben. Diese Methode lässt sich ohne weiteres allerdings nur anwenden, wenn die Verbindung die folgenden Bedingungen erfüllt: In einem offenen System sei der Schmelzvorgang inkongruent, während ein kongruentes Schmelzen im Gleichgewicht mit einer Dampfphase, die nahezu nur aus der leichtflüchtigen Komponente besteht, möglich sei. Die Löslichkeit der Komponenten in der betrachteten festen Verbindung sei vernachlässigbar.

Die Methode besteht im wesentlichen darin, dass eine Schmelze zum einseitigen Erstarren gebracht wird, wobei der Gleichgewichtsdampfdruck von Versuch zu Versuch geändert wird. Der gesuchte Dampfdruck war vorhanden, falls ein so hergestellter Kristall vollständig frei von Einschlüssen ist. Dieser Dampfdruck wird berechnet aus der Menge der leichtflüchtigen Komponente, die sich zur Zeit des Erstarrungsprozesses in der Dampfphase befand.

An einigen $A^{III}B^{V}$–Verbindungen wurden Messungen durchgeführt und dabei die folgenden Werte für den Dampfdruck am Schmelzpunkt ermittelt : InAs : 0,25 atm. ; GaAs : 0,89 atm. ; InP $>$ 15,5 atm. ; GaP $>$ 13,5 atm. Einige Folgerungen für die Herstellung und das Umschmelzen von Verbindungen der genannten Art werden diskutiert.

**Abstract**—A new method for the measurement of the vapour-pressure of a binary compound at its melting point is described. This method, however, is only applicable if the following conditions are met :

The melting process must be accompanied by a decomposition of the compound in an open system, whereas a melting without decomposition must occur, if the melting takes place in equilibrium with a vapour phase consisting almost entirely of the high-volatility component of the compound and if a certain pressure is applied. The solubilities of the components in the solid compound must be negligible.

The proposed method consists substantially of a normal freezing of a melt in equilibrium with a vapour phase. Freezing processes are carried out under different pressures. If the resulting solid consists completely of a single phase, the chosen vapour pressure equals the equilibrium-vapour-pressure of this compound at the melting point. This vapour-pressure can be calculated from the amount of the high-volatility component in the vapour phase during the freezing process. Measurements on some $A^{III}B^{V}$–compounds gave the following values : InAs : 0,25 atm. GaAs : 0,89 atm. ; InP $>$ 15,5 atm; GaP $>$ 13,5 atm. Some conclusions about the preparation and the remelting of compounds of this kind are discussed.

## 1. EINLEITUNG

Die binären Systeme In-As, Ga-As, In-P und Ga-P sind gleichartig aufgebaut. Sie enthalten bei 50 Atomprozent eine Verbindung der Art $AB$ ($A$ = In bzw. Ga ; $B$ = As bzw. P), während die Teilsysteme $A$–$AB$ bzw. $AB$–$B$ eutektisch aufgebaut sind, wobei das Eutektikum z.T. entartet ist, und die Existenzgebiete der Einzelphasen $A$, $AB$ und $B$ sehr eng sind.[1,2,3,4,9]

Die Verbindungen schmelzen nur unter einem nicht vernachlässigbaren Dampfdruck der leichterflüchtigen Komponente $B$ (As bzw. P) kongruent, während sie sich beim Erhitzen in einem offenen Tiegel in eine $A$-reichere Schmelze und einen $B$-reicheren Dampf zersetzen.[5,6] Systeme dieser Art sind schon früher eingehend beschrieben worden.[7]

Seit der Halbleitercharakter der genannten

Verbindungen entdeckt[8] und näher untersucht worden ist,[9] stellt sich immer dringender die Aufgabe, diese Verbindungen in einphasiger, homogener, möglichst einkristalliner Form herzustellen.[5,6,10] Dazu ist die genaue Kenntnis des Zustandsdiagrammes in der allgemeinen Form eines $p$-$T$-$x$-Diagrammes wünschenswert ($p$ = Druck, $T$ = Temperatur, $x$ = Konzentration). Zur ersten Orientierung reicht es allerdings aus, wenn man den kongruenten Schmelzpunkt der jeweiligen Verbindung $AB$ und den dort herrschenden Gleichgewichtsdampfdruck kennt. Mit Hilfe der bekannten thermodynamischen Daten der Komponenten $A$ und $B$ lassen sich damit, auf Grund der eingangs beschriebenen gleichartigen Charakteristik der hier interessierenden Systeme, diese in groben Zügen skizzieren.

## 2. PRINZIPIELLES ZUR DAMPFDRUCKMESSUNG UND BISHERIGE ERGEBNISSE

Der kongruente Schmelzpunkt einer in 1 beschriebenen Verbindung $AB$ ist—entsprechend der Gibbschen Phasenregel — ein nonvarianter Punkt, d.h. die Umwandlung eines Kristall $AB$ in eine Schmelze derselben Zusammensetzung geschieht nur unter einer bestimmten Temperatur $T_s$, einem bestimmten Dampfdruck $p_s$ und einer bestimmten Dampfkonzentration $x_s^D$. Da die Komponente $A$ um mehrere Grössenordnungen schwerflüchtiger ist als die Komponente $B$, bezeichnet die Zusammensetzung $x_s^D$ nahezu reines $B$. Der gesamte Gleichgewichtsdampfdruck $p_s$ ist also dem Partialdampfdruck $p_s^B$ nahezu gleichzusetzen, während der Partialdampfdruck $p_s^A$ der schwerflüchtigen Komponente $A$ bzw. der Partialdampfdruck $p_s^{A_mB_n}$ einer eventuellen dampfförmigen Verbindung $A_mB_n$ dagegen vernachlässigbar ist.[3] Wir werden im folgenden daher $p_s^B = p_s$ setzen.

Die bisher bekanntgewordenen Dampfdruckmessungen an Systemen der hier interessierenden Art sind Reihenmessungen über Gleichgewichtsphasen unterschiedlicher Zusammensetzung (festes $AB$ und nichtstöchiometrische Schmelze). Der Dampfdruck am kongruenten Schmelzpunkt (Gleichgewicht zwischen festem $AB$ und Schmelze derselben stöchiometrischen Zusammensetzung) wurde daraus durch Extra- bzw. Interpolation gewonnen.[3,11] Die Bestimmung des Dampfdruckes selbst erfolgt dabei auf verschiedene Weise. Entweder wurde er nach der „Taupunktsmethode" bestimmt,[11] oder es wurde an der kältesten Stelle des Systems dauernd ein Bodenkörper der leichtflüchtigen Komponente $B$ aufrechterhalten, dessen Temperatur den Druck $p$ im gesamten System bestimmt.[3]*

Die so ermittelten Werte für den Gleichgewichtsdampfdruck $p_s$ am Schmelzpunkt sind in Tabelle 2 verzeichnet. Die Werte stimmen untereinander sehr schlecht überein, so dass eine Nachprüfung mit einer weiteren Methode, die die Fehlerquellen der bisherigen Methoden ausschliesst, als zweckmässig angesehen wurde.

## 3. MESSMETHODE

Die hier angewandte Messmethode unterscheidet sich in zwei wesentlichen Punkten von den bisher bekanntgewordenen: (Absatz 2)

($\alpha$) Der Dampfdruck wird direkt am Schmelzpunkt gemessen.

($\beta$) Die Berechnung des Dampfdruckes geschieht nicht im Umweg über Dampfdruckkurven des Bodenkörpers der leichtflüchtigen Komponente $B$. Man umgeht damit (insbesondere bei den Phosphiden) die Unsicherheiten, die durch die Polymorphie des Phosphors hervorgerufen werden.

Im einzelnen wird wie folgt verfahren :

In ein Schiffchen aus Graphit oder bekohltem Quarz wird eine Menge $a$ der schwerflüchtigen Komponente $A$ eingewogen. Das gefüllte Schiffchen wird daraufhin in eine Ampulle aus Quarzglas eingeschmolzen. In dieselbe Ampulle wird eine Menge $b+\Delta b$ der leichtflüchtigen Komponente $B$ eingeschmolzen. Da die Ampulle etwa doppelt so lang (Länge $\approx$ 25 bis 30 cm, Durchmesser $\approx$ 2 cm) wie das Schiffchen ist und sich die beiden Komponenten $A$ und $B$ an den entgegengesetzten Enden der Ampulle befinden, sind

* Dieses ist in guter Näherung richtig, da nach den Ausführungen am Anfang des Absatzes die Dampfphase beinahe nur aus $B$ besteht. So kann sowohl das hier interessierende Teilsystem (festes $AB$ mit Schmelze) als auch das Teilsystem, das aus dem Bodenkörper $B$ besteht, je für sich mit der Dampfphase (näherungsweise) im Gleichgewicht stehen, ohne sich untereinander ins Gleichgewicht zu setzen. Die beiden Teilsysteme sind dabei zwar räumlich getrennt, aber im selben Dampfraum angeordnet.

sie zunächst nicht in unmittelbarer Berührung (Abb. 1). Ob die Ampulle ansonsten evakuiert oder zusätzlich mit einem neutralen Gas gefüllt wurde, ist für das weitere Geschehen ohne prinzipielle Bedeutung, da durch eine solche Gasfüllung lediglich eine Dämpfung der Reaktionsgeschwindigkeit erreicht werden kann.

Die Mengen $a$ und $b$ sind so gewählt, dass daraus gerade die stöchiometrische Verbindung $AB$ gebildet werden kann, während $\Delta b$ einen bestimmten Überschuss der Komponente $B$ darstellt.

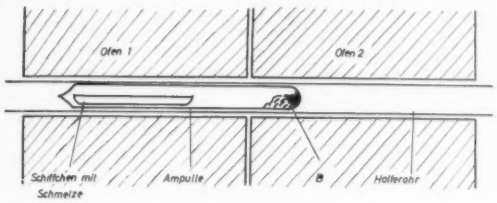


Versuchsanordnung
(schematisch)

ABB. 1. Versuchsanordnung (schematisch).

Die so vorbereitete Ampulle wird in einen „Zwei-Temperatur-Ofen" eingeführt. Die eine Temperaturzone $T_1$ umfasst den Teil der Ampulle, der das Schiffchen enthält, die andere Temperaturzone $T_2$ den Teil mit der Komponente $B$. Daraufhin wird $T_1$ zunächst erhöht bis etwas über den Schmelzpunkt der herzustellenden Verbindung $AB$ ($T_1 \geqslant T_s$). Danach wird auch die Temperatur $T_2$ erhöht. Der Dampfdruck über der Komponente $B$ beginnt zu steigen, der Dampfraum beginnt sich mit dampfförmigem $B$ zu füllen, und die Schmelze beginnt $B$ aus der Dampfphase aufzunehmen. Der Gleichgewichtsdampfdruck über der Schmelze bleibt immer (auch in der Umgebung der stöchiometrischen Konzentration) für gleiche Temperaturen wesentlich kleiner als der Gleichgewichtsdampfdruck des Bodenkörpers. Daher wird bei einer Temperatur $T_2 = T_B < T_s$ der Bodenkörper verschwunden sein. Der Grossteil von $B$ befindet sich nun in der Schmelze, während ein kleiner Teil sich in der Dampfphase befindet und ihren wesentlichen Teil ausmacht. Die Zusammensetzung der Schmelze wird nach der beschriebenen Versuchsführung stöchiometrisch sein — also gleiche molare Mengen an $A$ bzw. $B$ enthalten — wenn die Zusatzmenge $\Delta b$ gerade ausreicht, um den Gleichgewichtsdampfdruck $p_s$ zu bilden.

Das weitere läuft also darauf hinaus, erstens die Stöchiometrie der Schmelze festzustellen und zweitens aus der bekannten eingewogenen Menge $\Delta b$ den Dampfdruck zu berechnen. Dazu wird die Ampulle, die sich zunächst z.T. im Ofen 1 mit der Temperatur $T_1 > T_s$ und zum anderen Teil im Ofen 2 mit der Temperatur $T_2$ (Abb. 1) befindet, langsam ($\approx$ 1 mm/min) in den Ofen 2 geschoben, so dass nach und nach die ganze Ampulle die Temperatur $T_2$ annimmt.* Dabei wird $T_2$ konstant gehalten, auf einem Wert zwischen $T_B$ und $T_s$. Da $T_2$ unterhalb der jeweiligen Schmelztemperatur $T_s$ der Verbindung liegt, erfolgt im Schiffchen ein gerichtetes Erstarren. Anschliessend wird die Ampulle auf Zimmertemperatur abgekühlt und geöffnet. Der im Schiffchen befindliche Kristall wird im allgemeinen weitgehend einphasig sein und aus der Verbindung $AB$ bestehen, jedoch zeigt das zuletzt erstarrte Ende u.U. Abweichungen. Dabei haben wir 3 Fälle zu unterschieden:

($\alpha$) Der Kristall ist vollständig einphasig. In diesem Falle entspricht das eingewogene $\Delta b$ gerade dem Gleichgewichtsdampfdruck der Verbindung $AB$ am Schmelzpunkt. Während des Erstarrens fand kein nennenswerter gerichteter Austausch von $B$ zwischen Schmelze und Dampfphase statt.

($\beta$) Der Kristall zeigt am zuletzt erstarrten Ende Einschlüsse von $A$. In diesem Falle entspricht das eingewogene $\Delta b$ einem kleineren Dampfdruck als im Falle $\alpha$. Die Schmelze war nicht stöchiometrisch, sondern enthielt einen Überschuss $\Delta a$ der Komponente $A$. Beim gerichteten Abkühlen kristallisierte aus dieser Schmelze zunächst einphasig stöchiometrisches $AB$ aus. Dadurch verarmte die Schmelze weiter an $B$, so dass die Schmelze $A$-reicher wurde. Zwar wurde der $B$-Mangel der Schmelze teilweise durch Nachlieferung aus der Dampfphase wieder ausgeglichen, gleichzeitig sank dadurch jedoch der Dampfdruck. Gegen Ende der Erstarrung ist

* Die Temperaturen wurden mit $Ni/Cr_{12,5}$ $Ni_{87,5}$ Thermoelementen gemessen. Für InP, GaAs und GaP wurde der Ofen 1 weggelassen und dafür die Schmelze induktiv erhitzt. Dies erwies sich als notwendig, da damit eine unnötig hohe Aufheizung der Quarzampulle vermieden wurde, welche sonst leicht zu Explosionen führt. In diesen Fällen wurde die Temperatur $T_1$ mit einem Strahlungspyrometer gemessen.

dieser Prozess soweit fortgeschritten, dass die Schmelze beinahe nur noch aus $A$ besteht. Der Kristall wird also in zunehmendem Masse Einschlüsse von $A$ aufweisen, ja am zuletzt erstarrten Ende sogar beinahe nur aus $A$ bestehen. Einschlüsse von $A$ werden allerdings nicht auftreten, wenn die Nachlieferung von $B$ aus der Dampfphase ausreicht, um vollständig einphasiges $AB$ zu bilden. Es wird dann der Fall $\alpha$ vorgetäuscht. Die dadurch entstehende Ungenauigkeit der Messmethode wird um so geringer sein, je kleiner die Dampfmenge in Bezug auf die Stabgrösse ist. Bei gleicher Geometrie sind also die Messungen bei geringem Dampfdruck genauer als bei hohem. Daraus folgt, dass für InAs und GaAs die erwähnte Ungenauigkeit keine Rolle spielt, hingegen bei den Phosphiden InP und GaP zu berücksichtigen ist.

($\gamma$) Der Kristall weist am zuletzt erstarrten Ende Blasen (Lunker) auf. In diesem Falle war der Dampfdruck höher als im Falle $\alpha$.

Die ursprüngliche Schmelze war also $B$-reicher als der Formel $AB$ entspricht. Zwar kristallisierte zunächst einphasiges $AB$ aus, gleichzeitig aber wurde die Schmelze noch $B$-reicher. Durch Austausch mit der Dampfphase stieg daher der Dampfdruck. Gegen Ende der Erstarrung ist dieser Prozess soweit fortgeschritten, dass an der Erstarrungsfront das jeweils überschüssige $B$ nicht vollständig an die Dampfphase oder Restschmelze abgegeben werden kann und daher als Gasbläschen vom Kristall eingeschlossen wird. Das Verfahren ist zwar hier nicht so wirksam wie im Falle $\beta$, weil ein Teil der in der Schmelze angereicherten Komponente $B$ in den Dampfraum entweichen kann und somit im Stabende nicht mehr erfassbar ist. Die Erkennbarkeit wird aber andererseits verbessert durch den Umstand, dass $B$ wie bereits betont, gasförmig eingeschlossen wird und eine sehr geringe Menge schon eine gut zu beobachtende Störung des Kristalls verursacht.

Für InAs und GaAs liess sich so durch Variation von $\Delta b$ der stöchiometrische Fall $\alpha$ mit $\Delta b = \Delta b^{St}$ auf etwa 10% genau angeben. Für InP und GaP machte sich der vorhin beschriebene systematische Fehler stark bemerkbar, so dass der Fall $\alpha$ für einen grösseren Dampfdruckbereich vorgetäuscht wurde. Der Fall $\gamma$ konnte nicht erreicht werden, da er der hohen Drucke wegen experimentell schwer zugänglich ist.

Die Berechnung des Gleichgewichtsdampfdruckes aus den gemessenen $\Delta b^{St}$-Werten ergab sich wie folgt: Der Druck $p_s$; wird einfach mit Hilfe der idealen Gasgleichung berechnet. Korrekturen wegen Nichtidealität des Dampfes wurden vernachlässigt, da die in Frage stehenden Drucke und Temperaturen recht weit entfernt von den kritischen Daten sind (für Arsen $T_k \approx 1400$°C; für Phosphor: $T_k = 948$°C, $p_k = 80$ atm.) Es gilt also

$$p_s = n.R.T_m/V \qquad (1)$$

Dabei bedeutet :

$n$ = Anzahl der Mole Dampf.
$R$ = allgemeine Gaskonstante
$T_m$ = mittlere absolute Dampftemperatur
$V$ = Dampfvolumen

$n$ ist aus $\Delta b$ ohne weiteres zu berechnen, wenn die im Dampf vorhandene Molekülart bekannt ist. Für Arsen dürfte in den hier interessierenden Druck-und Temperaturbereichen, weitgehend mit $As_4$-Molekeln zu rechnen sein.[12] Ein kleiner Bruchteil davon ist in $As_2$-Moleküle zerfallen, doch kann das in guter Näherung vernachlässigt werden.

Über die Molekülart von Phosphor gibt es zwei ältere, sich widersprechende Arbeiten.[13,14] Auf Grund neuerer kritischer Überlegungen[15,16] darf die Arbeit von A. Stock und Mitarbeitern[13] als zutreffend anzusehen sein. Danach hat man bei einem Druck von 1 atm und 800°C mit 99% und bei 1000°C noch mit 90% $P_4$-Molekülen zu rechnen. Diese Prozentsätze dürften mit steigendem Druck noch höher liegen, so dass wir in dieser Arbeit durchweg mit $P_4$-Molekülen rechnen dürfen, ohne einen nennenswerten Fehler zu machen.

$T_m$ = die mittlere Temperatur in °K, unter der das System steht. Die Temperatur in der Ampulle ist nicht einheitlich, so dass eine mittlere Temperatur $T_m$ in die Gleichung (1) eingesetzt werden muss. Zu Beginn des Erstarrungsprozesses befindet sich etwa die Hälfte der Ampulle auf der Temperatur $T_s$, die andere Hälfte auf der Temperatur $T_2$; gegen Ende des Prozesses ist fast die ganze Ampulle auf der Temperatur $T_2$. Wir werden also für $T_m$ im wesentlichen $T_2$ einsetzen und nur leicht nach oben korrigieren. Prinzipiell lässt sich der Unterschied zwischen $T_1$ und $T_2$ beliebig klein machen und somit $T_m$ sicher bestimmen. In den vorliegenden Experimenten wurde allerdings der Unterschied $T_1$–$T_2$ in der Grössenordnung 100°C (InAs) bis 400°C (GaP) gewählt, um einerseits stabile Abkühlungs- und Erstarrungsbedingungen zu erhalten und um andererseits die Quarzampulle thermisch nicht unzulässig hoch zu belasten. Diese Unsicherheit von $T_m$ ist nicht sehr entscheidend, da ja in Formel (1) $T_m$ nur proportional eingeht. Man ist hierbei den anderen Methoden überlegen,[3,11] bei denen die zu messende Temperatur sehr viel empfindlicher (im wesentlichen exponentiell) in die Berechnung des Dampfdruckes eingeht. Die Unsicherheiten in $T_m$ dürften sich in einer Genauigkeit der berechneten Dampfdruckwerte zwischen ±5% und ±10% bemerkbar machen.

VOL.
7
1958

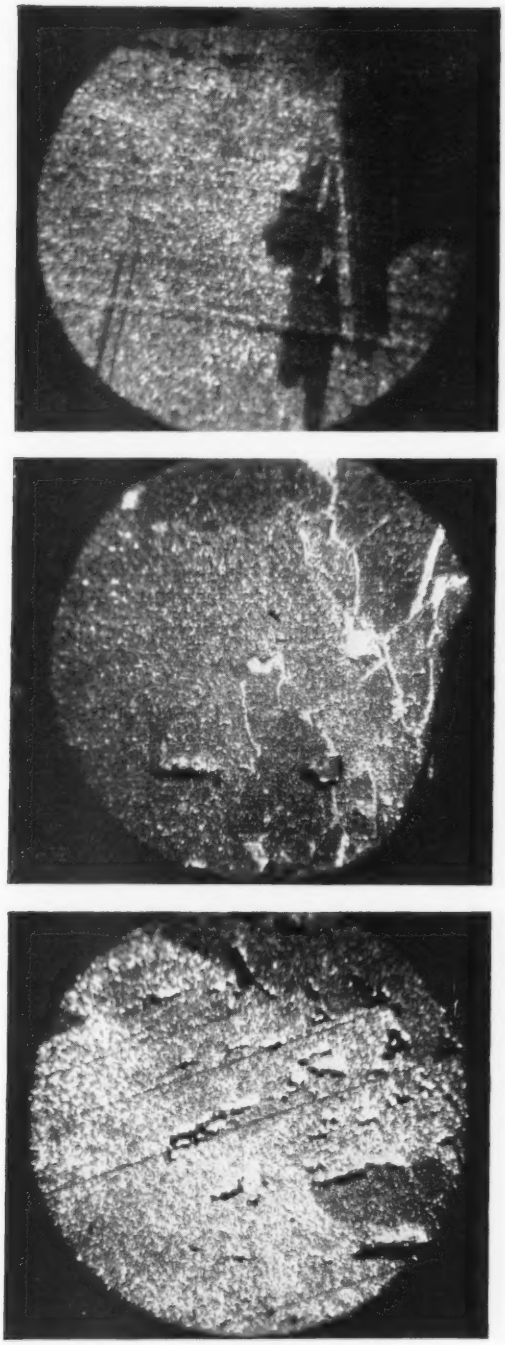

ABB. 2. Schliffbilder vom zuletzt erstarrten Ende dreier InAs-Proben mit verschiedenem Überschuss $\Delta b$ (Vergrösserung 50 mal). (Fall $\alpha$) $\Delta b = \Delta b^{st} = 50$ mg. Die Probe ist einphasig (Fall $\beta$) $\Delta b = 40$ mg. Die Probe enthält gegen Ende (rechts) In-Einschlüsse, die als helle Fäden sichtbar sind. (Fall $\gamma$) $\Delta b = 60$ mg. Die Probe enthält gegen Ende Lunker.

[*facing p.* 298

VOL
7
195

$V$ = Dampfvolumen der Ampulle. Es wurde jeweils durch Auffüllen der Ampulle mit Wasser und anschliessender Messung des Wasservolumens in Messzylinder festgelegt.

## 4. ERGEBNISSE

Die Messergebnisse sind in Tabelle 1 zusammengefasst. Abb. 2 zeigt als Beispiel Schliffbilder von InAs. Das zuletzt erstarrte Ende wurde mit einer Diamant-Blattsäge vom Stab getrennt und in Längsrichtung in zwei gleiche Teile zersägt. Das Bild zeigt diese Schnittfläche ohne weitere Bearbeitung für 3 verschiedene $\Delta b$-Einwaagen.

*Tabelle* 1. *Messwerte*

| | $\Delta b^{St}$ in mg | $n$ in Mol | $T_m$ in °K | $V$ in Litern | $P_s$ in atm |
|---|---|---|---|---|---|
| InAs | 50 | $1{,}67.10^{-4}$ | 1000 | 0,056 | 0,25 |
| GaAs | 110 | $3{,}68.10^{-4}$ | 1050 | 0,034 | 0,89 |
| InP | >750 | $6{,}06.10^{-3}$ | 1020 | 0,033 | >15,5 |
| GaP | >1300 | $1{,}05.10^{-2}$ | 1100 | 0,070 | >13,5 |

## 5. DISUSSION

In Tabelle 2 sind die bisher bekanntgewordenen Messungen über den Gleichgewichtsdampfdruck am Schmelzpunkt für die hier untersuchten Verbindungen zusammengestellt.

*Tabelle* 2. *Gleichgewichtsdampfdruck $p_s$ einiger $A^{III}B^{V}$-Verbindungen am Schmelzpunkt in atm.*

| | nach[3] | nach[11] | eig. Messg. |
|---|---|---|---|
| InAs | 0,33 | – | 0,25 |
| GaAs | 0,9 | – | 0,89 |
| InP | 60,0 | 5 | >15,5 |
| GaP | — | – | >13,5 |

Aus Tabelle 2 ist zu entnehmen, dass die jeweiligen Messwerte für InAs bzw. GaAs recht gut übereinstimmen. Die Abweichungen liegen innerhalb der Genauigkeitsgrenzen beider Verfahren.

Dagegen zeigen die Messwerte für InP grosse Abweichungen. Die Ursache könnte in der schon erwähnten Polymorphie des Phosphors liegen, die in den Methoden nach[3] und,[11] nicht aber im vorliegenden Messverfahren, die Messwerte stark beeinflusst. Eine andere Fehlerquelle besteht darin, dass das Verfahren nach[11] bei Annäherung an den Schmelzpunkt ungenau wird. Die in dieser Arbeit mitgeteilten Werte für InP und GaP können nur als untere Grenzwerte angesehen werden. Die Werte für den Gleichgewichtsdampfdruck am Schmelzpunkt liegen höher, der Wert von 60 atm für InP nach[3] dürfte richtig sein.

## 6. FOLGERUNGEN FÜR DIE HERSTELLUNG UND DAS UMSCHMELZEN DER VERBINDUNGEN

Nach dem in 3/α angegebenen Verfahren lassen sich ohne weiteres die genannten Verbindungen einphasig herstellen,[5,17] und umschmelzen.[5,10,17] Im Falle von InP und GaP braucht man dabei nicht den unangenehm hohen Gleichgewichtsdampfdruck am Schmelzpunkt aufzubringen, sondern es reichen die in Tabelle 1 angegebenen Werte, um bei Vorschubgeschwindigkeiten von $\approx$ 1 mm/min durchweg einphasige Kristalle zu erschmelzen. Verfahren dieser Art sind einfacher (und im Falle von P als leichtflüchtiger Komponente auch sicherer) als Herstellungs-und Umschmelzverfahren, bei denen dauernd ein Bodenkörper der leichtflüchtigen Komponente im Schmelzgefäss vorhanden ist.[6,18] Das vorgeschlagene Verfahren ist allerdings nur dann ohne weiteres anwendbar, wenn die Löslichkeit der Komponenten in der festen Verbindung vernachlässigbar ist. Eine höslichkeit konnte bei den hier in Frage stehenden Verbindungen bisher in keinem Falle (auch nicht mit elektrischen Methoden) nachgewiesen werden, was aber für halbleitende Verbindungen durchaus nicht allgemein gültig ist (siehe z.B.[6]). Die beschriebenen Methoden lassen sich selbstverständlich auch auf andere Verbindungen anwenden, soweit diese die genannten Bedingungen erfüllen.

Für photo-technische Hilfe danke ich Herrn Dr. H. J. HENKEL.

## LITERATUR

1. LIU T. S. und PERETTI E. A., *Trans. Amer. Soc. Met.* **45,** 677 (1953).
2. KÖSTER und THOMA B., *Z. Metallk.* **46,** 292 (1955).
3. VAN DEN BOOMGAARD J. und SCHOL K., *Phil. Res. Rep.* **12,** 127 (1957).
4. SHAFER M. und WEISER K. *J. Phys. Chem.* **61,** 1424 (1957).

5. FOLBERTH O. G. und WEISS H., *Z. Naturf.* **10a,** 615 (1955).
6. VAN DEN BOOMGAARD J., KRÖGER F. A., und VINK H. J., *J. of Electronics* **1,** 212 (1955).
7. VOGEL R., *Handbuch der Metallphysik* Bd. II. Akad. Verlagsgesellschaft Leipzig (1937) insb.s. 188 ff.
8. WELKER H., *Z. Naturf.* **7a,** 744 (1952).
9. WELKER H. und WEISS H., *Solid State Phys.* III (1956).
10. GREMMELMAIER R., *Z. Naturf.* **11a,** 511 (1956).
11. WEISER K., *J. Phys. Chem.* **61,** 513 (1957).
12. D'ANS J. und LAX E., *Taschenbuch für Chemiker und Physiker*, insb. 863 Springer, Berlin (1946).
13. STOCK A., GIBSON H. H., und STAMM E., *Berichte* **45,** 3527 (1912).
14. PREUNER G. und BROCKMÖLLER J., *Z. phys. Chem.* **81,** 129 (1913).
15. JOST D. M. und RUSSEL H., *Systematic Inorganic Chemistry* Prentice-Hall Inc. (1946) insb.S. 166 ff.
16. BREWER L. und KANE J. S., *J. Phys. Chem.* **59,** 105 (1955).
17. SCHILLMANN E., *Z. Naturf.* **11a,** 463 (1956).
18. KRÖGER F. A. und DE NOBEL D., *J. of Electronics* **1,** 190 (1955).

VOL.
7
195

*J. Phys. Chem. Solids* Pergamon Press 1958. Vol. 7. pp. 301–306.

# ULTRAVIOLET AND INFRARED ABSORPTION OF FUSED GERMANIA*

**ALVIN J. COHEN† and HERBERT L. SMITH†**

Mellon Institute, Pittsburgh, Pennsylvania

(*Received* 28 *May* 1958)

**Abstract**—Fused germania ($GeO_2$) contains an intense absorption band centered at 2445 Å and caused by a reduced germanium species, probably Ge(II). This band has a half-width comparable to that of a band centered at 2429 Å in certain fused silicas and produced by the same reduced germanium species contained as an impurity. The band in germania is bleached by ultraviolet light and X-rays accompanied by an increase in absorbency below 2200 Å. The energy gap for fused germania is slightly higher than a value published for hexagonal germanium dioxide, which indicates the latter is probably in error. The infrared spectrum of fused germania is also presented.

## 1. INTRODUCTION

DENNIS and LAUBENGAYER[1] produced the first optical-quality fused germania by heating the crystalline oxide in platinum at 1400–1425°C (20 min) and stirring with a platinum rod. The impurity content was given as not more than 0·2 per cent. It was found that a 2·5-mm-thick wafer did not transmit light below 3250 Å.

SHAW[2] investigated the spectrum of fused germania from the same source[1] and found the transmission cut-off at 315 mμ for a 2 mm-thick sample. He reported infrared bands at 2·86, 4·24, and 5·40 μ (inflection) and found the long-wavelength transmission cut-off at 6·15 μ. The present work is not in agreement with this earlier infrared work, as will be discussed in a following section.

KREIDL and HENSLER[3] found the ultraviolet cut-off at 280 mμ for a 2·51-mm-thick sample of high-purity fused germania, using the same source of crystalline germanium dioxide as that used in this present work.

Earlier COHEN[4] discussed the ultraviolet spectra of two thin sections of high-purity optical-quality fused germania, using a Beckman DU Spectrophotometer. He found an optical density of 1·940 at 272·5 mμ in a 72-μ-thick wafer, and in a 100-μ-thick wafer he found an absorption maximum at 245 mμ with $k = 3{\cdot}6 \times 10^2$ cm$^{-1}$. In the latter specimen the absorption edge was at 222 mμ. These specimens were from the same batch of fused germania as studied here.

## 2. EXPERIMENTAL

*Materials used*

The hexagonal crystalline form of germanium dioxide was obtained from the Eagle-Picher Company, Miami, Oklahoma, Batch No. M-86 Lot No. 1–2329–802. Company analysis: Si 5·8, Mg 0·3, and Ca 2·6 ppm. The results of the emission analyses carried out in this laboratory are given in Table 1.

*Table* 1. *Emission analyses of germanium dioxide*

| Impurity | Content in starting material* (ppm) | Content in glass produced* (ppm) | Limit of detection (ppm) |
|---|---|---|---|
| Al | N.F. | 10 | 10 |
| Ca | 10 | 10 | 1 |
| Fe | 3(?) | 10 | 3 |
| Pb | N.F. | 10 | 10 |
| Mg | trace (?) | 10 | 3 |
| Mn | N.F. | 10 | 3 |
| Si | 10 | 100 | ~ 10 |

* Absolute values between $\frac{1}{3}$ and 3 times values indicated. N.F. = not found.

* Presented before the Philadelphia Meeting of the American Physical Society in March 1957 (*Bull. Amer. Phys. Soc.* **2**, 150 (1957)).

† Pittsburgh Plate Glass Company Fellowship.

*Method of glass preparation*

Germanium dioxide powder (41·5 g) was placed in a cleaned platinum crucible and covered with a platinum lid. This was placed inside a fused silica crucible fitted with a fused silica lid. The material was heated slowly to 1625°C in a globar furnace. The glass was allowed to remain at this temperature for several hours and then removed from the furnace and allowed to cool in air without annealing. The resulting colorless glass was of optical quality, being free of all bubbles. Polished surfaces slowly devitrify on long standing to the hexagonal form of germanium dioxide as determined by X-ray powder diffraction.

*Absorption spectra measurements*

The specimens were prepared for optical studies by wafering with metal-bonded diamond wheels, grinding down with various abrasives, and finally polishing with cerium oxide polishing compound. The thickness of the specimens was obtained with a metric measure micrometer to ±0·001 mm. All of the absorption spectral data were taken on a Cary Model 14M Recording Spectrophotometer, Serial 66.

*Irradiations*

The X-ray irradiations were made with a Picker Industrial X-ray Unit designed for continuous operation at 50 pkV, 40 mA. The tube used was a Machlett AEG5OT with tungsten target and beryllium window. The irradiations were at 45 pkV, 35 mA, 6 cm from the X-ray tube window. The dosage rate is in the order of $2–3 \times 10^6$ r/hr in air at the surface of the wafer. The ultraviolet bleaching was done with a General Electric UA-3 360-W photochemical lamp. All irradiations and optical measurements were performed at room temperature.

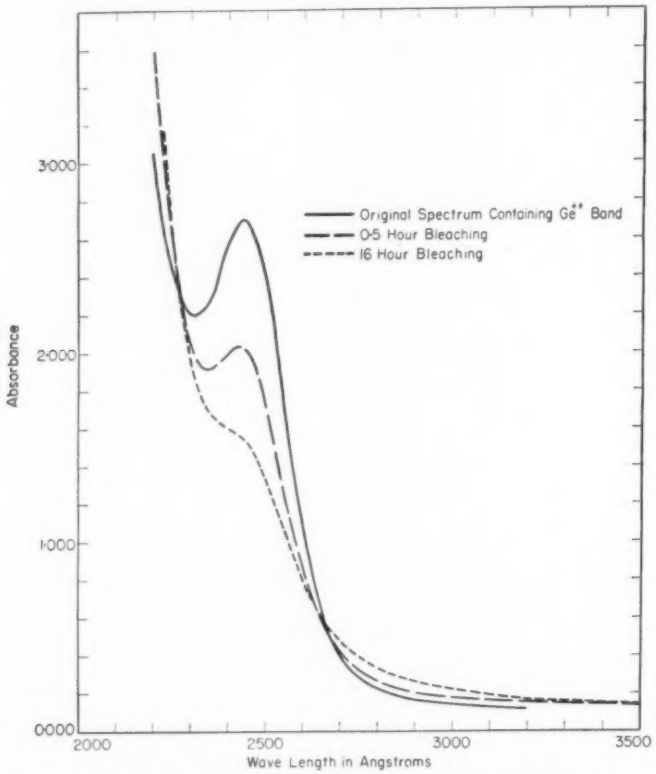


FIG. 1. Bleaching of the 2445 Å band in fused germania of 80 $\mu$ thickness with ultraviolet light.

## 3. RESULTS AND DISCUSSION

Since earlier workers[1–3] reported the absorption edge in fused germania at various longer wavelengths than the absorption band of a reduced

germanium species contained as an impurity in certain fused silicas,[4] it was proposed to study the absorption spectrum of fused germania in thin section in order to determine whether an absorption band were present in the region of 242 m$\mu$. The absorption spectrum of an 80-$\mu$-thick specimen is shown in Fig. 1. The spectrum is indeed characterized by a band at 2445 Å. On long standing in light this band was found to slowly decrease in absorbance. The band bleaches at a much greater rate when illuminated with ultraviolet light, as shown in the second and third curves in Fig. 1. It is to be noted that the bleaching of this band at 2445 Å is accompanied by an increase in the absorption on both sides of the band, indicating that the ultraviolet light or the resultant bleaching of the band causes a more intense growth at shorter wavelengths. Since the absorption coefficient in this ultraviolet region is so high as to give an apparent absorption edge, the band growth could not be followed. Fig. 2 shows the rate of decrease of the absorbance at 2450 Å with ultraviolet radiation.

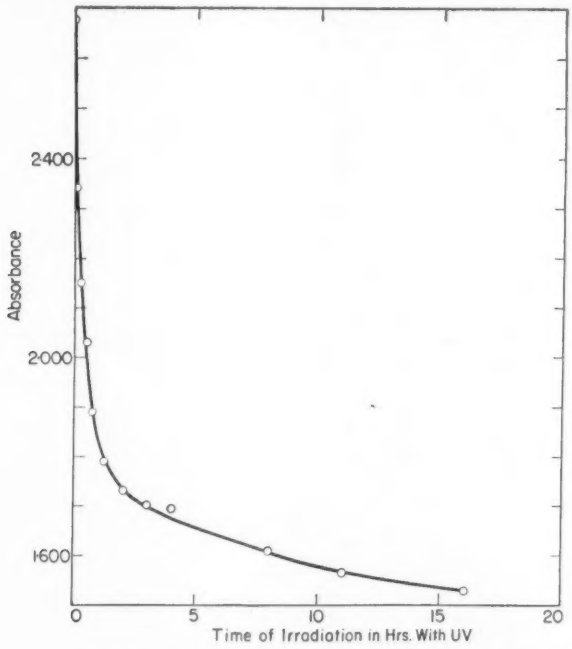


FIG. 2. Bleaching in the 2450 Å region in fused germania of 80 $\mu$ thickness with ultraviolet radiation.

Fig. 3 shows the apparent growth of the long-wavelength tail of the absorption edge at 2450 Å on X-irradiation of the fused germania after 16 hr of optical bleaching. There is no growth in the 2445 Å absorption band itself upon X-ray treatment; all of the growth is confined to a band or bands at lower wavelengths. X-ray treatment of a specimen of fused germania that has not been optically bleached gives the same results as optical bleaching. The 2445 Å absorption band decreases while the absorbance of the apparent absorption edge increases.

In the spectral regions studied, no color center bands are produced in this material upon X-ray treatment. If color centers similar to the 215 m$\mu$ band in fused silica[4] or to bands found recently in the vacuum region of fused silica[7] exist in fused germania, they are located below the apparent absorption edge at 2200 Å. It is planned to produce additional specimens of fused germania under oxidizing conditions to determine whether the apparent absorption edge is indeed the true one. It

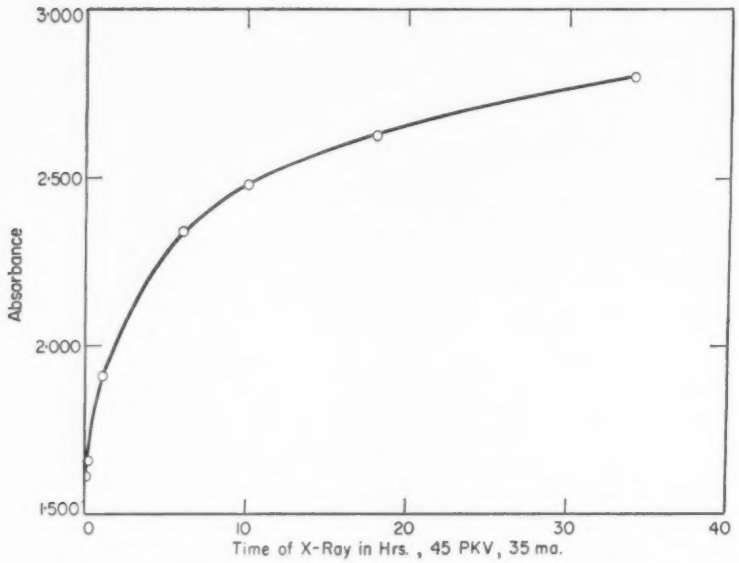


FIG. 3. Enhancement of the absorbance at 2450 Å in fused germania upon X-irradiation after 16 hr of optical bleaching; growth is not related to the 2445 Å absorption band. Data from same specimen as in Figs. 1 and 2.

could be due to trace impurities in a reduced state or a reduced species of germanium present unless the glass is made under strictly oxidizing conditions.

(a) *The absorption band at* 2445 Å

The production of a band at 2429 Å in fused silica containing a reduced species of germanium as an impurity has been discussed earlier.[4,5] It is of interest to compare this band in fused silica with the 2445 Å band in fused germania. In Table 2 the bands are compared. The widths at half maximum obtained in this laboratory are very close, the width of the band in the fused germania being 0·50 eV compared with 0·47 eV in the fused silica. It is concluded that the bands are due to the same reduced germanium species.[4] However, the number of atoms of the reduced germanium species responsible for the absorption band is over a thousand times as great in the fused germania as in the GE Type VI fused silica, assuming that the oscillator strength is the same in both media. If the fused germania were made under slightly more reducing conditions, the intensity of the band could undoubtedly be made so great as to give an apparent absorption edge. This could be the case in the work of earlier investigators.

*Table 2. Comparison of the* 2445 Å *(fused germania) and* 2429 Å *(fused silica) bands*

| Specimen | Absorption coefficient ($cm^{-1}$) | Width of band at half-maximum (eV) | $Nf/cm^3$* |
|---|---|---|---|
| Fused germania | 361·2 | 0·50 | $1·72 \times 10^{18}$ |
| Ge Type VI fused silica | 0·222 | 0·47 | $1·11 \times 10^{15}$ |
| Calculated from fused silica spectrum of GARINO–CANINA† | 4·05 | 0·41 | $1·76 \times 10^{16}$ |

* Calculated using Smakula equation, where $N$ is the number of centers and $f$ is the oscillator strength.

† Fig. 2, curve 3 of reference 5.

(b) *The energy gap*

PAPAZIAN[6] has recently grown small crystals of hexagonal germanium dioxide and observed the ultraviolet spectrum. He finds the absorption edge to be at 2230 Å, from which we calculate the energy gap as 5·56 eV. This compares with a value of 2200 Å for the absorption edge of fused germania in the present work, which gives 5·63 eV for the energy gap. However, MITCHELL and PAIGE[7] find that the energy gap in optical-quality fused silica is 8·1 eV and that of crystalline quartz is 8·5 eV ($k = 400$ cm$^{-1}$). The crystalline form thus has an energy gap 0·4 eV higher than that of the glass. This difference is accounted for by the regularity of the crystalline quartz lattice in comparison with the amorphous state in fused silica according to these workers. Since hexagonal germanium dioxide is isomorphous with the α-quartz structure and the amorphous states of these Group IV elements are expected to be quite similar, it follows that one would expect the energy gap of the crystalline form of germanium dioxide to be greater than that of the glassy form. However, in comparing the two values one finds they differ by only 0·07 eV, with the glass having the higher value. One concludes that the value in the hexagonal germanium dioxide is too low. This may be accounted for by the presence of trace impurity in this material. Therefore, from our analogy with the silica system, it is probably that the energy gap of crystalline germanium dioxide is somewhat higher than the value reported by PAPAZIAN.[6]

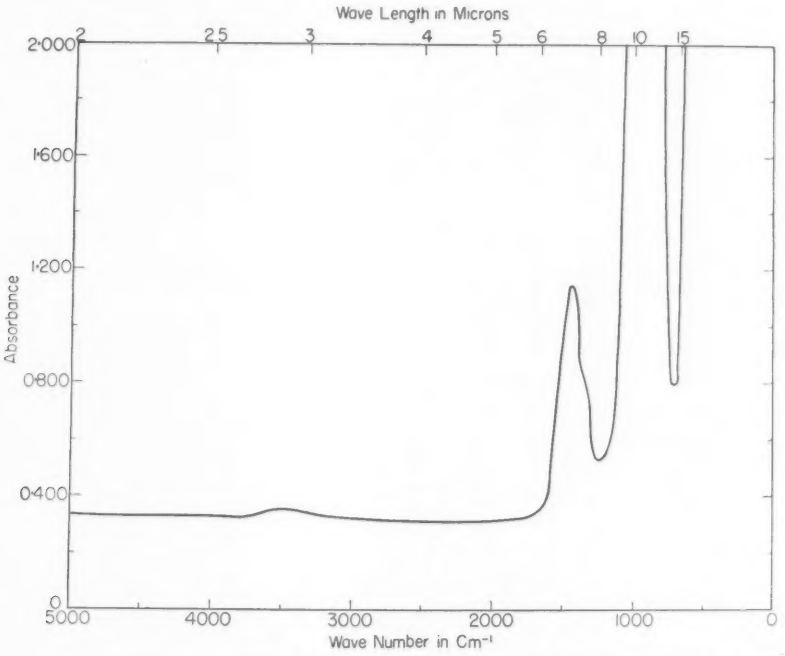


FIG. 4. The infrared spectrum of fused germania ~ 100 μ thickness.

(c) *The infrared spectrum*

The infrared spectrum of fused germania is shown in Fig. 4, encompassing the region 2–15·5 μ. The weak band at 2·86 μ (3500 cm$^{-1}$) which was mentioned by SHAW[2] as being a characteristic absorption is undoubtedly due to the fundamental —OH stretching vibration and is not characteristic of fused $GeO_2$. It would be difficult to remove all traces of the band after long storage periods due to the ease of hydration of germania. It is probable that a portion of the band seen here was in the original glass when produced. The band

found by SHAW at 4·24 $\mu$ is absent in this specimen. In the thin wafer studied here there is a vibrational band maximum at 6·94 $\mu$ (1440 $cm^{-1}$) and one on the shoulder of this band at approximately 7·3 $\mu$ (1370 $cm^{-1}$). In addition there is a very intense absorption between 9·35 $\mu$ (1070 $cm^{-1}$) and 12·66 $\mu$ (790 $cm^{-1}$) and an absorption edge at 15·5 $\mu$ (645 $cm^{-1}$).

*Acknowledgements*—The emission analyses were performed by Dr. E. S. HODGE and W. K. BAER; the infrared spectrum was run by G. L. CARLSON and the X-ray powder diffraction analysis was made by Dr. S. S. POLLACK, all of the Department of Research in Chemical Physics.

## REFERENCES

1. DENNIS L. M. and LAUBENGAYER A. W., *J. Phys. Chem.* **30,** 1510 (1926).
2. SHAW R. W., *Phys. Rev.* **51,** 146 (1937).
3. KREIDL N. J. and HENSLER J. R., Paper VII–3, Fourth International Congress on Glass, Paris, July 1956 (to be published).
4. COHEN A. J., *Phys. Rev.* **105,** 1151 (1957).
5. GARINO-CANINA V., *C.R. Acad. Sci., Paris* **242,** 1982 (1956).
6. PAPAZIAN H. A., *J. Appl. Phys.* **27,** 1253 (1956).
7. MITCHELL E. W. J. and PAIGE E. G. S., *Phil. Mag.* **1,** 1085 (1956).

VOL
7
195

*J. Phys. Chem. Solids* Pergamon Press 1958. Vol. 7. pp. 307–326.

# NEUTRON-IRRADIATION EFFECTS ON COPPER–ALUMINUM ALLOYS

**M. S. WECHSLER and R. H. KERNOHAN**

Solid State Division, Oak Ridge National Laboratory,* Oak Ridge, Tennessee

(*Received* 2 *June* 1958)

**Abstract**—The effect of neutron irradiation and subsequent thermal treatment on the electrical resistivity of α-phase Cu–Al alloys has been studied. It is found that a solid-state reaction that causes a decrease in resistivity is triggered or accelerated by irradiation at 32–45°C. The effect is absent in pure copper and increases with aluminum content. The resistivity decrease for the 15 atomic per cent aluminum alloy is about 0·2 μΩ-cm. When the irradiation is conducted at −120°C, no decrease in resistivity is observed, but the decrease in resistivity sets in upon subsequent warming above −50°C. Several explanations for these effects are discussed.

VOL. 7 1958

## 1. INTRODUCTION

IRRADIATION effects on metals and alloys have been studied from two points of view.† In the case of pure metals, the attempt is made to prepare samples that are, as closely as possible, in an equilibrium state and to investigate the manner in which bombardment causes the material to depart from equilibrium by the introduction of lattice defects. For this reason pure noble metals, particularly copper, have been irradiated at low temperatures where the bombardment-produced defects are immobile and changes in physical properties are measured as a function of irradiation dosage at the low temperature and as a function of subsequent thermal annealing. In recent years, such experiments have been performed using neutron[2,3] (below 25°K), deuteron[4–6] (below 20°K), and electron[7] (near 10°K) irradiations at the temperatures indicated. In general, it is found that, at least in the early portion of the irradiation exposure a linear increase in electrical resistivity takes place and that the subsequent recovery upon raising the temperature occurs in a number of stages, with a range of activation energies, starting at temperatures as low as 30–40°K and continuing to above room temperature. The fact that the thermal recovery is rather complicated even in the electron-irradiation case indicates that the annealing does not take place entirely by the simple recombination of vacancy-interstitial pairs. For this reason two consequences of the radiation seem likely to persist at higher temperatures: (1) damage clusters that result from the high density of displacements produced at the end of the path of a primary knock-on (cf. discussion by BRINKMAN[8,9]), and (2) vacancies, largely isolated or in small-number aggregates that remain after the higher mobility interstitials have become annihilated at grain boundaries, dislocations, or at the surface of the crystal.

These effects have led, in alloys, to another method of investigating the nature of radiation-induced disarrangements. Alloys are useful for the study of atomic movements in solids for two reasons. Firstly, the properties of alloys are sensitive to the relative arrangement of the constituent atoms. Thus, large changes in properties take place upon ordering or precipitation from solid solution, and a study of these reactions upon irradiation gives information concerning atomic movements and how they are affected by the bombardment.

* Oak Ridge National Laboratory is operated by Union Carbide Corporation for the U.S. Atomic Energy Commission.

† Reviews of the effects of irradiation on solids have been given by DIENES and VINEYARD,[1a] SEITZ and KOEHLER,[1b] BROOKS,[1c] and COTTRELL.[1d]

Secondly, there is reason to expect[10] that, because of the interaction between vacancies and solute atoms, the energy of formation, $\epsilon_F$, for vacancies in alloys is lower than in the pure metal, whereas the reverse is true for the activation energy for motion, $\epsilon_M$. This would have the consequence that many more vacancies are retained upon cooling in alloys as compared with pure metals and, indeed, it has been observed that changes in properties upon quenching of alloys (Ag–Zn,[11,12] Cu–Al,[13,14] and Au–Cd[15,16]) are indicative of the retention of concentrations of vacancies that are one or two orders of magnitude greater than those quenched into pure metals (Au,[17] Al,[18] Pt[19]). Furthermore, an examination of the relative magnitudes of $\epsilon_F$ and $\epsilon_M$ shows[13] that $\epsilon_M < \epsilon_F$ for pure metals, whereas $\epsilon_F < \epsilon_M$ for alloys. The possibility suggests itself that in some alloys, where the energy of interaction between solute and vacancy is great, it is virtually impossible to cool sufficiently slowly to avoid retaining an excess concentration of vacancies. It is of interest to investigate the way in which radiation affects the annealing of vacancies produced by thermal treatment.

The rate at which diffusion-controlled processes such as ordering, precipitation, and the annealing-out of defects occur depends upon the ease with which they are nucleated, the mobility of the diffusing entity, and the "scale" of the process, i.e. the number of atomic jumps necessary for completion. Each of these factors may be altered by irradiation, and it is usually observed[20c] that the reaction rates are increased upon irradiation. This may be the result of the introduction of nucleation sites, as in the case of the white-to-grey tin transformation,[21] the production of vacancies which increases atomic mobilities, or the introduction of annihilation sites in the case of the annealing of thermally-induced defects, thus reducing the number of jumps necessary for the annealing. For the most part, previous investigators have considered radiation-induced vacancies to be the cause of accelerated reaction rates, although the matter is by no means settled at the present time. In any case, a comparison of the experiments on pure metals and alloys indicates a certain duality in the nature of radiation effects. In the case of pure metals, the sample is initially at equilibrium and non-equilibrium defects are produced by means of low-temperature bombardments. This is what one normally associates with the term "radiation damage". In the case of alloys, in many experiments the material is initially in a non-equilibrium condition, as for example an ordering alloy quenched from above the critical temperature or a precipitating alloy that has been solution-annealed and quenched, and the enhancement of the ordering or precipitation process is observed either during or after the irradiation. Thus, the irradiation has the effect of accelerating the return to equilibrium, often by permitting the reaction to proceed at a temperature below that which is normally possible. This is of practical significance in the case of alloys used in radiation environments, since many alloys are prepared to have special properties by allowing an ordering or precipitation reaction to occur to a critical point at a high temperature. The sample is then returned to room temperature, where it remains in metastable equilibrium because of low reaction rates. However, if the sample is irradiated, the reaction rate may increase sufficiently to allow the properties to change significantly even at room temperature.

The compositions of the alloys used in the present investigation are in the α-solid-solution field of the Cu–Al phase diagram and no ordering or precipitation reaction is expected. Despite this, it will be seen that the neutron irradiation triggers or activates a diffusion-controlled solid-state reaction that brings about a decrease in resistivity. A similar decrease in resistivity upon neutron[20b,22] and electron[23] irradiation has been reported for α Cu–Zn alloys, which also do not display a superstructure. An interpretation[22,23] of these observations was made in terms of the radiation enhancement of short-range order. In support of this view, DAMASK[24] has shown that the relaxation times for annealing of the resistivity of quenched, cold-worked, and neutron-irradiated (at 50°C) samples are consistent with those obtained by stress-relaxation measurements on annealed samples.[24,25] The conclusion that short-range ordering is the cause of the decrease in resistivity upon irradiation was then based on the treatment of LECLAIRE and LOMER,[26] which relates the stress-relaxation effect to changes in lattice parameter upon short-range ordering. It will be indicated below that this conclusion is not necessarily valid. An attempt to detect short-range order directly by means of X-ray

and neutron diffraction met with negative results.[27] However, a measurement of order parameters in Cu–Zn alloys by using diffraction techniques is difficult because of the similarity of the scattering powers of copper and zinc in the X-ray case and because of difficulties inherent in the use of neutron diffraction. It was believed possible[27] that an amount of short-range order consistent with the changes observed by ROSENBLATT *et al.*[22] could have existed and not have been detected by the diffraction experiments.

The measurement of short-range order by X-ray techniques is more favorable for Cu–Al alloys, and this was one of the reasons that α Cu–Al alloys were chosen for the present study. Secondly, despite the lower α solubility limit (~ 18 atomic per cent aluminum at 750°C), the decrease in resistivity for Cu–Al alloys near the solubility limit is larger than that for Cu–Zn alloys. Thirdly, the shortness of the half-life of the neutron-induced aluminum isotope, $Al^{28}$, makes aluminum a convenient element for radiation experiments.

As will be described below, in-pile measurements at 35°C show that a sharp decrease in resistivity takes place in the early stage of the exposure. The resistivity then reaches a minimum, followed by a linear increase. The depth of the minimum increases with aluminum content and no decrease is observed for pure copper. When the irradiation is carried out at −120°C, no decrease is observed, but there remains a linear increase of somewhat greater slope than that observed in the later portion of the exposure at 35°C. These results are analyzed in terms of two processes, *A* and *B*. Process *A* causes a linear increase in resistivity due to the direct effect of the bombardment in producing defects. This process proceeds more rapidly when the irradiation is performed at a lower temperature, since less annealing (of the type observed[3] after irradiation at very low temperatures) goes on simultaneously with the radiation. On the other hand, Process *B* is a diffusion-controlled solid-state reaction that produces a decrease in resistivity that saturates with exposure at 35°C. Hence, in contrast to Process *A*, the rate at which Process *B* proceeds is greatly reduced by a decrease in temperature. Thus, when the reaction is carried out at −120°C, it is completely suppressed. It will be seen, however, that if the sample is warmed above about −50°C after irradiation at 120°C, Process *B* will set in* and this procedure provides a convenient method for studying the kinetics of Process *B* and for determining its activation energy.

## 2. EXPERIMENTAL DETAILS

The alloys were furnished by the Metallurgy Division at ORNL in the form of homogenized and vacuum-cast ingots. Electrolytic copper was used of 99·92 per cent purity and the aluminum was of 99·99 per cent purity. The single-crystal samples were prepared by melting the homogenized material in a split graphite mold and lowering the mold slowly through a temperature gradient in a vacuum furnace. The polycrystalline samples were swaged from the homogenized ingots. All the samples were $\frac{1}{8}$ in. in diameter and received an anneal of several hours at about 750°C, followed by slow cooling at a rate of about 15°C/hr to room temperature. The grain size of the polycrystalline samples after this treatment was about 200 grains/mm².

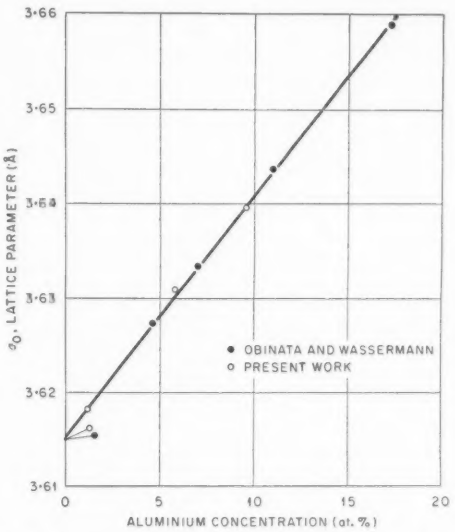


FIG. 1. Lattice parameter versus concentration of aluminum.

* The statement that the rate of Process *B* is greatly reduced by decreasing the temperature requires some qualification. This is true for the case where Process *B* is carried out subsequent to irradiation at −120°C. But when Process *B* goes on in the reactor it appears to be retarded only below a critical range of temperatures below room temperature. As will be discussed, there is reason to believe that Process *B* is relatively temperature-independent when it goes on in the reactor above room temperature.

The alloys were prepared with approximately 1, 6, 10, and 15 atomic per cent aluminum, although no resistivity measurements are described here on the 1 per cent sample. Chemical analyses of the three samples of lower aluminum content yielded the values 1·2, 5·8, and 9·6 atomic per cent aluminum, but chemical analyses from two sources gave inconsistent results for the 15 per cent material. Therefore, the composition of the 15 per cent aluminum alloy was checked, using the lattice parameter as a measure of the composition. Fig. 1 shows the results of OBINATA and WASSERMANN[28] and of present work for the dependence of lattice parameter on composition. The data of OBINATA and WASSERMANN were converted by the factor 1·0020 Å/kX to conform to the current definition of the Ångström unit. The lattice parameter of our 15 per cent aluminum material was found to lie between 3·653 and 3·654 Å, so using the results of Fig. 1 we assign to it the composition 15·0 atomic per cent aluminum. However, all compositions are best considered to be accurate to only $\pm 0{\cdot}5$ atomic per cent aluminum. It is interesting to note from Fig. 1 that Vegard's law is rather well satisfied for aluminum concentrations that extend to the solubility limit.

The neutron irradiations were carried out in three facilities of the ORNL Graphite Reactor: Holes C, 52, and 1768. The fast neutron fluxes are estimated to be about $3 \times 10^{11}$ neutrons/cm² sec for both Holes C and 52. Irradiations in Hole 1768 are performed in the center of a hollow uranium fuel element. In this facility, the amount of fast flux should be greater by several times the fast flux in Holes C or 52. Hole 52 is equipped with a low-temperature facility in which helium gas precooled with liquid nitrogen is circulated about the capsule containing the samples. In this way, it was possible to irradiate samples at −120°C for several weeks. Three types of irradiations of 15 atomic per cent aluminum samples were performed in Hole 52. In the first experiment in Hole 52, measurements of a single crystal and a polycrystalline sample were made at an irradiation temperature of 45°C. A wire-wound heater, surrounding the samples in the reactor, was used to control the temperature at 45°C. During a pile shutdown period at the conclusion of the irradiation run, the samples were given a step-annealing treatment. They were held for 30 min at increasingly higher temperatures up to about 250°C, and between each 30-min anneal the samples were returned to 45°C for measurement. In the second Hole 52 experiment, the same kind of experiment as the first one was performed, except that the irradiation was done at −120°C. At the conclusion of this experiment, a step-annealing treatment was again applied; this time the annealing was done in the range between −120 and 160°C and the temperature of measurement was −120°C. In the third Hole 52 experiment, a number of 15 atomic per cent aluminum single crystals were irradiated at −120°C; but no resistivity measurements were made. At the conclusion of the irradiation period, the samples were removed from the reactor without allowing them to warm-up. They were then stored in liquid nitrogen where they decayed to sufficiently low radioactivity levels so that they could be handled in the laboratory. At this time, they were removed from the liquid nitrogen and measured individually in the laboratory upon thermal treatment at higher temperatures. The experiments in Holes C and 1768 were performed at ambient reactor temperature. Changes in the resistivity due to variations in the temperature of measurement were cancelled out, using the temperature coefficient of resistivity that was measured for each sample before the irradiation. In Hole C, polycrystalline samples of 0, 6, 10, and 15 atomic per cent aluminum and one single crystal of 15 atomic per cent aluminum were used. The samples in Hole 1768 were of 15 atomic per cent aluminum composition and consisted of a single crystal and a polycrystalline sample of $\frac{1}{4}$ in. diameter and a polycrystalline wire 0·044 in. in diameter.

The resistivity measurements were made using standard techniques. The double potentiometer method was used for the in-pile measurements. The leads making current and voltage connections to the samples were led out of the reactor through a shield-plug and into an adjacent room containing the measuring apparatus. For the out-of-pile isothermal annealing, a Kelvin-bridge circuit was used. In this case, the resistivity of the irradiated sample was measured with respect to a comparison sample of the same composition, and thermal fluctuations in the annealing bath tended to cancel out. The out-of-pile isochronal annealing measurements and the resistivity versus temperature measurements were made using the double potentiometer system. These measurements were made with respect to a calibrated external standard resistor.

## 3. RESULTS

### (a) *Hole C Experiment*

Five samples were irradiated simultaneously at ambient pile temperature (~ 35°C) in Hole C; they were polycrystalline samples containing 0, 6, 10 and 15 atomic per cent aluminum and one single crystal containing 15 atomic per cent aluminum. The changes in resistivity are plotted in Fig. 2 versus integrated neutron flux. It is seen that a decrease in resistivity occurs in the early portion of the irradiation, whose magnitude increases with aluminum content. No decrease is observed for pure copper. The resistivity reaches a minimum, followed by a linear increase. The increase in resistivity continues linearly to exposure times of about 50 weeks, where a slight tendency toward a decrease in slope is noted. The long-time portion of the curves is not shown in Fig. 2. We have made an estimate of the contribution to the resistivity changes made by transmutation effects in the case of the 15 atomic per cent aluminum alloy. Four nuclear reactions were taken into consideration.

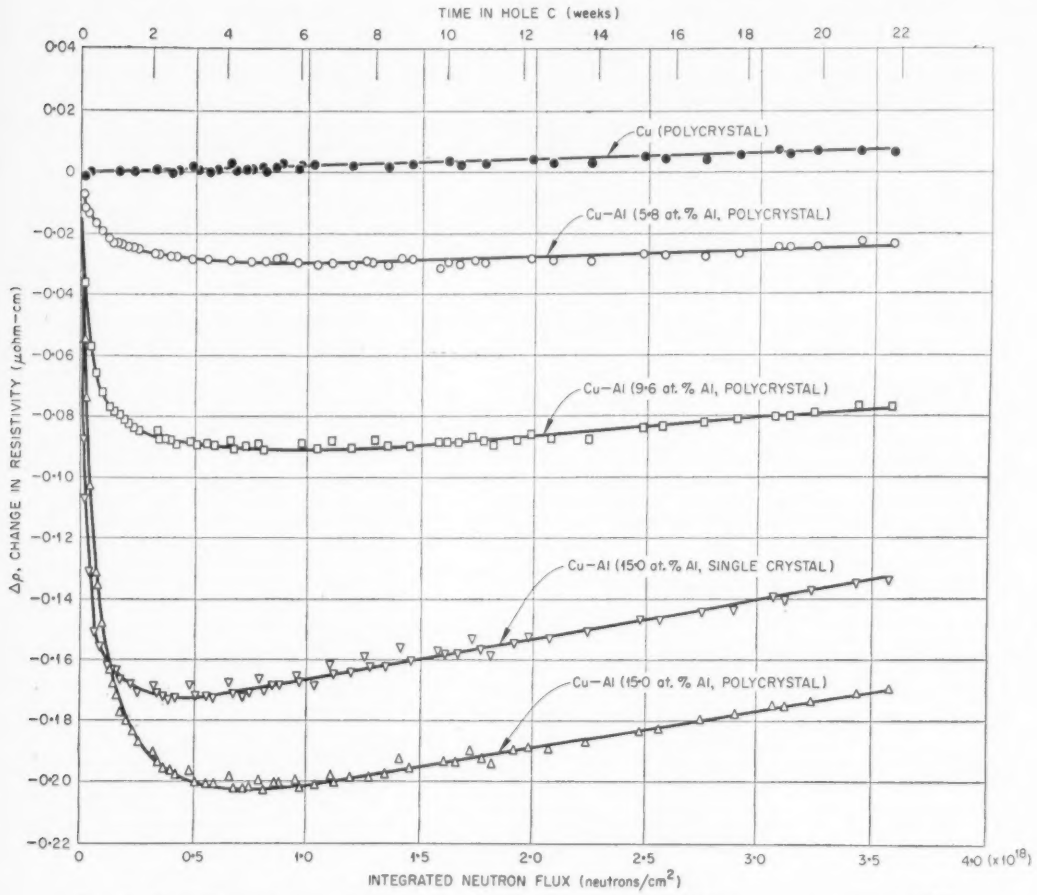


FIG. 2. Hole C experiment: Change in resistivity (corrected to 20°C) versus exposure at 35°C.

The 69 per cent abundant $^{63}Cu$ is converted to $^{64}Zn$ and to $^{64}Ni$, whereas the 31 per cent abundant $^{65}Cu$ forms $^{66}Zn$. Aluminum has only one stable isotope, $^{27}Al$, which becomes $^{28}Si$. The absorption cross-sections for these reactions were taken from the compilation of SULLIVAN,[29] and the contributions to the electrical resistivity of the various impurities were taken from the work of LINDE.[30] When account is taken of the fractional amounts of each reaction, the total added resistivity due to transmutation effects is less than 0·002 $\mu\Omega$-cm after 22 weeks of irradiation or less than 1 per cent of the change observed for the 15 atomic per cent aluminum alloys upon irradiation.

As mentioned above, the results shown in Fig. 2 are considered to be the superposition of two effects. The first of these, Process A, is the direct contribution of radiation-produced defects, giving rise to a linear increase in the resistivity upon neutron exposure. Process A occurs for pure metals, as well as alloys, and is largely independent of temperature, although it is expected to give a somewhat larger effect at lower temperatures where less simultaneous radiation-annealing takes place. On the other hand, Process B is a saturating, diffusion-controlled solid-state reaction that depends upon the presence of the aluminum atoms in solid solution. It, therefore, occurs to a much lesser extent at lower temperatures. The superposition of the observed results is illustrated schematically in Fig. 3.

The curves shown in Fig. 2 can be separated into Processes A and B by using the observed

slope of Process $A$ past the minimum. The dependence of the slope of Process $A$ and the saturation value of Process $B$, i.e. the amount of the decrease, upon the aluminum concentration for the polycrystalline samples is given in Fig. 4. The saturation value for Process $B$ appears to be fitted fairly well with a parabolic dependence as shown by the curve. The slope of Process $A$ also increases rather sharply with the concentration of aluminum, but the increase in resistivity observed for pure copper prevents the fitting with a parabola through the origin. However, there would appear to be no reason to expect the slope of Process $A$ and the saturation value of Process $B$ to have the same composition dependence.

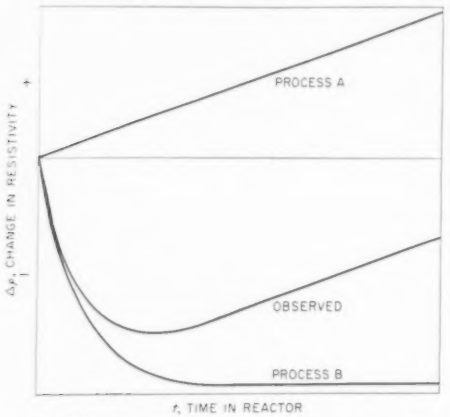


FIG. 3. Schematic separation into Processes $A$ and $B$ of the observed changes in resistivity upon irradiation at ~ 35°C.

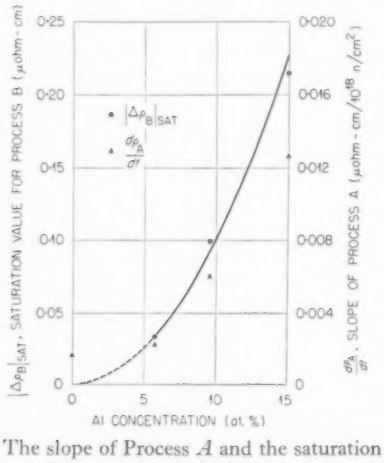


FIG. 4. The slope of Process $A$ and the saturation value for Process $B$ versus concentration of aluminum. The curve represents parabolic fit for the circles.

(b) *Hole 52 Experiments*

The results of the first Hole 52 experiment, conducted at 45°C, are shown in Fig. 5. A single-crystal sample and a polycrystalline sample were irradiated and measured at 45°C for 2 weeks, a time sufficient to reduce the resistivity to a value close to the minimum. The polycrystalline sample was observed to decrease somewhat less rapidly than the single crystal and to reach a somewhat lower value of resistivity at the end of the irradiation. Then, during the regular reactor-off period, the samples were step-annealed for periods of 30 min and returned to 45°C for measurement between each anneal. The resistivity of both samples was observed to increase upon the step-annealing treatment, the single crystal having first decreased after annealing at about 160°C to the resistivity attained by the polycrystalline sample. After annealing at about 250°C, the resistivity exceeds the pre-irradiation value. At the time this observation was made, it was thought to be anomalous and inherent in the difficulties of doing such in-pile annealing. However, it was later learned (Fig. 13) that the increases in resistivity are derived from a quenching effect and take place in the unirradiated material as well.

In the second Hole 52 experiment, the irradiation and the measurements were done at −120°C. The irradiation was continued for 1 week, an amount of time sufficient to produce a decrease of 0·17 $\mu\Omega$-cm upon irradiation at 45°C. However, as can be seen in Fig. 6, no decrease in resistivity took place upon irradiation at −120°C and, in fact, a linear increase of about 0·005 $\mu\Omega$-cm in this period was noted instead. A step-annealing treatment was applied at the conclusion of the week-long irradiation, in which the sample was held for 30 min periods at increasing temperatures between −120 and 160°C and returned between each anneal for measurement at −120°C. The results at the right of Fig. 6 show that the irradiation effect in producing Process $B$ can be stored in the samples to be released upon subsequent raising of the temperature. Although there is some scatter in the step-annealing data, it is apparent that the polycrystalline

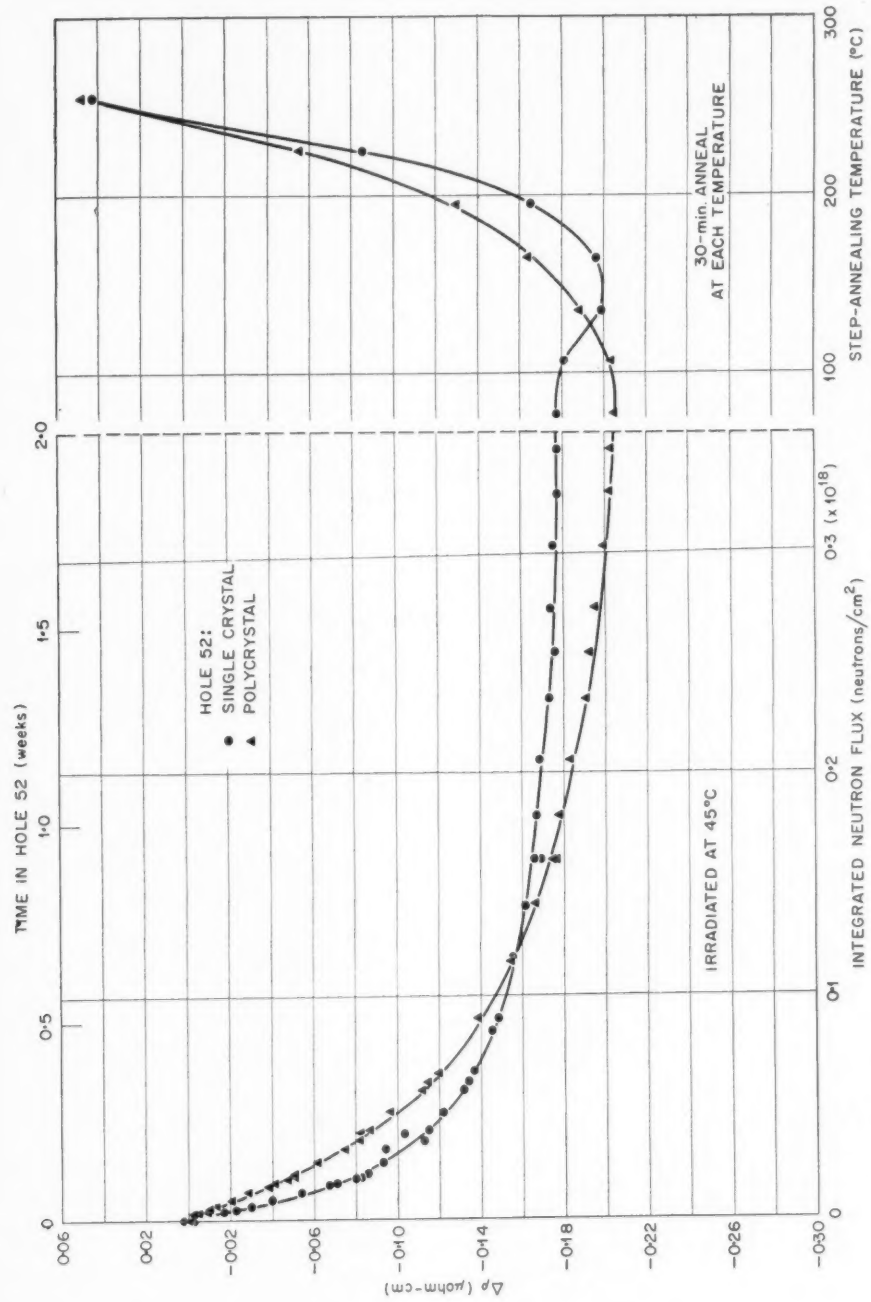


FIG. 5. Hole 52, experiment No. 1: Changes in resistivity of Cu–Al alloy (15 atomic per cent aluminum) versus neutron exposure at 45°C, followed by step-annealing. All measurements at 45°C.

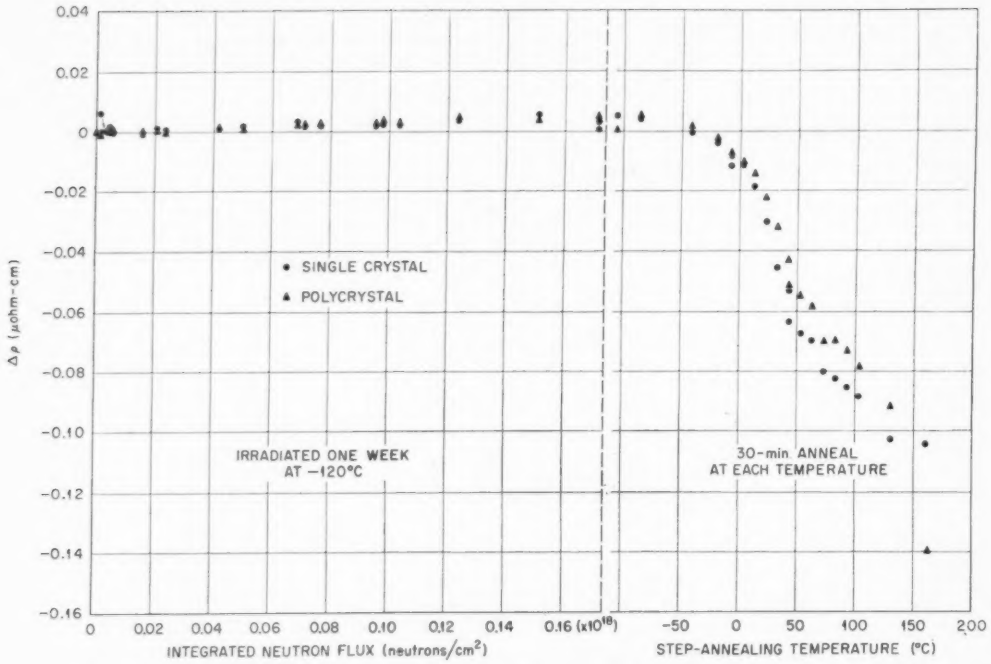


FIG. 6. Hole 52, experiment No. 2: Changes in resistivity of Cu–Al (15 atomic per cent aluminum) versus neutron exposure at −120°C, followed by step-annealing. All measurements at −120°C.

sample decreases in resistance somewhat less rapidly than the single crystal, as was the case for the experiments shown in Figs. 2 and 5. It was decided, as a result of this experiment, that the nature of the process responsible for the decrease in resistance could be better studied by irradiating the samples at −120°C and removing the samples without allowing them to warm-up, whereupon the kinetics of the decrease in resistance could be examined by isothermal and isochronal annealing in the laboratory. The results of such experiments are described in Section (d) below.

### (c) *Hole* 1768 *Experiment*

Since the instantaneous fast-neutron flux is thought to be several times greater in Hole 1768 than in either Holes C or 52, an irradiation at ambient pile temperature was carried out in Hole 1768 on a single-crystal sample and a polycrystalline sample of the 15 atomic per cent aluminum alloy. The results of this experiment are shown in Fig. 7; for comparison, the data for the experiments in Holes C and 52 are also plotted. It is to be noted that the abscissa is the time of neutron exposure rather than integrated neutron flux. When the data are presented in this way, the results of measurements in the three facilities superimpose, particularly for the single crystals. This would indicate that Process *B* is rather insensitive to the magnitude of the neutron flux at these flux levels. A 44-mil Cu–Al wire of the same composition as the $\frac{1}{8}$-in diameter samples was also irradiated in Hole 1768. No significant difference in behavior was noted for the wire as compared with the samples of larger cross-section.

### (d) *Annealing Following Irradiation at* −120°C

Prior to irradiation, a number of single-crystal samples containing 15 atomic per cent aluminum were annealed and measured at −196°C and at a number of temperatures between −80 and 200°C. They were then irradiated in Hole 52 for the 3 weeks at −120°C, removed from the reactor, and placed in liquid nitrogen. The transfer was made in

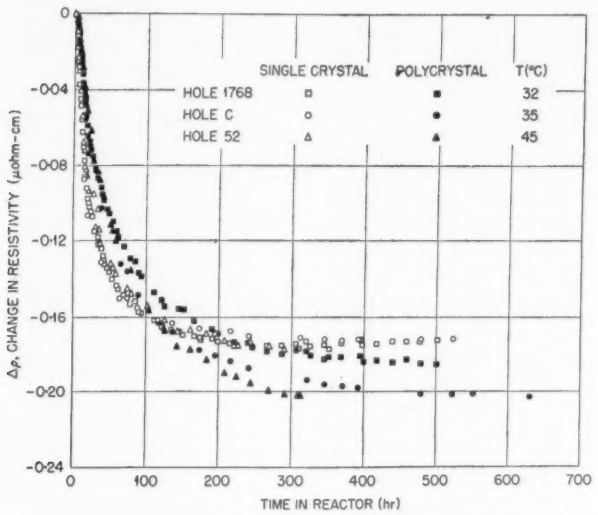


FIG. 7. The change in resistivity upon irradiation versus time in three facilities of the ORNL Graphite Reactor. Cu–Al (15 atomic per cent aluminum) alloy.

such a way as to minimize warming the samples in the process. The samples were stored in liquid nitrogen for at least several weeks to allow them to decay radioactively. We estimate from the linear increase observed in the second Hole 52 experiment (Fig. 6) that the samples should have increased in resistivity by about 0·014 $\mu\Omega$-cm as a result of the irradiation. A measurement at −196°C was made on each sample before the annealing studies were begun, in order to determine whether the samples had warmed sufficiently during removal from the reactor or handling in the laboratory to permit any decrease in resistivity to take place. For each sample, this measurement at −196°C showed that the resistivity had not decreased below the pre-irradiation value, although in most cases values less than 0·014 $\mu\Omega$-cm above the pre-irradiation values were obtained.

The results of annealing in the range 0–34°C after irradiation at −120°C are shown in Fig. 8. The changes in resistivity are measured with respect to the pre-irradiation values at the temperatures indicated. It is seen that when the change in resistivity is plotted versus log time, each curve exhibits two roughly linear portions. The long-time part of the curve continues to decrease extremely slowly at the temperatures investigated. This factor makes a determination of the final, asymptotic value difficult. Therefore, another point must be chosen at which to normalize the curves. For this purpose we define the "knee" of

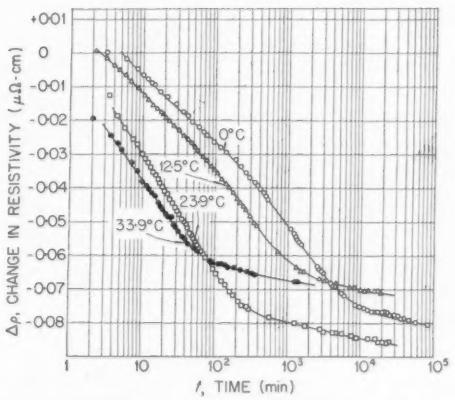


FIG. 8. Isothermal annealing of Cu–Al single crystals (15 atomic per cent aluminum) following irradiation for 3 weeks at −120°C.

the curve as the point where the change in slope takes place in Fig. 8, and we consider the same stage in the process to be reached at the times corresponding to the knee at each temperature. If we

define $f$ as the fractional amount of the process not completed at time $t$, then $f$ is given by

$$f = \frac{\rho - \rho_f}{\rho_i' - \rho_f}$$

where $\rho$ is the resistivity at time $t$, $\rho_f$ is the final value that would be obtained if the process were allowed to go to completion, and $\rho_i'$ is the initial value obtained after irradiation at $-120°C$, i.e. $\rho_i'$ is equal to $\rho_i + 0{\cdot}014$ $\mu\Omega$-cm, where $\rho_i$ is the original pre-irradiation value. We find that reasonable values for $\rho_f$ are obtained if we assign a value of 0·12 to $f$ at the knee of the curves.

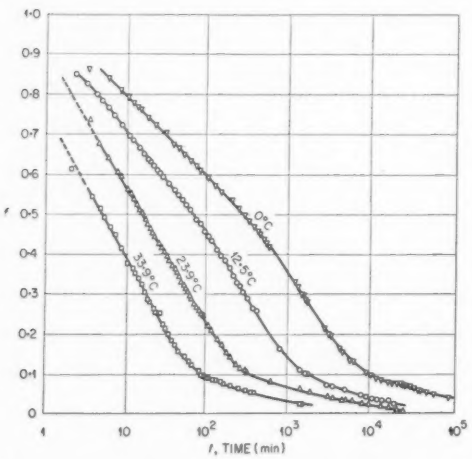


FIG. 9. Normalized isothermal annealing curves of Cu–Al single crystals (15 atomic per cent aluminum) following irradiation for 3 weeks at $-120°C$. $f$ is the fractional amount of the process not completed at time $t$.

The normalized curves that result are shown in Fig. 9. From these curves we may evaluate the activation energy, $\epsilon_M$, for the process corresponding to various $f$ values by plotting on a log scale the time, $t$, to reach a given value of $f$ versus the reciprocal annealing temperature. When this is done (Fig. 10), we find that the activation energy increases as the process progresses, as is seen by the increase in the slopes of the lines as $f$ decreases. The variation of $\epsilon_M$ with $f$ is shown in Fig. 11.

The annealing curves shown in Figs. 8 and 9 suggest that the decrease in resistivity after irradiation at $-120°C$ takes place in two stages. The first stage is rather rapid at temperatures between 0 and

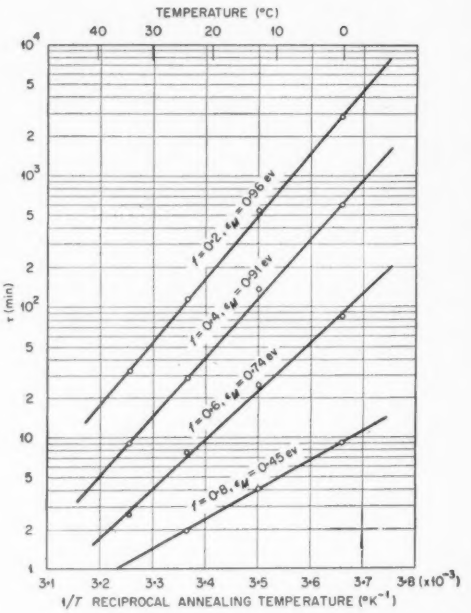


FIG. 10. Activation energy plot for annealing after 3 weeks' irradiation at $-120°C$.

34°C, and the second is quite slow at these temperatures. This aspect of the annealing is seen more clearly as a result of the experiment illustrated in Fig. 12. Here we have plotted the variation in

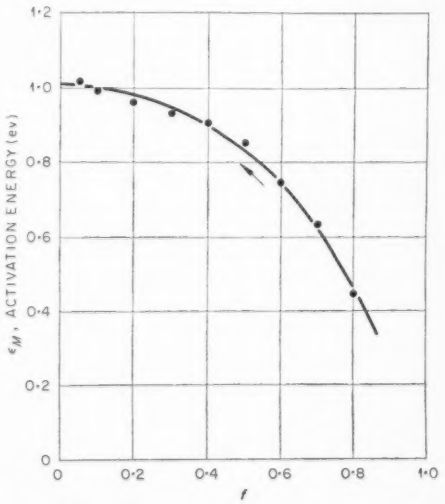


FIG. 11. Activation energy for annealing versus $f$. The arrow indicates the direction of Process $B$.

resistivity of a sample previously irradiated for 3 weeks at −120°C as a function of isothermal annealing at successively higher temperatures. At 34°C, the resistivity decreases about 0·08 μΩ-cm below the as-irradiated resistivity in about 100 min corresponding to the first stage of the annealing process. Upon continuation of the annealing at higher temperatures, little further decline in the resistivity is observed until the sample is held for about 2000 min at 75°C. A further slight decrease is seen at 125°C. Thus, Fig. 12 suggests that a second annealing stage occurs between 75 and 125°C. When the annealing is continued at 175°C, however, the resistivity increases and after some $2\times10^4$ min the resistivity has returned close to the pre-irradiation value. A failure in the temperature-control system during the 175°C anneal occurred for an unknown length of time between the points indicated by crosses on the 175°C curve. The succeeding points were plotted so as to continue the curve smoothly.

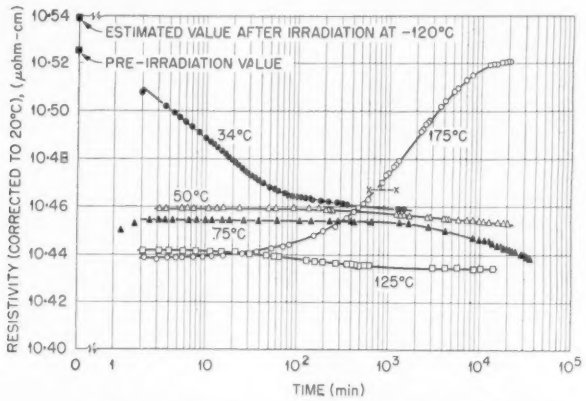


FIG. 12. Isothermal annealing behavior of a Cu–Al (15 atomic per cent aluminum) single crystal following 3 weeks' irradiation at −120°C. The resistivity was measured at temperature with respect to an unirradiated sample and all values are corrected to 20°C. The annealing was carried out at successively higher temperatures shown adjacent to the curves.

The nature of the decrease in resistivity after irradiation at −120°C was also studied by means of isochronal annealing. After the irradiation at −120°C and storage in liquid nitrogen, a 15 atomic per cent aluminum single crystal was held for 30 min at successively higher temperatures and returned to liquid nitrogen for measurement after each anneal. The same procedure was followed with an unirradiated sample of the same composition. Above 30°C the annealing steps were 20°C apart, and the samples were cooled in air to room temperature before insertion into liquid nitrogen, where the resistivities were measured. Fig. 13 shows that little change took place in the unirradiated sample below 200°C. At the beginning of the isochronal annealing, the resistivity of the sample that had been previously irradiated at −120°C was greater than its pre-irradiation value by 0·012 μΩ-cm due to the increase (Process *A*) upon the cold irradiation. No change in this value was observed upon isochronal annealing below −50°C. However, between 0 and 150°C the resistivity is observed to decrease about 0·08 μΩ-cm. There is some indication of a second dip in the curve between 130 and 170°C that is suggestive of the second annealing stage mentioned above. This dip in the curve is also reminiscent of the decrease observed for the single-crystal sample in the first Hole 52 experiment (Fig. 5) upon step-annealing between 100 and 150°C. A slight decrease in the curve for the unirradiated sample is also apparent in Fig. 13. When the step-annealing is continued above 150°C, the resistivity is observed to increase

and eventually to surpass the pre-irradiation value. Again, this is what was observed upon step-annealing after irradiation at 45°C (Fig. 5). Furthermore, the same general behavior is observed for the unirradiated sample above 200°C. A discussion of the origin of this increase upon annealing above 200°C and the reason for the decrease for temperatures above 310°C is deferred until this aspect of the work is explored in more detail. However, a reasonable approach seems to be that lattice defects or a lesser amount of short-range order come into equilibrium at temperatures above 150 or 200°C and are quenched-in upon air-cooling to room temperature. The reason for the decrease in $\Delta\rho$ for temperatures above 310°C depends upon the detailed nature of the quenching process. The similarity in the curves for the irradiated and unirradiated samples above 200°C indicates that the effect of the irradiation in producing Process *B* is dissipated upon raising the temperature above this point. This idea is supported by the result, not shown here, of retracing the experiment of Fig. 13 by *decreasing* the temperature of the irradiated sample from 500°C to room temperature. In this case, the points shown above 200°C are largely reproduced, but below 200°C no evidence of the decrease is found.

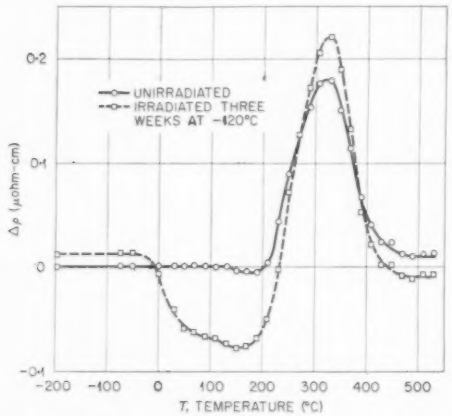


FIG. 13. Isochronal annealing of Cu–Al (15 atomic per cent aluminum) single crystals. Samples were held 30 min at each temperature and brought to −196°C for measurement.

A matter that is of some importance in this work is the relative effect of the irradiation on the residual and temperature-dependent contributions to the resistivity. ROSENBLATT *et al.*[22] have reported measurements on α-brass before and after neutron irradiation at 50°C for exposures of $7\times10^{17}$ and $3\times10^{18}$ neutrons/cm$^2$. A decrease in resistivity was observed for the lighter irradiation and an increase for the heavier irradiation. This was interpreted as being due to a larger negative change in the residual resistivity than positive change in the temperature-dependent part of the resistivity for the lighter irradiation and the reverse for the heavier one. In view of this, it was of interest to investigate whether changes in the temperature-dependent resistivity take place upon irradiation at −120°C or upon subsequent annealing at 0°C. The results of such an experiment are shown in Table 1 and in Fig. 14. The resistivity of a 15 atomic per cent aluminum sample was measured before irradiation in baths of liquid helium, liquid nitrogen, and dry ice and acetone and at a number of temperatures between 192 and 323°K. The sample was measured in liquid helium, liquid nitrogen, and dry ice and acetone baths following irradiation at −120°C. The results are shown in the second column of Table 1. The sample was then annealed at 0°C for $2\times10^4$ min, whereupon the resistivity decreased to 0·064 μΩ-cm below the pre-irradiation value at 0°C. The corresponding values measured at liquid helium, liquid nitrogen, and dry ice and acetone temperatures are shown in the third column of Table 1. It is believed likely that the measurements in the dry ice and acetone baths

*Table* 1. *Changes in resistivity measured at various temperatures upon irradiation for* 3 *weeks at* −120°C *and after annealing at* 0°C. *Values given are with respect to the pre-irradiation resistivity. Single crystal of* Cu–Al (15 *atomic per cent aluminum*) *alloy*

| Temperature (°K) | Δρ upon irradiation (μΩ-cm) | Δρ upon annealing (μΩ-cm) |
|---|---|---|
| 4 | 0·009 | −0·067 |
| 77 | 0·008 | −0·067 |
| 196 | 0·019 | −0·086 |
| 273 | | −0·064 |

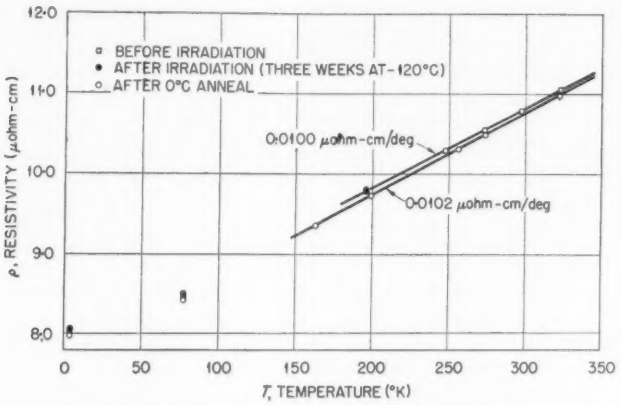


FIG. 14. Resistivity versus temperature measurements for Cu–Al (15 atomic per cent aluminum) alloy.

VOL. 7 1958

were inaccurate because of temperature gradients. If we take this into account, we find that the changes in resistivity at 4°K are the same as those measured at higher temperatures. Furthermore, as can be seen in Fig. 14, only a negligible change in the temperature coefficient corresponding to the linear portion of the curve above 200°K takes place upon annealing at 0°C. It is concluded from these measurements that only changes in the residual resistivity are significant in the effects considered here.

### (e) *X-Ray Work*

Debye–Scherrer X-ray photographs were taken of annealed Cu–Al (15 atomic per cent) filings before and after neutron irradiation for several weeks at about 35°C. In both cases, no superstructure reflections were observed and no evidence was found for the formation of a new phase upon irradiation.

## 4. DISCUSSION

According to our analysis of the changes in resistivity upon irradiation, Process *A* is considered to be produced directly by the impinging neutrons and the primary knock-ons that they set into motion. The pattern of imperfections developed by Process *A* endows the material with the ability to carry on Process *B*. We wish first to consider the Process *A* aspect of the irradiation effect in more detail. The values of the slopes of Process *A* obtained under various circumstances are shown in Table 2. We see that the magnitude of Process *A* increases with increasing neutron flux and with decreasing temperature. The comparison between the results in Holes C and 1768 indicates that the slope of Process *A* is roughly proportional to the instantaneous fast flux, when the measurements are done at the same temperature. The curves for resistivity versus exposure time in the long-time region indicate that Process *A* begins to saturate after 50 weeks in Hole C and about 16 weeks in Hole 1768. These times are inversely proportional to the instantaneous flux, as is to be expected. The comparison between experiments in Holes C and 52 illustrates the effect of lowering the temperature. It can be seen that the effect of simultaneous "self-annealing" during irradiation causes the slope of Process *A* to decrease as the temperature of irradiation is raised.

*Table 2. Slopes of Process* A *obtained under various circumstances for* Cu–Al (15 *atomic per cent*) *single crystals*)

| Reactor facility | Temperature (C°) | Fast neutron flux (neutron/cm² sec) | Slope of Process *A* (μΩ-cm/sec) |
|---|---|---|---|
| Hole C | 35 | $3\times10^{11}$ | $3{\cdot}4\times10^{-9}$ |
| Hole 1768 | 32 | $9\times10^{11}$ | $12{\cdot}1\times10^{-9}$ |
| Hole 52 | −120 | $3\times10^{11}$ | $8{\cdot}2\times10^{-9}$ |

The rate of the primary damage, Process *A*,

increases with aluminum content as is shown in Fig. 4. This observation is consistent with that of BLEWITT *et al.*,[2] who found that the low-temperature annealing after neutron irradiation is suppressed when beryllium, gold, silicon, or zinc is added to copper. It is reasonable to expect that the addition of aluminum to copper also decreases the rate at which Process *A* anneals out and therefore, as the aluminum content is raised, the amount of self-annealing at a given temperature (in this case 35°C) is decreased. The origin of this dependence on solute content may lie in the lower energy of formation and a higher activation energy for motion of a defect in the alloy as compared with the pure metal,[10] which is a result of interactions between point defects and solute atoms. As a result, more defects are produced in the alloy upon irradiation, and a lesser amount of annealing takes place at a given temperature. Another factor that may be involved is the possibility that a lower displacement energy is valid for alloys. DUGDALE[31] has indicated that the displacement energy for $Cu_3Au$ is less than 13·5 eV to be compared with a value of about 25 eV usually considered appropriate for pure copper.

A discussion of the structural details of the Process *A* damage depends on assumptions concerning the nature of Process *B*. We shall consider two general possibilities for the origin of the radiation-enhancement of diffusion-controlled reactions: (1) the increased atomic mobilities arising from vacancies produced by the irradiation, and (2) the introduction of nucleation or annihilation sites for the annealing of thermally-produced defects. In the case of the first mechanism, the enhanced diffusion resulting from the radiation-induced vacancies may cause short-range ordering or clustering to take place. The irradiation must be performed in the range of temperatures where vacancies are mobile; when the sample is irradiated below these temperatures, these reactions cannot take place and no decrease in resistivity results, as is shown in Fig. 6. However, the irradiation effect can be stored in the solid, since the decrease in resistivity will take place subsequent to the cold irradiation if the temperature is raised. In terms of this mechanism, the radiation-produced vacancies are immobile at the lower temperature, but when the temperature is raised they migrate to their annihilation sites, in the course of which atomic rearrangements take place that produce the short-range ordering or clustering. The fact that the irradiation effect can be stored in this way indicates that the primary effect of the radiation upon rate processes is not a result of the high temperatures of thermal spikes. In the case of the annealing after cold irradiation, all of the radiation-induced vacancies are available for migration at the outset of the isothermal anneal, whereas when the decrease in resistivity is produced in the reactor at 32–45°C, the vacancies are introduced gradually. This shortens the time for annealing after cold irradiation relative to that for annealing in the reactor. Thus, we find that the time for half-annealing at 34°C after cold irradiation is about 5 min (Fig. 9), whereas the corresponding time for in-pile annealing is about $10^3$ min (Fig. 7).

The number of vacancies introduced by the bombardment during 3 weeks at −120°C in Hole 52 may be estimated from the rise of 0·014 $\mu\Omega$-cm in resistivity observed during that period. If we assume 1·3 $\mu\Omega$-cm per atomic per cent vacancies, as calculated by JONGENBURGER[32] for pure copper, we obtain a concentration of about $10^{-4}$ vacancies. An estimate of effectiveness of these excess vacancies in producing atomic rearrangements may be made with the use of the activation energy $\epsilon_M = 0{\cdot}85$ eV corresponding to half completion of the annealing process after irradiation at −120°C (Fig. 11) and a relaxation time, $\tau$, of about 250 min at 0°C (Fig. 9). The number of jumps, $n_J$, that an average vacancy makes during its lifetime is given by

$$n_J = \tau\Gamma \tag{1}$$

where $\Gamma$, the jump rate, is given by

$$\Gamma = \Gamma_0 \exp\left(-\frac{\epsilon_M}{kT}\right) = z\nu \exp\left(\frac{s_M}{k} - \frac{\epsilon_M}{kT}\right) \tag{2}$$

and $z \cong 10$, $\nu = 10^{13}$ sec$^{-1}$, and $\exp(s_M/k) = 1$ ($s_M$ is the entropy associated with the motion of a vacancy). In this way, we find that approximately 300 jumps are made by an average vacancy. Thus, for a vacancy concentration of $10^{-4}$, we find that approximately one out of thirty atoms shifts position as a result of the motion of the excess vacancies. An average of 300 vacancy jumps is much lower than is found for the annealing of vacancies in unirradiated metals, where the annihilation is

VOL. 7 1958

presumably at dislocations. If we assume that each position on the dislocation lines serves as a sink for vacancies, then, for a concentration of $10^8$ dislocations/cm$^2$ and lattice parameter of 3·6 Å, one atomic position in $10^7$ is an annihilation site. Thus, on the average, a vacancy makes $10^7$ jumps for annihilation in annealed metals. The low number of jumps after irradiation indicates that the radiation must produce vacancy sinks as well as the vacancies themselves, thereby reducing the distance that a vacancy must travel before annihilation. This supposition is supported by the observation that the decrease in resistivity (−0·18 Ω-cm, Fig. 7) when Process *B* occurs during irradiation close to room temperature is larger than the decrease (−0·08 Ω-cm, Fig. 8) observed upon annealing subsequent to irradiation at −120°C. This follows from the fact that early in the irradiation at 35°C few sinks have been produced by the irradiation and therefore a vacancy makes many jumps during its lifetime. However, when the annealing is done after the irradiation at −120°C is completed, all vacancy motion must be carried out in a field that contains the full complement of radiation-produced sinks. Hence, fewer vacancy jumps are made and less ordering takes place. A suggestion as to the nature of the vacancy sinks introduced by the radiation is made below in the course of discussion of the second general mechanism for Process *B*.

It should be pointed out that caution should be applied in ascribing the effects reported here on Cu–Al alloys or those reported elsewhere on Cu–Zn alloys[22–24] to an increase in short-range order as a result, chiefly, of measurements of decreases in electrical resistivity upon irradiation. The point has been made[33] that the effect of short-range order on resistivity is very small, if it exists at all, and more evidence is needed to establish a relation between the two effects. Also, in the case of $Cu_3Au$, evidence has been found[34,35] that the increase in short-range order obtained by decreasing the temperature above the critical temperature causes an increase in resistivity. A theoretical basis for this increase in resistivity upon short-range ordering of $Cu_3Au$ is given by GIBSON[36] who, in fact, predicts a slight increase in resistivity for α-brass upon short-range ordering. Indeed, even as concerns long-range order, MUTO and TAKAGI[37] cite several examples of increases in resistivity upon the formation of a superlattice and others in which a change in resistivity on ordering is quite small or almost absent. Because of the lack of correspondence between resistivity changes and short-range ordering, it is impossible at present to correlate the amount of atomic rearrangement calculated above with the observed decrease in resistivity. It would seem equally reasonable to postulate that clustering takes place as a result of the presence of radiation-induced vacancies. Since the clustering of aluminum would result in a matrix richer in copper, such a clustering may result in a decrease in resistivity. Based on our measurements of resistivity for Cu–Al alloys of various compositions, we find the slope of the resistivity-versus-composition curve to be 0·25 μΩ-cm per atomic per cent aluminum at the 15 atomic per cent aluminum composition. Thus, a decrease of 0·08 μΩ-cm after irradiation at −120°C would imply the removal of about 0·3 atomic per cent aluminum from solid solution.

Another mechanism that depends upon radiation-induced vacancies concerns the migration of these vacancies to solute atoms. A number of authors[10,38–40] have commented on the existence of an interaction between solute atoms and vacancies and its effect on diffusion processes in metals. A large attractive interaction is expected between vacancies and aluminum atoms in copper because of the large size difference between the two atoms. Also, it appears not unlikely that a decrease in resistivity accompanies the trapping of a vacancy by a solute aluminum atom. Thus, we suggest the possibility that the decrease in resistivity of Cu–Al alloys is associated with the pairing of radiation-produced vacancies and aluminum atoms. The effect would be expected to increase with aluminum content. However, in the 15 atomic per cent aluminum alloy, one or two nearest neighbor sites to a given site are occupied by an aluminum atom and some solute-vacancy pairs would be expected to be formed even upon low temperature irradiation. Therefore, it is difficult to understand, on the basis of this model, why no decrease in resistivity took place upon irradiation at −120°C.

All of the mechanisms for Process *B* discussed above rely upon the introduction of vacancies by the irradiation, and the radiation enhancement of short-range ordering or clustering depends specifically on the increased diffusion rates that are the

result of the extra concentration of vacancies. However, another explanation for the observed radiation effects may lie in the introduction of annihilation sites for defects that were present in the material before the bombardment had begun. This implies that the sample has initially an excess concentration of defects despite the procedure normally used in its preparation, i.e. holding at a high temperature and slowly cooling to room temperature. As was mentioned earlier, because of the lower energy of formation of vacancies in alloys as compared to pure metals and the higher activation energy for motion, it is conceivable that no reasonable cooling rate is low enough to avoid the quenching-in of vacancies. Also, since the annealing is extremely slow at temperatures at which measurable concentrations exist in equilibrium, no thermal treatment can be given that will allow the excess vacancies to anneal out. However, the neutron irradiation may introduce sites that are particularly favorable for the annihilation of vacancies. The suggestion is made, therefore, that the decrease in resistivity observed upon irradiation of Cu–Al alloys is associated with the annealing-out of vacancies that were inadvertently quenched-in as a result of prior thermal treatment. The decrease in formation energy of vacancies upon alloying results in greater amounts of such quenched vacancies for the samples of greater aluminum content. Therefore, the more highly alloyed sample show a greater decrease in resistivity as is shown in Figs. 2 and 4. Furthermore, despite the introduction of favorable sites for vacancy annihilation, the quenched vacancies must be mobile or no annealing is observed during irradiation, as in the case of the irradiation at −120°C.

The damage cluster that results when a primary knock-on rapidly partitions its energy at the end of its path would appear to be an excellent sink for vacancies. We use the picture developed by BRINKMAN,[8,9] although we need not consider the proposal that melting and resolidification take place. The damage cluster is pictured as a pear-shaped region populated by vacancies toward the center and surrounded by a shell of interstitials (see Fig. 3, Ref. 9; Fig. 2.6, Ref. 1(a); or Fig. 1, Ref. 1(d)). The vacancies in the interior of the damage cluster may agglomerate into a void that collapses forming a sessile dislocation loop. However, since the low-temperature radiation annealing attributed to the motion of interstitials is suppressed in alloys, we may consider the shell of interstitials to be stable. Also, it has been pointed out[41] that, because of the anisotropic elastic interactions discussed by ESHELBY,[42] appropriately oriented interstitials may trap one another and form a fairly stable configuration. Thus, we adopt the picture that the irradiation introduces damage clusters at whose surfaces lie a preponderance of interstitials. The introduction of these damage clusters is our Process *A*. Such damage clusters will enhance the annealing-out of pre-existing lattice vacancies because, firstly, their presence shortens the distance a vacancy must travel before it is annihilated, and, secondly, there would be an attractive interaction between such clusters and vacancies lying within the stress field that the clusters exert.* These vacancies would move directly to their annihilation point and would not execute diffusive, random-walk motion. Thus, the number of jumps for annihilation would be greatly reduced.

The shorter relaxation time for annealing after irradiation at −120°C as compared to that for the in-pile annealing at 35°C follows from the fact that all the damage clusters are present before the annealing starts in the former case. Therefore, the distance over which the quenched vacancies must travel is short at the start and less time is required for the annealing. Each vacancy cancels out an interstitial as it is annihilated at the damage cluster. Therefore, a damage cluster disappears when it has absorbed a number of vacancies equal to the number of displacements produced per primary. A calculation may be made of the number of displacements produced in the cluster. If we use 1·3 $\mu\Omega$-cm/atomic per cent vacancies, we calculate that, corresponding to 0·08 $\mu\Omega$-cm, about $6{\cdot}2\times10^{-4}$ vacancies are required to eliminate the damage clusters. The number of clusters is given by

$$n_c = \sigma_s \phi t$$

* It has been pointed out to us by H. B. HUNTINGTON that no interaction exists between spherically symmetric centers of distortion in an isotropic medium that obeys Hooke's Law. In view of this, the suggestion of an interaction between damage clusters and vacancies must assume either a departure from isotropy and Hooke's Law or that the damage clusters are non-spherical, as would be the case if there were a collapse of the void at the center of the cluster.

where $\sigma_s = 3{\cdot}5\times10^{-24}$ cm$^2$, $\phi = 3\times10^{11}$ neutrons/cm$^2$ sec, and $t$, the time the reactor is on during the 3-week irradiation period, is $1{\cdot}7\times10^6$ sec. Thus, the number of clusters per atom is about $1{\cdot}8\times10^{-6}$, and the number of vacancies annihilated per cluster is $6{\cdot}2\times10^{-4}/1{\cdot}8\times10^{-6}$ or about 340. This must also equal the number of interstitials at the cluster or the number of displacements per primary knock-on. Other estimates[1] of the number of displacements vary from 100 to 1000. For copper, DIENES and VINEYARD[1a] give 380 displacements per primary as a result of neutron bombardment. Other types of bombardment such as electrons or $\gamma$-rays may also give rise to stable aggregates of interstitials in alloys, but these irradiations would be expected to be less effective in enhancing the annealing of vacancies than those resulting from neutron irradiation.

Fig. 11 shows that the activation energy for the annealing after cold irradiation of the inadvertently quenched vacancies increases as the annealing proceeds. We interpret this as an indication that vacancies lying within the stress field of a damage cluster move with considerably less energy than those lying without the stress field. Therefore, at the start of the annealing, when most of the vacancies being annihilated have originated from within the stress field, the activation energy is quite low. In fact, the curve in Fig. 11 appears to extrapolate to zero energy at the very start of the process. However, the annealing becomes increasingly difficult as the process continues; and finally, when all of the damage clusters have been dissolved, the remaining vacancies anneal with an activation energy of $1{\cdot}01\pm0{\cdot}03$ eV corresponding to $f = 0$ in Fig. 11. The annealing of vacancies at the high $\epsilon_M$ is responsible for the slow decrease, shown in Fig. 8, that persists at 0–34°C even after $10^4$ or $10^5$ min. Also, these vacancies, annealing at an energy of 1·0 eV may be responsible for what appears to be a second annealing stage between 150 and 200°C in Fig. 13. LI and NOWICK[13] have studied atomic mobility in a Cu–Al (17 atomic per cent aluminum) alloy after quenching and neutron irradiation, using stress-relaxation techniques. As a result of their quenching experiments, they deduce the value $1{\cdot}08\pm0{\cdot}08$ eV for the activation energy for motion of vacancies, in good agreement with the value 1·01 eV obtained here in the latter portion of the annealing after irradiation at −120°C. This fact also leads to the conclusion that, at the end of the annealing after irradiation, the damage clusters have been removed and the kinetics of vacancy motion have returned to that characteristic of the unirradiated solid.

We may use the value $\epsilon_M = 1{\cdot}01$ eV to check the plausibility of the suggestion that vacancies are inadvertently quenched into the lattice in the initial preparation of the sample. For annihilation at dislocations of concentration $10^8$ cm$^{-2}$, the effective freezing-in temperature is that below which fewer than $10^7$ jumps are made upon cooling to lower temperatures. The instantaneous jump rate is given by

$$\Gamma = \frac{dn_J}{dt}$$

whereby

$$n_J = \int_{t=0(T=T_0)}^{t=t_f(T=T_f)} \Gamma dt$$

where $\Gamma$ is given by (2), $t = (T_0 - T)/\alpha$, and $\alpha$ is the cooling rate. For values of $T_f$ close to room temperature, $n_J$ is well approximated by the expression

$$n_J = \frac{\Gamma_0 T_0}{\alpha\beta_0} e^{-\beta_0}, \quad \beta_0 = \epsilon_M/kT_0.$$

Our samples were cooled at a controlled constant rate of about 15°C/hr. Corresponding to this cooling rate, to $\epsilon_M = 1{\cdot}01$ eV, and to $\Gamma_0 = 10^{14}$ sec$^{-1}$, it is found that $n_J = 10^7$ jumps for $T_0 = 204$°C. $T_0$ is not very sensitive to the value taken for $n_J$; for example, $T_0 = 165$°C for $10^6$ jumps and 249°C for $10^8$ jumps. Thus, it appears reasonable that vacancies are frozen into the lattice in concentrations characteristic of about 200°C, even upon slow cooling. The presence of a significant concentration of vacancies in equilibrium at 200°C implies a low energy of formation in Cu–Al alloys. Equilibrium and quenching experiments have been reported[14] that indicate that this is indeed the case.

LI and NOWICK[13] also reported that no changes in the relaxation times for stress relaxation of Cu–Al alloys were observed after neutron exposures of about $10^{19}$ neutrons/cm$^2$ at 50, 35°C,

and liquid-nitrogen temperature. However, since their first measurement was made after at least 5000 sec at room temperature, we see from Figs. 8 and 9 that most of the irradiation effect would have annealed out by that time even in the case of the samples exposed at liquid-nitrogen temperature. Nevertheless, on the basis of the interpretation we are now considering, we would have expected the post-irradiation values of $\tau$ to be somewhat longer than those observed before irradiation. But LI and NOWICK's irradiation experiment may not be strictly comparable to ours, since their samples received 10–20 times the neutron dose necessary to bring the samples to minimum resistivity.

Since the activation energy is so small at the outset of the process, in-pile annealing would be expected to show little temperature-dependence inasmuch as the damage clusters are introduced continuously while the annealing is going on. This is indicated by the in-pile annealing curves shown in Fig. 7, although the temperature range is too small here (32–45°C) to allow definite conclusions to be drawn. We should not be surprised, however, if the time for annealing remained rather constant upon in-pile annealing at higher temperatures below 200°C.

Fig. 11 and the results of LI and NOWICK show that the activation energy returns upon completion of Process *B* to the value of about 1·0 eV characteristic of vacancy motion in unirradiated Cu–Al alloys. If the temperature is then raised to above about 200°C, the equilibrium concentration of vacancies characteristic of these temperatures will then be created. The relaxation time for this process will be controlled by the equilibrium activation energy for diffusion, since the energy for both creation and movement of vacancies is involved. This would explain why the relaxation time and activation energy for the increase in resistivity of α-brass after irradiation at 50°C were found by DAMASK[24] to be consistent with those obtained by CHILDS and LECLAIRE[25] by equilibrium stress-relaxation methods. The theory of LECLAIRE and LOMER[26] is designed to explain the origin of the damping peak observed in stress-relaxation experiments and relates the *strength* of the relaxation to changes in lattice parameter that accompany local ordering. In their analysis, it is pointed out that the degree of order, $\sigma$, is a function of the mixing energy and, since the mixing energy varies with lattice parameter, straining a crystal will lead to a change in $\sigma$. Thus, according to their development, small fluctuations in $\sigma$ about an average value give rise to corresponding small fluctuations in strain, and this results in the anelastic effects. Other interpretations of the relaxation phenomenon have been given,[43,44] but even if the view of LECLAIRE and LOMER is adopted, the relaxation times observed in a stress-relaxation experiment are governed, not by the small fluctuations of short-range order associated with their measurement, but by the concentration and motion energy of the vacancies that control the diffusion. Therefore, it should not be concluded from the fact that resistivity changes after irradiation follow the same kinetics as stress-relaxation measurements that the resistivity changes arise from changes in short-range order.[24] A determination by diffuse-scattering techniques of the short-range-order parameters and the effect of irradiation on them has not yet been made. Such an experiment is under way for the case of Cu–Al alloys. But until such an experiment is completed, it is advisable to consider other mechanisms in addition to short-range ordering as possible explanations for the irradiation effects. Several additional approaches to the problem have been discussed.

## 5. SUMMARY

(1) Upon neutron irradiation at 32–45°C, the resistivity of α Cu–Al alloys decreases, reaches a minimum, and then increases linearly upon further exposure. This behavior is considered to be due to the superposition of two effects: Process *A*, causing a linear increase in resistivity due to displacements produced directly by the bombardment, and Process *B*, a saturating diffusion-controlled reaction that brings about a decrease in resistivity. The slope of Process *A* and the saturation decrease for Process *B* increase in magnitude with aluminum content. There is no Process *B* for pure copper. For the 15 atomic per cent aluminum alloy, the decrease is about 0·2 μΩ-cm (2 per cent).

(2) When the irradiation is carried out at −120°C, no decrease in resistivity is found. However, upon subsequent warming above −50°C the decrease sets in. The kinetics of the decrease (Process *B*) were studied by isothermal annealing at 0–34°C following irradiation at −120°C. The

activation energy increases as the process continues starting with a very low value and ending with an energy of 1·0 eV. Annealing above about 150°C causes the resistivity to increase again, and the pre-irradiation value is exceeded if the annealing is continued above 200°C. No change in the temperature coefficient of resistivity was observed after irradiation at −120°C or after Process *B* was completed.

(3) Several mechanisms to explain these effects are discussed:

A. Based upon radiation-produced vacancies

(1) short-range ordering
(2) clustering
(3) solute atom–vacancy pairing.

B. Based upon radiation-produced nucleation or annihilation sites

(1) annealing of thermally-quenched vacancies.

*Acknowledgements*—The advice and co-operation of D. S. BILLINGTON and other members of the Solid State Division are greatly appreciated. We also wish to thank A. B. LEWIS, J. M. WILLIAMS and F. A. RUSSO, for assistance in the setting up of apparatus and the making of resistivity measurements, and F. A. SHERRILL for help with the X-ray work.

## REFERENCES

1. (a) DIENES G. J. and VINEYARD G. H., *Radiation Effects in Solids*. Interscience Publishers Inc., New York (1957).
   (b) SEITZ F. and KOEHLER J. S., *Solid State Physics* Vol. 2, p. 305. Academy Press Inc., New York (1956).
   (c) BROOKS H., *Annual Reviews of Nuclear Science* Vol. 6, p. 215. Annual Reviews Inc., Stanford University, Palo Alto, California (1956).
   (d) COTTRELL A. H., *Met. Rev.* **1,** 479 (1956).
2. BLEWITT T. H., COLTMAN R. R., KLABUNDE C. E. and NOGGLE T. S., *J. Appl. Phys.* **28,** 639 (1957).
3. BLEWITT T. H., COLTMAN R. R., HOLMES D. K. and NOGGLE T. S., *Creep and Recovery* p. 84. American Society for Metals, Cleveland, Ohio (1957).
4. VOOK R. and WERT C. *Phys. Rev.* **109,** 1529 (1958).
5. SIMMONS R. O. and BALLUFFI R. W., *Phys. Rev.* **109,** 1142 (1958).
6. COOPER H. G., KOEHLER J. S. and MARX J. W., *Phys. Rev.* **97,** 599 (1955).
7. CORBETT J. W., DENNEY J. M., FISKE M. D. and WALKER R. M., *Phys. Rev.* **108,** 954 (1957).
8. BRINKMAN J. A., *J. Appl. Phys.* **25,** 961 (1954).
9. BRINKMAN J. A., *Amer. J. Phys.* **24,** 246 (1956).
10. LOMER W. M., *Vacancies and Other Point Defects in Metals and Alloys* p. 79. Institute of Metals, London (1957).
11. ROSWELL A. E. and NOWICK A. S., *Trans. Amer. Inst. Min. (Metall) Engrs.* **197,** 1259 (1953).
12. NOWICK A. S. and SLADEK R. J., *Acta Met.* **1,** 131 (1953).
13. LI C. Y. and NOWICK A. S., *Phys. Rev.* **103,** 294 (1956).
14. WECHSLER M. S. and KERNOHAN R. H., *Bull. Amer. Phys. Soc.* **3,** 118 (1958).
15. WECHSLER M. S., *Acta Met.* **5,** 150 (1957).
16. STURM W. J. and WECHSLER M. S., *J. Appl. Phys.* **28,** 1509 (1957).
17. BAUERLE J. E. and KOEHLER J. S., *Phys. Rev.* **107,** 1493 (1957).
18. DESORBO W. and TURNBULL D., *Bull. Amer. Phys. Soc.* **2,** 262 (1957).
19. BRADSHAW F. J. and PEARSON S., *Phil. Mag.* **1,** 812 (1956).
20. Earlier investigations of the effect of neutron irradiation on diffusion-controlled reactions in copper-base alloys are reported in: (a) BILLINGTON D. S. and SIEGEL S., *Metal Progr.* **58,** 847 (1950) and (b) MURRAY G. F. and TAYLOR W. E., *Acta Met.* **2,** 52 (1954). For a general review see (c) THOMAS D. E., in *Nuclear Metallurgy* Vol. 3, p. 13. American Institute of Mining and Metallurgical Engineers, New York (1956).
21. FLEEMAN J. and DIENES G. J., *J. Appl. Phys.* **26,** 652 (1955).
22. ROSENBLATT D. B., SMOLUCHOWSKI R. and DIENES G. J., *J. Appl. Phys.* **26,** 1044 (1955).
23. DAMASK A. C., *J. Phys. Chem. Solids* **4,** 177 (1958).
24. DAMASK A. C., *J. Appl. Phys.*, **27,** 610 (1956).
25. CHILDS B. G. and LECLAIRE A. D., *Acta Met.* **2,** 718 (1954).
26. LECLAIRE A. D. and LOMER W. M., *Acta Met.* **2,** 731 (1954).
27. KEATING D. T., *Acta Met.* **2,** 885 (1954).
28. OBINATA I. and WASSERMANN G., *Naturwissenschaften* **21,** 382 (1933).
29. SULLIVAN W. H., *Trilinear Chart of Nuclides* U.S. Government Printing Office, Washington, D.C. (1957).
30. LINDE J. O., *Elektrische Widerstandseigenschaften der verdünnten Legierungen des Kupfers, Silbers and Goldes*. Ohlsson, Lund (1939).
31. DUGDALE R. A., *Defects in Crystalline Solids* p. 246. Physical Society, London (1955).
32. JONGENBURGER P., *Phys. Rev.* **90,** 710 (1953); *Appl. Sci. Res.* B**3,** 237 (1953).
33. BROOM T., *Advanc. Phys.* **3,** 26 (1954).
34. BURNS F. P. and QUIMBY S. L., *Phys. Rev.* **97,** 1567 (1955).
35. DAMASK A. C., *J. Phys. Chem. Solids* **1,** 23 (1956).
36. GIBSON J. B., *J. Phys. Chem. Solids* **1,** 27 (1956).

37. MUTO F. and TAKAGI Y., *Solid State Physics* Vol. 1, p. 193. Academy Press Inc., New York (1955).
38. LOMER W. M. and COTTRELL A. H., *Phil. Mag.* **46,** 711 (1955).
39. ALFRED L. C. R. and MARCH N. H., *Phil. Mag.* **2,** 985 (1957).
40. JOHNSON R. P., *Phys. Rev.* **56,** 814 (1939).
41. MAGNUSSON G. D., PALMER W. and KOEHLER J. S., *Phys. Rev.* **109,** 1990 (1958).
42. ESHELBY J. D., *Solid State Physics* Vol. 3, p. 79. Academy Press Inc., New York (1956).
43. ZENER C., *Phys. Rev.* **71,** 34 (1947).
44. NOWICK A. S., *Progress in Metal Physics* Vol. 4, p. 1. Interscience Publishers Inc., New York (1953).

VOL
7
195

*J. Phys. Chem. Solids* Pergamon Press 1958. Vol. 7. pp. 327–344.

# THERMODYNAMIC PROPERTIES OF A DISORDERED LATTICE*

**GEORGE WEISS† and ALEXEI MARADUDIN**

Institute for Fluid Dynamics and Applied Mathematics, University of Maryland
Department of Physics, University of Maryland, College Park, Maryland

(*Received* 15 *May* 1958; *revised* 26 *June* 1958)

**Abstract**—We present in this paper a new method for evaluating additive functions of the normal mode frequencies of disordered isotopic lattices as a perturbation-type expansion. The method is constructive; a recipe is given for writing down the general term of the expansion. The expression for the general term depends only on the evaluation of certain sums and integrals. A further advantage of the present method is that we are able to discuss the convergence of the resulting series solution. This is generally difficult, if not impossible, to do for the usual perturbation expansions.

Several simple examples have been considered to illustrate the method. We have rederived and generalized the result of PRIGOGINE *et al.* (*Physica* **20,** 383, 516 (1954)) for the zero-point energy of a one-dimensional lattice and have obtained higher-order terms in the expansion. In two dimensions the agreement between our more accurate calculation and that of PRIGOGINE *et al.*, indicates that their use of the Debye frequency spectrum as a zeroth approximation does not lead to appreciable error. In addition to our calculation of additive functions of the normal mode frequencies, we are able to discuss the low-frequency end of the frequency-distribution function.

## 1. INTRODUCTION

THE problem of determining the vibrational properties of a randomly disordered many-component lattice has received much attention recently and has stimulated a great deal of ingenious mathematical thought. The interest in this problem is due in part to the light it throws on such properties of many-component lattices as the vibrational contribution to the thermodynamic functions of binary alloys and the separation of isotopic mixtures into separate phases at very low temperatures. This model has in addition a direct application to the evaluation of electronic energy levels in disordered alloys as well as to certain aspects of the spin-wave theory of magnetism.

The earliest work in this field was done by DYSON[1] who reduced the problem in the one-dimensional case to the solution of an integral equation. However, his approach appears to be quite difficult: DYSON has presented no complete calculations except for a physically unrealistic model. The mathematics for more realistic cases seems intractable. Furthermore DYSON's method is inapplicable in higher dimensions. Other developments which depend on some form of perturbation theory have been pursued.[2–4] Several authors[5–8] have discussed the linear chain by the use of transfer matrices. None of these treatments has any convincing or notable success in describing the frequency spectrum and none, except for the work of PRIGOGINE *et al.*,[2] discusses the effects of disorder on thermodynamic functions of the normal mode frequencies. For a further discussion of previous work on this subject, see reference (9).

In this paper we evaluate several additive functions of the normal mode frequencies of an $n$-dimensional ($n = 1, 2, 3$) two-component lattice. We assume that each lattice site is occupied by a particle of mass $M_1$ with probability $p$ and by a particle of mass $M_2$ with probability $(1-p)$. We

* This research was supported by the United States Air Force through the Air Force Office of Scientific Research, Air Research and Development Command under Contracts #AF18(600)1315 and #AF18(600)1015.

† This is based on a thesis submitted to the University of Maryland in partial fulfillment of the requirements for the Ph.D. degree.

average the additive functions over all the configurations of the particles, and we show that in the limit that the number of particles in the lattice becomes infinite our results approach those for a lattice containing *precisely* a fraction $p$ of masses $M_1$ and a fraction $(1-p)$ of masses $M_2$. The method used in the following analysis is to write the sum over the normal mode frequencies formally in terms of a contour integral and then to use an expansion of the integral to get an approximate expression for the sum. The method does not depend on dimension and is limited only by the number and complexity of the integrals involved. It will be seen that the technique presented here can actually be applied to more complicated situations. For example, we could consider several different masses $M_1, M_2 \ldots, M_n$ randomly distributed over the lattice sites (as does SCHMIDT[5]), or force constants which depend on the masses they couple, or we could allow correlations between the occupants of the lattice sites. These refinements can be handled in the process of averaging the additive functions over the configurations which the defect masses can assume. However, all of the advantages and the difficulties of our method will become evident from the present calculation.

We shall chiefly be concerned with the calculation of the zero-point energy and the specific heat of the disordered lattice. Results will be given for one- and two-dimensional lattices in detail. So far the three-dimensional lattice presents great computational problems although none in principle.

## 2. PRELIMINARY REMARKS

We denote the normal mode frequencies of a lattice by $\{\omega_j\}$. In what follows we shall be interested in evaluating sums of functions of the normal mode frequencies

$$S = \sum_j g(\omega_j). \tag{1}$$

In particular we will be interested in evaluating the zero-point energy of the lattice which is given by $S$ if $g(z) = \hbar z/2$; the Laplace transform of the frequency distribution function for which $g(z) = N^{-1}e^{-\alpha z}$, where $N$ is the number of degrees of freedom of the lattice; and the specific heat of the lattice for which $g(z) = k(\hbar z/2kT)^2/\sinh^2(\hbar z/2kT)$.

The frequencies are the roots of a determinantal equation

$$|M(\omega)| = 0. \tag{2}$$

Then it is a well-known result from the theory of contour integration that[14]

$$S = \sum_j g(\omega_j) = \frac{1}{2\pi i}\int_C g(z)d\ln|M(z)| \tag{3}$$

where $C$ is any closed counter-clockwise contour which encloses all the positive zeroes of $|M(z)|$ but none of the poles of $g(z)$.*

Let us now formally decompose $M(\omega)$ into the sum of two square matrices:

$$\begin{aligned} M(\omega) &= M_0(\omega)+\delta M(\omega) \\ &= M_0(\omega)[I+M_0^{-1}(\omega)\delta M(\omega)] \\ &= M_0(\omega)\Delta(\omega) \end{aligned} \tag{4}$$

where $\Delta(\omega) = I+M_0^{-1}(\omega)\delta M(\omega)$ and $I$ is a unit matrix. Since the determinant of the product of two matrices is equal to the product of the determinants of the individual matrices, the determinant $|M(\omega)|$ can be written as

$$|M(\omega)| = |M_0(\omega)|\,|\Delta(\omega)|. \tag{5}$$

Using the decomposition of equation (5) we find

$$\begin{aligned} S &= \frac{1}{2\pi i}\int_C g(z)d\ln|M_0(z)| + \frac{1}{2\pi i}\int_C g(z)d\ln|\Delta(z)| \\ &= S_0+\Delta S. \end{aligned} \tag{6}$$

If we now regard $M_0(\omega)$ as the secular determinant of an unperturbed lattice for which the various additive functions $S_0$ of the normal mode frequencies are known, then the evaluation of $S$ is reduced to the evaluation of $\Delta S$. If, further, we can assume that the elements of $\delta M(\omega)$ are small in some sense and that the elements of $M_0^{-1}(\omega)$ are easily found then an expansion of $\ln|\Delta(\omega)|$ in powers of the elements of $\delta M(\omega)$ would seem to be appropriate.

The details of such an expansion now follow. Let the matrix $M_0^{-1}(\omega)\cdot\delta M(\omega)$ be denoted by $D(\omega)$. We denote the set of eigenvalues of this

* The first use of contour integration in physical problems to evaluate additive functions of the zeroes of secular equations seems to be by WENTZEL.[11]

VOL 7 195

matrix by $\{\lambda_j\}$. Then we can express the determinant $|\Delta(\omega)|$ in the form

$$|\Delta(\omega)| = \prod_j (1+\lambda_j). \tag{7}$$

Therefore an expression for $\ln|\Delta(\omega)|$ can be written

$$\ln|\Delta(\omega)| = \sum_j \ln(1+\lambda_j). \tag{8}$$

When $|\lambda_j| < 1$, we can expand the logarithms in equation (8) to find

$$\ln|\Delta(\omega)| = \sum_j \lambda_j - \tfrac{1}{2}\sum_j \lambda_j^2 + \tfrac{1}{3}\sum_j \lambda_j^3 - \ldots. \tag{9}$$

The sum of the $k$th power of the eigenvalues of a matrix is equal to the trace of the $k$th power of the matrix, hence we obtain

$$\ln|\Delta(\omega)| = Tr(D) - \tfrac{1}{2}Tr(D^2) + \tfrac{1}{3}Tr(D^3) - \ldots. \tag{10}$$

It is clear that this expansion is valid for any choice of crystal lattice. In order to apply it to the evaluation of additive functions of the normal mode frequencies of a perturbed lattice, we must choose a particular model of a crystal lattice for which the inverse to the matrix of the secular determinant is readily found. Such a model is the one originally due to ROSENSTOCK and NEWELL,[12] which has subsequently been the basis of investigations by MONTROLL[13] and by MONTROLL and POTTS.[14]

We consider an $n$-dimensional simple-cubic lattice, each point of which is occupied by a particle of either mass $M_1$ or $M_2$. The number of particles in an edge of our lattice is $N$ so that the total number of lattice points is $N^n$. Born–von Karman boundary conditions will be used. We assume that a given lattice site is occupied by a particle of mass $M_1$ with probability $p$ and by a particle of mass $M_2$ with probability $(1-p)$. Each particle is in Hookean interaction with its $2n$ nearest neighbors. To insure stability of the lattice against shear, both central and non-central force interactions between particles are assumed. This model has the physically unrealistic feature that the components of displacement of a particle in any single direction are independent of those in all other directions. However, it does have the advantage of sufficient mathematical simplicity so that many of its properties can be studied analytically rather than numerically.

Although the mass at any given lattice site is a random variable, the force constants will be assumed to depend only on the relative direction of displacement of the interaction particles. The equation of motion for the $x$-component of displacement of the particle with co-ordinates $(m_1, m_2, \ldots m_n)$ is

$$M_{m_1, m_2, \ldots, m_n}\ddot{x}_{m_1, m_2, \ldots, m_n} =$$

$$= \sum_{j=1}^{n} \gamma_j [\chi_{m_1, m_2, \ldots, m_j+1, \ldots, m_n} - \tag{11}$$

$$-2\chi_{m_1, m_2, \ldots, m_j, \ldots, m_n} +$$

$$+\chi_{m_1, m_2, \ldots, m_j-1, \ldots, m_n}]$$

where $\gamma_j$ is the force constant associated with displacement of particles which lie along the $j$th coordinate axis. Similar equations hold for the other components of displacement. We choose solutions of the form

$$\chi_{m_1, m_2, \ldots, m_n} = e^{i\omega t} u_{m_1, m_2, \ldots, m_n}.$$

The equation for the $u$'s takes the form

$$\omega^2 M_{m_1, m_2, \ldots, m_n} u_{m_1, m_2, \ldots, m_n} +$$

$$+ \sum_{j=1}^{n} \gamma_j [u_{m_1, m_2, \ldots, m_j+1, \ldots, m_n} - \tag{12}$$

$$-2u_{m_1, m_2, \ldots, m_j, \ldots, m_n} +$$

$$+u_{m_1, m_2, \ldots, m_j-1, \ldots, m_n}] = 0.$$

The matrix $M(\omega)$ is the matrix of coefficients of $u_{m_1 \ldots m_n}$ in equation (12).

We wish to decompose $M(\omega)$ into the sum of two matrices $M_0(\omega)$ and $\delta M(\omega)$ such that the eigenvectors, eigenvalues, and elements of the matrix $M_0(\omega)$ are known and the remaining matrix $\delta M(\omega)$ has elements that can be regarded as small in a sense to be specified later. Here and in what follows we use the single index $\boldsymbol{m}$ to represent the $n$-tuple $(m_1, m_2, \ldots m_n)$. We define the mass at lattice site $\boldsymbol{m}$ to be

$$M(\boldsymbol{m}) = \bar{M} + \sigma_m \Delta M \tag{13}$$

where now $\sigma_m$ is a random variable with the property

$$\sigma_m = \begin{cases} \dfrac{M_1 - \bar{M}}{\Delta M} & \text{with probability } p \\ \dfrac{M_2 - \bar{M}}{\Delta M} & \text{with probability } 1-p. \end{cases} \tag{14}$$

We also will use the notation $\mu = \Delta M/\bar{M}$.

The choice of $\bar{M}$ is restricted by the condition that the expansion of equation (10) converge. This point will be discussed more carefully below.

We now define the matrix $M_0(\omega)$ to be the matrix of coefficients of the $u$'s in

$$\omega^2 \bar{M} u_{m_1, m_2, \ldots, m_n} + \sum_j \gamma_j [u_{m_1, m_2, \ldots, m_j+1, \ldots m_n} - 2u_{m_1, m_2, \ldots m_j, \ldots, m_n} + u_{m_1, m_2, \ldots, m_j-1, \ldots, m_n}] = 0 \tag{15}$$

while the matrix $\delta M(\omega)$ is diagonal with elements $\Delta M \omega^2 \sigma_m$. The matrix $M_0$ describes a crystal lattice with all masses equal to $\bar{M}$. Its eigenvectors and eigenvalues have been obtained by MONTROLL and POTTS.[13] They are

$$u_s(\boldsymbol{m}) = N^{-n/2} \exp(2\pi i \boldsymbol{s} \cdot \boldsymbol{m}/N) \tag{16}$$

$$\lambda_0(\boldsymbol{s}) = \bar{M}\omega^2 - 2\sum_j \gamma_j \left(1 - \cos\frac{2\pi s_j}{N}\right) \tag{17}$$

where $\boldsymbol{s} = (s_1, s_2, \ldots, s_n)$. The largest normal mode frequency of the lattice described by $M_0$, $\omega_L$, is defined by the equation

$$\bar{M}\omega_L^2 = 4\sum_{j=1}^{n} \gamma_j. \tag{18}$$

The elements of the matrix $M_0$ can be expressed as

$$a_{m, m'} = N^{-n} \sum_s \lambda_0(s) \exp[2\pi i \boldsymbol{s} \cdot (\boldsymbol{m} - \boldsymbol{m}')/N] \tag{19}$$

while the elements of $M_0^{-1}$ are

$$a^{(-1)}_{m, m'} = N^{-n} \sum_s [\lambda_0(s)]^{-1} \exp[2\pi i \boldsymbol{s} \cdot (\boldsymbol{m} - \boldsymbol{m}')/N]. \tag{20}$$

The elements of $\delta M$ are

$$(\delta M)_{m, m'} = \Delta M \omega^2 \sigma_m \delta_{m, m'} \tag{21}$$

where $\delta_{m, m'}$ is a Kronecker delta. The elements of the matrix $D$ then become

$$D_{m, m'} = \Delta M \omega^2 a^{(-1)}_{m, m'} \sigma_{m'}. \tag{22}$$

With these results we can now write $Tr(D^k)$ as

$$Tr(D^k) = (\Delta M \omega^2)^k \times \times \sum_{m_1} \cdots \sum_{m_k} a^{(-1)}_{m_1 m_2} a^{(-1)}_{m_2 m_3} \cdots a^{(-1)}_{m_k m_1} \sigma_{m_1} \cdots \sigma_{m_k}. \tag{23}$$

## 3. THE CHARACTERISTIC VALUES OF D(ω)

We have assumed in the preceding section that a convergent expansion of $\ln|\Delta(\omega)|$ in terms of traces of powers of the matrix $D(\omega)$ exists. A necessary condition that the expansion given by equation (10) be convergent is seen to be that

$$|\lambda_j(\omega)| < 1 \tag{24}$$

where $\{\lambda_j\}$ are the characteristic values of the matrix $D$. We now examine carefully the conditions under which this condition is satisfied.

By definition $D(\omega) = M_0^{-1}(\omega)\delta M(\omega)$, so that the condition of equation (24) imposes a certain restriction on our choice of the matrix $M_0$ and the perturbation matrix $\delta M$. It will be shown that not all choices of $M_0$ and $\delta M$ lead to a convergent series of the type given in equation (10).

It is usually simpler to study the eigenvalues, $\{\lambda_j^{-1}\}$, of the matrix inverse to $D$,

$$D^{-1}(\omega) = [\delta M(\omega)]^{-1} M_0(\omega), \tag{25}$$

rather than the eigenvalues of $D$ itself. Thus, we now discuss under what conditions the eigenvalues of $D^{-1}$ are greater than one in absolute value. We restrict ourselves here to the one-dimensional case; however, the results obtained here are valid with only slight modification in the higher-dimensional cases as well.

The matrix $D^{-1}$ for the one-dimensional case is

$$D^{-1}(\omega)=\begin{vmatrix} \dfrac{\bar{M}\omega^2-2\gamma}{\Delta M\omega^2\sigma_1} & \dfrac{\gamma}{\Delta M\omega^2\sigma_1} & 0 & \cdots & \dfrac{\gamma}{\Delta M\omega^2\sigma_1} \\ \dfrac{\gamma}{\Delta M\omega^2\sigma_2} & \dfrac{\bar{M}\omega^2-2\gamma}{\Delta M\omega^2\sigma_2} & \dfrac{\gamma}{\Delta M\omega^2\sigma_2} & 0 & \cdots \\ 0 & \dfrac{\gamma}{\Delta M\omega^2\sigma_3} & \dfrac{\bar{M}\omega^2-2\gamma}{\Delta M\omega^2\sigma_3} & \dfrac{\gamma}{\Delta M\omega^2\sigma_3} & 0\ \cdots \\ \vdots & & & & \\ \dfrac{\gamma}{\Delta M\omega^2\sigma_N} & \cdots & & & \cdots \end{vmatrix} \tag{26}$$

To discuss bounds on the eigenvalues of this matrix, we use the following result due to GERSHGORIN:[15]

Let $B=(B_{k\lambda})$ be an arbitrary square matrix of order $N$ and set

$$P_k=\sum_{\substack{\lambda=1\\ \lambda\neq k}}^{N}|B_{k\lambda}|. \tag{27}$$

Then each eigenvalue of $B$ lies in the interior or on the boundary of at least one of the $N$ circles

$$|z-B_{kk}|\leqslant P_k. \tag{28}$$

If some of the circles are completely disjoint from any others, then they must contain at least one eigenvalue.

In our case the elements $B_{kk}$ and $P_k$ are given by

$$B_{kk}=\frac{\bar{M}\omega^2-2\gamma}{\Delta M\omega^2\sigma_k}, \qquad P_k=\left|\frac{2\gamma}{\Delta M\omega^2\sigma_k}\right|. \tag{29}$$

Since $\sigma$ can assume only two values (cf. equation (14)) the system of circles given by equation (28) reduces to only two circles whose equations are

$$\left|z-\frac{1}{\mu\sigma_k}+\frac{2\gamma}{\Delta M\omega^2\sigma_k}\right|\leqslant\left|\frac{2\gamma}{\Delta M\omega^2\sigma_k}\right|. \tag{30}$$

Hence the two circles in which the eigenvalues lie are the following:

$$\text{center: } \frac{\bar{M}}{M_j-\bar{M}}-\frac{2}{\omega^2(M_j-\bar{M})};$$

$$\text{radius: } \frac{2}{|\omega^2(M_j-\bar{M})|}. \tag{31}$$

We will be interested in the special case corresponding to the contour of integration to be described later. This case is $\omega=i\omega'$ where $\omega'$ is real. In particular we seek to find the conditions under which $|\lambda_j^{-1}|>1$.

When $\omega=i\omega'$ the two circles have centers lying on the real axis. The intercepts of the circles on this axis are

$$\left(\frac{\bar{M}+(4\gamma/\omega'^2)}{M_1-\bar{M}},\ 0;\ \frac{\bar{M}}{M_1-\bar{M}},\ 0\right)$$
$$\text{and} \tag{32}$$
$$\left(\frac{\bar{M}+(4\gamma/\omega'^2)}{M_2-\bar{M}},\ 0;\ \frac{\bar{M}}{M_2-\bar{M}},\ 0\right).$$

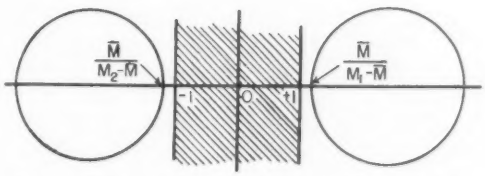


FIG. 1. Circles containing the eigenvalues of $D^{-1}$.

The two circles are shown in Fig. 1. The circles lie on either side of the $y$-axis and the intercepts closest to the $y$-axis are $\bar{M}/(M_j-\bar{M})$, $j=1, 2$. As $\omega'\to\infty$ the circles shrink to these points. Hence, in order to have $|\lambda_j^{-1}|>1$ we must have the conditions

$$\bar{M}>|M_j-\bar{M}| \tag{33}$$

satisfied.

The criterion of equation (33) leads to an interesting conclusion. An obvious choice for $\bar{M}$ would be such as to insure that $\langle\sigma\rangle = 0$. By equations (13) and (14) this means that*

$$\bar{M} = pM_1 + (1-p)M_2. \tag{34}$$

If we substitute this definition into the criterion equation (33), we find the following conditions must be satisfied for $|\lambda_j| < 1$,

$$\begin{aligned} \frac{p(M_1-M_2)+M_2}{(1-p)(M_1-M_2)} &> 1 \\ \frac{p(M_1-M_2)+M_2}{p(M_1-M_2)} &> 1. \end{aligned} \tag{35}$$

It is easily seen that the second of equations (35) is always satisfied regardless of the values of $M_1$, $M_2$, and $p$. However, the first question is satisfied only if

$$\frac{M_2}{M_1} > \frac{1-2p}{2-2p} \text{ or } 2p > \frac{M_1-2M_2}{M_1-M_2}. \tag{36}$$

This condition, therefore, restricts the class of lattices for which the choice of $\bar{M}$ given by equation (34) leads to a convergent expansion for $\ln|\Delta(\omega)|$. Notice that for $p \geqslant \frac{1}{2}$ there is no restriction on the masses for the convergence of the expansion using this definition. It is easily shown that if $\bar{M} \geqslant M_1$ then $|\lambda_j| < 1$.

## 4. THE STATISTICS OF DISORDERED LATTICES

We are now in a position to discuss the statistical aspects of the problem under consideration. The model that we examine in this paper postulates that there is no correlation between the position of atoms of different masses. If each atom in a lattice of $N$ atoms has mass $M_1$ with probability $p$, then the lattice will contain $k$ atoms of mass $M_1$ with probability $\binom{N}{k}p^k(1-p)^{N-k}$. If we now consider an ensemble of binomial lattices, then the distribution of the number of lattices with $k$ atoms is found to be approximately Gaussian with mean $Np$ and standard deviation equal to $N^{\frac{1}{2}}\sqrt{p(1-p)}$. As $N$ goes to infinity the law of large numbers assures us that the probability of a large deviation from the mean number goes to zero. Hence, our following remarks will apply to a good approximation to the problem of a lattice containing *exactly* $Np$ atoms of mass $M_1$ randomly placed.

If we assume that $|\lambda_j| < 1$, then by equation (10) we have for $\Delta S$ as a function of the random variables $\sigma_{m_j}$

$$\Delta S = \frac{1}{2\pi i}\int_C g(z)d\left\{\sum_{n=1}^{\infty}\frac{(-1)^{n+1}}{n}(\Delta M z^2)\times\right.$$

$$\times \sum_{m_1}\cdots\sum_{m_n} a^{(-1)}_{m_1m_2}\, a^{(-1)}_{m_2m_3}\cdots a^{(-1)}_{m_nm_1}\times$$

$$\left.\times\,\sigma_{m_1}\sigma_{m_2}\cdots\sigma_{m_n}\right\}. \tag{37}$$

To proceed generally one must now study the moments of $\Delta S$ with respect to the probability distribution over all configurations of atoms. It is of interest to note that if $(M_1-M_2)/\bar{M}$ is small enough so that higher powers of this quantity can be neglected in comparison to the first, we can say a bit more about the distribution of $\Delta S$. We see from equation (20) that $a^{(-1)}_{mm}$ is independent of $m$. Hence, we can write as an approximation for $\Delta S$:

$$\Delta S \sim \frac{\Delta M}{2\pi i}\int_C (\sum_m \sigma_m)g(z)d\{z^2 a^{(-1)}_{m,m}\}. \tag{38}$$

In this situation all of the random behavior of $\Delta S$ is described by the term $\sum_m \sigma_m$, which is a sum of independent random variables. If $N$ is large enough, we may infer from the central limit theorem that the sum $\sum_m \sigma_m$ has a Gaussian distribution with mean equal to

$$\frac{N^n}{\Delta M}[pM_1 + (1-p)M_2 - \bar{M}]$$

and variance equal to

$$\frac{N^{2n}}{(\Delta M)^2}[p(1-p)(M_1-M_2)^2].$$

In general we shall have to be content with a good deal less than the complete distribution of $\Delta S$; we shall find only the first moment. Denoting configuration averages by $\langle\ \rangle$ and $\langle\sigma^j\rangle$ by $\beta_j$, we find

* This definition was used by PRIGOGINE *et al.*[2].

VOL 7 195

$$\beta_1=\frac{1}{\Delta M}\{pM_1+(1-p)M_2-\bar{M}\}$$

$$\beta_2=\frac{1}{(\Delta M)^2}\{pM_1^2+(1-p)M_2^2+\bar{M}^2-2pM_1\bar{M}-2(1-p)M_2\bar{M}\} \tag{39}$$

$$\beta_3=\frac{1}{(\Delta M)^3}\{pM_1^3+(1-p)M_2^3-3pM_1^2\bar{M}-3(1-p)M_2^2\bar{M}+3pM_1\bar{M}^2+3(1-p)M_2\bar{M}^2-\bar{M}^3\}.$$

We must now begin to distinguish between subscripts in averaging over products of $\sigma$'s since, for example, $\langle\sigma_m{}^2\rangle \neq \langle\sigma_m\rangle^2$. Let us first consider the double sum in equation (37). There are two types of averages included in the summation: $\langle\sigma_m{}^2\rangle$ and $\langle\sigma_{m_1}\sigma_{m_2}\rangle=\langle\sigma_m\rangle^2$ when $\boldsymbol{m}_1\neq\boldsymbol{m}_2$ by the hypothesis of independence. Each average itself is independent of the actual subscripts. We, therefore, write for the double summation

$$\sum_{m_1}\sum_{m_2} a^{(-1)}_{m_1m_2}\,a^{(-1)}_{m_2m_1}\,\langle\sigma_{m_1}\sigma_{m_2}\rangle$$

$$=\beta_2\sum_{m_1}\{a^{(-1)}_{m_1m_1}\}^2+\beta_1{}^2\sum_{m_1}{\sum_{m_2}}'\,a^{(-1)}_{m_1m_2}\,a^{(-1)}_{m_2m_1} \tag{40}$$

where the stroke indicates that all terms with $\boldsymbol{m}_1\neq\boldsymbol{m}_2$ are to be omitted. In a similar fashion we must partition all of the $r$-fold summations according to how many of the $\sigma$'s in $\langle\sigma_{m_1}\sigma_{m_2}\ldots\sigma_{m_r}\rangle$ have different indices. To study this type of partition we introduce the notion of a $k$-vector, $\boldsymbol{k}=(k_1,\,k_2,\ldots k_r)$ where $k_j$ is the number of $j$-tuples of equal indices. For an $r$-fold product $\langle\sigma_{m_1}\sigma_{m_2}\ldots\sigma_{m_r}\rangle$ the components of the associated $k$-vector must satisfy

$$\sum_{j=1}^{r} jk_j=r. \tag{41}$$

We will be interested in the degeneracy of each $k$-vector (i.e. the number of different realizations of each $k$-vector) and for a specific expansion we will need the actual $k$-vectors. The problem is formally equivalent to a combinatorial problem* arising in the theory of cluster integrals as applied to the theory of the equation of state of imperfect gases. The result is that for a given $k$-vector the degeneracy is

$$\frac{r!}{k_1!k_2!\ldots k_r!(1!)^{k_1}(2!)^{k_2}\ldots(r!)^{k_r}}. \tag{42}$$

We may now proceed to a more detailed consideration of the sums appearing in equation (37). If we define

$$a_k(\omega)=N^{-n}(\Delta M\omega^2)^k\sum_{m_1}\cdots\sum_{m_k} a^{(-1)}_{m_1m_2}\,a^{(-1)}_{m_2m_3}\cdots a^{(-1)}_{m_km_1}$$

$$=N^{-n}(\Delta M\omega^2)^k\sum_{s}[\lambda_0(s)]^{-k} \tag{43}$$

$$b_k(\omega)=N^{-n}(\Delta M\omega^2)^k\sum_{m_1}\sum_{m_2}(a^{(-1)}_{m_1m_2})^k$$

* Namely, in how many ways can one arrange $r$ distinguishable objects into $k_1$ groups of one object, $k_2$ groups of two objects, etc.?

then all the sums appearing in equation (37) can be written (to order $\mu^4$) in terms of these two. For example, we have that

$$N^{-n}\Delta M\omega^2\sum_{m_1} a^{(-1)}_{m_1m_1} = \Delta M\omega^2 a^{(-1)}_{00} \tag{44}$$

since $a^{(-1)}_{m_1m_1}$ is independent of $m_1$ (see equation (20)). In a similar fashion we find, for example, that

$$N^{-n}(\Delta M\omega^2)^4\sum_{m_1}\sum_{m_2}\sum_{m_3}\sum_{m_4} a^{(-1)}_{m_1m_2}a^{(-1)}_{m_2m_3}a^{(-1)}_{m_3m_4}a^{(-1)}_{m_4m_1}$$
$$= a_4(\omega)+10a_1^2(\omega)a_2(\omega)+b_4(\omega)-4a_1(\omega)a_3(\omega)-6a_1^4(\omega)-2a_2^2(\omega). \tag{45}$$

If we were to take our expansion of $N^{-n}\langle\ln|\Delta(\omega)|\rangle$ to higher powers of $\Delta M$, we would find that new "irreducible" sums $c_k$, $d_k$, . . . would have to be introduced in terms of which all sums over combinations of the $a^{(-1)}_{m_1m_2}$'s could be expressed. The situation here is somewhat analogous to the expansion of cluster integrals in terms of irreducible integrals in the theory of imperfect gases.

It is easily shown from the definition of equation (43) that the $a_k(\omega)$ satisfy the following differentiation formula:

$$\frac{da_k}{d\omega} = \frac{2k}{\omega}[a_k(\omega)-\mu^{-1}a_{k+1}(\omega)]. \tag{46}$$

Unfortunately no such simple formula holds for the derivative of $b_k(\omega)$.

Using equations (37) and (43)–(46), we obtain the general expression for $N^{-n}d/d\omega\langle\ln|\Delta(\omega)|\rangle$ up to second order in $\mu$

$$N^{-n}\frac{d}{d\omega}\langle\ln|\Delta(\omega)|\rangle = \frac{2}{\omega}\{\beta_1+\beta_1^2a_1(\omega)-\beta_2a_1(\omega)\}$$
$$\times\{a_1(\omega)-\mu^{-1}a_2(\omega)\}-\frac{2\beta_1^2}{\omega}[a_2(\omega)-\mu^{-1}a_3(\omega)]+\ldots \tag{47}$$

Additional terms covering up to $\mu^4$ can be found in reference 18.

This result in connection with the equation

$$\frac{\langle\Delta S\rangle}{N^n} = \frac{1}{2\pi iN^n}\int_C g(z)d\langle\ln|\Delta(z)|\rangle \tag{48}$$

constitutes a formal solution to our problem. We will use the contour $C$ shown in Fig. 2. As $R\to\infty$ the contribution from the semi-circle vanishes for the class of functions $g(z)$ of physical interest. Hence we are left only with an integration on the imaginary axis.

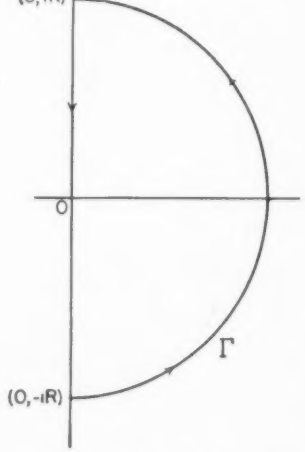


FIG. 2. The contour of integration C.

## 5. EVALUATION OF $a_k(\omega)$ AND $b_k(\omega)$

We have seen in Section 4 that the trace of the $k$th power of the matrix $D$ breaks up into several subsidiary sums when we average $\Delta S$ over all configurations of the masses. It has been shown that all of these subsidiary sums are expressible in terms of certain "irreducible" sums which we have labelled $a_k$, $b_k$, $c_k$, . . . . In this section we evaluate the first two of these sums.

The simplest of these sums is $a_k(\omega)$ defined by

$$N^n a_k(\omega) = (\Delta M\omega^2)^k \sum_{m_1} \cdots \sum_{m_k} a^{(-1)}_{m_1 m_2} a^{(-1)}_{m_2 m_3} \cdots a^{(-1)}_{m_k m_1}$$

$$= (\Delta M\omega^2)^k \sum_s [\lambda_0(s)]^{-k} \tag{49}$$

where the $\lambda_0(s)$ are the eigenvalues of $M_0(\omega)$ and are given by equation (17). If we assume that $\omega^2 < 0$, then

$$N^n a_k(i\omega) = (\Delta M\omega^2)^k \sum_s \left[\bar{M}\omega^2 + 2\sum_j \gamma_j \left(1 - \cos\frac{2\pi s_j}{N}\right)\right]^{-k}. \tag{50}$$

Using the recurrence relation of equation (46), one needs only to calculate $a_1(i\omega)$ in order to obtain all of the $a_k(i\omega)$.

In order to evaluate the expression for $a_k(i\omega)$, we let $N \to \infty$ and replace the sum in equation (50) by a Riemann integral

$$a_k(i\omega) = \pi^{-n}(\Delta M\omega^2)^k \int_0^\pi \cdots \int \frac{d\phi_1 d\phi_2 \ldots d\phi_n}{[\bar{M}\omega^2 + 2\sum_j \gamma_j(1-\cos\phi_j)]^k}. \tag{51}$$

(a) *The one-dimensional case*

In one dimension the integral in equation (51) can be evaluated in terms of Legendre polynomials[16]

$$a_k(i\omega) = (\Delta M\omega^2)^k P_{k-1}\left(\frac{\bar{M}\omega^2 + 2\gamma}{\sqrt{\bar{M}^2\omega^4 + 4\gamma\bar{M}\omega^2}}\right) / (\bar{M}^2\omega^4 + 4\gamma\bar{M}\omega^2)^{k/2}. \tag{52}$$

We define $\omega_L$ through the relation $\bar{M}\omega_L^2 = 4\gamma$, transforming equation (52) into

$$a_k(i\omega) = \mu^k |\omega|^k (\omega^2 + \omega_L^2)^{-k/2} P_{k-1}\left(\frac{2\omega^2 + \omega_L^2}{2|\omega|\sqrt{\omega^2 + \omega_L^2}}\right). \tag{53}$$

(b) *The two-dimensional case*

To simplify succeeding expressions we make the following definitions

$$\omega_{L_1}^2 = \frac{4\gamma_1}{\bar{M}}, \quad \omega_{L_2}^2 = \frac{4\gamma_2}{\bar{M}}, \quad \omega_L^2 = \omega_{L_1}^2 + \omega_{L_2}^2. \tag{54}$$

The integral of equation (51) can be written in terms of Legendre functions[17]; thus for $a_1(i\omega)$ we obtain

$$a_1(i\omega) = \frac{2\mu\omega^2}{\pi\omega_{L_1}\omega_{L_2}} Q_{-\frac{1}{2}}\left(\frac{2\omega^4 + 2\omega^2\omega_L^2 + \omega_{L_1}^2\omega_{L_2}^2}{\omega_{L_1}^2\omega_{L_2}^2}\right) \tag{55}$$

where $Q_n(z)$ is the $n$th Legendre function of the second kind. But this function can be expressed in

terms of a complete elliptic integral of the first kind by use of the relations[17]

$$Q_{-\frac{1}{2}}(z)=\frac{\pi}{\sqrt{2(z+1)}}F(\tfrac{1}{2},\tfrac{1}{2},1;2(z+1)^{-1})=\sqrt{\frac{2}{1+z}}K\left(\sqrt{\frac{2}{z+1}}\right). \tag{56}$$

Hence for $a_1(i\omega)$ we have

$$a_1(i\omega)=\frac{2\mu\omega^2}{\pi(\omega^2+\omega_{L_1}{}^2)^{\frac{1}{2}}(\omega^2+\omega_{L_2}{}^2)^{\frac{1}{2}}}\,K\left(\frac{\omega_{L_1}\omega_{L_2}}{\sqrt{(\omega^2+\omega_{L_1}{}^2)(\omega^2+\omega_{L^2}{}^2)}}\right). \tag{57}$$

The next two $a_k$'s are

$$a_2(i\omega)=\frac{\mu^2\omega^2}{\pi\sqrt{(\omega^2+\omega_{L_1}{}^2)(\omega^2+\omega_{L_2}{}^2)}}\left(\frac{2\omega^2+\omega_L{}^2}{\omega^2+\omega_L{}^2}\right)E\left(\frac{\omega_{L_1}\omega_{L_2}}{\sqrt{(\omega^2+\omega_{L_1}{}^2)(\omega^2+\omega_{L_2}{}^2)}}\right) \tag{58}$$

and

$$\begin{aligned}a_3(i\omega)=\frac{\mu^3}{\pi}\Bigg[&\frac{3\omega^{10}+6\omega^8\omega_L{}^2+\omega^6(4\omega_L{}^4+\omega_{L_1}{}^2\omega_{L_2}{}^2)+\omega^4(\omega_L{}^2\omega_{L_1}{}^2\omega_{L_2}{}^2+\omega_L{}^6)}{(\omega^2+\omega_L{}^2)^2(\omega^2+\omega_{L_1}{}^2)^{\frac{3}{2}}(\omega^2+\omega_{L_2}{}^2)^{\frac{3}{2}}}+\\&+\frac{1}{2}\frac{\omega_L{}^2\omega_{L_1}{}^2\omega_{L_2}{}^2\omega^2}{(\omega^2+\omega_L{}^2)^2(\omega^2+\omega_{L_1}{}^2)^{\frac{3}{2}}(\omega^2+\omega_{L_2}{}^2)^{\frac{3}{2}}}\Bigg]E\left(\frac{\omega_{L_1}\omega_{L_2}}{\sqrt{(\omega^2+\omega_{L_1}{}^2)(\omega^2+\omega_{L_2}{}^2)}}\right)-\\&-\frac{\mu^3}{4\pi}\frac{\omega^4(2\omega^2+\omega_L{}^2)^2}{(\omega^2+\omega_L{}^2)(\omega^2+\omega_{L_1}{}^2)^{\frac{3}{2}}(\omega^2+\omega_{L_2}{}^2)^{\frac{3}{2}}}K\left(\frac{\omega_{L_1}\omega_{L_2}}{\sqrt{(\omega^2+\omega_{L_1}{}^2)(\omega^2+\omega_{L_1}{}^2)}}\right).\end{aligned} \tag{59}$$

(c) *The three-dimensional case*

In three dimensions $a_k(i\omega)$ is given by

$$a_k(i\omega)=\frac{(\Delta M\omega^2)^k}{\Gamma(k)}\int_0^\infty t^{k-1}e^{-(\bar{M}\omega^2+2\sum_j\gamma_j)t}I_0(2\gamma_1 t)I_0(2\gamma_2 t)I_0(2\gamma_3 t)\,dt. \tag{60}$$

If we assume that $\gamma_1=\gamma_2\neq\gamma_3$ and set

$$\alpha=\gamma_3/\gamma_1 \qquad \beta=1+\bar{M}\omega^2[2\gamma_1(2+\alpha)]^{-1} \tag{61}$$

then the following series can be derived[18] for $a_k(i\omega)$:

$$a_k(i\omega)=\mu^k\left(\frac{\omega}{\omega_L}\right)^{2k}\frac{(4+2\alpha)^k}{\Gamma(k)}\sum_{m=0}^{\infty}\frac{(2m)!\Gamma(2m+k)}{2^{2m}(m!)^4}\frac{P_{2m+k-1}\left(\dfrac{(2+\alpha)\beta}{\sqrt{(2+\alpha)^2\beta^2-\alpha^2}}\right)}{[(2+\alpha)^2\beta^2-\alpha^2]^{m+k/2}}. \tag{62}$$

The second type of irreducible sums to be considered are the $b_k(\omega)$ defined by

$$b_k(\omega)=N^{-n}(\Delta M\omega^2)^k\sum_{m_1}\sum_{m_2}(a^{(-1)}_{m_1m_2})^k. \tag{63}$$

Notice that $b_2(\omega)=a_2(\omega)$. Terms involving $b_3(\omega)$ do not appear in any calculation, so that we need

only consider the $b_k(\omega)$ for $k \geqslant 4$. We will work only with $b_k(i\omega)$. It is possible to evaluate the $b_k$'s in a usable form only in the one-dimensional case, although formal expressions in terms of generalized hypergeometric functions can be given in two and three dimensions.

A general expression for $a^{(-1)}_{m_1 m_2}(i\omega)$ is

$$a^{(-1)}_{m_1 m_2}(i\omega) = \frac{-1}{\pi^n} \int_0^{\pi} \cdots \int \frac{e^{i\phi \cdot (m_1 - m_2)}\, d\phi_1 \ldots d\phi_n}{\bar{M}\omega^2 + 2\sum_j \gamma_j (1 - \cos\phi_j)}, \tag{64}$$

where the interchanges of integrals can be justified, when $\omega \neq 0$. The vector $\boldsymbol{m}_j$ has components $(m_1{}^j, m_2{}^j \ldots)$. In one dimension we find[14]

$$a^{(-1)}_{m_1 m_2}(i\omega) = -\frac{1}{\bar{M}\omega\sqrt{\omega^2 + \omega_L{}^2}} \times \times \left(2\frac{\omega^2}{\omega_L{}^2} + 1 + \frac{2\omega}{\omega_L}\sqrt{1 + \frac{\omega^2}{\omega_L{}^2}}\right)^{-|m_1 - m_2|} \tag{65}$$

If we use the notation introduced by MONTROLL and POTTS[14]

$$\frac{\omega}{\omega_L} = \sinh\frac{z}{2}, \tag{66}$$

equation (65) assumes the simpler form

$$a^{(-1)}_{m_1 m_2}(i\omega) = -\frac{2}{\bar{M}\omega_L{}^2} \frac{\exp(-|\boldsymbol{m}_1 - \boldsymbol{m}_2|z)}{\sinh z}. \tag{67}$$

With this result and the definition equation (43) for $b_k(i\omega)$, we obtain

$$b_k(i\omega) = \frac{2^k(\Delta M\omega^2)^k}{N(\bar{M}\omega_L{}^2)^k} \sum_{m_i} \sum_{m_2} \frac{e^{-|m_1 - m_2|kz}}{\sinh^k z} = \left\{N\left(\frac{1 + e^{kz}}{e^{kz} - 1}\right) + \frac{1 - e^{-Nkz}}{1 - \cosh z}\right\} \frac{2^k(\Delta M\omega^2)^k}{N(\bar{M}\omega_L{}^2)^k \sinh^k z} \tag{68}$$

The second term is negligible in comparison with the first except when $|z|$ is very small. However, there will only be a negligible contribution to any integral from this region because the factor which multiplies the geometric series causes $b_k$ to vanish at the origin for $k > 1$ as a power of $z$. Thus we may write in the limit $N \to \infty$

$$b_k(i\omega) = \mu^k \tanh^k\left(\frac{z}{2}\right) \coth\left(\frac{kz}{2}\right). \tag{69}$$

In particular we have

$$\frac{db_4(i\omega)}{d\omega} = \frac{\mu^4\omega^2}{4} \frac{(64\omega^6\omega_L{}^2 + 96\omega^4\omega_L{}^4 + 40\omega^2\omega_L{}^6 + 3\omega_L{}^8)}{(\omega^2 + \omega_L{}^2)^{7/2}(2\omega^2 + \omega_L{}^2)^2}. \tag{70}$$

With this term we can calculate terms of order up to $\mu^4$ in an expansion of any $\langle \Delta S \rangle$ in the one-dimensional case.

## 6. ZERO-POINT ENERGY OF DISORDERED LATTICES

We are now in a position to apply the formalism developed in the preceding sections to the calculation of the simplest additive function of the normal mode frequencies, viz. the zero-point energy. For this case the function $g(z)$ is $(\frac{1}{2})\hbar z$; consequently the results of Section 2 yield

$$\frac{\langle \Delta E_0 \rangle}{N^n} = -\frac{\hbar}{2\pi N^n} \int_0^{\infty} \omega d\langle \ln|\Delta(i\omega)| \rangle. \tag{71}$$

(a) *The one-dimensional case*

The integrals of equation (71) are all elementary. When they are evaluated, there results the following expression for $(E_0 + \langle \Delta E_0 \rangle/N)$ up to terms which are $0(\mu^4)$:

$$E_0+\langle\Delta E_0\rangle = N\pi^{-1}\hbar\omega_L[1-0{\cdot}5\beta_1\mu+(0{\cdot}3927\beta_2-0{\cdot}0177\beta_1^2)\mu^2+(0{\cdot}6073\beta_1\beta_2-0{\cdot}3333\beta_3-0{\cdot}5862\beta_1^3)\mu^3+$$
$$+(0{\cdot}2946\beta_1+0{\cdot}0933\beta_2^2+1{\cdot}6667\beta_1\beta_3+1{\cdot}7687\beta_1^4-3{\cdot}7358\beta_1^2\beta_2)\mu^4+0(\mu^5)]. \quad (72)$$

For a special set of definitions

$$\bar{M}=pM_1+(1-p)M_2 \qquad \mu=(M_1-M_2)/(pM_1+(1-p)M_2)$$
$$\omega_L=2(\gamma/\bar{M})^{\frac{1}{2}} \qquad \beta_n=p(1-p)^n+(-1)^n p^n(1-p) \quad (73)$$

the expression in equation (72) simplifies to

$$E_0+\langle\Delta E_0\rangle = N\hbar\omega_L\pi^{-1}[1+0{\cdot}3927p(1-p)\mu^2-0{\cdot}3333[p(1-p)^3-p^3(1-p)]\mu^3+$$
$$+\{0{\cdot}2945p(1-p)(1-6p+6p^2)+0{\cdot}9769p^2(1-p)^2\}\mu^4+0(\mu^5)]. \quad (74)$$

This definition is used in the work of PRIGOGINE *et al.*,[2] however, the expansion of $\langle\log|I+D|\rangle$ cannot be justified by the methods of this paper except when the masses and probabilities satisfy equation (36). For a CuAu alloy ($M_2=63$, $M_1=197$, $p=0{\cdot}50$) the term in brackets is equal to 1·13, the convergence being quite slow. The term in $\mu^2$ gives a contribution of 0·10 and the term in $\mu^4$ gives a contribution of 0·03.

Another convenient definition for $\bar{M}$ and $\Delta M$ is

$$\bar{M}=(\tfrac{1}{2})(M_1+M_2) \qquad \mu=(M_1-M_2)/(M_1+M_2)$$
$$\omega_L=2(\gamma/\bar{M})^{\frac{1}{2}} \qquad \beta_{2k}=1, \quad \beta_{2k+1}=2p-1. \quad (75)$$

of convergence about the same as in the last case. Notice that the actual expressions for the zero-point energy by the two methods will differ in general because of the two choices for $\omega_L$. However, $\omega_L$ is the same for the two definitions in the case of CuAu.

(b) *The two-dimensional case*

In this case we assume that the central and non-central force constants are different. For convenience we say that $\gamma_2=\theta^2\gamma_1$, where $\theta^2\leqslant 1$. The zero-point energy for a uniform lattice, that is, one with only one mass, can be derived from an integral representation first given by MONTROLL[13]

$$E_0=\frac{\hbar N^2}{\sqrt{2M}}\sum_{j=1}^{2}\gamma_j\int_0^\infty x^{-\frac{1}{2}}e^{-(\gamma_1+\gamma_2)x}\frac{I_0(x\gamma_1)I_0(x\gamma_2)}{I_0(x\gamma_j)}[I_0(x\gamma_j)-I_1(x\gamma_j)]\,dx. \quad (76)$$

The detailed form for $E_0$ can be shown to be[16]

$$\frac{E_0}{N^2}=\frac{\hbar\omega_L}{2\sqrt{2\theta}}\Big\{\sqrt{1+\theta^2}P_{-\frac{1}{2}}(\sqrt{1+\theta^2})P_{-\frac{1}{2}}(\sqrt{1+\theta^{-2}})-\frac{1}{2\sqrt{1+\theta^2}}P_{\frac{1}{2}}(\sqrt{1+\theta^2})P_{-\frac{1}{2}}^{-1}(\sqrt{1+\theta^{-2}})-$$
$$-\frac{\theta^2}{2\sqrt{1+\theta^2}}P_{\frac{1}{2}}(\sqrt{1+\theta^{-2}})P_{-\frac{1}{2}}^{-1}(\sqrt{1+\theta^2})\Big\} \quad (77)$$

The expansion of $\langle\log|I+D|\rangle$ is always convergent for this choice of parameters. For CuAu the term multiplying $(\hbar\omega_L)/\pi$ is 1·13, with the rate

where $P_\nu^\mu$ is the associated Legendre function. These, in turn, may be evaluated for numerical computations by using their representations in

terms of complete elliptic integrals of the first and second kind.[17] When $\theta$ is small, an expansion of $E_0/N^2$ is

$$\frac{E_0}{N^2}=\frac{\hbar\omega_{L_1}}{\pi}\left[1-\frac{\theta^2}{8}\ln\theta+\left(\frac{3}{16}+\frac{3}{8}\ln 2\right)\theta^2+0(\theta^4\ln\theta)\right]. \tag{78}$$

In two dimensions we are fortunate in having the $a_k$'s expressible in terms of complete elliptic integrals, as given in equations (57)–(59). The coefficients of the $\mu$'s in the expansion for the zero-point energy must be found by numerical integration. The results of performing these integrations, accurate to two places are

$$\theta^2=0{\cdot}16\colon\ E_0+\langle\Delta E_0\rangle=N^2\hbar\omega_L[0{\cdot}33-0{\cdot}14\beta_1\mu+0{\cdot}12\beta_2\mu^2+\ldots]$$
$$=E_0(\bar{M})[1-0{\cdot}42\beta_1\mu+\{0{\cdot}37\beta_2-0{\cdot}01\beta_1^2\}\mu^2+\ldots] \tag{79a}$$

$$\theta^2=0{\cdot}49\colon\ E_0+\langle\Delta E_0\rangle=N^2\hbar\omega_L\{0{\cdot}35-0{\cdot}15\beta_1\mu+0{\cdot}12\beta_2\mu^2+\ldots\}$$
$$=E_0(\bar{M})\{1-0{\cdot}43\beta_1\mu+0{\cdot}37\beta_2\mu^2+\ldots\}. \tag{79b}$$

Notice that the expansion does not seem to depend very much on $\theta^2$. If we choose $\bar{M}$ and $\Delta M$ so that $\beta_1=0$, then equation (79) becomes

$$\theta^2=0{\cdot}16\quad E_0+\langle\Delta E_0\rangle$$
$$=E_0(\bar{M})\{1+0{\cdot}73p(1-p)\mu^2+\ldots\} \tag{80a}$$

$$\theta^2=0{\cdot}49\quad E_0+\langle\Delta E_0\rangle$$
$$=E_0(\bar{M})\{1+0{\cdot}73p(1-p)\mu^2+\ldots\}. \tag{80b}$$

Both of these expansions are slightly different from the corresponding ones given by PRIGOGINE *et al.*[2] Their expressions would replace the factor 0·37 in equation (79) by 0·38. It is believed that this difference is due to his use of the Debye model in the calculations as opposed to our use of a more accurate frequency spectrum.

## 7. SPECIFIC HEAT

In this section we shall present the first few terms in the expansion of the specific heat in one dimension. The function $g(z)$ is, in this case, given by

$$g(z)=c_v(z)=k\frac{(\beta z)^2}{\sinh^2\beta z} \tag{81}$$

where $\beta=\hbar/2kT$ and $k$ is Boltzmann's constant. One can see from this equation that if the integral were taken down the imaginary axis as in previous sections, then the contour would have to be indented at each zero of $\sinh\beta z$. The resulting integrals are quite difficult to evaluate, hence we present another method which is of some interest in its own right.

For this purpose we let $\langle h(\omega)\rangle$ be the averaged distribution of frequencies, i.e. $\langle h(\omega)\rangle d\omega$ measures the average number of frequencies in $(\omega, \omega+d\omega)$ as $d\omega$ approaches zero. Notice that by our remarks of Section 8 there is a frequency $\omega_m$ such that $\langle h(\omega)\rangle\equiv 0$ for $\omega\geqslant\omega_m$. We define $\langle H(\alpha)\rangle$ as the Laplace transform or characteristic function of $\langle h(\omega)\rangle$, that is,

$$\langle H(\alpha)\rangle=\int_0^\infty\langle h(\omega)\rangle e^{-\alpha\omega}d\omega=\int_0^{\omega_m}\langle h(\omega)\rangle e^{-\alpha\omega}\,d\omega. \tag{82}$$

Since $\omega_m$ is finite the moments, $\overline{\omega^n}$, defined by

$$\overline{\omega^n}=\int_0^{\omega_m}\omega^n\langle h(\omega)\rangle\,d\omega \tag{83}$$

exist for all values of $n$. This implies that $\langle H(\alpha)\rangle$ can be expanded in a Taylor's series,

$$\langle H(\alpha)\rangle=1-\alpha\bar{\omega}+\frac{\alpha^2}{2!}\overline{\omega^2}-\ldots. \tag{84}$$

If we invert this series we find that $\langle h(\omega)\rangle$ can formally be expressed as

$$\langle h(\omega)\rangle = \sum_{n=0}^{\infty} (-1)^n \frac{\overline{\omega^n}}{n!} \frac{d^n\delta(\omega)}{d\omega^n}. \tag{85}$$

In this way we replace every term of the form $\alpha^k$ in the expression for $\langle H(\alpha)\rangle$ by the operator $(-1)^k d^k\delta(\omega)/d\omega^k$ in any integral over $\omega$. For any power $\omega^k$ we have

$$\int_0^{\omega_m} \omega^k \frac{d^n\delta(\omega)}{d\omega^n} d\omega = \begin{matrix} (-1)^n\, 1 & n=k \\ 0 \quad \frac{1}{2}(n!) & n\neq k. \end{matrix} \tag{86}$$

For any polynomial $f(\omega) = \sum_{j=0}^{n} f_j\omega^j$ we therefore have

$$\int_{0+}^{\omega_m} \left(\sum_{j=0}^{n} f_j\omega^j\right) \sum_{n=0}^{\infty} (-1)^n \frac{\overline{\omega^n}}{n!} \frac{d^n\delta(\omega)}{d\omega^n} d\omega$$

$$= \frac{1}{2}\sum_{j=0}^{n} f_j\overline{\omega^j}. \tag{87}$$

Hence by WEIERSTRASS's theorem[10] the representation of $\alpha^n$ by a delta function operator is permissible for all continuous functions in $(0, \omega_m)$. In a similar manner we can show that a term of the form $\alpha^n e^{-\alpha\omega_L}$ corresponds to the operator $(-1)^n d^n \delta(\omega-\omega_L)/d\omega^n$.

In one dimension an expression for $\langle H(\alpha)\rangle$ can be found which contains all terms up to and including those of order $\mu^2$. We now consider $\langle \Delta H(\alpha)\rangle$ that is, the change in characteristic function due to disordering. As before we may integrate down the imaginary axis so that $\langle \Delta H(\alpha)\rangle$ is

$$\langle \Delta H(\alpha)\rangle = -\frac{1}{\pi i}\int_0^{\infty} e^{-i\alpha\omega} d\langle \ln|\Delta(i\omega)|\rangle. \tag{88}$$

When the specific functions for $d/d\omega\langle \ln|\Delta(i\omega)|\rangle$ are substituted into equation (88) and are evaluated there results,

$$\begin{aligned}\langle \Delta H(\alpha)\rangle = {} & \frac{\beta_1\omega_L\mu\alpha}{2}[\boldsymbol{L}_{-1}(\alpha\omega_L) - I_1(\alpha\omega_L)] + (\tfrac{1}{4})(\beta_1^2-\beta_2)\mu^2\omega_L\alpha e^{-\alpha\omega_L} + \\ & + \left(\frac{1}{3\pi}\right)\beta_1\mu^2\omega_L\alpha - \frac{\beta_1^2\mu^2\omega_L\alpha}{6}[\boldsymbol{L}_{-1}(\alpha\omega_L) - I_1(\alpha\omega_L)] - \\ & - \frac{\beta_1^2\mu^2\omega_L{}^2\alpha^2}{6}[I_0(\alpha\omega_L) - \boldsymbol{L}_0(\omega\alpha_L)] - \frac{\beta_1^2\mu^2\omega_L{}^2\alpha^2}{24}[I_2(\alpha\omega_L) - \boldsymbol{L}_{-2}(\alpha\omega_L)] + 0(\mu^3)\end{aligned} \tag{89}$$

where $L_\nu$ is Struve's function of order $\nu$ and $I_\nu$ is a Bessel function of imaginary argument.

We may derive an operator which corresponds to terms of the form

$$\alpha^n[I_n(\alpha\omega_L) - \boldsymbol{L}_{-n}(\alpha\omega_L)]$$

appearing in the expansion of the characteristic function. To this end we employ the identity[18]

$$I_n(y) - \boldsymbol{L}_{-n}(y) = \sqrt{\frac{2y}{\pi}}\{\Gamma(n-\tfrac{1}{2})\Gamma(n+\tfrac{1}{2})\}^{-1} \int_0^{\pi/2} \cos^{n+\frac{1}{2}}\theta K_{n-\frac{1}{2}}(y\cos\theta)\, d\theta$$

$$= \{\Gamma(n-\tfrac{1}{2})\Gamma(n+\tfrac{1}{2})\}^{-1} \sum_{r=0}^{n-1} \frac{(n-1+r)!}{r!(n-1-r)!2^r y^r} \int_0^{\pi/2} \cos^{n-r}\theta e^{-y\cos\theta}\, d\theta, \tag{90}$$

VOL 7 195

where the second line is valid for integral $n$ and $K_n(x)$ is a modified Bessel function of the second kind. We have seen that a term $\alpha^n e^{-\alpha r}$ in the expansion of the characteristic function corresponds to an operator

$$(-1)^n \frac{d^n \delta(\omega - r)}{d\omega^n}.$$

This fact suggests that

$$\alpha^m [I_m(\alpha\omega_L) - \boldsymbol{L}_{-n}(\alpha\omega_L)]$$

should be replaced by the operator

$$\{\Gamma(n-\tfrac{1}{2})\Gamma(n+\tfrac{1}{2})\}^{-1} \sum_{r=0}^{n-1} \frac{(n-1+r)!}{r!(n-1-r)!2^r\omega_L{}^r} \times$$

$$\times \int_0^{\pi/2} \cos^{n-r}\theta \frac{d^{n-r}\delta(\omega - \omega_L\cos\theta)}{d\omega^{n-r}} d\theta \quad (91)$$

in any integral over $f(\omega)$. It is easily verified that this operator is correct for all polynomial $f(\omega)$, and therefore for all continuous $f(\omega)$.

With this result we may write, in the one-dimensional case

$$\langle g(\omega)\rangle = \frac{\beta_1\omega_L\mu}{\pi}\left(1 - \frac{\mu}{3}\right)\int_0^{\pi/2} g'(\omega_L\cos\theta)\cos\theta\, d\theta + \tfrac{1}{4}(\beta_2 - \beta_1{}^2)\mu^2\omega_L g'(\omega_L) -$$

$$- \frac{\beta_1\mu^2\omega_L}{3\pi} g'(0) - \frac{1}{3\pi}\beta_1{}^2\mu^2\omega_L{}^2 \int_0^{\pi/2} g''(\omega_L\cos\theta)\, d\theta - \quad (92)$$

$$- \frac{1}{9\pi}\beta_1{}^2\mu^2\omega_L{}^2 \int_0^{\pi/2} \left[g''(\omega_L\cos\theta)\cos^2\theta - g'(\omega_L\cos\theta)\frac{\cos\theta}{\omega_L}\right] d\theta + \ldots.$$

In the particular case where the definition of equation (73) is valid, the integrals all drop out and we are simply left with

$$\langle g(\omega)\rangle = \frac{\beta_2\mu^2\omega_L}{4} g'(\omega_L). \quad (93)$$

Using this definition, we find for the specific heat

$$\langle \Delta c_v \rangle = \tfrac{1}{2}p(1-p)\mu^2\omega_L k\beta^2\left(\frac{\omega_L}{\sinh^2\beta\omega_L} - \right.$$

$$\left. - \beta\omega_L{}^2 \frac{\cosh\beta\omega_L}{\sinh^3\beta\omega_L}\right) + 0(\mu^3). \quad (94)$$

In the limit $T \to 0$, $\beta \to \infty$ we find

$$\langle \Delta c_v \rangle = -2p(1-p)k\mu^2\beta^3\omega_L{}^3 e^{-2\beta\omega_L} + 0(\mu^3) \quad (95)$$

and in the limit $T \to \infty$ we find

$$\langle \Delta c_v \rangle = -\frac{p(1-p)\hbar^2\mu^2}{24kT^2} + 0(\mu^3). \quad (96)$$

Using this same set of definitions, we find for the $\mu^2$ correction to the Helmholtz free energy for which $g(z) = kT \ln(2\sinh(\hbar z/2kT))$,

$$\langle \Delta F \rangle = \tfrac{1}{8}p(1-p)\hbar\omega_L\mu^2 ctnh\left(\frac{\hbar\omega_L}{2kT}\right) + 0(\mu^3). \quad (97)$$

In general the integrals which appear in equation (92) cannot be evaluated in closed form. If $g(\omega)$ is taken to be the specific heat, we could not evaluate the low-temperature corrections. At high temperatures we may use the approximation

$$c_v(z) \sim k\left(1 - \frac{\beta^2 z^2}{3}\right). \quad (98)$$

The integrals of equation (92) can all be evaluated

leading to the result

$$\langle \Delta c_v \rangle \sim \frac{k\beta^2\omega_L{}^2\mu}{3}\left[\frac{\beta_1}{2}\left(\frac{\mu}{3}-1\right)-\right.$$

$$\left.-\frac{\beta_2\mu}{2}+\frac{5}{6}\beta_1{}^2\mu\right]+0(\mu^3). \qquad (99)$$

## 8. BOUNDS ON THE MAXIMUM FREQUENCY OF A DISORDERED LATTICE

It is of some interest to notice that the frequency spectrum of the disordered lattice considered in this paper is unequal to zero over a finite range only. To see this point consider a lattice made up only of light atoms of mass $M_2$. We call this our base lattice. Then any lattice containing atoms of masses $M_1$ and $M_2$ with $M_1 > M_2$ can be thought of as being constructed from the base lattice by the addition of masses $(M_1-M_2)$ at the proper lattice sites. According to a theorem of RAYLEIGH,[19] the addition of mass to a vibrating system can only decrease the normal mode frequencies associated with the system; hence an upper bound for the frequencies will be the maximum frequency appearing in the spectrum of the base lattice. If we consider a lattice with only the masses chosen at random, then the maximum frequency will be equal to that of a lattice containing only light atoms with probability $p^N$ (where $p$ is the probability that a light atom occupies a given site). Hence the frequency spectrum is non-zero in a finite region whose upper bound is the maximum frequency of a lattice with light atoms only. Similarly, the frequency spectrum would be unequal to zero over a finite range if spring constants were changed as well by the addition of impurities. If both masses and spring constants are randomly distributed over the lattice, then the maximum frequency of the lattice may coincide with the maximum frequency of a base lattice consisting of light atoms and stiff springs. However, if we were to assign masses at random but specify that the force constants of the springs coupling masses $M_1$ to $M_1$ and those coupling $M_2$ to $M_2$ differed from those coupling $M_1$ to $M_2$, then we could locate exactly the maximum possible frequency only if we knew that the largest force constants were associated with the coupling between the lightest masses.

In any event the procedure of the last paragraph provides us with upper and lower bounds for the averaged maximum frequency of any lattice. A lower bound for this frequency is the maximum frequency of a base lattice consisting of heavy atoms coupled by stiff springs. If we now consider a lattice consisting of a fixed proportion of atoms of one type, then we may improve the bounds for the averaged maximum frequency by using some results of MONTROLL and POTTS.[14] For example, let us suppose that we have a linear chain with two types of masses such that there is a non-zero fixed concentration of light atoms in heavy atoms. Then an upper bound for the maximum frequency is the maximum frequency of a base lattice containing the

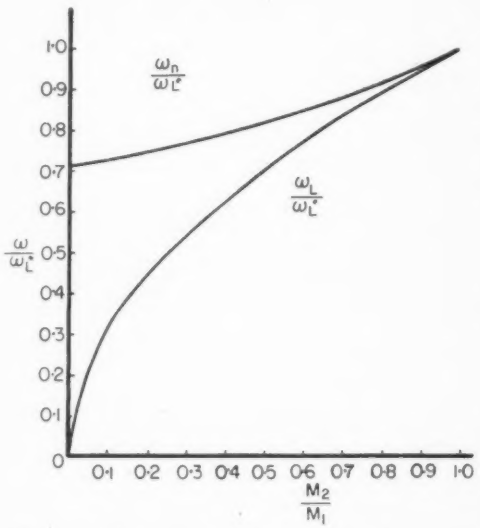


FIG. 3. Lower bounds of the maximum frequency.

light atoms only. A lower bound is the maximum frequency of a base lattice containing heavy atoms only. An improved lower bound is the maximum frequency of a base lattice containing heavy atoms with one light atom as a defect. It is shown by MONTROLL and POTTS that the maximum frequency of such a lattice is given by

$$\frac{\omega_n}{\omega_L{}^*}=\left(2-\frac{M_2}{M_1}\right)^{-1} \qquad M_1>M_2>0 \quad (100)$$

where $\omega_L{}^*$ is the maximum frequency of the base lattice consisting of light atoms only. The ratio of

the maximum frequency to $\omega_L^*$ of the base lattice consisting of heavy atoms is given by

$$\frac{\omega_L}{\omega_L^*} \quad \left(\frac{M_2}{M_1}\right)^{\frac{1}{2}}. \tag{101}$$

It is seen from Fig. 3 that for $M_2/M_1$ small the lower bound provided by the lattice with a defect is a substantial improvement over that provided by the lattice of heavy atoms. A similar analysis can be made for changes in force constants, using the results of MONTROLL and POTTS. This analysis will not be given here.

In the one case for which he could obtain an explicit solution, DYSON[1] found a frequency spectrum which was non-zero over an infinite range. However, this was due to the fact that neither the masses nor the spring constants were limited to any finite range. The approximate spectrum found by SCHMIDT[5] is also non-zero over an infinite range, but this is probably due to his method of solution rather than to his model.

## 9. THE LOW-FREQUENCY END OF THE FREQUENCY SPECTRUM

It is well known that any additive function of the normal mode frequencies can be expressed as an average over the frequency-distribution function, $g(\omega)$. As we have seen in Section 7, the calculation of this frequency-distribution function is an extremely difficult task, and it has been by-passed by methods which give the additive function of interest directly without the necessity of knowing $g(\omega)$. However, for discussing the low-temperature thermodynamic properties of crystals, it is very convenient to know the form for the low-frequency end of the frequency-distribution function, since it is just this portion of the spectrum on which these properties depend.

For example, if the frequency spectrum, $g(\omega)$, has a Taylor expansion about $\omega = 0$ of the form

$$g(\omega) = a_0 + a_2\omega^2 + a_4\omega^4 + \dots \tag{102}$$

the Helmholtz free energy of the crystal has the following low-temperature expansion

$$A = E_0 - NkT \sum_{m=0}^{\infty} a_{2m} \frac{(2m)!}{(2m+2)!} B_{m+1} \left(\frac{2kT}{\hbar}\right)^{2m+1} \tag{103}$$

where $B_n$ is the $n$th Bernoulli number, $N$ is the total number of degrees of freedom in the lattice, and $E_0$ is the zero-point energy of the lattice.

In this section we present a method for obtaining the coefficients $a_{2m}$ which is valid both for ordered as well as for disordered lattices.

The small $\omega$ behavior of the frequency spectrum can be given in terms of $\Omega(\omega) = N^{-n}(d/d\omega) \ln |\Delta(i\omega)|$. We consider the function $|\Delta(i\omega)|$ where $\Delta(\omega)$ is the matrix $I + M_0^{-1}(\omega)\delta M(\omega)$ discussed in Section 2. This function can be written

$$|M_0(i\omega)||\Delta(i\omega)| = \prod_j (\omega^2 + \omega_j^2) \tag{104}$$

or equivalently,

$$\ln|M_0(i\omega)| + \ln|\Delta(i\omega)| = \sum_j \ln(\omega^2 + \omega_j^2)$$

$$= N^n \int_0^{\nu_L} \ln(\omega^2 + \nu^2) g(\nu)\, d\nu. \tag{105}$$

Differentiating this formula, we find

$$\Omega_0(\omega) + \Omega(\omega) = \int_0^{\nu_L} \frac{2\omega}{\omega^2 + \nu^2} g(\nu)\, d\nu$$

$$= \int_0^{\nu_L} \left\{\frac{1}{\omega - i\nu} + \frac{1}{\omega + i\nu}\right\} g(\nu)\, d\nu. \tag{106}$$

Let us assume that there exists some region around $\nu = 0$ in which $g(\nu)$ can be expanded in a Taylor's series

$$g(\nu) = \sum_{m=0}^{\infty} \frac{g^{(2m)}(0+)}{(2m)!} \nu^{2m}. \tag{107}$$

We know that $g(\nu) = g(-\nu)$ and that $g(\nu)$ is non-zero over a finite range only. This implies that $g(\nu)$ can be represented by a Fourier cosine series, which in turn implies a Taylor series containing only even powers of $\nu$ valid for $\nu > 0$ (notice that $g(\nu) = |\nu|$ is even in $\nu$, so that in any bounded region $(-\nu_L, \nu_L)$ it can be approximated by a power series containing even powers only).

Because of the identity

$$\frac{\partial^{2m}}{\partial\omega^{2m}}\left\{\frac{2\omega}{\omega^2+\nu^2}\right\}=\frac{\partial^{2m}}{\partial\omega^{2m}}\left\{\frac{1}{\omega-i\nu}+\frac{1}{\omega+i\nu}\right\}$$

$$=\frac{(2m)!}{(\omega-i\nu)^{2m+1}}+\frac{(2m)!}{(\omega+i\nu)^{2m+1}} \quad (108)$$

$$=(-1)^m\frac{\partial^{2m}}{\partial\nu^{2m}}\left\{\frac{2\omega}{\omega^2+\nu^2}\right\}$$

we may write

$$\Omega_0^{(2m)}(\omega)+\Omega^{(2m)}(\omega)$$

$$=(-1)^m\int_0^{\nu_L}\frac{\partial^{2m}}{\partial\nu^{2m}}\left\{\frac{2\omega}{\omega^2+\nu^2}\right\}g(\nu)\,d\nu. \quad (109)$$

Successive integration by parts yields

$$\Omega_0^{(2m)}(\omega)+\Omega^{(2m)}(\omega)$$

$$=(-1)^m\left\{\left[\frac{(2m-1)!}{i(\omega-i\nu)^{2m}}-\frac{(2m-1)!}{i(\omega+i\nu)^{2m}}\right]g(\nu)\Big|_0^{\nu_L}-\right.$$

$$\left.-\ldots+\int_0^{\nu_L}\frac{2\omega}{\omega^2+\nu^2}g^{(2m)}(\nu)\,d\nu\right\}. \quad (110)$$

The Dirac delta function can be represented in the form

$$\delta(\nu)=\lim_{\omega\to 0+}\frac{1}{\pi}\frac{\omega}{\omega^2+\nu^2}$$

hence we find from equation (110)

$$\Delta g^{(2m)}(0+)=\frac{(-1)^m}{\pi}\Omega^{(2m)}(0+). \quad (111)$$

Notice that if $\Omega(\omega)$ is a function only of $\omega^2$ in a neighborhood of $\omega=0$, the function $g(\omega)$ can be found in terms of $\Omega(\omega)$ near the origin simply by replacing $\omega$ by $i\omega$. Hence we may use equations (47), (54), and (70) to determine the form of the small $\omega$ part of the one-dimensional frequency spectrum of the disordered chain. Unfortunately it does not seem possible to say more about the radius of convergence of this representation.

*Acknowledgement*—We would like to thank Professor E. W. MONTROLL for helpful discussions during the course of this work.

## REFERENCES

1. DYSON F. J., *Phys. Rev.* **92,** 1331 (1953).
2. PRIGOGINE I., BINGEN R. and JEENER J., *Physica* **20,** 383, 516 (1954).
3. PARMENTER R. H., *Phys. Rev.* **104,** 22 (1956).
4. LIFSHITZ I. M. and STEPANOVA G. I., *Zh. eksp. teor. phys. SSSR* **3,** 656 (1956).
5. SCHMIDT H., *Phys. Rev.* **425** (1957).
6. KERNER E. H., *Proc. Phys. Soc.* A**69,** 234 (1956).
7. HORI J. and ASAHI T., *Progr. teor. phys.* **17,** 523 (1957).
8. HORI J., *Progr. teor. phys.* **18,** 367 (1957).
9. MARADUDIN A. A., MAZUR P., MONTROLL E. W. and WEISS G. H., *Rev. Mod. Phys.* **30,** 175 (1958).
10. TITCHMARSH E. C., *The Theory of Functions.* Oxford University Press (1939).
11. WENTZEL G., *Helv. Phys. Acta* **15,** 111 (1942).
12. ROSENSTOCK H. B. and NEWELL G. F., *J. Chem. Phys.* **21,** 1607 (1953).
13. MONTROLL E. W., *Proc. Third Berkeley Symp. on Math. Stat. and Prob.* Vol. 3, p. 209 (1956).
14. MONTROLL E. W. and POTTS R. B., *Phys. Rev.* **100,** 525 (1955); **102,** 72 (1956).
15. GERSCHGORIN S., *Izv. Akad. Nauk SSSR* 749 (1931).
16. ERDELYI A., *Tables of Integral Transforms.* McGraw-Hill Book Co., New York (1954).
17. ERDELYI A., *HigherT ranscendental Functions.* McGraw-Hill Book Co., New York (1954).
18. WEISS G. H., Ph.D. Dissertation, University of Maryland (1958).
19. RAYLEIGH (Lord), *The Theory of Sound,* Second edition. Reprinted by Dover Publications, New York (1945).

VOL 7 195

*J. Phys. Chem. Solids* Pergamon Press 1958. Vol. 7. pp. 345–350.

# SUR LA RELAXATION NUCLEAIRE DANS LES CRISTAUX IONIQUES

**P-G DE GENNES**

Centre d'Etudes Nucléaires de Saclay Gif-sur-Yvette (S & O)

(*Received* 6 *June* 1958)

**Résumé**—On montre que dans les cristaux ioniques où la relaxation nucléaire est contrôlée par des impuretés paramagnétiques, la composante de l'aimantation nucléaire *globale* parallèle au champ statique obéit a une équation simple de relaxation. L'inverse du temps de relaxation est proportionnel a :

(a) la concentration en impureté
(b) le coefficient de diffusion de spin
(c) une certaine «longueur de relaxation», $a$, dont la valeur exacte dépend du comportement des spins nucléaires au voisinage immédiat des impuretés paramagnétiques. La relaxation est modifiée si les impuretés forment des amas ou se groupent sur des dislocations.

**Abstract**—It is shown that in ionic crystals where nuclear relaxation is due to paramagnetic impurities, the part of the *total* nuclear magnetisation which is parallel to the static field obeys a simple relaxation equation. The inverse relaxation time is proportional to :

(a) the impurity concentration
(b) the spin diffusion coefficient
(c) a «relaxation length», $a$, whose exact value depends on the behavior of the nuclear spins in the near vicinity of the paramagnetic impurities. The relaxation rates are modified if the impurities are grouped in clusters or on dislocation lines.

## 1. INTRODUCTION

La relaxation nucléaire spin-réseau dans les cristaux ioniques est conrôlée par la présence d'impuretés paramagnétiques fortement couplées au réseau.[1] Le champ magnétique fluctuant dû à ces impuretés induit des transitions nucléaires dans leur voisinage immédiat. La portée de cet effet est augmentée par la possibilité d'un échange des orientations de deux spins nucléaires voisins («diffusion» de l'aimantation nucléaire). Le but du présent travail n'est pas d'améliorer ce modèle physique. (En particulier, nous ne pensons pas que le calcul, pourtant assez rustique, du coefficient de diffusion, mérite d'être repris dans l'état actuel de l'expérimentation).

Nous nous proposons de montrerici que l'étude expérimentale de la relaxation spin-réseau fournit des informations quantitatives sur la *concentration* et la *répartition* des impuretés paramagnétiques. De ce point de vue, on doit distinguer dès le départ deux situations fondamentalement distinctes :

(a) Impuretés distribuées de façon homogène, avec une (faible) concentration $N$ (sec. II, III, IV). Le fait physique fondamental est le suivant : chaque spin nucléaire subit l'effet (indirect) d'un grand nombre d'impuretés, même si ces impuretés sont très diluées. Dans ces conditions, en régime stationnaire, l'aimantation nucléaire prend une valeur uniforme (qui dépend seulement de l'intensité du champ de radiofréquence) dans la majeure partie du cristal. En régime transitoire, l'aimantation nucléaire s'égalise rapidement, et relaxe ensuite de façon *exponentielle*; seule la première phase est sensible au détail des conditions initiales. Pour des impuretés diluées, la deuxième phase est beaucoup plus longue que la première, et c'est elle qui est observée en pratique.

(b) Impuretés groupées en amas, ou sur des dislocations, etc. (section V). Ici, l'ordre de grandeur

des constantes de temps peut être fortement modifié : on a donc là un moyen d'étude des groupements d'impuretés paramagnétiques, même si elles sont très diluées.

Le point de départ de notre calcul sera l'équation de transport de l'aimantation, qui s'écrit sous sa forme la plus simple :

$$\frac{\partial p}{\partial t} = D\nabla^2 p - C(p-p_0)[\sum_n |\boldsymbol{R}-\boldsymbol{R}_n|^{-6}] - 2Ap \quad (1)$$

$p(\boldsymbol{R}, t)$ est l'aimantation d'un spin nucléaire situé au point $R$, $p_0$ sa valeur à l'équilibre thermique, $D$ le coefficient de diffusion. $C(\boldsymbol{R}-\boldsymbol{R}_n)^{-6}$ est la probabilité d'une transition induite par la $n^{\text{ème}}$ impureté. Enfin $2A$ est la probabilité de transition due à la présence du champ de radiofréquence. On trouvera une estimation de $C$ et de $D$ dans l'article de BLOEMBERGEN.[1] L'équation (1) néglige l'anisotropie de la diffusion pour des interactions dipolaires, la dépendence angulaire de $C$, etc... Nous préférons cependant centrer notre exposé sur ce modèle simple et montrer ensuite que les conclusions essentielles sont, en fait, plus générales.

## 2. MÉTHODE DU PSEUDOPOTENTIEL

Pour débrouiller l'équation (1), envisageons d'abord le cas *d'une seule* impureté paramagnétique, l'intensité du champ $RF$ étant presque nulle. La distribution stationnaire des spins nucléaires est régie par

$$D\nabla^2 p + CR^{-6}(p_0-p) = 0 \quad (2)$$

Pour $R = 0$ on doit avoir $p = p_0$, car les spins nucléaires immédiatement voisins de l'impureté sont toujours en équilibre thermique. La solution de (2) qui est nulle à l'infini a la forme asymptotique

$$p = p_0 \frac{a}{R} \quad (R \gg a) \quad (3)$$

La longueur $a$ doit être déterminée par la solution exacte de (2) qui se raccorde à (3) aux grandes distances, et qui est égale à $p_0$ à l'origine. On trouve[2]

$$a = 0{\cdot}68\left(\frac{C}{D}\right)^{\frac{1}{3}} \quad (4)$$

$a$ mesure la portée de la relaxation en régime stationnaire. Dans les expériences de Bloembergen, on prévoit d'après (4) une portée de quelques Å. Il est essentiel de noter que $a$ est très inférieur aux autres longueurs caractéristiques qui interviennent dans notre problème, à savoir :

1° la distance moyenne entre impuretés (d'ordre $N^{-\frac{1}{3}}$, où $N$ est le nombre d'impuretés par cm$^3$).

2° la longueur de diffusion de l'aimantation entre deux transitions induites par la radiofréquence. Cette longueur est de l'ordre de

$$k_0^{-1} = \left[\frac{D}{2A}\right]^{\frac{1}{2}} \quad (5)$$

On verra plus loin que $k_0 a \ll 1$ même pour des valeurs de $A$ qui correspondent à la saturation.

L'équation (1) décrit donc un régime de diffusion libre, sauf dans de très petites régions violemment perturbées au voisinage de chaque impureté. Comme on s'intéresse uniquement à l'aimantation nucléaire globale, qui fait surtout intervenir des spins éloignés des impuretés, on est en droit de remplacer (1) par une équation plus simple, qui restitue les mêmes propriétés asymptotiques pour les points éloignés des impuretés :

$$\frac{\partial p}{\partial t} = D\nabla^2 p - 2Ap \quad (6)$$

à l'extérieur d'une sphère de rayon $a$ entourant chaque impureté

$$p = p_0 \quad (7)$$

à l'intérieur de chaque sphère

On vérifiera aisément que (6) et (7) conduisent bien à la solution (3) pour le cas d'une impureté isolée.

La méthode que nous employons ici à propos d'une équation de diffusion est inspirée de techniques analogues pour la résolution d'une équation de Schrödinger d'où le nom de pseudopotentiel que nous avons choisi pour la décrire. Elle est correcte lorsque l'on s'intéresse à des temps $t \gg a^2/D$ et à des distances très supérieures à $a$.

## 3. ETUDE DE LA SATURATION

La distribution stationnaire de l'aimantation nucléaire, $p_s(R)$, en présence d'un fort champ de

radiofréquence (caractérisé par la quantité $2A$) s'obtient en faisant $\partial p/\partial t = 0$ dans (6).

Il est possible de construire explicitement la solution pour $k_0 a \ll 1$, en posant

$$p_s(\boldsymbol{R}) = p_0 \xi \sum_n g(\boldsymbol{R} - \boldsymbol{R}_n) \tag{8}$$

$$g(R) = \begin{cases} \dfrac{a}{R} e^{-k_0 R} & R > a \\ e^{-k_0 a} & R < a \end{cases} \tag{9}$$

$g(R)$ satisfait à l'équation de diffusion dans la région extérieure ($k_0$ étant défini par (5)). $\gamma$ est un facteur de normalisation dont on détermine la valeur en écrivant la condition (7) pour chaque site d'impureté.

$$p_0 \xi e^{-k_0 a} + p_0 \xi N \int d_3 R g(R) = p_0 \tag{10}$$

Le premier terme de (10) représente la contribution à la somme (8) de l'impureté pour laquelle on écrit la condition aux limites. Le deuxième terme est la contribution *moyenne* des autres impuretés.

(On peut vérifier par un calcul direct que l'écart quadratique réduit, qui mesure la dispersion par rapport à cette valeur moyenne, est $1/2k_0 a$, donc négligeable dans notre approximation). Finalement on déduit de (10) la valeur du coefficient $\xi$

$$\xi = \frac{2A}{2A + 4\pi NaD} \tag{11}$$

et le pourcentage de l'aimantation nucléaire globale qui subsiste en présence du champ de radiofréquence

$$\frac{\int p_s(\boldsymbol{R}) d_3 R}{p_0 \int d_3 R} = \frac{4\pi NaD}{2A + 4\pi NaD} \tag{12}$$

La quantité mesurée par Bloembergen, dans ses expériences, était l'intensité du champ de RF nécessaire pour diviser par 2 l'aimantation nucléaire globale. Il correspond à cette intensité une certaine valeur $A_{\frac{1}{2}}$ de $A$, que l'on déduit de (12) (déjà obtenu par un argument simplifié par KHOUTSICHVILI[2])

$$2A_{\frac{1}{2}} = 4\pi NaD \tag{13}$$

Avant de discuter ce résultat, il convient de vérifier que notre hypothèse de base $k_0 a \ll 1$ est correcte, même lorsque $A$ est de l'ordre de $A_{\frac{1}{2}}$. On déduit effectivement de (13) et (5) que dans ces conditions $k_0 a \sim (Na^3)^{\frac{1}{2}}$, donc très inférieur à 1.

Nous pouvons aussi vérifier une remarque faite dans l'introduction : le nombre d'impuretés qui ont un effet sensible sur un spin nucléaire est de l'ordre de $Nk_0^{-3} \sim (Na^3)^{-\frac{1}{2}}$ donc très supérieur à 1.

(13) montre que la quantité $(4\pi NaD)^{-1}$ joue le rôle d'un temps de relaxation spin réseau pour l'aimantation nucléaire globale, en régime stationnaire. Pour les concentrations d'impuretés $N$ étudiées par Bloembergen, $(4\pi NaD)^{-1}$ varie approximativement entre $\frac{1}{10}$ et 100 sec.

## 4. RÉGIMES TRANSITOIRES

L'ordre de grandeur des constantes de temps que nous venons d'étudier rend possible, entre autres, l'expérience suivante : le spécimen, en équilibre à la température $T$ en l'absence de tout champ, est amené rapidement dans le champ statique. L'aimantation nucléaire atteint aussitôt sa valeur d'équilibre pour les spins qui sont très voisins des impuretés paramagnétiques. Puis par diffusion, les autres spins nucléaires tendent à s'orienter pour atteindre finalement la distribution d'équilibre donnée par (8) et (9). On suit le phénomène en appliquant un champ RF assez faible pour ne pas perturber la distribution. Le signal de résonance est proportionnel à l'aimantation nucléaire globale.

Son évolution peut être analysée de la façon suivante : posons

$$p(\boldsymbol{R}, t) = p_s(\boldsymbol{R}) + \sum_k d_k \theta_k(\boldsymbol{R}) e^{-\mu_k t} \tag{19}$$

Les fonctions $\theta_k(\boldsymbol{R})$ sont les solutions de

$$(\mu_k - 2A)\theta_k(\boldsymbol{R}) + D \nabla^2 \theta_k(\boldsymbol{R}) - \\ - C\theta_k(\boldsymbol{R}) \sum_n |\boldsymbol{R} - \boldsymbol{R}_n|^{-6} = 0 \tag{20}$$

Cette équation a même forme que l'équation de Schrödinger d'une particule se déplaçant dans une assemblée de diffuseurs répartis au hasard, chaque diffuseur créant un potentiel (répulsif) proportionnel à $1/R^6$.

Nous connaissons un tel cas de propagation en présence de perturbations très localisées : il s'agit des neutrons thermiques, dans un milieu matériel

rigide. Leur propagation peut être décrite au moyen d'un indice de réfraction. La méthode que nous allons développer ici est une méthode «optique», inspirée de cette analogie.

Si les termes «potentiels» étaient absents, les fonctions propres de (20) seraient des ondes planes

$$\theta_k(\boldsymbol{R}) = e^{i\boldsymbol{k}\cdot\boldsymbol{R}} \tag{21}$$

avec

$$k = k_1(\mu_k)$$

$$k_1^2(\mu) \equiv \frac{\mu - 2A}{D} \tag{22}$$

En présence des termes en $CR^{-6}$, les fonctions propres ont encore une certaine analogie avec des ondes planes, mais la relation entre la valeur propre $\mu_k$ et le vecteur d'onde $k$ est modifiée.

Nous obtiendrons cette relation de la façon suivante : construisons d'abord les fonctions propres $\theta_k(\boldsymbol{R})$ définies par (20) en substituant à cette équation la forme approchée dérivée de (6) et (7).

$$D\nabla^2\theta_k - (2A - \mu_k)\theta_k = 0 \tag{23}$$

à l'extérieur d'une sphère de rayon $a$ autour de chaque impureté

$$\theta_k(\boldsymbol{R}) = 0$$

à l'intérieur

Nous essayons la solution :

$$\theta_k(\boldsymbol{R}) = \sum_n \gamma_k(\boldsymbol{R} - \boldsymbol{R}_n) e^{i\boldsymbol{k}\cdot\boldsymbol{R}_n} \tag{24}$$

$$\gamma_k(R) = \begin{cases} \dfrac{a}{R}\cos(k_1 R) & R > a \\ \cos(k_1 a) & R < a \end{cases} \tag{25}$$

$k_1$ est défini en fonction de $\mu_k$ par (22) et ceci assure que (23) est satisfaite dans les régions extérieures. Dans les régions intérieures, la nullité de $\theta_k(R)$ impose par un raisonnement analogue à celui de l'équation (10), et avec les mêmes limitations :

$$\cos(k_1 a) + N\int d_3 R \frac{a}{R}\cos(k_1 R) e^{i\boldsymbol{k}\cdot\boldsymbol{R}} = 0 \tag{26}$$

Pour $k_1 a \ll 1$, (26) peut être récrite

$$1 + \frac{4\pi N a}{k^2 - k_1^2} = 0 \tag{27}$$

C'est la relation classique entre l'indice de réfraction $n$ et la longueur de diffusion rencontrée notamment en physique du neutron

$$n^2 \equiv \frac{k^2}{k_1^2} = 1 - \frac{4\pi N a}{k_1^2} \tag{28}$$

La présentation usuelle de (28), par exemple dans le livre de FERMI,[3] revient à calculer le déphasage produit par une lame à faces parallèles. Ici, nous avons préféré construire explicitement la forme approchée de $\theta_k(\boldsymbol{R})$, qui servira dans la suite.

Finalement (27) permet d'écrire le spectre des valeurs propres de (23) sous la forme

$$\mu_k = 4\pi N a D + 2A + Dk^2 \tag{29}$$

Cette équation étant correcte à part des termes d'ordre $Nk^2$ ou d'ordre supérieur en $N$.

Nous allons maintenant appliquer ces résultats à l'étude d'un régime transitoire. Envisageons plus particulièrement le cas cité plus haut, où la radiofréquence a un effet négligeable ($2A = 0$), et où, au temps 0, l'aimantation nucléaire est nulle sauf au voisinage des impuretés.

$$p(\boldsymbol{R}, t = 0) = p_0$$

à l'intérieur d'une sphère de rayon $a$ autour de chaque impureté,

$$p(\boldsymbol{R}, t = 0) = 0 \tag{30}$$

à l'extérieur

Le choix de $a$ comme «rayon initial» est arbitraire mais simplifie le calcul sans en modifier les conclusions. La solution est en effet pour ce cas

$$p(\boldsymbol{R}t) = p_0[1 + \theta_0(\boldsymbol{R})e^{-\mu_0 t}] \tag{31}$$

En effet, cette fonction

1° satisfait à l'équation de diffusion simplifiée (6)

2° se réduit à la valeur stationnaire $p_0$ aux temps élevés

3° vérifie la condition (30) au temps 0. Pour vérifier ce dernier point, il suffit de calculer la valeur moyenne de $\theta_0(R) =$ dans les régions intérieures, cette valeur moyenne est nulle d'après (26). Dans les régions extérieures

VOL 7 195

$$\langle\theta_0(\boldsymbol{R})\rangle = N\int d_3R\frac{a}{R}\cos(k_{1(\mu_0)}R) = -1 \quad (32)$$

ce qui est justement la valeur désirée.

La partie transitoire du signal est donc proportionnelle à

$$\frac{\int d_3R[p(\boldsymbol{R}t)-p_s(\boldsymbol{R})]}{p_0\int d_3R} = e^{-4\pi NaDt} \quad (33)$$

Cette dépendance exponentielle du régime transitoire se retrouve pour une large classe de conditions initiales, et en particulier lorsque l'aimantation au temps 0 a une valeur uniforme (quelconque) dans la majeure partie de l'espace entre impuretés : dans ce cas, en effet, le développement (19) ne fait intervenir pratiquement que $\theta_0(R)$.

Dans toutes les situations pratiques rencontrées jusqu'à présent, on est donc en droit de décrire le mouvement de l'aimantation globale $M_z$ par une équation de la forme

$$\frac{dM_z}{dt} = 4\pi NaD(M_{z0}-M_z)-2AM_z \quad (34)$$

L'intérêt de (33) ou de (34) est de montrer que c'est la même constante de temps $(4\pi NaD)^{-1}$ qui intervient pour le régime stationnaire et pour le régime transitoire. La forme exponentielle (33) a été vérifiée qualitativement par BLOEMBERGEN,[1] mais l'identité des deux constantes de temps n'a pas encore été vérifiée à notre connaissance.

### 5. IMPURETÉS GROUPÉES

Nous nous tournons maintenant vers des situations plus complexes où les impuretés paramagnétiques sont groupées, soit qu'elles s'attirent, soit qu'elles soient fixées sur certains départs géométriques du réseau. Qualitativement, à concentration égale en impuretés paramagnétiques, on peut prévoir que la relaxation spin-réseau est d'autant plus *lente* que la tendance à former des groupes est plus forte. Quantitativement, lorsque le specimen est macroscopiquement homogène, l'aimantation nucléaire globale est encore régie par une équation linéaire :

$$\frac{dM_z}{dt} = \frac{1}{T_1}(M_{z0}-M_z)-2AM_z \quad (35)$$

mais $T_1$ est supérieur à $(4\pi NaD)^{-1}$

(35) est valable même lorsqu'il existe simultanément plusieurs types de groupements (une partie des impuretés étant par exemple fixée sur des dislocations, une autre formant des paires); (35) peut être établi par la méthode «optique» employée plus haut, ou encore justifié par l'argument suivant : après une courte phase transitoire, l'aimantation nucléaire atteint toujours une valeur uniforme $p_1(t)$ dans la majeure partie du specimen et :

$$M_z(t) = Vp_1(t) \quad (36)$$

où $V$ est le volume du specimen. Les groupes d'impuretés étant supposés isolés les uns des autres et de dimensions finies, chacun de ces groupes, le $n^{\text{ème}}$ par exemple, peut être considéré comme agissant seul dans un milieu infini où, à grande distance, $p$ est égal à $p_1(t)$. La quantité d'aimantation qui diffuse par seconde vers ce groupe est : $-D(p_1(t)-p_0)Bn$ où $Bn$ est un coefficient dépendant de $a$ et de la forme du groupe. On a alors :

$$\frac{dM_z}{dt} = D(p_0-p_1(t))[\sum_n Bn]-2AM_z \quad (37)$$

et on obtient (35) avec :

$$\frac{1}{T_1} = \frac{D}{V}\sum_n Bn \quad (38)$$

Après cette discussion générale, nous passons à l'étude numérique de deux exemples, en faisant toujours usage de l'approximation du pseudo-potentiel (celle-ci n'est plus entièrement correcte si les impuretés forment des groupes très denses, mais elle suffit en pratique).

*Premier exemple : impuretés en amas.* Soit $N_2(R)$ le nombre moyen d'impuretés rencontré par unité de volume au point $\boldsymbol{R}$, sachant qu'il existe une impureté à l'origine. Nous faisons choix pour $N_2(R)$ de la forme simple

$$N_2(R) = N+\frac{\nu-1}{8\pi\rho^3}e^{-R/\rho} \quad (39)$$

qui exprime que chaque impureté paramagnétique est en moyenne coordonnée à $\nu-1$ autres impuretés dans un domaine dont les dimensions linéaires sont de l'ordre de $\rho$. La relation qui remplace (26) dans ces conditions est :

$$\cos(k_1 a)+Na\int d_3R\frac{\cos(k_1R)}{R}e^{i\mathbf{k}\cdot\mathbf{R}}+$$

$$+\frac{(\nu-1)a}{8\pi\rho^3}\int d_3R\frac{\cos(k_1R)}{R}e^{-R/\rho}e^{i\mathbf{k}\cdot\mathbf{R}}=0 \tag{40}$$

ou encore, avec les mêmes approximations :

$$1+\frac{4nNa}{k^2-k_1^2}+\frac{(\nu-1)a}{2\rho}\frac{1}{1+(k^2-k_1^2)\rho^2}=0 \tag{41}$$

le cas qui nous intéresse est celui où $\rho$ reste fini pour $N\to 0$. On peut alors simplifier l'équation ci-dessus, et l'on trouve finalement :

$$\frac{1}{T_1}=\frac{4nNaD}{1+(\nu-1)\dfrac{a}{2\rho}} \tag{42}$$

*Deuxième exemple : impuretés fixées sur des dislocations.* Soient $\Delta$ la densité de dislocation par cm$^2$ et $1/b = N\Delta^{-1}$ la densité d'impuretés sur une dislocation. (26) est alors remplacé par :

$$\cos k_1 a+Na\int d_3R\frac{\cos(k_1R)}{R}e^{i\mathbf{k}\cdot\mathbf{R}}+$$

$$+\frac{2a}{b}\left[\cos(k_1a)+\int_a^\infty\frac{\cos(k_1z)}{z}e^{ik_zz}dz\right]=0 \tag{43}$$

dont la solution donne :

$$\frac{1}{T_1}\cong\frac{4\pi NaD}{1-\dfrac{a}{b}\mathrm{Log}_e(5{\cdot}4Na^3)} \tag{44}$$

## 6. CONCLUSIONS

Nous voudrions insister maintenant sur le fait que (34) ou (35) ont un domaine de validité plus large que l'équation de transport (1) dont nous sommes partis. Outre les effets d'anisotropie déjà mentionnés, l'équation (1) souffre du défaut suivant : dans les régions où le champ local dû aux ions est comparable au champ local nucléaire, comme l'a remarqué Bloembergen, les fréquences de Larmor de deux noyaux voisins ne sont plus égales; et la diffusion de spin est bloquée. Il y a donc une région (de rayon $b \cong 10$ Å) autour de chaque impureté dans laquelle le mécanisme de transport est profondément modifié. Toutefois, il suffit d'admettre que l'aimantation (ou mieux, l'énergie magnétique) obéit encore dans cette zone à une équation *linéaire*, pour pouvoir définir une longueur de relaxation $a$ par la forme asymtotique (3). Avec cette nouvelle valeur de $a$, la formule (34) restera valable. Enfin, pour l'étude des groupements paramagnétiques, on remarque qu'il intervient toujours *trois constantes* : $NaD$, $p$ et $\nu$ dans le premier exemple, $NaD$, $\Delta$ et $b$ dans le deuxième. Ces constantes doivent être déterminées par des expériences successives (recuits, etc) ou par l'adjonction d'informations indépendantes (mesures directes de $\Delta$, etc).

Pour conclure, nous tenons à remercier le Professeur A. ABRAGAM, qui nous a suggéré ce problème.

## REFERENCES

1. BLOEMBERGEN N., *Physica* **XV,** 386 (1949).
2. KHOUTSICHVILI G. R., *Acad. des Sciences de Géorgie* **IV,** 3 (1956).
3. FERMI E. *Nuclear Physics.* University of Chicago Press (1950).

VOL 7 195

*J. Phys. Chem. Solids* Pergamon Press 1958. Vol. 7. pp. 351–360.

# CRYSTALLOGRAPHIC AND MAGNETIC PROPERTIES OF SEVERAL SPINELS CONTAINING TRIVALENT JA-1044 MANGANESE*

**D. G. WICKHAM† and W. J. CROFT‡**

Lincoln Laboratory, Massachusetts Institute of Technology, Lexington, Massachusetts

(*Received* 14 *May* 1958; *in revised form* 4 *June* 1958)

VOL. 7 1958

**Abstract**—Many useful ferrimagnetic oxides which crystallize with the spinel structure contain several transition metals, each of which can exist in two or more possible oxidation states. A specific formulation for many such materials is very difficult. An approach to this problem, in some cases, can be made through crystallographic studies. The tetragonal distortion from cubic symmetry exhibited by several spinels containing manganese has been attributed to characteristic properties of $Mn^{3+}$ ions occupying the octahedral positions in the lattice. Several new compositional systems containing manganese and crystallizing with the spinel structure have been prepared and studied crystallographically and magnetically. The following solid-solution systems were chosen because they appeared to present a minimum of ambiguity in composition and in the distribution of cations among tetrahedral and octahedral positions: $Zn_xGe_{1-x}Mn_2O_4$, $Zn_xGe_{1-x}Co_{2-2x}Mn_{2x}O_4$, and $Zn_xLi_{1-x}Mn_2O_4$. The tetragonal distortions from cubic symmetry observed for these systems can be accounted for by assuming that the octahedral sites are occupied by more than a critical fraction, 60–65 per cent, of $Mn^{3+}$ ions. A complete range of solid solutions in the system $Co_{3-x}Mn_xO_4$ was prepared and formulas assigned on the basis of this rule. The configuration, for values of $x$ between 0 and 2, appears to be $Co^{2+}[Co^{3+}_{2-x}Mn_x^{3+}]O_4$. The observed magnetic properties (saturation magnetization at 4·3°K and Curie temperatures) can be interpreted in terms of this configuration. The magnetization measured for cubic materials is the result of Néel-type magnetic coupling between $Co^{2+}$ ions on tetrahedral sites and $Mn^{3+}$ ions on octahedral sites. Tetragonal materials apparently have a more complex magnetic structure. The configuration of $Co_{3-x}Mn_xO_4$ for values of $x$ between 2 and 3 appears to be $Co^{2\pm}_{3-x}Mn^{2\pm}_{x-2}[Mn_2^{3+}]O_4$. The crystal-lattice constants, saturation magnetization (4·3°K) and Curie temperatures are given for a number of materials, including $GeMn_2O_4$, $LiMn_2O_4$, $Co_3O_4$, $MnCo_2O_4$, $CoMn_2O_4$ and $Mn_3O_4$.

## 1. INTRODUCTION

THE element manganese is a common constituent of many useful ferrimagnetic materials which crystallize with the spinel structure. The several possible oxidation states of manganese often make it difficult to represent these compositions with a specific formulation. The manganese–magnesium ferrite composition from which millions of memory elements for automatic computers have been fabricated is a case in point. After the most thorough chemical analysis possible, this material can be assigned a chemical formula only within certain limiting concentrations of specific oxidation states of iron and manganese.[1]

The possible oxidation states existing in the tetragonally distorted spinel structure of $Mn_3O_4$ and $ZnMn_2O_4$ have been the subject of considerable thought and experiment. At room temperature the axial ratio $c/a$ for $Mn_3O_4$ has the value 1·16 while at 1170°C $Mn_3O_4$ is cubic. The electrical conductivities of $Mn_3O_4$ and $ZnMn_2O_4$ ($c/a = 1{\cdot}144$) show definite thermal hysteresis between 1075 and 1150°C., and between 950 and 1125°C, respectively.[2] These properties were

* The research in this document was supported by the U.S. Army, Navy, and Air Force under contract with the Massachusetts Institute of Technology.

† Staff Member, Lincoln Laboratory, M.I.T.

‡ Now with R.C.A. Laboratories, Needham, Massachusetts.

explained by GOODENOUGH and LOEB[3] who described them as a consequence of the tendency of trivalent manganese ions which have the outer electronic structure $3d^4$ to form square planar $dsp^2$ bonds when occupying octahedral sites in a face-centered-cubic oxygen lattice. In each $MnO_6$ group there are four coplanar, shortened covalent bonds extended toward four of the near-neighbor anions. (This explanation is compatible with ligand-field theory as was shown by DUNITZ and ORGEL.)[4] The third axis ($c$-axis) of the octahedron is relatively longer. If the $c$-axes of all octahedra are parallel, the crystals are tetragonally distorted from cubic symmetry and the axial ratio $c/a$ has its maximum value. The probable configurations for $Mn_3O_4$ and $ZnMn_2O_4$ are thus, $Mn^{2+}[Mn^{3+}Mn^{3+}]O_4$ and $Zn^{2+}[Mn^{3+}Mn^{3+}]O_4$.*

According to the theory of GOODENOUGH and LOEB, the distortion of the spinel crystal from cubic to tetragonal must be regarded as a cooperative phenomenon. If, for example, a solid solution system $A[B_{2-x}Mn_x^{3+}]O_4$ is considered, the following sequence of changes can be anticipated. For small values of $x$, most of the $Mn^{3+}$ ions will occupy isolated positions in the cubic lattice, and the distortion of individual octahedra will be inhibited by the strain energy. As the value of $x$ is increased, so also does the probability that several $Mn^{3+}$ ions will occupy adjacent octahedral positions. Localized, small regions in the crystal may develop in which the energy gain associated with a cooperative distortion of several octahedra is sufficient to overcome the strains imposed by the surrounding cubic lattice. Within each of these regions the longer axes of the octahedra are parallel, but these axes in respect to the whole crystal are oriented randomly along all three equivalent cubic axes. As long as the regions of oriented octahedra are too small to be detected by X-ray diffraction measurements, the crystal appears cubic. This situation will be referred to below as short-range order. Finally, at a certain critical value of $x$, a long range ordering sets in and a tetragonal distortion of the crystal as a whole takes place. A two-phase system containing a $Mn^{3+}$ rich, tetragonal phase may form depending on the thermal history of the sample.

* Brackets enclose ions occupying octahedral sites in the spinel structure. The ions outside the brackets occupy the tetrahedral sites.

MASON[5] studied the crystallographic properties of the solid solution system $Fe_3O_4$-$Mn_3O_4$ (or $Fe_{3-x}Mn_xO_4$) in which one end member is cubic, the other tetragonal. Synthetic materials prepared by igniting oxides above 1200°C exhibited a cubic structure at room temperature from 0 to 60 per cent $Mn_3O_4$, a tetragonal structure from 60 to 100 per cent $Mn_3O_4$: through the latter region the value of $c/a$ increased from 1·00 to 1·16. The temperature at which the transition from tetragonal to cubic symmetry takes place was studied by MCMURDIE *et al.*[6] and found to increase from 400–500°C for 65 per cent $Mn_3O_4$ to 1175°C for pure $Mn_3O_4$. However, MASON[5] studied some mineral specimens belonging to the $Fe_3O_4$–$Mn_3O_4$ system and found evidence that compositions containing from approximately 54 per cent to 91 per cent $Mn_3O_4$, will form two phases if allowed to reach equilibrium: one cubic, poor in manganese and one tetragonal, rich in manganese. VAN HOOK and KEITH[15] have described more completely the solid-phase equilibria for this system. Complete equilibrium at temperatures below 900°C is approached very slowly so that it is possible to prepare a complete range of single-phase solid solutions in this system by reacting the appropriate oxides at a sufficiently high temperature and cooling the products not too slowly.

The configuration of $Fe_3O_4$ has been established by magnetic measurements and neutron diffraction studies as $Fe^{3+}[Fe^{2+}Fe^{3+}]O_4$. If it is assumed that the solid solutions between $Fe_3O_4$ and $Mn_3O_4$ can be formed without changing the oxidation states present or the distribution of cations in the pure end members, the composition containing the greatest quantity of manganese which remains cubic at room temperature can be written $Fe^{3+}_{0.40}Mn^{2+}_{0.60}[Fe^{2+}_{0.40}Fe^{3+}_{0.40}Mn^{3+}_{1.20}]O_4$. It could be inferred from this formula that if more than 60 per cent of the octahedral sites are occupied by $Mn^{3+}$ ions, the symmetry of the spinel structure becomes tetragonal. The assumption that $Fe_3O_4$ and $Mn_3O_4$ dissolve in each other unchanged cannot be made without reason and several other formulas can be written to express the same composition. An example is the formula $Mn^{2+}_{0.80}Fe^{2+}_{0.20}[Fe^{2+}_{1.00}Mn^{4+}_{1.00}]O_4$ which represents a 2–4 spinel containing the manganese as highly oxidized as possible.

VOL. 7 1958

FINCH *et al.*[7] have studied the solid-solution systems $Mn_3O_4$–$NiFeO_4$, $Mn_3O_4$–$CoFe_2O_4$, $Mn_3O_4$–$MnFe_2O_4$ and $Mn_3O_4$–$Fe_3O_4$ and state that 62·5 per cent, 55·5 per cent, 50 per cent, and 60 per cent, respectively, of the octahedral sites are occupied by $Mn^{3+}$ ions where a tetragonal distortion first appears at room temperature. These authors have assumed that the end member ferrites in each solid solution series are ideal inverse spinels and that they have mixed with no redistribution of the cations among the two kinds of lattice sites. It is necessary to point out that the system $Mn_3O_4$–$MnFe_2O_4$, if prepared under similar conditions, is in reality another way of representing two-thirds of the system $Mn_3O_4$–$Fe_3O_4$. The observation that 50 per cent in one case and 60 per cent in the other represents the critical fraction of $Mn^{3+}$ must be attributed to a lack of information concerning the distribution of cations and the oxidation states present. Indeed, the ferrite $MnFe_2O_4$ has been found to possess a structure essentially that of a normal spinel. HASTINGS and CORLISS[16] through a neutron diffraction study established the fact that approximately 80 per cent of the manganese ions in $MnFe_2O_4$ occupy tetrahedral sites.

In order to investigate further the possible relationships between crystal symmetry, magnetic properties, and the amount of $Mn^{3+}$ present in substances with the spinel crystal structure and thus to resolve some of the ambiguities encountered in assigning specific formulations to complex systems, several new compositional systems have been studied. These particular systems were chosen because they provide a chemical situation which is not as complex as that found in manganese-iron oxide systems. In three of the systems, ($Zn_xGe_{1-x}Mn_2O_4$, $Zn_xGe_{1-x}Co_{2-2x}Mn_{2x}O_4$, and $Li_{1-x}Zn_xMn^{3+}_{1+x}Mn^{4+}_{1-x}O_4$), an attempt was made to introduce into the spinel structure ions of unambiguous oxidation state which would occupy tetrahedral sites exclusively. This would permit chemical analysis for the oxidation value of ions in octahedral sites. The interesting results of these experiments led to an investigation of the apparently more complex system $Co_{3-x}Mn_xO_4$.

The crystallographic data reported below is taken from measurements made with a Philips Norelco Diffractometer. MENYUK and DWIGHT made the magnetic measurements using a modified vibrating-coil magnetometer recently described by DWIGHT, MENYUK and SMITH.[8] The measurements of saturation magnetization were made in a magnetic field of 10,000 Oe and are accurate within ca. 2 per cent. Curie temperatures were found by extrapolation to zero moment of the linear portion of the magnetization vs. temperature curves. Details of the techniques for powdered samples are given in reference 9.

### 2. THE SYSTEM $Zn^{2+}_xGe^{4+}_{1-x}Mn^{2+}_{2-2x}Mn^{3+}_{2x}O_4$

This composition system may be referred to as a solid-solution series between $GeMn_2O_4$ and $ZnMn_2O_4$. Pure, almost white, manganous germanate $Ge^{4+}Mn_2^{2+}O_4$ was prepared by sintering together the appropriate quantities of MnO and $GeO_2$ under an inert atmosphere. It was found by X-ray analysis to be isomorphous with the mineral olivine $(Mg, Fe)_2SiO_4$. The symmetry is orthorhombic with $a_0 = 5{\cdot}05$ Å, $b_0 = 10{\cdot}70$ Å, and $c_0 = 6{\cdot}28$ Å. In the olivine structure the divalent ions occupy octahedral sites, the tetravalent ions tetrahedral sites, in an approximately close-packed, hexagonal array of oxygen anions. Although the same number of tetrahedral and octahedral sites are occupied as in the spinel $AB_2O_4$, the arrangement of these sites is less symmetrical than in the spinel structure. The olivine structure can become stable when the ratio of the radius of the B ion to that of the A ion exceeds a certain limit. Nickel and cobalt germanates, $GeNi_2O_4$ and $GeCo_2O_4$ crystallize as normal cubic spinels[10] ($r_{Ni^{++}} = 0{\cdot}69$ Å, $r_{Co^{++}} = 0{\cdot}73$ Å, whereas $r_{Mn^{2+}} = 0{\cdot}80$ Å).

By heating mixtures of ZnO, $GeO_2$, and $Mn_2O_3$ at 1150°C in air, it was possible to prepare the compositions $Zn_xGe^{4+}_{1-x}Mn^{2+}_{2-2x}Mn^{3+}_{2x}O_4$ which consist of a single, reddish brown spinel phase for values of $x$ greater than 0·5. Preparations ignited below 1100°C do not consist of a single phase. X-ray diffraction patterns, chemical analyses, and saturation magnetization measurements were made for each composition. The results are shown graphically in Fig. 1.

A tetragonal distortion is observed for values of $x$ greater than ca. 0·6. It is reasonable to assume that in this system the $Zn^{2+}$ and $Ge^{4+}$ occupy tetrahedral positions in the spinel structure and that no oxidation–reduction reactions have taken

place between germanium or zinc and manganese. The average valence found experimentally for the manganese in the composition with $x = 0{\cdot}6$ is that represented by 0·8 $Mn^{2+}$ ions and 1·2 $Mn^{3+}$ ions

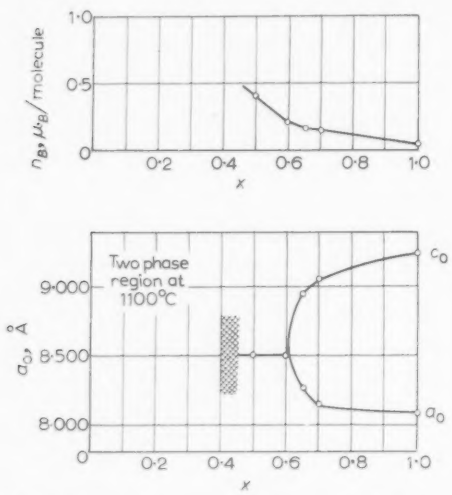


FIG. 1. Saturation magnetization $n_B$ and lattice constant $a_0$(25°C) as a function of $x$ for the system $Zn_{1-x}Ge_{1-x}Mn^{++}_{2-2x}Mn^{+++}_{2x}O_4$.

per molecule $AB_2O_4$. Therefore, the formula $Zn^{2+}_{0.6}Ge^{4+}_{0.4}[Mn^{2+}_{0.8}Mn^{3+}_{1.2}]O_4$ can be written to represent the configuration for the composition containing the most $Mn^{3+}$ which will remain cubic at room temperature. This formula is analogous in terms of $Mn^{3+}$ to that one given above for the critical composition in the $Fe_3O_4$–$Mn_3O_4$ system, $Fe^{3+}_{0.40}Mn^{2+}_{0.60}[Fe^{2+}_{0.40}Fe^{3+}_{0.40}Mn^{3+}_{1.20}]O_4$.

The saturation magnetization (4·2°K) decreases with increasing values of $x$. An inflection in the curve occurs for a value of $x$ between 1·2 and 1·3 corresponding to the appearance of a tetragonal distortion.

Since analogous formulas may be written for the critical compositions in both of the systems described above, in terms of other possible oxidation states of manganese (e.g., $Mn^{3+} \rightleftharpoons 0{\cdot}5Mn^{2+} + 0{\cdot}5Mn^{4+}$), experiments were undertaken to synthesize some materials with the spinel structure containing $Mn^{4+}$ ions.

### 3. THE SYSTEM $Li^{+}_{1-x}Zn^{2+}_{x}Mn^{3+}_{1+x}Mn^{4+}_{1-x}O_4$

When lithium carbonate and any oxide of manganese are taken in such quantities that the molar ratio Li/Mn equals exactly 0·5, mixed intimately together and reacted at 800–900°C in the air, repeatedly ground and reacted at this temperature until the sample has reached constant weight, the bluish-black product has a composition which can be formulated $Li^{+}Mn^{3+}Mn^{4+}O_4$. X-ray diffraction patterns demonstrate that it crystallizes as a cubic spinel with $a_0 = 8{\cdot}246$ Å. The most likely configuration for this compound would be $Li_{+}[Mn^{3+}Mn^{4+}]O_4$. The (220) and (224) reflections usually observed in the X-ray powder patterns of spinels are absent in the pattern for $LiMn_2O_4$. The intensities of these two reflections are chiefly dependent upon the atomic scattering factors of the ions occupying tetrahedral sites.[11] Therefore, the light lithium atoms ($Z = 3$) with their low scattering power for X-rays are probably the occupants of the tetrahedral sites in the structure of $LiMn_2O_4$.

If the configuration $Li^{+}[Mn^{3+}Mn^{4+}]O_4$ is correct, $Mn^{3+}$ ions occupy 50 per cent of the octahedral positions in the spinel structure without causing a tetragonal distortion, and this is consistent with the inference above that 60 per cent is the critical fraction. Tetravalent manganese ions here occupy 50 per cent of the octahedral sites also without causing a distortion from cubic symmetry. The critical compositions in the $Fe_3O_4$–$Mn_3O_4$ and $Zn_{1-x}Ge_xMn_2O_4$ systems can be formulated $Mn^{2+}_{0.8}Fe^{2+}_{0.2}[Fe^{2+}_{1.0}Mn^{4+}_{1.0}]O_4$ and $Zn^{2+}_{0.6}Ge^{4+}_{0.4}[Mn^{2+}_{1.4}Mn^{4+}_{0.6}]O_4$. Neither of these two substances contain more $Mn^{4+}$ than $Li^{+}[Mn^{3+}Mn^{4+}]O_4$. An effort was made to increase the amount of $Mn^{4+}$ present by increasing the value of the atomic ratio Li/Mn slightly. The result was the appearance of a brightly-colored, red, second phase which was identified as the compound $Li_2Mn^{4+}O_3$. An effort was made also to increase the amount of $Mn^{3+}$ present by decreasing the value of Li/Mn. The result here was the appearance of $Mn_2O_3$ as a second phase.

An alternate method of varying the amount of $Mn^{3+}$ present in the octahedral positions appeared in the possible synthesis of the system $Li^{+}_{1-x}Zn_x{}^{2+}[Mn^{3+}_{1+x}Mn^{4+}_{1-x}]O_4$, i.e., a solid solution system $LiMn^{3+}Mn^{4+}O_4 - ZnMn_2{}^{3+}O_4$. The value of $x$ was varied from 0·2 to 0·6 by sintering mixtures of the appropriate oxides at temperatures ranging from 800 to 950°C. Two phases were present in all samples, one cubic and one tetragonal. The

tetragonal lattice constants indicated a composition close to that of pure $ZnMn_2O_4$. This behavior is similar to that described by MASON for the system $Fe_3O_4$–$Mn_3O_4$ at equilibrium below 950°C.

Preparations in this series were not attempted at temperatures above 950°C because $LiMn_2O_4$ decomposes above 950° with the evolution of oxygen and simultaneous reduction of tetravalent manganese. The decomposition temperature was determined by differential thermal analysis and the reduction of the manganese was discovered by chemical analysis of samples quenched from 1000°C. The possible values of $x$ for single-phase compositions in this system, although they have not been determined accurately, are restricted to very narrow ranges and all single-phase compositions are probably cubic for values of $x$ less than 0·6.

The saturation magnetization observed for $LiMn_2O_4$ is essentially zero.

#### 4. THE SYSTEM $Zn_x^{2+}Ge_{1-x}^{4+}Co_{2-2x}^{2+}Mn_{2x}^{3+}O_4$

It was possible to obtain single-phase preparations throughout this series by sintering mixtures of the appropriate molar quantities of ZnO, CoO, $GeO_2$ and $Mn_2O_3$ at 950–1100°C. The end-member, $Ge^{4+}Co_2^{2+}O_4 (x = 0)$ is a pink, normal

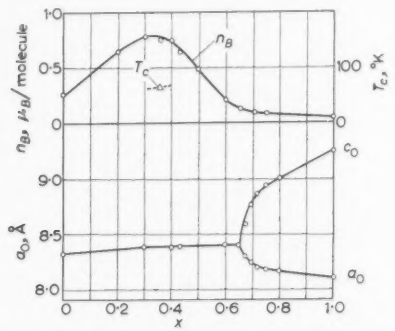


FIG. 2. Saturation magnetization $n_B$(4°K) and lattice constant $a_0$(25°C) as a function of $x$ for the system $Zn_xGe_{1-x}Co_{2-x}^{2+}Mn_{2x}^{3+}O_4$.

cubic spinel with $a_0 = 8{\cdot}318$ Å (ROMEIJN gives $a_0 = 8{\cdot}3175 \pm {\cdot}0005$ Å).[10] The other end-member ($x = 1$) is the yellow-brown, tetragonal $ZnMn_2O_4$ ($a_0 = 8{\cdot}087$ Å, $c_0 = 9{\cdot}254$ Å, $c/a = 1{\cdot}144$ Å). The value of $a_0$ for the black, solid solutions increases almost linearly from 8·318 for $x = 0$ to 8·395 Å for $x = 0{\cdot}65$. A tetragonal distortion is observed for values of $x$ greater than 0·65 with $c/a$ increasing from 1·00 to 1·144 for $x = 1{\cdot}0$. The data is shown graphically in Fig. 2.

Two reasonable formulas can be written for the critical composition: (1) $Zn_{0.65}^{2+}Ge_{0.35}^{4+}[Co_{0.70}^{2+}Mn_{1.30}^{3+}]O_4$ and (2) $Zn_{0.65}^{2+}Ge_{0.35}^{4+}[Co_{0.70}^{3+}Mn_{0.70}^{2+}Mn_{0.60}^{3+}]O_4$. The first formula showing 65 per cent of the octahedral sites occupied by $Mn^{3+}$ ions, is analogous to the formulas which may be written for the like members of the two systems described above, $Fe_3O_4$–$Mn_3O_4$ and $Zn_xGe_{1-x}Mn_2O_4$. The slightly greater value for $x$ required to produce a tetragonal distortion at room temperature in the $Zn_xGe_{1-x}Co_{2-2x}Mn_{2x}O_4$ system perhaps can be explained by assuming that some of the cobalt ions exist as $Co^{3+}$ ions so that a slightly greater manganese content is required to fill 60 per cent of the octahedral sites with $Mn^{3+}$. Other explanations are possible.

The saturation magnetization curve for this system is presented and compared with the crystallographic data in Fig. 2. There is a maximum value for $n_B$ of 0·78 $\mu_B$/molecule observed for a value of $x$ equal to ca. 0·32, i.e., $Zn_{0.32}^{2+}Ge_{0.68}^{4+}[Co_{1.36}^{2+}Mn_{0.64}^{3+}]O_4$. There is an inflection in the curve corresponding to the value of $x$ for which a tetragonal distortion of the lattice first appears. The values of $n_B$ for the tetragonal samples are uniformly very small varying from 0·1 $\mu_B$/molecule for $x$ equal to 0·65 to 0·034 $\mu_B$/molecule for $x$ equal to 1·00. A magnetization curve for the system $Zn_xGe_{1-x}Mn_2O_4$ was obtained only for values of $x$ greater than 0·5 because of the limited single-phase region. This curve is similar in shape, however, to the curve for the $Zn_xGe_{1-x}Co_{2-2x}^{2+}Mn_{2x}^{3+}$ system.

#### 5. THE SYSTEM $Co_{3-x}Mn_xO_4$

##### 5.1. *Preparation*

A complete range of solid solutions in this system was prepared by sintering in the air intimate mixtures of cobalt and manganese oxides obtained by the thermal decomposition of coprecipitated cobalt and manganese oxalates. The composition of each sample was determined entirely by chemical analysis because the preparative procedure was not quantitative. It was necessary to prepare a few samples of particularly desired compositions from pure oxides.

It was necessary also to determine the oxidizing power of each sample in order to find a proper reaction temperature. This follows from the fact that the pure oxide $Co_3O_4$ is stable in air only below ca. 900°C and $Mn_3O_4$ is stable in the air only above ca. 950°C. The results of two reaction temperatures are presented graphically in Fig. 3.

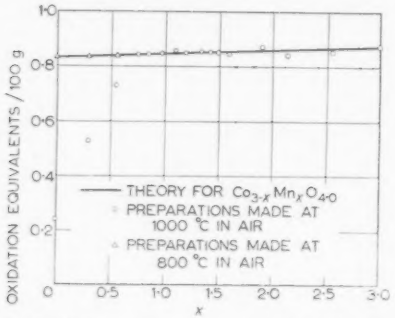


FIG. 3. Oxidizing power vs. composition for the system $Co_{3-x}Mn_xO_{4-\lambda}$ prepared at 800°C and 1000°C.

8·083 Å* for $x$ equal to zero to 8·316 for $x = 1{\cdot}20$. For values of $x$ greater than 1·20, the samples crystallize with tetragonal symmetry. The $c/a$ ratio increases in value from 1·000 to 1·148 for $x = 2{\cdot}00$. (See Fig. 4). This latter composition $CoMn_2O_4$ possesses a $c/a$ ratio almost as great as that of pure $Mn_3O_4$($c/a = 1{\cdot}16$) and thus can be assumed to have an analogous configuration, $Co^{2+}[Mn^{3+}Mn^{3+}]O_4$. BONGERS[12] has arrived at the same result; his value for the axial ratio $c/a$ is 1.15.

It is possible again to account for the tetragonal distortion of a spinel structure by assuming that more than a critical fraction, viz., 60 per cent, of the octahedral sites are occupied by $Mn^{3+}$ ions. COSSEE[13] has shown that the most probable configuration for $Co_3O_4$ is $Co^{2+}[Co^{3+}Co^{3+}]O_4$. Therefore, as $x$ is varied from 0 to 2·00, in the system $Co_{3-x}Mn_xO_4$, $Mn^{3+}$ ions will be substituted for $Co^{3+}$ ions on the octahedral sites. The composition which contains the most $Mn^{3+}$ and yet remains

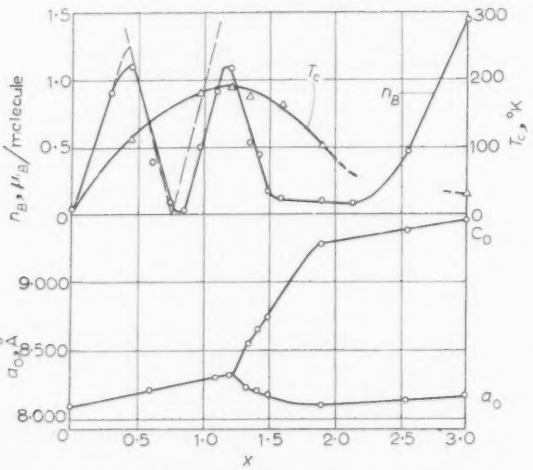


FIG. 4. Saturation magnetization ($n_B$), Curie temperature ($T_c$), and unit-cell dimensions vs. composition for the system $Co_{3-x}Mn_xO_4$.

### 5.2. *Crystallographic properties*

X-ray diffraction measurements show that compositions in the system $Co_{3-x}Mn_xO_4$ crystallize with a cubic spinel structure for values of $x$ from zero to 1·2. The length of the unit-cell edge increases almost linearly through this region from cubic at room temperature is approximately $Co^{2+}[Co^{3+}_{0.80}Mn^{3+}_{1.20}]O_4$ in analogy to similar substances in the two systems, $Zn_xGe_{1-x}Mn_2O_4$ and $Zn_xGe_{1-x}Co^{2+}_{2-2x}Mn^{3+}_{2x}O_4$.

* Measured by R. J. ARNOTT for a sample whose composition is $Co_3O_{4.008}$.

5.3. *Magnetic properties*

The values for the saturation magnetic moment ($n_B$) measured at 4·2°K and the Curie temperature ($T_c$) are plotted along with the lattice constants of the system $Co_{3-x}Mn_xO_4$ in Fig. 4.

The magnetization curve for values of $x$ from 0 to 1·2 can be interpreted quite easily in terms of the spinel configuration deduced above from crystallographic considerations. This configuration for values of $x$ from zero to 2·00 can be written $Co^{2+}[Co^{3+}_{2-x}Mn^{3+}_x]O_4$.

COSSEE[13] has studied the paramagnetic susceptibility of a number of substances with the spinel crystal structure which contain $Co^{3+}$ ions. He finds that generally this ion, when occupying octahedral positions, is diamagnetic. This property can be attributed to the tendency of the $Co^{3+}$ ion to form covalent bonds with its six oxygen neighbors through six hybridized $d^2sp^3$ orbitals. It acquires in this way a completely full $3d$ electron shell and does not contribute to a net magnetic moment.

The magnetic moments for $Co^{2+}[Co^{3+}_{2-x}Mn^{3+}_x]O_4$ would be the result of indirect Néel type coupling between the $Co^{2+}$ ions on the tetrahedral sites (A-sites) and the $Mn^{3+}$ ions on the octahedral sites (B-sites). The values indicated by the dashed line in Fig. 4 are calculated using the "spin only" (orbital moments quenched) values of 3·0, 4·0 and 0 $\mu_B$ for the moments contributed by $Co^{2+}$, $Mn^{3+}$ and $Co^{3+}$ ions, respectively. The composition ($x = 0{\cdot}75$) for which the moments on the tetrahedral sites are exactly equal to the moments on octahedral sites has a net moment of zero. The experimental curve beginning at zero for the paramagnetic $Co_3O_4$ reaches a theoretical value for $x$ equal to 0·45 and then follows the theoretical curve until $x$ is equal to 1·2. The experimental "compensation point" occurs for $x$ equal to about 0·8. An increasing small divergence from theoretical values for $n_B$ appears to begin for $x =$ ca. 0·7. The number of $Mn^{3+}$ ions on octahedral sites increases through this composition range ($0 \leqslant x \leqslant 1{\cdot}2$) and hence the number of A–B interactions increases producing a constantly rising Curie temperature which reaches a maximum of 191°K at $x = 1{\cdot}2$. An abrupt change in the magnetization curve occurs also for this value of $x$. These changes coincide with the change in crystal symmetry at $x$ equal to 1·2.

An appreciable magnetic moment appears again for values of $x$ greater than 2·1 reaching a maximum of 1·4 $\mu_B$/molecule for pure $Mn_3O_4$. The Curie temperature of $Mn_3O_4$ is 30°K. BOROVIK–ROMANOV and ORLOVA have reported a value of 42·5°K for $T_c$.[18]

## 6. DISCUSSION

Three solid solution systems crystallizing with the spinel structure have been studied in each of which a tetragonal distortion at room temperature is associated with a critical composition. The formulas expressing these compositions and a reasonable distribution of cations are: $Zn^{2+}_{0.60}Ge^{4+}_{0.40}[Mn^{2+}_{0.80}Mn^{3+}_{1.20}]O_4$, $Zn^{2+}_{0.65}Ge^{4+}_{0.35}[Co^{2+}_{0.70}Mn^{3+}_{1.30}]O_4$, and $Co^{2+}[Co^{3+}_{0.80}Mn^{3+}_{1.20}]O_4$. Thus, with $Zn^{2+}$ + $Ge^{4+}$, or $Co^{2+}$ ions occupying the tetrahedral sites and $Mn^{2+}$, $Co^{2+}$, or $Co^{3+}$ ions besides $Mn^{3+}$ ions occupying octahedral sites, 60–65 per cent of $Mn^{3+}$ ions on the latter type sites can cause a distortion of the spinel lattice from cubic to tetragonal symmetry. Other ions present in octahedral sites must be indifferent, however, and not in themselves influence the symmetry of the structure either through bonding properties or packing considerations, for this rule to apply.

The critical compositions given by FINCH, SINHA and SINHA[7] for the systems $Fe_3O_4$–$Mn_3O_4$ and $NiFe_2O_4$–$Mn_3O_4$ are respectively $Fe^{3+}_{0.4}Mn^{2+}_{0.6}[Fe^{2+}_{0.4}Fe^{3+}_{0.4}Mn^{3+}_{1.2}]O_4$ and $Fe^{3+}_{0.375}Mn^{2+}_{0.625}[Ni^{2+}_{0.375}Fe^{3+}_{0.375}Mn^{3+}_{1.25}]O_4$ which obey the above rule very well. The critical composition given by these authors for the system $MnFe_2O_4$–$Mn_3O_4$ (50 per cent $Mn^{3+}$) should be the same as that for the system $Fe_3O_4$–$Mn_3O_4$ (see Introduction). The critical composition in terms of $Mn^{3+}$ for the system $MnFe_2O_4$–$Mn_3O_4$ can be recalculated on the basis of the known distribution of iron and manganese cations in $MnFe_2O_4$ among tetrahedral and octahedral sites determined by HASTINGS and CORLISS.[16] If the distribution of oxidation states given by HARRISON *et al.*[17] for $MnFe_2O_4(Mn^{2+}_{0.8}Fe^{3+}_{0.2}[Fe^{2+}_{0.2}Fe^{3+}_{1.6}Mn^{3+}_{0.2}]O_4)$ is accepted the critical composition becomes $Mn^{2+}_{0.90}Fe^{3+}_{0.10}[Fe^{3+}_{0.80}Fe^{2+}_{0.10}Mn^{3+}_{1.1}]O_4$. Here 55 per cent of the octahedral sites are occupied by $Mn^{3+}$ ions and a better agreement is found with the value for the $Fe_3O_4$–$Mn_3O_4$ system and with the value 60–65 per cent deduced in the present work. It was pointed out in the Introduction that it is frequently unsafe to assume that solid solutions can be formed without changing

the oxidation states present or the distribution of cations in the pure end members. The remaining lack of agreement between two values which should be identical is possibly due to the invalidity of this assumption.

The configuration of the system $CoFe_2O_4$–$Mn_3O_4$ (FINCH *et al.* give 55·5 per cent $Mn^{3+}$ for the critical composition) is particularly difficult to deduce because there are present three metals each with more than one possible oxidation state.

The mechanism given by GOODENOUGH and LOEB[3] can be invoked to explain the tetragonal distortion of crystals containing more than the critical fraction of $Mn^{3+}$ ions. The distorted octahedra of oxygen anions surrounding the $Mn^{3+}$ ions

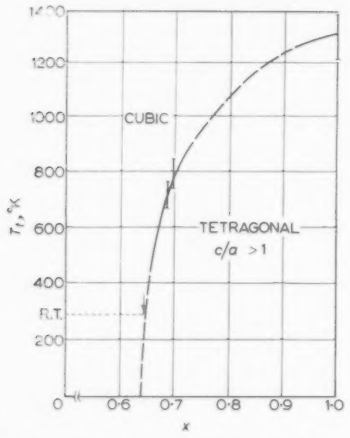


FIG. 5. Transition temperature $T_t$ for tetragonal-to-cubic phase change in the system $Zn_xGe_{1-x}[Co^{2+}\ Mn^{3+}_{2x}]O_4$.

are forced by elastic energy considerations to align their longer axes parallel and the whole crystal becomes increasingly tetragonal. Reference to Figs. 1, 2 and 4 shows that the tetragonality, when it appears, develops rapidly for a small increment in $x$.

FINCH *et al.* have treated this problem mathematically as an ordering phenomenon and conclude that the mechanism of bulk distortion is best described in terms of a net fraction of distorted octahedra with their electrovalent bond direction parallel to the $c$-axis of the crystal. The dependence of this fraction on temperature is reflected in the increasing tetragonal to cubic phase-transition temperature for the system $Fe_{3-x}Mn_xO_4$ measured through the region from $x$ equal to 1·95 to $x$ equals 3·00.[6] It would be interesting to know if compositions containing a little less than the critical concentration of $Mn^{3+}$ which are cubic at room temperature become tetragonal at a lower temperature. Two transition temperatures for the system $Zn_xGe_{1-x}[Co^{2+}_{2-2x}Mn^{3+}_{2x}]O_4$ were determined.* These values and a value for pure

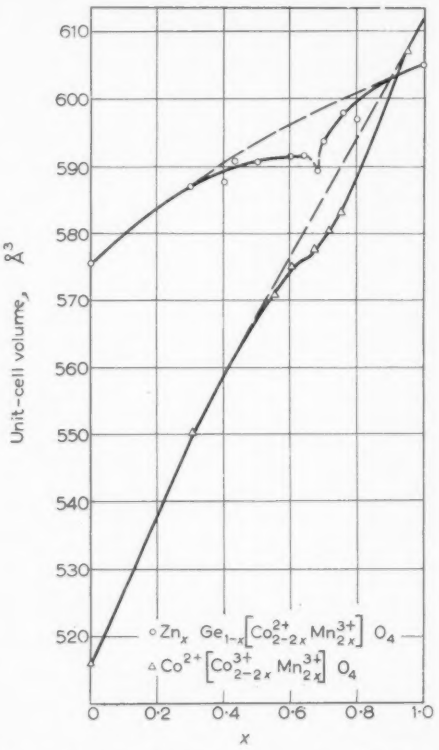


FIG. 6. Unit-cell volume (Å³) as a function of composition for the systems $Zn_xGe_{1-x}[Co^{2+}_{2-2x}Mn^{3+}_{2x}]O_4$ and $Co^{2+}[Co^{3+}_{2-2x}Mn^{3+}_{2x}]O_4$.

$ZnMn_2O_4$ reported by ROMEIJN permit the construction of the graph shown in Fig. 5. If the extrapolation to absolute zero is allowed, the critical fraction of $Mn^{3+}$ ions required to produce a tetragonal distortion at 0°K is at the most only a few per cent smaller than it is at room temperature.

* Measurements made by R. J. ARNOTT—limited in number by unavailability of apparatus.

FINCH *et al.* observed in the systems they studied a linear relationship between the cube-root of the unit-cell volume and composition. They concluded on this basis that the orientation of distorted octahedra in cubic crystals is completely randomized.

The unit-cell volume is plotted in Fig. 6 as a function of composition for two of the systems studied in the present work, $Zn_xGe_{1-x}[Co^{2+}_{2-2x}Mn^{3+}_{2x}]O_4$ and $Co^{2+}[Co^{3+}_{2-2x}Mn^{3+}_{2x}]O_4$. A significant departure from normal behavior occurs for values of $x$ equal to approximately 0·3. There is a sharp inflection in both curves corresponding to the change in crystal symmetry ($x = 0{\cdot}60$–$0{\cdot}65$). This behavior is possibly caused by an increasing degree of short-range order existing among the distorted $MnO_6$ octahedra like that described in the Introduction. As the critical composition is approached, localized regions of parallel-oriented, distorted octahedra increase in number and effect a relative contraction of the lattice previous to the long-range cooperative distortion of the entire crystal.

The $Mn^{3+}$ ions in distorted interstices can be expected to couple magnetically in a different sense through the short covalent bonds than through the long electrovalent bonds.[14] Although the predominant magnetic coupling in the system $Co_{3-x}Mn_xO_4$, for values of $x$ between 0 and 1·2, is Néel-type coupling between $Co^{2+}$ ions in tetrahedral sites and $Mn^{3+}$ ions in octahedral sites, more complex magnetic ordering may develop in the localized regions of distorted octahedra. The experimental magnetization curve shown in Fig. 4 is seen to diverge slightly from the theoretical curve for a value of $x$ equal to ca. 0·7. The divergence of the unit-cell volume curve begins for approximately the same composition. The divergence of each increases gradually with increasing $Mn^{3+}$ content until, at the point where the crystal becomes tetragonal, an abrupt change in both the magnetization and unit-cell volume curves takes place. The fact that the Curie temperature remains relatively high after the magnetization has abruptly fallen off indicates that relatively strong magnetic interactions persist into the tetragonal region, but that a new and more complex orientation of ionic moments exists throughout the crystal. If a similar orientation of magnetic moments were to occur within the localized regions of ordered $MnO_6$ octahedra, it could account for the experimental fact that the observed magnetic moments are slightly lower than expected values.

The source of the magnetization observed in the system $Zn_xGe_{1-x}[Co^{2+}_{2-2x}Mn^{3+}_{2x}]O_4$ cannot be stated with any certainty. If the structure has exactly the configuration indicated, the magnetic interactions leading to a net magnetic moment would have to be between ions on octahedral sites only. If a small percentage of the $Co^{2+}$ ions were to occupy the tetrahedral positions, the magnetic moment would be the result of ferrimagnetic coupling between these and $Mn^{3+}$ ions on octahedral sites. The low Curie temperature ($T_c = 62°K$ for $x = 0{\cdot}36$) is consistent with either view. The fact that the magnetization curves for this system and for the system $Zn_xGe_{1-x}Mn^{2+}_{2-2x}Mn^{3+}_{2x}O_4$ each show a similar inflection corresponding to the change in crystal symmetry suggests that their magnetic properties can eventually be interpreted in terms of the peculiar behavior of trivalent manganese.

*Acknowledgements*—The helpful advice and generous assistance of J. B. GOODENOUGH, R. J. ARNOTT, N. MENYUK and K. DWIGHT have been invaluable in the pursuit of this work. The authors wish to thank J. FITZGERALD, E. WHIPPLE, and L. DOCTOR for performing the many necessary chemical analyses.

## REFERENCES

1. WICKHAM D. G. Lincoln Laboratory Technical Report No. 164, August 23, 1957 (Not generally available).
2. ROMEIJN F. C. *Philips Res. Rep.* **8,** 304 (1953).
3. GOODENOUGH J. B. and LOEB A. *Phys. Rev.* **98,** 391–408 (1955).
4. DUNITZ J. D. and ORGEL L. E. *J. Phys. Chem. Solids* **3,** 20 (1957).
5. MASON B. Dissertation, Geol. Fören. Stock. För. **65,** 97–180 (1943).
6. MCMURDIE H. F., SULLIVAN B. M. and MAUER F. A. *J. Res. Nat. Bur. Stand.* **45,** 35 (1950).
7. FINCH G. I., SINHA A. P. B. and SINHA K. P. *Proc. Roy. Soc.* A**242,** 28 (1957).
8. DWIGHT K., MENYUK N. and SMITH D. *J. Appl. Phys.* **29,** 491 (1958).
9. GOODENOUGH J. B., WICKHAM D. G. and CROFT W. *J. Chem. Phys. Solids* **5,** 107–116 (1958).
10. ROMEIJN F. C. *Philips Res. Rep.* **8,** 327 (1953).
11. BARTH T. F. W. and POSNJAK E. *Z. Krist.* **82,** 325 (1932).

12. BONGERS P. F. Thesis, University of Leiden, July 4, 1957.
13. COSSEE P. Doctoral Thesis, University of Leiden, October 4, 1956.
14. GOODENOUGH J. B. To be published.
15. VAN HOOK H. J. and KEITH M. L. *Amer. Min.* **43,** 69 (1958).
16. HASTINGS J. M. and CORLISS L. M. *Phys. Rev.* **104,** 328 (1956).
17. HARRISON F. W., OSMOND W. P. and TEALE R. W. *Phys. Rev.* **106,** 865 (1957).
18. BOROVIK–ROMANOV A. S. and ORLOVA M. P. *Zh. eksp. teor. fiz.* **5,** 1023 (1957).

VOL
7
195

**Zonal specificity and nonspecificity of certain impurities during growth of synthetic α-quartz**

(*Received* 15 *August* 1958)

IT is now generally known that an aluminum (III) ion replacing silicon in the α-quartz lattice enters certain zones of the growing quartz more readily than others.[1] This fact was apparently discovered by HAMMOND *et al.*[2] by X-irradiation of a thin slice of *Y*-bar synthetic crystal cut perpendicular to the *Y* axis, coupled with emission analyses of the *X* and *Z* zones. The present note concerns the analyses of *Y*-bar and *Z*-seed crystals, both grown *simultaneously* from a NaOH solution to which $GeO_2$ had been intentionally added. These crystals were grown by Mr. FRANK AUGUSTINE of the Clevite Research Center, Cleveland, Ohio.

Table 1 presents emission analyses of several of the different zones present in the *Y*-bar crystal as well as that of predominant growth in the *Z*-seed crystal. The slight amount of rhombohedral growth in the latter crystal containing most of the substitutional aluminum was not analyzed. Fig. 1 illustrates the zones in the *Y*-bar crystal that were analyzed. The $x(51\bar{6}1)$ and $x_s^-$ zones were not analyzed because of the difficulty in obtaining enough material completely separated from the other zones. The depth of color due to the visible color centers associated with substitutional aluminum[3] increases in the order:

$$Z(0001) < X_f^+ (0010) < s(11\bar{2}1) < x(51\bar{6}1).$$

These relations can be seen in Fig. 1.

Fig. 2 is a cross-section of the same crystal as that illustrated in Fig. 1. The α-quartz has been heated slowly through the $\alpha$–$\beta$ transition and slowly cooled. A lithium–aluminum silicate was observed to precipitate on cooling at the transition temperature, since aluminum was incorporated interstitially in the sample during growth.[1] In comparing the $X_f^+$ regions in both figures, it is seen that the light striations where no darkening is present due to color-center formation in Fig. 1 are just the regions where interstitial aluminum is present in the structure as shown by precipitated regions in Fig. 2. This phenomenon will be discussed in detail elsewhere.[1] It is introduced here in order to point out that the aluminum has two roles in the quartz structure: generally, trace quantities of aluminum are incorporated interstitially in the regions of *Z* growth; in addition, when large quantities of aluminum are present during growth, substitution for silicon may occur. The latter case is

*Table* 1. *Emission analyses of synthetic* α*-quartzes* (*Clevite run* 50*C*–5)*

| Impurity | on *s* (p.p.m. Si)† | *Y*-bar, growth on $X_f^+$ (p.p.m. Si)† | on *Z* (p.p.m. Si)† | *Z*-seed plate growth on *Z* (p.p.m. Si)† |
|---|---|---|---|---|
| Ag | <0·1 | <0·1 | <0·1 | N.F. |
| Al | 38 | 29 | 24 | 24 |
| Ba | 0·5 | N.F. | N.F. | N.F. |
| Ca | 3 | 1 | 1 | 2 |
| Fe | 7 | 5 | 2 | 2 |
| Ge | 54 | 54 | 54 | 54 |
| Li | 32 | 11 | 8 | 8 |
| Mg | 5 | 4 | 3 | 2 |
| Mn | <0·2 | <0·2 | <0·2 | N.F. |
| Na | 46 | 23 | 17 | 6 |
| Ni | 0·4 | 0·7 | N.F. | N.F. |
| Ti | 0·6 | 0·6 | 0·3 | 0·6 |

* All numerical values in the table should be multiplied by the factor 4·6.

† Absolute values one-half to twice the stated values.
N.F. = Not Found.

sometimes accompanied by flawing due to rhombohedral growth of the macromosaics.

Upon examination of the emission analyses, one is struck with the close similarity between the *Z* zones in both crystals. They differ appreciably only in the sodium analyses. It is of interest that the samples were analyzed some weeks apart and prior to any anticipation of such correspondence in composition. The results not only show the continuing precision of the emission analyses but also indicate that when separate crystals are grown from seeds of different orientation but in the same autoclave (under conditions of good solution circulation), then corresponding zones have the same impurity content.

Further examination of the analyses shows:

(1) Germanium (IV) replaces silicon (IV) independently of the type of zonal growth in the quartz, being invariant in the four analyses presented here.

(2) Lithium (I) and sodium (I) ions follow the same order of concentration in various zones as the aluminum (III) ion.

(3) Iron (II and/or III) and magnesium (II) ions also follow the same order of concentration in different zones as the aluminum (III) ion.

(4) When germanium is present, aluminum will appear in the *Z* zones substitutionally as well as interstitially.

One may then conclude from these facts that:

(a) Tetravalent cations substitutional for silicon in the α-quartz lattice are incorporated uniformly throughout the structure.

(b) Trivalent (and possibly divalent) cations substitutional for silicon in the α-quartz lattice tend to concentrate during growth in certain growing zones.

(c) The incorporation of certain impurities in the structure seems to influence the incorporation of others, viz. germanium in the *Z* zone causes greater incorporation of substitutional aluminum; incorporation of lithium and sodium seems to depend on the presence of trivalent (or possibly divalent) impurities. The incorporation of interstitial lithium and sodium, thus, gives ionic-charge balance to the crystal.

*Acknowledgements*—The authors wish to acknowledge the aid of Mr. TOM KONDIS in performing the analyses and Mr. HERBERT L. SMITH in specimen preparation.

*Mellon Institute* ALVIN J. COHEN*
*Pittsburgh, Pa.* EDWIN S. HODGE†

VOL
7
195

## REFERENCES

1. COHEN A. J., Symposium on Defect Structure of Quartz and Glassy Silica, Mellon Institute (May 1957); paper entitled *Substitutional and Interstitial Aluminum Impurity in Quartz Structure and Color-Centre Interrelationships* to be published.
2. HAMMOND D. L., CHI A. R., and STANLEY J. M., *Engineering Report E*-1162, *Signal Corps Task No.* 142*a*, *D.A. Project No.* 3-99-11-000(1955). P.B.131,087.
3. COHEN A. J., *J. Chem. Phys.* **25,** 908 (1956).

* Pittsburgh Plate Glass Company Fellowship.
† Department of Research in Chemical Physics.

VOL.
7
1958

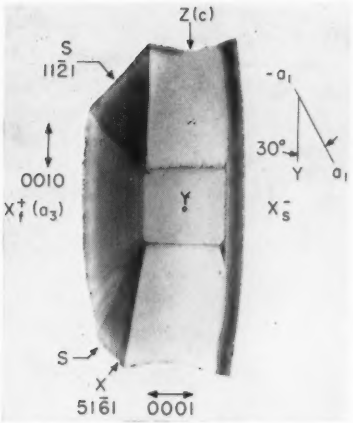


FIG. 1. X-rayed cross-section (normal to the *Y* axis) of *Y*-bar synthetic α-quartz crystal, Clevite run 50C–5. The relative darkness of the area indicates roughly the amount of substitutional aluminum present.

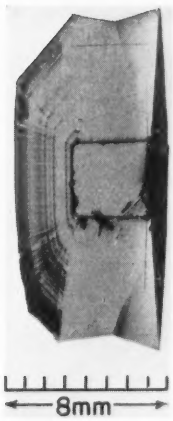


FIG. 2. Cross-section similar to that in Fig. 1 after heat treatment to precipitate a lithium–aluminum silicate in regions where substitutional aluminum is absent.

[*facing p.* 362

VOL.
7
1958

# CONTENTS LISTS OF VOLUME 6, NOS. 1–4

## Volume 6 No. 1


page

ROBERT W. KEYES:
Effets de la diffusion électron–électron sur les propriétés électriques des semi-conducteurs 1

WILLIAM PAUL et D. M. WARSCHAUER:
Propriétés optiques des semi-conducteurs sous pression hydrostatique—III Alliages germanium–silicium . . . . . 6

A. TAYLOR et R. M. JONES:
Constitution et propriétés magnétiques des alliages fer-aluminium à haute teneur en fer . 16

R. NATHANS, M. T. PIGGOT et C. G. SHULL:
La structure magnétique de $Fe_3Al$ . . . . . 38

P. G. DE GENNES:
Diffusion des neutrons par les corps antiferromagnétiques au-dessus du point de Néel . 43

A. SMAKULA et J. KALNAJS:
Impureté d'oxygène dans des monocristaux de silicium . . . . . 46

V. L. GINZBURG et A. P. LEVANYUK:
Diffusion de la lumière au voisinage d'une transition du second ordre et des points de Curie 51

A. ASCOLI, M. ASDENTE, E. GERMAGNOLI et A. MANARA:
Energies d'activation pour la production et le déplacement des lacunes dans le platine . 59

J. L. BIRMAN:
Calcul des potentiels coulombiens dans un cristal . . . . . 65

H. FRITZSCHE:
Résistivité et coefficient de Hall du Germanium traité à l'antimoine aux basses températures 69

THOMAS A. SANDEBAW et ROBERT B. GIBNEY:
La résistivité électrique et la conductibilité thermique du plutonium métallique. . . . 81

D. G. WORDEN et G. C. DANIELSON:
Résistivité électrique de films minces de potassium à 100°K. . . . . 89

Lettres aux éditeurs:

A. W. CZANDERNA et J. M. HONIG:
Composition, résistivité et pouvoir thermoélectrique des oxydes de cérium au-dessous de 500°C . . . . . 96

R. A. ORIANI et R. N. HALL:
Caractère endothermique et excès positif d'entropie des solutions solides dans le germanium et le silicium . . . . . 97

C. KITTEL et W. MARSHALL:
Sur le nombre des électrons 3d dans le fer . . . . . 99

J. L. PANKOVE:
Effets radiatifs de surface dans le germanium . . . . . 100

DAVID DUTTON:
Anisotropie de la luminescence verte du sulfure de cadmium. . . . . 101

Revue de livre . . . . . 103

Volume 6 Nos. 2/3

page

M. Ya. Azbel' et E. A. Kaner:
Résonance cyclotron dans les métaux . . . . . 113

G. Bogner et E. Mollwo:
Sur la fabrication de cristaux d'oxyde de zinc de composition définie . . . . . 136

H. Rupprecht:
Sur la concentration et la mobilité des électrons dans les cristaux d'oxyde de zinc de composition définie . . . . . 144

Gerhard Heiland:
Effet de champ et photoconductibilité sur des cristaux d'oxyde de zinc . . . . . 155

J. M. Whelan et G. H. Wheatley:
La préparation et les propriétés des monocristaux d'arséniure de galium . . . . . 169

C. S. Fuller et J. M. Whelan:
Diffusion, solubilité et comportement électrique du cuivre dans l'arséniure de gallium . 173

Bipin K. Agarwal et M. Parker Givens:
Absorption des rayons X mous par le manganèse et l'oxyde de manganèse . . . . 178

R. A. Eppler et H. G. Drickamer:
L'influence de la pression sur les spectres de l'ion $Tl^+$ dans les réseaux d'halogénures alcalins . . . . . 180

D. H. Roberts et J. E. Baines:
Photoconductibilité de films de séléniure de plomb déposés chimiquement . . . . 184

G. F. Newell:
Fréquences extrêmes des vibrations du réseau pour les alliages binaires désordonnés . 190

Chr. Lehmann et G. Leibfried:
Traitement par les méthodes de la théorie des réseaux cristallins d'une dislocation vis dans les métaux alcalins . . . . . 195

E. Daniel:
Influence du potentiel du réseau et contribution des couches d à l'annihilation du positon dans le cuivre . . . . . 205

O. Flint et J. H. O. Varley:
Sur le mécanisme de la formation de film d'oxyde sur le zirconium . . . . . 213

L. P. Kao et E. Katz:
Théorie phénoménologique des effets galvanomagnétiques isothermes anisotropes . . 223

Evan O. Kane:
L'influence de l'échange sur le formalisme de la masse effective . . . . . 236

E. Schlömann:
Analyse en ondes de spin de la résonance ferromagnétique dans les ferrites polycristallins . 242

Ernst Schlömann:
Résonance ferromagnétique dans les ferrites polycristallins de grande anisotropie . . 257

A. H. Mones et E. Banks:
Ferrimagnetisme dans le système $Na_2O$–$ZnO$–$Fe_2O_3$ . . . . . 267

R. E. Schlier et H. E. Farnsworth:
Structure du cuivre déposé en épitaxie par évaporation sur une face propre (00·1) d'un cristal de titane . . . . . 271

VOL
7
195

*page*

R. A. ORIANI et W. K. MURPHY:
Thermodynamique de l'ordre des alliages—III Energies de transformations des phases $Au_{\frac{1}{2}}Cu_{\frac{1}{2}}$ . . . . . 277

EDGAR F. WESTRUM, JR. et D. M. GRIMES:
Chaleurs spécifiques à basse température et propriétés thermodynamiques des ferrites de zinc—II Influence de l'histoire thermique et de l'addition d'atomes métalliques. . . . 280

JOHN B. GOODENOUGH:
Une interprétation des propriétés magnétiques des cristaux mixtes du type de la perovskite $La_{1-x}Sr_xCoO_{3-\lambda}$ . . . . . 287

Lettres aux éditeurs:

A. B. LIDIARD:
Diffusion des anions dans les cristaux d'halogénures alcalins . . . . . 298

GERALD W. SEARS:
Limite élastique des whiskers de fluorure de lithium . . . . . 300

F. J. BLATT:
La susceptibilité magnétique des métaux . . . . . 301

## Volume 6 No. 4

C. H. L. GOODMAN:
La prédiction des propriétés semi-conductrices des composés minéraux. . . . . 305

W. LOW et D. SCHALTIEL:
Spectre de résonance paramagnétique du gadolinium dans des monocristaux d'oxyde de thorium . . . . . 315

HELMUT BROSS et ALFRED SEEGER:
Recherches sur la théorie électronique des défauts dans les métaux VI. La résistivité électrique des paires de lacunes dans les métaux monovalents . . . . . 324

FRANK S. HAM:
Théorie de la précipitation limitée par la diffusion . . . . . 335

W. DESORBO et G. E. NICHOLS:
Un calorimètre pour la région de températures 1–20°K. La chaleur spécifique de quelques spécimens de graphite . . . . . 352

J. C. BOWMAN et J. A. KRUMHANSL:
La chaleur spécifique de basse température du graphite . . . . . 367

K. KOMATSU:
Effet de la taille des particules sur la chaleur spécifique du graphite aux basses températures 380

I. BROSSER et R. BROSER-WARMINSKY:
Sur le mécanisme du transport d'énergie dans les cristaux de sulfure de cadmium . . 386

Lettres aux éditeurs:

M. BALKANSKI:
Sur le mecanisme du transport d'energie . . . . . 401

J. A. MORRISON et R. RUDHAM:
Diffusion de l'anion dans les cristaux de chlorure de potassium dopés . . . . 403

GERALD W. SEARS:
Influence des impuretés solubles sur la résistance mécanique des cristaux parfaits . 404

Revue de livre . . . . . 406

Volume 6 No. 1

page

Р. Кейес:
Эффекты электрон-электронного рассеяния в электрических свойствах полупроводников . . . . . 1

В. Паул и Д. М. Варшауер:
Оптические свойства полупроводиников—III. Сплавы германия с кремнием . 6

А. Тейлор и Р. М. Джонс:
Состав и магнитные свойства богатых железом сплавов железа с алюминием 16

Р. Матанс, М. Т. Пиггот. К. Шелл:
Магнитная структура $Fe_3Al$ . . . . . 38

П. Дж. де Дженнес:
Рассеивание нейтронов антифферомагнитами выше точки Ниля . . . 43

А. Смакула и Дж. Калнайс:
Примеси кислорода в монокристаллах кремния . . . . . 46

В. Л. Гинзбург и А. П. Леванюк:
Рассеяние света вблизи точек фазовых переходов второго рода и точек Кюри . 51

А. Асколи, М. Асденте, Е. Германьоли и А. Манара:
Энергии активации для образования и миграции вакансий в платине . . 59

Дж. Бирман:
Вычисление кулоновских потенциалов кристалла . . . . . 65

Г. Фритцше:
Сопротивление и коэффициент Холла при низких температурах у германия, загрязненного мышьяком . . . . . 69

Томас А. Санденау и Роберт Б. Гибней:
Электрическое сопротивление и термическая проводимость металла плутония 81

Д. Дж. Уорден и Дж. С. Даниелсон:
Электрическое сопротивление тонких пластинок калия при температуре 100° К . 89

Письма в редакцию:

А. В. Чандерна и Ж. М. Гониг:
Композиция, сопротивление и термоэлектрическая мощность церийных кислот при температуре ниже 500° Ц. . . . . 96

Р. Ориани и Р. Холл:
Эндотермичность и положительный избыток энтропии в твердых растворах в германии и кремнии . . . . . 97

Ч. Киттель и В. Маршалл:
О числе 3d электронов в железе . . . . . 99

Ж. Панков:
Радиационный поверхностный эффект в германии . . . . . 100

Д. Дуттон:
Анизотропия границы люминесценции в сульфиде кадмия . . . . 101

Рецензия . . . . . 103

Volume 6 Nos. 2/3

*page*

М. Я. Азбель и Э. А. Канер:
Циклотронный резонанс в металлах . . . . . 113

Г. Богрен и Е. Мольво:
Приготовление монокристаллов окиси цинка с определенными примесями . . 136

Г. Руппрехт:
О концентрации и подвижности электронов в монокристаллах окиси цинка с определенными примесями . . . . . 144

Г. Хейланд:
Влияние поля и фотопроводимость монокристаллов ZnO . . . . . 155

Дж. М. Велан и Г. Уитли:
Изготовление и свойства монокристаллов мышьяковистого галлия . . . 169

К. Фуллер и Дж. Велан:
Диффузия, растворимость и электрическое поведение меди в арсениде галлия . 173

В. К. Агарвал и М. П. Гивенс:
Поглощение мягких X-лучей марганцем и окисью марганца . . . . . 178

Р. А. Эпплер и Г. Дриккамер:
Влияние давления на спектры иона $Tl^+$ в решетках галогенидов щелочных металлов . . . . . 180

Д. Робертс и Дж. Бейнс:
Фотопроводимость химически осажденных пленок селенида свинца . . 184

Г. Ф. Ньювелл:
Граничные частоты колебаний решетки в неупорядоченных бинарных сплавах . 190

Хр. Леманн и Г. Лейбфрид:
Рассмотрение винтовых дислокаций в кристаллах щелочных металлов с помощью теории решеток . . . . . 195

Е. Даниель:
Влияние решеточного потенциала и вклад *d*-оболочки в аннигиляцию позитронов в меди . . . . . 205

О. Флинт и Дж. Варлей:
О механизме образования оксидной пленки на цирконии . . . . . 213

Л. П. Као и Е. Катц:
Феноменологическая теория анизотропных изотермических гальваномагнитных эффектов . . . . . 223

И. О. Кейн:
Учет обмена в формализме эффективных масс . . . . . 236

Е. Шлеманн:
Спин-волновой анализ ферромагнитного резонанса в поликристаллических ферритах . . . . . 242

Э. Шлеманн:
Ферромагнитный резонанс в поликристаллических ферритах с большой анизотропией . . . . . 257

А. Монес и Е. Банкс:
Ферримагнетизм системы $Na_2O$–ZnO–$Fe_2O_3$ . . . . . 267

VOL. 7 1958

*page*

Р. Шлир и Г. Фарнсворт:
Структура пленок меди, осажденных на поверхности грани (001) кристалла титана 271

Р. А. Орнани и В. К. Мерфи:
Термодинамика упорядочения растворов—III. Энергии превращения фаз $Au_{1/2}Cu_{1/2}$ 277

Э. Ф. Веструм мл. и Д. М. Граймс:
Низкотемпературные теплоемкость и термодинамические свойства ферритов цинка. II. Влияние термической предистории и металлических примесей . . 280

Дж. Гуденаф:
Интерпретация магнитных свойств смешанных кристаллов типа перовскита $La_{1-x}Sr_xCoO_{3-\lambda}$ . . . . . 287

Письма в редакцию:
А. Б. Лидиард:
Диффузия анионов в кристаллах галогенидов щелочных металлов . . 298

Джералд В. Сирс:
Прочность контактной пружины из лития флурида . . . . . 300

Ор. Ж. Влатт:
Магнетическая восприимчивость металлов . . . . . 301

## Volume 6 No. 4

К. Гудман:
Предсказание полупроводниковых свойств в неорганических соединениях . 305

В. Лоу и Д. Шальтьель:
Спектр парамагнитного резонанса гадолиния в монокристаллах окиси тория . 315

Г. Бросс и А. Зеегер:
Электронно-теоретические исследования дефектов в металлах-VI. Электрическое сопротивление двойных вакансий в одновалентных металлах . . . . . 324

Ф. С. Хем:
Теория ограниченной диффузией преципитации . . . . . 335

В. де Сорбо и Г. Никольс:
Калориметр для температурной области 1–20°К: теплоемкость некоторых образцов графита . . . . . 352

Дж. Боуман и Дж. Крумгансль:
Низкотемпературная теплоемкость графита . . . . . 367

К. Комацу:
Влияние размеров частиц графита на его теплоемкость при низких температурах 380

И. Брозер и Р. Брозер-Варминский:
О механизме переноса энергии в кристаллах сульфида кадмия . . . 386

Письма в редакцию:
М. Балканский:
О механизме трансмиссии энергии . . . . . 401

Ж. А. Моррисон и Р. Рудам:
Рассеяние анионов в изолированных кристаллах хлористого калия . . 403

Джеральд В. Сирс:
Влияние растворимых примесей на прочность совершенных кристаллов . 404

Реценции: . . . . . 406

Volume 6 No. 1

*page*

ROBERT W. KEYES:
Der Einfluss der Elektron–Elektronstreuung auf die elektrischen Eigenschaften von Halbleitern . . . . . 1

WILLIAM PAUL und D. M. WARSCHAUER:
Optische Eigenschaften von Halbleitern unter hydrostatischem Druck—III Germanium–Siliziumlegierungen . . . . . 6

A. TAYLOR und R. M. JONES:
Konstitution und magnetische Eigenschaften von eisenreichen Eisen–Aluminiumlegierungen . . . . . 16

R. MATHAES, M. T. PIGOTT und C. G. SHULL:
Die magnetische Struktur von $Fe_3Al$ . . . . . 38

P. G. DE GENNES:
Neutronenstreuung durch Antiferromagneticis oberhalb des Néelpunktes . . . . 43

A. SMAKULA und J. KALNAJS:
Sauerstoffverunreinigungen in Siliziumeinkristallen . . . . . 46

V. L. GINZBURG und A. P. LEVANYUK:
Lichtstreuung an Curiepunkten und an Phasenumwandlungen zweiter Ordnung . . 51

A. ASCOLI, M. ASDENTE, E. GERMAGNOLI und A. MANARA:
Aktivierungsenergien für Bildung und Wanderung von Leerstellen in Platin . . . . 59

JOSEPH L. BIRMAN:
Die Berechnung von Coulomb-Kristallpotentialen . . . . . 65

H. FRITZSCHE:
Elektrischer Widerstand und Hallkoeffizient von antimondotiertem Germanium bei tiefen Temperaturen . . . . . 69

THOMAS A. SANDENAW und ROBERT B. GIBNEY:
Elektrischer Widerstand und Wärmeleitfähigkeit von metallischem Plutonium . . 81

D. G. WORDEN und G. C. DANIELSON:
Elektrischer Widerstand dünner Kaliumschichten bei 100°K . . . . . 89

Briefe an die Herausgeber:

A. W. CZANDERNA und J. M. HONIG:
Zusammensetzung, elektrischer Widerstand und Thermokraft der Ceroxyde unterhalb 500°C . . . . . 96

R. A. ORIANI, R. N. HALL:
Endotherme Reaktionswärmen und positive Zusatzentropie bei festen Lösungen von Germanium und Silizium . . . . . 97

C. KITTEL und W. MARSHALL:
Über die Zahl der 3 d-Elektronen in Eisen . . . . . 99

JACQUES I. PANKOVE:
Strahlungseffekt an der Oberfläche von Germanium . . . . . 100

DAVID DUTTON:
Anisotropie der Kantenluminiszenz in Cadmiumsulfid . . . . . 101

Buchbesprechung . . . . . 103

VOL. 7 1958

Volume 6 Nos. 2/3

page

M. Ya. Azbel' und E. A. Kaner:
Zyklotronresonanz in Metallen . . . . . 113

G. Bogner und E. Mollwo:
Über die Herstellung von Zinkoxydeinkristallen mit definierten Zusätzen . . . 136

H. Rupprecht:
Über Konzentration und beweglichkeit von Elektronen in Zinkoxydeinkristallen mit definierten Zusätzen . . . . . 144

Gerhard Heiland:
Feldeffekt und Photoleitung an ZnO-Einkristallen . . . . . 155

J. M. Whelan und G. H. Wheatley:
Herstellung und Eigenschaften von Galliumarsenid-Einkristallen . . . . . 169

C. S. Fuller und J. M. Whelan:
Diffusion, Löslichkeit und elektrisches Verhalten von Kupfer in Galliumarsenid . . 173

Bipin K. Agarwal und M. Parker Givens:
Die Absorption wiecher Röntgenstrahlen bei mangan und Manganoxyden . . . 178

R. A. Eppler und H. G. Drickamer:
Der Einfluss von Druck auf die Spektren von $Tl^+$-Ionen in Alkalihalogenidgittern . . 180

D. H. Roberts und J. E. Baines:
Photoleitfähigkeit in chemisch niedergeschlagenen Schichten des Bleiselenids . . . 184

G. F. Newell:
Extreme Frequenzen der Gitterschwingungen bei ungeordneten binären Legierungen . 190

Chr. Lehmann und G. Leibfried:
Gittertheoretische behandlung einer Schraubenversetzung in Alkalimetallen . . . 195

E. Daniel:
Der Einfluss des Gitterpotentials und der *d*-Schalen auf die Zerstrahlung der Positronen in Kupfer . . . . . 205

O. Flint und J. H. O. Varley:
Über den Mechanismus der Bildung einer Oxydschicht auf Zirkon . . . . . 213

L. P. Kao und E. Katz:
Eine phänomenologische Theorie anisotroper isothermer galvanomagnetischer Effekte . 223

Evan O. Kane:
Der Einfluss der Wechselwirkung auf den Formalismus der effektiven Masse . . . 236

E. Schlömann:
Eine Spinwellenanalyse der ferromagnetischen Resonanz in polykristallinen Ferriten . . 242

Ernst Schlömann:
Ferromagnetische Resonanz in polykristallinen Ferriten mit grosser Anisotropie . . 257

A. H. Mones und E. Banks:
Ferrimagnetismus im System $Na_2O$–ZnO–$Fe_2O_3$ . . . . . 267

R. E. Schlier und H. E. Farnsworth:
Die Struktur von orientiert aufgewachsenem Kupfer, das durch Verdampfen auf eine reine (001)-Fläche eines Titankristalls niedergeschlagen wurde . . . . . 271

VOL
7
195

*page*

R. A. ORIANI und W. K. MURPHY:
Die Thermodynamik geordneter Legierungen—III Umwandlungsenergien der $Au_{\frac{1}{2}}Cu_{\frac{1}{2}}$-Phasen . . . . . 277

EDGAR F. WESTRUM JR. und D. M. GRIMES:
Warmekapazität und thermodynamische Eigenschaften von Zinkferriten—II. Der Einfluss der thermischen Behandlung und metallischer Zusätze . . . . . 280

JOHN B. GOODENOUGH:
Eine Deutung der magnetischen Eigenschaften der Mischkristalle $La_{1-x}Sr_xCoO_3$-vom Perovskittyp . . . . . 287

Briefe an die Herausgeber:

A. B. LIDIARD:
Anionendiffusion in Alkalihalogenidkristallen . . . . . 298

GERALD W. SEARS:
Die Grösse von Lithiumfluorid-Whiskers . . . . . 300

F. J. BLATT:
Die magnetische Suszeptibilität bei Metallen . . . . . 301

OL.
7
958

## Volume 6 No. 4

C. H. L. GOODMAN:
Die Vorhersage halbleitender Eigenschaften in anorganischen Verbindungen . . . 305

W. LOW und D. SHALTIEL:
Das paramagnetische Resonanzspektrum des Gadoliniums in Einkristallen des Thoriumoxyds . . . . . 315

HELMUT BROSS und ALFRED SEEGER:
Elektronentheoretische Untersuchungen uber Fehlstellen in Metallen—VI. Der elektrische Widerstand von Doppelleerstellen in einwertigen Metallen . . . . . 324

FRANK S. HAM:
Die Theorie der diffusionsabhängigen Bedampfung . . . . . 335

W. DESORBO und G. E. NICHOLS:
Ein Kalorimeter für den Temperaturbereich 1–20°K—Die spezifische Wärme einiger Graphitproben . . . . . 352

J. C. BOWMAN und J. A. KRUMHANSL:
Die spezifische Wärme von Graphit bei tiefen Temperaturen . . . . . 367

K. KOMATSU:
Ein Effekt der Partikelgrösse auf die spezifische Wärme von Graphit . . . . . 380

I. BROSER und R. BROSER-WARMINSKY:
Über den Mechanismus der Energiewanderung in Kadmiumsulfid-Kristallen. . . . 386

Briefe an die Herausgeber:

M. BALKANSKI:
Über den Mechanismus des Energietransports . . . . . 401

J. A. MORRISON und R. RUDHAM:
Anionendiffusion in dotierten Kristallen des Kaliumchlorides . . . . . 403

GERALD W. SEARS:
Der Einfluss loslicher Verunreingungen auf die Fliesspannung eines idealen Kristalls 404

Buchbesprechung . . . . . 406